

The 12th International Symposium on Medical Information and Communication Technology

ISMICT 2018
26-28 March 2018
University of Technology Sydney



Overview

The 12th International Symposium on Medical Information and Communication Technology, ISMICT 2018, aims to establish a forum to present new research and development results, exchange ideas, discuss practices, and share experiences among Technology and Medicine sides, including healthcare, wellness, clinical therapy, and surgery, as well as ICT, mechanical, and biomedical engineering.

Moreover, activities of standard, regulation and business for medical ICT devices, systems and services will be promoted by national and international government and industry.

The Symposium is technically co-sponsored by IEEE Communications Society and Engineering in Medicine and Biology Society.

Copyright



2018 12th International Symposium on Medical Information and Communication Technology (ISMICT) took place 26-28 March 2018 in Sydney, AU-NSW, Australia.

IEEE catalog number:	CFP1841M-ART
ISBN:	978-1-5386-3389-2
ISSN:	2326-8301

Copyright and Reprint Permission: Abstracting is permitted with credit to the source. Libraries are permitted to photocopy beyond the limit of U.S. copyright law for private use of patrons those articles in this volume that carry a code at the bottom of the first page, provided the per-copy fee indicated in the code is paid through Copyright Clearance Center, 222 Rosewood Drive, Danvers, MA 01923. For other copying, reprint or republication permission, write to IEEE Copyrights Manager, IEEE Operations Center, 445 Hoes Lane, Piscataway, NJ 08854. All rights reserved. Copyright © 2018 by IEEE.

Welcome Message

It is my great pleasure to welcome the participants of ISMICT 2018 to Sydney, Australia. It is our honour and pleasure to host this conference for the first time in Australia and to continue to enhance the prestige of this conference.

ISMICT 2018 features:

- Keynote addresses by eminent speakers from around the world
- Health Data Panel
- Medical Device Regulatory Science Workshop
- Special Session on Emerging Technologies in Biomedical Devices
- Technical Sessions on key topics

I would like to thank the Organising Committee and the TPC Members for their hard work that ensured high quality of the papers accepted to the conference. I would also like to thank the Steering Committee Co-Chairs, Prof. Ryuji Kohno and Prof. Jari Iianatti, for providing invaluable advice on many important issues.

I would like to thank CWC Nippon and University of Technology Sydney for their generous patronage.

I hope that you and your partners will enjoy the best that Sydney and Australia can offer and that you will have fond memories of the conference when you return home.



Prof. Eryk Dutkiewicz
ISMICT 2018 General Chair

Committees

Organizing Committee

Honorary Chair

Ian Opperman, NSW Government Data Analytics Centre, Australia

General Chair

Eryk Dutkiewicz, University of Technology Sydney, Australia

Steering Committee Co-Chairs

Ryuji Kohno, Yokohama National University, Japan
Jari Iinatti, University of Oulu, Finland

Technical Program Co-Chairs

Ren Ping Liu, University of Technology Sydney, Australia
Matti Hamalainen, University of Oulu, Finland
Kohei Ohno, Meiji University, Japan
Graeme Woodward, University of Canterbury, New Zealand

Publications Chairs

Diep Nguyen, University of Technology Sydney, Australia

Publicity Co-Chairs

Ying He, University of Technology Sydney, Australia
Shinsuke Hara, Osaka City University, Japan
John Farserotu, CSEM, Switzerland
Yi Qian, Macquarie University, Australia
Ilangko Balasingham, Norwegian University of Science and Technology, Norway

Workshops Co-Chairs

Beeshanga Abewardana Jayawickrama, University of Technology Sydney, Australia
Rajan Shankaran, Macquarie University, Australia
Masayuki Fujise, Yokohama National University, Japan

Panel Co-Chairs

Zenon Chaczko, University of Technology Sydney, Australia
Valerie Gay, University of Technology Sydney, Australia

Tutorials Co-Chairs

Chika Sugimoto, Yokohama National University, Japan
Rein Vesilo, Macquarie University, Australia

Poster Co-Chairs

Mehmet Yuce, Monash University, Australia
Thuy Pham, University of Technology Sydney, Australia

Special Sessions Chair

Yang Yang, University of Technology Sydney, Australia
Forest Zhu, University of Technology Sydney, Australia

IEEE Liaison Chair

Stefan Mozar, NSW EMBS Chapter Chair, Australia

Local Arrangements Chair

Peter Beadle, Academic Event Services, Australia

Web Chair

Noman Haider, UTS, Australia

Technical Program Committee

Huda A. Majid	Universiti Tun Hussein Onn Malaysia	Malaysia
Mohamad Kamal A. Rahim	Universiti Teknologi Malaysia	Malaysia
Qammer H Abbasi	University of Glasgow	United Kingdom (Great Britain)
Otman Aghzout	ENSA Tetouan - UAE	Morocco
Emmanuel Agu	Worcester Polytechnic Institute	USA
Tahsin Akalin	Université de Lille 1	France
Ertugrul Aksoy	Gazi University	Turkey
Isam Alawneh	Ruhr University Bochum	Germany
Antonio Almeida	Instituto Superior Tecnico	Portugal
Pedro Almeida	Instituto de Biofísica e Engenharia Biomédica - Faculdade de Ciências da Universidade de Lisboa	Portugal
Hasim Altan	University of Sharjah	United Arab Emirates
Slawomir Ambroziak	Gdansk University of Technology	Poland
Max Ammann	Dublin Institute of Technology	Ireland
Noemen Ammar	University el manar	Tunisia
Dimitris Anagnostou	South Dakota School of Mines and Technology	USA
Andrey Andrenko	eNFC Inc.	Japan

Marco Antoniadès	University of Cyprus	Cyprus
Eva Antonino-Daviu	Universitat Politècnica de València	Spain
Daisuke Anzai	Nagoya Institute of Technology	Japan
Takahiro Aoyagi	Tokyo Institute of Technology	Japan
Wellington Araujo	Universidade Estadual da Paraíba	Brazil
Javid Atai	University of Sydney	Australia
Hervé Aubert	Laboratory of Analysis and Architecture of Systems	France
Leyre Azpilicueta	Tecnologico de Monterrey	Mexico
Ilangko Balasingham	Norwegian University of Science and Technology	Norway
H. W. Peter Beadle	Academic Event Services	Australia
Nader Behdad	University of Wisconsin	USA
Gennaro Bellizzi	Mediterranea University of Reggio Calabria	Italy
Ahmet Ozan Bicen	Georgia Institute of Technology	USA
Huynh Thi Thanh Binh	HUST	Vietnam
Toni Björninen	Tampere University of Technology	Finland
Davor Bonefačić	University of Zagreb, Faculty of Electrical Engineering and Computing	Croatia
Halim Boutayeb	Huawei Technologies	Canada
Djuradj Budimir	University of Westminster	United Kingdom (Great Britain)
Rafael Caldeirinha	IPL - Polytechnic Institute of Leiria	Portugal
Francisco José Cano	Sener	Spain
Eryk Dutkiewicz	University of Technology Sydney	Australia
Matti Hämäläinen	University of Oulu	Finland
Ying He	University of Technology Sydney	Australia
Marco Hernandez	NICT	Japan
Anne Julien-Vergonjanne	University of Limoges	France
Pawel Kabacik	Wroclaw University of Science and Technology	Poland
Faeyz Karim	Nanyang Technological University	Singapore
Heikki Karvonen	University of Oulu, Centre for Wireless Communications	Finland
Andrzej Karwowski	Silesian University of Technology	Poland
Elsayed Esam Khaled	Assiut University	Egypt
Minseok Kim	Niigata University	Japan
Asimina Kiourti	The Ohio State University	USA
Peter Knott	Fraunhofer FHR	Germany
Panagiotis Kosmas	King's College London	United Kingdom (Great Britain)
Ioannis Koufogiannis	Huber+Suhner AG	Switzerland
Stavros Koulouridis	University of Patras	Greece
Maria Koutsoupidou	King's College London	Greece
István Kovács	Nokia Bell Labs	Denmark
Viktor Krozer	Goethe University of Frankfurt am Main	Germany
Ketavath Kumar Naik	K L University	India
Yoshihiko Kuwahara	Shizuoka University	Japan
George Kyriacou	Democritus University of Thrace	Greece
Saeed Latif	University of South Alabama	USA
Antonino Laudani	University of Roma Tre	Italy
Antonio Lazaro	URV	Spain
Philippe Le Thuc	Université Côte d'Azur, CNRS, LEAT	France

Fedor Lehocki	Slovak University of Technology	Slovakia
Huan-Bang Li	National Institute of Information and Communications Technology	Japan
Maokun Li	Tsinghua University	P.R. China
Xinrong Li	University of North Texas	USA
Jau-Jr Lin	National Changhua University of Education	Taiwan
Nguyen Linh-Trung	Vietnam National University, Hanoi	Vietnam
Changjun Liu	Sichuan University	P.R. China
Ren Ping Liu	University of Technology Sydney	Australia
RPtest Liu	UTStest	Australia
Xiaoming Liu	Anhui Normal University	P.R. China
Zi-Liang Liu	National University of Singapore	Singapore
Guido Lombardi	Politecnico di Torino	Italy
Hoi-Shun Lui	The University of Queensland	Australia
Arye Nehorai	Washington University in St. Louis	USA
Diep Nguyen	University of Technology Sydney	Australia
Symeon Nikolaou	Frederick Research Center	Cyprus
Nurul Noordin	Universiti Malaysia Pahang	Malaysia
Martin O'Halloran	National University of Ireland, Galway	Ireland
Kohei Ohno	Meiji University	Japan
Mahdi Oliaei	Research Assistant, Telecommunication Engineering, KNTU	Iran
Bárbara Oliveira	National University of Ireland, Galway	Ireland
Abbas Omar	University of Magdeburg	Germany
Teruo Onishi	NTT DOCOMO	Japan
Lotfi Osman	Higher School of Communication of Tunis - University of Carthage	Tunisia
Anna Papiro Toda	Energous Corporation	USA
Daniele Pinchera	University of Cassino	Italy
Pedro Pinho	ISEL	Portugal
Cristina Ponti	Roma Tre University	Italy
Milica Popović	McGill University	Canada
Emily Porter	National University of Ireland Galway	Ireland
Xianming Qing	Institute for Infocomm Research	Singapore
Zbynek Raida	Brno University of Technology	Czech Republic
Khalid Rajab	Queen Mary University of London	United Kingdom (Great Britain)
Sujith Raman	Bharathiar Universitiy, Coimbatore, Tamilnadu	India
Yogesh Ranga	Macquarie University	Australia
Jalil Rashed-Mohassel	School of Electrical and Computer Engineering College of Engineering	Iran
Arie Reichman	Ariel University	Israel
Alejandro Rivera-Lavado	Universidad Carlos III de Madrid	Spain
Francois Rivet	University of Bordeaux	France
Christophe Roblin	Telecom ParisTech	France
Juan Antonio Romo	University of the Basque Country	Spain
Ruth Rotman	Tel Aviv University	Israel
Theodoros Samaras	Aristotle University of Thessaloniki	Greece
Hoang Tuan	University of Technology, Sydney	Australia
Yang Yang	University of Technology Sydney	Australia
Xi Zhu	University of Technology Sydney	Australia

Keynote Speech

Keynote Speakers

Speaker 1:

Title: Medical Healthcare Big Data Mining and Managing by Integrated ICT and Data Science for Regulatory and Commercial Uses

Speaker: Professor Ryuji Kohno, Director, Centre of Medical Information and Communication Technology, and Professor, Division of Physics, Electrical & Computer Engineering, Yokohama National University, Japan

Abstract: Personal vital data should be primarily employed for their owners' medical healthcare and wellness in a sense of primary use. EHR and EMR have been developed and applied for medical health record for medical analysis and therapy because a huge size of citizens' vital data can be easily collected with less load of medical staffs and be useful for medical research and clinical activities including regulatory compliance exam for drugs and medical devices. To collect various vital data, medical wireless body area network (BAN) has been researched and developed to be a medical platform by connecting with medical database, registry or repository through cloud network for network therapy and remote medicine and international standard of medical BAN IEEE802.15.6 was established in February 2012. Such a medical platform of BAN, cloud network and data mining server could be a key subject of research and social services to be discussed in a field of medical ICT. There are a lot of research subjects for such a medical platform such as (1) network architecture and database management, (2) security and dependability, (3) regulatory compliance, (4) secondary use of medical big data. This talk will address technical aspects in (1) and (2) in a term of enhanced dependability and security of medial networking and data mining technologies, and regulatory aspects in (3) and (4) in a term of cyber physical security and authentication for medical personal data and compliance of medical data uses. It may cover a latest status report of activities of MDD, IVDD and AIMD in EU, CFDA and CFE in China, FDA in USA and PMDA in Japan.

Speaker Bio: Ryuji Kohno received the Ph.D. degree from the University of Tokyo in 1984. Since 1998 he has been a Professor and the Director of Centre on Medical Information and Communication Technology, in Yokohama National University in Japan. In his career he played a part-time role of a director of Advanced Telecommunications Laboratory of SONY CSL during 1998-2002, directors of UWB Technology and medical ICT institutes of NICT during 2002-2012. Since 2012 he is CEO of University of Oulu Research Institute Japan - CWC-Nippon Co. Since 2007 he has been a distinguished professor in University of Oulu in Finland and since 2014 a director of Kanagawa Medical Device Regulatory Science Centre. He was a member of medical devices committee in PMDA during 2012-2014 and the Science Council of Japan since 2006. He was a member of the Board of Governors of IEEE Information Theory Society in 2000-2009, and editors of IEEE Transactions on Communications, Information Theory, and ITS. He was Vice-president of Engineering Sciences Society of IEICE during 2004-2005, Editor-in chief of the IEICE Trans. Fundamentals during 2003-2005. He is a founder of series of international symposia of medical information and communication technologies (ISMICT) since 2006.

Speaker 2:

Title: The Power of Diversity - Examining non-traditional data in Health.

Speaker: Dr. Ian Oppermann, Chief Data Scientist, NSW Government and CEO of the NSW Data Analytics Centre, Australia.

Abstract: Industries had used data analytics to achieve impressive results in the personalisation of services and create greater customer intimacy. In the broad area of health, advances in non-medical data analysis have led to improved understanding of patient flow and resource management. By casting a wide net and considering a diverse range of data sets, we can see the first steps in the transformation from health being sickness management to wellness

management. This presentation will highlight some real world examples from NSW.

Speaker Bio: Dr. Ian Oppermann is the NSW Government's Chief Data Scientist and CEO of the NSW Data Analytics Centre. Ian has 25 years' experience in the ICT sector and, has led organizations with more than 300 people, delivering products and outcomes that have impacted hundreds of millions of people globally. He has held senior management roles in Europe and Australia as Director for Radio Access Performance at Nokia, Global Head of Sales Partnering (network software) at Nokia Siemens Networks, and then Divisional Chief and Flagship Director at CSIRO. Ian is considered a thought leader in the area of the Digital Economy and is a regular speaker on "Big Data", broadband enabled services and the impact of technology on society. He has contributed to 6 books and co-authored more than 120 papers which have been cited more than 3500 times. Ian has an MBA from the University of London and a Doctor of Philosophy in Mobile Telecommunications from Sydney University. Ian is a Fellow of the Institute of Engineers Australia, a Fellow of the IEEE, a Fellow of the Australian Academy of Technological Sciences and Engineering, is Vice President of the Australian Computer Society, and a graduate member of the Australian Institute of Company Directors. Ian is also president of the Australia National Committee of the IEC and president of the JTC1 strategic advisory committee in Australia.

Speaker 3:

Title: Innovations in Health Technologies and data analytics for remote monitoring. Business models and regulatory issues.

Speaker: Professor Branko Celler, Emeritus Professor at UNSW, Australia.

Abstract: The irresistible digitization of our lives coupled with the innovative application of analytics have led to astonishing changes in the way we understand the world, the services we create and how we connect. It can also allow us to tackle some of the biggest problems we face in the environment, food security and dealing with a growing and aging population. This presentation highlights some of the opportunities and challenges of living in a digital world.

Speaker Bio: Professor Celler is internationally recognized as an innovator and pioneer in the development and use of biomedical software and instrumentation for the telemonitoring of chronically ill patients at home. He was Head of School of Electrical Engineering at UNSW for nine years and established the Biomedical Systems Laboratory which was successful in winning more than \$15m in competitive grants. He has an abiding and on-going interest in supporting health and socio-economic development of rural and remote communities through the smart use of ICT. Prof Celler has previously held positions as Executive Dean of the College of Health and Science at Western Sydney University and Chief Scientist at the CSIRO ICT Centre. He is a Fellow of the IEEE and a Fellow of the Australian Academy of Technological Science and Engineering and an inaugural Fellow of the Australian College of Health Informatics. He has published more than 200 Journal Articles and Refereed Conference Proceedings. In 2006 Prof. Celler established a start-up company Telemedcare Pty Ltd which now operates internationally and is respected for its innovation and excellence in telehealth. Professor Celler is Emeritus Professor and an active researcher at the University of New South Wales.

Speaker 4:

Title: The doable, conceivable and improbable of health analytics.

Speaker: Dr. Federico Girosi, Assoc. Prof. at School of Medicine, Western Sydney University, Australia.

Speaker Bio: Federico Girosi is an Associate Professor of Population Health at the School of Medicine, Western Sydney University and the Head of Research of the Health Market Quality program of Capital Markets CRC. Dr. Girosi is a health economist and a data scientist whose interests span a wide range of topics. He is currently working in collaboration with federal and state organizations, as well as the private sector, on projects that apply data analytics to the solution of problems of immediate interest. Examples of his current projects include the development of a microsimulation for the prediction of health and health care utilization under different policy scenarios, the detection of clusters and anomalies in health trajectories, the design of customizable catchment areas and the analysis of the Australian hospital payment system. He is also a Principal Investigator in three NHMRC sponsored project grants. Dr. Girosi earned a Ph.D. in Health Policy from Harvard University in 2003 and worked 8 years at the RAND Corporation (Santa Monica, U.S.A.). He also holds a Ph.D. in Physics from the University of Genoa, Italy, and conducted research

for 10 years at the Artificial Intelligence Laboratory at the Massachusetts Institute of Technology (MIT) in the areas of machine learning and computer vision. Dr. Giroso has published in a number of peer-reviewed international journals, including the New England Journal of Medicine, Health Affairs, Nature, Science and the Proceedings of the Institute of Electrical and Electronics Engineers. He is also the author of a book, published by Princeton University Press in 2008 and co-authored by Gary King, entitled "Demographic Forecasting".

Speaker 5:

Title: Precision Medicine: Combining Electronic Health Records, Genomics, Wearable and Sensor Data.

Speaker: Dr. Lucila Ohno-Machado, Professor of Medicine and Founding Chair, Health System Department of Biomedical Informatics, University of California San Diego.

Abstract: Integrating different types of health data has the potential to fill important: individuals can better understand their health status and healthcare providers can provide better care for their patients. To build effective predictive models, it is necessary to have data on a large number of individuals. The All of Us Research Program (formerly known as Precision Medicine Initiative) has started to recruit participants across the USA. I will describe the California Precision Medicine Consortium, which is awarded by the All of Us Research Program. Our goal is to recruit about 100,000 participants to compose a diverse cohort of 1 million people for the next 10 years. Researchers from anywhere will be able to compute with the data. This effort intersects several disciplines, from informatics to genetics to epidemiology. It is expected that engineers will play a significant role in designing and managing the computational environments for the program as well as integrating data from wearables and other sensors.

Speaker Bio: Lucila Ohno-Machado, MD, MBA, PhD Received her medical degree from the University of São Paulo and her doctoral degree in medical information sciences and computer science from Stanford. She is Associate Dean for Informatics and Technology, and the founding chair of the Health System Department of Biomedical Informatics at UCSD, where she leads a group of faculty with diverse backgrounds in medicine, nursing, informatics, and computer science. Prior to her current position, she was faculty at Brigham and Women's Hospital, Harvard Medical School and at the MIT Division of Health Sciences and Technology. Dr. Ohno-Machado is an elected fellow of the American College of Medical Informatics, the American Institute for Medical and Biological Engineering, and the American Society for Clinical Investigation. She serves as editor-in-chief for the Journal of the American Medical Informatics Association since 2011. She directs the patient-centered Scalable National Network for Effectiveness Research funded by PCORI (and previously AHRQ), a clinical data research network with over 24 million patients and 14 health systems, as well as the NIH/BD2K-funded Data Discovery Index Consortium. She was one of the founders of UC-Research eXchange, a clinical data research network that connected the data warehouses of the five University of California medical centers. She was the director of the NIH-funded National Center for Biomedical Computing iDASH (integrating Data for Analysis, 'anonymization,' and Sharing) based at UCSD with collaborators in multiple institutions. iDASH funded collaborations involving study of consent for data and biospecimen sharing in underserved and under-represented populations.

Program

	Monday, March 26	Tuesday, March 27	Wednesday, March 28
9:00 - 10:00	K1: Keynote 1	K2: Keynote 2	K3: Keynote 3
10:00 - 10:30			F9: Morning Tea
10:30 - 11:00			
10:30 - 11:00	F1: Morning Tea	F5: Morning Tea	S3: IoT Applications in Medical and Health Care Fields - I S4: Body Area Networks: PHY and MAC Layers
11:00 - 12:00	P1: Panel: "Should you care about your health data? How to provide privacy-aware solutions for data collection?"	Special 1: Emerging Technologies in Biomedical Devices, Systems and Applications	
12:00 - 12:30	O1: Students Posters Session		
12:30 - 13:30	F2: Lunch	F6: Lunch	
13:30 - 15:00	S1: Data Science in Medical and Healthcare Applications	W1: Workshop: Medical Device Regulatory Science Workshop (Part 1)	S5: IoT Applications in Medical and Health Care Fields - II S6: Human Body Wireless Communications
15:00 - 15:30	F3: Afternoon Tea	F7: Afternoon Tea	F11: Afternoon Tea
15:30 - 16:30	S2: Privacy and Security: Medical Data Collecting and Storage	W2: Workshop: Medical Device Regulatory Science Workshop (Part 2)	
16:30 - 17:00			
17:00 - 18:00	F4: Welcome Reception		
18:00 - 19:00			
19:00 - 21:00			F8: Conference Banquet

Monday, March 26, 09:00 - 10:30

K1: Keynote 1

Room: Harris

Chair: Ren Ping Liu (University of Technology Sydney, Australia)

Opening: Prof. Eryk Dutkiewicz, University of Technology Sydney, Australia

Speaker: Prof. Branko Celler, University of New South Wales, Australia

Title: Innovations in Health Technologies and data analytics for remote monitoring. Business models and regulatory issues

Speaker: Dr. Federico Giroi, Western Sydney University, Australia

Title: The doable, conceivable and improbable of health analytics

Monday, March 26, 10:30 - 11:00

F1: Morning Tea

Room: Foyer

Monday, March 26, 11:00 - 12:00

P1: Panel: "Should you care about your health data? How to provide privacy-aware solutions for data collection?"

Room: Harris

Chairs: Zenon D Chaczko (University of Technology, Sydney & SEDE, Australia), Valérie Gay (University of Technology Sydney, Australia)

Panelists:

Prof. Branko Celler, University of New South Wales, Australia

Dr. Federico Giroi, Western Sydney University, Australia

Prof. Prasuna Reddy, University of Technology Sydney, Australia

Assoc. Prof. Gyorgy Hutvagner, University of Technology Sydney, Australia

Monday, March 26, 12:00 - 12:30

O1: Students Posters Session

Room: Harris

12:00 Body-to-Body Communication: Applications, System Design Aspects and Performance Evaluation

Rida Khan (Tallinn University of Technology, Estonia & Istanbul Technical University, Turkey);

Muhammad Mahtab Alam (Tallinn University of Technology, Estonia)

Wireless body area networks (WBANs) contain set of wearable and/or implantable sensors that are located in, on, around or in immediate proximity to the human body. WBANs have immensely attracted the research efforts of scientific community due to

their current and prospective applications in different walks of life. The fundamental concept of WBANs can be developed into future body-to-body (B2B) communication systems by attaining the existence of multiple co-located WBANs as well as their mutual coordination and communication. The huge scope of challenges and potential applications (i.e., sports and fitness, rescue and critical operations etc.) associated with body to body communication has led to many publications. On the other hand, a thorough characterization of B2B propagation channels is the foremost step whether the purpose is minimizing the interference from neighboring WBANs or maintaining a good quality communication link between adjacent WBANs. Therefore, we highlight different candidate applications of B2B communication systems and present a thorough investigation of various B2B channel models. Moreover, several physical and medium access control (MAC) parameters are enlisted and discussed with regards to their impact on packet reception rate (PRR) performance in B2B communication systems

12:10 Performance Comparison of Routing Protocols for Vital Data Monitoring from a Large Number of Exercisers

Atsushi Niino, Shintaro Yamaguchi, Kazuki Okita and Hiroyuki Yomo (Kansai University, Japan)

In recent years, there have been significant research effort on vital data monitoring of people playing sports, which provides us with the information on their physical conditions and training effect. In this work, we assume a system configuration in which sensor nodes attached to exercisers with their back-waist positions sense vital data and send them to a sink node. The communication range of each sensor node is limited in this environment, therefore, the sensed data needs to be delivered to the sink node through multi-hop transmissions. There have been several routing protocols developed for ad hoc and sensor networks, however, their performances have not been evaluated in this application scenario including high node density and mobility with specific types of exercises. In this poster, we present simulation results of several routing protocols, such as RPL (IPv6 Routing Protocol for Low power and Lossy Networks) and OLSR (Optimized Link State Routing), when they are applied to vital data monitoring of people playing various types of exercises. With the radio link model assuming IEEE 802.15.4g as an employed communication standard and mobility model obtained with our experiments, we evaluate data collection rate of the above routing protocols as well as conventional flooding. With obtained numerical results, we discuss the fundamental challenges in multi-hop transmissions for vital data monitoring of a large number of exercisers.

pp. 1-2

12:20 Autocorrelation Based Transmission Power Control in WBANs

Hongyun Zhang (University of Wollongong, Australia); Farzad Safaei (ICT Research Institute, University of Wollongong, Australia); Le Chung Tran (University of Wollongong, Australia)

Spurred by the autocorrelation characteristic of in the real daily life WBAN scenarios, we propose an autocorrelation-based transmission power control (A-TPC) method to increase the transmission reliability and reduce the energy consumption. In A-TPC, data packets from multiple sensor nodes are scheduled in TDMA-fashion. The transmission power level and the slot scheduling are jointly optimized based on a temporal autocorrelation model. The newly proposed scheme is designed to be compatible with IEEE 802.15.6. The channel datasets collected from real WBAN daily scenarios are imported into our simulation model to evaluate the performance of A-TPC. Simulation results demonstrate that the A-TPC significantly improve the transmission reliability and extend the system lifetime by reducing the energy consumption.

Presenter bio: Dr Le Chung Tran received the Bachelor of telecommunications engineering degree (with the 1st class Hon, highest distinction) from University of Communications and Transport, and Master of telecommunications engineering degree (highest distinction) from Hanoi University of Technology, Vietnam, in 1997 and 2000, respectively. He achieved the PhD degree in telecommunications engineering from University of Wollongong, Australia, in 2006. From 1997 to 2005, he was a lecturer at the University of Communications and Transport, Vietnam. From 2005 to 2006, he was an associate research fellow at the University of Wollongong. From 2006 to 2008, he was a postdoctoral fellow at the Institute for Signal Processing, University of Luebeck, Germany, under the Alexander von Humboldt (AvH) fellowship. He has been with the University of Wollongong since 2009 to date. Dr Tran has achieved the World University Services awards (twice), Vietnamese Government's doctoral scholarship, International Postgraduate Research Scholarship, and the prestigious Humboldt postdoctoral fellowship. He is an editorial board member of the Electrical Engineering: An International Journal, a Technical Program Committee member of 23 IEEE conferences, and a regular reviewer for a number of international journals and conferences. He is a co-author of 59 publications, including one book and one book chapter. His research interests include multiple-input multiple-output systems, ultra-wideband communications, space-time-frequency processing for wireless and mobile communications, cooperative and cognitive communications, software defined radio, wireless personal area networks, and wireless body area networks.

pp. 3-4

Monday, March 26, 12:30 - 13:30

F2: Lunch

Room: Foyer

Monday, March 26, 13:30 - 15:00

S1: Data Science in Medical and Healthcare Applications

Room: Harris

Chair: Nguyen Linh-Trung (Vietnam National University, Hanoi, Vietnam)

13:30 A Dynamic Model Estimation Scheme for Model Predictive Control of Anesthesia Using Recurrent Neural Network

Yoshitomo Sakuma (Yokohama National University, Japan); Ryuji Kohno (Yokohama National University & University of Oulu, Japan)

In this paper, we proposed a dynamic estimation scheme of drug effect model for model predictive control of anesthesia. To control anesthesia with satisfy complicated requirements to guarantee safety, using model predictive control are effective. In the model predictive control of anesthesia, estimation accuracy using patient model are very important to guarantee control performance and maintain value of vital during surgery into the desired range. However, the drug response to the patients are modeled by nonlinear mathematical model and difficult to estimate using estimation algorithm for linear model. From this point of view, we proposed recurrent neural network to estimate nonlinear model of the drug response and track dynamic change of dose response.

Presenter bio: was born in Fukushima, Japan, in 1992. He received the Bachelor's degree in Engineering from Yokohama National University, Yokohama, Japan, in 2016. He is currently working toward the M.S. degree in Physics, Electrical and Computer Engineering at Yokohama National University, Yokohama, Japan. His research interests dependable communication and control theory and machine learning for Medical IoT.

pp. 5-9

13:45 Proposal for Feature Enhancement of Bioinformation Using Attractor Pattern and Frequency Analysis

Makoto Kikuchi (National Institute of Technology, Ibaraki College, Japan)

When recognising signals using deep learning, it is essential to extract features efficiently. In this study, we propose an individual identification method using medical data itself as identification information as part of research on medical malpractice prevention technology. In particular, to efficiently emphasise the features of the signal, we proposed a pretreatment method combining attractor pattern and frequency analysis. As a biological signal, we focused on the centre of gravity fluctuation of a standing posture, which is one of the human's whole body movements. We extract the component in one direction from the centre of gravity fluctuation and create the attractor pattern using that signal and its rate of change. Moreover, classification and individual identification of unknown data of the centre of gravity fluctuation were performed using the weight space obtained by machine learning. As a result, the effectiveness of the method proposed this time confirmed from the viewpoint of feature extraction. The process of this study has less information loss compared with the case using a convolution layer and has a small computation processing load. Therefore there is a possibility that it can apply to a failsafe system for medical malpractice prevention or a medical diagnosis system.

Presenter bio: Makoto Kikuchi received his master's degree from University of Tsukuba, Japan, in 1988, his doctor's degree in control systems engineering from the Ibaraki University, Japan, in 2001. He is current stuff at National Institute of Technology, Ibaraki College, Japan. His research interests include biomedical measurement, modelling, physiological characteristic of nerve-musculoskeletal systems and automatic analysis of physiological parameters.

pp. 10-15

14:00 Feature Analysis for Discrimination of Motor Unit Action Potentials

Thuy T. Pham (University of Technology Sydney & Garvan Medical Institute, Australia); Diep N. Nguyen and Eryk Dutkiewicz (University of Technology Sydney, Australia); Alistair McEwan and Philip Leong (The University of Sydney, Australia); Andrew Fuglevand (The University of Arizona, Australia)

In electrophysiological signal processing for intra- muscular electromyography data (nEMG), single motor unit activity is of great interest. The changes of action potential (MUAP) morphology, motor unit (MU) activation, and recruitment provide the most informative part to study the nature causality in neuromuscular disorders. In practice, for a single nEMG recording, more than one motor unit activities (in the surrounding area of a needle electrode) are usually collected. Such a fact makes the MUAP discrimination that separates single unit activities a crucial task. Most neurology laboratories worldwide still recruit specialists who spend hours to manually or semi- automatically sort MUAPs (e.g. using template matching). From a machine learning perspective, this task is analogous to the clustering-based classification problem in which the number of classes and other class information are unfortunately missing. In this paper, we present a feature analysis strategy to help better utilize unsupervised (i.e., totally automated) methods for MUAP discrimination. To that end, we extract a large pool of features from each MUAP. Then we select the top ranked candidates using clusterability scores as selection criteria. We found spectrograms of wavelet decomposition as a top-ranking feature, highly correlated to the motor unit reference and was more separable than existing features. Using a correlation-based clustering technique, we demonstrate the sorting performance with this feature set. Compared with the reference produced by human experts, our method obtained a comparable result (e.g., equivalent number of classes was found, identical MUAP morphology in each pair of corresponding MU class, and similar histograms of MUs). Taking the manual labels as references, our method got a much higher sensitivity and accuracy than the compared unsupervised sorting method. We obtained a similar result in MUAP classification to the reference.

pp. 16-21

14:15 Deep Holistic Representation Learning from EHR

Edmond Zhang and Reece Robinson (Orion Health, New Zealand); Bernhard Pfahringer (University of Waikato, New Zealand)

In recent years there has been a surge of interest in applying deep neural networks to electronic health records (EHRs) for predictive clinical tasks. EHR data cannot be mined like traditional image or text data because it has unique characteristics including temporality, irregularity, heterogeneity (both structured and unstructured) and incompleteness. We begin by identifying weaknesses in the way deep learning is currently being applied to health data. Then, leveraging these insights, we propose an end-to-end strategy for extracting complimentary deep feature representations from EHRs. This strategy is based on a "bringing model to data" machine learning approach instead of "transforming data to model". It uses multiple neural networks, that have each been optimised for the characteristics of their input data, to extract features. Then, the output of these neural networks is combined. We show that prediction accuracy improves as the output of each neural network is contributed. This work demonstrates the value of extracting relevant insights from different aspects of a patients record, which is analogous to how a clinician makes decisions.

pp. 22-27

14:30 An Efficient Ant Colony Optimization Algorithm for Protein Structure Prediction

Dong Do Duc (VNU, Hanoi, Vietnam); Phuc Thai Dinh (Vietnam National University Hanoi, Vietnam); Ngọc Anh Vũ (The Hanoi College of Industrial Economics, Vietnam); Nguyen Linh-Trung (Vietnam National University, Hanoi, Vietnam)

Protein structure prediction (PSP) is considered as one of the most challenging and computationally intractable combinatorial problem and is classified as an NP-hard problem. The 3-dimensional structure of a protein exposes its properties and features. Therefore, the identification of protein structure is a significant step towards understanding the protein's function which is an important role to synthesize new drugs and vaccine design; since many diseases are shown to result from malfunctioning of proteins. In this paper, we present K-ACO algorithm to tackle PSP, in which the pheromone is calculated according to k-degree Markov model. Its effectiveness is shown by comparing the experiment result against the state-of-the-art algorithms. pp. 28-33

14:45 EEG Affective Modelling for Dysphoria Understanding

Norhaslinda Kamaruddin (MARA University of Technology, Malaysia); Mohd Hafiz Mohd Nasir (Universiti Teknologi MARA, Malaysia); Abdul Wahab Abdul Rahman (IIUM, Malaysia)

Dysphoria is a state of dissatisfaction, restlessness or fidgeting. It is a state of feeling unwell in relation to mental and emotional discomfort. If this state is not carefully handled, it may lead to depression, anxiety, and stress. To date, 21-item instruments of Depression, Anxiety and Stress Scale (DASS) is employed to measure dysphoria. Although DASS provides a quantitative assessment of the human affective state, it is subjected to interpretation. To complicate matters, pre-cursor emotion and pre-emotion of the participants can result in biasness of the DASS report. Hence, a more direct method in measuring human affective state by analyzing the brain pattern is proposed. The approach can also address the dynamic affective state which is needed in detecting dysphoria. Brain waves pattern are collected using the electroencephalogram (EEG) device and used as the input to analyze the underlying emotion. In this paper, relevant features were extracted using Mel-frequency cepstral coefficients (MFCC) and classified with Multi-Layer Perceptron (MLP). The experimental results show potential of differentiating between positive and negative emotion with comparable accuracy. Subsequently, it is envisaged that the proposed model can be extended as a tool that can be used to measure stress and anxiety in work places and education institutions. pp. 34-39

Monday, March 26, 15:00 - 15:30

F3: Afternoon Tea

Room: Foyer

Monday, March 26, 15:30 - 17:00

S2: Privacy and Security: Medical Data Collecting and Storage

Room: Harris

Chair: Zenon D Chaczko (University of Technology, Sydney & SEDE, Australia)

15:30 On Path Length Estimation for Wireless Capsule Endoscopy

Anders Bjørnevik (Kongsberg Seatex, Norway); Pål Anders Floor (Oslo University Hospital, Norway); Ilangko Balasingham (Norwegian University of Science & Technology & Oslo University Hospital, Norway)

Wireless capsule endoscopy (WCE) is a non-invasive technology used for inspection of the gastrointestinal tract. Localization of the capsule is a vital part of the system enabling physicians to identify the position of anomalies. Due to intestinal motility, the positions of the intestines will change significantly within the abdominal cavity over time. However, the distance from one position to another within the intestines changes much less. In this paper a method for calculating the pathlength travelled by a WCE is proposed. The method is based on Kalman- and particle filters and is simulated using a model that approximately replicates the movement through the small intestine. The travelled distance was estimated to an accuracy within a few millimeters. pp. 40-44

15:48 Fine Grained Attribute Based Access Control of Healthcare Data

Edward Mrema and Vimal Kumar (University of Waikato, New Zealand)

One of the biggest threats to the healthcare data stored by healthcare organizations comes from malicious insiders. The first layer of protection against such adversaries is access control, however if an adversary is able to bypass that then the data becomes exposed. In this paper we propose an access control method based on Hidden Vector Encryption. In our approach access control policies are written using attributes of entities. The Hidden Vector Encryption system then embeds the policies in the ciphertext such that it can be decrypted only when the relevant attributes are presented. This provides a higher level of access control where a malicious insider cannot decrypt data unless they possess the right attributes. pp. 45-49

16:06 POSTCODE Middleware for Post-market Surveillance of Medical Devices for Cyber Security in Medical and Healthcare Sector in Australia

Junaid Chaudhry (Embry-Riddle Aeronautical University Prescott AZ, USA); Michael Crowley (ECU, Australia); Peter Roberts (Edith Cown University, Australia); Craig Valli (Edith Cowan University, Australia); Jon Jon Haass (Embry-Riddle Aeronautical University, USA)

Postmarket surveillance for cyber security of medical devices is an area within the critical infrastructure of health care and public health that has been largely neglected. In developed countries post market quality assurance is passive following complaints from the health care institutions to the manufacturers of the medical devices. Recently, the individual devices can be made traceable allowing any malfunctions to be uniquely identified in each device. There is a lack of clarity on post-sale ownership and management of devices and the updates to the device software. These devices, once plugged into Healthcare Information Systems (HIS) act as FDA approved black boxes that can not be patched, updated, or secured by anyone other than the manufacturer. Moreover, these unpatched devices provide back doors to cyber criminals to invade the HIS. These devices are soft targets for cyber criminals. So far, we have not come across any mechanisms that address the surveillance of these devices for cyber security. In this paper, we analyse the post-sale surveillance regulations in Australia. Based on our findings, we present fog-based POSTmarket SurveillanCe Of DEvices (POSTCODE) middleware that provides the operational details (excluding the private data of patient) of the devices directly to the manufacturers. The introduction of the POSTCODE will give device manufacturers the means to closely monitor the functioning of their devices. Manufacturers will be able to up-grade devices, patch security vulnerabilities and monitor device performance thereby enhancing health care outcomes. The POSTCODE middleware enhances device security whilst building partnerships between the health care facilitators and the device manufacturers.

Presenter bio: Junaid has over 15 years of exciting experience in academia, industry, law- enforcement, and in corporate world in information and cyber security. He has demonstrated capability of project management and cyber security management. He was training by Harvard Business School, University of Amsterdam, and Kaspersky Lab in cyber security hunting and training. Currently, he is conducting cutting edge research on safeguarding the weakest and the most vulnerable of the society in healthcare and public health sector at Security Research Institute (SRI). He is a Senior Member of IEEE, High Technology Crime Investigation Association (HTCIA), Australian Computing Society, Australian Information Security Association, and frequently volunteers in promotion of science through public speaking, conference organisation, and by editing the scientific journals i.e. IEEE Access, Computer and Security by Elsevier, IEEE Internet Policy and IEEE Future Directions.

pp. 50-59

16:24 Game-Theory Based Cognitive Radio Policies for Jamming and Anti-Jamming in the IoT

Zenon D Chaczko (University of Technology, Sydney, Faculty of Engineering and IT, School of Data and Electronic Engineering); Shaher Slehat (Faculty of Engineering and Information Technology, University of Technology, Sydney, Australia); Tamer Shnoudi (University of Technology, Sydney, Australia)

Cognitive Radio can be considered as a mandatory part of the Body Area Networks. It helps to solve the sacristy issues in the frequency bands of the wireless network component of the technology. However, the security problem is the primary challenge that needs to be carefully mitigated. Specifically, defending the Cognitive Radio mechanism against the jamming attacks. The aim this research paper is to investigate and provide a reliable and adaptive Cognitive Radio protection methods against the jamming attacks. Thus, improving the performance of the wireless network of IoT technology, enhancing the bandwidth and solving the issue of the sacristy of the frequency bands. The mentioned objectives will be accomplished by the aid of the game theory which is modelled as an anti-jamming game and by adapting the multi-arm bandit (MAB) policies. However, to solve the sacristy issue in the frequency band spectrum of the cognitive radio, some MAB policies were adapted such as Upper Confidence Bound (UCB), Thompson Sampling and Kullback-Leibler Upper Confidence Bound (KL-UCB). The results show some improvements and enhancements to the sacristy problem in the frequency band spectrum. To conclude, the Thompson Sampling MAB policy was the best to be adapted for solving the problem, as it resulted with lowest regrets and highest rewards compared to the other MAB policies.

Presenter bio: Dr Zenon Chaczko is currently the Senior Lecturer of Software Engineering at UTS and an active member of CRIN. After 25 years of R/D experience in ICT and marine systems industry as well as concurrent 4 years of P/T lecturing at the University of Technology Sydney, he moved to the F/T academic position at UTS in 2002. Since then he has been Program Head of Information and Communications Technologies. He is an experienced lecturer and researcher, consistently receiving excellent teaching results and reviews from students. He is an expert software and system engineer, research supervisor, having supervised/co-supervised many candidates to completion in the last 8 years. He has completed his PhD in Engineering at UTS. His specialisation is anticipatory (AI) and biomimetic middleware systems for the IOT. He is an author of several innovative theories and AI computational models.

pp. 60-65

16:42 Detection Scheme of Selfish Node in WBAN Utilizing CSMA/CA Based on IEEE 802.15.6

Yuto Omuro, Kento Takabayashi and Katsumi Sakakibara (Okayama Prefectural University, Japan)

This paper proposes a detection scheme of a selfish node in a wireless body area network (WBAN) utilizing CSMA/CA (Carrier Sense Multiple Access / Collision Avoidance) defined in IEEE 802.15.6. In the Internet of Things (IoT) era, the existence of a selfish node giving disadvantage to the network by acting selfishly is a problem. Especially, its influence is large in a WBAN dealing with medical and healthcare information. Hence, we proposed a detection method of such a node. Specifically, we focused on an illegal act of arbitrarily changing parameters of CSMA/CA in IEEE 802.15.6. In the proposed method, the illegal act was detected using measured values of back-off time. As a result of computer simulations, it was found that the detection effect can be enhanced by selecting the ratio of measured values according to the assumed illegal act and environment.

Presenter bio: Kento Takabayashi received the Ph.D. degree in Electrical and Computer Engineering from Yokohama National University, Yokohama, Japan, in 2017. He currently works at Okayama Prefectural University. His research interests in MICT such as Wireless Body Area Network and coding theory in wireless communications.

pp. 66-69

Monday, March 26, 17:00 - 19:00

F4: Welcome Reception

Room: Jones

Tuesday, March 27

Tuesday, March 27, 09:00 - 10:30

K2: Keynote 2

Room: Harris

Chair: Eryk Dutkiewicz (University of Technology Sydney, Australia)

Speaker: Dr Ian Oppermann, NSW Data Analytics Centre, Australia

Title: The Power of Diversity - Examining non-traditional data in Health

Speaker: Prof. Ryuji Kohno, Yokohama National University, Japan

Title: Medical Healthcare Big Data Mining and Managing by Integrated ICT and Data Science for Regulatory and Commercial Uses

Tuesday, March 27, 10:30 - 11:00

F5: Morning Tea

Room: Foyer

Tuesday, March 27, 11:00 - 12:30

Special 1: Emerging Technologies in Biomedical Devices, Systems and Applications

Room: Harris

Chairs: Xi Zhu (University of Technology Sydney, Australia), Yang Yang (University of Technology Sydney, Australia)

11:00 Self-powered Wireless Urinary-incontinence Sensor System Detecting Urine Amount and Diaper Change Timing in Under 10 Minutes

Hiroya Sakamoto, Ami Tanaka, Ryota Suematsu, Yo Nakajima and Takakuni Douseki (Ritsumeikan University, Japan)

A self-powered wireless urinary-incontinence sensor system composed of a wireless sensor and a receiver has been developed that detects the amount of urine and the time for a diaper change. The wireless urinary-incontinence sensor, which consists of a urine-activated battery, an intermittent power-supply circuit with a storage capacitor, and a wireless transmitter, makes it possible to detect the number of urinations and the amount of urine from the spacing between the output signals. The urine-activated battery, which consists of two long flexible electrodes embedded in a diaper and placed under a piece of absorbent material with a trench structure, makes fast detection of less than 10 minutes possible. A prototype urinary-incontinence sensor system detected the amount of urine in a diaper from the spacing between the sensing signals with a resolution of 100 cm³ and detected the time for a diaper change 7 minutes after urinations.

pp. 70-73

11:15 Non-Laboratory-Based Risk Factors for Automated Heart Disease Detection

Ha Mai (Garvan Medical Institute, Australia); Thuy T. Pham (University of Technology Sydney & Garvan Medical Institute, Australia); Diep N. Nguyen and Eryk Dutkiewicz (University of Technology Sydney, Australia)

Developing a heart disease detection model using simple non-laboratory risk factors plays an important role in preventive care, especially for high risk subjects. The model allows physicians/epidemiologists to effectively diagnose a person as having

heart disease. In this work, we aim to develop a non-invasive risk prediction model for automated heart disease detection that involves age, gender, rest blood pressure, maximum heart rate, and rest electrocardiography. We examine four public datasets from 1071 participants who were referred for a special X-ray of the heart's arteries (i.e., to see if they are narrowed or blocked). The subjects also undertook a physical examination and three non-invasive tests. To estimate the heart disease status, we apply a generalized linear model with regularization paths via coordinate descent. Even without laboratory-based data (e.g., serum cholesterol, fasting blood sugar), we observed a prediction accuracy as high as 72%, compared with 76% of other comprehensive models. This observation suggests that few non-invasive factors utilizing recent advances in data analytics can replace the current practices of heart disease risk assessment.
pp. 74-79

11:30 PDMS-Embedded Conductive Fabric: A Simple Solution for Fabricating PDMS-Based Wearable Antennas with Robust Performance

Roy B. V. B. Simorangkir (Macquarie University, Australia); Shilun Feng (Macquarie University & ARC Centre of Excellence for Nanoscale BioPhotonics (CNBP), Australia); Abu Sadat Md. Sayem and Karu Esselle (Macquarie University, Australia); Yang Yang (University of Technology Sydney, Australia)

A new and simple fabrication method to realize robust flexible wearable antennas by combining conductive fabric and polydimethylsiloxane (PDMS) is proposed. The conductive fabric acts as the conductive part of the antenna, while PDMS acts as the substrate as well as the encapsulation layers. The method takes advantage of the porous structure of the conductive fabric and the initial liquid form of PDMS to attain a significantly strong integration between the two, leading to a robust PDMS-based wearable antenna. A number of patch antennas have been designed, fabricated, and tested to validate the proposed concept and the results are presented, showing robust performance. The fabricated prototypes have a resonance frequency approximately at 2.46 GHz with a 10 dB return-loss bandwidth ranging from 3.3 to 5.7%.

Presenter bio: Dr Yang received PhD in Electrical and Computer System Engineering in 2013 from Monash University and currently is working as a research assistant at Monash University Clayton Campus. Dr Yang has published 2 book chapters 5 international journals and 6 international conference papers during the past 4 years. His major research interests are microwave and electronics active and passive component and system level designs.

pp. 80-82

11:45 Safety Consideration for Emerging Wireless Technologies - Evaluations of Temperature Rise in Eyes for RF Radiations Up to 10GHz

Yinliang Diao, Weinong Sun and Sai Wing Leung (City University of Hong Kong, Hong Kong); Mengze Li (Xiamen University, P.R. China); Yixin Cai (China Agricultural University, P.R. China); Xi Zhu and Yang Yang (University of Technology Sydney, Australia)

The study of temperature rise distribution in the human eye under plane electromagnetic wave exposure up to 10 GHz is presented in this paper. The effects of different frequencies and different blood perfusion rates of sclera to thermal calculations are investigated by finite difference method. The results reveal that the changes in the thermal parameter produce a maximum relative standard deviation of ~15% in the temperature rise in lens.

pp. 83-85

12:00 A Design and Implementation of an Ambulatory Electrocardiogram (ECG) Acquisition Circuit for Emergency Application

Jiewei Feng and Shahriar Shehab (Monash University, Australia); Yang Yang (University of Technology Sydney, Australia); Nemai Karmakar (MONASH University, Australia); Samir Gupta (Monash University, Australia)

This paper presents the design and development of an ECG data acquisition circuit for emergency applications. The ECG signal extraction method and the design of the analogue front-end circuit are discussed. This design has been implemented in a printed circuit board (PCB), with comparable size to a 50 cent Australian coin. By applying the testing approach with this prototype, the output ECG trace quality is overall satisfactory with a clear display of QRS complex and certain robustness to motion artifacts.

pp. 86-91

12:15 Development of Novel Gold/PDMS Sensors for Medical Applications

Anindya Nag (Macquarie University, Australia)

The paper presents the design and fabrication of novel gold/PDMS sensors using the sputtering method to use them for biomedical applications. The electrodes on the sensor patches were formed by placing a masked template containing the design over the PDMS. The sensor patches were flexible in nature with interdigitated electrodes formed on them. CTx-I, being one of the significant bone turnover biomarkers to determine the condition of the bones was tested at different concentrations to validate the functionality of the patches for this purpose. The results look promising to upgrade this idea into a fully-functionalized system for medical applications.

pp. 92-96

Tuesday, March 27, 12:30 - 13:30

F6: Lunch

Room: Foyer

Tuesday, March 27, 13:30 - 15:00

W1: Workshop: Medical Device Regulatory Science Workshop (Part 1)

Room: Harris

Chair: Masayuki Fujise (Yokohama National University, Japan)

Keynote Speakers:

Dr. Seigo Hara, MD, CEO of MICIN, Inc. Japan

Prof. Dr. Yi Qian, Professor of Biomechanics, the Faculty of Medicine and Health Sciences, Macquarie University, Australia

Tuesday, March 27, 15:00 - 15:30

F7: Afternoon Tea

Tuesday, March 27, 15:30 - 16:30

W2: Workshop: Medical Device Regulatory Science Workshop (Part 2)

Panel: Medical Network Therapy & Big Data Registry

Room: Harris

Chair: Ryuji Kohno (Yokohama National University & University of Oulu, Japan)

Panelists:

Dr. Ian Oppermann, NSW Data Analytics Centre, Australia

Prof. Dr. Yi Qian, Professor of Biomechanics, the Faculty of Medicine and Health Sciences, Macquarie University, Australia

Prof. Lucila Ohno-Machado, MD, PhD, Division of Biomedical Informatics, University of California San Diego, USA

Dr. Seigo Hara, MD, CEO of MICIN, Inc. Japan

Prof. Jari Iinatti, Dr.Sc. (Tech.), Centre for Wireless Communications, University of Oulu, Finland

Prof. Chika Sugimoto, PhD., Medical ICT Center, Yokohama National University, Japan

Tuesday, March 27, 18:00 - 21:00

F8: Conference Banquet

Room: Darling Harbour Convention Jetty (MV Morpheus)

Wednesday, March 28

Wednesday, March 28, 09:00 - 10:00

K3: Keynote 3

Chair: Ryuji Kohno (Yokohama National University & University of Oulu, Japan)

Speaker: Prof. Lucila Ohno-Machado, University of California San Diego, USA (by video link)

Wednesday, March 28, 10:00 - 10:30

F9: Morning Tea

Room: Foyer

Wednesday, March 28, 10:30 - 12:30

S3: IoT Applications in Medical and Health Care Fields - I

Room: Harris

Chair: Ilanko Balasingham (Norwegian University of Science and Technology, Norway)

10:30 A Study on the Effect of Sports on Academic Stress Using Wearable Galvanic Skin Response

Khalid Oweis, Moudar Zgoul, Assal Haddad and Hussam Quteishat (American University of Madaba, Jordan)

Wearable sensors have opened a new door for research to understand different human emotions and states. This is the first study to employ wearable devices in the measurement of Galvanic Skin Response (GSR) of students. A set of Microsoft Band 2 was used to collect data from nineteen engineering students while attending the same class. The data was collected throughout a whole semester. Students were later divided into categories according to their weekly activity level. This activity level was determined by an online survey that the students filled out. One-Way Analysis of Variance was performed to assess differences between groups. Correlation Analysis was also performed to evaluate the correlations between groups. Findings of this work include significant intra-group differences. Significant correlations were also found between GSR values and activity level. Significant correlations were also found within the GSR values between the groups themselves.

Presenter bio: Dr. Khalid Oweis has finished his Bachelor's degree in Electrical Engineering from the University of Jordan. His Master's degree in Computer Engineering from the University of Massachusetts - Lowell. And his PhD degree in Electrical Engineering with Biomedical focus from the George Washington University in 2011. He is currently an Assistant Professor at the American University of Madaba. His main research interests are medical image processing and biomedical signal processing.

pp. 97-102

10:45 Development of Printed Sensors for Shoe Sensing Applications

Anindya Nag (Macquarie University, Australia)

The paper presents the design and implementation of a low-cost shoe sensing system using laser-induced graphene sensors. Commercial polymer films were laser-induced to photo-thermally form graphene, which was then used as electrodes on Kapton tapes to form sensor patches. Experiments were then conducted with these sensor prototypes to validate its functionality as pressure sensors to be used in shoe sensing system. Different weights were tested with the developed system to ensure the capability of these sensor patches to be used as pressure sensing. The results look promising to be a system for monitoring the movement of a person wearing a shoe containing these low-cost pressure sensors.

pp. 103-108

11:00 A Network Simulator to Develop Wireless Networking Protocols Suited for Vital Information Collection from a Group of Exercisers

Hirofumi Ogura (Osaka City University, Japan); Takuma Hamagami (Oki Electric Industry Co., Ltd., Japan); Ryusuke Miyamoto (Meiji University & School of Science and Technology, Japan); Hiroyuki Yomo (Kansai University, Japan); Shinsuke Hara (Osaka City University, Japan)

To develop a wireless networking protocol suited for real-time vital information collection from a group of exercisers, it is mandatory to compare the performances among different protocol candidates by experiments using a group of subjects as a matter of course. However, fair comparison is almost impossible because the experiments have no repeatability. In this paper, we propose a software network simulator to fairly compare the performances of different networking protocols. The simulator is composed of two unique functions such as mobility model and channel model, both of which were developed through real experiments using a group of subjects. The mobility model outputs data sets for the time-series of locations of persons during different kinds of sports and exercises, and the channel model determines the channel characteristics between persons taking into consideration the transmission power, antenna pattern and blocking by other persons. We demonstrate by the simulator the performance of a wireless networking protocol using different types of antennas for the case of football game.

pp. 109-113

11:15 A Non-Linear Tensor Tracking Algorithm for Analysis of Incomplete Multi-Channel EEG Data

Nguyen Linh-Trung (Vietnam National University, Hanoi, Vietnam); Truong Minh-Chinh (Hue University of Education, Vietnam); Viet-Dung Nguyen (University of Paris Saclay, France); Karim

Abed-Meraim (Polytech'Orléans & University of Sharjah, UAE, France)

We consider the problem of tensor tracking for analyzing incomplete multi-channel EEG signals. In recent years, there has been an increasing interest in analyzing EEG signals by using tensor decomposition. There exist three challenging tasks: high computational complexity when working with tensor data, non-linearity of EEG signals and incomplete data. To overcome those problems, we propose a new adaptive tensor completion algorithm to simultaneously complete and track data in efficient way. Moreover, our algorithm copes with the non-linearity by minimizing the cost function with an embedded non-linear function. We illustrate the effectiveness of the proposed algorithm by tracking real-life EEG data.
pp. 114-119

11:30 PPG Based Respiration Signal Estimation Using VMD-PCA

Hangyang Ye and Jin Zhu (Tongji University, P.R. China); Yongqiang Cheng (University of Hull, United Kingdom (Great Britain))

The photoplethysmography (PPG) waveform is a pulsatile physiological waveform reflecting the blood volume changes attributed to cardiac synchronous activities, and with the lower frequency waveform components attributed to respiration, sympathetic nervous system activities and thermoregulation. Therefore, PPG waveforms are commonly used as non-invasive approach to extract cardiorespiratory signals such as heart beat and respiration rate. The existing methods either only estimate the respiration rate or sensitive to noises. In this paper, an algorithm based on variational mode decomposition with principal component analysis (VMD-PCA) is proposed as a novel approach to both recover the respiration signal (RS) and estimate respiration rate (RR) from PPG signal. Some 80 PPG samples from the MIMIC database (Physionet ATM data bank) are used to validate the performance of our algorithm. The results are examined with respect to the capnograph-based respiration signal as the ground truth. The performance measurement matrix is composed of mean normalized root mean square deviation (NRMSE), magnitude squared coherence (MSC) and Pearson's correlation coefficient (PCC) with values of 0.434, 0.382 and 0.209 respectively. The proposed method has also achieved 6.67 and 3.34 times faster than EEMD-PCA and EWT-PCA algorithms respectively.
pp. 120-124

11:45 SAM: Smart Asthma Monitoring: Focus on Air Quality Data and Internet of Things (IoT)

Nikita Isaac (University of Technology, Sydney, Australia); Naveenaa Sampath and Valérie Gay (University of Technology Sydney, Australia)

Nowadays, mobile technologies and in particular the Internet of Things (IoT), data and machine learning technologies can have a positive impact on the way we manage our health. This paper focuses on Asthma, a condition that affects 10% of Australians. This research collects and analyses data about air quality using New South Wales regional area data and data obtained from our faculty smart building (UTS building 11). Based on a persons location and travel plans, we analyze the Air Quality Index (AQI) and provide a personalized and localized feedback to individuals living with asthma and help them manage their condition better.
pp. 125-130

12:00 Secured Cancer Care and Cloud Services in IoT/WSN Based Medical Systems

Adeniyi Onasanya and Maher N Elshakankiri (University of Regina, Canada)

In recent years, the Internet of Things (IoT) has constituted a driving force of modern technological advancement, and it has become increasingly common as its impacts are seen in a variety of application domains, including healthcare. IoT is characterized by the interconnectivity of smart sensors, objects, devices, data, and applications. With the unprecedented use of IoT in industrial, commercial and domestic, it becomes very imperative to harness the benefits and functionalities associated with the use of IoT technology in (re)assessing the provision and positioning of healthcare that will ensure efficient and improved healthcare delivery. In this research, we are focusing on two important services in healthcare systems, which are cancer care services and business analytics/cloud services. These services incorporate the implementation of an IoT that provides solution and framework for analyzing health data gathered from IoT through various sensor networks and other smart devices in order to improve healthcare delivery and to help health care providers in their decision-making process for an enhanced and efficient cancer treatment. In addition, we discuss the wireless sensor network (WSN), WSN routing and data transmission in the healthcare environment. Finally, some operational challenges and security issues associated with IoT-based smart healthcare system are discussed.
pp. 131-136

12:15 Design and Implementation of Portable Health Monitoring System

Seema Khadirnaikar and Aparna P (National Institute of Technology Karnataka, India)

Advancement in technology is paving way for the development of portable/remote health monitoring devices. These devices have a significant role to play in day-to-day lives of the people living in the remote areas as they do not have proper access to health care centers. Since Heart Rate (HR) and Haemoglobin count have a vital role to play in determining the health condition of an individual, this paper presents a prototype of the health monitoring unit to monitor ECG and a noninvasive method to obtain Haemoglobin count. ECG signals acquired using surface electrodes are pre-processed and digitized. These are then analyzed using an efficient algorithm that computes heart rate and also distinguishes Normal Sinus Rhythm (NSR) from various cardiac ailments. This setup is tested using a standard database and real-time data. A LED-photodetector setup containing two wavelengths are used to obtain the PPG signals, which is further processed and mathematically modeled to obtain the Haemoglobin count.

S4: Body Area Networks: PHY and MAC Layers

Room: Jones

Chair: Jari Iinatti (University of Oulu, Finland)

10:30 Joint PHY-MAC Realistic Performance Evaluation of Body-to-Body Communication in IEEE 802.15.6 and SmartBAN

Rida Khan (Tallinn University of Technology, Estonia & Istanbul Technical University, Turkey);
Muhammad Mahtab Alam (Tallinn University of Technology, Estonia)

This paper presents the joint physical-medium access control (PHY-MAC) performance analysis of inter-BAN communication systems using realistic body-to-body (B2B) wireless channel model in IEEE 802.15.6 and smartBAN standards. The time-varying distances for the space-time B2B link variations are generated by real-time motion capture traces which are then introduced into already established B2B wireless channel model to give the actual path-loss values in dynamic environments. The SNR (Signal to Noise Ratio), BER (Bit Error Rate) and PER (Packet Error Rate) computations are briefly discussed to give an overview of the radio link modeling employed in the simulations. Using the mobility and the proposed radio link models, a more tangible performance assessment of B2B systems with IEEE 802.15.6 and SmartBAN specifications is achieved. Consequently, transmission power, packet length and data rate variations are investigated and the obtained results of packet reception rate (PRR) identify "head" as the best position to place the coordinator nodes for B2B communication.
pp. 137-142

10:45 Performance Comparison Between ETSI SmartBAN and Bluetooth

Andrea D'Souza (University of Florence, Italy); Harri Viitala and Matti Hämäläinen (University of Oulu, Finland); Lorenzo Mucchi (University of Florence, Italy)

This paper introduces the comparative performance analysis between ETSI SmartBAN and Bluetooth low energy (BLE) in the interfered additive white Gaussian noise (AWGN) channel as well as in multipath fading channel. Both technologies are possible solutions for wireless body area networks (WBAN) to implement services like delivering the vital signs data of an individual. The results show how the SmartBAN can outperform BLE in both AWGN and fading channel. In addition, SmartBAN can take advantages of repetition and coding features, which are not present in BLE to increase its performance even more.

Presenter bio: Dr. Hämäläinen received his M.Sc. and Dr.Sc. degrees from Telecommunications Laboratory at University of Oulu, Oulu, Finland in 1994 and 2006, respectively. Currently he is working as a University Researcher and research group coordinator at Centre for Wireless Communications (CWC), University of Oulu, Finland. He is also an Adjunct Professor at CWC and IAS Visiting Professor at Yokohama National University. His research interests include ultra wideband technology, radio channel modeling, wireless body area networks and medical ICT in general. He has published more than 150 scientific articles.

pp. 143-147

11:00 A New Optimal Relay Selection Strategy for the Coincident Multi-user Access

Jiajia Mei, Jie Zeng, Bei Liu, Xin Su and Chang Wang (Tsinghua University, P.R. China); Qi Liu (China Unicom Company, P.R. China); Shihai Shao (University of Electronic Science and Technology of China, P.R. China)

Non-orthogonal multiple access (NOMA) has been recognized as one of the promising multiple access technologies to provide higher spectral efficiency and system capacity to address several challenges in the fifth generation (5G) wireless systems. Telemedicine in the process of being greatly advanced by the high-reliable communication in future 5G wireless systems. This paper proposed a novel optimal relay selection (RS) strategy for the cooperative NOMA to achieve the minimum outage probability, which means that the number of retransmissions in hybrid automatic repeat request (HARQ) is decreased and hence indirectly reduce the communication latency. Small latency ensures the validity of medical data, thereby improving the quality of service (QoS) in medical communications. In addition, compared to another optimal relay selection, namely two-stage strategy, the proposed enhanced max-min RS has a lower computational complexity and lower storage overhead. The proposed enhanced max-min RS strategy can reduce almost 43% storage overhead and 95% latency caused by selection strategy in the cooperative RS-NOMA system used for wireless medical communications.

pp. 148-152

11:15 Impact of the Sternotomy Wires and Aortic Valve Implant on the On-Body UWB Radio Channels

Mariella Särestöniemi (University of Oulu, Finland); Carlos Pomalaza Raez (Purdue University, USA); Timo Kumpuniemi, Matti Hämäläinen and Jari Iinatti (University of Oulu, Finland)

In this paper, the impact of the sternotomy wires and aortic valve implant on the ultra wideband (UWB) channel characteristics is studied. The evaluations are performed by calculations, measurement data analysis, and power flow simulations. The aim is to show that implants, which consist of steel, titanium, and other highly conductive materials, do have clear effect on the signal propagation even inside the tissues. This impact should be taken into account when using in-body or on-body communication devices, such as endoscopy capsules etc.

Presenter bio: Dr. Hämäläinen received his M.Sc. and Dr.Sc. degrees from Telecommunications Laboratory at University of Oulu, Oulu, Finland in 1994 and 2006, respectively. Currently he is working as a University Researcher and research group coordinator at Centre for Wireless Communications (CWC), University of Oulu, Finland. He is also an Adjunct Professor at CWC and IAS Visiting Professor at Yokohama National University. His research interests include ultra wideband technology, radio channel modeling, wireless body area networks and medical ICT in general. He has published more than 150 scientific articles.

pp. 153-157

11:30 Simulation-based Body Motion Classifier Using Radio Channel Characteristics

Minseok Kim and Yuki Ichikawa (Niigata University, Japan)

Human motion classification is emerging technology which can improve healthcare system and to realize context-aware body area network (BAN). This paper focused the fact that the radio channel characteristics between sensor devices and coordinator may have stronger potential for motion classification than the conventional methods using accelerometer and the video sensor. Due to extremely large variety of possible combination of the channel components it is actually very difficult to obtain the accurate motion classifier based on measurement. Therefore, this study proposed a simulation-based classifier that is generated by large amount of data from the combination of individual channel components in computer simulation. This paper presented the current development that included only the free-space path loss variation by body motion. The automatic motion classification for 6 motion scenarios by using the radio channel between four sensor devices and coordinator was evaluated. From the results, it was seen that the method using radio channel entirely outperforms the method using acceleration, particularly in static motion scenarios.

Presenter bio: Prof. Kim was born in Seoul, Republic of Korea. He received the B.S degree in Electrical Engineering from Han Yang University, Seoul, Korea, M.E and Ph.D degrees in Division of Electrical and Computer Engineering, Yokohama National University (YNU), Japan in 1999, 2002, and 2005, respectively. He joined Tokyo Institute of Technology (Tokyo Tech) as an assistant professor from July 2007. He has been on leave to Georgia Institute of Technology as a visiting scholar in 2010. From April 2014, he joined Niigata University as an associate professor. His research interests include digital signal processor implementation, radio propagation

measurement, array processing, smart antenna system, software defined radio/cognitive radio. He is a member of IEEE and IEICE.

pp. 158-161

11:45 Evaluating Contemporary Physical Activity Self-Monitoring Technology Performance

Reem Altamimi and Geoff Skinner (The University of Newcastle, Australia)

Encouraging physical activity is becoming an increasingly relevant issue in modern society. Studies have shown that being involved in regular physical activity is essential for individuals' physical, mental and social development. The field of Information and Communication Technology (ICT) has been applied in several areas of research. One of the main domains that utilize the applications of ICT is the health domain. The definition of eHealth has appeared in the literature describing this integrated area of research. Health technologies have been increasingly utilized in physical activity promotion and intervention. Physical Activity Self-Monitoring Technologies (PAMTs) are a popular example of such technologies. New wearable activity monitoring technologies, such as fitness bracelets that track everyday activity, provide a technological solution for promoting active lifestyles. This research presents a pilot test that makes a valuable contribution within the area of valid and accurate trackers in terms of distance walked, using a treadmill walking activity, and a manual counting of steps, taken in a stair climbing activity. This study might assist other researchers in their choice of reliable equipment to use in research that involves reliable and accurate distance and steps calculations.

pp. 162-169

12:00 Modernising Asthma Management; Personalised Asthma Action Plans Using a Smartphone Application

Nikita Isaac (University of Technology, Sydney, Australia); Naveenaa Sampath and Valérie Gay (University of Technology Sydney, Australia)

Asthma is a chronic disease affecting one in nine Australians. With symptoms such as coughing, wheezing and shortness of breath, asthma can significantly impact a patient's quality of life. Asthma action plans are said to be one of the most effective asthma interventions available. However, in Australia only one in five people aged 15 and over, with asthma, have a written asthma action plan. Even less of which, refer to their plan. A review of related literature and work showed a gap regarding accessibility of information on asthma action plans in a written form. In an attempt to mitigate this problem, this paper focuses on the design and development of a smartphone application. The application is currently a high-fidelity prototype designed and built using proto.io software. In addition to this conversion, the application incorporates aspects of the Internet of Things (IoT) whereby real-time data regarding environmental triggers such as temperature, humidity and pollen in surroundings can be accessed from the app. The application ultimately aims to help asthmatics improve their health and quality of life by providing them, or their carer with the knowledge needed to better understand and manage their asthma when and where they need it.

pp. 170-174

12:15 Performance Study for Multimodal Client Identification System Using Cardiac and Speech Signals

Hadri Hussain (Faculty of Biosciences and Medical Engineering & Universiti Teknologi Malaysia, Malaysia); Sh-Hussain Salleh and Chee-Ming Ting (Universiti Teknologi Malaysia, Malaysia); Fuad Noman (UTM & UTM, Malaysia); Mohd Murtadha Mohamad (Universiti Teknologi Malaysia, Malaysia); Zubaidi Abdul Latif (Universiti Sultan Zainal Abidin, Malaysia); Osamah Al-Hamdani (Cisco System, Malaysia)

A person's physiological or behavioral characteristic can be used as a biometric and provides automatic identification. There are several advantages of this identification method over the traditional approaches. Overall, biometric techniques can potentially prevent unauthorized access. Unlike the traditional approach which uses keys, ID, and password, these approach can be lost, stolen, forged and even forgotten. Biometric systems or pattern recognitions system have been acknowledged by many as a solution to overcome the security problems in this current times. This work looks into the performance of these signals at a frequency samples of 16 kHz. The work was conducted for Client Identification (CID) for 20 clients. The building block for these biometric system is based on MFCC-HMM. The purpose is to evaluate the system based on the performance of training data sets of 30%, 50% and 70%. This work is evaluated using biometric signals of Electrocardiogram (ECG), heart sound (HS) and speech (SP) in order to find the best performance based on the complexity of states and Gaussian. The best CID performance was obtained by SP at 95% for 50% training data at 16 kHz. The worst CID performance was obtained by ECG achieving only 53.21% for 30% data training.

pp. 175-180

Wednesday, March 28, 12:30 - 13:30

F10: Lunch

Room: Foyer

Wednesday, March 28, 13:30 - 15:00

S5: IoT Applications in Medical and Health Care Fields - II

Room: Harris

Chair: Diep N. Nguyen (University of Technology Sydney, Australia)

13:30 Monitoring and Controlling Two Applications of a Magnetic Screw in the Gastrointestinal Tract

Hidetoshi Ohta (Sapporo Orthopaedics and Cardiovascular Hospital, Japan)

Several magnetic devices have been introduced into the gastroenterology. We indicated that the magnetic navigation in the capsule endoscopy is available. We have applied the magnetic control to the intragastric balloon therapy and the preparation of capsule colonoscopy. Though both procedures are well-known as non-invasive modalities, there are some drawbacks such as an unstable efficacy of the body weight loss for long term or the poor acceptability due to onerous amount of preparation. In this study, we clarified that the magnetic screw could control the intragastric balloon volume frequently, which was expected to keep the body weight loss for long time. Also, the ingestible magnetic cleansing device could reduce the amount of preparation to the acceptable dose. To date, there are no real-time monitoring systems for frequently checking the balloon volume or cleansing effects during preparation. We have also developed a simple real-time estimation of volume and flow by mean of resonant frequency shift related to the coil inductances on the devices and clarified that the accuracy of estimation was within 20%. The monitoring data was expected to contribute to the control of magnetic screw.

Presenter bio: Hidetoshi Ohta received the B.S. and M.S. degrees in Electronic Engineering from Hokkaido University in 1971 and 1973, the B.S. and Ph.D. in Medicine from Sapporo Medical University in 1988 and 1994 respectively. During 1973-1982, he stayed in Yokosuka Telecommunication Laboratory, NTT to study coaxial cable and optical fiber transmission system. After 1988, he has worked at several clinical hospitals, Sapporo Medical University Hospital, Bibai Municipal Hospital, Hokkaido Prefectural Sapporo Kitano Hospital, Hokkaido Cancer Center, Tomakomai Oji Hospital and studied medical engineering related to gastroenterology. During 2004-2011 he educated resident doctors as clinical associate professor in Sapporo Medical University. He is now vice chair in Sapporo Orthopaedics and Cardiovascular Hospital.

pp. 181-185

13:45 Applying Multi-channel Flooding to Vital Data Monitoring of a Large Number of Exercisers: Mobility and Link Modeling and Performance Evaluation

Shintaro Yamaguchi and Atsushi Niino (Kansai University, Japan); Hirofumi Ogura (Osaka City University, Japan); Hiroyuki Yomo (Kansai University, Japan); Ryusuke Miyamoto (Meiji University & School of Science and Technology, Japan); Shinsuke Hara (Osaka City University, Japan); Takashi Kawabata (Kansai University, Japan)

In recent years, there have been significant research effort on vital data monitoring of people playing sports, which provides us with the information on their physical conditions and training effect. In this paper, we assume a system configuration in which sensor nodes attached to exercisers with their back-waist positions sense vital data and send them to a sink node. In order to evaluate data collection performance by computer simulations, we first conduct experiments to collect position data of people playing football and footrace. Furthermore, we measure communication performance of sensor nodes with IEEE802.15.4g with experiments. Based on these experimental data, we construct mobility model and radio link model, which are applied to computer simulations investigating the performance of data collection employing a location-based flooding with multi-channel setting. Based on the obtained simulation results, we analyze the trade-off between the alleviation of congestion level and reduction of connectivity, which are observed when varying the number of allocated channels in the location-based flooding.

pp. 186-190

14:00 Resource-Constrained Device for Unobtrusive Estimation of Sleep Stages Using R-R Interval Data

Jaspal Singh (CDAC, Mohali, India); Rajender Kumar Sharma (National Institute of Technology Kurukshetra & National Institute of Technology Kurukshetra, India)

Identifying the Sleep stages is an essential component of sleep studies. It is normally done by observing collective behavior of various physiological signals, including EEG, EMG, EOG, etc. Recently it has been demonstrated that respiration and ECG can be computationally augmented to reasonably estimate the sleep stages. This paper describes a dedicated wireless device developed to acquire the cardio-respiratory data to distinguish the sleep stages. The device extracts R-R intervals and respiration data from the ECG and transmits it over the Bluetooth. The miniature hardware device and its energy efficient firmware design, presented in this work, are tested against the standard ECG machine for accuracy of R-R interval periods and ECG derived respiration (EDR). The experimental results show very good agreement of observed data with that obtained using commercial wired machine. The device is found to be very useful in unobtrusively screening the patients suffering with sleep related problems, especially in an out of center setting.

pp. 191-194

14:15 Modeling of a Cardiovascular System to Investigate Factors Affecting Hypertension

Kento Kadoya (The University of Tokyo, Japan); Shigehiko Kaneko (The University of Tokyo, Japan)

In this study, we construct a cardiovascular model considering the interaction of cardiac and vascular systems, and investigate factors affecting hypertension. In the cardiovascular model, stroke volume, the blood volume pumped by a heart per beat, is determined based on the operating conditions of the system. In addition, positions of baroreceptors, pressure sensors of cardiac system, in blood vessels are also considered. Consequently, the functions proportionally controlling the baroreceptor activities and determining the activities of autonomic nerves have significant effects on hypertension, which are comparable to those of arterial stiffness.

pp. 195-200

14:30 Impact of Enhancement Features on Image Registration for Liver Cancer Interventions Using CT Images

Luu Manh Ha (University of Technology and Engineering, VNU, Hanoi & AVITECH, Vietnam); Son Hoang (AVITECH, UET, VNU, Hanoi, Vietnam); Hong Thinh Nguyen (University of Engineering and Technology, VNU Hanoi & Signal and System Laboratory, Vietnam); Adriaan Moelker (Erasmus MC, The Netherlands); Tan Duc Tran (University of Technology and Engineering, VNU, Hanoi, Vietnam); Theo van Walsum (Erasmus MC, The Netherlands)

In minimal invasive intervention of liver cancer treatment, image registration is a powerful technique to align the diagnostic information such as tumor and vessels from diagnostic image to interventional images, in which the information is barely visible due to limited use of contrast agent. In this paper we investigate how the contrast-enhanced features such as tumor and vessels help the registration. For this, we decontrast-enhance the contrast enhanced CT image of the liver in the intervention; and then we compare accuracy of the registration between the diagnostic image and the original interventional image versus the diagnostic image and the decontrast-enhanced image. In addition, we use a rigidity term to improve the registration using the decontrast-enhanced image. The method is evaluated on 11 clinical data and shows promising results. pp. 201-204

14:45 Electronic Design of a Semi-Automated Micromanipulator Cell Injection System

Asad Hameed, Nabeel Kamal and Osman Hasan (National University of Sciences and Technology, Pakistan); Saad Qaiser (NUST, Pakistan); Nasir Jalal (School of Pharmaceutical Science and Technology Tianjin University, P.R. China)

A cell microinjection system is a widely used tool in the domain of cell biology and it allows us to deliver a specific amount of substance into a cell using a fine tipped needle (or a microinjection pipette) under the observation of a microscope. Cell microinjection systems are widely used for delivering drugs to a single cell for the treatment of diseases, like Cancer, Alzheimer's, Sickle cell anemia and Cystic fibrosis etc., developing organs, like heart, lungs and kidney, and in-vitro fertilization. This paper surveys the state-of-the-art microinjection techniques and cell microinjections systems and proposes an electronic design for the semi-automated micro cell injection system, which works on the principle of capillary pressure microinjection (CPM). The distinguishing feature of the proposed system is its low cost without compromising on the accuracy or movement precision.

Presenter bio: Currently, Osman Hasan is an Assistant Professor at the NUST School of Electrical Engineering and Computer Science (SEECS) since September 2009. He is the founder and director of the System Analysis and Verification (SAVE) Lab at SEECS and his research interests include Embedded System design, Formal Methods and e-health. He received the Quaid-e-Azam Award, Ministry of Education, Pakistan (1998), the Best University Teacher Award 2010 from HEC, Pakistan, Ideal ICT Excellence Award 2012 from Ideal Distributions, Pakistan, the Excellence in IT Education Award 2013 from Teradata Pakistan, the Best Young Research Scholar Award from HEC, Pakistan, the Best Teacher Award (2012-13) from NUST-SEECS, Best Researcher Award (2014) from NUST-SEECS, Excellence in IT Research and Development Award 2014 from Teradata Pakistan and the President's Gold Medal for the Best Teacher of the University (2015) from NUST.

pp. 205-209

S6: Human Body Wireless Communications

Room: Jones

Chair: Matti Hämäläinen (University of Oulu, Finland)

13:30 Resource Allocation in PDMA with Wireless Information and Power Transmission

Chang Wang, Jie Zeng, Bei Liu, Mingyao Peng and Xin Su (Tsinghua University, P.R. China); Shihai Shao (University of Electronic Science and Technology of China, P.R. China); Qi Liu (China Unicom Company, P.R. China)

With the development of the fifth generation (5G) wireless systems, the mobile medical will face a profound change. Pattern division multiple access (PDMA) is a novel non-orthogonal multiple access scheme proposed to increase throughput and the number of connections by combining the design of transmitters and receivers. In this paper, we propose a resource allocation scheme to achieve the trade-off between rate and energy. In our system model, we also exploited energy harvesting to optimize the efficiency of the entire system, although this makes it harder to solve the problem. To figure out the problem, an iterative algorithm based on optimized power allocation and the pattern matrix is proposed to improve the performance of downlink PDMA networks. Simulation results show that the proposed algorithm needs less total transmitting power when reaching the same rate and energy value.

pp. 210-214

13:45 Beacon-based Localization Middleware for Tracking in Medical and Healthcare Environments

Zenon D Chaczko (University of Technology, Sydney & SEDE, Australia); Kevin Casareo (University of Technology, Sydney, Australia)

This paper proposes a middleware solution for a Localization System that may be used in Medical environments such as Hospitals to track staff, patients and equipment. It investigates literature regarding indoor localization methods and limitations to determine a suitable algorithm that may be implemented in software. The methodology used to build and test the software is then explained. It then illustrates the concept of the Localization middleware in how it may be applied when used inside a room such as a hospital ward, the functional responsibilities it is expected to offer and the implementation of the distance measurement algorithm for Received Signal Strength and the Linear Least-Squares localization algorithm. The simulations of the localization algorithm appeared to be promising with the given simulation results; however, the real-time tests demonstrated that the range measurement was insufficiently precise to be reliable. Given a more accurate and reliable distance measurement, a more precise localization result could be attained.

Presenter bio: Dr Zenon Chaczko is currently the Senior Lecturer of Software Engineering at UTS and an active member of CRIN. After 25 years of R/D experience in ICT and marine systems industry as well as concurrent 4 years of P/T lecturing at the University of Technology Sydney, he moved to the F/T academic position at UTS in 2002. Since then he has been Program Head of Information and Communications Technologies. He is an experienced lecturer and researcher, consistently receiving excellent teaching results and reviews from students. He is an expert software and system engineer, research supervisor, having supervised/co-supervised many candidates to completion in the last 8 years. He has completed his PhD in Engineering at UTS. His specialisation is anticipatory (AI) and biomimetic middleware systems for the IOT. He is an author of several innovative theories and AI computational models.

pp. 215-220

14:00 Resource Allocation in Multi-user NOMA Wireless Systems

Mingyao Peng, Jie Zeng, Bei Liu, Jiajia Mei, Xin Su, Xibin Xu and Limin Xiao (Tsinghua University, P.R. China)

Non-orthogonal multiple access (NOMA) is a promising multiple access technologies for the fifth generation (5G) wireless systems due to its superior spectral efficiency and system capacity. With the rapid development of wireless body sensor networks (WBSNs) and wireless communications, supporting real-time communications in the telemedicine communication becomes a very important challenge. In this article, our goal is to optimize subchannel allocation and power allocation to maximize the sum rate, thereby improving real-time performance in telemedicine communications. Assuming that the base station could obtain perfect channel state information, we propose a suboptimal sub-channel allocation algorithm and a power allocation scheme with low complexity. In the power allocation scheme, the closed-loop expressions of power allocation proportional factors for multiplexed users on each subchannel is obtained by using Karush-Kuhn-Tucker (KKT) optimization conditions. The simulation results show that our proposed scheme has comparable performance to ideal sub-channel allocation based on the exhaustive search and is superior to other schemes.

pp. 221-225

14:15 A Low Complexity SCMA Detector Based on Avoiding Redundant Iterations

Shuliang Hao (Chongqing University of Posts and Telecommunications, P.R. China); Xin Su and Jie Zeng (Tsinghua University, P.R. China); Xin Ma (Shenzhen Gongjin Electronics Co., Ltd, P.R. China); Tiejun Lv (Beijing University of Posts and Telecommunications, P.R. China)

Sparse code multiple access (SCMA), as a competitive air-interface technology for the fifth-generation (5G) mobile communication networks, has a broad application prospect, in which the message passing algorithm (MPA) is employed at the receiver. However, the computational complexity of MPA is still an extreme challenge for SCMA decoding. In this paper, a low complexity multiuser detection algorithm based on avoiding redundant iterations, Avoiding Redundant Iterations-MPA (ARIMPA), is proposed for uplink SCMA system. ARI-MPA can achieve low complexity by avoiding redundant iterations, in which the number of iterations required is determined by the convergence rate of codeword probability. Numerical results demonstrate that the proposed scheme can achieve an affordable trade-off between bit error ratio (BER) performance and decoding complexity for SCMA system.

pp. 226-230

14:30 A Channel Estimation Method Based on the Improved LMS Algorithm for MIMO-OFDM Systems

ZhenFeng Zhang (Chongqing University of Posts and Telecommunications, P.R. China); Limin Xiao, Xin Su, Jie Zeng and Xibin Xu (Tsinghua University, P.R. China)

The least mean square(LMS) algorithm is a kind of typical adaptive filter algorithm. The algorithm of channel estimation based on that does not need to know the characteristics of channel and noise statistics, which make full use of channel correlation between front and back to reduce the influence of noise on channel estimation performance. In this paper, is presented in this paper, the LMS algorithm has been improved under the MIMO-OFDM systems and a revised method about variable step size has been put forward which make it accelerate the rate of convergence to improve performance preferably. The simulation results show that the algorithm proposed in this paper not only has the fastest convergence compared with LMS and NLMS algorithm, but also has a better channel estimation(CE) performance than other estimation algorithms.

pp. 231-235

14:45 Method of CS-IC Detection in Grant-Free NOMA System

Bin Fan (Chongqing University of Posts and Telecommunications, P.R. China); Xin Su and Jie Zeng (Tsinghua University, P.R. China); Xin Ma (Shenzhen Gongjin Electronics Co., Ltd, P.R. China); Tiejun Lv (Beijing University of Posts and Telecommunications, P.R. China)

With the development of mobile communication and the Internet of Things, non-orthogonal multiple access (NOMA) has become one of the hottest candidates for 5G. In the uplink NOMA system, there is a large number of connected users with multi-user detection, fewer active users and sparse signals in a certain period of time. In this paper, combined with the compressive sensing (CS) technique, a compressive sensing based multi-user interference cancellation (CS-IC) method is proposed to detect the active users and data of the grant-free nonorthogonal multiple access (GF-NOMA) system. It greatly reduces the signaling overhead and control transmission delay, because the active users do not send the active status information to the base station and do not need to interact with the base station in advance. Simulation results show that the proposed CS-IC multiuser detection can obtain much better BLER performance than the IC and MMSE-IC multi-user detection, greatly improving the spectrum efficiency.

pp. 236-240

Wednesday, March 28, 15:00 - 15:30

F11: Afternoon Tea

Performance comparison of routing protocols for vital data monitoring from a large number of exercisers

Atsushi Niino, Shintaro Yamaguchi, Kazuki Okita, and Hiroyuki Yomo
Graduate School of Engineering Science, Kansai University

Abstract—In this work, we focus on vital data monitoring of people playing various types of sports. We assume a system configuration in which sensor nodes attached to exercisers with their back-waist positions sense vital data and send them to a sink node. The communication range of each sensor node is limited in this environment, therefore, the sensed data needs to be delivered to the sink node through multi-hop transmissions. In this paper, we present simulation results of RPL (IPv6 Routing Protocol for Low power and Lossy Networks) that is a widely-used routing protocol in wireless sensor networks. We evaluate data collection rate of RPL, and compare its performance with that of conventional flooding when these schemes are applied to vital data monitoring of people playing various types of exercises. With obtained numerical results, we discuss challenges in multi-hop transmissions for vital data monitoring of a large number of exercisers.

I. INTRODUCTION

In recent years, there has been an increasing interest in monitoring vital data of exercisers, which enables us to study efficient training methods and to prevent injuries of players. In order to realize such a vital data monitoring, data generated by a large number of sensors must be reliably gathered in a realtime manner [1]. In this work, we focus on the collection of vital data from several tens to hundreds of exercisers by using wireless sensor networks (WSNs) technologies. A sensor node based on IEEE 802.15.4g is attached to their back-waist position. In such an environment, the communication range of each node is limited and varies due to the movement of exercisers as well as propagation effects such as the shadowing of human body. In this work, we consider applying data collection through multi-hop communication by RPL (IPv6 Routing Protocol for Low power and Lossy Networks) [2], which is widely used in many applications of WSNs, and flooding where each sensor node repeats broadcast to deliver sensing data to a sink node. We also consider applying multi-channel communication that reduces the congestion level of the frequency band by distributing the traffic into several channels. With the obtained results, we discuss the effectiveness of each approach when they are applied to vital data monitoring of a large number of exercisers.

II. SYSTEM MODEL

In this work, we assume that each sensor node is attached to back-waist position of each exerciser to sense vital data

and transmit it to a data collection node (sink). Each sensor node generates 5 types of data: heartrate (200 Bytes), energy expenditure (2 Bytes), body temperature (2 Bytes), humidity (2 Bytes), and sequence number (1 Byte). The generation period of these data is set to be 10 seconds. As a communication module, we adopt ARIB STD-T108 [3] that is based on IEEE802.15.4g standard as physical layer operating over 920 MHz band and IEEE802.15.4 as MAC layer. We employ multi-channel transmissions where sink node is equipped with multiple interfaces supporting different frequency channels while each sensor node operates with a single interface with a randomly assigned frequency channel.

III. SIMULATION MODEL

In this paper, we focus on two scenarios with different types of exercises, football and warming-up exercise in a sports-day event. Football is a sports suitable for assessing the communication protocols for vital data monitoring since it includes various movements such as jumping and sliding. The field size of football model is set to $81.08\text{m} \times 101.58\text{m}$. The number of players is 22. On the other hand, warming-up exercise is commonly played during a sports-day event at schools in Japan. The field size of warming-up model is set to $100\text{m} \times 150\text{m}$. We assume that 300 students (which is supposed to be a total number of students in a school) play a warming-up exercise within the field at uniformly located positions. The mobility model was created by using an object-tracking technique that is applied to video data of actual football game and warming-up exercise.

We employ link model constructed based on experiments of nodes following ARIB STD-T108 standard [4]. The other simulation parameters are shown in Table I.

IV. SIMULATION RESULTS

Fig. 1 shows data collection rate against number of channels for football model. From this figure, we can first see that data collection rate is improved when the number of channels is increased from 1 to 2. This is thanks to the reduction of congestion level that is achieved by distributing traffic into multiple channels. However, when the number of channels is further increased, data collection rate deteriorates for both schemes. With large number of channels, each node has less number of neighboring nodes operating with the same

TABLE I
SIMULATION PARAMETERS

Parameter	Value
Simulation Time	540s (football) 730s (warming-up)
Number of nodes	22 (football) 300 (warming-up)
Data Rate	100 kbps
Transmission power	20mW
DIO frame size	24 Bytes
DIS frame size	2 Bytes
Min. Backoff Exponent (BE)	3
Max. Backoff Exponent (BE)	5
Max. Number of Backoffs	4
Number of Simulation Trials	10

channel, which reduces the connectivity of overall network, thereby degrading data collection rate. By comparing the results of RPL and flooding, we can find that flooding achieves much higher data collection rate than RPL for football model. With football, the mobility of each node is so high that the route constructed by RPL can become invalid frequently while flooding can enjoy route diversity effect. This contributes to the superiority of flooding to RPL for football model.

Next, Fig. 2 shows data collection rate against number of channels for warming-up exercise model. From this figure, we can see that data collection rate is continuously improved as the number of channels is increased. With warming-up exercise model, we have 300 nodes within the field, and the number of nodes over a single channel is sufficiently high even for a large number of channels. Therefore, the reduction of network connectivity is not observed. For smaller number of channels, we can find that RPL shows better performance than flooding. With warming-up exercise, the node mobility is small, therefore, a route constructed by RPL can be valid for a long period of time. On the other hand, the congestion level over smaller number of channels is so high that flooding cannot achieve high data collection rate. This is the reason why RPL has superior performance to flooding for smaller number of channels. When the number of channel is larger, the performance of flooding is improved since the congestion level is reduced, and the performance of RPL and flooding becomes almost same. However, the largest data collection rate is around 80 % for both schemes, which requires us to develop more advanced routing techniques for enhancing reliability of vital data collection.

V. CONCLUSIONS

In this paper, we have investigated the effectiveness of RPL and flooding when they are applied to vital data collection from a large number of exercisers. Our numerical results have shown that flooding is suited for a scenario with smaller number of nodes and high mobility while RPL works well when nodes are static and the congestion level is relatively high. However, both of them cannot achieve data collection rate higher than 90 % when the number of nodes is larger. In our future work, we will develop more advanced

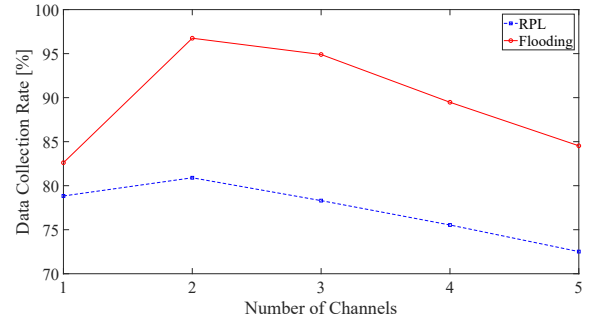


Fig. 1. Data collection rate against number of channels for football model.

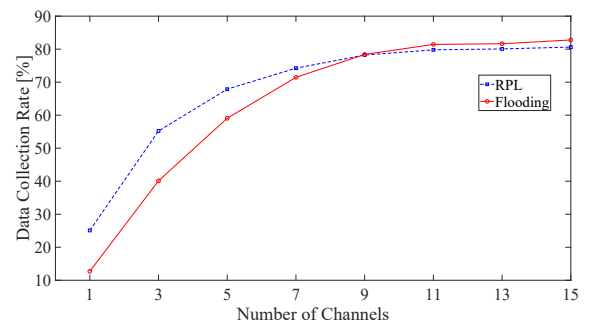


Fig. 2. Data collection rate against number of channels for warming-up exercise model.

routing/flooding techniques that can achieve high reliability in vital data monitoring of a large number of exercisers.

VI. ACKNOWLEDGEMENT

This work was supported by the Research and Development of Innovative Network Technologies to Create the Future of National Institute of Information and Communications Technology (NICT) of Japan.

REFERENCES

- [1] S. Hara, H. Okuhata, T. Kawabata, H. Nakamura, and H. Yomo, "Real-Time Vital Monitoring for Persons during Exercises-Solutions and Challenges," *IEICE Trans. Commun.*, vol. E99-B, no. 3, pp. 556-564, March 2016.
- [2] RPL: IPv6 Routing Protocol for Low power and Lossy Networks, IETF RFC 6550, March 2012.
- [3] Association of Radio Industries and Businesses, ARIB STD-T108, version 1.0, 2011.
- [4] S. Yamaguchi, A. Niino, H. Ogura, H. Yomo, R. Miyamoto, S. Hara, and T. Kawabata, "Applying Multi-channel Flooding to Vital Data Monitoring of a Large Number of Exercisers: Mobility and Link Modeling and Performance Evaluation," *Proc. of ISMICT 2018*, Sydney, Australia, March 2018.

Autocorrelation Based Transmission Power Control in WBANs

Hongyun Zhang*, Farzad Safaei*, Le Chung Tran*

*School of Electrical, Computer and Telecommunications Engineering

Faculty of Engineering and Information Sciences, University of Wollongong, NSW 2522, Australia

Email: hz697@uowmail.edu.au, (farzad,lctran)@uow.edu.au

Abstract—In this paper, we propose an autocorrelation-based transmission power control (A-TPC) method to increase the transmission reliability and reduce the energy consumption. In A-TPC, data packets from multiple sensor nodes are scheduled in the TDMA-fashion. The transmission power level and the slot scheduling are jointly optimized based on a temporal autocorrelation model. The channel datasets collected from real WBAN daily scenarios are imported into our simulation model to evaluate the performance of A-TPC. Simulation results demonstrate that A-TPC significantly improves the transmission reliability and reduces the energy consumption.

I. INTRODUCTION

Transmission power control (TPC) approach refers to the adaptive method which optimizes the transmission power based on the change of channel condition or QoS (Quality of Service) requirements. Due to the peculiarity of WBANs [1], simply adopting the TPC methods designed for other networks, e.g., cellular networks and WSNs (Wireless Sensor Networks), is not appropriate. Spurred by the autocorrelation characteristic of on-body channels, we propose an autocorrelation-based transmission power control (A-TPC) method which jointly optimizes the transmission power level and slot scheduling for real daily WBAN scenarios.

II. SYSTEM MODEL

We consider a one-hop WBAN composed of n on-body sensor nodes (denoted as SN_1, SN_2, \dots, SN_n) and one hub node, the sensor nodes periodically upload monitoring data to the hub. Figure 1 illustrates the superframe structure, which is split into two phases: Random Access Phase (RAP1) and Managed access phase (MAP). The CSMA/CA access method is adopted by the RAP1 phase to exchange management and control packets. The scheduled upload intervals (SUIs) assigned to the sensor nodes are located in the MAP to upload data packets to the hub. All sensor nodes are allocated with the same length and No Acknowledgment (N-Ack) policy is adopted in the uplink. Moreover, both the hub and the sensor nodes are considered to operate in the half-duplex mode.

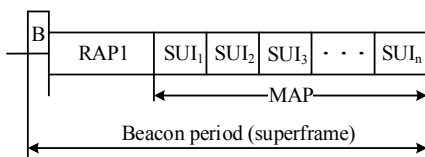


Fig. 1. Superframe structure.

Instead of utilizing the distance-based formula to quantify the path loss [2], we adopt channel gain datasets collected from the real daily scenarios. The portable wireless transceivers introduced in [3], [4] are used to collect the channel gain data. We adopt the energy consumption model in network simulator *Castalia* [5], which is one of the most accurate energy models for WBANs.

III. THE PROPOSED TPC SCHEME

In A-TPC, all control and calculation operations are carried out on the hub side, as the hub is typically more powerful than the rest of the nodes in terms of storage and computational resources implement. Specifically, A-TPC consists of three main steps, which are summarized as follows:

A. Channel Information Collection

Upon receiving the data packets from a sensor node, the hub node records the RSSI values. Meanwhile, the hub node knows the transmission power levels for all sensor nodes, it is easy to calculate the channel gain (or path loss) after receiving the RSSI value. By this approach, the hub keeps track of the channel gain from all sensor nodes.

B. Channel Quality Prediction

We use a “lite version” of the temporal autocorrelation model (TAM) introduced in [6] to predict the channel quality for next superframe. The “lite version” TAM only requires the autocorrelation coefficient between two consecutive superframes. In short, the conditional distribution of channel gain in the next superframe can be expressed by:

$$G_i(S+1) \sim \mathcal{N}((1-\rho_i)\mu_i + \rho_i G_i(S), (1-\rho_i^2)\sigma_i^2) \quad (1)$$

where $G_i(S)$ and $G_i(S+1)$ are the channel gains of channel $SN_i - \text{hub}$ at the superframe S and $S+1$, respectively. ρ_i denotes the autocorrelation coefficient for the two channel gains recorded in the two adjacent superframes. The following parameters: $G_i(S)$, μ_i , σ_i and ρ_i are required by (1) to estimate the channel quality. Firstly, the latest channel gain record in the previous superframe is chosen as $G_i(S)$. Then, the channel gain expectation μ_i and standard deviation σ_i can be estimated by the sample mean and sample standard deviation, i.e., $\hat{\mu}_i$ and $\hat{\sigma}_i$. At last, the autocorrelation coefficient σ_i is calculated based on the following equation:

$$\rho_i = \frac{\sum_{x=1}^N (G_i(x) - \hat{\mu}_i)(G_i(x+1) - \hat{\mu}_i)}{\sum_{x=1}^N (G_i(x) - \hat{\mu}_i)^2} \quad (2)$$

where $G_i(1) \dots G_i(N)$ are sample channel gain values recorded in N consecutive superframes, and N is the sample size.

C. Transmission Power Control

At the beginning of each superframe, the hub calculates $G_i(S)$, $\hat{\mu}_i$, $\hat{\sigma}_i$ and ρ_i for each channel. Then Algorithm 1 is carried out to decide the transmission power level and slot scheduling for the current superframe. These decisions are embedded into the beacon packet which would be broadcasted to all sensor nodes to execute the configurations.

Algorithm 1: Adaptive transmission power control

Input: The known channel gains in last superframe, i.e., $G_1(S), G_2(S), \dots, G_n(S)$.
Input: Autocorrelation coefficients between two consecutive superframe, i.e., $\rho_1, \rho_2, \dots, \rho_n$.
Input: Sample means, i.e., $\mu_1, \mu_2, \dots, \mu_n$.
Input: Sample standard deviations, i.e., $\hat{\sigma}_1, \hat{\sigma}_2, \dots, \hat{\sigma}_n$.
Output: The transmission power levels of n sensor nodes for the current superframe, i.e., $TX_1(S+1), TX_2(S+1), \dots, TX_n(S+1)$.
Output: The scheduled SUI orders of n sensor nodes for the current superframe, i.e., $O_1(S+1), O_2(S+1), \dots, O_n(S+1)$.

```

1 Define
  Txlevel = [-25, -15, -10, -7, -5, -3, -1, 0];
2 for  $i \leftarrow 1$  to  $n$  do
3    $\hat{G}_i(S+1) = (1 - \rho_i)\hat{\mu}_i + \rho_i G_i(S)$ ;
4 end
5 Sorting array  $\hat{G}_1(S+1), \hat{G}_2(S+1), \dots, \hat{G}_n(S+1)$  with
  the greatest in front;
6  $O_i(S+1)$  = the order of  $\hat{G}_i(S+1)$  in the sorted array;
7 for  $i \leftarrow 1$  to  $n$  do
8    $M_i(S+1) = \hat{\sigma}_i \times (BasicMargin + O_i(S+1) \times$ 
      $GradientMargin)$ ;
9    $TX_i(S+1) = \arg \min_x TxLevel[x] \geq$ 
      $(\hat{G}_i(S+1) + M_i(S+1))$ ;
10 end

```

IV. PERFORMANCE EVALUATION

The channel dataset collected from real WBAN scenarios is imported into the simulation model, and the dataset contains channel gains of five sensors. We compare the performance of A-TPC with the following three methods:

- 1) **Static:** The hub does not adjust the transmission power (remain 0 dBm) and the SUIs order for sensor nodes.
- 2) **Xiao's:** The method adapts the transmission power level according to the estimated average RSSI value [7].
- 3) **Ideal:** The hub controls the transmission power based on the exact channel gain value. Note that the ideal method is infeasible in real WBANs.

Figure 2 shows the performance of average packet loss ratio (PLR) when the Rx sensitivity in the hub varies. It can be seen from the figure that the PLR performance of A-TPC is close to the ideal method and much lower than the Xiao's scheme.

Figure 3 shows the energy efficiency. As shown in the figure, the energy efficiency of A-TPC is much higher than the static method and better than that of Xiao's method.

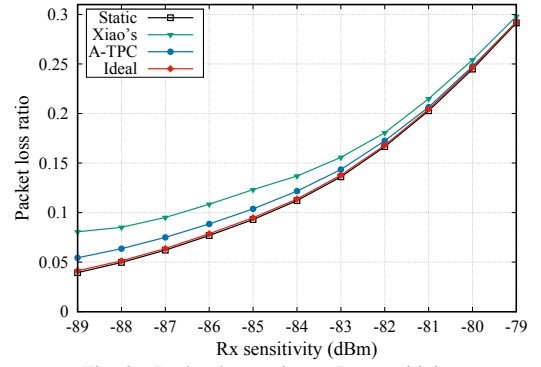


Fig. 2. Packet loss ratio vs. Rx sensitivity

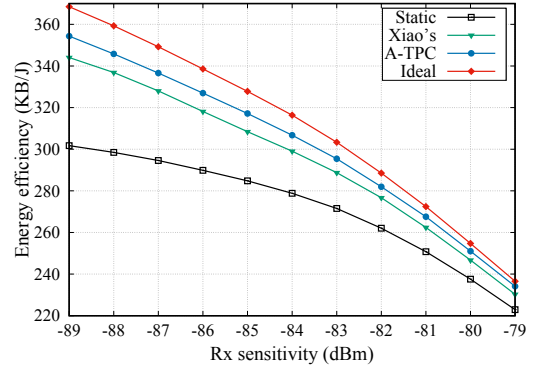


Fig. 3. Energy efficiency vs. Rx sensitivity

V. CONCLUSION

Motivated by the significant autocorrelation characteristic of on-body channels in the daily WBAN scenarios, we propose an autocorrelation-based transmission scheme, named A-TPC, in which transmission power control and slot scheduling are jointly optimized based on a temporal autocorrelation model. We evaluate the performance of the newly proposed scheme by importing the channel dataset collected from real WBAN daily scenarios into our simulation model. Simulation results demonstrate that compared to classical method, A-TPC achieves a better performance in terms of packet loss ratio and energy efficiency.

REFERENCES

- [1] M. Sudjai, L. C. Tran, and F. Safaei, "Performance analysis of STFC MB-OFDM UWB in WBAN channels," in *Proc. IEEE PIMRC*, Sept. 2012, pp. 1710–1715.
- [2] H. Zhang, F. Safaei, and L. C. Tran, "Joint analog network coding and channel allocation in the walking scenario for WBAN," in *Proc. IEEE ISCC*, Jun. 2016, pp. 604–609.
- [3] H. Zhang, F. Safaei, and L. C. Tran, "Measurement-based characterizations of on-body channel in the human walking scenario," in *Proc. IEEE VTC2017-Spring*, Jun. 2017, pp. 1–5.
- [4] H. Zhang, F. Safaei, and L. C. Tran, "A novel cooperation-based network coding scheme for walking scenarios in WBANs," *Wireless Communications and Mobile Computing*, vol. 2017, pp. 1–20, Sept. 2017.
- [5] A. Boulis. (2017) Castalia: A simulator for wireless sensor networks and body area networks. [Online]. Available: <https://github.com/boulis/Castalia/>
- [6] H. Zhang, F. Safaei, and L. C. Tran, "Channel autocorrelation based dynamic slot scheduling for body area networks," *Submitted to EURASIP Journal on Wireless Communications and Networking*, 2017.
- [7] S. Xiao, A. Dhamdhere, V. Sivaraman, and A. Burdett, "Transmission power control in body area sensor networks for healthcare monitoring," *IEEE J. Sel. Areas Commun.*, vol. 27, no. 1, pp. 37–48, Jan. 2009.

A Dynamic Model Estimation Scheme for Model Predictive Control of Anesthesia Using Recurrent Neural Network

Yoshitomo Sakuma, and Ryuji Kohno

Graduate School of Engineering, Yokohama National University

79-5 Tokiwadai, Hodogaya, Yokohama, 240-8501

Email: {sakuma-yoshitomo-cm, kohno-ryuji-ns} @ynu.jp

Abstract—In this paper, we proposed a dynamic estimation scheme of drug effect model for model predictive control of anesthesia. To control anesthesia with satisfy complicated requirements to guarantee safety, using model predictive control are effective. In the model predictive control of anesthesia, estimation accuracy using patient model are very important to guarantee control performance and maintain value of vital during surgery into the desired range. However, the drug response to the patients are modeled by nonlinear mathematical model and difficult to estimate using estimation algorithm for linear model. From this point of view, we proposed recurrent neural network to estimate nonlinear model of the drug response and track dynamic change of dose response.

I. INTRODUCTION

Recently, Information communication technology(ICT) for medical application has attracted attention due to the arrival of aging society and shortage of medical staff.

In particular, a dosage control system for total intravenous anesthesia (TIVA) used Propofol¹⁾ as the anesthetic drug has been studied in order to help anesthesiologist and make up for their shortage.

In the general anesthesia, constraints of dosage of the Propofol¹⁾ and the value of biological information indicating anesthetic depth must be taken into account. Bispectral Index(BIS)²⁾ is often used as the index of anesthetic depth which shows BIS value during surgery is from 40 to 60 based on the requirement.

TABLE I
BISPECTRAL INDEX²⁾

Condition of the patients	Value of BIS
Awaken	From 90 to 100
Light Hypnosis	From 60 to 90
Desired range	From 40 to 60
Deep Hypnosis	From 0 to 40

On the other hand, control scheme for the TIVA using Model Predictive Control(MPC) are proposed⁴⁾ considering those requirements. Also, estimation scheme of time variation of BIS using Extended Karman Filter^{5,6)} are proposed. However, the Extended Karman Filter uses linear approximation and time variation of BIS are expressed by

nonlinear equation. Thus, an estimation scheme considering nonlinearity of the time variation of BIS is needed.

To solve this problem, we proposed a dynamic estimation scheme of BIS behavior. In the scheme, we made a recurrent neural network model of the anesthetic effect in order to predict time varying response to drug administration.

Numerical results have shown the proposed scheme enables to estimate BIS behavior compared to Extended Karman Filter and our proposal can track BIS behavior when parameter of the patient model are changed during surgery.

II. BACKGROUND

A. Supposed use cases

Firstly, we explain the supposed use cases in this study. We supposed that the system is controlled remotely by anesthesiologists who are outside of the operation room. Also, vital data is sent to the server which is outside of the operation room and the data is used to estimate drug effects.

B. Numerical model of drug effects

In this study, we used a numerical model to predict effect of the anesthetic drug.

1) *Compartmental model*: We used the fourth-order compartmental model proposed by Schnider and Minto⁹⁾ as the pharmacokinetic(PK) and pharmacodynamics(PD) model for Propofol. The model are expressed by following equations:

$$\begin{aligned}
 \dot{C}_1(t) &= -[k_{1o} + k_{12} + k_{13}] \cdot C_1(t) + k_{21} \cdot C_2(t) \\
 &\quad + k_{31} \cdot C_3(t) + \frac{\dot{u}(t)}{V_1} \\
 \dot{C}_2(t) &= k_{12} \cdot C_1(t) - k_{21} \cdot C_2(t) \\
 \dot{C}_3(t) &= k_{13} \cdot C_1(t) - k_{31} \cdot C_3(t) \\
 \dot{C}_e(t) &= -k_e \cdot C_e(t) + k_e \cdot C_1(t).
 \end{aligned} \tag{1}$$

In eq. 1, C_i represents the concentration in the compartment i and C_e denotes the concentration in the effect site compartment[g/L]. The parameter k_{ij} ($i \neq j$) denotes the drug transfer frequency from compartment i to j , k_{1o} denotes the drug metabolize frequency from compartment

1 and k_e denotes the drug transfer frequency from compartment 1 to effect site compartment and the frequency of drug removal from effect site compartment. The parameter \dot{u} represents the drug infusion rate [g/s] and V_i denotes the volume of the compartment i .

In this study, we expressed PK-PD model by the following state equation (discrete time) supposing that the infusion rate \dot{u} [g/s] is constant during sampling time in the discrete-control system

$$\begin{aligned} \mathbf{x}_{k+1} &= \mathbf{A}_d \mathbf{x}_k + \mathbf{B}_d u_k \\ \mathbf{A}_d &= e^{\mathbf{A}T_s} = \mathcal{L}^{-1}[(s\mathbf{I} - \mathbf{A})^{-1}] \\ \mathbf{B}_d &= \int_0^{T_s} e^{\mathbf{A}(T_s-\tau)} d\tau \mathbf{B}. \end{aligned} \quad (2)$$

where, u_k denotes the dosage[g] of the Propofol in discrete time k , \mathbf{x}_k denotes the quantity of state of the PK-PD model and defined as

$$\mathbf{x}_k^T = [C_{1,k}, C_{2,k}, C_{3,k}, C_{e,k}], \quad (3)$$

\mathbf{A} and \mathbf{B} are the parameters of the PK-PD model and defined as

$$\mathbf{A} = \begin{bmatrix} -k_{10} - k_{12} - k_{13} & k_{21} & k_{31} & 0 \\ k_{12} & -k_{21} & 0 & 0 \\ k_{13} & 0 & -k_{31} & 0 \\ k_e & 0 & 0 & -k_e \end{bmatrix}$$

$$\mathbf{B}^T = [\frac{1}{V_1 T_s}, 0, 0, 0], \quad (4)$$

\mathbf{I} are identity matrix of fourth dimension and T_s represents sampling period in the discrete-control. Each rate constant and Volume of each compartment depends on age, weight, height and gender⁹.

2) *Hill equation*: The Bispectral index(BIS) value is related to the effect site concentration. The empirical static relationship is typically expressed by the nonlinear function: Hill equation⁷

$$BIS_k = f_b(C_{e,k}) = E_0(1 - \frac{C_{e,k}^\gamma}{C_{e,k}^\gamma + EC_{50}^\gamma}) \quad (5)$$

where, E_0 denotes the value of BIS when effect site concentration C_e is zero, EC_{50} denotes concentration of effect site compartment when value of BIS is 50 and γ denotes steepness of BIS variation depending on change of effect site concentration C_e . Average value and standard deviation (SD) of each parameter are shown in table II. Shown in eq.

TABLE II
PARAMETER OF HILL FUNCTION⁷

Parameter	Average value(SD)
E_0	97.3(0.8)
EC_{50} [g/L]	$3.90 \times 10^{-3}(1.05 \times 10^{-3})$
γ	1.81(0.67)

5, hill function are nonlinear function and those parameter cannot be estimated accurately using estimation algorithm for linear equation.

C. Extended Kalman Filter

The Extended Kalman filter (EKF)⁵⁾⁶⁾ is a state estimator for nonlinear systems using approximating to the linear system. The performance of the filter depends on the accuracy of the linear approximation. It can be regarded as the problem when the EKF is applied to the estimator of the BIS value. Therefore, we proposed the Recurrent Neural Network for estimate nonlinear behavior of the BIS value.

III. PROPOSED SCHEME

A. System model

The system model our proposed scheme is shown in fig. 1.

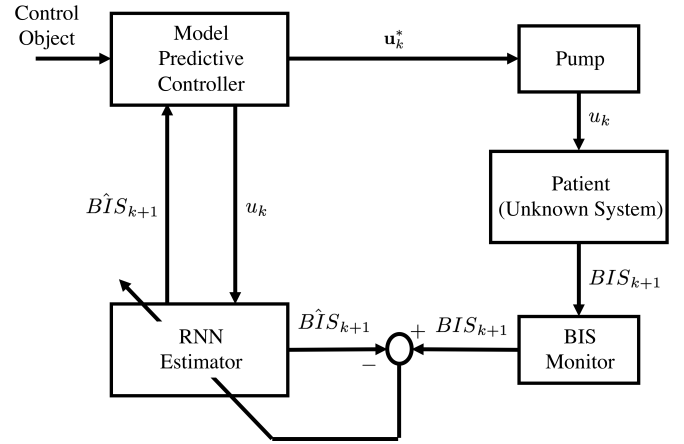


Fig. 1. The block diagram of the proposed system

In the system, drug dosages in each step time are controlled based on prediction using estimator of the BIS behavior using Recurrent Neural Network. Also, parameter of the Recurrent Neural Network are updated using BIS value sensed from the patient.

B. Proposal of Recurrent Neural Network for dynamic estimation of anesthetic effect

Firstly, we transform the hill equation (5) in order to compose recurrent neural network model of the anesthetic effect. The hill equation (5) can be transformed into

$$y_k = 1 - \frac{BIS_k}{E_0} = \frac{1}{1 + (\frac{C_{e,k}}{EC_{50}})^{-\gamma}}. \quad (6)$$

Above equation (6) can be approximated as sigmoid function:

$$y_k \simeq \frac{1}{1 + e^{-(w_1 C_{e,k} + w_0)}}. \quad (7)$$

Notice that, w_0 and w_1 are weight parameter for the approximation.

From eq. (2) and (7), we composed recurrent neural network model shown in fig. 2 in order to predict variation of BIS value by drug dosing.

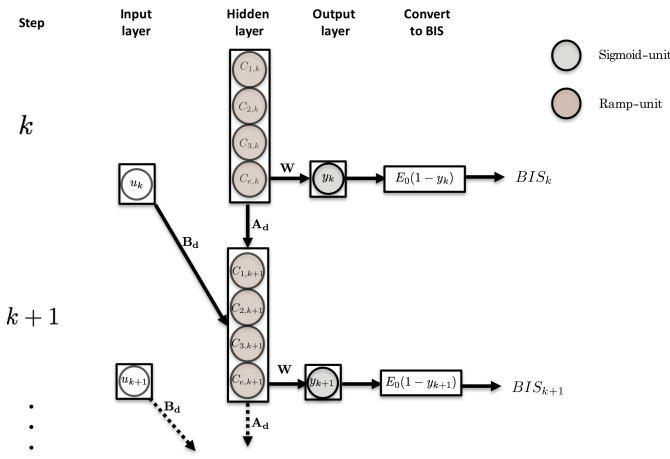


Fig. 2. Proposed RNN

In our proposed RNN, drug dosages in each step time u_k are input of the RNN. In the hidden layer, drug concentration of each compartments ($\mathbf{x}_k^T = [C_{1,k}, C_{2,k}, C_{3,k}, C_{e,k}]$) in the PK-PD model are estimated. From eq. (2), Weights between input layer and hidden layer can be expressed as B_d and hidden layer and hidden layer (recurrent) can be expressed as A_d . In the output layer, y_k are expressed. Notice that, from eq. (7), weights between hidden layer and output layer are $\mathbf{W} = [w_0, w_1]$, w_1 is multiplied by effect site compartment $C_{e,k}$ and w_0 is bias. Also, output of the RNN y_k are converted to BIS by the following equation:

$$\hat{BIS}_k = E_0(1 - y_k). \quad (8)$$

Notice that, \hat{BIS}_k denotes BIS value estimated by our proposed RNN.

C. Flowchart of the proposed scheme

The flowchart of our proposed system is shown in fig. 3.

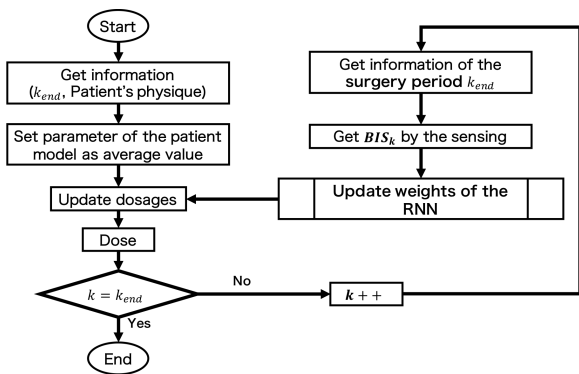


Fig. 3. Main routine of the proposed scheme

Notice that k_{end} denotes end time of the surgery period. In this algorithm, dosages are updated adaptively. Also, BIS value are sensed from patients and used to update RNN

model for prediction. In each step time, subroutine to update RNN is called and the routine are shown in fig. 4.

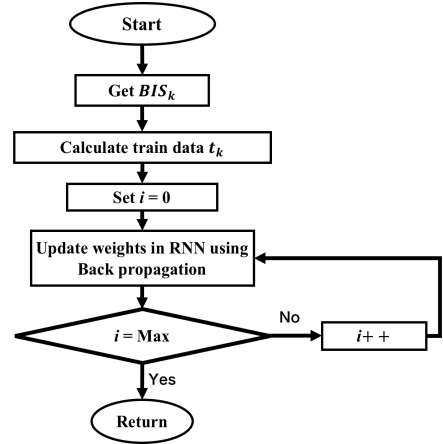


Fig. 4. Subroutine of the proposed scheme

Where, i denotes number of iteration. In the subroutine, weights the RNN are updated using back propagation through time (BPTT) algorithm. When subroutine are stated, train data for training the RNN are calculated by the following equation:

$$t_k = 1 - \frac{BIS_k}{E_0}. \quad (9)$$

Also, objective function for updating weights using back propagation are defined as

$$J_k = (y_k - t_k)^2. \quad (10)$$

Based on the objective function (10), weight are updated by the BPTT algorithm while number of iteration are lower than defined Maximum number of epoch.

IV. COMPUTER SIMULATION

A. Condition of evaluations

In the evaluation, we evaluate accuracy of the prediction by our proposed RNN compared with existing method: Extended Kalman Filter. We used two sets of the parameter of the hill function. the sets are shown in table III.

TABLE III
PARAMETER OF HILL FUNCTION IN EACH CASES

Set	E_0	$EC_{50}[\text{g/L}]$	γ
1	97.3	2.85×10^{-3}	2.48
2	97.3	4.95×10^{-3}	1.14

We supposed the situation that parameter set are switched from Set1 to Set2 in the evaluation in order to evaluate performance of the proposed scheme to the dynamic change of the behavior of the BIS. In the evaluation, the parameter

set are switched when 60 minutes after the start of dosing in the simulation.

Also, dosages in each step time are controlled by the proportional control that object value of BIS is 50. Other simulation parameter are shown in table IV.

TABLE IV
SIMULATION PARAMETERS

simulation time[min.]	180
Surgery period[min.]	120
Sampling Period T_s [sec.]	0.10
Gain of the controller	3.0×10^{-5}
Object value of BIS in the control	50.0
Learning late in the back propagation	0.10
Maximum number of the iteration	5,10,15,20
Patient	
Age	40
Weight[kg]	70
Height[cm]	170
Gender	Male

B. Simulation results

The transition of the BIS value are shown in fig. 5, 6, 7 and 8. From those graphs, we can see proposed scheme could estimate BIS behavior accurately compared with EKF. In particular, proposed scheme can estimate overshoot and undershoot from the desired range in each maximum number of iteration while EKF scheme could not. Also, from the transition of the BIS value around 60 minutes in the simulation, our proposal can track to the dynamic change of the dose response of the patient. From those results, our proposed scheme can be applied to the model predictive control compared with the EKF.

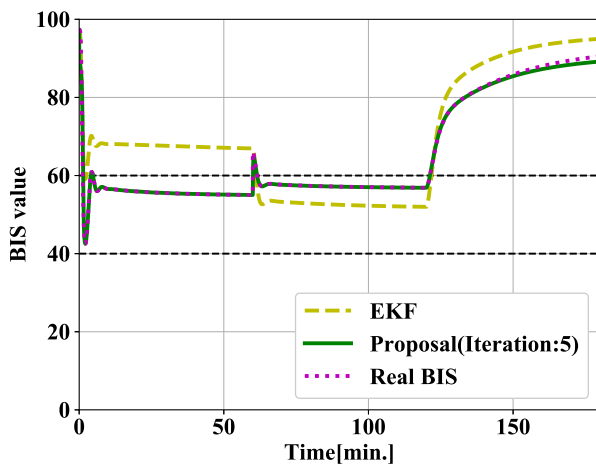


Fig. 5. Transition of the BIS value(Number of iteration:5)

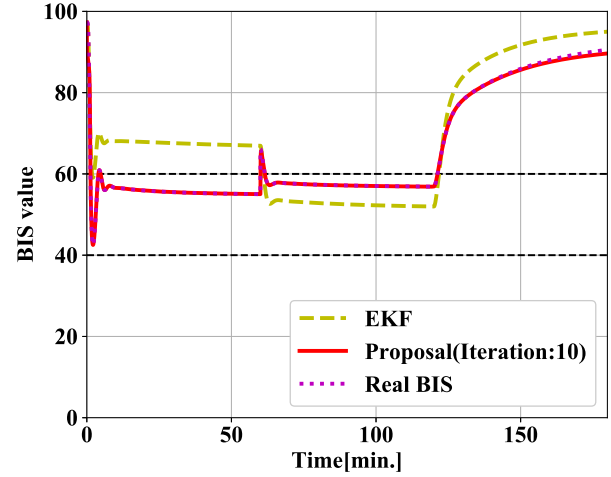


Fig. 6. Transition of the BIS value(Number of iteration:10)

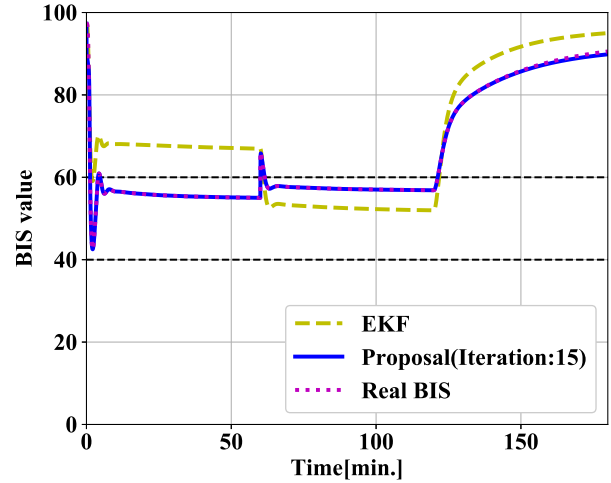


Fig. 7. Transition of the BIS value(Number of iteration:15)

Next we evaluated absolute error between estimated value and real value. The transition of the absolute error are shown in fig. 9 and 10. From fig. 9, we can observed the more number of iteration increases, the faster absolute error converges. On the other hand, from 10, the more number of iteration increases, the better tracking performance to the dynamic change of the dose response of the patient.

From those result, It can be concluded that our proposed scheme can guarantee the estimation accuracy for applying model predictive control compared with Extended Kalman Filter. Also, optimization of the number of iteration are needed. In the optimization, tradeoff between tracking performance and calculation complexity need to be considered. It can be regarded as one of the important theme in the study.

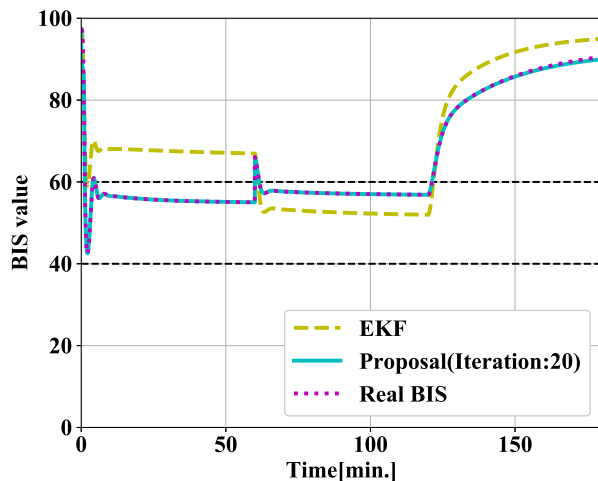


Fig. 8. Transition of the BIS value(Iteration:20)

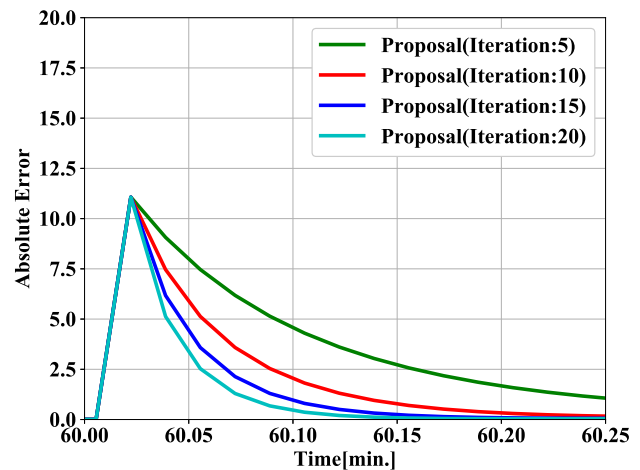


Fig. 10. Absolute error(From 60.00[min.] to 60.25[min])

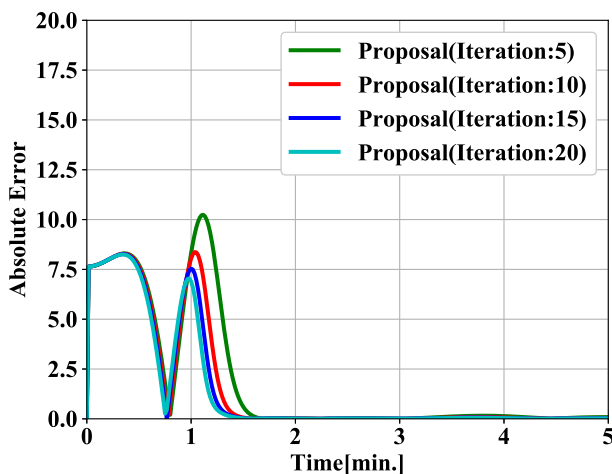


Fig. 9. Absolute error(From 0[min.] to 5[min])

V. CONCLUSION

In this paper, we proposed the dynamic estimation scheme of drug effect model for model predictive control of anesthesia. We confirmed our proposed scheme can guarantee the estimation accuracy for applying model predictive control compared with conventional scheme. Also, our proposal can track the dynamic change of the dose response of the patient.

In the future, we'll propose adaptive control scheme of anesthesia using our proposal in this paper.

REFERENCES

- [1] DIPRIVAN(R) (Propofol) INJECTABLE EMULSION, USP, (http://www.accessdata.fda.gov/drugsatfda_docs/label/2014/019627s062lbl.pdf).
- [2] Bispectral Index Monitor An Evidence-Based Analysis, Ontario Health Technology Assessment Series 2004, Vol. 4, No. 9, 2004.
- [3] M.M.R.F.Struys, T.D.Smet, J.B.Glen, H.E.M.Vereecke, A.R. Absalom, T.W.Schnider, The History of Target-Controlled Infusion, *Anesthesia & Analgesia*, Vol.122, Issue 1, pp.56-69, 2016.
- [4] Y.Sakuma, K.Sameshima, and R.Kohno, "An Adaptive Scheme of Controlling Dosage and Dosing Interval in General Anesthesia by Model Predictive Control Using Anesthetic Depth Model," the 11th International Symposium on Medical Information and Communication Technology (ISMICT2017), Lisbon, Portugal, February. 2017.
- [5] S.Rezvanian, F.Towhidkhah, N.Ghahramani, A. Rezvanian, "Increasing Robustness of the Anesthesia Process from Difference Patient's Delay Using a State-Space Model Predictive Controller", *Procedia Engineering* 15, Advanced in Control Engineering and Information Science, pp-928-932, 2011
- [6] S.Rezvanian, F.Towhidkhah, N.Ghahramani, "Controlling the Depth of Anesthesia Using Model Predictive Controller and Extended Kalman Filter", *Proc. IEEE, 2011 1st Middle East Conference on Biomedical Engineering (MECBME) 2011*:213-216.
- [7] Y.Sawaguchi, E.Furutani, G.Shirakami, M.Araki, and K.Fukuda, A Model-Predictive Hypnosis Control System Under Total Intravenous Anesthesia, *IEEE TRANSACTIONS on Biomedical Engineering*, Vol.55, No.3, pp-874-887, 2008.
- [8] I.N.Nascu, A.Krieger, C.M Ionescu, and E.N.Pistikopoulos, Advanced Model-Based Control Studies for the Induction and Maintenance of Intravenous Anaesthesia, *IEEE TRANSACTIONS on Biomedical Engineering*, Vol.62, No.3, 2015.
- [9] T.W.Schnider, C.F.Minto, P.L.Gambus, C.Andersen, D.B.Goodale, and S.L.Shafer, The Influence of Method of Administration and Covariates on the Pharmacokinetics of Propofol in Adult Volunteers, *Anesthesiology*, Ver.88, No.5, pp.1170-1182, 1998.

Proposal for Feature Enhancement of Bioinformation Using Attractor Pattern and Frequency Analysis

Makoto KIKUCHI

National Institute of Technology, Ibaraki College
866 Nakane, Hitachinaka-shi, Ibaraki-ken, 312-8508, Japan,
mkikuchi@asme.org

Abstract— When recognising signals using deep learning, it is essential to extract features efficiently. In this study, we propose an individual identification method using medical data itself as identification information as part of research on medical malpractice prevention technology. In particular, to efficiently emphasise the features of the signal, we proposed a pretreatment method combining attractor pattern and frequency analysis. Especially, as a biological signal, in this study, we focused on the centre of gravity fluctuation of a standing posture, which is one of the human's whole body movements. This movement is representative biological information and is being studied not only as a diagnosis of diseases and functional disorders however also as an index for evaluating health condition. In this study, we extract the component in one direction from the centre of gravity fluctuation and create the attractor pattern using that signal and its rate of change. Moreover, from the difference in the model, the identification of the subject and the state of the standing posture control system are identified. The attractor pattern is two-dimensionally Fourier transformed to emphasise a part of the characteristics of signals. After filtering the result, it used for supervised machine learning as the input signal of the hierarchical neural network. Furthermore, classification and individual identification of unknown data were performed using the weight space obtained by machine learning. As a result, the effectiveness of the method proposed this time confirmed from the viewpoint of feature extraction. The process of this study has less information loss compared with the case using a convolution layer and has a small computation processing load. Therefore there is a possibility that it can apply to a failsafe system for medical malpractice prevention or a medical diagnosis system.

Keywords— *Identification, pre-processing, neural network, attractor pattern, bio-information, medical error*

I. INTRODUCTION

When pattern recognition function and depth learning using a neural network performed, lack of arrangement information by the convolution layer and high-speed processing in convolution and filter processing are necessary. Feature extraction consisting of preprocessing of target data, convolution layer, pool layer, normalisation layer, calculation by feature sharpening layer, etc. is a heavy load. The way to speed up this process more efficiently is worth extending the scope of the application and reducing the burden on the hardware. One of the applications is to a management of medical information. For example, the quality of advanced medical care is support by patient's

objective medical data. For this reason, hospitals possess various medical measurement devices. At the same time, the medical team must strictly manage the measurement results as patient's data. However now, its management is not perfect. In reality, the medical team sometimes mistake on the patient's medical data. Of course, methods to prevent medical malpractice have developed, however, the rate of medical mismanagement has not reduced. Therefore, a safer fail-safe system is essential in this field. On the other hand, biometrics is also a significant technology to maintain a more stable global society. Under these circumstances, the primary methods of these techniques have been developed by many research groups [1] - [9]. The primary purpose of this study is to find an efficient and realistic feature emphasis method for these technologies. Furthermore, for verily the study, this study proposes an individual identification method that uses medical data itself as identification information as part of research on medical malpractice prevention technology. Specifically, individually, the medical evidence controlled by the label or header of the data. In the unlikely event that the data name or header disappears, it is tough to distinguish the medical data. Here, we assumed that all medical data encompassed individual characteristics, and aim at verification of technology to identify medical data by utilizing the unique features contained therein. By applying this method, even if the nature of medical data is lost or exchanged, it is possible to doubt the medical error mechanically. In this study, correctly, as the biometric information, the centre of gravity fluctuation in walking was selected as an example of data. However, since the fundamental analysis was necessary for this preliminary research, in the present study, as the first step, we verified the proposed method by using the swaying of the centre of gravity at the standing position.

II. AUTOMATIC DETECTION SYSTEM FOR MISHANDLING

In many cases, a mistake in handling medical data occurs in an early step. For instance, that happens when a measuring medical data and an inputting individual data by hands into a computer. Therefore, this study aims to establish a technology for to prevent lack of different information and miss exchanging of personal information. Especially, the primary purpose of this study is to find an efficient and realistic feature emphasis method for these technologies. First, this study proposes a new identification method shown in Fig. 1. In this approach, index data obtained from biometric data by using attractors and neural networks [1], [6], [9]. After this, the index data used for the

detection of a medical error. For example, as in Fig. 2, if personal information about the medical data exchanged for other individual information, we can detect the medical error by using a database that has prepared in advance. In the following contents, this paper is experimentally verifying an effectiveness of the new identification method.

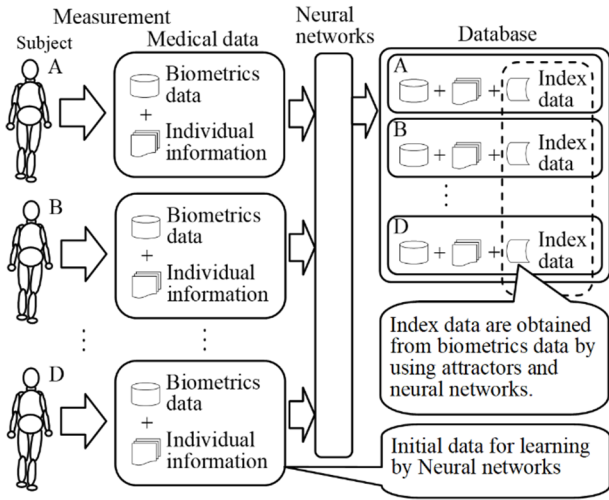


Fig. 1. Feature extraction system using attractors and neural networks

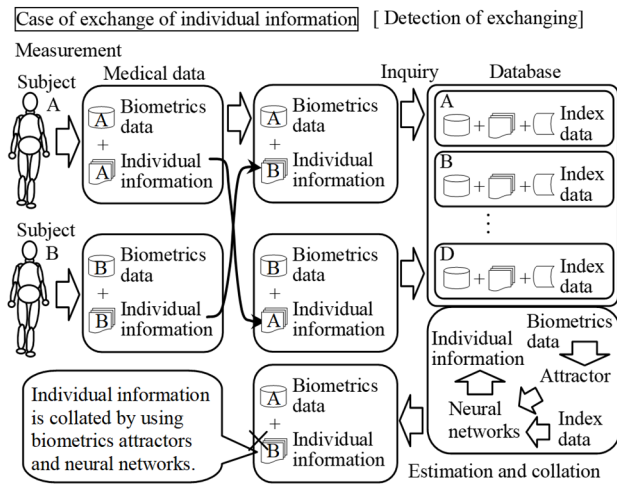


Fig. 2. Detection system on miss exchanging of individual information

III. MEASURING DEVICE OF BODY-SWAY

The stance condition measurement method hitherto has been using to appraise the phase of a physical handicap patients. In this study, we are improved upon the technique to measure the body sway of healthy persons in the standing condition [1], [2], [7]. Figure 3 shows the measuring device and the system. Also, the procedure of experiments shown in Fig. 4. The test subject is keeping standing posture on the measurement instrument for body sway. In the following, we have described the experimental cooperators as "test subject" or "person". At the time, the display device can indicate a square mark of 1cm on the left or right side of a screen. The test subject keeps a standing posture by the left leg or right leg according to the orders from a display. In the experiments, test subjects are requested to keep

standing position by their left leg or right leg alternately for five seconds each, for a total of twenty seconds. We define this type of measurement as "measurement I" in this study. The measurement instrument measures the sway of centre of gravity r_G along the x -axis during this measurement. Moreover, this output signal is digitised by an Analog/Digital converter and sent to a computer. Also, in this study, "measurement I" is repeated fifteen times at sixty seconds intervals, and these measures collectively defined to as "measurement II". We performed "measurement II" at two-hour intervals from 10 a.m. to 4 p.m. in the experiments.

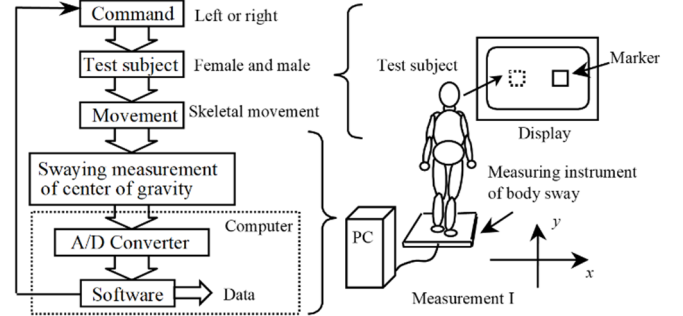


Fig. 3. Measuring system

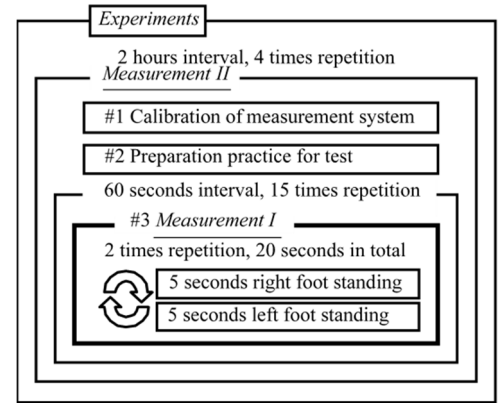


Fig. 4. Procedure of experiments

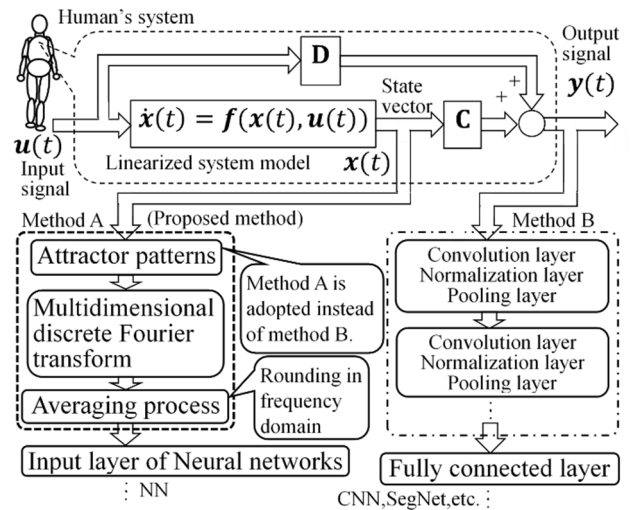


Fig. 5. Concept of proposed feature extraction

IV. ALGORITHM AND BASIC CONCEPTS FOR PREPROCESSING

In this study, regardless of the linearity and nonlinearity of the system, it is assumed that the system that generates phenomena has a structure and can describe mathematically. Also, it is expected that the response of the system changes due to the difference in construction and the variation in parameters. Furthermore, we assume that the reaction generated by reconstructing the internal state of the system. Figure 5 shows the basic structure of the system and the concept of feature extraction. In this, the input $u(\kappa)$ and the output $y(\kappa)$ of the order of discrete representation are known, and the system $f(x(\kappa), u(\kappa)) = Px(\kappa) + Qu(\kappa)$ can approximate. Where, $x(\kappa)$ is a state vector, P is a discrete system matrix of $(\eta \times \eta)$, Q is a discrete system input matrix, and κ is an integer such $\kappa = 0, 1, 2, \dots, \lambda$. Also, assume that the output $y(\kappa)$ is $y(\kappa) = Cx(\kappa) + Du(\kappa)$, matrix $D = 0$. Where matrix D is the direct transmission matrix. At this time, if the system is observable, the state vector $x(\kappa)$ can be estimated from input $u(\kappa)$ and output $y(\kappa)$. In the case of a controllable real control system in general, controllable and observable are most examples. In other words, suppose that you can calculate the state $x(0)$ at $\kappa=0$ by observing the measurable output $y(\kappa)$ with the time interval $0 \leq \kappa T \leq \lambda T$. Where T is the discretisation time. In this case, since the inverse matrix exists in the observability matrix U_o , the Eq. (1) holds.

$$x(0) = U_o^{-1} \{M_y(\lambda) - M_1(\lambda)M_u(\lambda)\} \quad (1)$$

Where, $M_y(\lambda) = [y(0) \ y(1) \ y(2) \ \dots \ y(\lambda-1)]^T$,

$M_u(\lambda) = [u(0) \ u(1) \ u(2) \ \dots \ u(\lambda-1)]^T$,

$$M_1(\lambda) = \begin{bmatrix} 0 & 0 & 0 & \dots & 0 & 0 \\ CQ & 0 & 0 & \dots & 0 & 0 \\ CPQ & CQ & 0 & & \vdots & \vdots \\ CP^2Q & CPQ & CQ & & \vdots & \vdots \\ \vdots & \vdots & \vdots & & 0 & 0 \\ CP^{\eta-2}Q & CP^{\eta-3}Q & CP^{\eta-4}Q & \dots & CQ & 0 \end{bmatrix}$$

By using Eq. (1), the λ th state $x(\lambda)$ is Eq. (2).

$$x(\lambda) = P^\lambda U_o^{-1} M_y(\lambda) + U_c I_a(\lambda) M_u(\lambda) - P^\lambda M_1(\lambda) M_u(\lambda) \quad (2)$$

Where U_c is a controllability matrix. I_a is an anti-diagonal matrix that size of each diagonal element is one. Also, when the system includes nonlinearity, it can deal with by limiting the application range to a slight disturbance. Although the above explanation is a story of a discrete system, by making the discretization time T extremely short, this discussion is effective also in a continuous system. Under the above conditions, if the state variable is defined as $x_1(t) = y(t)$, $x_2(t) = dy(t)/dt$, \dots , $x_\eta = d^{(\lambda-1)}y(t)/dt^{(\lambda-1)}$, there is a high correlation between the state variable $x(t)$ and the matrices P , Q , C of the function f . Moreover, considering the state space composed of the state variables $x_1(t)$, $x_2(t)$, \dots , $x_\eta(t)$, the locus of the end point of the state vector becomes the attractor $C_a(M_x)$, in which convert to a specific orbit, where $M_x(\lambda) = [x(0) \ x(1) \ x(2) \ \dots \ x(\lambda-1)]^T$. This attractor $C_a(M_x)$ can encompass the characteristic features of the system and its change depends on changes in system structure or

control parameters can be inferred. Next, in this study, as a first step of extracting features, multi-dimensional spatial discrete Fourier transform is performed on attractor patterns, and geometric features of attractor patterns replaced with frequency spectra. In general, the frequency spectrum recognises as a method of expressing the characteristics of a signal. On the other hand, the resolution of the frequency spectrum at this stage is high, and it is not suitable as an input to the neural network as it is. Therefore, in this study, this frequency spectrum is partitioned in the frequency domain, and the value in the region rounded to the average as the representative value. As is also known in voice recognition, even if rounding performed in the frequency domain, the whole image of the frequency spectrum does not change significantly. Thus, without altering the original signal information much, It can be input to the input layer of the networks. In this study, binding of features is performed by attractors, and multidimensional complex discrete Fourier transform and averaging processing are introduced instead of convolution layer and the filter layer. This method combining the attractor pattern and the multifaceted, complex discrete Fourier transform can shorten the processing time while compensating for the disadvantage that the arrangement information becomes ambiguous in the convolution layer and the filter layer of CNN (Convolutional Neural Network). In this study, to verify this method, assuming that the order of the system that generates the output signal $y(t)$ is $\eta=2$ with the centre of gravity fluctuation in the standing posture described in the previous section as the theme, preprocessing for feature extraction. It also shows that this attempt may be helpful in preventing malpractice.

V. ATTRACTOR PATTERNS OF SWAY OF CENTER OF GRAVITY

In a point of view of control engineering, the sway of centre of gravity can regard as one of information that derives from characteristics of the posture regulation system [1], [2]. Although we cannot represent the actual position control system as a perfect model, simplifying some feature makes it possible to define a functional model by using some ordinary differential equations [3], [4], [5]. Furthermore, we can eliminate chaotic factors from these simplified differential equations. If the form of differential equations is temporally invariant and stable, the attractors absorbed into the characteristic point by the states obtained from the differential equations. Thus, the attractors are invariant. The attractor has a high correlation with the features of the posture control system. In short, we can regard that the attractor is one-to-one correspondence with the characteristics of the position control system. However, because chaotic mechanisms in our body are thought to contain within actual posture regulation systems, the attractors sway around that point according to tiny differences in initial values and condition of persons. From this causality, it is possible to estimate temporal changes in the structure of the system, by observing the variations in the attractor pattern of the posture regulation system. Therefore, we calculated the position r_G and the velocity of the centre of gravity by using the data obtained in "measurement I". Furthermore, we investigated the changes in the locus of these state variables within state space. First, because the data r_G of the centre of gravity has high-frequency noise, we reduce the noise by using a digital low pass filter. The digital low-pass filter has a damping factor of 0.707, and a cut-

off frequency of 30Hz, and a sampling rate of 500Hz. Finally, we plotted the data on an r_G-v phase plane. Figure 6 shows the pattern of attractor obtained by executing "measurement I" at 12 a.m. These "measurement I" was performed at 10 a.m., 2 p.m., and 4 p.m. in the same way at midday. Figure 6(a) shows typical results for "measurement I", which obtained at 10 a.m. with a 23 years old female test subject "A". Figure 6(b) shows typical an attractor pattern of subject "B" (36-year-old male). This attractor pattern starts from a neighbourhood of origin and obeys orders on the screen. Approximately, the attractor pattern changes between the left foot position $(-0.14, 0)$ and the right foot position $(0.12, 0)$. It can also see that the centre of gravity of test subject moves with a slight swaying at close to the left/right foot positions. Thus, Fig. 6(a) and Fig. 6(b) indicated the almost same trend. However, person A and B differ in point of view of the overall sway intensity and the shape of attractors. We focused on this difference and considered an extraction method that emphasises features of subjects using objective approach. Therefore, we propose the following method for automatically differentiating from the attractor patterns the characteristics of test subjects.

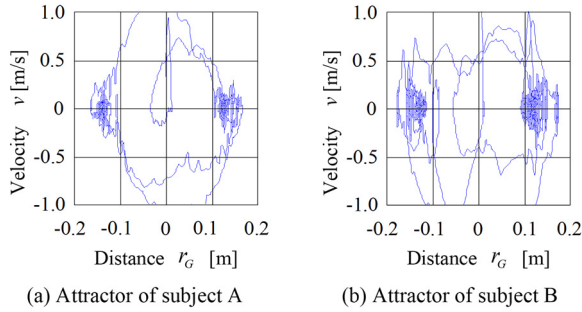


Fig. 6. Typical examples of attractor by measurement I at 12 a.m.

VI. PREPROCESSING FOR FEATURE EXTRACTION FROM ATTRACTORS

Figure 7 shows typical representative examples of attractor patterns in experiments. Although it is subjective, according to the figure, we can find the difference between patterns (a) and patterns (b). We aim to extract this difference objectively. Thus we propose a new algorithm in the following. Figure 8 shows an algorithm of the feature extraction based on attractor patterns in experiments. A Two-Dimensional Fourier transformation applied to the attractor data images to extract the features. It is possible to analyse the power spectrum of frequency component contained in attractor data. In this study, we consider that this signal processing is valid because the frequency components of a signal include the information on dynamic characteristics of a system. In other words, it will be considered to contain some information on a structure and coefficients for the mathematical model of systems. At first, we plot the attractor pattern on data to the r_G-v phase plane. Moreover, the graph captures as an image and assign the shading of the image $F_d(i,j)$ as 200×200 pixels to a variable. Next, the pixel data $F_d(i,j)$ process by a two-dimensional complex discrete Fourier transformation (DFT). In short, this processing is defined in the form of $F_{td}(i,j)$ as shown in Eq. (3).

$$F_{td}(i,j) = DFT_i(DFT_j(F_d(i,j))) \quad (3)$$

Where i and j are integers in the range $1 \leq i \leq 200$ and $1 \leq j \leq 200$. Equation (3) means that a one-dimensional discrete Fourier transformation calculates for each column of matrix $F_d(i,j)$, and Moreover, these results transform for each row. Figure 9 shows representative typical examples of obtained from the attractors of Fig. 6. Next, we define a new matrix $F_{cd}(k,l)$ obtained by select a 100×100 domain that frequencies are greater than or equal to zero in $F_{td}(i,j)$.

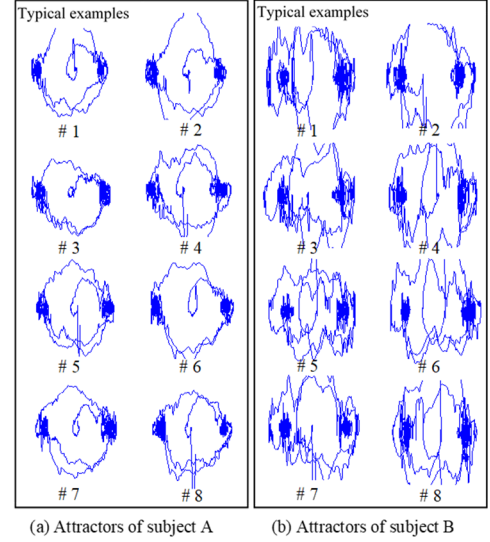


Fig. 7. Comparison of attractor patterns between subject A and subject B

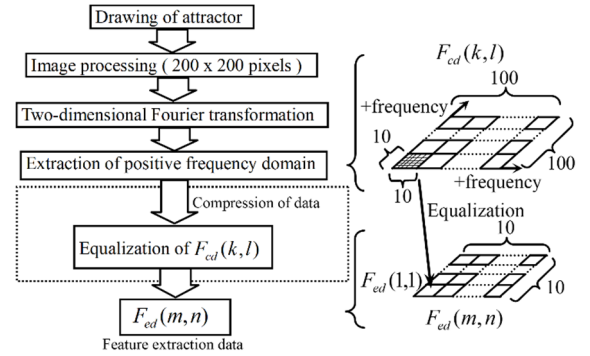


Fig. 8. Algorithm for feature extraction

Furthermore, the region of $F_{cd}(k,l)$ classified into total 100 groups by dividing $F_{cd}(k,l)$ into groups of 10 elements in the row and column directions. The average value of the power spectrums in each cluster is calculated by Eq. (4), and the results stored in a 10×10 matrix $F_{cd}(m,n)$. Where, $k = i - 100$ (i is an integer in the range $101 \leq i \leq 200$) and $l = j - 100$ (j is an integer in the range $101 \leq j \leq 200$).

$$F_{cd}(m,n) = \frac{1}{100} \sum_{k=10(m-1)}^{10m} \left\{ \sum_{l=10(n-1)}^{10n} F_{cd}(k,l) \right\} \quad (4)$$

These steps described in the above can convert a part of the information in attractor into a matrix of 100 elements. Figure 10(a) shows a result obtained from the attractor in Fig. 6(a). That figure is a three-dimensional expression of values of the 10×10 matrix stored in $F_{cd}(m,n)$. Where the height direction shows

power spectrum values, the depth direction shows rows of the matrix, and the width direction shows columns of the matrix. In Fig. 10(a), the bigger column number and row number means to be higher frequency components.

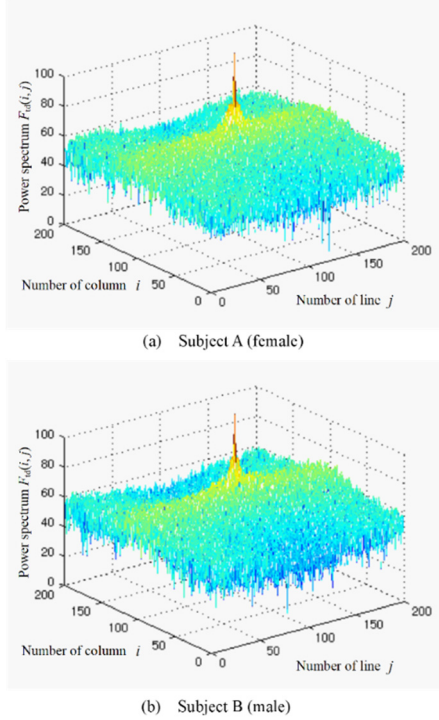


Fig. 9. $F_{id}(i, j)$ result obtained from attractors of Fig. 6

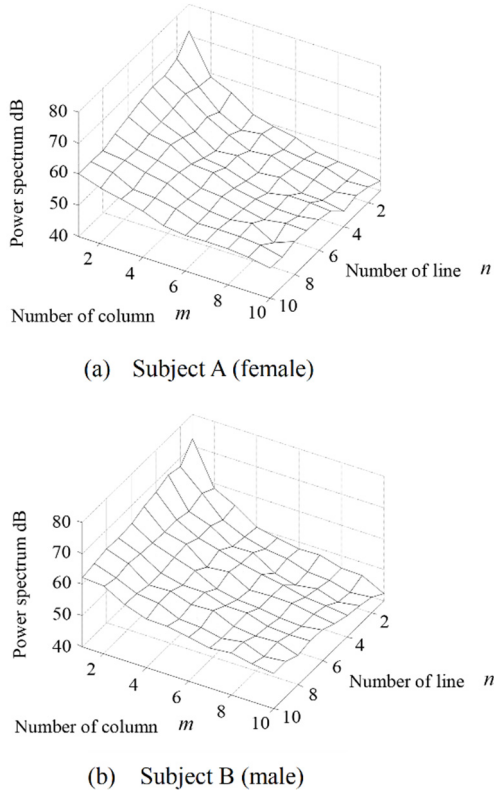


Fig. 10. $F_{cd}(m, n)$ result obtained from attractors of Fig. 6

Similarly, Fig. 10(b) shows a result obtained from the attractor in Fig. 6(b). Although Fig. 10(a) and (b) have fundamentally almost curved surface shapes, the component in the neighbourhood of $F_{cd}(10, 4)$ of test subject B is approximately 10 dB larger than test subject A. If there is a correlation between the features of test subjects and these curved surface profiles, it is possible to objectively estimate the state of test subject's functions from the information of curved surface profiles.

VII. IDENTIFICATION BY USING NEURAL NETWORKS

Neural networks are known to be suitable for recognising images and sound. Where, neural network learned the correlation between test subjects and curved surface profiles by using the $F_{cd}(m, n)$ data for 12 a.m. on test subjects A and B. Finally, we examined to identify the test subjects from any new attractor data. Figure 11 shows the structure of the neural network. These neural networks are a hierarchical structure comprising an input layer, a hidden layer, and an output layer. The learning algorithm in this experiments is an error-back-propagation method. The input layer includes 100 units. The Hidden layer includes 30 units. The output layer includes two units. For instance, we want to increase the number of learning patterns enhance the number of units in the output layer. In that case, it must also improve the number of units in the hidden layer in conjunction with this extension.

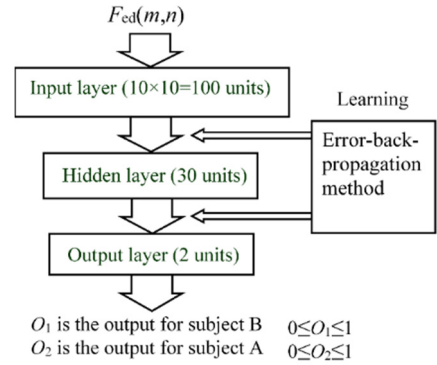


Fig. 11. Structure of neural networks

A. Estimation Results

We identified test subjects A and B by using fifteen sets of measured value started from 10 a.m. Those results show in Fig. 12. Because in this study subjects were two persons, the number of neurone in a final layer set up two neurone units " O_1 " (for person B) and " O_2 " (for person A). When the $F_{cd}(m, n)$ values of person B input, as the values to be calculated accordingly, the result of output " O_1 " is indicated in this figure. The big dot symbols indicate the values of output unit " O_2 " for person A in a neural network, and the square shows the values of output unit " O_1 " for person B. According to the calculated results, the standard deviation and average of the values of output neurone for person A are 0.111 and 0.814. Similarly, the values of person B are 0.074 and 0.806. The vertical axis shows the values of output units corresponding to each test subject and the horizontal axis indicates the number of measurements. In this figure, output values closer to 1 for person A and B mean that inferences were successful. Furthermore, measurements where results are 0.5 or less, indicate that inferences were incorrectness

(the shaded parts of Fig.12). For instance, the first measurement of person A in the figure shows a result of 0.522, which means that even if inference was favourable, the margin of accuracy was not very large. In short, this result of estimation suggests a possibility that recognises person A as person B. However, according to all inference results in this figure, test subjects A and B identified with a success rate 100%. Strictly speaking, if except for the first value of test subject A, the success rate is 93.3%. Where the recognition the success rate is defined as a value obtained by dividing the amount of achievement by the total number. This inference result supports that there is a significant interrelation between output values of neural networks and posture control behaviour. In this study, we have confirmed that the neural network enables it possible to identify the person by using the $F_{ed}(m,n)$ values.

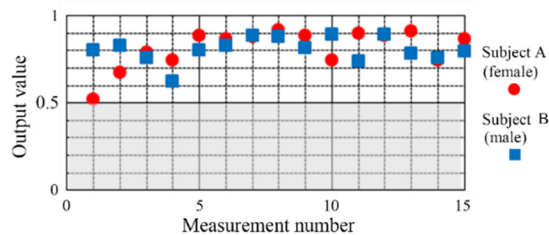


Fig. 12. Estimated result at 12 a.m. Subject A: average is 0.814, standard deviation is 0.111. Subject B: average is 0.806, standard deviation is 0.074.

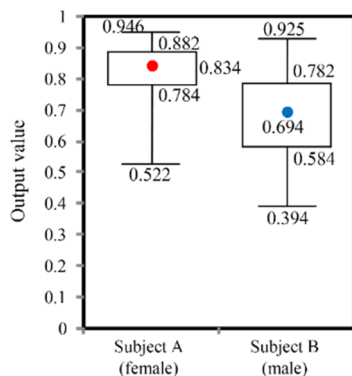


Fig. 13. Estimation results by average values of the output of neural networks. Some performed "measurement I" is 60 times per one subject.

Also, Fig.13 shows distributions of mean value on individuals A and B. This is a box-and-whisker plot when measured 60 times. According to this figure, the average value of person A is 0.834. The maximum value is 0.946. The minimum value is 0.522. In this case, the new identification method is effective to such data for person A because the position and size of the box are proper. Similarly, the new identification method is effective to such data for person B. However, the distribution of "test subject A" and the "test subject B" are different. Thus, it is concerned that the new identification method has specificity for data.

VIII. CONCLUSIONS

In this study, we propose a method of feature extraction by combining attractor pattern, frequency analysis and neural network, with the theme of fluctuation of the centre of gravity of standing posture which is one of the whole body movements of humans, and verified its effectiveness. Furthermore, using this

method, we propose that there is a possibility of restoring that information even if the association between the subject's report and the medical data lost. It can be applied to studies to prevent malpractice. The following knowledge obtained in this study. (1) Attractor analysis using the state quantities of the control system is possible as a method of extracting features of the body sway. (2) To automatically distinguish between differences in biometric information, preprocessing that combines attractor patterns and frequency analysis is efficient, which is valid for subsequent recognition in neural networks.

Since the signal of interest in this study was a one-dimensional physical quantity which varies with time, there is a possibility that it can apply to electrocardiogram waveforms, electroencephalograms and body movements. However, an application of this study is limited, because Number of subjects included in the study is insufficient. Also, it is necessary to control changes in image resolution due to the scaling for attractor patterns. Furthermore, it is required to increase the number of intermediate layers and the number of neurons in the neural network to improve the discrimination ability. The future works are to classify the information of many subjects and to verify the signal generation sources with different physical models.

ACKNOWLEDGMENT

The author is grateful to every one of the test subjects and Prof. M. Shiraishi. This work was supported by Japan Society for the Promotion of Science (JSPS) KAKENHI Grant-in-Aid for Scientific Research (C), Grant Number JP16K06205, 2017.

REFERENCES

- [1] M. Shiraishi, H. Watanabe, Pneumatic Assist Device for Gait Restoration, Trans. ASME, J. Dyn. Syst., Meas., 1996, 118.
- [2] M. Kikuchi, M. Shiraishi, Characteristic Mapping of Human Dynamics and Evaluation of Its Control Performance (1st Report)-Identification of Stance Posture Control System and Its Pole Assignment-, The Japan Society for Precision Engineering, 65, 6, 1999, 840-844, in Japanese.
- [3] B. Tondou, P. Lopez, McKibben artificial muscle robot actuators, IEEE Control System Magazine, 20, 2, 2000, 15-37.
- [4] M. Kikuchi, Effect of finger nerve-musculoskeletal system on medical micromanipulator based on a physiological modelling, International Journal of Modelling and Simulation, Vol. 32, Issue 4, ACTA Press, DOI: 10.2316/Journal.205.2012.4.205-5509, 2012, 221-228.
- [5] M. Kikuchi, M. Shiraishi, Effect of Grasping Musculoskeletal System on Operative Force Feedback Micromanipulator, Proc. of 2004 JUSFA 2004 Japan-USA Symposium on Flexible Automation, Denver, Colorado, July 19-21, 2004, 1-4 of a CD.
- [6] J. D. Enderle, S. M. Blanchard, J. D. Bronzino, Introduction to Biomedical Engineering, Academic Press, 2000, 279-368.
- [7] M. Kikuchi, M. Shiraishi, Characteristic Mapping of Stance Posture Control Systems from a Control Engineering Standpoint, Human-Friendly Mechatronics, Issued by Elsevier Science, 2000, 135-140. Trans. Roy. Soc. London, vol. A247, pp. 529-551, April 1955.
- [8] M. Kikuchi, A Proposal of Neuron Model Capable of Neurite Elongation by NGF Based on Physiological Characteristics, Proceedings of the 29th IASTED International Conference on Modelling, Identification and Control, Austria, 2010, 347-351.
- [9] M. Kikuchi, An Application of Time Delayed Neural Network to Machine Tool Condition Monitoring System, Proceedings of the 30th Meeting of the Institute of Measurement and Automatic Control, July 1991, pp. 609-610.

Feature Analysis for Discrimination of Motor Unit Action Potentials

Thuy T. Pham^{*12}, Diep N. Nguyen¹, Eryk Dutkiewicz¹,
Alistair L. McEwan², and Philip H.W. Leong², Andrew J. Fuglevand³,

¹Faculty of Engineering and IT, University of Technology Sydney, NSW, Australia.

²Department of Electrical and Information Engineering, University of Sydney, NSW, Australia.

³Department of Physiology, University of Arizona, AZ, USA.

Abstract—In electrophysiological signal processing for intramuscular electromyography data (nEMG), single motor unit activity is of great interest. The changes of action potential (MUAP) morphology, motor unit (MU) activation, and recruitment provide the most informative part to study the nature causality in neuromuscular disorders. In practice, for a single nEMG recording, more than one motor unit activities (in the surrounding area of a needle electrode) are usually collected. Such a fact makes the MUAP discrimination that separates single unit activities a crucial task. Most neurology laboratories worldwide still recruit specialists who spend hours to manually or semi-automatically sort MUAPs. From a machine learning perspective, this task is analogous to the clustering-based classification problem in which the number of classes and other class information are unfortunately missing. In this paper, we present a feature analysis strategy to help better utilize unsupervised (i.e., totally automated) methods for MUAP discrimination. To that end, we extract a large pool of features from each MUAP. Then we select the top ranked candidates using clusterability scores as selection criteria. We found spectrograms of wavelet decomposition as a top-ranking feature, highly correlated to the motor unit reference and was more separable than existing features. Using a correlation-based clustering technique, we demonstrate the sorting performance with this feature set. Compared with the reference produced by human experts, our method obtained a comparable result (e.g., equivalent number of classes was found, identical MUAP morphology in each pair of corresponding MU class, and similar histograms of MUs). Taking the manual labels as references, our method got a much higher sensitivity and accuracy than the compared unsupervised sorting method. We obtained a similar result in MUAP classification to the reference.

Index Terms—Spike sorting, feature learning

I. INTRODUCTION

Motor unit activity analysis provides crucial information towards diagnosis and treatment of neuromuscular disorders. In intramuscular electromyography data, when recording small voluntary contractions with a needle electrode, the electrical signal obtained is often a combination of more than one motor unit (MU) from the surrounding area of the needle tip. Therefore, a motor unit action potential (MUAP) consists of several muscle fiber action potentials (MFAPs) within the anatomical MU.

To obtain the changes of MUAP morphology, MU activation, and MU recruitment that yield valuable information, one would require activities from a single MU. Neuropathic conditions occur with decreased recruitment whereas myopathic conditions happen with MUAP morphology changes. As an example, a MUAP examination can confirm myopathic

conditions and identify the differential to find an appropriate biopsy site [1]. For each recording, most neurology laboratories employ experts who spend hours to classify action potentials (“spikes”) using commercial software tools (e.g., Spike2 [2], Cerebus [3]). This de-facto standard practice relies on human-based assessment which is subjective (hence prone to mistake/errors of the expert) and time-consuming. An unsupervised/automated classification method is hence very much desirable.

A spike discrimination procedure involves three basic phases: spike detection, feature extraction, and spike clustering. Spike detection often involves aligning spikes to a common temporal point. The feature extraction phase provides principal information that highlights differences among spikes. Common spike feature extraction algorithms are based on principal component analysis (PCA) [4], the discrete wavelet transform (DWT) [5], or discrete derivatives [6]. A dimensionality reduction step may be used to select only the few best coefficients. In the final phase, spikes are assigned into different MU classes. Existing spike sorting algorithms using distances (e.g., k-means clustering [7][8]), mean shift [9][10]), likelihood (e.g., Bayesian classification (BC) [11]), or super paramagnetic clustering (SPC) [12] have all been proposed.

In the literature of MUAP discrimination, the relevance and clusterability of the above existing features have failed to be addressed. Most previous automated efforts often only yielded excellent performance for subject-dependent settings. We hypothesize that higher correlated and more separable features across classes may improve the classification performance of unsupervised subject-independent MUAP classifiers. We propose to evaluate feature candidates using our voting-based selection approach for the MUAP sorting application. This hybrid selection scheme is a data-driven approach and can compare a comprehensive set of candidates including existing features and novel variants. The strategy has been shown successfully in detecting respiratory artefacts in lung function data [13] and freezing of gait epochs in acceleration data [14]. However, under the context of MUAP sorting, the classification involves an unknown number of class discrimination. In this work, we demonstrate that such feature analysis approach is also applicable to MUAP discrimination. The main contributions of this work are:

- This is the first reported feature analysis approach using clusterability criterion for MUAP sorting in nEMG data.
- The spectrograms of wavelet decomposition is more

*: correspondence thuy.pham@uts.edu.au. Faculty of Engineering and IT, University of Technology Sydney, NSW, Australia

relevant and discriminative than existing features.

- The accuracy of our proposed is comparable with the manual reference.

The rest of the paper is as follows. The method details including data collection, the feature analysis process, sorting algorithms, and performance metrics are presented in Section II. The obtained results are reported and discussed in Section III and IV. Conclusion is drawn in Section V.

II. METHODS

A. Data Collection

1) *Physiologically-Based Synthetic Data*: We used the nEMG simulation algorithm by Hamilton-Wright and Stashuk [15] for our development phase. Note that the algorithm was shown to produce nEMG data consistent with those acquired from real muscle (the developed muscle) [15]. We run the simulator on a Microsoft Windows personal computer for a concentric electrode during a 10% contraction maximal voluntary (*MVC*). Figure 1 illustrates a synthetic epoch of 100 *ms*. The voltage range is $-516.05 \rightarrow 1019.84 \mu V$. The full settings used for the experiments can be found in [15].

2) *Human Recorded Data*: We also collected a real data set recording from a healthy young male at the Fuglevand Laboratory [16] using a rack-mounted electro-physiological recording system CED [2]. Data were sampled at 55.5 *kHz*. The experiment settings for force used to create nEMG data was: time interval of 0.1 *ms* for force, scale of 0.0023, unit of “*N*”. We used the concentric needle electrode. A neurologist manually provided labels of MUAP appearances together with its associated MU. Note that though most of the manual labeling procedure was aided by a commercial software tool (Spike2 [2]), the human operator is still needed for the final template matching and adjusting. These labels are referred to as “reference” during our evaluation.

B. Feature Analysis

1) *Selection Scheme*: Given a large exploratory feature pool, a voting process with different selection levels and criteria (saliency, robustness, and accuracy) is used to figure out the best feature. After each level, selected candidates become more favourable. Specifically, the first round suggests the most salient and discriminative subset of features using mutual information (MI) and separability calculated using the Euclidean distance (DIS). These features are evaluated against the reference for detection performance assessment.

Selection criteria, i.e., MI and DIS are calculated as follows. Let X be a discrete random variable $X \in \mathbb{X}$ and C be a target variable ($c \in \mathbb{C}$, class label set). The entropy $H_b(X)$ of X measures its uncertainty [17].

$$H_b(X) \stackrel{\text{def}}{=} - \sum_{x \in \mathbb{X}} p(x) \log_b p(x)$$

where b is the base of the logarithm. In this work, $b = 2$, and hence entropy will be measured in bits.

Let C be a target variable ($c \in \mathbb{C}$, class label set). The conditional entropy of X given C is defined by:

$$H(X|C) = - \sum_{c \in \mathbb{C}} p(c) \sum_{x \in \mathbb{X}} p(x|c) \log p(x|c).$$

The mutual information [17] between X and C , $MI(X;C)$, measures the amount of information “shared” by X and C . MI is then interpreted as the relevance of X and C :

$$I(X;C) = \sum_{x \in \mathbb{X}} \sum_{c \in \mathbb{C}} p(xc) \log \frac{p(xc)}{p(x)p(c)}$$

To assess discrimination of features, relevant candidates are considered having nearest instances (by Euclidean distances) of same class closer and having nearest ones of other classes more far apart. The weighting of these distances, called DIS, is calculated using the *RELIEF* algorithm [18] (as similarly implemented in [19] or built-in packages of MATLAB, The MathWorks Inc., Natick, MA, 2000).

2) *Feature Pool*: We extracted twelve groups of features in both time and frequency domains (Table I). In the table, existing features include amplitude range information of EMG data, DWT, top ten selected by KS tests [20] of DWT, top ten percentage selected by ICA or PCA. Our new feature candidates are singular value decomposition (SVD) of spectral analysis and spectrograms of raw amplitude data or DWT transformed data.

TABLE I: List of candidates in the EMG feature pool.

Group ID	Domain	Description	New or not?*	Feature ID
1	Time	Maximum amplitude of EMG	No	1
2	Time	Minimum amplitude of EMG	No	2
3	Time	Range amplitude of EMG	No	3
4	Frequency	DWT level d3	No	4-128
5	Frequency	DWT level d4	No	129-253
6	Frequency	DWT level a3	No	254-378
7	Frequency	SVD of spectral analysis	Yes	379-386
8	Time	ICA (ten percentage)	No	387-398
9	Time	PCA (ten percentage)	No	399-410
10	Frequency	KS test of DWT (top ten coefficients)	No	411-420
11	Frequency	Spectrograms of raw amplitude	Yes	421-1065
12	Frequency	Spectrograms of DWT	Yes	1066-1710

Several methods used for the *new* feature extraction (i.e., they have not been proposed for nEMG spike sorting) are described as follows. Discrete wavelet analysis that represents signals in both frequency and time is a very useful tool in the neuroscience field [21]. Transient differences in high frequency features (sharp edges and steep leading or trailing slopes) and/or in low frequency features (duration of the repolarization phase) can present the morphology of spikes. In this work, MUAPs are first decomposed into wavelet coefficients using the DWT method [5]. These coefficients represent differences among spikes based on the quantification of energy found in specific frequency bands at specific time locations. We implemented a 4-level decomposition and *Haar* window using built-in functions of MATLAB (The MathWorks Inc., Natick, MA, 2000).

Due to the multi-modal distribution of coefficients [22], we rank these candidates by scores calculated by deviation from normality, using a modification of Kolmogorov-

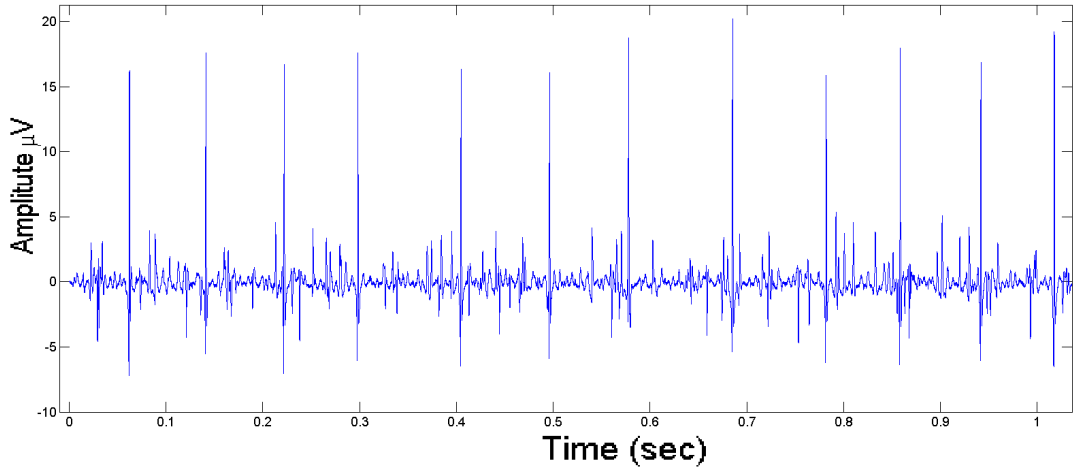


Fig. 1: Example of a 100-ms epoch of the simulated nEMG.

Smirnov (KS) test [20]. Let X be a data set, the score is $\max(|F(x)G(x)|)$ where $F(x)$ is the cumulative distribution function of X and $G(x)$ is a Gaussian cumulative distribution function with the same mean and variance. To minimize the effect of overlapping spikes, for each coefficient, only values within three standard deviations (both directions) are considered [22]. In order to create a compressed input to the sorting process, only the ten largest score candidates are selected to best separate spikes.

Finally, these selected coefficients are transformed to a series of spectral snapshots (spectrograms) using the short Fourier transform (STFT [23]). Specifically, let v be the wavelet feature of a spike. A Hamming window is used with STFT to transform v into an image of spectrogram. Hence, *distance* between spikes are the correlation coefficients between these images.

C. Automated Spike Sorter

1) *Preprocessing*: Intramuscular data is corrupted by spike-like correlated noise. Thus, we need to make data points statistically independent (“pre-whitening”). A practical approach employs a linear prediction filter [24] to whiten the input signal itself before we extract any MUAP. In this work, we use a third-order forward linear predictor (FIR filter) that predicts the current value of the real-valued original data based on past three samples [24]. Using timing labels from the reference, we extract the spike set together with labels of MU classes. All spikes are extracted with the same window size of 8 ms.

To focus on sorting evaluation, overlapping spikes (i.e., have more than two MU in the same window) relate more to spike detection than sorting algorithms. Thus, we removed overlapping spikes with small delay by detecting multiple peaks within a spike window. For overlaps without delay (i.e., they may look like the firing of a new neuron), we do a re-sorting step as described in the post-preprocessing section.

2) *x-Class Sorter*: After feature extraction steps, based on MUAP morphology, the correlation between spikes is used as the similarity measure for an number x -class sorting application [25], [26] where x is unknown. Instead of using the Euclidean distance metric, to account for electrode drift and

normalized values that suit for subject-independent settings, we proposed to use the correlation metric that ranges from 0 to 1.

Let I_X and I_Y be two feature vectors of MUAP X and MUAP Y , respectively. $r_{X,Y}$ is the correlation between two feature vectors of X and Y $r_{X,Y} = \frac{\mathcal{C}\{X,Y\}}{\sigma_X \sigma_Y}$ where $r_{X,Y}$ is the correlation coefficient between MUAP X and MUAP Y . $\mathcal{C}\{X,Y\}$ is the covariance of two feature vectors X and Y . σ_X and σ_Y are the variances of X and Y , respectively. The class assignment variable of X is defined by the correlation based sorting scheme. The sorter starts with a single class contains all spikes having high correlation $r_{X,Y}$ with the initial spike given a desired threshold level (e.g., 0.9). Then the sorter stops when the unsorted pool of remaining spikes is empty.

3) *Post-processing*: Because the firing behaviour of an individual MU relates to its recruitment threshold [27] [28], the size of a valid cluster corresponding to a MU should exceed a parameter. According to the recruitment threshold assignment derived from the work of Fuglevand [29]) and popular settings found in the literature, we set this parameter to 40. All clusters with size smaller than 40 were merged into a group, called *catch-all* class. We assume that these small clusters may associate with overlapping spikes without delay. To assign the labels for clusters (or individual spike if that is the catch-all cluster), we measure the correlation between the mean waveform of the cluster and the one of the reference group. A label is chosen if the match has the highest correlation score.

D. Reference Works

The objective reference clustering results are available for the synthetic data as the simulator is controlled during data generation. However, this is usually not available for the recorded data. Ideally the reference could be derived from simultaneous intra-cellular recording, but availability of such data is limited. The most common practice in physiology laboratories involves using commercial software (e.g., *Spike2* in our work) and manual checking by an (human) operator. This approach was used to obtain the reference in this work for real recordings.

We also compare our proposed method with a relevant work using the DWT extraction and super paramagnetic clustering (SPC) [12]. We applied settings for the SPC method as recommended in [30]. Specifically there were $q = 20$ states, $K = 11$ nearest neighbours, and $N = 500$ iterations for clustering. The range of temperature was from 0 to 0.201 in steps of 0.01. The implementation was provided by the authors of [12] (MATLAB packages, The MathWorks Inc., Natick, MA, 2000) .

E. Performance Metrics

Performance metrics for a multi-class classification task are derived from the confusion matrix. Let M be the confusion matrix of sorting outcome. The successful predicted events (*True*) for a class are on the diagonal of M . All other members of M are incorrectly predicted events (*False*). Let M_{ij} denote the number of test outcomes (i.e., *ground truth* labels, Ground_i) of class i , that were predicted as class j , Predicted_j . The successful predicted events (*True*) for class i , denoted T_{ii} , are on the diagonal of M . All other members of M are incorrectly predicted events (*False*), denoted F_{ij} where $i \neq j$.

$$M = \begin{pmatrix} \text{Predicted}_1 & \dots & \text{Predicted}_i & \dots & \text{Predicted}_C \\ T_{11} & \dots & F_{1i} & \dots & F_{1C} \\ \vdots & \ddots & \vdots & \dots & \vdots \\ F_{i1} & \dots & T_{ii} & \dots & F_{iC} \\ \vdots & \dots & \vdots & \ddots & \vdots \\ F_{C1} & \dots & F_{Ci} & \dots & T_{CC} \end{pmatrix} \begin{matrix} \text{Ground}_1 \\ \vdots \\ \text{Ground}_i \\ \vdots \\ \text{Ground}_C \end{matrix} \quad (1)$$

The sensitivity and positive predictive value (PPV) of class i , Sen_i and PPV_i , are defined as follows.

$$\text{Sen}_i = \frac{T_{ii}}{T_{ii} + \sum_{j \neq i} F_{ij}} \quad (2)$$

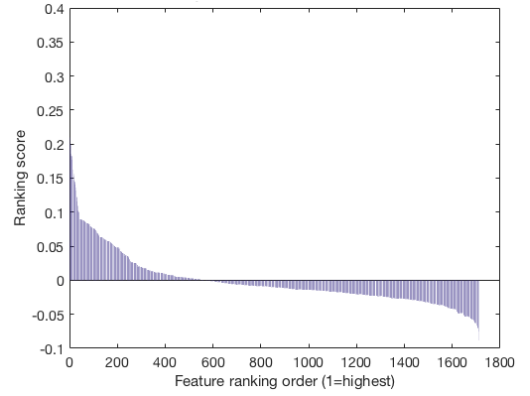
$$\text{PPV}_i = \frac{T_{ii}}{T_{ii} + \sum_{j \neq i} F_{ji}} \quad (3)$$

III. RESULTS

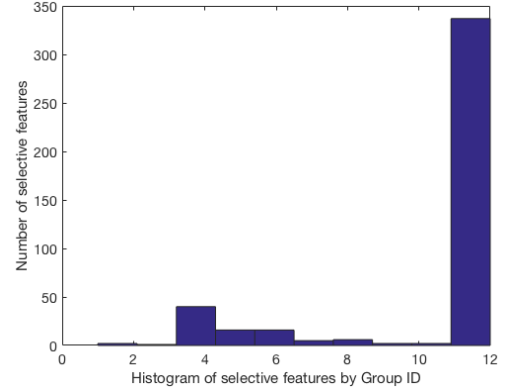
A. Selective Features

Ranking over the entire exploratory pool, each feature candidate was found with a ranking score by aforementioned saliency criteria (Fig. 2; sorted from high to low scores). The higher saliency score indicated the higher ranking order. Among the top quarter (i.e., highest 25% ranking) of the pool, the distribution of feature groups (Fig. 2b) shows that the list includes DWT and Spectrograms of DWT coefficient features (Table I).

As can be seen, scores dropped quickly outside of the top 25 percent candidates by DIS criterion and only after 80 percent candidates by the MI score. We found that, by MI criterion, except for the single feature of Group 1, all other members of the top 25 percent belong to Group 12. Meanwhile, by DIS criterion, though the top 25 percent includes several groups, Group 12 still dominates the high score area. Hence, we proposed to use the feature set Group 12 for the next evaluation in terms of sorting performance.



(a) Ranking of the entire feature pool.



(b) The histogram of the top 25 percent candidates.

Fig. 2: Example of feature ranking by DIS criterion. (a) Ranking scores for the entire feature pool. Vertical: saliency scores; Horizontal: ranking order (highest = 1, lowest = 1710). (b) The histogram of the top 25 percent highest-score candidates by feature groups (Table I).

B. Sorting Performance

1) *Synthetic Data*: After preprocessing, spike sets were prepared for the sorting stage as in Table II. In the reference set, the MU1 class has much larger amplitude range than other four classes. Classes MU2-5 have only slight difference in the waveforms. Our sorter produced five clusters that match with five reference classes. After assigning labels, the histograms were compared with the reference histogram (Fig. 3). In terms of the confusion matrix, the general classification accuracy and class-wise sensitivities as well as predictivities are reported in Table III.

TABLE II: Spike set inputs. Class proportions are in order of the MU names in the labels.

	Synthetic data	Recorded data
Number of spikes	1230	1220
Number of classes	5	3
Class proportion	336:269:226:207:192	440:483:535

2) *Recorded Data*: Table IV depicts the distribution of spikes in large clusters corresponding to the reference classes from the recorded dataset. Both automatic clustering methods had about 19% *catch-all* spikes. There were three reference classes. While the amplitude range of spikes in MU1 and

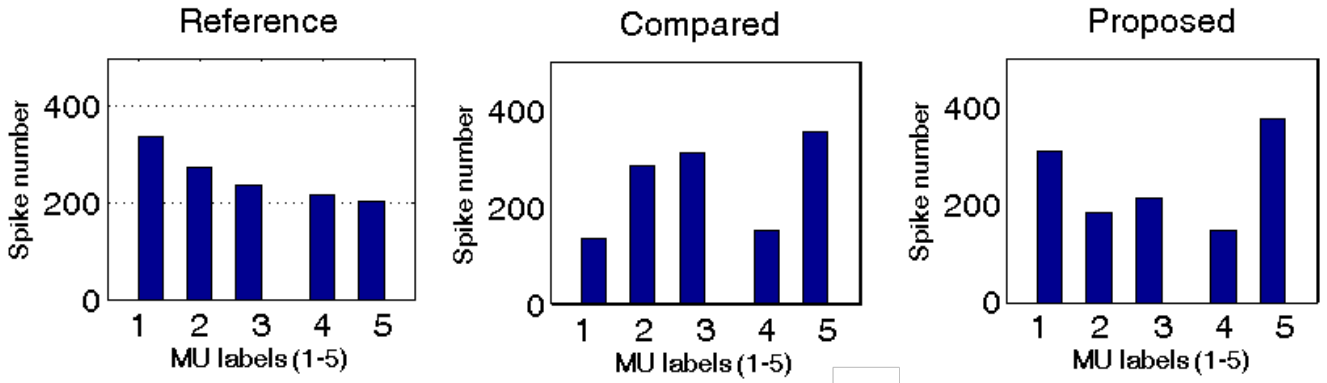


Fig. 3: Agreement in histograms of automatic methods against the reference for synthetic data.

TABLE III: Synthetic data MUAP sorting comparisons between automatic methods and the reference. Accuracy measures (in %) use simulation settings as reference. True/False are MU matching or not with the reference labels.

Metrics	Class name	Include catch-all		Not include catch-all	
		SPC-based	Our method	SPC-based	Our method
Sensitivity	MU1	39.3	92.5	100.0	100.0
	MU2	85.1	67.6	100.0	98.4
	MU3	74.7	75.2	98.8	98.3
	MU4	71.9	69.5	99.3	88.9
	MU5	19.3	88.0	0	72.9
PPV	MU1	100.0	100.0	100.0	100.0
	MU2	81.2	98.9	98.2	98.9
	MU3	54.5	80.2	54.5	80.2
	MU4	98.6	97.9	54.6	97.9
	MU5	10.4	44.9	0	100.0
Average accuracy		58.2	79.3	81.9	94.8

MU2 are $\pm 0.5 \mu V$, MU3 ranges much larger ($\pm 1 \mu V$). Sorting performance for each MU and the general accuracy were depicted in Table V.

TABLE IV: Distribution of spike count in large clusters corresponding to the reference classes from the recorded dataset.

Clusters	Our method	SPC-based	Manual reference
MU1 MUAPs	314	368	383
MU2 MUAPs	283	335	408
MU3 MUAPs	378	284	429
un-sorted MUAPs	245	233	0

In contrast with our superior results against the SPC when applied to the synthetic data, results of both automatic techniques were comparable with recorded data. However, it might be due to the small size of dataset and a small number of active MUs recorded. We may also need an inter-rater measurement to alleviate the human subjectivity of the manual reference in evaluation. These should be addressed in future work for the method. In general, all performance measurements we achieved in this study are among the most accurate outcomes in spike sorting evaluation works.

IV. DISCUSSION

Given a large exploratory feature pool, to select the best feature, a voting process consists of three levels: saliency,

TABLE V: Comparison of sorting performance using recorded data between automatic methods. Accuracy measures (in %) use manual labels as reference. True/False are MU matching or not with the reference labels.

Metrics	Class name	Include catch-all		Not include catch-all	
		SPC-based	Our method	SPC-based	Our method
Sensitivity	MU1	99.7	99.7	99.7	99.6
	MU2	89.9	68.6	100.0	99.6
	MU3	74.6	83.9	100.0	100.0
PPV	MU1	71.8	65.8	100.0	99.6
	MU2	99.7	99.6	99.7	99.6
	MU3	100.0	100.0	100.0	100.0
General accuracy		87.6	83.7	99.9	99.8

robustness, and accuracy selection. This strategy has been successfully demonstrated with anomaly detection scenarios in our earlier works [13], [14]. However, both of the cases are two-predefined-class detection tasks. Though MUAP sorting involves an unknown-class-number classification task, the feature analysis scheme still addresses the best feature candidate for the clustering purpose. Synthetic and human recorded datasets of motor unit action potentials were used to demonstrate the performance. Compared with the manual reference, our MUAP sorting method is comparable (regarding to the number of MUs found and histograms of MUs). Moreover, in the compared method (SPC-based), the *temperature* terminology used for reviewing outcome is less intuitive than the correlation as in our method. The correlation values range $0 \rightarrow 1$ while the measure of *temperature* is difficult to tune.

V. CONCLUSION

In this work, a feature analysis approach for spike sorting in MUAP is reported. We analyzed a large pool of candidates for MUAP feature extraction. We used ranking scores by several saliency criteria including mutual information, Euclidean distance based discrimination. This hybrid selection scheme is a data-driven approach and can compare a comprehensive set of candidates including existing features and novel variants. The most selective features learnt from this process are most applicable to the unsupervised and subject-independent applications. We demonstrated the classification performance with this feature using both synthetic nEMG and human recorded data. Compared with the reference produced by

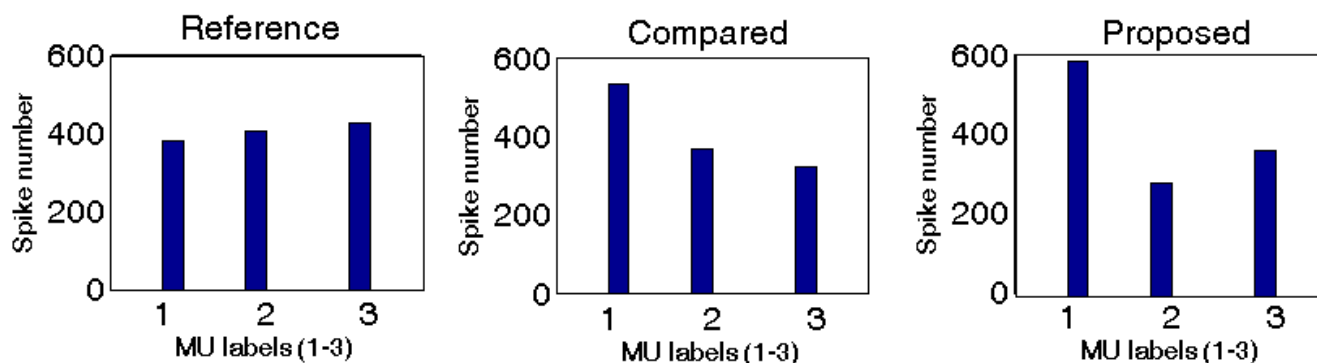


Fig. 4: Agreement in histograms of automatic methods against the reference for recorded data.

human experts, our method obtained a comparable result (e.g., equivalent number of classes was found, identical MUAP morphology in each pair of corresponding MU class, and similar histograms of MUs).

REFERENCES

- [1] S. Paganoni and A. Amato, "Electrodiagnostic evaluation of myopathies," *Physical medicine and rehabilitation clinics of North America*, vol. 24, no. 1, pp. 193–207, 2013.
- [2] *Cambridge Electronic Design: Spike2*, www.ced.co.uk.
- [3] *Cerebus*, www.cyberkineticsinc.com.
- [4] E. M. Glaser and W. B. Marks, "Separation of neuronal activity by waveform analysis," *Advances in Biomedical Engineering*, vol. 5, pp. 137–156, 1968.
- [5] J. C. Letelier and P. P. Weber, "Spike sorting based on discrete wavelet transform coefficients," *Journal of Neuroscience Methods*, vol. 101, no. 2, pp. 93 – 106, 2000.
- [6] V. Karkare, S. Gibson, and D. Markovic, "A 130 μ W, 64-channel spike-sorting DSP chip," in *Solid-State Circuits Conference, 2009. A-SSCC 2009. IEEE Asian*, 2009, pp. 289 –292.
- [7] S. P. Lloyd, "Least squares quantization in pcm," *Information Theory, IEEE Transactions on*, vol. 28, no. 2, pp. 129–137, 1982.
- [8] S. Takahashi, Y. Anzai, and Y. Sakurai, "A new approach to spike sorting for multi-neuronal activities recorded with a tetrode—how ICA can be practical," *Neuroscience Research*, vol. 46, no. 3, pp. 265 – 272, 2003.
- [9] Y. Cheng, "Mean shift, mode seeking, and clustering," *Pattern Analysis and Machine Intelligence, IEEE Transactions on*, vol. 17, no. 8, pp. 790–799, 1995.
- [10] Z. Yang, Q. Zhao, and W. Liu, "Improving spike separation using waveform derivatives," *Journal of Neural Engineering*, vol. 6, pp. 046 006–046 018, 2009.
- [11] P. Cheeseman, J. Kelly, M. Self, J. Stutz, W. Taylor, and D. Freeman, "Autoclass: A Bayesian classification system," *Proc of the Fifth Intl Workshop on Machine Learning*, pp. 54–64, 1988.
- [12] M. Blatt, S. Wiseman, and E. Domany, "Superparamagnetic clustering of data," *Phys. Rev. Lett.*, vol. 76, pp. 3251–3254, 1996.
- [13] T. T. Pham, S. T. Moore, S. J. Lewis, D. N. Nguyen, E. Dutkiewicz, A. J. Fuglevand, A. L. McEwan, and P. H. Leong, "Freezing of gait detection in parkinsons disease: A subject-independent detector using anomaly scores," *IEEE Transactions on Biomedical Engineering*, 2017.
- [14] T. T. Pham, C. Thamrin, P. D. Robinson, A. McEwan, and P. H. Leong, "Respiratory artefact removal in forced oscillation measurements: A machine learning approach," *IEEE Transactions on Biomedical Engineering*, 2016.
- [15] A. Hamilton-Wright and D. W. Stashuk, "Physiologically based simulation of clinical emg signals," *IEEE Transactions on biomedical engineering*, vol. 52, no. 2, pp. 171–183, 2005.
- [16] *Fuglevand Laboratory of motor control neurophysiology*, Department of Physiology, University of Arizona, USA.
- [17] C. Shannon, "A mathematical theory of communication," *Bell System Technical Journal, The*, vol. 27, no. 3, pp. 379–423, July 1948.
- [18] K. Kira and L. A. Rendell, "The feature selection problem: traditional methods and a new algorithm," in *Proceedings of the tenth national conference on Artificial intelligence*, ser. AAAI'92. AAAI Press, 1992, pp. 129–134.
- [19] G. Brown, A. Pocock, M.-J. Zhao, and M. Luján, "Conditional likelihood maximisation: a unifying framework for information theoretic feature selection," *The Journal of Machine Learning Research*, vol. 13, no. 1, pp. 27–66, 2012.
- [20] H. W. Lilliefors, "On the kolmogorov-smirnov test for normality with mean and variance unknown," *Journal of the American Statistical Association*, vol. 62, no. 318, pp. 399–402, 1967.
- [21] V. J. Samar, "Wavelet analysis of neuroelectric waveforms," *Brain and Language*, vol. 66, pp. 1 – 6, 1999.
- [22] R. Quiroga, Z. Nadasdy, and Y. Ben-Shaul, "Unsupervised spike detection and sorting with wavelets and superparamagnetic clustering," *Neural Comput.*, vol. 16, pp. 1661–1687, 2004.
- [23] D. Gabor, "Theory of communication. part 1: The analysis of information," *Electrical Engineers-Part III: Radio and Communication Engineering, Journal of the Institution of*, pp. 429–441, 1946.
- [24] L. B. Jackson *et al.*, *Digital filters and signal processing*. Springer, 1989, vol. 3.
- [25] T. T. Pham, A. J. Fuglevand, A. L. McEwan, and P. H. Leong, "Unsupervised discrimination of motor unit action potentials using spectrograms," in *Engineering in Medicine and Biology Society (EMBC), 2014 36th Annual International Conference of the IEEE. IEEE*, 2014, pp. 1–4.
- [26] T. T. Pham and C. M. Higgins, "A visual motion detecting module for dragonfly-controlled robots," in *Engineering in Medicine and Biology Society (EMBC), 2014 36th Annual International Conference of the IEEE. IEEE*, 2014, pp. 1666–1669.
- [27] J. V. Basmajian and C. De Luca, "Muscles alive," *Muscles alive: their functions revealed by electromyography*, vol. 278, p. 126, 1985.
- [28] C. J. De Luca, "Physiology and mathematics of myoelectric signals," *IEEE Transactions on Biomedical Engineering*, no. 6, pp. 313–325, 1979.
- [29] A. J. Fuglevand, D. A. Winter, and A. E. Patla, "Models of recruitment and rate coding organization in motor-unit pools," *Journal of neurophysiology*, vol. 70, no. 6, pp. 2470–2488, 1993.
- [30] M. Blatt, S. Wiseman, and E. Domany, "Data clustering using a model granular magnet," *Neural Comput.*, vol. 9, pp. 1805–1842, 1997.

Deep Holistic Representation Learning from EHR

Edmond Zhang

Orion Health

Auckland, New Zealand

Email: edmond.zhang@orionhealth.com

Reece Robinson

Orion Health

Auckland, New Zealand

Email: reece.robinson@orionhealth.com

Bernhard Pfahringer

The University of Waikato

Hamilton, New Zealand

Email: bernhard.pfahringer@gmail.com

Abstract—In recent years there has been a surge of interest in applying deep neural networks to electronic health records (EHRs) for predictive clinical tasks. EHR data cannot be mined like traditional image or text data because it has unique characteristics including temporality, irregularity, heterogeneity (both structured and unstructured) and incompleteness. We begin by identifying weaknesses in the way deep learning is currently being applied to health data. Then, leveraging these insights, we propose an end-to-end strategy for extracting complimentary deep feature representations from EHRs. This strategy is based on a “bringing model to data” machine learning approach instead of “transforming data to model”. It uses multiple neural networks, that have each been optimised for the characteristics of their input data, to extract features. Then, the output of these neural networks is combined. We show that prediction accuracy improves as the output of each neural network is contributed. This work demonstrates the value of extracting relevant insights from different aspects of a patients record, which is analogous to how a clinician makes decisions.

Keywords—EHR, deep neural networks, holistic learning, patient representation

I. INTRODUCTION

Electronic health records (EHRs) are rapidly being adopted by health care providers. This has resulted in a significant increase in the quantity and availability of EHR data. According to a recent report from the Office of the National Coordinator for Health Information Technology, more than 80% of hospitals in the United States had some form of EHR system implemented in 2015[1].

While the primary use of EHR data is improving clinical efficiency, there is a renewed and growing interest in the secondary application of EHR data for various clinical tasks, such as disease diagnosis[2]-[6], readmission prediction[7]-[10], automatic coding[11]-[14], and future disease modelling[5][15][16].

To date, most of these applications were based on traditional machine learning techniques such as Support Vector Machines, Random Forest, and various ensemble learning methods. More recently, applications have started using the same deep learning techniques shown to be effective in other domains such as images and text. Many of these research efforts have demonstrated that there is improved performance when neural networks are trained on a large volume of digital patient data[2]-[10]. Most of this deep learning has worked by either 1) transforming a single data source (e.g. discharge summaries) into an appropriate input format before feeding it into the neural network for training; or 2) transforming and combining multiple data sources (e.g. prescriptions and ICD-9 codes) before feeding them into the neural network for training.

We argue that EHR data, which captures several different aspects of patient health, should be processed and learned in a more holistic way - to more closely replicate what clinicians do. Our end-to-end neural network extracts and combines insights from different aspects of the patient record. We believe this is the first of its kind and fundamentally different to the current popular approaches that only look at one single aspect of the EHR data at a time.

It is important to point out the following contributions of this research:

- To the best of our knowledge, the proposed technique is the first to use multiple neural network architectures to extract and learn from multiple data sources or observations in EHR data.
- For the two multi-label classification tasks detailed in this paper, we show that this technique achieves better prediction accuracy for than models trained on a single source.

Section I of this paper provides some background on EHR data and deep learning. Section II looks at recent work that has applied deep learning to EHR data. Section III details our proposed end-to-end neural network model. Section IV describes the dataset. Section V evaluates the results of using the proposed technique with the dataset. Section VI concludes this paper by exploring options for future work.

II. BACKGROUND

This section provides an in-depth description of EHRs before looking at the rationale and context for applying machine learning and deep learning to EHR data.

A. EHRs

EHRs capture relevant information about a patient and their health - including demographics, historical admissions and discharges, lab test results, prescriptions, medical images and clinical notes.

They present a number of challenges that are not present in traditional text or image data, such as temporality, irregularity, heterogeneity, and incompleteness.

B. Secondary Application of the EHR

Earlier work in leveraging EHRs for secondary applications was primarily focused on using traditional machine learning methodologies such as Bags-of-Words. These traditional methodologies extract relevant information from the records, as vector-based representations, and then train a shallow classifier on top of the features. They require intensive

manual effort and do not scale well in different settings. In addition, they require the domain knowledge of experts to develop effective feature representations.

In more recent work, researchers have found the application of deep learning techniques to EHR data has yielded consistently better results. An important characteristic of this technique is that little or no domain knowledge is required because feature representations are learned automatically. Different feature sets are learned from the input based on the problem or loss function that model tries to minimize. Given the same input data and model architecture, deep learning techniques both maximize and minimize the weight or contribution of the same input representation to produce the optimal result for the relevant problem.

1) Patient Representative Learning: Inspired by the success of applying deep learning techniques for addressing NLP problems, patient representative learning represents the patient as vectors of feature embeddings. Varied medical information is concatenated into a single vector embedding[4][5][6].

The Deep Patient representation by Miotto et al.[5][6] is one of the most popular works on feature learning from patient EHR data. Their method transforms relevant patient information (e.g., medication, diagnoses, and procedures) into a single word2vec style of vector embedding and then feeds it into a three-layer stack of de-noising auto-encoders that capture the hierarchical inter-dependencies of input features.

2) Information Extraction: Extracting information from EHRs is a popular research topic. Clinical concepts, medical events, procedures and abbreviation expansion can be derived from both free text and structured data. In the past, extracting this data has been very time consuming - even for human annotators. Recent applications of deep learning techniques have yielded impressive results. For the task of extracting clinical concepts, Jagannatha et al.[18][19] experimented with several neural networks such as LSTM, Bi-LSTM and GRUs.

3) Predictive Modelling: In Predictive modelling, machine learning models use patient representations and information extracted from EHRs to predict future clinical outcomes. A wide variety of clinical applications are being proposed - including heart failure, hypertension, suicide risk, re-admission risk, ICD-9 code recognition, and diabetes risk. Leveraging word2vec vectors for patient representation (using only categorical codes), Choi et al. [21] found that simple MLP neural networks performed the best for heart failure prediction.

III. METHODOLOGY

Most of the deep learning frameworks currently being applied to EHR datasets work by either 1) using a single specific data source (e.g., discharge summary), or 2) transforming and combining multiple data sources into a single vector before feeding it into the network. We argue that these approaches are not optimal for feature extraction and learning from EHR data because of the inherent information loss. In addition, they do not reflect the way a clinician uses data in practice. Clinicians do not base their diagnoses on a single data source. They take in, and process, all relevant observations in their *natural form* discharge summaries as text documents, clinical images as images, and lab test quantity results as numbers.

A. Feature Transformations

We use four of the observations, associated with an admission, as inputs into our model - discharge summaries, prescriptions, vital signs, and lab test orders. This section describes how each of these inputs is pre-processed and transformed.

1) Discharge Summaries: As discharge summaries consist of unstructured text, we leverage the one-hot encoding with 1D convolutional network method proposed by Kim et al [24]. We load a pre-trained 200-dimensional Glove word embedding from [25] into a lookup table. For each word in the discharge summary, we try to find the matching 200-dimension vector from the look up table. If a match is not found, we return a vector of zeros. Figure 1 demonstrates how word embedding works.

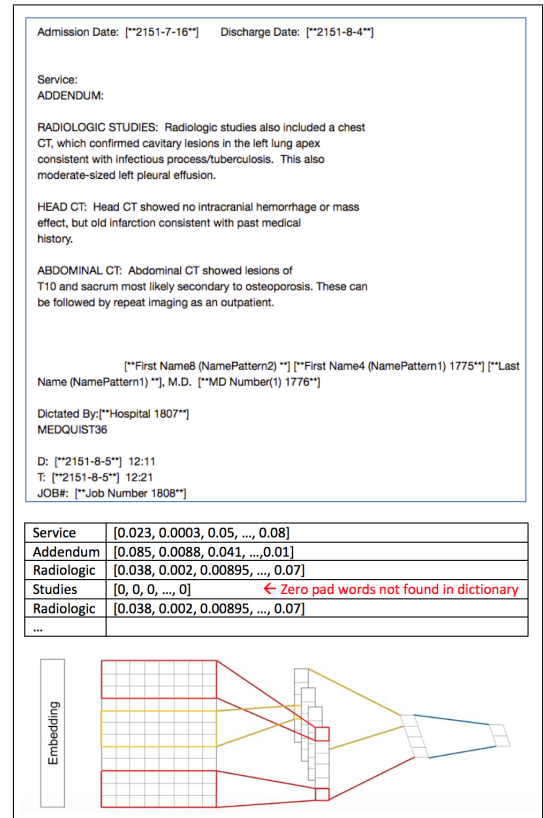


Fig. 1. 1D convolution word2vec embedding for text.

After the matching encoding has been assigned to each of the words, the shape of the input tensor is a matrix with height equal to the number of words and width equal to 200.

2) Prescriptions: Prescriptions are the drugs administered during the ICU stay. The Prescriptions are found by combining several attributes into a single string for each admission (e.g., *Drug_type*, *Drug_name_generic*, *Dose_val_rx*, and *Route*). Once prescriptions have been transformed into text, we apply the one-hot encoding technique described in the previous section. However, instead of using the concatenated word-level encoding strategy, we take the average of normalized word vectors of all the words in the text. This approach produces a one-dimensional vector which is used as input into the model.

3) Vital Signs: Vital Signs were selected from the four most common measurements taken at the bedside during a

patients stay. These were: Heart Rate, Noninvasive Blood Pressure (NBP) systolic, NBP diastolic, and NBP mean. Typically, each measurement would be recorded hourly.

For training, a 48-hour window of hourly vitals measurement was chosen. The window started when a patient was admitted to the ward. Where there were multiple measurements in an hour the maximum value was chosen. Where values were missing a zero was used for that hour. For ward stays that were shorter than 48 hours, zero padding was employed. Figure 2 is the matrix representation of the training data:

Time Step	NBP Mean	NBP Systolic	NBP Diastolic	Heart Rate
0	122	192	100	121
1	103	165	85	118
2	76	119	64	118
...
...
...
47	0	0	0	0

Fig. 2. The matrix representation of vital signs.

This data has obvious temporal characteristics and can be viewed as a time sequence of values. Alternatively, the time dimension can be ignored and each time step can be horizontally stacked to form a 1D input vector.

4) *Lab Test Orders*: The Lab test orders training dataset contained 575 unique lab test result types. For each patient the one hot encoding technique was applied to create vectors that contained a one ('1') if that test was ordered during their stay, and zero ('0') otherwise. This test data is presented during training as a 1D vector that is 575 dimensions wide. See Figure 3 for an example of this.

Admission	Embedding (n=575)
1	[0, 0, 0, 0, 0, 0, 0, 0, 1, 0, 0, 0, 0, 0, ..., 0]
...	
m	[0, 0, 1, 0, 0, 1, 0, 0, 0, 0, 0, 1, 1, 0, 0, ..., 1]

Fig. 3. The vector representation of lab tests.

B. Model Architecture

The proposed deep learning framework extracts and transforms features from multiple data sources before training a final classifier on the combined outputs.

It has two distinct stages. In stage one, specific data types are extracted from the EHR and then transformed. For each data type, we apply the most appropriate feature transformation before feeding it into a neural network architecture optimized for that data type. In stage two, a classifier is trained using the combined outputs (last hidden layer) of all the stage one models. The strength of the proposed method is that it allows you to apply the transformation and model architecture that will extract the most out of each of the different data sources. The proposed framework is an example of end-to-end learning because the combined model is optimized globally, without the need to train each network independently.

For example, free text discharge summaries are processed using the word2vec feature transformation and then ingested into a 1-Dimensional Convolutional network architecture for learning. This architecture was chosen for the free text discharge summaries because previous researchers have demonstrated good performance in applying it to free text. By contrast, time series may require an RNN style architecture.

Figure 4 lists the transformations and network architectures for each of the sub-models; Figure 5 describes the combined architecture used in this research.

Input Transformation	Discharge Summaries (Word2Vec)	Vitals (48x1hr time-steps)	Medications (Avg. Norm Word2Vec)	Lab Test Orders (OHE Vector)
Stage One Model Type	CNN	CNN	CNN & LSTM	MLP
Stage One Output	Hidden State	Hidden State	Hidden State	Hidden State
Stage Two Model Type	Dense Layer			
Stage Two Output	Sigmoid			

Fig. 4. Transformations and network architectures for the combined model.

We evaluated a number of model architectures to select the best models; first for each data source and then for the combined model. To illustrate this process, we detail how we selected the best model for Vitals data source.

Vitals data was prepared as a time sequence of values with 48 time steps. We initially investigated the Recurrent Neural Network (RNN) model architecture because it uses the temporal dimension of data. To decide which RNN memory cell type to use we evaluated the performance of four cell type options (ie: Simple RNN, Long Short-Term Memory (LSTM), Bidirectional Long Short-Term Memory (Bi-LSTM), and Gated Recurrent Units (GRU)). We also investigated the performance of a Convolutional Neural Network (CNN) model which ignores the temporal dimension of the data. In this configuration the vitals data is presented to the input as a 1D vector.

Figure 6 summarizes the results of training the various vitals model architectures and batch sizes.

Figure 7 shows the RNN memory cell and CNN performance values plotted by batch size. Of the RNN models, Bi-LSTM performed the best with LSTM being the next best. However, the CNN model out-performed the RNN architecture for this dataset. Based on this analysis the CNN architecture was chosen for the vitals data in the final combined model.

IV. DATASET

The framework proposed in this research was evaluated using the public MIMIC III dataset[23]. This is the largest public dataset of this type. It contains approximately 60,000 ICU admission records from Beth Israel Deaconess Medical Center in Boston over an 11 year period. Each admission is associated with various observations and information about the patient including demographics, vital signs, discharge summaries, lab tests, clinical notes, prescriptions, ICD-9 codes and charts. The De-identification processing on the data was done according to the Health Insurance Portability And Accountability Act (HIPAA) standards meaning that all of the eighteen identifiable elements were removed.

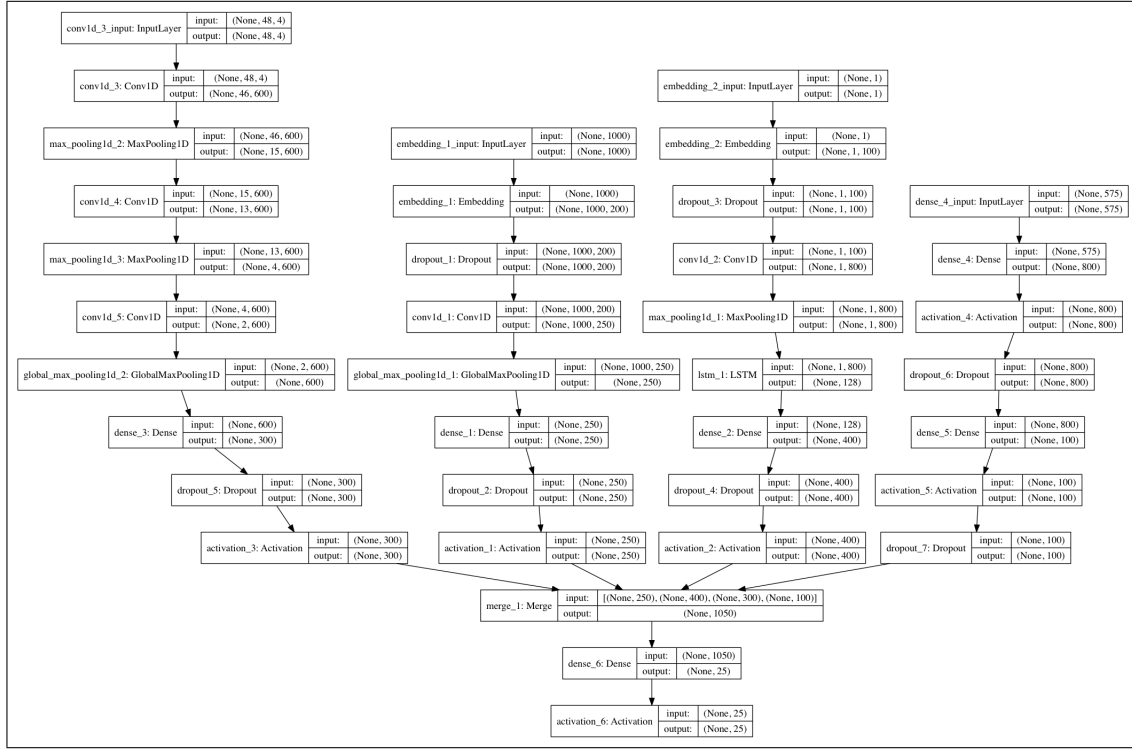


Fig. 5. The proposed end-to-end deep learning architecture transforms and extracts features from multiple data sources, before training a final classifier on the combined outputs. From left to right, the sub-network architecture and parameters for vital signs, discharge summaries, prescriptions, and lab test orders.

	Cell Type		Memory Cell Type							1D Convolution (Three Layers)	
Single Layer of:	SimpleRNN		LSTM		GRU		Bi-LSTM				
with Batch Size	Mean	StdDev	Mean	StdDev	Mean	StdDev	Mean	StdDev		Mean	StdDev
32	0.429	0.025	0.413	0.025	0.433	0.027	0.398	0.011		0.335	0.013
64	0.445	0.035	0.409	0.034	0.415	0.041	0.388	0.022		0.324	0.041
128	0.435	0.036	0.398	0.019	0.412	0.036	0.383	0.022		0.325	0.034
256	0.422	0.040	0.406	0.012	0.411	0.011	0.378	0.024		0.324	0.030
512	0.422	0.037	0.362	0.027	0.405	0.034	0.377	0.022		0.327	0.030
1024	0.416	0.037	0.380	0.026	0.401	0.034	0.371	0.025		0.334	0.035
2048	0.411	0.036	0.373	0.029	0.382	0.026	0.353	0.030			
4096	0.408	0.036	0.374	0.024	0.377	0.024	0.360	0.024			
8192	0.410	0.035	0.384	0.028	0.414	0.012	0.354	0.024			
16348	0.409	0.026	0.387	0.027	0.403	0.025	0.364	0.028			

Input not normalised, train/test = 90/10 split, Epoch = 20

Fig. 6. Multi-Label Hamming Distance by Batch Size for ICD-9 Code Group prediction using ICU Vitals.

V. EVALUATION

This section details our experiments using the proposed framework on the MIMIC III dataset. We evaluated two multi-label classification tasks - ICD-9 group prediction and lab test order prediction.

We used the deep learning library Keras with a Tensorflow backend for both tasks. When we conducted our research, the version of the Keras library did not directly support multi-label output. For each label, we used a thresholding technique based on Matthews Correlation Coefficient to determine the best cut-off threshold value for converting the label probabilities into ones and zeros. Specifically, our neural network was trained with binary cross-entropy loss function with a Sigmoid

activation function. The model also uses the efficient Adam optimization algorithm for gradient descent and is trained over 20 epochs.

We ran the same experiment with 10-fold cross-validation, with different random seeds, ten times with different train/test data sets. We reported averaged prediction accuracy of the test data. The Hamming loss (See Equation 1, which essentially is the fraction of labels that are incorrectly predicted), and average AUC score over all labels were used as the evaluation metrics for the two multi-label problems.

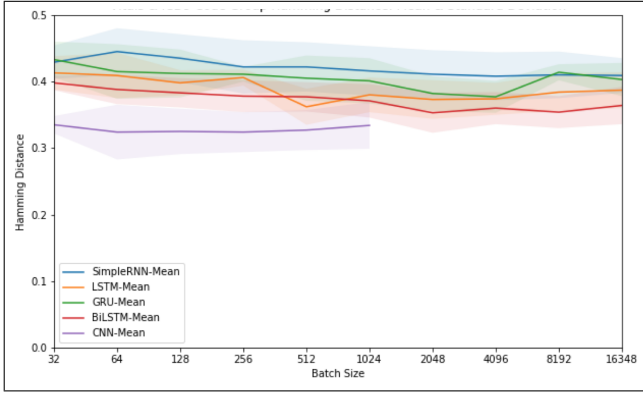


Fig. 7. Multi-Label Hamming Distance by Batch Size for ICD-9 Code Group prediction using ICU Vitals.

Data Source	Hamming Loss	Standard Deviation
Baseline (All Zeros)	0.1854	0.0004
Discharge Summary (DS)	0.1202	0.0027
Prescription (P)	0.1759	0.0050
Vital Signs (VS)	0.1854	0.0093
Lab Test Orders (LT)	0.2058	0.0071
DS + P	0.1163	0.0025
DS + P + VS	0.1160	0.0045
DS + P + VS + LT	0.1130	0.0018

TABLE I. EVALUATING ICD-9 GROUP PREDICTION WITH HAMMING LOSS.

$$HammingLoss(x_i, y_i) = \frac{1}{|D|} \sum_{i=1}^{|D|} \frac{xor(x_i, y_i)}{|L|}, \quad (1)$$

Where $|D|$ is the number of samples, $|L|$ is the number of labels, y_i is the ground truth, and x_i is the prediction.

A. Task 1: ICD-9 Group Prediction

This task predicts a patient's ICD-9 Group labels using the admission data. ICD-9 Group labels are used to categorize medical conditions. We used the 25 Adult ICU-related ICD-9 Group labels described in [26].

To assign one or more of the 25 ICD-9 Group labels to an admission we followed the guideline published by Health Cost and Utilization (HCUP). Since nearly all admissions have more than one diagnoses, we formulated this as a multi-label classification problem. See Table I and II for evaluation performance.

We can see that the Hamming Loss score decreased as each new data source was added into the network. The best

Data Source	Average AUC	Standard Deviation
Baseline (All Zeros)	0.593	0.0004
Discharge Summary (DS)	0.706	0.0034
Prescription (P)	0.585	0.0005
Vital Signs (VS)	0.443	0.0005
Lab Test Orders (LT)	0.550	0.0006
DS + P	0.716	0.0005
DS + P + VS	0.715	0.0005
DS + P + VS + LT	0.723	0.0005

TABLE II. EVALUATING ICD-9 GROUP PREDICTION WITH AVERAGE AUC.

Data Source	Hamming Loss	Standard Deviation
Baseline (All Zeros)	0.1162	0.0002
Discharge Summary (DS)	0.0494	0.0008
Prescription (P)	0.0565	0.0005
Vital Signs (VS)	0.0758	0.0020
DS + P + VS	0.0445	0.0001

TABLE III. EVALUATING LAB TEST ORDERS PREDICTION WITH HAMMING LOSS.

Data Source	Average AUC	Standard Deviation
Baseline (All Zeros)	0.558	0.0002
Discharge Summary (DS)	0.802	0.0002
Prescription (P)	0.776	0.0007
Vital Signs (VS)	0.704	0.0002
DS + P + VS	0.820	0.0002

TABLE IV. EVALUATING LAB TEST ORDERS PREDICTION WITH AVERAGE AUC.

single observation was discharge summaries, which achieved a score of 0.1202. The combined model was able to improve on this score (ie: 0.1130), after adding all data sources, despite the fact that the individual data sources performed significantly worse on their own. Similar performance gains were also realised using the averaged AUC score, where the best single observation was 0.706 for discharge summaries and 0.723 after combining all available data sources.

B. Task 2: Lab Test Order

This task predicts which lab tests will be ordered using the admission data. We found a total of 575 unique lab tests in the dataset (e.g. Monocytes, Hemoglobin A and Cancer Ag 125 tests). As it is highly likely that multiple lab tests are ordered for a patient admitted to ICU, we also formulated this as a multi-label classification problem. See Table III and IV for evaluation performance.

Again, we saw an improvement over the best single data source when multiple data sources were combined. As with Task 1, the best single feature was the discharge summaries with a Hamming loss score of 0.0494. Again, the combined model was able to improve this score (ie: 0.0445), after adding the prescriptions and vital signs data sources. Similar performance gains were also realised using the averaged AUC score, where the best single observation was 0.802 for discharge summaries and 0.820 after combining all available data sources.

VI. CONCLUSIONS

This work proposed an original end-to-end strategy for *holistic* learning from EHRs. The main contribution is two-fold. First, to account for the heterogeneous nature of the EHR data, we adopted the concept of bringing model to data instead of the common transforming data to model learning approach. Second, we combined the contributions from multiple neural networks for improved prediction accuracy for two tasks. We tested our deep learning model on the popular MIMIC III dataset, which achieved improved performance when the model was provided with more data sources belonging to the same admission. This is analogous to how a clinician makes decisions.

In future work, it would be good to investigate how transfer learning can be applied to deep EHR models. It should be possible to improve the accuracy of a single holistic EHR model, trained on a large population, for different tasks using very little new data. This is a popular and successful approach in image recognition, where millions of images are used to train the general baseline model before fine-tuning it for other tasks.

ACKNOWLEDGMENT

This research was supported by Precision Driven Health (www.precisiondrivenhealth.com) under PDH project 1213 - Deep Representation Learning. PDH had no role in study design, data collection and analysis, decision to publish or preparation of the manuscript.

REFERENCES

- [1] Henry, J., Pylypchuk, Y., Searcy, T., Patel, V. (2016). Adoption of electronic health record systems among US non-federal acute care hospitals: 2008-2015. The Office of National Coordinator for Health Information Technology.
- [2] Cheng, Y., Wang, F., Zhang, P., Hu, J. (2016, June). Risk prediction with electronic health records: A deep learning approach. In Proceedings of the 2016 SIAM International Conference on Data Mining (pp. 432-440). Society for Industrial and Applied Mathematics.
- [3] Lipton, Z. C., Kale, D. C., Elkan, C., Wetzell, R. (2015). Learning to diagnose with LSTM recurrent neural networks. arXiv preprint arXiv:1511.03677.
- [4] Pham, T., Phung, D.Q., Tran, T., Venkatesh, S. (2016). DeepCare: A Deep Dynamic Memory Model for Predictive Medicine. PAKDD.
- [5] Miotto, R., Li, L., Kidd, B. A., Dudley, J. T. (2016). Deep patient: An unsupervised representation to predict the future of patients from the electronic health records. Scientific reports, 6, 26094.
- [6] Miotto, R., Li, L., Dudley, J. T. (2016, March). Deep Learning to predict patient future diseases from the electronic health records. In European Conference on Information Retrieval (pp. 768-774). Springer International Publishing.
- [7] Pham, T., Tran, T., Phung, D., Venkatesh, S. (2017). Predicting healthcare trajectories from medical records: A deep learning approach. Journal of biomedical informatics, 69, 218-229.
- [8] Nguyen, O. K., Makam, A. N., Clark, C., Zhang, S., Xie, B., Velasco, F., ... Halm, E. A. (2016). Predicting allcause readmissions using electronic health record data from the entire hospitalization: Model development and comparison. Journal of hospital medicine, 11(7), 473-480.
- [9] Makam, A. N., Nguyen, O. K., Clark, C., Zhang, S., Xie, B., Weinreich, M., ... Halm, E. A. (2017). Predicting 30-day Pneumonia Readmissions Using Electronic Health Record Data. Journal of hospital medicine, 12(4), 209-216.
- [10] Nguyen, P., Tran, T., Wickramasinghe, N., Venkatesh, S. (2017). Deeppr: A Convolutional Net for Medical Records. IEEE journal of biomedical and health informatics, 21(1), 22-30.
- [11] Berlin, Z.I., Bruer, J. (2017). Clinical Entity Recognition for ICD-9 Code Prediction in Clinical Discharge Summaries.
- [12] Zhao, S., He, D., Zhang, D., Li, L., Meng, R. (2017). Automatic ICD Code Assignment to Medical Text with Semantic Relational Tuples. iConference 2017 Proceedings Vol. 2.
- [13] Dermouche, M., Velcin, J., Flicoteaux, R., Chevret, S., Taright, N. (2016). Supervised Topic Models for Diagnosis Code Assignment to Discharge Summaries. In Proceedings of the 17th International Conference on Intelligent Text Processing and Computational Linguistics (CICLing16).
- [14] Helwe, C., Elbassuoni, S., Geha, M., Hitti, E., Makhoul Obermeyer, C. (2017, July). CCS Coding of Discharge Diagnoses via Deep Neural Networks. In Proceedings of the 2017 International Conference on Digital Health (pp. 175-179). ACM.
- [15] Choi, E., Bahadori, M. T., Schuetz, A., Stewart, W. F., Sun, J. (2016, December). Doctor ai: Predicting clinical events via recurrent neural networks. In Machine Learning for Healthcare Conference (pp. 301-318).
- [16] Mehrabi, S., Sohn, S., Li, D., Pankratz, J. J., Therneau, T., Sauver, J. L. S., ... Palakal, M. (2015, October). Temporal pattern and association discovery of diagnosis codes using deep learning. In Healthcare Informatics (ICHI), 2015 International Conference on (pp. 408-416). IEEE.
- [17] Mehrabi, Saaed, et al. "Temporal pattern and association discovery of diagnosis codes using deep learning." Healthcare Informatics (ICHI), 2015 International Conference on. IEEE, 2015.
- [18] Jagannatha, A. N., Yu, H. (2016, November). Structured prediction models for RNN based sequence labeling in clinical text. In Proceedings of the Conference on Empirical Methods in Natural Language Processing. Conference on Empirical Methods in Natural Language Processing (Vol. 2016, p. 856). NIH Public Access.
- [19] Jagannatha, A. N., Yu, H. (2016, June). Bidirectional rnn for medical event detection in electronic health records. In Proceedings of the conference. Association for Computational Linguistics. North American Chapter. Meeting (Vol. 2016, p. 473). NIH Public Access.
- [20] Wu, Y., Jiang, M., Lei, J., Xu, H. (2015). Named entity recognition in Chinese clinical text using deep neural network. Studies in health technology and informatics, 216, 624.
- [21] Choi, E., Bahadori, M. T., Searles, E., Coffey, C., Thompson, M., Bost, J., ... Sun, J. (2016, August). Multi-layer representation learning for medical concepts. In Proceedings of the 22nd ACM SIGKDD International Conference on Knowledge Discovery and Data Mining (pp. 1495-1504). ACM.
- [22] Tran, T., Nguyen, T. D., Phung, D., Venkatesh, S. (2015). Learning vector representation of medical objects via EMR-driven nonnegative restricted Boltzmann machines (eNRBM). Journal of biomedical informatics, 54, 96-105.
- [23] Johnson, A. E., Pollard, T. J., Shen, L., Lehman, L. W. H., Feng, M., Ghassemi, M., ... Mark, R. G. (2016). MIMIC-III, a freely accessible critical care database. Scientific data, 3.
- [24] Kim, Y. (2014). Convolutional neural networks for sentence classification. arXiv preprint arXiv:1408.5882.
- [25] Pennington, J., Socher, R., Manning, C. (2014). Glove: Global vectors for word representation. In Proceedings of the 2014 conference on empirical methods in natural language processing (EMNLP) (pp. 1532-1543).
- [26] Harutyunyan, H., Khachatrian, H., Kale, D. C., Galstyan, A. (2017). Multitask Learning and Benchmarking with Clinical Time Series Data. arXiv preprint arXiv:1703.07771.

An Efficient Ant Colony Optimization Algorithm for Protein Structure Prediction

Dong Do Duc, Phuc Thai Dinh, Vu Thi Ngoc Anh, Nguyen Linh-Trung

AVITECH Institute, University of Engineering and Technology, Vietnam National University Hanoi, Vietnam

Abstract—Protein structure prediction is considered as one of the most long-standing and challenging problem in bioinformatics. In this paper, we present an efficient ant colony optimization algorithm to predict the protein structure on three-dimensional face-centered cubic lattice coordinates, using the hydrophobic–polar model and the Miyazawa–Jernigan model to calculate the free energy. The reinforcement learning information is expressed in the k -order Markov model, and the heuristic information is determined based on the increase of the total energy. On a set of benchmark proteins, the results show a remarkable efficiency of our algorithm in comparison with several state-of-the-art algorithms.

I. INTRODUCTION

Proteins are essential components of all living cells and play a vital role in biological processes of living organisms. They are sequential chains of amino acid connected by single-peptide bonds, and therefore also known as polypeptides. The three-dimensional (3D) structure of a protein exposes its properties and features. A misfolded protein can cause many dangerous diseases, such as Alzheimer, diabetes, cancer [1]. Analyzing the structure of proteins allow us to understand their features and produce medicines for diseases caused by protein misfolding [2], [3].

Unfortunately, it is complex and difficult to simulate a protein nature into 3D structure [4], [5]. Therefore, protein structure prediction (PSP) remains as a highly challenging problem for both the biological and computational communities. Several *in-vitro* methods were proposed to study proteins at atom-level like, such as X-ray crystallography, nuclear magnetic resonance (NMR). However, these methods is time-consuming and costly, unsuitable for large-scale situations. For this reason, computational methods for predicting the structure of proteins are promising alternatives [6], [7].

So far, there are three computational approaches: homology modeling, threading and *ab initio*. The first two approaches can only be used when compatible labels exist in the Protein Data Bank [8], limiting their applications. Methods in the *ab initio* approach predict the 3D structure of proteins, relying only on its primary amino acid sequence. From a given amino acid sequence, they predict the 3D structure of the protein by finding a unique 3D conformation with minimal interaction energy [4]. The model for solving this problem has been optimized by the search space and the target function.

In practice, the search space is very large and determining interaction energies is a complex and costly task. High-resolution methods can only handle proteins with length below 150 amino acids. That is why the lattice structure is used, wherein every amino acid corresponds to a node in a discretized search space. This simplicity allows developing highly efficient algorithms, especially when applied to longer proteins.

Many methods to apply the lattice structure have been considered [9]–[11], and among them, 3D face-centered cubic lattice (3D-FCC) possesses many advantages over other methods [12], [13] and have been used by many researchers [10], [14]–[16].

There are two popular energy models, approximating the optimal structure of proteins: Hydrophobic–Polar (HP) energy model [10], [17] and Miyazawa–Jernigan (MJ) energy model [18]. In the HP

model, every amino acid is considered a bead labelled as hydrophobic (H) and polar (P), and energy is determined from the physical interactions among H-nodes, whereas P-nodes are seen as neutral. The MJ model considers interactions between specific pairs of amino acids, thus being closer to the realistic model of free energy.

PSP has been classified as an NP-hard problem [19], [20], and so heuristic and metaheuristic algorithms have been proposed to solve it. Many of those are based on population, such as: ant colony optimization (ACO) [21], artificial learning system [22], generic algorithm (GA) [23]–[25], population-based algorithm [26], particle swarm optimization (PSO) [27], firefly algorithm [14]. Recently, Rashid *et al.* has proposed two methods based on the GA: GAPlus [15] (HP energy model) and MH-GA [16] (graded energy, strategically mixing the MJ energy with the HP energy). The performance of these algorithms is outstanding in comparison with several the state of the art algorithms.

In this paper, we propose the K-ACO algorithm for PSP, in which the pheromone trail is calculated according to k -order Markov model, which is suitable for 3D structure reception. When using the HP energy model, a local search algorithm is applied to the best solution at each iteration step. Its effectiveness is shown by comparing the simulation study against GAPlus [15], TLS [28] MH-GA [16], Hybrid [29], Local Search [30].

The rest of this paper is organized as follows. In Section II, we briefly provide the background knowledge about the FCC lattice protein representation, the HP and MJ models and some related works. Section III is dedicated for the new algorithm, K-ACO. The simulation study is shown in Section IV. The conclusion is presented in the last section.

II. PROBLEM STATEMENT AND RELATED WORKS

In this section, we briefly describe PSP from its native amino acid sequence in the FCC lattice representation of proteins, the objective functions (HP and MJ), some related works, and the ACO method.

A. FCC lattice and presentation of protein

The FCC lattice is obtained by discretizing the 3D space, formed around triangles. Each node only has 12 neighbors whose relative coordinates to the current node are (1, 1, 0), (1, 1, 0), (1, 1, 0), (1, 1, 0), (0, 1, 1), (0, 1, 1), (1, 0, 1), (1, 0, 1), (0, 1, 1), (1, 0, 1), (0, 1, 1) and (1, 0, 1). This is illustrated in Fig. 1. Given a primary amino acids sequence, a feasible protein sequence is a sequence where any pair of consecutive amino acids in the primary sequence are neighbors. Compared to other lattices, the FCC lattice is close to the natural structure of proteins, with many advantages [12], [13], such as highest packing density, smaller root mean square deviation values.

B. The energy models

Two energy models frequently used to determine the target function of this problem are the HP and MJ models.

TABLE I: Energy values between every protein pairs

	CYS	MET	PHE	ILE	LEU	VAL	TRP	TYR	ALA	GLY	THR	SER	GLN	ASN	GLU	ASP	HIS	ARG	LYS	PRO
CYS	-1.06	0.19	-0.23	0.16	-0.08	0.06	0.08	0.04	0.0	-0.08	0.19	-0.02	0.05	0.13	0.69	0.03	-0.19	0.24	0.71	0.0
MET	0.19	0.04	-0.42	-0.28	-0.2	-0.14	-0.67	-0.13	0.25	0.19	0.19	0.14	0.46	0.08	0.44	0.65	0.99	0.31	0.0	-0.34
PHE	-0.23	-0.42	-0.44	-0.19	-0.3	-0.22	-0.16	0.0	0.03	0.38	0.31	0.29	0.49	0.18	0.27	0.39	-0.16	0.41	0.44	0.2
ILE	0.16	-0.28	-0.19	-0.22	-0.41	-0.25	0.02	0.11	-0.22	0.25	0.14	0.21	0.36	0.53	0.35	0.59	0.49	0.42	0.36	0.25
LEU	-0.08	-0.2	-0.3	-0.41	-0.27	-0.29	-0.09	0.24	-0.01	0.23	0.2	0.25	0.26	0.3	0.43	0.67	0.16	0.35	0.19	0.42
VAL	0.06	-0.14	-0.22	-0.25	-0.29	-0.29	-0.17	0.02	-0.1	0.16	0.25	0.18	0.24	0.5	0.34	0.58	0.19	0.3	0.44	0.09
TRP	0.08	-0.67	-0.16	0.02	-0.09	-0.17	-0.12	-0.04	-0.09	0.18	0.22	0.34	0.08	0.06	0.29	0.24	-0.12	-0.16	0.22	-0.28
TYR	0.04	-0.13	0.0	0.11	0.24	0.02	-0.04	-0.06	0.09	0.14	0.13	0.09	-0.2	-0.2	-0.1	0.0	-0.34	-0.25	-0.21	-0.33
ALA	0.0	0.25	0.03	-0.22	-0.01	-0.1	-0.09	0.09	-0.13	-0.07	-0.09	-0.06	0.08	0.28	0.26	0.12	0.34	0.43	0.14	0.1
GLY	-0.08	0.19	0.38	0.25	0.23	0.16	0.18	0.14	-0.07	-0.38	-0.26	-0.16	-0.06	-0.14	0.25	-0.22	0.2	-0.04	0.11	-0.11
THR	0.19	0.19	0.31	0.14	0.2	0.25	0.22	0.13	-0.09	-0.26	0.03	-0.08	-0.14	-0.11	0.0	-0.29	-0.19	-0.35	-0.09	-0.07
SER	-0.02	0.14	0.29	0.21	0.25	0.18	0.34	0.09	-0.06	-0.16	-0.08	0.2	-0.14	-0.14	-0.26	-0.31	-0.05	0.17	-0.13	0.01
GLN	0.05	0.46	0.49	0.36	0.26	0.24	0.08	-0.2	0.08	-0.06	-0.14	-0.14	0.29	-0.25	-0.17	-0.17	-0.02	-0.52	-0.38	-0.42
ASN	0.13	0.08	0.18	0.53	0.3	0.5	0.06	-0.2	0.28	-0.14	-0.11	-0.14	-0.25	-0.53	-0.32	-0.3	-0.24	-0.14	-0.33	-0.18
GLU	0.69	0.44	0.27	0.35	0.43	0.34	0.29	-0.1	0.26	0.25	0.0	-0.26	-0.17	-0.32	-0.03	-0.15	-0.45	-0.74	-0.97	-0.1
ASP	0.03	0.65	0.39	0.59	0.67	0.58	0.24	0.0	0.12	-0.22	-0.29	-0.31	-0.17	-0.3	-0.15	0.04	-0.39	-0.72	-0.76	0.04
HIS	-0.19	0.99	-0.16	0.49	0.16	0.19	-0.12	-0.34	0.34	0.2	-0.19	-0.05	-0.02	-0.24	-0.45	-0.39	-0.29	-0.12	0.22	-0.21
ARG	0.24	0.31	0.41	0.42	0.35	0.3	-0.16	-0.25	0.43	-0.04	-0.35	0.17	-0.52	-0.14	-0.74	-0.72	-0.12	0.11	0.75	-0.38
LYS	0.71	0.0	0.44	0.36	0.19	0.44	0.22	-0.21	0.14	0.11	-0.09	-0.13	-0.38	-0.33	-0.97	-0.76	0.22	0.75	0.25	0.11
PRO	0.0	-0.34	0.2	0.25	0.42	0.09	-0.28	-0.33	0.1	-0.11	-0.07	0.01	-0.42	-0.18	-0.1	0.04	-0.21	-0.38	0.11	0.26

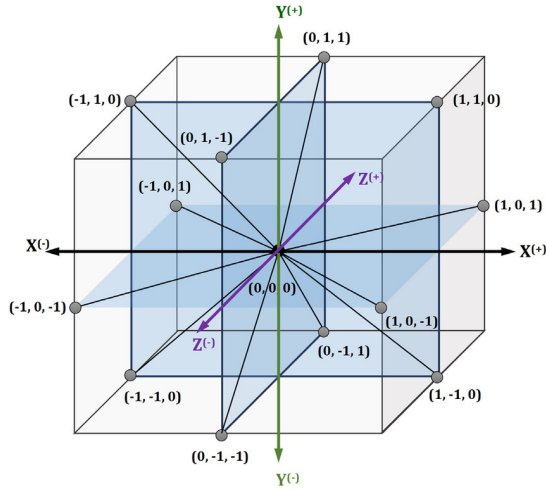


Fig. 1: Basis vectors of 12 neighbors of the origin (0,0,0).

1) *HP energy model*: The HP energy model proposed by Lau and Dill in 1972 [17]. In this model, the amino acids Gly, Ala, Pro, Val, Leu, Ile, Met, Phe, Tyr, Trp are labeled as hydrophobic (H), others are labeled as polar (P). Two consecutive H-labeled amino acids will create negative energy (-1). The complete HP energy of the model for two amino acids i and j is calculated by

$$E_{HP} = \sum_{i < j-1} c_{ij} * e_{ij}, \quad (1)$$

where

$$c_{ij} = \begin{cases} 1, & \text{if } i \text{ and } j \text{ not consecutive but neighbors,} \\ 0, & \text{otherwise,} \end{cases} \quad (2)$$

$$e_{ij} = \begin{cases} -1, & \text{if } i \text{ and } j \text{ both hydrophobic,} \\ 0, & \text{otherwise.} \end{cases} \quad (3)$$

2) *MJ energy model*: Relying on the interactive trend of amino acids, Miyazawa and Jernigan proposed the MJ energy model in 1985 [31]. The complete MJ energy is calculated by

$$E_{MJ} = \sum_{i < j-1} c_{ij} * e_{ij}, \quad (4)$$

where c_{ij} is determined by Eq. (2) and e_{ij} is taken from Table I.

C. The optimal problem and related algorithms

The optimal problem: for each given protein with the native amino acid sequence of length m , the PSP problem is transformed into finding the representation with optimal E_{HP} or E_{MJ} energy.

Recently, MH-GA [16] has been proven to be the most efficient algorithm to solve the PSP problem by comparing its experimental results with the MJ model against other state-of-the-art algorithms, such as Hybrid algorithm [29], and Local Search [30].

III. THE PROPOSED K-ACO ALGORITHM

ACO is a stochastic metaheuristic method proposed by Dorigo [32] for the traveling salesman problem (TSP). Many variants have been developed to tackle difficult optimization problems. In this paper, we build a structure graph and transform the original problem into a problem where solutions can be found by sequentially executing a certain procedure on the built structure graph. An ant colony executes the said procedure based on heuristic and reinforcement learning information (i.e., pheromone) in a random manner. When a solution is found, the algorithm appraises it then updates the pheromone to improve the chance of finding better solutions on the next searches, this is repeated till the termination requirement is met. The properties affecting the quality of the algorithm are: (i) a suitable structure graph, (ii) heuristic information, and (iii) how pheromone is stored and updated.

A. Construction graph

Without loss of generality, the first amino acid is placed at the origin (0,0,0) and start there. The 12 neighbors of each node are indexed from 1 to 12. The structure graph for a protein with the

length of m has $(m - 1)$ columns put in order after the start vertex. There are edges directed from each vertex to all vertices in the next column. The graph is illustrated in Fig. 2. With this, any feasible sequence of length m will correspond to a path on this graph.

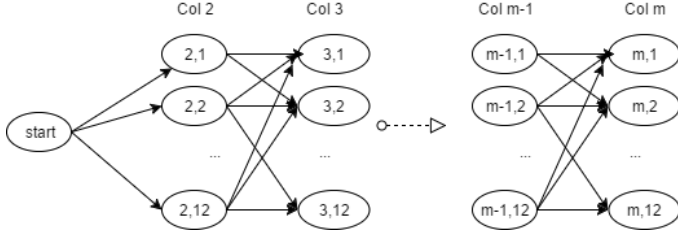


Fig. 2: Construction graph.

B. Randomized procedure to find solution

Each ant will begin at the start vertex and randomly select a vertex on the next column to go. Suppose the ant is on vertex i of column n (or the start vertex), it will select vertex j out of 12 vertices on the next column with the probability $P_{i,j}$ calculated by the following formula:

$$P_{i,j} = \frac{[\tau_{i,j(k)}]^\alpha [\eta_{i,j}]^\beta}{\sum_{l \in C_{n+1}} [\tau_{i,l(k)}]^\alpha [\eta_{i,l}]^\beta}, \quad (5)$$

where $\eta_{i,j}$ is the heuristic information (see III-C), $\tau_{i,j(k)}$ is the pheromone information of the k -degree Markov model (see III-D), C_t is the set of vertices on column t , α and β are parameters of the ACO system, deciding the impact of heuristic and pheromone information on making decisions.

To ensure self-avoiding walk constraint, we set $P_{i,j} = 0$ when selecting vertex would cause two amino acids to have the same coordinate on the protein representation.

C. Heuristic information

After the first $(i - 1)$ amino acids were successfully represented and vector j is the selected direction to go next, let η_{ij} be the heuristic value, E_{ij} be the amount of increased energy, and $E_{\max} = \max(E_{ij})$. Then $\eta_{ij} = E_{\max} - E_{ij} + \epsilon$, where ϵ is a small positive number to ensure η_{ij} always positive. In our implements, we set it to 0.01.

D. Pheromone update

Instead of making choice based only on the pheromone information in the current column, we can also take previously selected vertices into consideration. Let $\tau_{i,j(k)}$ be the pheromone when vertices $(i, j), (i - 1, v_{i-1}), \dots, (i - k + 1, v_{i-k+1})$ are selected. This way, the pheromone will give more accurate information during the searches.

After every round of search, we update pheromone using the SMMAS algorithm [33], by

$$\tau_{i,j(k)} = (1 - \rho)\tau_{i,j(k)} + \Delta_{ij}, \quad (6)$$

where

$$\Delta_{ij} = \begin{cases} \rho\tau_{\min}, & \text{if } (i, j) \in T, \\ \rho\tau_{\min}, & \text{otherwise.} \end{cases} \quad (7)$$

Above, T is the set of selected vertices in the best solution found in this round.

E. Local Search

At each step of the local search procedure, we first identify the hydrophobic core center (HCC) as the center of the hydrophobic amino acid (H). The coordinates of HCC are determined as follows:

$$x_{\text{HCC}} = \frac{1}{n_H} \sum_{i=1}^{n_H} x_i, \quad y_{\text{HCC}} = \frac{1}{n_H} \sum_{i=1}^{n_H} y_i, \quad z_{\text{HCC}} = \frac{1}{n_H} \sum_{i=1}^{n_H} z_i, \quad (8)$$

where n_H is the number of amino acids H. Then, we choose an amino acid H to move closer to the HCC so as not to increase the free energy of the protein.

Algorithm 1 Procedure of Local Search

```

1: while stop conditions not satisfied do
2:   Calculate the HCC coordinates
3:   Move ← SelectMove()
4:   if Move = Null then
5:     Break
6:   ApplyMove()

```

Algorithm 2 Procedure of K-ACO algorithm

```

1: Initialize pheromone trail matrix and set A of p ants
2: while stop conditions not satisfied do
3:   for a ∈ A do
4:     Ant a build a solution by random walk procedure
5:   Update pheromone trail follows SMMAS rule
6:   Use local search on the best solution
7:   Update the best solution
8: Decode solution and save the best solution

```

IV. SIMULATION

A. Different values of K

E_{MJ} is the average of energy values returned by our algorithm and N_{loops} is the average of the number of loops that our algorithm will be convergent. From Table II, we see that the number of loops needed for convergence increases when K increases. However, the value of E_{MJ} increases significantly when K increases from 1 to 3. Values of E_{MJ} when $K \in \{3, 4, 5\}$ do not differ much. The larger K , the more running time and memory our algorithm needed to complete. Hence, we choose $K = 3$ as default for the algorithm.

B. HP energy model

The data sets were used are H,F90,S,F180,R (Peter Clote laboratory¹) and 3MSE, 3MR7, 3MQZ, 3NO6, 3NO3, 3ON7 from Critical Assessment of Protein Structure Prediction competition², used in [15].

¹<http://bioinformatics.bc.edu/clotelab/FCCproteinStructure>.

²<http://predictioncenter.org>.

TABLE II: The result when trying multiple values of K

K	3NO3		3NO6		3ON7	
	E_{MJ}	N_{loops}	E_{MJ}	N_{loops}	E_{MJ}	N_{loops}
1	-110.29	494	-118.56	456	-120.18	565
2	-128.36	1043	-134.67	1126	-136.8	1247
3	-141.03	2230	-150.13	2371	-154.8	2612
4	-141.99	3104	-150.44	3462	-154.26	3790
5	-141.24	3407	-148.62	3821	-154.34	4207

TABLE III: Results when HP energy model was used

Protein details				State-of-the-art					ACO			
SEQ	size	HS	LBFE	TLS		GA plus		time(s)	best	avg	time(s)	RI(%)
				best	avg	best	avg					
H1	48	24	-69	-68	-66	-69	-69	1800	-69	-69	308	0.00
H2	48	24	-69	-68	-65	-69	-69		-69	-69	321	0.00
H3	48	24	-72	-69	-66	-72	-72		-72	-72	316	0.00
H4	48	24	-71	-70	-65	-71	-71		-71	-71	316	0.00
H5	48	24	-70	-68	-65	-70	-70		-70	-70	321	0.00
H6	48	24	-70	-69	-66	-70	-69		-70	-70	324	1.45
H7	48	24	-70	-69	-66	-70	-70		-70	-70	320	0.00
H8	48	24	-69	-67	-64	-69	-69		-69	-69	320	0.00
H9	48	24	-71	-68	-66	-71	-71		-71	-71	313	0.00
H10	48	24	-68	-68	-65	-68	-68		-68	-68	324	0.00
F90_1	90	50	-168	-164	-160	-168	-166	7200	-168	-166	584	0.00
F90_2	90	50	-168	-165	-158	-168	-165		-167	-165	589	0.00
F90_3	90	50	-167	-165	-159	-167	-164		-165	-163	596	-0.61
F90_4	90	50	-168	-165	-159	-168	-165		-167	-163	592	-1.21
F90_5	90	50	-167	-165	-159	-167	-166		-167	-166	590	0.00
S1	135	100	-357	-351	-341	-355	-348		-357	-354	878	1.72
S2	151	100	-360	-355	-343	-356	-349		-356	-352	996	0.86
S3	162	100	-367	-355	-340	-361	-348		-359	-353	1062	1.44
S4	164	100	-370	-354	-343	-364	-352		-360	-355	1077	0.85
F180_1	180	100	-378	-338	-326	-351	-341	18000	-352	-343	1194	0.59
F180_2	180	100	-381	-345	-333	-362	-346		-350	-343	1185	-0.87
F180_3	180	100	-378	-352	-338	-361	-350		-363	-357	1189	2.00
R1	200	100	-384	-332	-318	-355	-345		-353	-341	1341	-1.16
R2	200	100	-383	-337	-324	-360	-346		-347	-337	1359	-2.60
R3	200	100	-385	-339	-323	-363	-344		-346	-337	1342	-2.03
3MSE	179	84	-323	-268	-251	-292	-278		-286	-278	1312	0.00
3MR7	189	93	-355	-304	-287	-330	-316		-326	-318	1324	0.63
3MQZ	215	120	-474	-404	-384	-427	-412		-426	-415	1547	0.73
3NO6	229	116	-455	-390	-372	-423	-402	28800	-410	-400	1689	-0.50
3NO3	258	122	-494	-388	-372	-421	-404		-425	-411	1751	1.73
3ON7	279	146	u/k	-491	-461	-519	-490		-510	-495	1803	0.00

To evaluate the performance of K-ACO, we use Relative Improvement (RI), defined as

$$RI = \frac{E_A - E_B}{E_B}, \quad (9)$$

where E_A and E_B are the average energy values achieved by the K-ACO algorithm and by the state-of-the-art one, respectively. K-ACO was compared with two other algorithms: TLS [28] and GA [15]. For each protein, each of the three algorithms were run 50 times. Table III shows the best and the average result of 50 runs for each protein. It can be seen that K-ACO performed better as compared to TLS. However, K-ACO and GA performed similarly; the difference between them always below 3%. K-ACO performed better than GA in 10 protein sequences while GA better than K-ACO in 7 protein sequences. To further compare with GA, we increased the number of loops to 60,000 and applied this new change for those 7 protein sequences where GA did better. We see that, when increasing the number of loops, K-ACO performance improved and approximately as good as GA, as shown in Table V.

C. MJ energy model

In this section, data in Table IV were used for the MJ energy model. These data were also used in [16].

We run K-ACO on the above dataset and compare the result with other algorithms, namely Hybrid [29], Local search [30] and GA [15]. This is the best and average result taken from 50 runs for each protein sequence. From the column RI in Table VII, we can see that for all proteins sequences, our algorithm improved the average energy.

V. CONCLUSION

In this paper, we presented the K-ACO algorithm to predict the protein structure on the FCC lattice, using two different energy models— HP and MJ. This algorithm has a simple structure graph, the use of pheromone information in the k -order Markov model is more suitable for the 3D structure prediction and increase the efficiency of the ACO method. The simulation study shows that the proposed algorithm outperforms the state-of-the-art algorithms both in quality and running time. The algorithm can be improved by applying local search techniques according to memetic schemes. In this algorithm, the pheromone trail in the k -order Markov model with $k = 3$ is appropriate. Increasing k costs more memory and time, but the efficiency is not much improved. This technique can be applied to ACO algorithms for other similar problems.

TABLE V: K-ACO vs GA with increased running time

Protein details				GA plus			K-ACO		
SEQ	size	HS	LBFE	best	avg	time(s)	best	avg	time(s)
F90_3	90	50	-167	-167	-164	7200	-165	-164	1763
F90_4	90	50	-168	-168	-165	7200	-167	-165	1782
F180_2	180	100	-381	-362	-346	18000	-350	-346	3496
R1	200	100	-384	-355	-345	18000	-353	-345	4107
R2	200	100	-383	-360	-346	18000	-348	-340	4092
R3	200	100	-385	-363	-344	18000	-346	-340	4128
3NO6	229	116	-455	-423	-402	28800	-411	-404	5092

TABLE IV: Benchmark proteins used in our experiments with MJ model

ID	Length	Protein sequence
4RXN	54	MKKYTCTVCGYIYNPEDGDPDNGVNPGETDFKIDIPDDWVCPCLCGVGKQDFEEVEE
1ENH	54	RPRTAFSSQLARLKREFNENRYLTERRRQQLSSELGLNEAQIKIWFQNKRAKI
4PTI	58	RPDFCLLEPPYTGPCKARIIRYFYNAKAGLCQTFVYGGCRAKRNNFKSAEDCMRTCGGA
2IGD	61	MTPAVTTYKLIVINGKTLKGETTTKAVDAETAETAEKAFKQYANDNGVDGVWVYDDATKTFTVTE
1YPA	64	MKTEWPELVGKAVAAAKKVILQDKPEAQIIVLPVGTIVTMEYRIDRVRLFVDKLDNIAQVPRVG
1R69	69	SISSRVKSKRIQLGLNQAELAQKVGTTQSSIEQLENGKTKRPRFLPELASALGVSDWLLNGTSDSNVR
1CTF	74	AAEEKTEFDVILKAAGANKVAVIKAVRGATGLGLKEAKDLVESAPAALKEGVSKDDAEALKKALEEAGAEVEVK
3MX7	90	MTDLVAVWDVALSDGVHKIEFEHGTTSGRKRVVYVDGKKEIRKEWMFKLVGKETFFYVGAAKTKATINIDAISGFA YEYTL- INGKSLKKYM
3NBM	108	SNASKELKVVLVLCAGSGTSAQLANAINEGANLTVRVIANSGAYGAHYDIMGVYDLIILAPQVRSYYREMKVDA ERLGIQIVATRGMEYIHLTKSPSKALQFVLEHYQ
3MQO	120	PAIDYKTAFFHLAPIGLVLSRDRVIEDCNDELAIFRCARADLIGRSFEVLYPSSDEFERIGERISPMIAHGSY ADDRIMKRAGGELFWCHVTGRALDRTPLAAGVWTFEDLSATRVA
3MRO	142	SNALSASEERFQLAVSGASAGLWDWNPKTGAMYLSPHFKKIMGYEDHELPEITGHRESIHPPDRARVLAALKA HLEHRDITYDVEYRVTRSGDFRWIQSRGQALWNSAGEPYRMVGWIMDVTDRKRDEDALRVREELRRL
3PNX	160	GMENKKMNLFFSGDYGKALASLIANAAREMEIEVTIFCAFWGLLLLRDPEKASQEDKSLYEQAFSSLTPREA EELPLSKMNLGGIGKKMLLEMMKEEKAPKLDLLSGARKKEVKFYACQLSVEIMGFKKEELFPEVQIMDVKEYL KNALESDLQLFI
3MSE	180	GISPVLNNMKSYSMKHSNIRNIINIMAHELSVINNHKIYNELFYKLDTNHNGSLSHREIYTVLASVGIKKWD INRILQALDINDRGNITYTEFMAGCYRWKNIESTFLKAFFNKIDKDEGDGYISKSDIVSLVHDKVLDNNDIDNFF LSVHSIKKGIPREHIINKISFQEFKDYMLSTF
3MR7	189	SNAERRLCAILAADMAGYSRLMERNETDVLNRQKLYRRELIDPAIAQAGGQIVKTTGDGMLARFDTAQAALRCA LEIQQAMQOREEDTPRKRIQYRIGINIGDIVLEDGDFGDAVNVAARLEAISEPGAICVSDIVHQITQDRVSE PFTDLGLQKVKNITRPIRVWQWVPDADRQSHDPQPSHVQH
3MQZ	215	SNAMSVQTIERLQDYLLPEWVSIFDIADFSGRMLRIRGDIRPALLRLASRLAELLNESPGRPWPYPHVASHMRRR VNPPETWALGPCKRGYKSYAHSGVFIIGRGLSVRFILKDEAIEERKNLGRWMSRSGPAFEQWKKKVGDLRDFG PVHDDPMADPPKVEWDPRVFGERLGLSKASLDIGFRVTFDTSLAGIVKTIRTFDLLYAEAEKGS
3NO3	238	GKDNTKVIAHRGYWKTEGSAQNSIRSLERASEIGAYGSEFDVHLTADNVLVVYHDNDIQGKHQISCTYDELKDLQ LSNGEKLPTLEQYLKRAKKLKNIRLIFELKSHDTPERNRDAARLSVQVMKRMKLAKRTDYISFNMDACKEFIRLC PKSEVSYLNGELSPMELKELGFTGLDYHYKVLQSHPDWVKDCKVLGMTSNVWTVDDPKLMEEMIDMGVDFITDDL PEETQKILHSRAQ
3NO7	248	MGSDKIHHHHHHENLYFQGMFTFSKELREASRPIIDDIYNDGFIQDLLAGKLSNQAVRQYLRADASYLKEFTNIYA MLIPKMSSMEDVKFLVEQIEFMLEGEVEAHEVLADFINEPYEEIVKEKVVWPPSGDHYIKHMYFNAFARENAAFI AAMAPCPYVYAVIGKRAMEDPKLNKESVTSKWFQFYSTEMDELVDVFDQLMDRLTKHCSETEKKEIKENFLQSTI HERHFFNMAYINEKWEYGGNNNE
3ON7	280	GMKLETIDYRAADSARFVESLRETGFGLVLSNHPIDKELVERIYTEWQAFFNSEAKNEFMFNRETHDGFPPASIS ETAKGHTVKDIKEYYHYVYPWGRIPDSLNRANILAYYEKANTLASELLEWIETYSPEIKAKFSLPEMIANSHKT LLRILHYPTMTGDEEMGAIRAAAHEDINLITVLTANEPGLQVKAADGGSWLDVPSDFGNIINIGMDLQEAESDGY FPSTSHRVINPEGTDKTSRISLPLFLPHPSVVLSERYTADSYLMERLRELGLV

TABLE VII: K-ACO vs other algorithms (bold values are the best one in their row)

Protein details			Hybrid		Local search		GA		K-ACO		
SEQ	size	H	best	avg	best	avg	best	avg	best	avg	RI(%)
4RXN	54	27	-32.61	-30.94	-33.33	-31.21	-36.36	-33.6	-37.98	-36.84	9.64
1ENH	54	19	-35.81	-35.07	-29.03	-28.18	-38.39	-35.67	-37.51	-36.49	2.3
4PTI	58	32	-32.07	-29.37	-31.16	-28.33	-35.65	-31.01	-37.2	-33.35	7.55
2IGD	61	25	-38.64	-32.54	-32.36	-28.29	-36.49	-33.75	-36.77	-35.09	3.97
1YPA	64	38	n/a	n/a	-33.33	-32.15	-40.14	-36.33	-40.52	-38.93	7.16
1R69	69	30	-34.2	-31.85	-33.35	-32.2	-40.85	-36.28	-39.73	-38.59	6.37
1CTF	74	42	-38	-35.28	-45.83	-40.94	-51.5	-47.29	-53.72	-51.09	8.04
3MX7	90	44	n/a	n/a	-44.81	-42.32	-56.32	-50.95	-58.1	-56.04	9.99
3NBM	108	56	n/a	n/a	-52.44	-49.51	-49.51	-49.9	-59.71	-57.5	15.23
3MQO	120	68	n/a	n/a	-64.04	-58.84	-62.25	-54.56	-70.62	-67.5	14.72
3MRO	142	63	n/a	n/a	-87.38	-82.24	-90.05	-82.32	-101.34	-98.2	19.29
3PNX	160	84	n/a	n/a	-103.04	-96.86	-102.55	-88.06	-116.31	-112.18	15.82
3MSE	180	83	n/a	n/a	n/a	n/a	-92.61	-84.6	-110.9	-106.44	25.82
3MR7	189	88	n/a	n/a	n/a	n/a	-93.65	-83.93	-120.64	-115.02	37.04
3MQZ	215	115	n/a	n/a	n/a	n/a	-104.29	-95.22	-132.09	-126.62	32.98
3NO3	238	102	n/a	n/a	n/a	n/a	-122.97	-108.7	-151.84	-147.86	36.03
3NO7	248	112	n/a	n/a	n/a	n/a	-133.95	-117.11	-163.89	-156.01	33.22
3ON7	280	135	n/a	n/a	n/a	n/a	-116.88	-96.64	-167.12	-160.29	65.86



Fig. 3: New best structure found by K-ACO for two largest datasets.

TABLE VI: Running time of K-ACO and GA

Protein details			K-ACO	GA
SEQ	size	H		
4RXN	54	27	706.97	3600
1ENH	54	19	708.4	
4PTI	58	32	770.32	
2IGD	61	25	798.04	
1YPA	64	38	848.82	
1R69	69	30	916.28	
1CTF	74	42	991.53	
3MX7	90	44	1183.9	
3NBM	108	56	1414.94	
3MQO	120	68	1584.95	
3MRO	142	63	1831.22	
3PNX	160	84	2061.74	
3MSE	180	83	2337.52	7200
3MR7	189	88	2461.5	
3MQZ	215	115	2806.42	
3NO3	238	102	3053.11	
3NO6	248	112	3154.14	
3ON7	280	135	3576.92	

REFERENCES

- [1] C. M. Dobson, "Protein folding and misfolding," *Nature*, vol. 426, no. 6968, pp. 884–890, 2003.
- [2] A. Breda, N. F. Valadares, O. N. de Souza, and R. C. Garratt, "Protein structure, modelling and applications," in *Bioinformatics in Tropical Disease Research: A Practical and Case-Study Approach*, A. Gruber, A. Durham, and C. Huynh, Eds. Oxford University Press, 2007.
- [3] P. Veerapandian, *Structure-based drug design*, 1997, vol. 11, no. 32.
- [4] C. B. Anfinsen, "Principles that govern the folding of protein chains," *Science*, vol. 181, no. 4096, pp. 223–230, 1973.
- [5] A. Bruce, A. Johnson, J. Lewis, M. Raff, K. Roberts, and P. Walters, "The shape and structure of proteins," *Molecular Biology of the Cell*, 2002.
- [6] C. A. Floudas, "Computational methods in protein structure prediction," *Biotechnology and Bioengineering*, vol. 97, pp. 207–213, 2007.
- [7] C. M. Dobson, "Computational biology: protein predictions," pp. 176–177, 2007.
- [8] H. Berman, "The protein data bank," *Nucleic Acids Res*, pp. 235–242, 2000.
- [9] A. Bechini, "On the characterization and software implementation of general protein lattice models," *PLoS ONE*, 2013.
- [10] I. Dotu, M. Cebrian, P. V. Hentenryck, and P. Clote, "On lattice protein structure prediction revisited," *IEEE/ACM Tr. Comp. Biol Bioinfo.*, 2011.
- [11] M. Mann and R. Backofen, "Exact methods for lattice protein models," *Bio-Algorithms and Med-Systems*, vol. 10, no. 4, pp. 213–225, 2014.
- [12] D. Covell and R. Jernigan, "Conformations of folded proteins in restricted spaces," *Biochemistry*, pp. 3287–94, 1990.
- [13] T. C. Hales, "A proof of the kepler conjecture," *The Annals of Mathematics*, vol. 162, no. 3, pp. 1065–1185, 2005.
- [14] B. Maher, A. A. Albrecht, M. Loomes, X.-S. Yang, and K. Steinhöfel, "A firefly-inspired method for protein structure prediction in lattice models," *Biomolecules*, pp. 56–75, 2014.
- [15] M. A. Rashid, F. Khatib, M. T. Hoque, and A. Sattar, "An enhanced genetic algorithm for ab initio protein structure prediction," *IEEE Transactions on Evolutionary Computation*, vol. 20, pp. 627–644, 2016.
- [16] M. A. Rashid, S. Iqbal, F. Khatib, M. T. Hoque, and A. Sattar, "Guided macro-mutation in a graded-energy based genetic algorithm for protein structure prediction," *Comp. Biology and Chemistry*, pp. 162–177, 2016.
- [17] K. F. Lau and K. A. Dill, "A lattice statistical mechanics model of the conformational and sequence spaces of proteins," *Macromolecules*, vol. 22, no. 10, pp. 3986–3997, 1989.
- [18] S. Miyazawa and R. L. Jernigan, "Residue–residue potentials with a favorable contact pair term and an unfavorable high packing density term, for simulation and threading," *Journal of Molecular Biology*, vol. 256, no. 3, pp. 623–644, 1996.
- [19] R. Unger and J. Moult, "Finding the lowest free energy conformation of a protein is an NP-hard problem: Proof and implications," *Bulletin of Mathematical Biology*, vol. 55, no. 6, pp. 1183–1198, 1993.
- [20] M. Paterson and T. Przytycka, "On the complexity of string folding," *Discrete Applied Mathematics*, vol. 71, no. 1–3, pp. 217–230, 1996.
- [21] A. Shmygelska and H. H. Hoos, "An ant colony optimisation algorithm for the 2D and 3D hydrophobic polar protein folding problem," *BMC Bioinformatics*, vol. 6, no. 1, p. 30, 2005.
- [22] V. Cutello, G. Nicosia, M. Pavone, and J. Timmis, "An immune algorithm for protein structure prediction on lattice models," *IEEE Transactions on Evolutionary Computation*, vol. 11, no. 1, pp. 101–117, 2007.
- [23] R. Unger and J. Moult, "A genetic algorithm for 3D protein folding simulations," in *5th Intl. Conf. Genetic Algorithms*, 1993, p. 581.
- [24] M. T. Hoque, M. Chetty, and A. Sattar, "Protein folding prediction in 3D FCC HP lattice model using genetic algorithm," in *IEEE Congress on Evolutionary Computation*, 2007, pp. 4138–4145.
- [25] S. R. D. Torres, D. C. B. Romero, L. F. N. Vasquez, and Y. J. P. Ardila, "A novel ab-initio genetic-based approach for protein folding prediction," in *9th Conf. Genetic and Evolutionary Computation*, 2007, pp. 393–400.
- [26] L. Kapsokalivas, X. Gan, A. A. Albrecht, and K. Steinhöfel, "Population-based local search for protein folding simulation in the MJ energy model and cubic lattices," *Comp. Biol. Chem.*, vol. 33, no. 4, pp. 283–294, 2009.
- [27] N. Mansour, F. Kanj, and H. Khachfe, "Particle swarm optimization approach for protein structure prediction in the 3D HP model," *Interdisciplinary Sciences, Comp. Life Sciences*, vol. 4, pp. 190–200, 2012.
- [28] M. Cebrián, I. Dotú, P. Van Hentenryck, and P. Clote, "Protein structure prediction on the face centered cubic lattice by local search," *23rd Conference on Artificial Intelligence*, vol. 8, pp. 241–246, 2008.
- [29] A. D. Ullah and K. Steinhöfel, "A hybrid approach to protein folding problem integrating constraint programming with local search," *BMC Bioinformatics*, vol. 11, no. 1, p. S39, 2010.
- [30] S. Shatabda, M. Newton, and A. Sattar, "Mixed heuristic local search for protein structure prediction," in *Conf. Arti. Intel.*, 2013, pp. 876–882.
- [31] S. Miyazawa and R. L. Jernigan, "Estimation of effective interresidue contact energies from protein crystal structures: Quasi-chemical approximation," *Macromolecules*, vol. 18, no. 3, pp. 534–552, 1985.
- [32] M. Dorigo, V. Maniezzo, and A. Colomi, "Positive feedback as a search strategy," *Tech. Rep.*, 1991.
- [33] D. Do Duc, H. Q. Dinh, and H. H. Xuan, "On the pheromone update rules of ant colony optimization approaches for the job shop scheduling problem," in *PRIMA Conference*. Springer, 2008, pp. 153–160.

EEG Affective Modelling for Dysphoria Understanding

Norhaslinda Kamaruddin

Faculty of Computer and
Mathematical Sciences
Universiti Teknologi MARA
Shah Alam, Selangor, Malaysia
norhaslinda@tmsk.uitm.edu.my

Mohd Hafiz Mohd Nasir

Faculty of Computer and
Mathematical Sciences
Universiti Teknologi MARA
Shah Alam, Selangor, Malaysia
mhafiz2201@gmail.com

Abdul Wahab Abdul Rahman

Kulliyah of Information and
Communication Technology
International Islamic University
Malaysia
Gombak, Kuala Lumpur, Malaysia
abdulwahab@iiu.edu.my

Abstract—Dysphoria is a state of dissatisfaction, restlessness or fidgeting. It is a state of feeling unwell in relation to mental and emotional discomfort. If this state is not carefully handled, it may lead to depression, anxiety, and stress. To date, 21-item instruments of Depression, Anxiety and Stress Scale (DASS) is employed to measure dysphoria. Although DASS provides a quantitative assessment of the human affective state, it is subjected to interpretation. To complicate matters, pre-cursor emotion and pre-emotion of the participants can result in biasness of the DASS report. Hence, a more direct method in measuring human affective state by analyzing the brain pattern is proposed. The approach can also address the dynamic affective state which is needed in detecting dysphoria. Brain waves pattern are collected using the electroencephalogram (EEG) device and used as the input to analyze the underlying emotion. In this paper, relevant features were extracted using Mel-frequency cepstral coefficients (MFCC) and classified with Multi-Layer Perceptron (MLP). The experimental results show potential of differentiating between positive and negative emotion with comparable accuracy. Subsequently, it is envisaged that the proposed model can be extended as a tool that can be used to measure stress and anxiety in work places and education institutions.

Keywords—*dysphoria; Electroencephalogram (EEG); Emotion; Affective Space Model; Multi-Layer Perceptron*

I. INTRODUCTION

While technology has helped most people to accelerate and improve in many areas of life, namely; transportation, work, and communication, some individual found it stressful and troubled that their quality of life is being compromised. For instance, the dependency to the gadget will be increased and the outcome of technological failure is not desirable. In addition, the widespread of social media may affect interpersonal relationship, give skewed perception of social norm and give more opportunities for cyber bullying. The recent survey #StatusOfMind collected by Royal Society of Public Health (RSPH) and Young Health Movement (YHM) from 13 February to 8 May 2017 among 1,500 people aged 14 to 24 years old in the United Kingdom revealed that 91% of 16-24 years old use the internet for social networking and the rates of anxiety and depression in young people have risen 70% in the past 25 years [1]. Almost similar outcome is also

reported by American Psychological Association in 2016 that observed more than one-third adults (approximately 34%) experienced increase level of stress in 2015 while only 16% adults from the survey gave a contrary response [2]. Stress was also found to be the main reason for absenteeism, reduced productivity, fast labor turnover, poor timekeeping and accidents [3]. According to Muzzaffar, 70% percent of Malaysian workers have occupational or work-related stress illnesses [4]. The report also revealed that 48% of the Malaysian respondents felt their occupational or work stress levels had risen over the years. Therefore, the state before full-blown stress occurrence should be identified to prevent unwanted consequences.

Dysphoria is a complex emotional state that is usually associated with discontent, frustration, dissatisfaction or crushed expectation. It is usually regarded as day-to-day reaction of a person facing disappointment in his/her life [5]. It acts as a possible trigger point of either positive or negative adaptation states starting with normal condition to the situation when an individual faces disappointment. If the disappointment is not discovered early and addressed, individual may fall into dysphoria state where the condition of disappointment can be acute. A well-adjusted person will recuperate from this stage by triggering the adaptation state. However, if adaptation state is not reached, the individual may experience stress that may lead to clinical depression if it is not properly handled. Since emotion is the manifestation of mental states that can be closely mapped to dysphoria, emotion measurement methods can be adopted [6].

Currently, there is no computational measurement tool that is easily assessable for the public to identify dysphoria tendency except questionnaire. Experienced psychologists normally examine the dysphoria symptoms by using the 21-item instruments of Depression, Anxiety and Stress Scale (DASS). The DASS test is used to measure the negative emotional states and can only provide subjective diagnostic measurement of the patients depending on the knowledge and experience of the psychiatrists and psychologists. Such situation posed a problem due to limited number of trained psychologist. Furthermore, the cost for such instrument is expensive. Malaysia at present does not have enough certified psychologist, psychiatrist, or neurologists to meet the demands.

According to WHO report [7], there are only 0.83 psychiatrists and 0.27 psychologists per 100,000 populations. Thus, a computational tool to assist in pre-screening dysphoria to complement the psychologists and psychiatrists is needed.

This paper is organized in the following manner. Section 2 describe the literature review focusing on dysphoria and current approaches implemented to detect dysphoria. The proposed approach as well as the data collection and experimental set-up are described in Section 3. The result and discussion are presented in Section 4. This paper concludes with Section 5 with summary and future work.

II. LITERATURE REVIEW

The term ‘dysphoria’ comes from a Greek word; dysphoros that means difficult to bear dissatisfaction or hard to adapt [8]. Generally, dysphoria can refer to mood disorder and it is associated with negatives mood deviations [9]. According to Starcevic [10], dysphoria denotes as a distress that is hard to bear. In addition, dysphoria can also be defined as a complex emotional state [5]. In this paper dysphoria is defined as the state after disappointment of event that is prior to stress and it is always associated with negative emotions.

To further understand dysphoria and its related studies, different research approaches are reviewed. Koster, Raedt, Leyman, and Lissnyder [11] observed that depression is characterized by mood congruent attention bias and memory bias in dysphoria. An experiment involving 41 participants who scored above 13 (denoted as stable) and another 41 participants who scored below 6 (denoted as dysphoric) are tested using spatial cueing task consists of 45 words based on Beck Depression Inventory (BDI-II). The experimental results show that the dysphoric participants tend to take longer time for the negative words regardless on their gender and age distribution. In addition, Yuan and Kring [12] studied the different responses between dysphoric and non-dysphoric group based on prediction and actual responses by winning and losing task using a computer. There are 72 participants involved in the study and divided into two groups of dysphoric and non-dysphoric based on their score in Beck Depression Inventory (BDI). Both groups showed that they experienced negative emotions after losing money. However, the dysphoric group showed that they experienced less happiness and contentment than non-dysphoric group when they were winning money. Such finding shows that after disappointment, everyone will experience dysphoria, but well-adjusted person may adapt and move on, but dysphoric person may dwell on the losing effects.

Since dysphoria is very closely related to negative emotions, Encephalogram (EEG) emotion identification study is reviewed. The EEG is a medical imaging technique where small electrical signals caused by neuron activation in the brain are captured. Its capability to record functional and physiological changes with high temporal resolution and portability compared to MEG or fMRI are the main reason the suitability of using EEG for data collection.

Typically, the International 10-20 system is used to place the electrodes at the scalp and the location of the nodes is determined by anatomical skull landmarks. Different regions

of the brain are identified as Fp (Frontopolar), F (Frontal), C (Central), P (Parietal), O (Occipital) and T (Temporal). For the midline placements, Z is used. A signifies an ear channel where A1 denotes for left ear and A2 denotes for right ear. Technologists measure the distance from the nasion to the inion and the head circumference, marking precise electrode locations based on 10% or 20% intervals of those distances, hence the name ‘10-20’ is used [13]. Figure 1 shows the 10-20 system electrode placement.

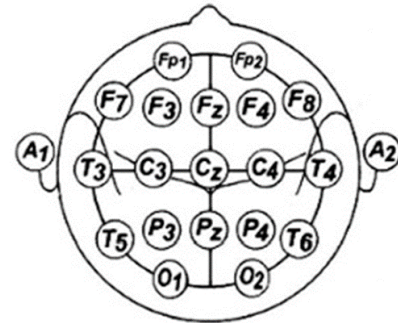


Fig. 1. The International 10-20 Electrode Placement System [13]

Frontal signal typically associated with emotion processing. It has dramatic expansions in emotional, behavioral and social capacities [14]. Moreover, according to Asakawa et al [15], the frontal region is known to handle emotions, with a sub-region specializing in information processing. It is observed that healthy participants show prompt emotion processing in a specific brain location while participants with strong mental illness tendency processed emotion in both brain hemispheres. Previously, Teplan [16] mentioned that different electrode placement can be used to measure different brain functions, for instance; F7 is for rational activities, Fz for intentional and motivational, F8 for emotional impulses, C3, C4 and Cz deals with sensory and motor function, P3, P4 and Pz contribute to activity of perception and differentiation, and T3 and T4 deal with emotional processor. In addition, T5 and T6 process certain memory functions and primary visual areas can be found in O1 and O2. In this work, 6 channels are selected, namely; F3, F4, F7, F8, FP1 and FP2. Further analysis on the way different channel behaves for negative emotion classification will be further studied.

Othman, Wahab, Karim, Dzulkifli and Alshaikli [17] focuses in EEG emotion recognition based on 2 dimensional models of emotions, which are recalibrated Speech Affective Space Model (rSASM) [18] and 12-Point Affective Circumplex (12-PAC) model [19]. The brain signal of 5 preschoolers with age ranging from 5 to 6 years old are captured when four emotions of happiness, sadness, calm and fear stimuli are presented. The stimuli are taken from the standard RadBound Faces Database (RafD). The relevant features are extracted using Kernel Density Estimation (KDSE) and Mel-Frequency Cepstral Coefficients (MFCC) coupled with Multi-Layer Perceptron (MLP) classification. Based on the homogeneous classification, the MFCC feature extraction method yielded mean squared error ranging 0.08 to 0.15 with disparity of 0.1 to 0.2 with 12-PAC model with mean squared error of 0.25 to 0.28 respectively. On contrary, 12-PAC model outperformed rSASM with mean squared error

ranging from 0.07 to 0.09 as opposed to 0.15 and 0.19 mean squared error once KSDE feature extraction is employed. Hence, in this paper MFCC feature extraction coupled with rSASM model approach will be employed in this paper due to its performance in homogeneous experiment to study the performance of different EEG channel with respect to negative emotions classification.

III. METHODOLOGY

A. Data Collection and Experimental Protocol

This research focuses on EEG signals garnered from multiple channels, namely: F3, F4, F7, F8, FP1 and FP2 to measure the negative emotion classification. Four different window sizes of 512, 1024, 2048 and 4096 for MFCC are prepared to see the performance disparity between these window size for each channel.

There are four participants involved in the data collection with age mean of 27.5 years and variance of ± 1.25 years. All participants are healthy male with no medical record of experiencing acute depression, anxiety and stress. Prior to the experiment, the participants are briefed about the study and signed the consent form to follow the International Islamic University Malaysia (IIUM) ethic committee procedure. They are in neutral state and not under the influence of medicine, drug or alcohol. Each of the participant took the DASS-21 test to coordinate the psychological result with the EEG experiment. The DASS-21 results show that the participants are not experiencing depression, anxiety and stress at the time of the data collection.

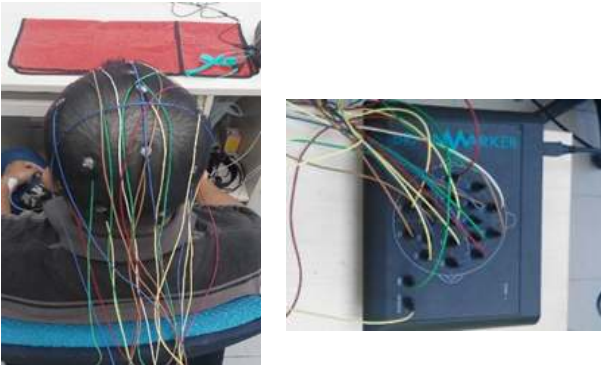


Fig. 2. (a) The Electrode Placement on the Participant Scalp and (b) The EEG Device Used for Data Collection.

Once the pre-EEG experiment set-up has been completed, the participants are needed to sit comfortably on a chair facing the laptop where selected stimuli will be presented. During the experiment, the participants are reminded to minimize the physical movement as the artefacts may disturb the EEG signals recorded. The electrodes are placed on the participants scalp using the reference of the international 10-20 electrode placement system [13]. In order to improve the conductivity of the brain electrical signals, conducting gel is placed between the electrode and the scalp. This is also to ensure the impedance is kept to a minimum. The experiment is conducted in the laboratory environment with controlled ambience to

ensure distraction and background noise are low. Before the EEG signals are captured, the electrode placement check is done to ensure good signal quality can be recorded. The device used to capture the brain signal is BrainMarker with 19 channels. Figure 2(a) depicts the electrode placement on the participants scalp and Figure 2(b) show the EEG device used for data collection.

Initially, the resting state of the participant is recorded. The resting state refers to the state before any stimuli are presented to the participants. They had to open their eyes for a minute and followed by closing their eyes for another minute. Then, emotional test will be conducted. In this test, participants need to look at four emotional stimuli representing happiness, sadness, calm and fear images in one minute each respectively. The images are taken from International Affective Picture System (IAPS) [21] developed by The Center for the Study of Emotion and Attention, University of Florida. This dataset is considered a standard dataset and widely used by the affective computing researchers in emotion elicitation. Video stimuli is presented for fear and sadness to gauge the video effect on negative emotion. The data collection protocol is concluded with resting state (after) with one-minute eye-opening and eye-closing. The overall time taken for data collection in this work is 10 minutes without considering the pre-EEG experiment and post-EEG experiment tasks. The summary of the experiment is provided in Figure 3. The EEG signals are captured and collected in the form of numeric values and kept in CSV format file.

Resting State		Emotion Test				Video Stimuli	
Eye Open	Eye Close	Happy	Sad	Calm	Fear	Fear Video	Sad Video
1 minute	1 minute	1 minute	1 minute	1 minute	1 minute	1 minute	1 minute
2 minutes		4 minutes				2 minutes	

Fig. 3. The EEG Experiment Protocol

B. Video Stimuli and Self-assessment Manikin (SAM)

Video data are collected to see whether the usage of different medium of data can better elicit the negative emotion as compared to static images as presented by IAPS [21]. To give some insights, a Self-Assessment Manikin (SAM) approach is adopted [22]. SAM is a picture-oriented instrument to access the valence, arousal and dominance associated with the emotional stimuli. Valence refers to the positive or negative impact of the stimuli to the participant whereas arousal can be defined as the level of activation ranging from active to passive. Subsequently, dominance is the impact of the stimuli to the participant. The participants need to select the value that they deemed appropriate to represent the feeling they experienced when the stimuli are presented. In this work, 5 volunteers are involved with the selection of the video stimuli (3 male and 2 females with age mean of 25.4 years and variance of ± 3.6 years). 3 videos are selected each for fear and sadness. The videos are typically about war, festival celebration, human kindness, abuse and spooky movie snippets that are gathered from the internet. Each video duration is approximately two minutes each. The volunteers watched the video and select the most appropriate value of valence, arousal

and dominance that they experienced. To ensure that the volunteers understand the difference between the emotion primitives, a brief explanation has been provided. Based on the survey, video Sad3 and Fear2 are selected based on the maximum SAM assessment value. The whole SAM assessment result is presented in Table 1. The result indicates that high negative valence with consistent arousal and dominance values are recorded for the selected video

TABLE I. THE SAM OVERALL RESULT

Vid	Volunteer 1			Volunteer 2			Volunteer 3			Volunteer 4			Volunteer 5		
	V	A	D	V	A	D	V	A	D	V	A	D	V	A	D
Sad1	3	5	7	2	4	8	4	5	6	5	6	6	3	6	7
Sad2	7	7	5	6	2	5	3	5	8	4	5	7	5	6	7
Sad3	3	5	5	3	5	6	7	4	6	6	5	5	5	6	7
Fear1	7	3	7	3	4	6	5	5	6	4	4	5	5	6	4
Fear2	3	3	7	5	6	4	2	7	9	3	5	6	4	6	8
Fear3	3	2	3	4	4	3	4	5	6	5	5	5	3	6	5

^a. V represents Valence, A represents Arousal and D represents Dominance

C. Dysphoria EEG Experiment General Architecture

Once the EEG data has been collected, the data pre-processing phase is conducted. The signal that is more than 50Hz are removed. This is because such high frequency data are typically artifacts resulting from hand, eye and muscle movements. The elliptic function is used to smoothen the signals. Then, relevant features are extracted using Mel-Frequency Cepstral Coefficient (MFCC) with four different window sizes of 512, 1024, 2048 and 4096 to study the impact of window size to emotion classification performance. Multi-Layer perceptron is then employed as classifier to recognize the emotion. MLP is selected to emulate the way the information is being processed in the brain. In this work, MLP with X neuron in X hidden layer is implemented. Figure 4 simplify the general architecture of the dysphoria EEG experiment.

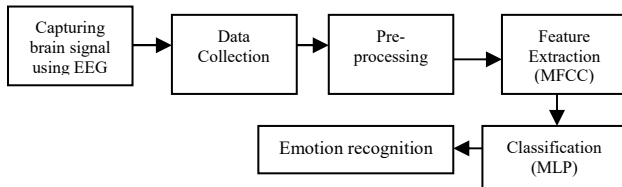


Fig. 4. The General Architecture of Dysphoria EEG Experiment.

IV. EXPERIMENTAL RESULT AND DISCUSSION

The EEG signals captured are classified using Multi-Layer Perceptron and the result is presented in Table II. In this work, two-classes classification results are compared, namely; calm vs happiness, calm vs fear and calm vs sadness. This is to give insight to the level of disparity of one emotion to another (in this case the differences between calm and other emotion. The yellow cells indicate the best performance whereas the green cells represent the minimum accuracy recorded respectively. The performance recorded ranging from 34.6% to 100%. The result in Table II indicates that window size of 4096 managed to yield consistently high accuracy across the three EEG emotion recognition experiments and mixed results are

obtained for worst performance. Hence, for channel performance analysis, only window size of 4096 is considered.

The performance of individual for emotion recognition experiment can be summarized as Figure 5. It can be observed that Subject2 scores the highest accuracy with mean accuracy of 96% followed by Subject3 with average performance of 90%. Subject 1 and Subject 4 recorded mean performance of 76% and 83% respectively. Calm vs Happiness experiment shows that the proposed approach can distinguish between calm and happiness with average accuracy of 91% followed by 9% and 7% decrement for Calm vs Fear and Calm vs Sadness experiment respectively. The result also indicates that the EEG calm signal is more similar to fear and sad EEG signals.

Further analyses are conducted to study the effect of emotion elicitation using video and IAPS stimuli as presented in Figure 6. It is obvious that IAPS stimuli performance is always outperformed video stimuli in all EEG emotion recognition experiments. This is because the brain need to process more information when video stimuli is presented as opposed to static images displayed in IAPS stimuli. Hence, lower performance is recorded.

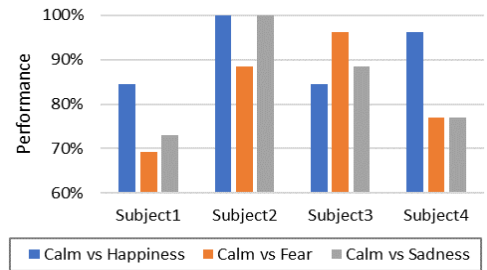


Fig. 5. The General Performance of Emotion Recognition Experiment.

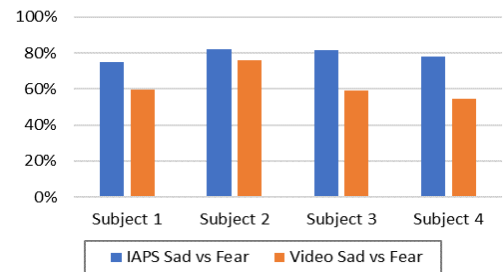


Fig. 6. The General Performance of Emotion Recognition Experiment.

In order to identify the performance of each channel, a radar diagrams are constructed for each participant with focus to the result from 4096 window size experiment. Average performance ranging from 51.28% to 91.03% are recorded for emotion recognition. It is observed that there is no channel can claim superiority and it can be seen in Figure 7(a) – 7(d) that different channel performs differently on different individual. For instance, the highest accuracy for Subject1 is recorded by channel FP1 with mean performance of 71.79% and the highest performance for Subject3 is yielded by F4 with mean performance of 82.05%. Both Subject2 and Subject4 recorded channel F8 as the highest accuracy with mean performance of

TABLE II. THE RESULT OF EEG EMOTION CLASSIFICATION

Participant	Channel	Calm vs Happiness				Calm vs Fear				Calm vs Sadness			
		512	1024	2048	4096	512	1024	2048	4096	512	1024	2048	4096
Subject 1	FP1	58.0%	54.5%	64.5%	84.6%	65.9%	56.0%	59.7%	65.4%	61.6%	62.7%	58.1%	65.4%
	FP2	67.0%	70.1%	80.6%	53.8%	55.1%	54.5%	59.7%	69.2%	59.8%	59.0%	61.3%	57.7%
	F3	53.6%	63.4%	67.7%	57.7%	55.8%	57.5%	40.3%	69.2%	64.9%	63.4%	48.4%	73.1%
	F4	65.9%	66.4%	61.3%	65.4%	61.2%	61.2%	64.5%	34.6%	56.5%	63.4%	58.1%	53.8%
	F7	67.4%	51.5%	75.8%	46.2%	65.9%	60.4%	62.9%	65.4%	70.7%	64.2%	72.6%	69.2%
	F8	59.8%	62.7%	64.5%	69.2%	55.4%	53.7%	48.4%	57.7%	55.4%	53.7%	53.2%	65.4%
Subject 2	FP1	59.1%	64.9%	54.8%	84.6%	50.0%	53.0%	46.8%	57.7%	49.6%	56.0%	54.8%	34.6%
	FP2	58.0%	55.2%	66.1%	76.9%	58.3%	59.0%	69.4%	73.1%	56.9%	58.2%	67.7%	61.5%
	F3	50.7%	56.7%	58.1%	88.5%	66.3%	64.2%	67.7%	88.5%	55.4%	53.7%	64.5%	57.7%
	F4	60.9%	61.9%	66.1%	53.8%	59.4%	62.7%	64.5%	80.8%	62.7%	65.7%	71.0%	76.9%
	F7	65.2%	64.2%	74.2%	69.2%	68.8%	79.1%	69.4%	84.6%	61.6%	67.9%	56.5%	84.6%
	F8	81.2%	81.3%	82.3%	100.0%	58.0%	65.7%	83.9%	73.1%	85.1%	85.8%	100.0%	100.0%
Subject 3	FP1	58.7%	54.5%	64.5%	65.4%	64.5%	63.4%	79.0%	96.2%	54.0%	53.7%	61.3%	69.2%
	FP2	57.2%	62.7%	62.9%	84.6%	58.3%	60.4%	69.4%	57.7%	53.6%	50.0%	61.3%	61.5%
	F3	56.5%	58.2%	53.2%	57.7%	53.3%	58.2%	69.4%	92.3%	55.1%	48.5%	58.1%	53.8%
	F4	55.1%	53.7%	61.3%	76.9%	59.1%	56.0%	62.9%	80.8%	58.7%	56.7%	67.7%	88.5%
	F7	62.0%	61.2%	61.3%	76.9%	67.4%	71.6%	82.3%	80.8%	54.7%	54.5%	62.9%	53.8%
	F8	60.5%	53.7%	56.5%	69.2%	55.4%	63.4%	71.0%	69.2%	54.3%	54.5%	74.2%	76.9%
Subject 4	FP1	82.6%	85.8%	79.0%	80.8%	59.4%	59.7%	59.7%	57.7%	69.2%	75.4%	72.6%	73.1%
	FP2	68.5%	74.6%	64.5%	76.9%	55.4%	58.2%	64.5%	61.5%	61.2%	72.4%	56.5%	73.1%
	F3	69.9%	68.7%	64.5%	76.9%	63.0%	57.5%	53.2%	76.9%	58.0%	57.5%	61.3%	53.8%
	F4	72.5%	75.4%	80.6%	84.6%	69.9%	76.1%	72.6%	73.1%	64.5%	73.1%	67.7%	76.9%
	F7	57.2%	58.2%	74.2%	92.3%	53.6%	61.9%	64.5%	46.2%	55.8%	60.4%	46.8%	65.4%
	F8	62.0%	67.2%	75.8%	96.2%	71.0%	73.1%	74.2%	76.9%	51.8%	64.2%	64.5%	69.2%

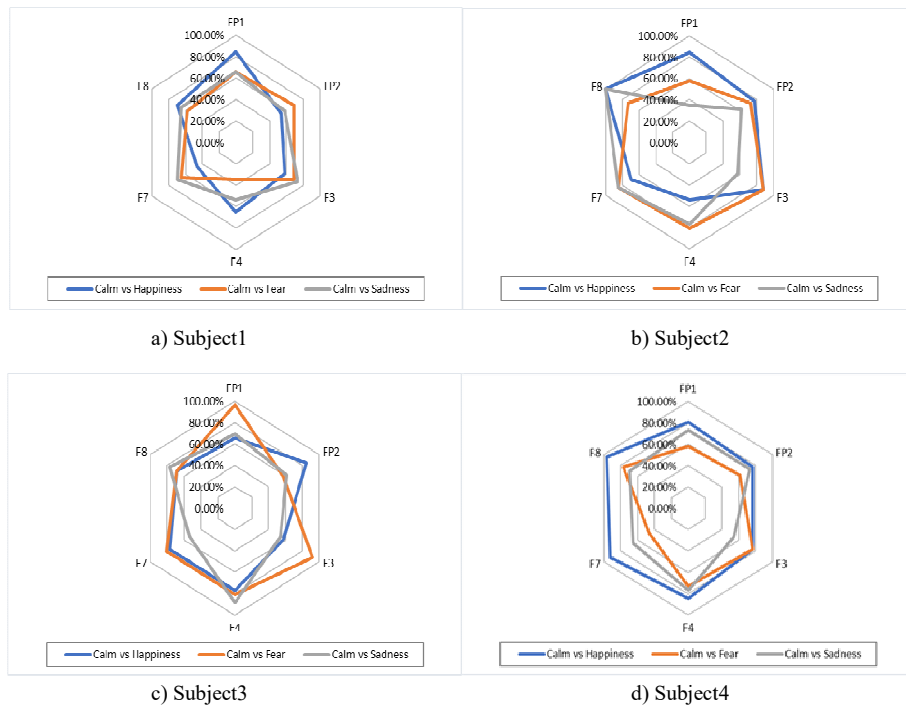


Fig. 7. The Different Channels Performance for Each Participant.

91.03% and 80.77% respectively. It can be said that the result conforms to the hypothesis that EEG emotion recognition is complex and more detailed studies are needed.

V. CONCLUSION AND FUTURE WORK

Early detection of dysphoria can help to identify the mental states of a patients before it become worse and the necessary treatment of mental states can be provided. This research proposes the usage of EEG signals with affective space model mapping to recognize dysphoria. Such measurement can be used to complement DASS-21 instrument to give empirical insight that can facilitate psychologists and psychiatrist in their patient's assessment in a timely manner. In addition, misleading response attempted by in-denial patient can be filtered because brain signals captured are dynamic and cannot be controlled as opposed to the answer given in the questionnaire. Hence, there is a high chance for the correct assessment can be made based on such input.

In this paper, the performance of EEG channels, namely; FP1, FP2, F3, F4, F7 and F8 are studied for emotion recognition experiment. Experimental result show that window size of 4096 can give slightly higher accuracy as compared to other window size of 512, 1024 and 2048 when MFCC is used for feature extraction. It is also observed that the performance of channel is inconclusive for emotion classification which is in-line with the understanding that the emotion classification task is complex and more studies are needed [23]. The effect of different medium of data (i.e still image and video) are compared. More detailed study is needed to give better insight to EEG emotion recognition task. More subjects, better stimuli, various classifiers as well as different feature extraction methods can be employed in the future to give better understanding and boost the classification performance. It is envisaged that this work will spark more interests and motivation for further dysphoria research.

REFERENCES

- [1] Young Health Movement and Royal Society for Public Health, "#StatusOfMind", 2017. [Online]. Available: <https://www.rsph.org.uk/our-work/policy/social-media-and-young-people-s-mental-health-and-wellbeing.html>. [Accessed: 22-November-2017]
- [2] American Psychological Association, "Stress in America: The Impact of Discrimination", 2016. [Online]. Available: <http://www.apa.org/news/press/releases/stress/2015/impact-of-discrimination.pdf>. [Accessed: 13-September-2017]
- [3] The Star Online, "Regus: 70% Malaysian Workers See Increase in Stress-related Illness", 2013. [Online]. Available: <https://www.thestar.com.my/business/business-news/2013/11/22/70-pct-of-malaysian-workers-see-increase-in-stress-related-illness-says-survey/>. [Accessed: 7-May-2017]
- [4] M. S. Mallow, "Occupational Stress in Malaysia: Causes, Effects and Possible Solutions", The Third International Conference on Education, Social Sciences and Humanities 2016 (SOCIOINT'16), 2016.
- [5] V. Starcevic, D. Berle, K. Viswasam, A. Hannan A, D. Milicevic, V. Brakoulis and E. Dale, "Specificity of the Relationship between Dysphoria and Related Constructs in an Outpatient", *Psychiatric Quarterly*, vol. 86, issue 4, pp. 459-469, 2015
- [6] N. Kamaruddin, A. Wahab and C. Quek, "Cultural Dependency Analysis for Understanding Speech Emotion", *Expert Systems with Applications*, vol. 39, issue 5, pp. 5115-5133, 2012.
- [7] World Health Organization, "Mental Health Atlas 2011", 2011, [Online]. Available: http://apps.who.int/iris/bitstream/10665/44697/1/9799241564359_eng.pdf. [Accessed: 1-September-2017].
- [8] G. Stanghellini, "The Doublets of Anger", *Psychopathology*, vol. 33, issue 4, pp. 155 – 158, 2000.
- [9] M. Musalek, H. Griengl, B. Hobl, G. Sachs and A. Zoghiani, "Dysphoria from a Transnosological Perspective", *Psychopathology*, vol. 33, issue 4, pp.209-214, 2000.
- [10] V. Starcevic, "Dysphoric about Dysphoria: Towards a Greater Conceptual Clarity of the Term", *Australasian Psychiatry*, vol. 15, issue 1, pp.9-13, 2007.
- [11] E. H. Koster, R. De Raedt, L. Leyman and E. De Lissnyder, "Mood-congruent Attention and Memory Bias in Dysphoria: Exploring the Coherence among Information-processing Biases", *Behaviour Research and Therapy*, vol. 48, issue 3, pp.219-225, 2010.
- [12] J. W. Yuan and A. M. Kring, "Dysphoria and the Prediction and Experience of Emotion", *Cognition and Emotion*, vol. 23, issue 6, pp.1221-1232, 2010.
- [13] L. J. Hirsch, R. P. Brenner, F. W. Drislane, E. So, P. W. Kaplan, K. G. Jordan, S. T. Herman, S. M. LaRoche, B. Young, T. P. Bleck, M. L. Scheuer, R. G. Emerson, "The ACNS Subcommittee on Research Terminology for Continuous EEG monitoring: Proposed Standardized Terminology for Rhythmic and Periodic EEG Patterns Countered in Critically Patients", *Journal of Clinical Neurophysiology*, vol. 22, pp.128–135, 2005.
- [14] J. T. Cacioppo, "Feelings and Emotions: Roles for Electrophysiological Markers", *Biological Psychology*, vol. 67, issue 1, pp.235-243, 2004.
- [15] T. Asakawa, T. Hayashi and Y. Mizuno-Matsumoto, "Coherence Analysis of EEG Under Emotional Stimuli Related to Mental States", *Electronics and Communications in Japan*, vol. 97, issue 8, pp.14-23, 2014.
- [16] M. Teplan, "Fundamentals of EEG Measurement", *Measurement Science Review*, vol. 2, issue 2, pp.1-11, 2002.
- [17] M. Othman, A. Wahab, I. Karim, M. A. Dzulkifli and I. F. T. Alshaikli, "EEG Emotion Recognition based on the Dimensional Models of Emotions", *Procedia-Social and Behavioral Sciences*, vol. 97, pp.30-37, 2013.
- [18] N. Kamaruddin and A. Wahab, "Human Behavior State Profile Mapping based on Recalibrated Speech Affective Space Model", *Annual International Conference of the IEEE Engineering in Medicine and Biology Society (EMBC 2012)*, pp. 2021-2024, 2012.
- [19] J. A. Russell, "A Circumplex Model of Affect", *Journal of Personality and Social Psychology*, vol. 39, issue 6, pp. 1161-1178, 1980.
- [20] Y. Liu and O. Sourina, "Real-time Subject-dependent EEG-based Emotion Recognition Algorithm", *Transactions on Computational Science XXIII*, pp. 199-223, 2014.
- [21] P. J. Lang, M. M. Bradley and B. N. Cuthbert, "International Affective Picture System (IAPS): Technical Manual and Affective Ratings", University of Florida, Center for Research in Psychophysiology; Gainesville, 1999.
- [22] M. M. Bradley and P. J. Lang, "Measuring Emotion: The Self-Assessment Manikin and the Semantic Differential", *Journal of Behavior Therapy and Experimental Psychiatry*, vol. 25, issue 1, pp.49-59, 1994.
- [23] I. Karim, A. Wahab and N. Kamaruddin, "Classification of Dyslexic and Normal Children during Resting Condition using KDE and MLP", *The 5th International Conference on Information and Communication Technology for the Muslim World (ICT4M 2013)*, pp. 1 – 5, 2013.

On Path Length Estimation for Wireless Capsule Endoscopy

Anders Bjørnevik

Dept. of Research and Development
Kongsberg Seatex
Trondheim, Norway
anderssb@gmail.com

Pål Anders Floor

Dept. of Computer Science
NTNU
Gjøvik, Norway
paal.anders.floor@ntnu.no

Ilangko Balasingham

Dept. of Electronic Systems
NTNU
Trondheim, Norway
ilangkob@iet.ntnu.no

Intervention Center, Oslo University Hospital
Institute of Clinical Medicine, University of Oslo
Oslo, Norway
ilangko.balasingham@medisin.uio.no

Abstract—Wireless capsule endoscopy (WCE) is a non-invasive technology used for inspection of the gastrointestinal tract. Localization of the capsule is a vital part of the system enabling physicians to identify the position of anomalies. Due to intestinal motility, the positions of the intestines will change significantly within the abdominal cavity over time. However, the distance from one position to another within the intestines changes much less. In this paper a method for calculating the pathlength travelled by a WCE is proposed. The method is based on Kalman- and particle filters and is simulated using a model that approximately replicates the movement through the small intestine. The travelled distance was estimated to an accuracy within a few millimeters.

Index Terms—Wireless capsule endoscopy, localization, tracking, distance estimation.

I. INTRODUCTION

Wireless capsule endoscopy (WCE) is an emerging technology for examination of the gastrointestinal (GI) system. The patient is examined by swallowing a capsule containing a small video camera. The capsule follows the gastrointestinal system from the esophagus to the colon, locomoted by natural contractions in the intestines [1]. The physician examines the recorded images for abnormalities, enabling non-invasive diagnosis of diseases.

The video has to be accompanied by WCE position information so that the physician can return to the location of abnormalities at a later stage. The position can be estimated by localization methods based on for example microwave imaging [2], radio frequency (RF) signals [3], [4] or by including a permanent magnet in the capsule [5]. Accuracy can be improved by applying algorithms that track the movement of the WCE [4], [6].

Due to intestinal motility, the intestines are constantly moving [7]. This makes a fixed position of little relevance, since the position of the abnormality may have moved significantly at the time of treatment. A better way to approach this problem, is to use the distance travelled from a known point in the intestine, for instance the entry of the stomach [8]. This

distance is not as greatly affected by the intestinal movement as a fixed position, and is therefore of greater value to the physician.

In this paper a method for estimating the distance traveled by a WCE is proposed. The proposed scheme computes the pathlength traveled by the WCE from estimated positional information obtained from localization- and tracking algorithms. Several tracking algorithms are compared using a simulation model that approximately replicates the movement through the small intestine. We simplify, and illustrate the model in two dimensions. The same principles can be extended to three dimensions.

II. PROPOSED METHOD

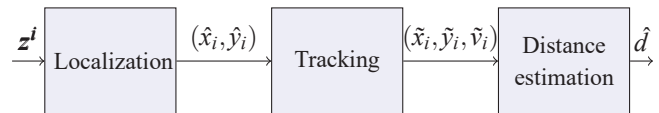


Fig. 1. Block diagram for distance estimation.

The system can be characterized by three different modules, as shown in Fig. 1. The tracking system receives (2D) position estimates, (\hat{x}_i, \hat{y}_i) , from the localization framework that refines the positions, $(\tilde{x}_i, \tilde{y}_i)$, and estimates the current velocity, \tilde{v}_i , both which are used to estimate the distance.

A set of measurements $\{z^i\}$ $i = 1, \dots, P$, is used to estimate the positions (\hat{x}_i, \hat{y}_i) . As mentioned in the introduction, there are many possible localization methods. Although localization is a crucial part, this paper is concerned with tracking and distance estimation. Generally, the more exact the localization is, the better the performance of the distance estimation (see Fig. 4). The efforts [4], [9], [10] evaluated localization accuracy within realistic media like the human abdominal model derived in [11] and a model based on measurements on a living porcine subject in [12]. It is shown that accuracy in the cm range is plausible for RF-based localization [9] and

Funding was given by the Research Council of Norway under the project MELODY II no. 225885.

that accuracy in the mm range is plausible for magnetic-based localization [13].

A. Distance Estimation

The problem of estimating the distance, \hat{d} , the WCE has travelled between a set of two-dimensional positions, $\{p_i\} i = 1, \dots, n$, can be solved by:

- 1) Integrating the velocity v between the points:

$$\hat{d} = \int_{p_1}^{p_n} v(t) dt \quad (1)$$

- 2) Summing the Euclidean distances between each position:

$$\hat{d} = \sum_{i=1}^{n-1} \sqrt{(x_{i+1} - x_i)^2 + (y_{i+1} - y_i)^2}. \quad (2)$$

As Eq. (2) is only dependent on the positions of the WCE, 2) is the simplest method to implement as the positions are already available. However, this solution alone is not suitable since the capsule may stop for periods of time, typically within bends in the intestine. Thus, small errors in the position estimates will accumulate to errors in the distance that cause the estimated length \hat{d} to be longer than the true length d . The capsule velocity is needed to reduce this problem. Due to power consumption, it is not preferable to have sensors measuring the WCE velocity. Therefore, the velocity has to be estimated from the observed positions. With prior information about the previous positions available, a Bayesian approach would be a reasonable choice for such an algorithm [14].

As both velocity and positions are applied, the relevant state vector, \mathbf{x} , is on the form

$$\mathbf{x} = [x \quad \dot{x} \quad y \quad \dot{y}]^T. \quad (3)$$

The problem of estimating the state \mathbf{x}_k at time instant k using Bayesian dynamic state estimation (BSE) is given as [15]

$$\mathbf{x}_k = g(\mathbf{x}_{k-1}, \mathbf{u}_{k-1}, \mathbf{w}_{k-1}), \quad (4)$$

$$\mathbf{z}_k = h(\mathbf{x}_k, \mathbf{n}_k), \quad (5)$$

where g is a function relating the previous state \mathbf{x}_{k-1} with \mathbf{x}_k and h is a function that relates \mathbf{x}_k with the measurements \mathbf{z}_k . \mathbf{u}_k denotes a vector of known *control inputs*, while \mathbf{w}_k and \mathbf{n}_k are process and measurement noise, respectively.

B. Movement Model and Data Sets

In order to evaluate tracking algorithms, a model describing the functions g and h in (4) have to be found. The problem of modelling the movement of a WCE in the intestines was considered in [4]: The capsule movement is governed by the stress and strain cycle of the intestine, which can be considered constant under normal conditions. The main factors determining the speed is the diameter of the capsule (which is constant) and the intestines. The inner diameter of the intestines was found to change for different parts of the intestine in [16], causing small changes in velocity. As in [4], we simplify and assume that the intestines consists of L tubes

of different diameters, implying that we have L speed modes. Then, at time step k , the capsule speed can be approximated to follow the Gaussian mixture distribution [4]

$$v_k \approx \sum_{n=-L}^L p(n) \mathcal{N}(v_k | \mu_n, q_n), \quad (6)$$

where $\mathcal{N}(v_k | \mu_n, q_n)$ is a Gaussian pdf with mean μ_n , covariance q_n , and probability $p(n)$. At the end of each tube the capsule stops for a moment due to bends in the intestine.

The movement of a WCE in the intestines can therefore be approximated by the model in Fig. 2: The straight lines is where the capsule is moving close to constant speed and at the nodes the capsule is at rest.

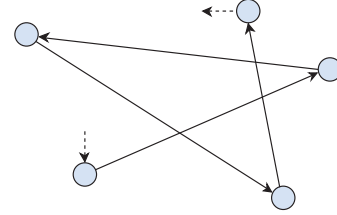


Fig. 2. A simplified motion model for the WCE movement. At the edges the WCE moves at approximately constant speed chosen from Eq. (6) and at the nodes it stops for a randomly chosen time interval.

The human model applied to generate relevant datasets is *HUGO* which is a complete anatomical three-dimensional model of the human body provided by the *Visible Human Project* [17]. The relevant datasets used for simulations were generated for the red dots shown in Figs. 3(a) and. 3(b), displaying two cross sections of the abdominal region of the HUGO model with a segment of about 30 cm of the small intestine included (the intestines are displayed as the black areas in the figures). The two cross-sections are located within the red rectangle shown in Fig. 3(c). For simplicity, the WCE was placed at the center of the intestine. In reality, more deviation from the midpoint is expected to occur. In the dataset generation, it was assumed that capsule positions were obtained every $T = 1$ seconds, which is in line with the existing WCE systems [18]. In every bend $< 135^\circ$ a random dwell time t_s was added to simulate the capsule stops.

C. Tracking Algorithms

For BSE, it is natural to use the *Kalman filter* (KF) [19]. However, since there are multiple speed modes as well as periods where the WCE is at rest one would assume that a *Multi model Kalman filter with variable noise level* (KF-VNL) [20], [21] would be a better choice. Further, the *particle filter* (PF) is a more general approach than the KF and applies to any state transition- and measurement model [22]. We will compare these three approaches, each of which is described in more detail in the following.

- i) **KF:** For the KF the state \mathbf{x}_k at time k is assumed to follow

$$\mathbf{x}_k = \mathbf{A}\mathbf{x}_{k-1} + \mathbf{B}\mathbf{u}_{k-1} + \mathbf{w}_{k-1}, \quad (7)$$

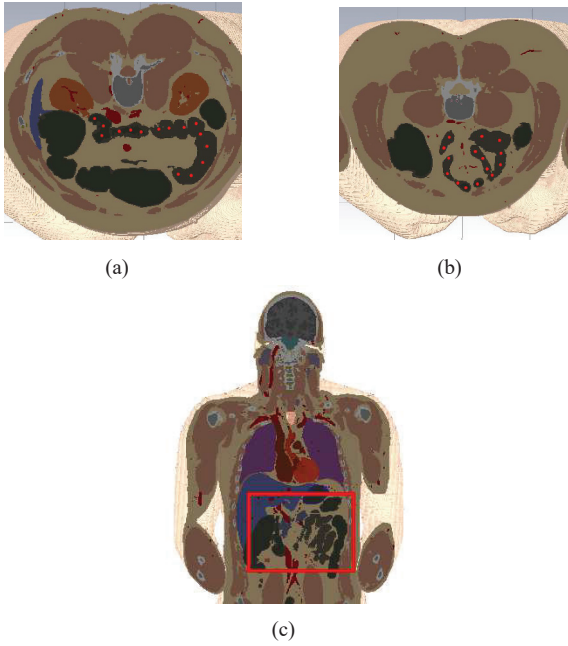


Fig. 3. Cross-sections of a human abdominal region. The red dots are points placed in the small intestine used as a reference when creating datasets for tracking: (a) Dataset 1. (b) Dataset 2. (c) Location of the two cross-sections within the HUGO model.

where the observation of \mathbf{x}_k is given as

$$\mathbf{z}_k = \mathbf{C}\mathbf{x}_k + \mathbf{n}_k. \quad (8)$$

\mathbf{w}_k and \mathbf{n}_k have distributions $p(\mathbf{w}) \sim \mathcal{N}(\mathbf{0}, \mathbf{Q})$ and $p(\mathbf{n}) \sim \mathcal{N}(\mathbf{0}, \mathbf{R})$ respectively. The covariance matrices \mathbf{Q} and \mathbf{R} are assumed constant. For constant velocity (\dot{x}, \dot{y}) with measurements of positions (x, y) and timestep T , the state transition matrix \mathbf{A} and the observation matrix \mathbf{C} are given by

$$\mathbf{A} = \begin{bmatrix} 1 & T & 0 & 0 \\ 0 & 1 & 0 & 0 \\ 0 & 0 & 1 & T \\ 0 & 0 & 0 & 1 \end{bmatrix}, \quad \mathbf{C} = \begin{bmatrix} 1 & 0 & 0 & 0 \\ 0 & 0 & 1 & 0 \end{bmatrix}. \quad (9)$$

The control input matrix \mathbf{B} was chosen as zero, with mismatch in the model compensated for by increased noise in the process noise covariance matrix \mathbf{Q} . The covariance matrix for observation noise was chosen as $\mathbf{R} = \text{diag}(\sigma_{r,x}^2, \sigma_{r,y}^2)$, where $\sigma_{r,x}^2$ and $\sigma_{r,y}^2$ are the variances of the measured noisy observations, while the covariance matrix $\mathbf{Q} = \text{diag}(0, \sigma_{q,x}^2, 0, \sigma_{q,y}^2)$ where $\sigma_{q,x}^2$ and $\sigma_{q,y}^2$ represent unmodelled accelerations when the capsule is moving. For more details on implementation of the KF see for example [4].

ii) KF-VNL: The KF-VNL operates with multiple observation noise covariance matrices, $\mathbf{Q}_1, \dots, \mathbf{Q}_n$, corresponding to different modes in the filter.

In this paper, a two-mode KF-VNL is considered with \mathbf{Q}_1 and \mathbf{Q}_2 , given by $\mathbf{Q}_1 = \text{diag}(0, \sigma_{q1,x}^2, 0, \sigma_{q1,y}^2)$ and $\mathbf{Q}_2 = \text{diag}(0, \sigma_{q2,x}^2, 0, \sigma_{q2,y}^2)$ respectively. The variances $\sigma_{q1,x}^2$ and $\sigma_{q1,y}^2$ represent unmodelled accelerations when the capsule is moving. $\sigma_{q2,x}^2$ and $\sigma_{q2,y}^2$ correspond to process noise that

compensates for the transition between the WCE moving and being stopped.

More details on how this 2-mode KF-VNL can be implemented is given in [21].

iii) PF: With a set of measurements $D_k = \{\mathbf{z}_i : i = 1, \dots, k\}$, the goal is to determine $p(\mathbf{x}_k | D_k)$ recursively: One can write [22]

$$p(\mathbf{x}_k | D_{k-1}) = \int p(\mathbf{x}_k | \mathbf{x}_{k-1}) p(\mathbf{x}_{k-1} | D_{k-1}) d\mathbf{x}_{k-1}. \quad (10)$$

When a new observation \mathbf{z}_k is available, then

$$p(\mathbf{x}_k | D_k) = \frac{p(\mathbf{z}_k | \mathbf{x}_k) p(\mathbf{x}_k | D_{k-1})}{p(\mathbf{z}_k | D_{k-1})}. \quad (11)$$

where the normalization $p(\mathbf{z}_k | D_{k-1})$ is as in (10) with \mathbf{x}_k replaced by \mathbf{z}_k and \mathbf{x}_{k-1} replaced by \mathbf{x}_k . Let $\{\mathbf{x}_{k-1}(i) : i = 1, \dots, N\}$ random samples from $p(\mathbf{x}_k | D_{k-1})$ be available. The PF approximates the relations in Eq. (10-11) through the two steps [22]:

Prediction: Pass each sample in the set through the system model to obtain

$$\mathbf{x}_k^*(i) = g(\mathbf{x}_{k-1}(i), \mathbf{w}_{k-1}(i)). \quad (12)$$

$\mathbf{w}_{k-1}(i)$ is drawn from the system noise pdf $p(\mathbf{w}_{k-1})$.

Update: When a new measurement \mathbf{z}_k is available, evaluate the likelihood of each prior sample and obtain the normalised weights

$$q_k(i) = \frac{p(\mathbf{z}_k | \mathbf{x}_k^*(i))}{\sum_{j=1}^N p(\mathbf{z}_k | \mathbf{x}_k^*(j))}. \quad (13)$$

The filtered posterior density is then

$$p(\mathbf{x}_k | D_k) \approx \sum_{i=1}^N q_k(i) \delta(\mathbf{x}_k - \mathbf{x}_k^*(i)), \quad (14)$$

where the approximation becomes equality as $N \rightarrow \infty$ [23].

The PF starts by initializing N particles $\mathbf{x}_0^1, \dots, \mathbf{x}_0^N$ according to $\mathcal{N}(\mathbf{x}_0, \Sigma)$, where \mathbf{x}_0 is the initial state provided to the filter and Σ are the variances of the initial particles. Using the constant velocity dynamic model with the state vector in Eq. (3), the state evolution in (12) becomes $\mathbf{x}_k^i = \mathbf{A}\mathbf{x}_{k-1}^i + \mathbf{n}$, where \mathbf{x}_k^i is particle number i representing one proposed state vector at time k . \mathbf{A} is as in (9) and $\mathbf{n} \sim \mathcal{N}(\mathbf{0}, \Sigma)$.

Since the noise model is assumed to be Gaussian, we have

$$p(\mathbf{z}_k | \mathbf{x}_k(i)) = \frac{1}{\sqrt{(2\pi)^M |\det(\mathbf{R})|}} \exp\left(-\frac{1}{2}(\boldsymbol{\pi}_k^i)^T \mathbf{R}^{-1} \boldsymbol{\pi}_k^i\right), \quad (15)$$

where $\boldsymbol{\pi}_k^i = \mathbf{z}_k - \mathbf{x}_k(i)$ and \mathbf{z}_k has covariance \mathbf{R} . The reconstruction is then $\hat{\mathbf{x}}_k = \sum_{i=1}^N \mathbf{x}_k(i) p(\mathbf{z}_k | \mathbf{x}_k(i))$.

For the PF resampling process, the cumulative distribution of the particle weights were used in order to discard particles with negligible probability. In order to weight both the position and the velocity estimate during resampling, the observation vector was chosen as

$$\mathbf{z}_k = [x_k \quad y_k \quad \sqrt{(x_k - x_{k-1})^2 + (y_k - y_{k-1})^2} / T]^T. \quad (16)$$

TABLE I
PARAMETERS USED UNDER
SIMULATION [4].

Parameter	Value
\bar{v}	0.5 mm/s
σ_v	0.05 mm/s
t_s	5 min
σ_s	10 min

TABLE II
SETTINGS USED FOR KF AND PF.

Description	Value
Noise level	SNR = 25 dB
Simulations	$S = 100$
Number of particles	$N = 10000$
Initial particle noise	$\sigma_{N_0} = 1$

III. SIMULATIONS

For all simulations the velocity was chosen as $\mathcal{N}(\bar{v}, \sigma_v)$, with the stop time, t_s , modelled as $|\mathcal{N}(t_s, \sigma_s)|$ following the investigations done in [4]. Specific values are given in Tab. I. The chosen values for all tracking algorithms are summarized in Tab. II. Timesteps for the 2nd mode of the KF VNL was chosen as $r = 100$.

The following measures are applied in order to evaluate the algorithms:

- i) Signal-to-noise ratio (SNR) [24]

$$\text{SNR} = 10 \log_{10} \left(\frac{1}{N \sigma_r^2} \sum_{n=1}^N x_n \right) \quad (17)$$

where x is the relevant signal and σ_r^2 is the (observation) noise variance.

- ii) For the distance estimation problem, the mean difference in length over S simulations is computed as

$$\Delta = \frac{1}{S} \sum_{n=1}^S (\hat{d}_n - d), \quad (18)$$

where d is the true distance and \hat{d}_n is the distance estimate.

In order to obtain the best estimate of the path length, all filters were tuned for the minimum Δ . The system should ideally be optimized for the most relevant SNR. However, this value will change throughout the intestine as well as from person to person depending on the size of the torso. Here we chose to optimize the system for SNR = 25 dB as was used for the detailed simulations in [24]. Due to the variation in SNR it is of interest to compare the effect of the varying observation noise on the distance estimates. The result can be seen in Fig. 4, where SNR levels between 10-45 dB have been used. The resulting Δ for each SNR value was found from 100 Monte-carlo simulations. For dataset 1, the KF-VNL has the best performance for most of the SNR values. For dataset 2, the KF performs best for low SNR. The PF is most susceptible to low SNR for both datasets, but has the best performance at high SNR. Due to the filters being tuned for operation at 25 dB SNR, the full performance of the KF-VNL is not utilized at low SNR, as the increased noise causes problems in detecting the capsule maneuvers.

IV. DISCUSSION AND CONCLUSIONS

In this paper a method for estimating the pathlength traversed by a wireless capsule endoscope (WCE) traveling

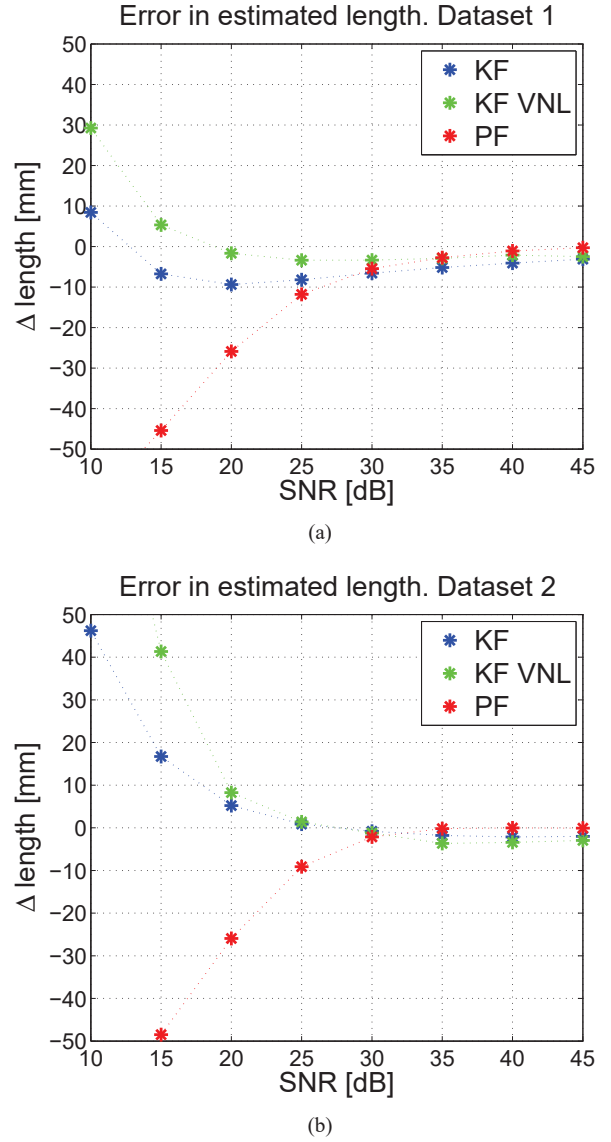


Fig. 4. Deviation from actual path length, Δ , for different SNR levels. (a) Dataset 1. (b) Dataset 2.

through the human gastrointestinal tract has been proposed. The method is built around known localization and tracking algorithms. Three tracking algorithms were tested: Kalman filter (KF), multi model KF with variable noise level (KF-VNL) and particle filter (PF). The distance is computed based on the output of the chosen tracking algorithm

The KF-VNL was found to have the most accurate distance estimation over the broadest range of position-to-observation signal-to-noise ratios (SNR), being within ± 3 mm above 25 dB SNR. However, if the SNR increases the PF becomes more accurate with an error approaching 0 mm. As the SNR drops below 15 dB, the KF outperforms the KF-VNL. The reason for this is probably that the KF-VNL was not tuned for SNR below 25 dB. The performance of the PF could be increased at low SNR with a larger amount of particles at the cost of

longer computation time.

For all tracking algorithms the performance increases as the observation noise is reduced. A high performance localization system combined with the tracking algorithms is expected to have a distance estimation accuracy in the order of millimeters.

In [25] a video-based distance estimation algorithm obtains an accuracy of 2.71 cm for a 500 cm long path with velocity within 0-4 mm/s. Comparing this to the result of ± 3 mm presented in Sec. III, it seems at first glance that our proposed scheme has a better performance for this specific setup. However, apart from being of different lengths, the datasets used for evaluation have significant differences: In [25], it is assumed that the capsule constantly changes velocity between 0-4 mm/s. The datasets we generated here have only minor deviations in the velocity when the capsule is moving, and has long periods when the capsule is at rest. It is unknown how well the algorithm in [25] performs for datasets that contain long periods with no capsule movement, and how our approach perform for a larger stretch of intestine. Further research is needed to conclude.

The results of this paper are entirely simulation based and meant to indicate a plausible accuracy for the proposed scheme. As a proof of concept it is important to evaluate the accuracy using real pillcams on several human test subjects of different sizes. This study will require a significant effort that should be pursued through future research.

REFERENCES

- [1] G. Ciuti, A. Menciassi, and P. Dario, "Capsule endoscopy: from current achievements to open challenges." *IEEE reviews in biomedical engineering*, vol. 4, pp. 59–72, Jan. 2011.
- [2] R. Chandra, A. J. Johansson, M. Gustafsson, and F. Tufvesson, "A microwave imaging-based technique to localize an in-body RF source for biomedical applications." *IEEE transactions on bio-medical engineering*, vol. 62, no. 5, pp. 1231–41, May 2015.
- [3] D. Fischer, R. Schreiber, D. Levi, and R. Eliakim, "Capsule endoscopy: the localization system." *Gastrointestinal endoscopy clinics of North America*, vol. 14, no. 1, pp. 25–31, Jan. 2004.
- [4] B. Moussakhani, "On Localization and Tracking for Wireless Capsule Endoscopy," Ph.D. dissertation, NTNU, 2013. [Online]. Available: <https://brage.bibsys.no/xmlui/handle/11250/2370705>
- [5] C. Hu, W. Yang, D. Chen, M. Q. H. Meng, and H. Dai, "An improved magnetic localization and orientation algorithm for wireless capsule endoscope." *Annual International Conference of the IEEE Engineering in Medicine and Biology Society. IEEE Engineering in Medicine and Biology Society. Annual Conference*, vol. 2008, pp. 2055–8, Jan. 2008.
- [6] G. Bao, K. Pahlavan, and L. Mi, "Hybrid Localization of Microrobotic Endoscopic Capsule Inside Small Intestine by Data Fusion of Vision and RF Sensors," *IEEE Sensors Journal*, vol. 15, no. 5, pp. 2669–2678, May 2015.
- [7] W. A. Kunze and J. B. Furness, "The enteric nervous system and regulation of intestinal motility." *Annual review of physiology*, vol. 61, pp. 117–42, Jan. 1999.
- [8] K. Pahlavan, G. Bao, Y. Ye, S. Makarov, U. Khan, P. Swar, D. Cave, A. Karellas, P. Krishnamurthy, and K. Sayrafian, "RF Localization for Wireless Video Capsule Endoscopy," *International Journal of Wireless Information Networks*, vol. 19, no. 4, pp. 326–340, Oct. 2012.
- [9] B. Moussakhani, J. Flåm, S. Støa, I. Balasingham, and T. Ramstad, "On localisation accuracy inside the human abdomen region," *IET Wireless Sensor Systems*, vol. 2, no. 1, p. 9, 2012.
- [10] A. Bjørnevik, *Localization and Tracking of Intestinal Paths for Wireless Capsule Endoscopy*. M.Sc. thesis, NTNU, 2015. [Online]. Available: <https://brage.bibsys.no/xmlui/handle/11250/2371524>
- [11] S. Stoa, R. Chavez-Santiago, and I. Balasingham, "An ultra wideband communication channel model for the human abdominal region," in *2010 IEEE Globecom Workshops*. IEEE, Dec. 2010, pp. 246–250.
- [12] P. A. Floor, R. Chavez-Santiago, S. Brovoll, O. Aardal, J. Bergsland, O.-J. Grymyr, P. S. Halvorsen, R. Palomar, D. Plettemeier, S.-E. Hamran, T. Ramstad, and I. Balasingham, "In-Body to On-Body Ultra Wideband Propagation Model Derived from Measurements in Living Animals." *IEEE journal of biomedical and health informatics*, vol. PP, no. 99, p. 1, Apr. 2015.
- [13] B. Moussakhani, T. A. Ramstad, J. Flåm, and I. Balasingham, "On localizing a capsule endoscope using magnetic sensors," in *Engineering in Medicine and Biology Society (EMBC), 2012 34th Annual International Conference of the IEEE*. ACM, 2012, pp. 4058–4062.
- [14] S. M. Kay, *Fundamentals of Statistical Signal Processing: Practical algorithm development*. Prentice-Hall PTR, 2013.
- [15] G. Welch and G. Bishop, "An Introduction to the Kalman Filter," Nov. 2006. [Online]. Available: <http://dl.acm.org/citation.cfm?id=897831>
- [16] X. Wang and M. Q.-H. Meng, "An experimental study of resistant properties of the small intestine for an active capsule endoscope." *Proceedings of the Institution of Mechanical Engineers. Part H, Journal of engineering in medicine*, vol. 224, no. 1, pp. 107–18, Jan. 2010.
- [17] M. Ackerman, "The Visible Human Project," *Proceedings of the IEEE*, vol. 86, no. 3, pp. 504–511, Mar. 1998.
- [18] J. L. Toennies, G. Tortora, M. Simi, P. Valdastrì, and R. J. Webster, "Swallowable medical devices for diagnosis and surgery: the state of the art," *Proceedings of the Institution of Mechanical Engineers, Part C: Journal of Mechanical Engineering Science*, vol. 224, no. 7, pp. 1397–1414, Jan. 2010.
- [19] R. E. Kalman, "A New Approach to Linear Filtering and Prediction Problems," *Journal of Basic Engineering*, vol. 82, no. 1, p. 35, Mar. 1960.
- [20] V. Jilkov, "Survey of maneuvering target tracking. part v: multiple-model methods," *IEEE Transactions on Aerospace and Electronic Systems*, vol. 41, no. 4, pp. 1255–1321, Oct. 2005.
- [21] B. Moussakhani, R. Chavez-Santiago, and I. Balasingham, "Multi Model Tracking for Localization in Wireless Capsule Endoscope," in *2011 4th International Symposium on Applied Sciences in Biomedical and Communication Technologies (ISABEL 2011)*. ACM, 2011.
- [22] N. Gordon, D. Salmond, and A. Smith, "Novel approach to nonlinear/non-Gaussian Bayesian state estimation," *IEE Proceedings For Radar and Signal Processing*, vol. 140, no. 2, pp. 107–113, 1993.
- [23] M. Arulampalam, S. Maskell, N. Gordon, and T. Clapp, "A tutorial on particle filters for online nonlinear/non-Gaussian Bayesian tracking," *IEEE Transactions on Signal Processing*, vol. 50, no. 2, pp. 174–188, 2002.
- [24] Z. Xiahou and X. Zhang, "Adaptive Localization in Wireless Sensor Network through Bayesian Compressive Sensing," *International Journal of Distributed Sensor Networks*, 2015.
- [25] Guanqun Bao, Liang Mi, Yishuang Geng, Mingda Zhou, and K. Pahlavan, "A video-based speed estimation technique for localizing the wireless capsule endoscope inside gastrointestinal tract." in *Engineering in Medicine and Biology Society (EMBC), 2014 36th Annual International Conference of the IEEE*, Aug. 2014, pp. 5615–5618.

Fine Grained Attribute Based Access Control of Healthcare Data

Edward Mrema
Department of Computer Science
University of Waikato
New Zealand
eam19@students.waikato.ac.nz

Vimal Kumar
Department of Computer Science
University of Waikato
New Zealand
vkumar@waikato.ac.nz

Abstract—One of the biggest threats to the healthcare data stored by healthcare organizations comes from malicious insiders. The first layer of protection against such adversaries is access control, however if an adversary is able to bypass that then the data becomes exposed. In this paper we propose an access control method based on Hidden Vector Encryption. In our approach access control policies are written using attributes of entities. The Hidden Vector Encryption system then embeds the policies in the ciphertext such that it can be decrypted only when the relevant attributes are presented. This provides a higher level of access control where a malicious insider cannot decrypt data unless they possess the right attributes.

I. INTRODUCTION

Security and privacy of healthcare data is paramount and consequently there has been therefore, a considerable amount of work on the protection of healthcare data from outside adversaries. Having said that, a big threat to healthcare data also comes from malicious insiders. According to an IBM X-Force report [1], 71% of the cyber-attacks in the healthcare industry in 2016 were from insiders which is exceptionally high when compared to other industries in the financial, ICT, manufacturing and retail sectors.

The threat of insider attacks arises due to people inside an organization that have the authorization and the access to information that is supposed to be secure. In most cases such insiders need that authorization and access to carry out their daily responsibilities because the security controls are not flexible enough and usually work in an all or nothing fashion (either everything is available or nothing is available). This creates a vulnerability where data is exposed to insiders that become malicious.

A security control that is used for protection against insider threats is Access Control List (ACL) or Access Control Matrix (ACM). ACLs/ACMs provide an individual with access to data based on their roles or attributes. ACLs/ACMs can restrict access based on policies but do not provide confidentiality of data. Traditionally confidentiality of data has been provided by encrypting it. Encryption is an example of the above mentioned all or nothing construct. If encryption is not used the data is unprotected but available and if encryption is used data is protected but unavailable. Encrypting healthcare data therefore, while provides security to the data, also creates an additional obstacle for the employees who need that data to

perform their duties. Organizations therefore have a reason for not choosing to encrypt data if it introduces a large amount of delay in the system. According to the HyTrust cloud adoption survey [2] 25% of healthcare organizations that use public cloud do not encrypt their data (Healthcare related Acts such as HIPAA do not force data encryption as a requirement). On the other hand some organizations encrypt healthcare data but have very lax key management, which means that even though data is encrypted, everyone has access to the key to decrypt the data.

To adequately protect healthcare data we need both an access control mechanism and an encryption mechanism. An ideal solution will be one, where the data is kept encrypted at all times and the access control mechanism is embedded into the data such that the data can be decrypted only by people who have the proper authorization. In this paper we propose a method of providing fine grained access control of encrypted data based on the concept of Hidden Vector Encryption (HVE). Functional encryption techniques such as HVE allow us to encrypt data and embed access control policies within the encrypted data. This eliminates the need of maintaining two separate security controls (ACL and encryption) for providing access control and confidentiality of data. It also means that data is kept encrypted at all times which enhances the security of the data.

The rest of the paper is organized as follows. In section II, we first elaborate on the concept of attributes and attribute based access control before going over Hidden Vector Encryption. We describe the proposed model in section III and go over its various components. We analyze the performance of the system in section IV and finally conclude the paper in section V.

II. PRELIMINARIES

A. Security Assumptions

The adversary in our system is a malicious insider who wants to access data that it is not authorized for. We also assume that the adversary is not able to create and present fake attributes. This can be ensured by storing credentials on a swipe card and asking users to swipe before each data access. We also assume that the adversary is not able to compromise any of the components of our system.

B. EMR vs EHR

Electronic Medical Record (EMR) and Electronic Health Record (EHR) are two related concepts and are frequently used interchangeably. The two terms however, refer to different kind of health data. We define the EMR as basically the digitized version of the patient's medical record which might include demographic information, scanned copies of the patient reports, medical images and any other information that might be collected by the healthcare provider about the patient. EHR on the other hand is the single aggregated medical information that is maintained by and shared across multiple entities. In this paper we are concerned about the storage and access control of EMRs at a single entity such as a clinic or a hospital. While our solution could be extended to EHRs, that would involve tackling the secure sharing of data which is outside the scope of this paper.

C. Attributes

Attributes are characteristics or properties that are associated with an entity. They can involve any quantity that describes or identifies the entity. In the healthcare system, entities can be healthcare staff, patients, EMRs etc, while attributes can be the role of a healthcare staff, the department of the healthcare staff, the age of a patient, the time of generation of an EMR, origin of an EMR, EMR sensitivity etc.

In many systems roles are used for access control [3] but attributes can be used to provide more fine grained and flexible access control than roles. With attributes, fine grained policies such as (*an EMR with a high sensitivity level can only be viewed by the doctor who created the document and at the same location as the origin of the EMR*) can be created. Attributes also allow us to provide the flexibility of creating and applying individual policies to documents by using Attribute Based Access Control (ABAC). HVE is an ABAC system which is discussed in the next subsection.

D. Hidden Vector Encryption

In traditional encryption, one can encrypt data under a public key or the secret key and only the owner of the secret key can decrypt the data. In a sense decryption can be described as all or nothing, if you have the secret key you can decrypt the message and if you don't have the secret key then you cannot decrypt the message. However, in applications such as electronic healthcare systems, users require fine grained control as to who can access the data and what can be learnt about the data.

Hidden Vector Encryption is a specific type of the more general Predicate Encryption which allows more flexible decryption than traditional encryption systems. With predicate encryption, users can specify predicates such as "*Department*" = "*Dermatology*" or "*Time*" < "*1700*" or even the conjunction of predicates such as ("*Department*" = "*Cardiology*") \wedge ("*Role*" = "*Nurse*") which can be embedded in the ciphertext such that the decryption will only be performed when those conditions are met.

In Hidden Vector Encryption the predicates are specified in the form of a vector of attributes. When the encryption is performed with the public key this attribute vector is embedded in the ciphertext. Decryption requires a separate vector of attributes along with the private key. Decryption will be successful only if the attributes in this vector satisfy the predicates specified in the encryption vector. HVE encryption allows the flexibility of having some don't care entries in the decryption vector, in case some predicates need to be ignored. We now provide a definition of HVE encryption.

Let $\vec{\delta}$ be a vector of attributes of length l , $\vec{\delta} = \{\delta_1, \delta_2, \dots, \delta_l\} \in \Sigma$, where Σ is the set of all attributes in the system. Also, let \vec{q} be a vector of the same length over $\{\Sigma \cup *\}$, where $*$ denotes don't care. A vector match($\vec{\delta}, \vec{q}$) is defined to be true if and only if the two vectors agree in all positions i where $q_i \neq *$. Given these two vectors a Hidden Vector Encryption scheme can be defined as a tuple of four efficient probabilistic algorithms (Key Gen, Encrypt, Gen Token and Decrypt) with the following semantics [4].

- 1) *Setup*(p)
 - Takes the security parameter p and generates the public key PK and secret key SK
- 2) *Encrypt*(PK, δ, d)
 - Takes as input, public key PK , the encryption vector δ and the data to be encrypted d
 - Outputs ciphertext $CT = Enc_{HVE}(PK, \delta, d)$
- 3) *GenToken*(SK, q)
 - Takes secret key SK and the query vector q as input.
 - Outputs a token $T_k = GenToken_{HVE}(SK, q)$
- 4) *Decrypt*(T_k, CT)
 - Takes the ciphertext CT and the token T_k as the input
 - If decryption is successful, output plaintext d , otherwise output *null*.

Fig. 1. Block Diagram of Hidden Vector Encryption

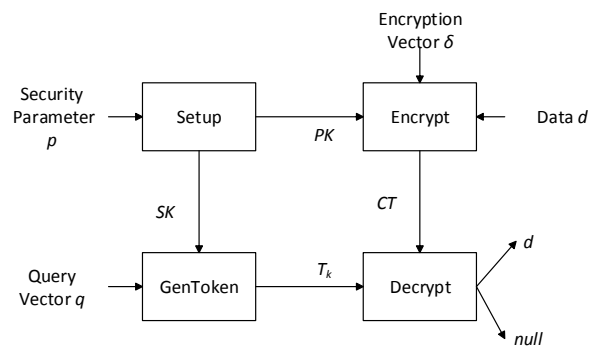
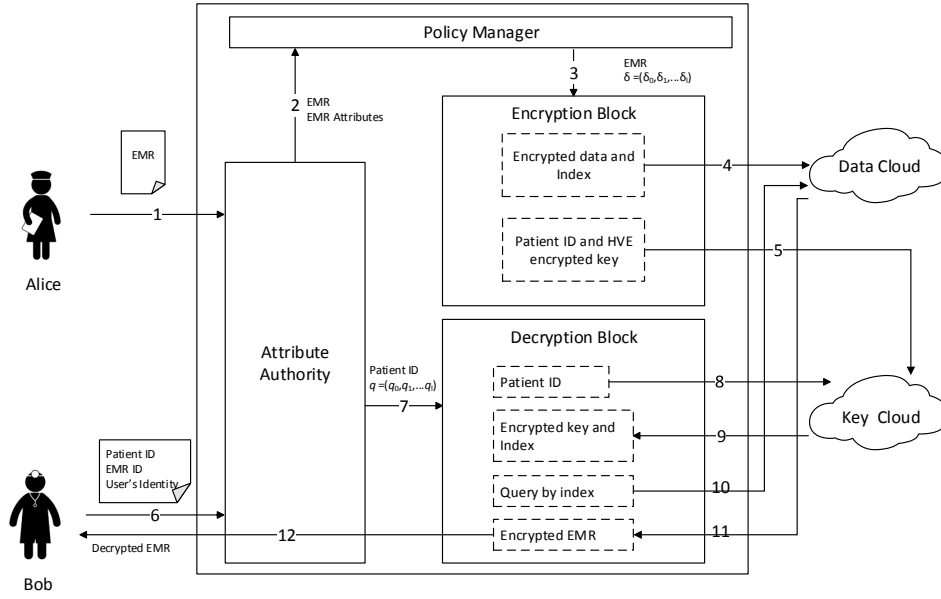


Figure 1 shows the block diagram representation of the four algorithms of HVE. While we do not provide the complete mathematical construction of the algorithms in this paper they can be found in [4], [5] and [6]. A dual of HVE also exists in which contrary to the original HVE, $\vec{\delta} \in \{\Sigma \cup *\}$ and $\vec{q} \in \Sigma$, while everything else remains the same. In our application we

Fig. 2. Proposed System Architecture



in fact use the dual of HVE, since it gives us the flexibility of using the don't care entries when creating the policies.

III. THE PROPOSED SYSTEM

Our proposed system consists of four functional entities, Attribute Authority, Policy Manager, Encryption Block, Decryption Block and two Cloud Servers, data cloud (DC) and key cloud (KC) for storing encrypted data and encrypted keys. Figure 2 shows a model of our system and how each of these entities interact with each other. We first provide an overview of our system before describing each of these entities in detail.

The component of the system that the healthcare staff directly interacts with is the Attribute Authority (AA). When a member of the staff say Alice wants to store an EMR of a patient in the system, Alice will interact with AA and provide it the EMR to be stored. AA will extract attributes from the EMR data as well as the meta-data. AA then converts the attributes in a numerical form and sends the attributes and the EMR to the Policy Manager (PM). The PM is the component of the system which stores the access control policies that are to be applied to the EMR. The PM then uses the numerical attributes to create a vector that has the access control policies to be enforced encoded. This is called the encryption vector δ . The PM then sends the EMR and the encryption vector to the Encryption Block (EB). The EB first encrypts the EMR with a randomly generated symmetric key and then encrypts the symmetric key with Hidden Vector Encryption using the encryption vector supplied by the PM. The encrypted EMR is stored in the Data Cloud (DC) while the encrypted key is stored in the Key Cloud (KC).

Now, say a user named Bob wants to access a particular EMR of a particular patient. Bob will communicate with AA for the data request. Bob provides AA with his identity as well

as information about the EMR that is being requested. AA then extracts relevant attributes from the request and creates a query vector of attributes (q). The query vector and the patient's ID is then sent to the Decryption Block DB in the form of the tuple $\langle q_i, PID_i \rangle$. The decryption block DB requests the records for the patient ID PID_i from the key cloud KC. DB then decrypts the records using the query vector q . If the attributes in the query vector satisfy the access control policies embedded in the ciphertext the decryption would be successful otherwise not. If the decryption is successful, it will give the DB the symmetric key ks_i and the unique identifier ID_i . The DB then requests the encrypted EMR corresponding to ID_i from DC and decrypts it using ks_i . The result is then returned back to Bob.

We now explain the function of each of the entities of our system in more detail.

A. Attribute Authority (AA)

During setup, the Attribute Authority chooses a unique random number x for each possible attribute value in the system. Let's say, Σ is an arbitrary set of all attributes in the system. $\Sigma = \{X_0, X_1, \dots, X_n\}$ where X_i can be attributes such as *Role, Department, Location etc.* and $\Lambda_i = \{\lambda_0, \lambda_1, \dots, \lambda_k\}$ be a set of all attribute values for a particular attribute X_i . For example, for the attribute *Role*, possible attribute values can be *Physician, Nurse, Ward clerk, Therapist etc.* For all possible values of all possible attributes in the system, the attribute authority randomly generates a unique number x .

The main goal of the attribute authority is the management of attributes and the generation of the encryption vector (δ) and the query vector (q) based on the attributes. When a medical staff say Alice, wants to store an EMR, she will submit it to the attribute authority. The attribute authority will extract

attributes from the EMR and forward the numerical vector $\vec{x} = (x_0, x_1 \dots x_n)$ corresponding to the attributes along with the EMR to the policy manager. Another medical staff say Bob, who only wants to access some data, will submit his attributes, patient ID and the meta-data of the document that he wants to the attribute authority. Attribute authority will generate a query vector (q) based on Bob's attributes and forward the tuple $\langle q_i, PID_i \rangle$ to the decryption block.

B. Policy Manager

The Policy Manager component of the system allows health-care providers to create, monitor and enforce policies that control the access to data. The health care provider can create a set of access policies and store these in the policy manager component. When some data needs to be encrypted the policy manager will receive attributes from the attribute authority. The policy manager will enforce the required access control policies by creating an encryption vector (δ) that corresponds to those policies. This encryption vector is then passed to the encryption block along with the EMR.

C. Encryption Block

The encryption block as the name suggests encrypts the data. The encryption block is provided with the HVE public key at the setup time. The encryption block will encrypt the healthcare data using the HVE public key and the encryption vector (δ). The encryption vector (δ) embeds the access policies in the ciphertext which ensures that the decryption takes place only when the correct attributes are provided. The encryption block works as follows.

- 1) First it generates a random symmetric key,
- 2) Then it encrypts the data with symmetric key encryption using the key generated above,
- 3) Then it generates a random number to be used as an identifier for this data,
- 4) Finally the symmetric key generated in step 1 is encrypted using Hidden Vector Encryption.

Let's say the EMR is represented by d_i . The data d_i is encrypted with the randomly generated key ks_i by symmetric encryption to produce ciphertext CT_i , where $CT_i = Enc_{ks_i}(d_i)$. The encryption block also generates a random number ID_i that will be used as an identifier for the CT_i . The tuple $\langle ID_i, CT_i \rangle$ is then sent to the data cloud DC for storage. The data is stored in the data cloud DC indexed by the identifier as shown in table I.

TABLE I
ENCRYPTED DATA STORAGE IN DC

Index	Encrypted data
ID_i	$Enc_{ks_i}(d_i)$
ID_j	$Enc_{ks_j}(d_j)$
\vdots	\vdots
ID_n	$Enc_{ks_n}(d_n)$

The encryption block then further encrypts the random key ks_i along with the identifier ID_i using HVE and vector δ . The ciphertext $Enc_{hve}(ks_i||ID_i)$, is then sent to the Key Cloud (KC) along with the patient ID PID_i as a tuple $\langle PID_i, Enc_{hve}(ks_i||ID_i) \rangle$. KC stores the encrypted key and identifier indexed by the patient IDs as shown in table II.

TABLE II
ENCRYPTED KEYS STORAGE IN KC

Patient ID	Encrypted Key
PID_i	$Enc_{hve}(ks_i ID_i)$
PID_j	$Enc_{hve}(ks_j ID_j)$
\vdots	\vdots
PID_n	$Enc_{hve}(ks_n ID_n)$

D. Decryption Block

To perform its function the decryption block receives the HVE private key at the setup time. The function of the decryption block is to receive a data request in the form of a query vector q and a patient ID PID_i from the AA and return data corresponding to the query, if the attributes in the query vector satisfy the access control criteria. The decryption block works as follows.

- 1) First it requests all the encrypted keys $Enc_{hve}(ks_i||ID_i)$ from Key Cloud KC for the patient ID PID_i received in the data request.
- 2) Then it uses the query vector q to perform HVE decryption on $Enc_{hve}(ks_i||ID_i)$ to retrieve ks_i and the identifier ID_i . If the decryption is unsuccessful, it quits the process otherwise it proceeds to the next step.
- 3) If step 2 is successful, it requests encrypted data CT_i from data cloud DC using the ID_i .
- 4) It then decrypts CT_i using ks_i to recover the original data d_i , where $d_i = Dec_{ks_i}(CT_i)$.
- 5) The data d_i is finally sent back to the user.

In step 2, when the HVE decryption is performed on the ciphertext, the decryption will only be successful if the attributes in the query vector, satisfy the access control policies embedded in the ciphertext at the time of encryption using the encryption vector δ . This will ensure the compliance with the policies. If the decryption is unsuccessful, the decryption block will inform the requestor that the access was denied.

IV. PERFORMANCE ANALYSIS

To evaluate the performance of our system we tested the execution time of the four core HVE algorithms *Setup*, *GenToken*, *Encrypt* and *Decrypt*. The implementation uses the Pairing Based Cryptography (PBC) library [7]. To test the execution time of our core algorithms we first tested the execution time of the various basic HVE functions that the algorithms are composed of. The system also uses other operations such as symmetric encryption/decryption and random number generation but because these operations are much

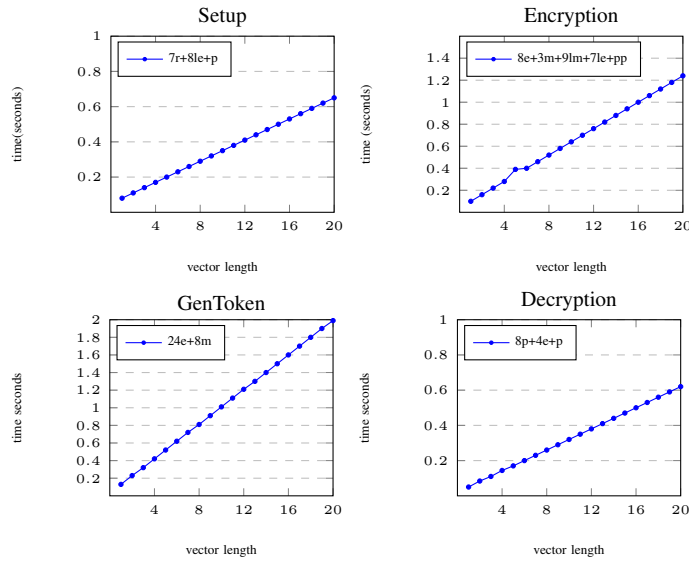


Fig. 3. Execution time of the algorithms

faster than the pairing based operations that HVE uses we did not analyze them in this work.

The tests were performed on an Oracle Virtual Box running 64-bit Ubuntu in a VM. The VM had 2048 MB of RAM and 40 GB of hard disk with a 2-core 2.2 GHz CPU. The VM thus mimicked a fairly low spec physical machine. Each basic function was executed 50 times and the average execution time was reported. Table III shows the HVE functions and their execution time. The four core HVE algorithms are composed of these basic functions and also depend on l , the length of the encryption vector δ . The mathematical details of the construction can be found in [6]. Table IV shows the composition of each of the algorithms in terms of the basic functions. The *Setup* for example is composed of 7 random element generations, $8l$ element exponentiations, where l is the length of the encryption vector δ , and 1 pairing function. The execution time of the algorithms can be calculated as a function of l using the compositions in table IV. Figure 3 shows the execution time as a function of the length l of the encryption vector. The time taken during setup is a one time cost at the system startup. The delay introduced by encryption when in the extreme case of $l = 20$ is only 1.24 seconds. In most cases the encryption vector would be smaller than that and accordingly the delay will be less than 1.24 seconds. The GenToken and the Decryption algorithms are executed when someone wants to access data. In the extreme case of $l = 20$, the combined execution time of the two algorithms is 2.61 seconds. This is admittedly slightly on the higher side and will cause a barely noticeable delay. This however, is the tradeoff for a higher level of security and access control.

V. CONCLUSIONS AND FUTURE WORK

In this paper we have proposed an attribute based access control mechanism for healthcare data. Using HVE, our system keeps the data encrypted at all times and embeds the

TABLE III
PAIRING BASED LIBRARY FUNCTIONS

Function	key	Runtime(s)
Random element generation	r	0.0021
Element addition	a	0.0032
Element division	d	0.0038
Element multiplication	m	0.0034
Element exponentiation	e	0.0041
Pairing generation	p	0.0036
Pairing multiplication	pp	0.0036

TABLE IV
COMPUTATION COMPLEXITY

Algorithm	Composition
Setup	$7r+8le+p$
Encryption	$8e+3m+9lm+7le+pp$
GenToken	$24e+8m$
Decryption	$8p+4e+p$

access control policies directly onto the encrypted data. This solution provides protection against both the outside adversary and the inside adversary and will be less cumbersome than having two separate controls for protection against the two types of adversaries. We implemented the HVE system on a low spec machine and found that the execution time of the system produces acceptable amount of delay which can be further reduced by the use of more efficient crypto libraries. In section II-A, we made 2 assumptions about our adversary. We assumed that the adversary is not able to present fake attributes to the system. As previously stated this can be established by using swipe cards. Our second assumption was that the adversary is not able to compromise the components of our system. This is a very strong assumption and our future work would entail making the system robust to such compromises. We are currently attempting to eliminate that assumption by using secret sharing and identity based systems.

REFERENCES

- [1] M. Alvarez, N. Bradley, P. Cobb, S. Craig, R. Iffert, L. Kessem, J. Kravitz, D. McMillen, and S. Moore, "Ibm x-force threat intelligence index 2017, the year of the mega breach," IBM X-Force Threat Research, Tech. Rep., March 2017.
- [2] HyTrust, "Whitepaper: Hytrust cloud adoption survey, despite security concerns multi-cloud adoption on the rise," HyTrust Inc, Tech. Rep., 08 2016.
- [3] Z. Pervaiz, A. Samuel, D. Ferraiolo, S. Gavrilu, and A. Ghafoor, "Access control for healthcare using policy machine," Purdue University, Tech. Rep. CERIAS TR 2009-20, 08 2009.
- [4] D. Boneh and B. Waters, "Conjunctive, subset, and range queries on encrypted data," in *Theory of Cryptography Conference*. Springer, 2007, pp. 535–554.
- [5] A. De Caro, V. Iovino, and G. Persiano, "Hidden vector encryption fully secure against unrestricted queries," *IACR Cryptology ePrint Archive*, vol. 2011, p. 546, 2011.
- [6] J. H. Park, K. Lee, W. Susilo, and D. H. Lee, "Fully secure hidden vector encryption under standard assumptions," *Information Sciences*, vol. 232, pp. 188–207, 2013.
- [7] B. Lynn, "The pairing-based cryptography library," *Internet: crypto.stanford.edu/pbc/[Nov. 1, 2017]*, 2011.

POStCODE Middleware for Post-market Surveillance of Medical Devices for Cyber Security in Medical and Healthcare Sector in Australia

Junaid Chaudhry
College of Security and Intelligence
Embry-Riddle Aeronautical University
Prescott, USA
chaudhrj@erau.edu

Craig Valli
Security Research Institute
Edith Cowan University
Joondaloup, Australia
c.valli@ecu.edu.au

Michael Crowley
School of Science
Edith Cowan University
Joondaloup, Australia
m.crowley@ecu.edu.au

Jon Haass
College of Security and Intelligence
Embry-Riddle Aeronautical University
Prescott, USA
haassj@erau.edu

Peter Roberts
School of Medicine
Edith Cowan University
Joondaloup, Australia
p.roberts@ecu.edu.au

Abstract—Postmarket surveillance for cyber security of medical devices is an area within the critical infrastructure of health care and public health that has been largely neglected. In developed countries post market quality assurance is passive following complaints from the health care institutions to the manufacturers of the medical devices. Recently, the individual devices can be made traceable allowing any malfunctions to be uniquely identified in each device. There is a lack of clarity on post-sale ownership and management of devices and the updates to the device software. These devices, once plugged into Healthcare Information Systems (HIS) act as FDA approved black boxes that cannot be patched, updated, or secured by anyone other than the manufacturer. Moreover, these unpatched devices provide back doors to cyber criminals to invade the HIS. These devices are soft targets for cyber criminals. So far, we have not come across any mechanisms that address the surveillance of these devices for cyber security. In this paper, we analyzed the post-sale surveillance regulations in Australia. Based on our findings, we present fog-based *POSTmarket SurveillanCe Of DEvices* (POStCODE) middleware that provides the operational details (excluding the private data of patient) of the devices directly to the manufacturers. The introduction of the POStCODE will give device manufacturers the means to closely monitor the functioning of their devices. Manufacturers will be able to upgrade devices, patch security vulnerabilities and monitor device performance thereby enhancing health care outcomes. The *POStCODE* middleware enhances device security whilst building partnerships between the health care facilitators and the device manufacturers.

Keywords—cyber security, critical infrastructure, healthcare, middleware, postmarket surveillance

I. INTRODUCTION

A. Medical Devices

In the past, Medical Devices (MDs) were isolated instruments that served in a closed loop: detection of physical

variables from a patient's physiological condition and translating that into electronic format. In [1] a device is defined as an instrument, apparatus, or machine which is intended for use in the diagnosis of disease or other conditions, or in the cure, mitigation, treatment, or prevention of disease and which does not achieve its primary intended purposes through chemical action. The MDs help in detection, cure, and prevention of medical, potentially fatal, health conditions. In [2] we proposed a detection system for cardiac abnormalities and we reported that misdiagnosis may lead to the death of the subject. It follows that any reasonable process that alerts manufacturers and users of devices to any operating anomalies is critical. A failure by manufacturers to evaluate and if appropriate take advantage of this new development could expose them to future legal liability.

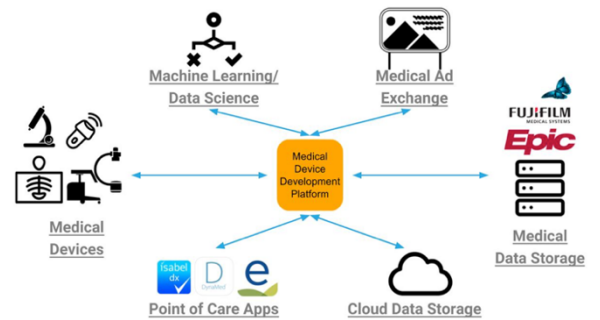


Fig. 1. Medical Devices connected to a centralized platform.

B. Healthcare Information System (HIS)

Any evaluation and or surveillance of MDs need to recognize that the data generated is patient data [3]. As such, this data is the property of the patient and the Healthcare Information System (HIS) is entrusted to keep that data secure and private for the owner [4]. This patient data is generated after the device applies manufacturer generated

standardized algorithms on the patients physiological condition [5]. These device operations are electronically administered either autonomously or with the assistance of a healthcare worker. At times, the operations promised by the MDs malfunction, such as the ones reported [6], [7] where remedial action is needed. Specific databases are maintained by the regulators who publish these device malfunction incidents. In this research we access these databases to extract information about past incidents related to cyber security in MDs [8]–[14]. A more comprehensive analysis is provided in the literature review section later in this paper.



Fig. 2. Healthcare Information Systems.

C. Food and Drug Administration

Once MDs are sold, their native operating system and application software is generally not updated or patched [15]. This failure to patch or update makes the operating system running in that MD vulnerable. Research has found that the MDs are often targeted by cyber criminals taking advantage of inbuilt outdated vulnerabilities [16]. Since these MDs are approved by the regulatory bodies, for example, the Food and Drug Administration (FDA) in the United States of America [17], it is illegal to alter the state of the device once implanted [20]. The only entity that can modify the software or hardware of an MD is its manufacturer. Kramer et.al. report inconsistencies in this MD governance cycle in [17]. After a medical device is brought onto the market, an ongoing postmarket surveillance begins. This is to ensure the safety and effectiveness of the MDs. In the United States of America, the postmarket surveillance may include per-market approval for high risk MDs or 522 studies [18] [20]. For new devices, the 510 process [21] clears the new devices on the grounds of substantial equivalence. This provides a gateway for the manufacturers to sell the new devices without substantial clinical testing. More details of the status of such devices can be found in reports [22], [23].

D. Security Problems in Healthcare Systems

In [24], Chaudhry et.al. identify cloud computing based system as the immediate solution to the cyber security problems of medical and healthcare sectors and Bildosola et.al. [25] also reports on the benefits of cloud adoption. Fog computing was proposed by Zhang et.al. [26] as a super set of

cloud-lets promising interoperability [27], dynamic work flows [28], security as a service [29], platform as a service etc. [30]. In this paper, we exploit the strengths of the fog computing environment, and propose a postmarket surveillance method. We propose that the MDs should report their operational context directly to the manufacturers via cloud portal. This will provide more transparency to the postmarket MD surveillance thereby promising an improved quality of service. It will also generate the clinical data for the new devices thereby assisting in keeping MDs safer. This process will allow the direct application of needed patches and enhance HIS administrator's trust in MDs. We aim at implementing this model in a test site to demonstrate the effectiveness of the solution.

E. Cloud-based Health Information Systems

The primary benefit of cloud based solutions for the industry is the shared platform, aggregating information and common methods [31]. Cloud systems can provide greater flow of data and support the multi-format data. According to [32], Infrastructure as a Service (IaaS) is a model that suits both the service providers and the service customers because it shares the risks equally amongst all parties. Because there are no definitive solutions to counter the reported frequent data breaches the medical sector looks to the cloud computing as an intermediate solution.

F. Fog Based Surveillance Solution

In this paper, we highlight the need for postmarket surveillance of medical devices and propose a fog-based surveillance solution that provides direct monitoring of the functional orientation of the MDs, quick and more localized response to the malfunctions and unauthorized access to MDs, provide access to Regulators so they can meet governance requirements of the surveillance of MDs, access to the live feed leading up to patient death for any subsequent legal and coronary investigations, improving the sharing of the security and safety risks of medical devices among the stakeholders.

The rest of this paper is organized as follows; a literature review followed by an analysis of the Australian postmarket surveillance market for the MDs. This is followed by a discussion of the POSTmarket SURVEILLANCE OF DEVICES (POSTCODE) middleware including coverage of relevant case studies. In concluding the paper we highlight options for future research in this area.

II. POSTMARKET SURVEILLANCE OF MEDICAL DEVICES

Medical devices play a critical role in diagnosing, maintaining, monitoring, and restoring the physiological state of a patient. An MD observes the state of the patient and uses the device intelligence programmed into it by the manufacturer, using the sensors and actuators at its disposal, to generate diagnostic data. This device intelligence is the intellectual property of the device manufacturers. Once data is generated, following the normal work flow of the device intelligence, it becomes a part of patient records. There is currently no way of tracking the control data to/from the

MDs (the control data that is used to issue commands to the sensors and actuators in the MDs) [114]. The security of patient records, is a tangent that is not addressed in this paper. Adverse events in the medical and healthcare environment may be caused by poorly trained staff [111], by external vectors i.e. cyber criminals [112], or by lack of best practice cyber hygiene [115]. Kramer et.al. [106] compare the strategies of the postmarket surveillance of MDs in the developed countries. Once a medical device is manufactured, it is tested for reliability and accuracy. Ruben et.al. present the number of patients studied prior to approval of new medicines [107]. However there are some comprehensive studies done in individual facets of the medical device surveillance technology [108], [109]. The question, should the MDs be tested by independent parties is a topic still unanswered [110]. Through POSTCODE we aim at also bringing transparency to the process of pre-deployment testing of the medical devices. The existing practices are not suited for mass development of devices because of unit cost in testing them. Moreover, the thoroughness of tests done on the new devices cannot be verified. Through data obtained from POSTCODE it is possible to perform fault localization.

TABLE I. APPLICATION AREAS OF FOG COMPUTING

<i>Scheme</i>	<i>Applications</i>
AlFaruque et.al. [37]	Energy As a Service for Fog Computing
Al-Fuqaha et.al. [38]	Integration of LoRaWAN into Fog Infrastructure
Alippi et.al. [39]	Autonomous Interactions in Fog Computing for the Smart Grid
Bader2016 et.al. [40], Bitencourt et.al. [41], and Yi et.al. [42]	Middleware Applications on Fog Platforms
Alrawais et.al. [43], Li et.al. [85], and Mollah et.al. [45]	Security Services on the Fog Platforms
Chiang et.al. [46], Park et.al. [47], Pu et.al. [48], Suto et.al. [49], Tao et.al. [50], Wang et.al. [51], and Taoxue et.al. [52]	Research Opportunities in particular domains in Fog Computing
Dantu et.al. [53]	Android suitability for Fog Platforms
Deng et.al. [54], Lu et.al. [55], Park et.al. [56], Peng et.al. [57], Mi et.al. [90], and Peng(1) et.al. [58]	Workload delegation for Fog Environments
CloudComp et.al. [59], Garcia et.al. [60], and Jalali et.al. [61]	Economics model of Fog computing models and associated costs
Ejaz et.al. [62], & Ku et.al. [63],	5G applications in Fog Computing
He et.al. [66], Gargees et.al. [65], Jayaraman et.al. [67], and Wang et.al. [68]	Applications of the Fog Computing in scalability issues in distributed video live streaming and assembly.
Chen et.al. [69], Hou et.al. [70], and Tandon et.al. [71],	Vehicular Networks and their integration into fog computing environments.
Lin et.al. [72], Hou et.al. [73], Tandon et.al. [74], Iotti et.al. [75], Nikoloudaki et.al. [80], Sharma et.al. [79], Shih et.al. [78], Zeng et.al. [76],	Quality of Service Improvement in Fog computing environments.
Farris et.al. [83], Jain et.al. [84], Li et.al. [85], and Li et.al. [86],	Various issues in Fog computing environments.
Kulatunga et.al. [87], Mubeen et.al. [88], Yannuzzi et.al. [89],	Smart Dairy and other smart spaces using Fog computing environments.

<i>Scheme</i>	<i>Applications</i>
and Nguyen et.al. [82].	

The collection of evidence of malfunction in MDs is no mean feat. The possibility of applying the postmarket surveillance proposed in developing countries is absolutely essential. Due to absence of enforcement of cyber medical law, the devices are often operated under hazardous conditions and may cause harm to either patients or to the machine operators. With POSTCODE we aim at bringing accountability in the MD audit and sharing of the control data among regulatory bodies and the device manufactures.

III. FOG COMPUTING AND MEDICAL HEALTHCARE SYSTEMS

Fog computing encompasses everything on the planet that can communicate [33]–[35]. Proposed first by Addepalli et.al. [36], [64] has fast growing applications in every facet of life. Although not without its challenges [83]–[86], [103], Chaudhry et.al. [102] proposed that cloud computing has a promising future in medical and Healthcare Information System (HIS). The primary application of the fog platform in the smart spaces [38], [82], [87]–[89] with extensive attention given so far to the improvement in quality of service [72]–[76], [78]–[80]. The integrated infrastructure also includes 5G environments and distributed video streaming applications associated with the Vehicular Networks [62], [63], [65]–[71]. With the help of research on workload delegation [54]–[58], [90] results reported in [59]–[61] present promising economic models for fog adaptation. Although there have been middleware applications proposed for fog platforms [37], [40]–[42], and security as a service being among those proposed [43], [45], [85], there are still many research opportunities in fog computing platforms [46]–[52]. See Tables I and II.

TABLE II. APPLICATION AREAS OF FOG COMPUTING IN MEDICAL AND PUBLIC HEALTH

<i>Scheme</i>	<i>Applications</i>
Hung et.al. [101], Tidbits et.al. [100], Wen et.al. [99], Malensek et.al. [98], and Manzalini et.al. [97]	On transitioning from legacy system to the Fog Infrastructure and user mode selection
Elkhatib et.al. [64]	Fog Middleware for automated compliance of OECD and privacy principles in Health-care IoT
Gao et.al. [96], Jantsch et.al. [95], and Jutila et.al. [94]	Data Dissemination in fog computing
Gargees et.al. [65], and Misra et.al. [93]	Cost effective fog in medical (OPSIT project)
Lu et.al. [92]	Privacy preservation in Fog computing
Moreno-vozmediano et.al. [81]	Cross site virtual networks in Fog
Yan et.al. [91]	Live data analysis in Fog

Different applications have been proposed for medical and healthcare infrastructure using Fog computing platforms.

Among them are [97]–[101] where transition strategies from legacy system to fog infrastructure are suggested. In [64] Elkhatib et.al. proposed a compliance middleware using fog computing for healthcare enterprises. The healthcare data that is in high demand among cyber criminals [104], is of empirical value to safeguard data. In [94]–[96] fog computing platforms are considered efficient in healthcare data dissemination and privacy preservation [92]. Because healthcare data is widely shared, so cross site [81] live data sharing [91] is of prime value. The healthcare data is frequently shared and requires archiving for later reference or to ease transition to a new provider. Among the healthcare data there is diagnostics data, first degree user data, and second degree user data [105]. The diagnostic data carries first degree user data that contains the meta data that the medical expert derives from the diagnostics data. The second degree user data is added for identification purposes.

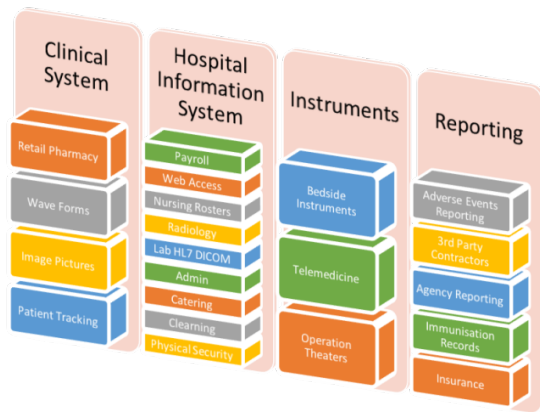


Fig. 3. HIS Reference Model.

IV. PROPOSED ARCHITECTURE OF THE POSTCODE MIDDLEWARE

The Hospital Information Systems (HIS) are integrated systems of sub-specialized information systems. In this research we classify an integrated HIS in following categories:

- 1) *Core Hospital Information Systems:* Provide information services to the core functions of the hospital.
- 2) *Multimedia Archiving System:* The long term storage of the patient records and imaging.
- 3) *Associated HIS subsystems:* Supports the functions that are associated with the core HIS i.e. Administrative systems, Financial systems, etc.
- 4) *External HIS systems:* The third party vendors who play an important role for the sustainability of the HIS i.e. Catering, Cleaning, Gas supplies, and Security services etc.

These components exchange Electronic Medical Data (EMD) among themselves in order to continue performing the integrated services to the patients. The standardization of the EMR is highlighted in [113]. This EMR can be of 1- Clinical, 2- Images, 3- Admin/Financial data or a combination of all three. The common interface data bus in

an HIS is known as an Integration Tool, which is not the topic of discussion in this research. A common HIS framework is shown in Figure3. Since the HIS are large enterprises, they are often an amalgamation of many different standards and typologies. Hence sharing of data among multifaceted systems is a challenge. While making it all work at the data link layer, often security vulnerabilities are left exposed. Moreover, the interoperability, data transformation, and translation become resource consuming tasks. In order to address this problem, cloud computing is proposed in [102] as an alternative solution. From a functional perspective, in certain areas of a hospital where the resources are shared, a Public cloud should be deployed. Public cloud are customarily conventional logic and rely on a self-service fine-grained foundation utilizing the Internet for transport, and rely on web services/applications, from third-party contributors who create bills and provide resources to the HIS. It is a pay as you go model that is adjustable enough for countering spikes to demand via cloud accretion. The resources of the HIS which are not shared with the entities outside the HIS are placed within a Private cloud. This term is being used by some cloud vendors to explain contributions that follow cloud computing model in confidential or closed networks. This system has been introduced inside a data center of a health organization. Within a private cloud, cloud purveyors provide virtual application and scaleable resources offering the flexibility without capital investment to size for peak loads.

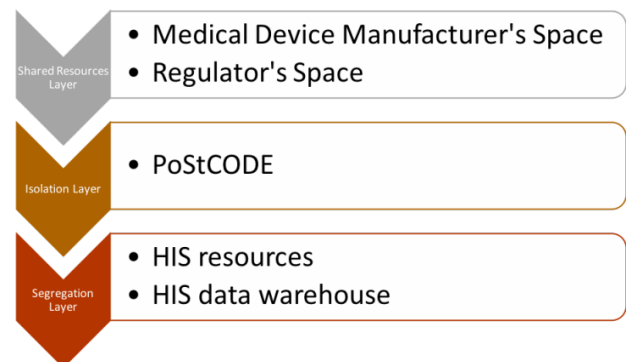


Fig. 4. Fog-let Architecture in HIS including the PoStCODE.

It is different from public cloud in the sense that organization itself supervises all applications and has the functionality of an intranet. Operation on private cloud is more sheltered than public cloud due to its additional authentication separation from the public network. Only delegated stakeholders and specific organizations have approaches to deal with explicit confidential cloud. In the HIS, some components that are external to the HIS i.e. External HIS systems frequently exchange data with the HIS and should be placed in Hybrid cloud. The portion of private cloud that is connected with one or many external cloud services is called hybrid cloud, that supervises centrally, rides as solitary unit, and restricts access by a network that is secure. It offers effective IT capabilities of both private and public clouds. Application and data are potentially more

secure in hybrid Cloud in comparison to a fully public Cloud even though it permits a variety of parties to access information via the Internet. Hybrid cloud solutions also possesses a public architecture to integrate with further systems of management. It explains configurations that combine a local device like Plug computer with services of cloud. It also explains configurations that combine physical and virtual collocation assets such as frequently virtualized environment required routers, physical server or further hardware like network appliances that act like a spam filter or firewall. The Figure 3 shows an overview of different cloud models. The PII that is generated by the MDs is the property of the patient sworn by the HIS to protect. We propose that the PII be managed by the HIS administrators while the control data from the MDs are transported out of the HIS and stored in the shared repository through a Virtual Private Network Coalition. The coalition provides the network isolation to the medical devices, which absolves the HIS administrators from MD security. The control data from the device is sent to the shared repository which is monitored by the device manufacturers and the regulators for accuracy and consistency. The figure 4 shows a sample Fog-let architecture.

V. POSTCODE IMPLEMENTATION

Many of the security vulnerabilities in MDs can be overcome by the direct monitoring of the devices. Until now, the MDs were connected to the HIS in an ad-hoc manner i.e. they are provided network access so that the PII data that is generated from those devices is stored by the HIS for investigation by healthcare workers. A predefined instruction set is provided to the healthcare workers on a console configured by the MD manufacturer. The POSTCODE provides a means of directly monitoring the functional orientation of the medical devices. Governance is an exercise in authority implying compliance and supervision by a regulator in an area of health care that is becoming increasingly congested with medical devices, associated software, and internet connectivity. Governance also implies a level of monitoring and supervision by manufacturers of both medical devices and associated software of their respective outputs to ensure compliance with accepted rules and regulations [116]. In the field of healthcare, a failure of governance can result in adverse outcomes for patients. The introduction of POSTCODE seeks to both enhance governance and improve medical outcomes for patients. The Australian regulator is the Therapeutic Goods Administration (TGA) whose responsibility covers pharmaceuticals and medical devices as well as other health related products. The TGA's powers flow from the Therapeutic Goods Act 1989 (Cth) and the Therapeutic Goods [116] Regulations 2002 (Cth). Chapter 4 of the Therapeutic Goods Act covers medical devices. Chapter 4 refers directly to the regulations (s.41CA), the powers of the Minister to determine standards (s.41CB) and to national and international standards (s.41CC) when establishing medical device standards. Listed international bodies include the European Committee for Standardization and the European Committee for Electro technical Standardization. Two principles seem to underpin the acceptance of medical devices in Australia, the first are

general principles covering health and safety and the second are essential principles related to design and construction. It is a reasonable assumption that any software interacting with medical devices complies with those two principles [117].

Software is picked up under Article 41BD of the Therapeutic Goods Act 1989 (Cth). This would include software that is relevant to the role of the POSTCODE in interacting with medical devices. The Australian Government Department of Health also has the Australian Regulatory Guidelines for Medical Devices (ARGMD) Part 2 (under review 2011) which is concerned with active medical devices and picks up 'all electronic devices and computers' under 'energy and also notes that:

Medical devices with telecommunications ports must comply with ACMA A-Tick requirements, for example, in-home patient- monitoring devices that have modem ports. Medical devices with radio-communications transmitters must comply with ACMA C-Tick requirements for radio-communications standards, for example, wrist-worn sphygmomanometers that connect to a mobile phone using Bluetooth. However, electrically- powered medical devices do not require C-Tick marking in relation to electromagnetic compatibility. They must comply with the more stringent requirements described in the Essential Principles. Active implantable medical devices (AIMDs) that utilize radio communications and the associated external radio transceiver such as an external programmer or data-logger, must also comply with ACMA radio spectrum licensing and C-Tick requirements. The ACMA Radio communications Class License (Low Interference Potential Devices) 2000 (also known as the LIPD Class License) makes specific allowance for some kinds of low-power radio communications for AIMDs, including those using Medical Implant Communications Systems (MICS), under specific conditions.

These regulations also cover software that operates as a controlling agent for an electronic device. The emphasis here is on the manufacturers purpose. That is, any regulation depends 'on the manufacturer's intended purpose for the software and how it is supplied'. Section 13 of the regulations concludes: The international standard IEC 62304 Medical device software—Software life cycle processes addresses requirements that are specific to software, while the IEC 62366 Medical devices — Application of usability engineering to medical de-vices standard addresses usability engineering requirements to all devices, including those that are wholly or partially software-based. The TGA considers these standards as representing the state-of- the-art for medical device software. The labeling requirements apply to medical device software, regardless of whether it is: downloaded from the Internet, installed from a CD, or pre-installed on a device. Manufacturers need to ensure that the product information, such as the graphical user interface, screenshots, CD labels, and product demonstrations meet the requirements of Essential Principle 13.

Because medical devices play a critical role in diagnosing, maintaining, monitoring, and restoring the physiological state of patients it is a reasonable expectation

that these medical devices will in themselves do no harm. Ideally, these devices will enhance the enjoyment of life of users whilst assisting manufacturers in achieving high standards of service. It is therefore incumbent upon hardware and software developers whose products directly or indirectly impact medical devices to ensure their products ‘do no harm’. Identifying what is covered by the principle ‘do no harm’ would be relatively straightforward but for the fact that the internet of things (IoT) is developing rapidly in a ‘world where science fiction quickly becomes scientific fact’. The principle of ‘do no harm’ encompasses not only appropriate maintenance and service of implanted medical devices but incorporates appropriate security.

The POSTCODE offers a clear benefit to users because it offers a viable interface for maintenance and service of medical devices whilst offering concurrent notification of malfunctioning devices. This process has the potential to enhance both general and essential principles mentioned above. It is however a new process. As such it needs to comply with present laws and regulation, not only in Australia but elsewhere in the world because a key feature of the internet is its connectivity. Or to put it another way, the internet is border-less requiring MD’s connected to the internet to take account of this connectivity in hardware and software design. Complying with the law does not in itself fulfill the requirement of ‘do no harm’ but it is an essential first step. In addition to the overarching requirements of legislation concerned directly with medical devices there are other laws and accepted codes that need to be kept in mind when introducing new processes into the medical device marketplace. There is also a concurrent ethical obligation to maintain confidentiality. Because the use of medical devices generally involves medical practitioners there is a concurrent code of professional conduct [119]. In Australia the Good medical practice has a section on guidelines for technology-based patient consultations [120]. The relevant definition is ‘[T]echnology- based patient consultations are patient consultations that use any form of technology, including, but not restricted to videoconferencing, internet and telephone, as an alternative to face-to-face consultations. The governing law for Australian Medical Practitioners is the Health Practitioner Regulation National Law Act [121], which has been replicated by each Australian state. Privacy in Australia is also covered by the Privacy Act 1988 (Cth) [122]. In that statute Section 16B is concerned with ‘the collection, use or disclosure of health information’ [123]. An important sub-section notes:

(3) A permitted health situation exists in relation to the use or disclosure by an organization of health information about an individual if:

(a) the use or disclosure is necessary for research, or the compilation or analysis of statistics, relevant to public health or public safety; and (b) it is impracticable for the organization to obtain the individual’s consent to the use or disclosure; and (c) the use or disclosure is conducted in accordance with guidelines approved under section 95A for the purposes of this paragraph and (d) in the case of disclosure—the organization reasonably believes that the

recipient of the information will not disclose the information, or personal information derived from that information [124].

It is a reasonable proposition that implementation of the POSTCODE proposal will comply with the above privacy codes and laws. However, there is more. The concern about unauthorized and/or illegal access to internet devices and storage has resulted in new laws focused on data protection. The purpose of this State of Victoria legislation is amongst other things to ‘provide for responsible collection and handling of personal information within the state of Victoria.’ It would not be unreasonable to expect other states within Australia to follow suit with similar legislation. The Australian Commission on Safety and Quality in Health Care [125] has also developed standards [126], which seek to improve the quality of health care in Australia. One component is E-health which for now is focused on hospital patient electronic records. The Australian Government entity, the Therapeutic Goods Administration [127] regulates the suppliers and manufacturers of therapeutic goods, specifically medical devices [128]. The connectivity of the internet requires a brief consideration of some international positions. The European Union has instituted a data protection regime through a directive on data protection [129] that is designed to protect both individual privacy and ensure personal data is protected from unauthorized use. This is about to be repealed and replaced by Regulation (EU) 2016/679. This new regulation entered into force on 24 May 2016 and will apply from 25 May 2018. European Union Member States are expected to have enacted complying legislation by 6 May 2018 [130]. Andrus Ansip, Vice-President of the Digital Single Market said:

Today’s agreement is a major step towards a Digital Single Market. It will remove barriers and unlock opportunities. The digital future of Europe can only be built on trust. With solid common standards for data protection, people can be sure they are in control of their personal information. And they can enjoy all the services and opportunities of a Digital Single Market. We should not see privacy and data protection as holding back economic activities. They are, in fact, an essential competitive advantage. Today’s agreement builds a strong basis to help Europe develop innovative digital services. Our next step is now to remove unjustified barriers which limit cross-border data flow: local practice and sometimes national law, limiting storage and processing of certain data outside national territory. So, let us move ahead and build an open and thriving data economy in the EU – based on the highest data protection standards and without unjustified barriers [131].

The important part of Ansips statement for non-European software developers is the impact on external digital storage and movement of data with a European link. The Press Release specifically noted that ‘companies based outside of Europe will have to apply the same rules when offering services in the EU’ and ‘that data protection safeguards are built into products and services from the earliest stage of development (Data protection by design)...’ [131]

A. Quick Anomaly Response to the MDs

To date, there is no means of detecting the anomalies in the MD. With POSTCODE, the anomalies are responded to much quicker than currently in practice. The anomalies are reported by the HIS either directly to the manufacturers or to regulatory body. POSTCODE would allow both manufacturer and regulator to receive data allowing monitoring and prevention of conflict of interest if sent only to manufacturer. The manufacturer may want to minimize reporting of anomalies. With POSTCODE the reporting of anomalies is a concern that is satisfied and also served for the purpose of direct governance of the postmarket surveillance process.

B. Downstream Applications of the PoStCODE

The connectivity of MDs raises an interesting area of future research into whether or not this connectivity can be used to cause the death of an MD user. What we propose here is a brief outline of the use of this process in ascertaining if a homicide has been caused by external interference with a MD. The novel portal access process can help investigators determine what, if any, external interference played a role in the homicide. However, this process would need to be accepted by the court systems before it could be utilized in the determination of cause of death. The admissibility of any evidence, in this case the 'novel portal process' in any Australian or USA court hearing requires acceptance by those same courts of the process. The courts will in determining admissibility apply certain tests. These tests may take into account whether or not the process monitoring the implanted MD's has met certain commercial and legal standards. For the former an established need, reliability and cost would be paramount. For the latter, legal reliability is paramount. Courts become interested in evidence when a party seeks to rely upon that evidence to influence a legal outcome. If we identify that evidence for these purposes as 'novel portal access' the following questions will need to be addressed:

Evidence is any matter of fact [118]: Would acceptance of this 'novel portal access' evidence, the fact(s) encompassed by this evidence effect any other fact. To put it another way, is the 'novel portal access' evidence relevant? That is, 'if accepted, could it rationally affect (directly or indirectly) the assessment of the probability of the existence of a fact in issue in the proceedings'. In our discussion here this latter fact is the cause of death. In those Australian jurisdictions that rely upon the common law the High Court of Australia has held that even though s55 of the Uniform Evidence Code does not apply in Western Australia the definition in s55 reflects the common law [132]. The next step after determining relevance is to ask if the 'novel portal access' evidence is admissible? This is a second test. At its simplest the test for admissibility says that even though 'novel portal access' evidence may be relevant it may nonetheless be found to be inadmissible if any of the exclusionary rules of evidence apply. The key word in 'novel portal access' is the word 'novel'. If this word 'novel' is being used because what is proposed is novel then what follows is relevant because leaving aside the main exclusionary rules there are rules about the admissibility of novel scientific evidence.

In *Mallard v The Queen* [132] the Western Australian Court of Appeal noted:

[E]xpert opinion evidence should not be rejected merely because the technique, instrument or methodology has not been used in court before (R v McHardie and Danielson [1983] 2 NSWLR 733 at 763). Likewise, even where such evidence has been rejected as not satisfying the requirements for admissibility at one time, that may change. Subsequent theoretical or practical scientific developments may later lead to a conclusion that in light of the more developed state of the particular field of expertise it may meet the requirements for admissibility.

Later the same court went on to say: the party offering the novel scientific evidence has the burden of demonstrating that it has been accepted as reliable among impartial and disinterested experts within the scientific field (emphasis added). This means that the proposed fog-based POSTmarket SurveillanCe Of DEvices (POSTCODE) middleware needs to be not only reliable, consistently fit for purpose, but has been independently tested and shown to be so. For the purposes of this paper the 'subsequent testing' is not needed at this point in time but the fact that this may be a requirement for any later use in court proceedings needs to be kept in mind opening up future research options the authors are pursuing. In essence, can what is proposed be replicated and independently tested?

C. Shared Risks among HIS Stakeholders

In modern day practice, health enterprises host Information Technology services in-house which consumes 60% of the resources of the organization [59]. Firstly, while outsourcing the IT infrastructure, the health organizations do outsource the infrastructure but the risks are not outsourced. These risks in-turn recoil back to the health enterprises in the form of security incidents. Secondly, since the health enterprises are large organizations with a considerable number of stakeholders the IT borne risks are not shared by the partners which puts health enterprises under considerable scrutiny. Thirdly, the HIS are evolving fast and it is logical to seek technological solutions that champion security over adaptability. Considering the enumerations mentioned above, the MDs that are somewhat standouts in HIS are closely monitored by the manufacturers which reduces some of the workload of HIS security engineers. As we discussed above, for different cloud models that are used in the HIS, the POSTCODE provides a corridor for the information technology components that are used in this HIS and delegates their security to their vendors who: 1-monitor their activities, 2- updating and patching components, 3- backup and restore the firmware, 4- replacing and tracking the MDs. The current practice of using the Unique Identifiers (UID) [9] (Sorenson C and in Perspective. *Milbank Q.* 2014;92(1):114–50 2014) is also outdated by the introduction of the POSTCODE.

VI. CONCLUSION

In this research we propose POSTmarket SurveillanCe Of DEvices (POSTCODE) middleware so that the secure tracking

and governance of the medical devices is performed in a cost effective way. The POSTCODE middleware provides the operational details (excluding the private data of patient) of the devices directly to the manufacturers. This way, the manufacturers will be able to closely monitor the functioning of their medical devices, bring up-gradation and build countermeasures of the vulnerabilities, adopt new technology through device performance analytics, etc. by virtue of this data available to them.

REFERENCES

- [1] United States Food and Drug Administration (2013) Medical Devices: Is the Product a Medical Devices? Available: <http://www.fda.gov/medicaldevices/deviceregulationandguidance/overview/classifyyourdevice/ucm051512.htm>. Accessed 17 May 2017. Conant GC, Wolfe KH.
- [2] Chaudhry, J., Qidwai, U., Zeeshan, H., Valli, C., (2017) Secure Detection of Critical Cardiac Abnormalities for Wireless Body Area Networks, Computer Systems Science and Engineering. May 2017.
- [3] The PLOS Medicine Editors (2016) Can Data Sharing Become the Path of Least Resistance? PLoS Med 13(1): e1001949.
- [4] Taichman DB, Backus J, Baethge C, Bauchner H, de Leeuw PW, Drazen JM, et al. (2016) Sharing Clinical Trial Data: A Proposal from the International Committee of Medical Journal Editors. PLoS Med 13(1): e1001950.
- [5] Piwek L, Ellis DA, Andrews S, Joinson A (2016) The Rise of Consumer Health Wearables: Promises and Barriers. PLoS Med 13(2): e1001953.
- [6] Hauser RG, Kallinen LM, Almquist AK, Gornick CC, Katsiyannis WT (2007) Early failure of a small-diameter high-voltage implantable cardioverter-defibrillator lead. Heart Rhythm 4: 892–896.
- [7] Hauser RG, Abdelhadi R, McGriff D, Retel LK (2012) Deaths caused by the failure of Riata and Riata ST implantable cardioverter-defibrillator leads. Heart Rhythm 9: 1227–1235.
- [8] Maisel WH (2004) Medical device regulation: an introduction for the practicing physician. Ann Intern Med 140: 296–302.
- [9] Sorenson C, Drummond M. Improving Medical Device Regulation: The United States and Europe in Perspective. Milbank Q. 2014;92(1):114–50.
- [10] Pharmaceuticals and Medical Devices Agency, Japan (2013) Approved Products databases. Available: <http://www.pmda.go.jp/english/service/approved.html>. Accessed 18 May 2017.
- [11] Liang Y (2010) Implementation of a postmarket traceability program for implantable medical devices adopting unique device identification. 2009-2012 GS1 Healthcare Reference Book. Available: <http://www.gs1.org/docs/healthcare/casestudies/Case20studyShanghai20FDAIMD20Traceability.pdf>. Accessed 18 May 2017.
- [12] Kevin Fu. Trustworthy medical device software. In Public Health Effectiveness of the FDA 510(k) Clearance Process: Measuring Postmarket Performance and Other Select Topics: Workshop Report, July 2011. IOM (Institute of Medicine), National Academies Press.
- [13] Daniel Halperin, Thomas S. Heydt-Benjamin, Benjamin Ransford, Shane S. Clark, Benessa Defend, Will Morgan, Kevin Fu, Tadayoshi Kohno, and William H. Maisel. Pacemakers and implantable cardiac defibrillators: Software radio attacks and zero-over defenses. In Proceedings of the 29th Annual IEEE Symposium on Security and Privacy, May 2008.
- [14] G.-Zheng, R.-Shankaran, M.-A. Orgun, L.-Qiao, and K.-Saleem, Ideas and challenges for securing wireless implantable medical devices: A review, IEEE Sensors Journal, vol.~17, no.~3, pp. 562--576, Feb 2017.
- [15] O'Connor B, Pollner F, Fugh-Berman A (2016) Salespeople in the Surgical Suite: Relationships between Surgeons and Medical Device Representatives. PLoS ONE 11(8): e0158510.
- [16] S. Movassaghi, M. Abolhasan, J. Lipman, D. Smith and A. Jamalipour, "Wireless Body Area Networks: A Survey," in IEEE Communications Surveys & Tutorials, vol. 16, no. 3, pp. 1658-1686, Third Quarter 2014.
- [17] Kramer DB, Xu S, Kesselheim AS (2012) How does medical device regulation perform in the United States and the European union? A systematic review. PLoS Med 9: e1001276.
- [18] Postmarket Surveillance Studies, <https://www.fda.gov/medicaldevices/postmarketsurveillance/>, Last Accessed: 20-06-2017.
- [19] General Controls for Medical Devices, Available: <https://www.fda.gov/MedicalDevices/DeviceRegulationandGuidance/Overview/GeneralandSpecialControls/ucm055910.htm>, Accessed 18 May 2017.
- [20] United States Food and Drug Administration (2013) 522 Postmarket Surveillance Studies. Available: <http://www.accessdata.fda.gov/pss.cfm>. Accessed 18 May 2017.
- [21] 510(k) Submission Methods, <https://www.fda.gov/MedicalDevices/>, Last Accessed: 20-06-2017.
- [22] United States Food and Drug Administration (2013) Post-Approval Studies website. Available: http://www.accessdata.fda.gov/pma_pas.cfm. Accessed 19 May 2017.
- [23] United States Food and Drug Administration (2013) 522 Postmarket Surveillance Studies. Available: <http://www.accessdata.fda.gov/scripts/cdrh/cfdocs/cfpMA/pss.cfm>. Accessed 19 May 2017.
- [24] Junaid Chaudhry, Uvais Qidwai, Mehdi Miraz, Healthcare Data Security among ISO/IEEE 11073 Personal Health Devices through Statistical Fingerprinting, 9th IEEE-GCC Conference and Exhibition 2017.
- [25] Bildosola I, Río-Belver R, Cilleruelo E, Garechana G (2015) Design and Implementation of a Cloud Computing Adoption Decision Tool: Generating a Cloud Road. PLoS ONE 10(7): e0134563.
- [26] McMillin, B., & Zhang, T. (2017). Fog Computing for Smart Living. Computer, 50(2), 5.
- [27] Cisco Delivers Vision of Fog Computing to Accelerate Value From Billions of Connected Devices, Available: <https://newsroom.cisco.com/articleId=1334100>. Accessed 19 May 2017.
- [28] Gao, L., Luan, T. H., Yu, S., Zhou, W., & Liu, B. (2017). FogRoute: DTN-Based Data Dissemination Model in Fog Computing. IEEE Internet of Things Journal, 4(1), 225–235.
- [29] Aazam, M., & Huh, E. N. (2016). Fog Computing: The Cloud-IoT/IoE Middleware Paradigm. IEEE Potentials, 35(3), 40–44.
- [30] T. H. Luan, L. Gao, Z. Li, Y. Xiang, G. Wei, L. Sun, "Fog computing: Focusing on mobile users at the edge", ArXiv e-print, Feb. 2015.
- [31] Singh G, Sood S & Sharma A. (2011). CM-Measurement Facets for Cloud Performance. IJCA. 23(3).
- [32] Problems Faced by Cloud Computing. Available at: LordCrusAd3r.dl.packetstormsecurity.net/ProblemsFacedbyCloudComputing.pdf, Accessed 18 May 2017.
- [33] Aazam M, Huh EN. Fog Computing: The Cloud-IoT/IoE Middleware Paradigm. IEEE Potentials. 2016;35(3):40–4.
- [34] H. Freeman, T. Zhang, "The emerging era of fog computing and networking [the president's page]", IEEE Commun. Mag., vol. 54, no. 6, pp. 4-5, Jun. 2016.
- [35] Zhanikeev M. A cloud visitation platform to facilitate cloud federation and fog computing. Computer (Long Beach Calif) [Internet]. 2015;48(5):80–3.
- [36] F. Bonomi, R. Milito, J. Zhu, and S. Addepalli, "Fog computing and its role in the internet of things," in Proceedings of the First Edition of the MCC Workshop on Mobile Cloud Computing, ser. MCC'12. ACM, 2012, pp. 13–16.
- [37] Al Faruque MA, Vatanparvar K. Energy Management-as-a-Service over Fog Computing Platform. IEEE Internet Things J. 2016;3(2):161–9.
- [38] Al-fuqaha A, Member S, Guizani M, Mohammadi M, Member S. Internet of Things : A Survey on Enabling. 2015;17(4):2347–76.

- [39] Alippi C, Fantacci R, Marabissi D, Roveri M. A Cloud to the Ground : The New Frontier of Intelligent and Autonomous Networks of Things. 2016;(December):14–20.
- [40] Bader A, Ghazzai H, Kadri A, Alouini M-S. Front-end intelligence for large-scale application-oriented internet-of-things. *IEEE Access* [Internet]. 2016;4:3257–72.
- [41] Bittencourt LF, Diaz-montes J, Member S, Buyya R, Rana OF, Member S, et al. Mobility-aware Application Scheduling in Fog Computing. 2015;14(8):1–8.
- [42] Yi S, Hao Z, Qin Z, Li Q. Fog computing: Platform and applications. In: *Proceedings - 3rd Workshop on Hot Topics in Web Systems and Technologies, HotWeb 2015*. 2016.
- [43] Alrawais A, Alhothaily A, Hu C, Cheng X. Fog Computing for the Internet of Things: Security and Privacy Issues. *IEEE Internet Comput [Internet]*. 2017;21(2):34–42.
- [44] Li Z, Zhou X, Liu Y, Xu H, Miao L. A non-cooperative differential game-based security model in fog computing [Internet]. Vol. 14, *China Communications*. 2017. p. 180–9.
- [45] Mollah MB, Azad MAK, Vasilakos A. Secure Data Sharing and Searching at the Edge of Cloud-Assisted Internet of Things. *IEEE Cloud Comput* 2017.
- [46] Chiang M, Zhang T. Fog and IoT: An Overview of Research Opportunities. *IEEE Internet Things J* [Internet]. 2016;4662(c):1–1.
- [47] Park SH, Simeone O, Shitz SS. Joint optimization of cloud and edge processing for fog radio access networks. *IEEE Int Symp Inf Theory - Proc*. 2016;2016–August(11):315–9.
- [48] Pu L, Chen X, Xu J, Fu X. D2D Fogging: An Energy-Efficient and Incentive-Aware Task Offloading Framework via Network-assisted D2D Collaboration. *IEEE J Sel Areas Commun* [Internet]. 2016;34(12):3887–901.
- [49] Suto K, Nishiyama H, Kato N, Huang CW. An Energy-Efficient and Delay-Aware Wireless Computing System for Industrial Wireless Sensor Networks. *IEEE Access*. 2015;3:1026–35.
- [50] Tao M, Ota K, Dong M. Foud: Integrating Fog and Cloud for 5G-Enabled V2G Networks. *IEEE Netw* [Internet]. 2017;31(2):8–13.
- [51] Wang W, Lee C, Chen L, Yu F, Su H-J. *IEEE Access Special Section Editorial : Emerging Cloud-Based Wireless*. *IEEE Access*. 2016;3:3122–4.
- [52] Yaoxue Z, Ju REN, Jiagang LIU, Chugui XU, Hui GUO, Yaping LIU. A Survey on Emerging Computing Paradigms for Big Data *. 2017;26(1).
- [53] Dantu K, Ko SY, Ziarek L. RAINA : Reliability and Adaptability in Android for Fog Computing. 2017;(April):41–5.
- [54] HR. Deng, R. Lu, C. Lai, T. H. Luan, and H. Liang, “Optimal workload allocation in fog-cloud computing toward balanced delay and powerconsumption,” *IEEE Internet Things J.*, vol. 3, no. 6, pp. 1171–1181, Dec. 2016.
- [55] R. Lu, H. Zhu, X. Liu, J. K. Liu, and J. Shao, “Toward efficient and privacy-preserving computing in big data era,” *IEEE Netw.*, vol. 28, no. 4, pp. 46–50, Jul./Aug. 2014.
- [56] Park S, Park J, Member S, Bong K. An Energy-Efficient and Scalable Deep Learning / Inference Processor With Tetra-Parallel MIMD Architecture for Big Data Applications. 2015;9(6):838–48.
- [57] Peng M, Member S, Zhang K. Recent Advances in Fog Radio Access Networks : Performance Analysis and Radio Resource Allocation. 2016;2016(c):1–6.
- [58] Peng M, Yan S, Zhang K, Wang C. Fog Computing based Radio Access Networks: Issues and Challenges. 2015
- [59] undefined, undefined, undefined, undefined, "The Economics of the Hybrid Multicloud Fog", *IEEE Cloud Comp* vol.4 no.1, p.16–21, 2017
- [60] García JM, Fernández P, Dustdar S, Wien TU. Edge and Cloud Pricing for the Sharing Economy. 2017;
- [61] Jalali F, Hinton K, Ayre R, Alpcan T, Member S, Tucker RS, et al. Fog Computing May Help to Save Energy in Cloud Computing. *Ieee J Sel Areas Commun*. 2016;34(5):1728–39.
- [62] Editorial G. Internet of Things (IoT) in 5G Wireless Communications. 2017;4:10310–4.
- [63] Ku Y, Lin D, Lee C, Hsieh P, Wei H, Chou C, et al. 5G Radio Access Network Design with the Fog Paradigm : Confluence of Communications and Computing. 2017;(April):46–52.
- [64] Elkhatib Y, Porter B, Ribeiro HB, Zhani MF, Qadir J, Riviere E. On Using Micro-Clouds to Deliver the Fog. *IEEE Internet Comput [Internet]*. 2017;21(2):8–15.
- [65] Gargees R, Morago B, Pelapur R, Chemodanov D, Calyam P, Oraibi Z, et al. Incident-Supporting Visual Cloud Computing Utilizing Software-Defined Networking. *IEEE Trans Circuits Syst Video Technol* [Internet]. 2016;27(1):1–1.
- [66] He Q, Zhang C, Ma X, Liu J. Fog-Based Transcoding for Crowdsourced Video Livecast. 2017;(April):28–33.
- [67] Jayaraman P, Gomes J, Nguyen H. Scalable energy-efficient distributed data analytics for crowdsensing applications in mobile environments. *IEEE Trans* [Internet]. 2015;2(3):109–23.
- [68] Wang W, Wang Q, Sohaby K. Multimedia Sensing as a Service (MSaaS): Exploring Resource Saving Potentials of at Cloud-Edge IoTs and Fogs. *IEEE Internet Things J* [Internet]. 2016;XX(c):1–1.
- [69] Chen X, Wang L. Exploring Fog Computing Based Adaptive Vehicular Data Scheduling Policies through a Compositional Formal Method - PEPA. *IEEE Commun Lett* [Internet]. 2017;21(4):1–1.
- [70] Hou X, Li Y, Chen M, Wu D, Jin D, Chen S. Vehicular Fog Computing: A Viewpoint of Vehicles as the Infrastructures. *IEEE Trans Veh Technol*. 2016;65(6):3860–73.
- [71] Tandon R, Simeone O. Harnessing cloud and edge synergies: Toward an information theory of fog radio access networks. *IEEE Commun Mag*. 2016;54(8):44–50.
- [72] Lin Y, Shen H. Leveraging Fog to Extend Cloud Gaming for Thin-Client MMOG with High Quality of Experience. *Proc - Int Conf Distrib Comput Syst*. 2015;2015–July(2):734–5.
- [73] Liang K, Zhao L, Zhao X, Wang Y, Ou S. Joint resource allocation and coordinated computation offloading for fog radio access networks, *China Communications*, Volume: 13, Issue: Supplement2, 2016.
- [74] Kapsalis A, Kasnesis P, Venieris IS, Dimitra I. CONNECTING FOG AND CLOUD COMPUTING Fog Approach for Effective Workload Balancing.
- [75] Iotti N, Picone M, Cirani S, Ferrari G. Improving Quality of Experience in Future Wireless Access Networks through Fog Computing. *IEEE Internet Comput* [Internet]. 2017;21(2):26–33.
- [76] Zeng D, Gu L, Guo S, Cheng Z, Yu S. Joint Optimization of Task Scheduling and Image Placement in Fog Computing Supported Software-Defined Embedded System. *IEEE Trans Comput*. 2016;65(12):3702–12.
- [77] Sun X, Member S, Ansari N. EdgeIoT : Mobile Edge Computing for Internet of Things. 2016;(December):1–7.
- [78] Shih Y, Chung W, Pang A, Chiu T, Wei H. Enabling Low-Latency Applications in Fog-Radio Access Networks. 2017;(February):52–8.
- [79] Sharma SK, Wang X. Live Data Analytics with Collaborative Edge and Cloud Processing in Wireless IoT Networks. *IEEE Access* [Internet]. 2017;1–1.
- [80] Nikoloudakis Y, Panagiotakis S, Markakis E. A Fog-Based Emergency System for Smart Enhanced Living Environments. 2016;
- [81] Moreno-vozmediano R, Montero RS, Huedo E. Cross-Site Virtual Network in Cloud and Fog Computing. 2017
- [82] C. Nguyen Le Tan, C. Klein, and E. Elmroth. Location-aware Load Prediction in Edge Data Centers. In *Proceedings of The 2nd IEEE International Conference on Fog and Edge Mobile Computing (FMEC 2017)*, Accepted, 2017.
- [83] Farris I, Girau R, Militano L, Nitti M, Atzori L, Iera A, et al. Social Virtual Objects in the Edge Cloud. *IEEE Cloud Comput*. 2015;2(6):20–8.
- [84] Jain A, Jain S, Bharadwaj S. Fog Computing. 2016;317–21.
- [85] Li S, Maddah-Ali MA, Avestimehr AS. Coding for Distributed Fog Computing. 2017;(April):34–40.
- [86] Li Z, Zhou X, Liu Y, Xu H, Miao L. A non-cooperative differential game-based security model in fog computing [Internet]. Vol. 14, *China Communications*. 2017. p. 180–9.

- [87] Kulatunga C. Opportunistic Wireless Networking for Smart Dairy. 2017;(April):16–23.
- [88] Mubeen S, Nikolaidis P, Didic A, Pei-Breivold H, Sandstrom K, Behnam M. Delay Mitigation in Offloaded Cloud Controllers in Industrial IoT. *IEEE Access* [Internet]. 2017;5:1–1.
- [89] Yannuzzi M, Van Ling F, Jain A, Parellada OL, Flores MM, Carrera D, et al. A new era for cities with fog computing. *IEEE Internet Comput*. 2017;21(2).
- [90] M X, M E, T G. Foggy Clouds and Cloudy Fogs : A Real Need for Coordinated Management of Fog-to-Cloud Computing Systems. 2016;(October):120–8.
- [91] Yan S, Peng M, Abana M, Wang W. An Evolutionary Game for User Access Mode Selection in Fog Radio Access Networks. *IEEE Access* [Internet]. 2017;5:1–1.
- [92] Lu R, Heung K, Lashkari A, Ghorbani A. A Lightweight Privacy-Preserving Data Aggregation Scheme for Fog Computing-Enhanced IoT. *IEEE Access* [Internet]. 2017;5:1–1.
- [93] Misra S, Sarkar S. Theoretical modelling of fog computing: a green computing paradigm to support IoT applications. *IET Networks* [Internet]. 2016;5(2):23–9.
- [94] Jutila M. An Adaptive Edge Router Enabling Internet of Things. *IEEE Internet Things J* [Internet]. 2016;4662(c):1–1.
- [95] Jantsch A, Wien TU. and Attention in Fog and Mist Computing. 2015;3745.
- [96] Gao L, Luan TH, Yu S, Zhou W, Liu B. FogRoute: DTN-based Data Dissemination Model in Fog Computing. *IEEE Internet Things J* [Internet]. 2017;4(1):1–1.
- [97] Manzalini A, Crespi N. An Edge Operating System Enabling Anything-as-a-Service. 2016;(March):62–7.
- [98] Malensek M, Pallickara SL, Pallickara S. CONNECTING FOG AND CLOUD COMPUTING Hermes : Federating Fog and Cloud Domains to Support Query Evaluations in Continuous Sensing Environments.
- [99] Wen Z, Yang R, Garraghan P, Lin T, Xu J, Rovatsos M. Fog Orchestration for Internet of Things Services. *IEEE Internet Comput* [Internet]. 2017;21(2):16–24.
- [100] Tidbits C. Connecting Fog and Cloud Computing. 2017;(October 2016):2017.
- [101] Hung S, Hsu H, Lien S. Architecture Harmonization Between Cloud Radio Access Networks and Fog Networks. 2016;3019–34.
- [102] Chaudhry J, Farmand S., Islam S., Islam R., Hannay P., Valli C., Discovering Trends for the Development of Novel Authentication Applications for Dementia Patients, ATCI2017.
- [103] Hao Z, Novak E, Yi S, Li Q. Challenges and Software Architecture for Fog Computing. *IEEE Internet Comput* [Internet]. 2017;21(2):44–53.
- [104] Chaudhry J, Ibrahim A, Basheer A. Internet of Threats and Context Aware Security: Part Two, <http://sites.ieee.org/futuredirections/tech-policy-ethics/march-2017/internet-of-threats-and-context-aware-security-part-two/>, Access Last: 22 May 2017.
- [105] Busch C. Inter-Patient Analysis of Tomographic Data. *Comput Based Med Syst*. 1997;173–8.
- [106] Kramer DB, Tan YT, Sato C, Kesselheim AS (2013) Postmarket Surveillance of Medical Devices: A Comparison of Strategies in the US, EU, Japan, and China. *PLoS Med* 10(9): e1001519.
- [107] Duijnhoven RG, Straus SMJM, Raine JM, de Boer A, Hoes AW, De Bruin ML (2013) Number of Patients Studied Prior to Approval of New Medicines: A Database Analysis. *PLoS Med* 10(3): e1001407.
- [108] Bourgeois FT, Kim JM, Mandl KD (2014) Premarket Safety and Efficacy Studies for ADHD Medications in Children. *PLoS ONE* 9(7): e102249.
- [109] Belknap R, Weis S, Brookens A, Au-Yeung KY, Moon G, DiCarlo L, et al. (2013) Feasibility of an Ingestible Sensor-Based System for Monitoring Adherence to Tuberculosis Therapy. *PLoS ONE* 8(1): e53373.
- [110] McKinney R, Korn D (2005) Should an Institution That Has Commercial Rights in a New Drug or Device Be Allowed to Evaluate the Technology, *PLoS Med* 2(1): e9.
- [111] Forster AJ, Taljaard M, Bennett C, van Walraven C (2012) Reliability of the Peer-Review Process for Adverse Event Rating. *PLoS ONE* 7(7): e41239. <https://doi.org/10.1371/journal.pone.0041239>
- [112] Halperin D, Heydt-Benjamin TS, Ransford B, et al. Pacemakers and Implantable Cardiac Defibrillators: Software Radio Attacks and Zero-Power Defenses; Paper presented at: Security and Privacy, 2008. SP 2008. IEEE Symposium; Oakland, California, USA. May 18–22, 2008.
- [113] Chaudhry J.A., Qidwai U.A., Malrey L. (2012) Dynamic Health Level 7 Packetizer for On-the-Fly Integrated Healthcare Enterprises (IHE) in Disaster Zones. *ICONIP* 2012.
- [114] S. Gringeri et.al., “Extending software defined network principles to include optical transport,” in *IEEE Communications Magazine*, March 2013, vol. 51, no. 3, pp. 32–40.
- [115] Chaudhry J., and R. G. Rittenhouse, "Phishing: Classification and Countermeasures," 2015 7th International Conference on Multimedia, Computer Graphics and Broadcasting (MulGraB), Jeju, 2015, pp. 28–31.sd
- [116] The regulation of medical devices in Australia - PowerPoint PPT Presentation - Australian Government, Department of Health, Therapeutic Goods Administration <http://www.slideserve.com/khoi/the-regulation-of-medical-devices-in-australia>, Last Accessed: 30/06/2017.
- [117] Kazunari Asanuma, Essential Principles of Safety and Performance of Medical Devices Study Group 1 of the Global Harmonization Task Force November 2 2012.
- [118] J. D. Heydon, Cross on Evidence, Butterworths Law; 8th Revised edition edition (December 2009).
- [119] Good medical practice and the International Code of Medical Ethics, <http://www.medicalboard.gov.au/./Code-of-conduct.aspx>, Last Accessed 20180211.
- [120] Guidelines for technology-based patient consultations, <http://www.medicalboard.gov.au/./Technology-based-consultation-guidelines.aspx>, Last Accessed 20180211.
- [121] Health Practitioner Regulation National Law Act, <http://www.ahpra.gov.au/./Legislation.aspx>, Last Accessed 20180211.
- [122] Australian Privacy Act 1988, <http://www.austlii.edu.au/./pa1988108/>, Last Accessed 20180211.
- [123] Disclosure of health information in Australia, http://www.austlii.edu.au/./consol_act, Last Accessed 20180211.
- [124] Australian legal Institute, <http://www.austlii.edu.au/./s16b.html>, Last Accessed 20170602.
- [125] The Australian Commission on Safety and Quality in Health Care, <https://www.safetyandquality.gov.au/./safety-in-e-health/>, Last Accessed 20180211.
- [126] Australian National Safety and Quality of Health Services Standards, <https://www.safetyandquality.gov.au/./national-safety-and-quality-health-service-standards/>, Last Access 20180211.
- [127] The Australian Government entity, the Therapeutic Goods Administration, {<https://www.tga.gov.au>, Last Accessed 20180211.
- [128] Therapeutic Goods Administration on medical devices, <https://www.tga.gov.au/medical-devices-ivds>, Last Accessed 20180211.
- [129] European Union's data protection directive (95/46/EC), <http://eur-lex.europa.eu/legal-content/>, Last Accessed 20180211.
- [130] European Union Data Protection Initiative Legalisation, http://ec.europa.eu/./index_en.htm, Last Accessed 20180211.
- [131] European Commission - Press release; Agreement on Commission's EU data protection reform will boost Digital Single Market http://europa.eu/rapid-press-release_IP-15-6321_en.htm, Last Accessed 20180211.
- [132] Washer v The State of Western Australia [2007] HCA 48, <http://eresources.hcourt.gov.au/showCase/2007/HCA/48>, Last Accessed 20180211

Game-Theory Based Cognitive Radio Policies for Jamming and Anti-Jamming in the IoT

Zenon Chaczko¹, Shaher Slehat² and Tamer Shnoudi³

^{1,2,3}School of Electronic and Data Engineering, Faculty of Engineering & IT,

University of Technology, Sydney – 2007, NSW, Australia

Emails: Zenon.Chaczko@uts.edu.au, Shaher.Slehat@uts.edu.au, Tamer.F.Shnoudi@student.uts.edu.au

Abstract—The Cognitive Radio can be considered as a mandatory part of the Internet of Things applications. It helps to solve the sacristy issues in the frequency bands of the wireless network component of the technology. However, the security problem is the primary challenge that needs to be carefully mitigated. Specifically, defending the Cognitive Radio mechanism against the jamming attacks. The aim this research paper is to investigate and provide a reliable and adaptive Cognitive Radio protection methods against the jamming attacks. Thus, improving the performance of the wireless network of IoT technology, enhancing the bandwidth and solving the issue of the sacristy of the frequency bands. The mentioned objectives will be accomplished by the aid of the game theory which is modelled as an anti-jamming game and by adapting the multi-arm bandit (MAB) policies. However, to solve the sacristy issue in the frequency band spectrum of the cognitive radio, some MAB policies were adapted such as Upper Confidence Bound (UCB), Thompson Sampling and Kullback-Leibler Upper Confidence Bound (KL-UCB). The results show some improvements and enhancements to the sacristy problem in the frequency band spectrum. To conclude, the Thompson Sampling MAB policy was the best to be adapted for solving the problem, as it resulted with lowest regrets and highest rewards compared to the other MAB policies.

Keywords— *IOT; Cognitive Radio; Jamming Attacks; Multiarmed Bandit*

I. INTRODUCTION

The Internet of Things (IoT) presents a new technology that is used to connect various heterogeneous devices (Things, nodes or smart objects). All these devices when deployed are interconnected, monitored and controlled in often dynamic and predominately wireless environment using smart radio installed on each node. According to some researchers and forecasts, by the year 2020, there will be more than 50 billion devices and items connected and communicating with each other (Rawat, Singh & Bonnin 2016). The idea behind the IoT has attracted the attention of researchers and people around the world. Many predict that everything would be connected to the Internet, which as a result can make human lives much easier. Also, the adoption of the Machine-to-Machine (M2M) technology that can connect various devices and objects has a great potential in helping to broaden the concept of IoT (Staff 2017).

There are a range of models, concepts, hardware, computational solutions and protocols that are being used to develop and make the IoT technology more secure, efficient and reliable. Thus,

many challenges can appear during the design and development of IoT technology, due to the introduction of new network architecture models and constraints imposed by limited radio resources (frequency spectrum sharing) available. These various challenges the IoT technology is facing need to be addressed and solved. The primary challenge is the sacristy in the frequency band spectrum, as the frequency bands can be used by different applications and protocols concurrently. Most, if not all, and technologies are somehow destine to follow the Cognitive Radio cycle which senses the environment parameters and performs decisions according to the collected data (Wang et al. 2015). The main objective of Cognitive Radio (CR) concept originally developed by Mitola & Maguire (1999) is to help in solving the sacristy problems of the frequency band spectrum, by choosing the best channel among many available. Another aim of the CR is to help in allowing the secondary users of the unlicensed bands to access the unused frequency of the licensed band spectrum. This will assist in solving the sacristy issues and provide a seamless Cognitive Radio. Furthermore, the Cognitive Radio enhance the spectrum efficiency by avoiding the collisions and system wastage. According to (Rawat, Singh & Bonnin 2016), the cognitive radios developed over the years, and are distributed into three major parts which are the Software Defined Radio (SDR), Cognitive Radio and Cognitive Networks. However, the Cognitive Radio can decide by gathering the data about the frequencies environment, and by previous experience. The Cognitive Radio collects the information by sensing the neighbours and adapt the collected information of the parameters to sense the network. The Cognitive Radio includes two types of users, which are the primary and secondary users. The primary users access the licenced frequency band, while the secondary users of the unlicensed band try to access the unused frequency band of the primary users by the aid of the cognitive radio. On the other hand, when the primary user becomes active, the Cognitive Radio feels this change and try to find another available frequency band. This type of radio is considered as an intelligent system that can adapt itself and provides a reliable connection to the user.

Performing in-depth research on the design and the architecture of the Cognitive Radio helped in enhancing and developing the cognitive radio. Akyildiz et al. (2008); Fragkiadakis, Tragos & Askoxylakis (2013); Wang, Wu & Liu (2010) presented the recent developments and the architecture

design of the cognitive radios. Akyildiz et al. (2008); Wang, Wu & Liu (2010) focused on the issues of the spectrum management and how to enhance these problems. While (Fragkiadakis, Tragos & Askoxylakis 2013) focused on security threats and the challenges that may alter the cognitive radios.

The jamming and anti-jamming types in the wireless networks were presented by Çakiroğlu & Özcerit (2008); Grover, Lim & Yang (2014); Lazos & Krunz (2011); Wang & Wyglinski (2011), and discussed in detail the detection and the countermeasures. The ability for defending against the jamming attacks need to be reviewed more and more. However, Bahl, Chandra & Dunagan (2004); Sampath et al. (2008) presented the impact of the cognitive radios based on the jamming attacks. The research is based on the multi-channel hopping in the wireless networks and what will be the impact after performing the channel hopping.

Improving the performance of the cognitive radios in the wireless networks depends on many factors. One of these factors is to provide secure Cognitive Radio against the attackers. However, many attacks can degrade the performance of the cognitive radios. Specifically, this research focuses on the jamming attacks, which occurs in the physical layer. Theoretically, many researchers proposed different approaches for enhancing the security of the cognitive radios against the jamming attacks. Thus, improving the throughput and reducing the delay. These approaches are based on the anti-jamming games theory, which will be discussed in this section.

The Jamming attacks have enticed (Chen et al. 2013) to help in finding a solution for securing the cognitive radios. The authors proposed jamming strategy that is based on the Markov decision process. The mentioned strategy helps in bypassing the jamming attacks that is initiated by the foreign attackers and thus magnifying the payoff function. First, the author uses a policy iteration technique to find the solution for the problem. However, the complexity of this technique obstructed the work of the authors. Thus, they used the Q-function as an alternative solution to avoid the complexity of the policy iteration technique. Also, they presented an algorithm that assists in finding a solution for the Q-function. The result of this approach proved that the mentioned technique helped in producing better results than the existing approaches.

Securing the cognitive radios against the jamming attacks is considered as the main aim for (Dabcevic et al. 2014; Li & Han 2009; Niyato, Hossain & Han 2009; Wu et al. 2012). The authors of the research papers proposed a defence strategy against the jamming attacks with the aid of the Markov decision process. At first, Niyato, Hossain & Han (2009); Wu et al. (2012) studied the set of circumstances where the secondary users can access one channel at a time and investigated the relationship between the attackers and the secondary users. Also, they expand the scheme where the SU's can use all the available channels at the same time and reformulate the anti-jamming game with unplanned and irregular power allocation

as the defensive approach. Finally, they used the Nash equilibrium to help in reducing the worst-case worsening. While (Li & Han 2009), they presented a dogfight technique in the one-stage study and the multi-stage study. For the one-stage study, it is represented as a zero-sum game, and the approach of the Nash equilibrium is achieved. While the multi-stage study, it is represented as a stochastic game with limited considerations and fault monitoring. The game is examined by adjusting the strategy of the SU and finding the preferable approach of the attacker with the aid of partially observable Markov decision process (POMDP). On the other hand, Dabcevic et al. (2014) reinforce the preliminary concepts and sub-edit a game which takes into consideration both the channel hopping and the power allocation, as a security technique against the external attackers. However, Dabcevic et al. (2014); Li & Han (2009) subedited the game as a zero-sum game.

Wang, Ghosh & Challapali (2011); Zhu & Cao (2010) proposed a Stochastic game model that is based on the Markov process. This model helps in reviewing and monitoring the strategies of the external attackers and the SU's in the jamming and the anti-jamming scheme. Besides, Zhu & Cao (2010) used three agents in their model (SU's, Primary User and jammers). The result of the research paper shows that the SU's can improve the defence level against the external attacks or increase their long-term payoffs, this can be done by enhancing their sensing performance and mystifying the jammer. While (Wang, Ghosh & Challapali 2011) proposed a technique that can adopt the dynamic spectrum allocation and channel quality.

The main aim of this research paper is to provide a secure and flexible Cognitive Radio by protecting it against the jamming attack. Thus, improving the performance of the wireless network technology, enhancing the bandwidth and solving the issue of the scarcity of the frequency bands. The mentioned objectives will be accomplished by the aid of the game theory which is modelled as an anti-jamming game, and by adapting the MAB policies. However, the main question to be answered in is how to provide a seamless wireless network application, and to solve scarcity issue in the frequency band spectrum of the cognitive radio. With the aid of state of the art, different essential points have been discovered. These helped in focusing on the main issue of the cognitive radio, and try to fill the gap by solving the scarcity problem of frequency band spectrum. However, in section 2 the policies used for solving the scarcity problem will be discussed, which include the UCB, Thompson Sampling and KLUCB. The results and discussion of the research are presented in section 3. Finally, the conclusion is proposed in section 4 to summarize all the outcomes and objectives of the project

In this section, the three primary MAB policies will be identified and described in detail. A pseudo-code that defines each policy will be presented as well. MAB policies are considered as a solution for the spectrum sensing and accessing problem, which is represented as exploration and exploitation dilemma. The mentioned problem is defined as gambler have a

different number of slot machines, and is trying to decide which slot machine to play with, how many times to play on that machine, and the order of play on the machines.

Number of slot machines or arms = Number of armed bandits

The MAB means that the use of several arms is required. Draw the result of one arm, and then scrutinise and monitor a sample from a distribution v_a , with mean ρ_a . To find the best arm from different number of arms K , refer to formula 1 and 2 below.

$$a^* = \operatorname{argmax}_a \rho_a \quad (1)$$

$$\rho^* = \max_a \rho_a \quad (2)$$

The main idea behind the Regret is that, if the gambler knew earlier what will be the best arm, then the gambler will only play with same arm all the time to increase the chances of winning and maximizing the rewards. On the other hand, the unavailability of the required information will affect the gambler by unavoidable loss due to suboptimal pulls. Equation 3 shows the how the regret is calculated.

A. Upper Confidence Bound (UCB)

In the beginning, the random bandit problem where identified by Robbins (1985). The bandit problem is a trade-off between exploration and exploitation, where there are a different number of trials out of different options. For the selected option, the rewards are assembled. While for the other options, the rewards are not unveiled. The main aim of the algorithm is to maximise the total rewards and decrease the regrets.

A new approach was proposed by (Auer, Cesa-Bianchi & Fischer 2002), which includes an uncomplicated solution for

$$R_T = T\rho^* - \mathbb{E}[\sum_{t=1}^T X_t] \quad (3)$$

the Multi-Arm Bandit problem. It involves performing arithmetic calculations of the Upper Confidence Bound indexes, which acquired much awareness from the researchers of machine learning. However, the type of algorithms that relies on the UCB has been shown to perform flawlessly on the complicated problems. The UCB algorithm pseudo-code is presented in Algorithm 1 below.

Algorithm 1 (UCB) pseudo-code (Gwon, Dastangoo & Kung 2013)

```

while  $t < I$ 
    Same as that of Algorithm 1
end
while  $t \geq I$ 
    Compute point estimate  $= \mu_i = R_i^t / T_i^t \forall i$ 
    Compute index  $g_i = \mu_i + \sqrt{\alpha \log \frac{t}{T_i^t}} \forall i$ 
    Access channel  $i^* = \operatorname{argmax}_i g_i$ 
    Update  $R_{i^*}^t$  and  $T_{i^*}^t$ 
end

```

B. Thompson Sampling

The Thompson Sampling which was first proposed by Thompson (1933), and it is used to solve the multiarmed bandit problem. However, many researchers ignored it, and especially the artificial intelligence community. Recently, the Thompson Sampling has been widely utilized in different online problems. Also, it is used in solving the jamming problem in the cognitive radios. The Algorithm assumes that for each arm reward is generated from some variable distribution v_i (Korda, Kaufmann & Munos 2013).

Then, the overall structure of the algorithm is as follows:

- For every arm, start with a prior belief on variables of the distribution.
- On making observations from an arm, update to posterior belief.
- At time t , play every arm with its posterior probability of being the most desired arm.

Algorithm 2 (Thompson Sampling) pseudo-code (Gwon, Dastangoo & Kung 2013)

```

Require:  $d = \{x, a, r\}$  for context  $x$ , action  $a$ , reward  $r$ ,
estimator  $p(\theta|d) \propto p(r|x, a, \theta)p(\theta)$  parameterized by  $\theta$ 
while  $t \geq 1$ 
    Acquire  $x^t$ 
    Draw  $\theta^t \sim p(\theta)$ 
    Choose  $a^t$  to access  $i^* =$ 
 $\operatorname{argmax}_i \mathbb{E}[r_i^t | x^t, \theta^t]$ 
    Observe actual  $r^t$ 
    Update  $d = d \cup \{x^t, a^t, r^t\}$ 
    Update  $p(\theta) = p(\theta|d)$ 
end

```

Algorithm 3 (KLUCB) pseudo-code (Gwon, Dastangoo & Kung 2013)

```

While  $t < I$ 
    Access each channel at least once
    Record  $R_i^t = \sum_{j=1}^t r_i^j$  and  $T_i^t$  for every channel  $i$ 
End

While  $t \geq I$ 
    Compute  $\mu_i = \frac{R_i^t}{T_i^t} \forall i$ 
    Find MPE Candidate  $C_{MPE} = i^* \text{ s.t. } \mu_{i^*} = \max \mu_i$ 
    Find RR Candidate  $C_{RR} = (t \bmod N) + 1$ 

    If  $D_{KL}(p_{PR} || p_{MPE}) > \log(t-1)/T_{C_{RR}}^t$ 
        Access  $C_{MPE}$  and observe  $r_{C_{MPE}}^t$ 
        Update  $R_{C_{MPE}}^t$  and observe  $T_{C_{MPE}}^t$ 
    Else
        Access  $C_{RR}$  and observe  $r_{C_{RR}}^t$ 
        Update  $R_C^t$ 
    End
End

```

C. Kullback-Leibler Upper Confidence Bound (KLUCB)

The KLUCB is based on the idea of gambling. By using a different number of gamblers for a specific time to play on various arms. After that, check choose the gambler with the optimal Maximum point estimate (MPE) (Lai & Robbins 1985).

II. RESULTS AND DISCUSSION

Different analysis and scenarios were performed to find the ideal technique of solving the sacristry issue of the frequency band spectrum in a wireless network application. These techniques were based on the anti-jamming game theory and the adaption of the multiarmed bandit policies to solve the sacristry problem. However, three scenarios were applied to the three primary policies of the MAB to enhance them, and find the best policy to be used. Specifically, to obtain the best result, the total rewards should be maximised, and the number of regrets should be minimised. This will help in finding the best arm to be used and solve the sacristry problem of the frequency band spectrum. The mentioned scenarios will be discussed in this section by showing some results and comparing the MAB policies. All the results in this section were simulated by MATLAB software.

A. Scenario #1

The first scenario is based on the Bernoulli Bandits which helps in finding the best arm to be used. Some random results were captured from a simulation of the first scenario. Figure (1) shows the results of the MAB policies after applying the first scenario.

As provided in figure 1, the three policies were enhanced after applying the changes on them. The noise decreased, and the number of regrets is low. However, the main issue is the significant difference between the lines.

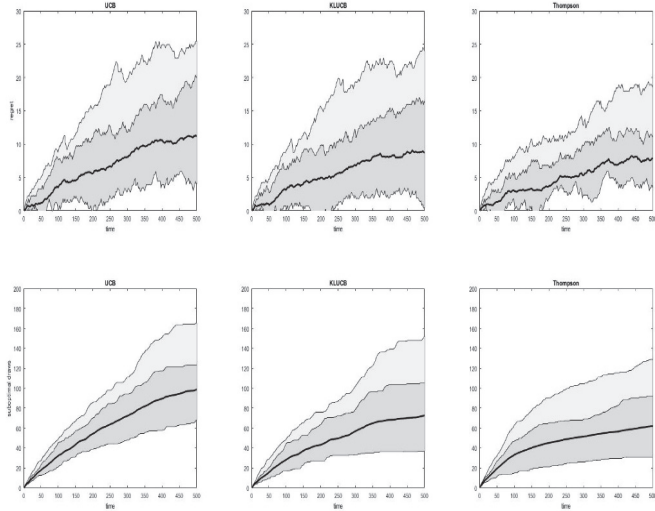


Figure 1: Results of MAB policies in Scenario #1

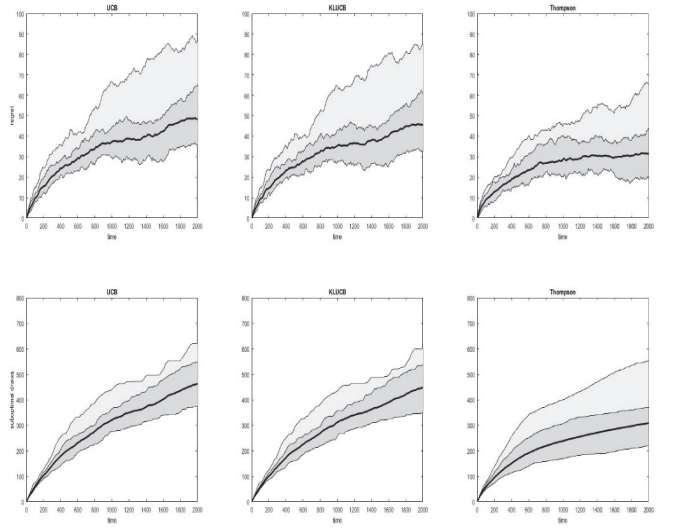


Figure 2: Results of MAB policies in Scenario #2

To obtain better results, the lines supposed to be near to each other, and in a straight line. However, by comparing the three policies in the first scenario, the best policy to be followed is the Thompson sampling. It is the only policy that shows approximate a straight line compared to the other policies.

B. Scenario #2

The second scenario is based on the Bounded Exponential Rewards which helps in increasing the number of rewards and decrease the number of regrets. Some random results were captured from a simulation of the second scenario. Figure 2 shows the results of the MAB policies after applying the second scenario. By following the second scenario changes, the noise was decrease compared to the first scenario. Also, the lines become much nearer to each other, and the straight lines are now much clearer than the first scenario. However, the Thompson sampling in the second scenario is the best policy to be used, as it resulted in the lowest number of regrets.

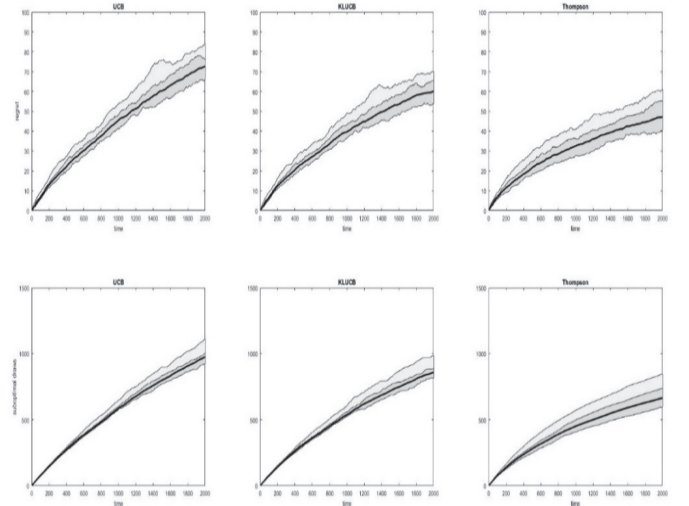


Figure 3: Results of MAB policies in Scenario #3

C. Scenario #3

The third scenario is based on the Bounded Poisson Rewards which plays a mandatory part in increasing the number of rewards and minimise the number of regrets. Some random results were captured from a simulation of the third scenario. Figure 3 shows the results of the MAB policies after applying the third scenario.

By following the third scenario changes, the noise decreased much more compared to the first and second scenario. Also, the lines became more attached to each other, and are nearly looking like a straight line. The number of regrets in the Thompson Sampling is lower than the other two policies and concludes that it is the best policy that can be adapted.

This analysis helped in planning about which policy to be adapted after providing different scenarios and applying changes to these three scenarios. The comparison between the three policies resulted in choosing the Thompson Sampling as the best policy to be adopted. This decision is made after finding that the Thompson Sampling will provide with the lowest number of regrets and the highest number of rewards. Also, the analysis shows that the Thompson Sampling will have the lowest noise compared to other two policies. To conclude, the Thompson Sampling is chosen as the best policy to adopt. Thus, it will help in finding the best frequency band spectrum to provide a secure Cognitive Radio by protecting it against the jamming attack and solve the sacristy issue in the frequency band spectrum. Also, it improves the performance of the wireless network technology and enhances the bandwidth of the network.

III. CONCLUSION

The recent developments of the IoT demonstrate that the technology is increasingly becoming a part of our lives. Every item and device around us will be connected to the internet, and these will be controlled by small sensors and actuators forming a network of interconnected smart devices (objects). A serious challenge arises after deploying this technology, which is the sacristy in the frequency band spectrum. The use of the Cognitive Radio technology is considered a suitable solution for this problem as it allows the secondary users to have access the unused frequency bands spectrum of the primary users. At the same time, the Cognitive Radios can be affected by the jamming attacks, which in turn can be defended or mitigated by adapting the MAB policies based on the anti-jamming game theory. It is suggested that the study of the adaptation of the MAB policies can help to solve the sacristy issues of the frequency band spectrum, as well as, enhance the performance, and reduce the bandwidth limitations of the shared wireless environment.

REFERENCES

- [1] Akyildiz, I.F., Lee, W.-Y., Vuran, M.C. & Mohanty, S. 2008, 'A Survey on Spectrum Management in Cognitive Radio Networks', *IEEE Communications magazine*, vol. 46, no. 4.
- [2] Auer, P., Cesa-Bianchi, N. & Fischer, P. 2002, 'Finite-Time Analysis of The Multiarmed Bandit Problem', *Machine learning*, vol. 47, no. 2-3, pp. 235-56.
- [3] Bahl, P., Chandra, R. & Dunagan, J. 2004, 'SSCH: Slotted Seeded Channel Hopping For Capacity Improvement in Ieee 802.11 Ad-Hoc Wireless Networks', *Proceedings of the 10th annual international conference on Mobile computing and networking*, ACM, pp. 216-30.
- [4] Çakiroğlu, M. & Özcerit, A.T. 2008, 'Jamming Detection Mechanisms for Wireless Sensor Networks', *Proceedings of the 3rd international conference on Scalable information systems*, ICST (Institute for Computer Sciences, Social-Informatics and Telecommunications Engineering), p. 4.
- [5] Chen, C., Song, M., Xin, C. & Backens, J. 2013, 'A Game-Theoretical Anti-Jamming Scheme for Cognitive Radio Networks', *IEEE Network*, vol. 27, no. 3, pp. 22-7.
- [6] Dabcevic, K., Betancourt, A., Marcenaro, L. & Regazzoni, C.S. 2014, 'Intelligent Cognitive Radio Jamming-A Game-Theoretical Approach', *EURASIP Journal on Advances in Signal Processing*, vol. 2014, no. 1, p. 171.
- [7] Fragkiadakis, A.G., Tragou, E.Z. & Askoxylakis, I.G. 2013, 'A Survey on Security Threats and Detection Techniques In Cognitive Radio Networks', *IEEE Communications Surveys & Tutorials*, vol. 15, no. 1, pp. 428-45.
- [8] Grover, K., Lim, A. & Yang, Q. 2014, 'Jamming And Anti-Jamming Techniques In Wireless Networks: A Survey', *International Journal of Ad Hoc and Ubiquitous Computing*, vol. 17, no. 4, pp. 197-215.
- [9] Gwon, Y., Dastangoo, S. & Kung, H. 2013, 'Optimizing Media Access Strategy for Competing Cognitive Radio Networks', *Global Communications Conference (GLOBECOM), 2013 IEEE*, IEEE, pp. 1215-20.
- [10] Korda, N., Kaufmann, E. & Munos, R. 2013, 'Thompson Sampling for 1-Dimensional Exponential Family Bandits', *Advances in Neural Information Processing Systems*, pp. 1448-56.
- [11] Lai, T.L. & Robbins, H. 1985, 'Asymptotically Efficient Adaptive Allocation Rules', *Advances in applied mathematics*, vol. 6, no. 1, pp. 4-22.
- [12] Lazos, L. & Krusz, M. 2011, 'Selective Jamming/Dropping Insider Attacks in Wireless Mesh Networks', *IEEE network*, vol. 25, no. 1.
- [13] Li, H. & Han, Z. 2009, 'Dogfight In Spectrum: Jamming and Anti-Jamming in Multichannel Cognitive Radio Systems', *Global Telecommunications Conference, 2009. GLOBECOM 2009. IEEE*, IEEE, pp. 1-6.
- [14] Mitola, J. & Maguire, G.Q. 1999, 'Cognitive Radio: Making Software Radios More Personal', *IEEE personal communications*, vol. 6, no. 4, pp. 13-8.
- [15] Niyato, D., Hossain, E. & Han, Z. 2009, 'Dynamics of Multiple-Seller And Multiple-Buyer Spectrum Trading in Cognitive Radio Networks: A Game-Theoretic Modeling Approach', *IEEE Transactions on Mobile Computing*, vol. 8, no. 8, pp. 1009-22.
- [16] Rawat, P., Singh, K.D. & Bonnin, J.M. 2016, 'Cognitive radio for M2M and Internet of Things: A survey', *Computer Communications*, vol. 94, pp. 1-29.
- [17] Robbins, H. 1985, 'Some Aspects of The Sequential Design of Experiments', *Herbert Robbins Selected Papers*, Springer, pp. 169-77.
- [18] Sampath, A., Yang, L., Cao, L., Zheng, H. & Zhao, B.Y. 2008, 'High Throughput Spectrum-Aware Routing For Cognitive Radio Networks', *Proc. of IEEE Crowncom*.
- [19] Staff, C. 2017, 'The internet of things', *Communications of the ACM*, vol. 60, no. 5, pp. 18-9.
- [20] Thompson, W.R. 1933, 'On The Likelihood That One Unknown Probability Exceeds Another in View of The Evidence of Two Samples', *Biometrika*, vol. 25, no. 3/4, pp. 285-94.
- [21] Wang, B., Wu, Y. & Liu, K.R. 2010, 'Game Theory for Cognitive Radio Networks: An Overview', *Computer networks*, vol. 54, no. 14, pp. 2537-61.
- [22] Wang, J., Feng, S., Wu, Q., Zheng, X. & Xu, Y. 2015, 'Hierarchical cognition cycle for Cognitive Radio networks', *China Commun.*, vol. 12, no. 1, pp. 108-21.

- [23] Wang, J., Ghosh, M. & Challapali, K. 2011, 'Emerging Cognitive Radio applications: A survey', *IEEE Communications Magazine*, vol. 49, no. 3.
- [24] Wang, L. & Wyglinski, A.M. 2011, 'A Combined Approach for Distinguishing Different Types of Jamming Attacks Against Wireless Networks', *Communications, Computers and Signal Processing (PacRim)*, 2011 IEEE Pacific Rim Conference on, IEEE, pp. 809-14.
- [25] Wu, Y., Wang, B., Liu, K.R. & Clancy, T.C. 2012, 'Anti-Jamming Games in Multi-Channel Cognitive Radio Networks', *IEEE Journal on Selected Areas in Communications*, vol. 30, no. 1, pp. 4-15.
- [26] Zhu, Q. & Cao, J. 2010, 'Stability analysis for stochastic neural networks of neutral type with both Markovian jump parameters and mixed time delays', *Neurocomputing*, vol. 73, no. 13, pp. 2671-80.

Detection Scheme of Selfish Node in WBAN Utilizing CSMA/CA based on IEEE 802.15.6

Yuto Omuro

*Department of Information and Communication Engineering,
Faculty of Computer Science and Systems Engineering,
Okayama Prefectural University
111 Kuboki, Soja-shi, Okayama, 719-1197 Japan
email:cd29009a@c.oka-pu.ac.jp*

Kento Takabayashi

*Department of Information and Communication Engineering,
Faculty of Computer Science and Systems Engineering,
Okayama Prefectural University
111 Kuboki, Soja-shi, Okayama, 719-1197 Japan
email:kent.hf@c.oka-pu.ac.jp*

Katsumi Sakakibara

*Department of Information and Communication Engineering,
Faculty of Computer Science and Systems Engineering,
Okayama Prefectural University
111 Kuboki, Soja-shi, Okayama, 719-1197 Japan
email:sakaki@c.oka-pu.ac.jp*

Abstract—This paper proposes a detection scheme of a selfish node in a wireless body area network (WBAN) utilizing CSMA/CA (Carrier Sense Multiple Access / Collision Avoidance) defined in IEEE 802.15.6. In the Internet of Things (IoT) era, the existence of a selfish node giving disadvantage to the network by acting selfishly is a problem. Especially, its influence is large in a WBAN dealing with medical and healthcare information. Hence, we proposed a detection method of such a node. Specifically, we focused on an illegal act of arbitrarily changing parameters of CSMA/CA in IEEE 802.15.6. In the proposed method, the illegal act was detected using measured values of back-off time. As a result of computer simulations, it was found that the detection effect can be enhanced by selecting the ratio of measured values according to the assumed illegal act and environment.

Index Terms—WBAN, IEEE802.15.6, CSMA/CA, Selfish node, Detection scheme

I. INTRODUCTION

Recently, various wireless devices have been developed with the development of wireless communication technology. Wireless body area network (WBAN) is one of them. A WBAN is constructed by a plurality of nodes arranged inside and outside the body and a hub for collecting data acquired from them. With the characteristic, it is expected to be widely used in medical and healthcare applications [1]–[12].

In Feb. 2012, IEEE 802.15.6 which is one of the standards of WBAN was issued [11]. In IEEE 802.15.6, CSMA/CA (Carrier Sense Multiple Access / Collision Avoidance) and Slotted Aloha can be used as a random access protocol in the media access control layer (MAC). In this study, we focused on the CSMA/CA protocol. This method is also used in common systems such as a wireless local area network (WLAN).

Identify applicable funding agency here. If none, delete this.

In the WLAN environment, the existence of a selfish node is a big problem. A selfish node attempts to increase transmission opportunities by changing various parameters on its own. An example of parameter change by a selfish node is to change the value of CW (Contention Window) used for back off control in CSMA / CA. Since CSMA/CA is also used in a WBAN, such a selfish node is likely to occur even in a WBAN. Hence, it is necessary to detect it in order for the WBAN to work properly.

In this research, we proposed a scheme of detecting a selfish node changing the value of CW on its own in WBAN using CSMA/CA based on IEEE 802.15.6. As a computer simulation, our proposed scheme had a good detection performance by adjusting the distribution of the measurement value with respect to the back-off time.

II. RELATED DESCRIPTION AND CONVENTIONAL SCHEME

A. CSMA/CA in IEEE 802.15.6

In order to prevent collision of data frames, CSMA / CA waits for time slots randomly determined from a predetermined CW (hereinafter referred to as back-off time), and then attempts transmission. Unlike IEEE 802.11 based CSMA/CA, that in IEEE 802.15.6 has only SIFS (Short Inter Frame Space) as IFS. In addition, eight levels of user priority (UP) from 0 to 7 can be set for handling data in IEEE 802.15.6. In the case of using CSMA/CA, CW_{min} is smaller as higher UP data to transmit with priority [11]. Here, CW_{min} is the initial value of CW.

B. Conventional detection scheme of selfish node

Many researches have been made on detection schemes of selfish nodes in WLAN using CSMA/CA. As a main research,

there is a method of measuring the back-off time for a certain period of time, and then using a threshold value for the collected measured value to judge whether it is a selfish node or not. For example, DOMINO [13], CTL [14], a scheme using the retry bit [15] and so on are mentioned.

III. SYSTEM MODEL AND PROPOSED METHOD

In this research, we assumed that one hub and multiple nodes handle data with a certain priority. It was assumed that a node always held a data frame. A hub measures the back-off time for each node for a certain period. If the average of the measured value falls below a preset threshold value, it is determined that the node is a selfish node. In addition, the threshold is set so as to achieve a desired false detection rate based on the known measurement value distribution assumed for the normal node and the central limit theorem [14].

In the measurement of the back-off time, a hub measures the back-off time subtracted between successful transmission frames for each node. The measurement values used for detection in the proposed method are classified into the following two types.

- 1) Measurement value in the case of not receiving a retransmission frame
- 2) Measurement value in case of that the number of collisions is 2 or less when receiving the retransmission frame

Using these two measured values, it is judged whether it is a selfish node. When it is determined that either one is a selfish node, it is determined that the node is a selfish one.

In the case of 1., the assumed distribution of the measurement value is a uniform distribution of $[1, CW_{min}]$ CSMA/CA in IEEE 802.15.6 doubles the value of CW when an even number of collisions of data frames occurs. Hence, the assumed distribution of the measured value of the back-off time when one collision occurs is $[1, CW_{min}] + [1, CW_{min}]$. Then, when collision occurs twice, it is $[1, CW_{min}] + [1, 2CW_{min}]$. These distributions are added at a fixed ratio to obtain the distribution of measurement value of a normal node.

The threshold used for selfish node detection is given by the following equation:

$$threshold = m - \frac{K\sigma}{\sqrt{n}}. \quad (1)$$

Here, m is the expected value assumed from the distribution of measurement value of a normal node. σ is a standard deviation assumed from the distribution of the normal node, K is a constant based on a desired false detection rate, n is the number of measurement values obtained within the measurement period. K is determined using a standard normal distribution table so as to obtain a desired false alarm rate.

Regarding the desired false alarm rate, there are two ranges to use as measured values in the proposed method. That is, after setting the desired false alarm rate, the false detection rate used in each range of measurement value is determined based on the desired one. Here, it is assumed that the desired

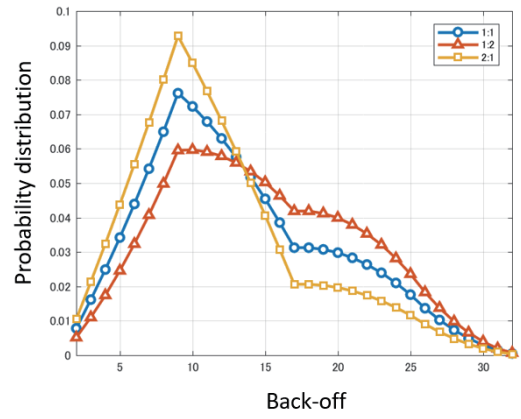


Fig. 1. Range and distribution of measurement values at retransmission in the case of UP2.

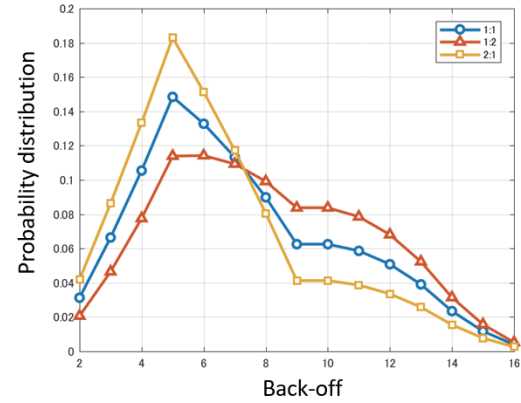


Fig. 2. Fig. 2. Range and distribution of measurement values at retransmission in the case of UP5.

false alarm rate is P_{FA} , and the false detection rates utilizing in each range of measurement value are P_0 and P_1 . Each relationship is expressed by the following equation:

$$P_0 = P_1 = 1 - \sqrt{1 - P_{FA}}. \quad (2)$$

IV. PERFORMANCE EVALUATION

A. Computer simulation parameters

In this computer simulation, we evaluated the proposed scheme assuming one selfish node. Also, it was assumed that there was only one UP. Specifically, the case of UP 2 and UP 5 was assumed. In addition, measurements were made on the case where the measured value distributions of the back-off time of one and two collisions were added at a ratio of 1: 1, 1: 2 and 2: 1. Fig. 1 and Fig. 2 show the measurement value distribution of the normal node when the number of collisions is 2 or less.

The illegal acts assumed this time are as follows:

- Case 1 Halve CW_{min} at collision.
- Case 2 Do not increase CW at even collision.
- Case 3 Halve CW_{min} at even collision.

TABLE I
CHANGES IN CW VALUES IN EACH ILLEGAL ACT

illegal act	UP	CW_{min}	2nd collision	4th collision
Normal nodes	2	8	16	$32 = CW_{max}$
To halve the value of CW_{min}	5	4	$8 = CW_{max}$	8
To halve the value of CW_{min}	2	4	8	16
Do not increase CW value	5	2	4	8
Do not increase CW value	2	8	8	8
Reduce CW_{min} value by half	5	4	4	4
Reduce CW_{min} value by half	2	8	4	2
Reduce CW_{min} value by half	5	4	2	1

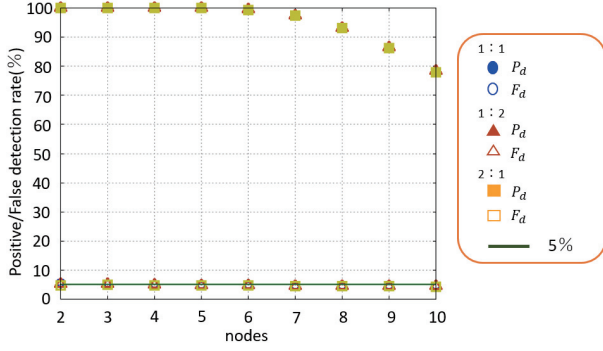


Fig. 3. Simulation result for case 1 (UP2)

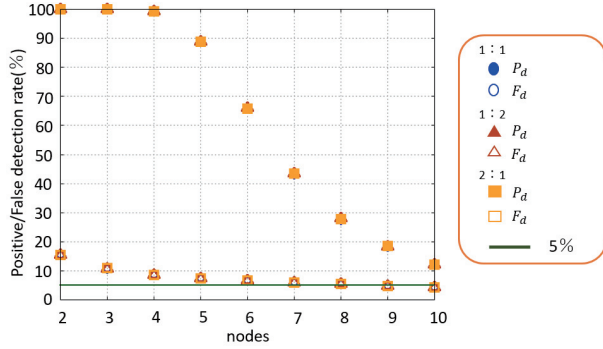


Fig. 4. Simulation result for case 1 (UP5)

Changes in CW values in each illegal act are shown in Table I. The rate at which a selfish node is detected correctly (Positive detection rate, P_d) and the rate at which a normal node is erroneously detected (False alarm rate, F_d) were used as an evaluation index.

B. Numerical result

1) *Case 1*: Fig. 3 and Fig. 4 show simulation results for illegal act in the case of halving the value of CW_{min} .

From Fig. 3, it can be seen that in the case of UP 2, substantially the same result was obtained in any ratio of usage measurement values. Since the P_d of 90% or more was obtained when the number of nodes was 8 or less, it can be seen that the proposed method detected a illegal act in the case of UP2. Also, with regard to the F_d , since the desired value and the measured values in all cases are almost the same, it can be considered that the assumed measurement value distribution

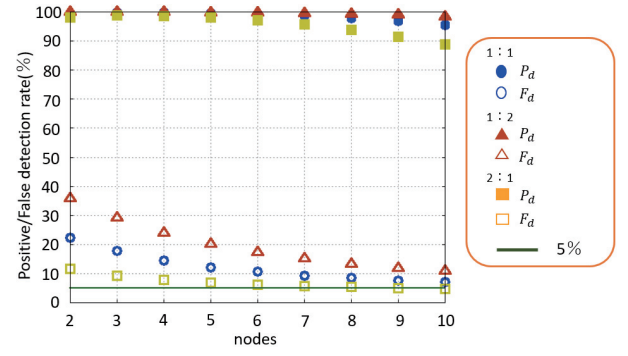


Fig. 5. Simulation results for case 2 (UP2)

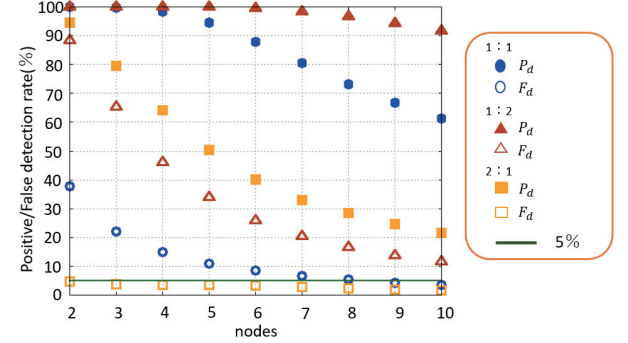


Fig. 6. Simulation results for case 2 (UP5)

of the normal node was correct. The reason why there was not much difference in F_d at all ratios is because it was possible to judge whether it was illegal or not based on the measured value at the time of receiving the non-retransmission frame.

As can be seen from Fig. 4, almost the same result was obtained in UP 5 irrespective of the ratio of the measured value at the time of receiving the retransmission frame. However, in case of UP 5, unlike UP 2, the P_d of 90% can only be achieved when the number of nodes is 4 or less. In addition, it can be seen that the F_d was larger than 5% while the number of nodes is small. For these reasons, in the case of UP 5, the backoff time that each node can take is smaller than that of the case of UP 2. It is considered that the back-off time of the normal node become almost the same as that of the selfish node.

2) *Case 2*: Fig. 5 and Fig. 6 show the simulation results in the case that CW was not doubled at the even number of collisions.

From Fig. 5, the highest P_d was obtained when the measured value ratio was 1:2. On the other hand, the F_d became the lowest when the ratio was 2:1. The reason is that since CW does not change in this case, it is not possible to judge a selfish node by the measured value at the time of receiving a non-retransmission frame. In addition, even in the measurement value at the time of receiving the retransmission frame, only when the collision occurs twice and the CW increases, it can be judged whether it is illegal or not.

From Fig. 6, in case of UP 5, the case that the ratio was 1:2 had the highest P_d and F_d , whereas that of the ratio of

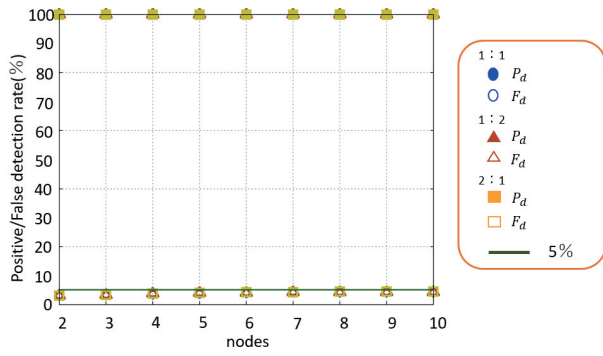


Fig. 7. Simulation results for case 3 (UP2)

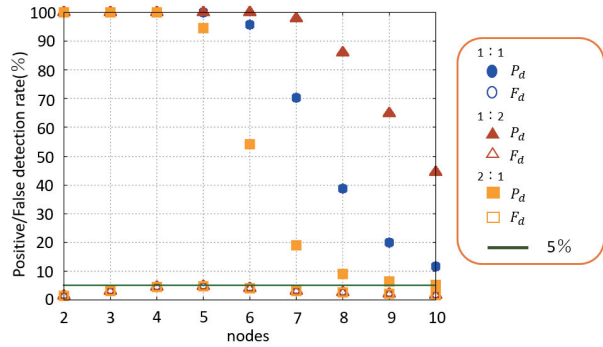


Fig. 8. Simulation results for case 3 (UP5)

2: 1 had the lowest P_d and F_d . This is because, CW_{min} and CW_{max} of UP 5 are smaller than those in UP 2. Hence, it was difficult to detect an illegal behavior.

3) *Case 3*: Fig. 7 and Fig. 8 show the simulation results in the case that CW_{min} is halved when an even number of collisions occur.

From Fig. 7, it can be seen that very high P_d was obtained in all cases, and the F_d was nearly 5% in the case of UP 2. The reason is that the assumed illegal act would reduce CW_{min} . In other words, it is considered that it was easier to judge whether it was a selfish node or not, since the difference in CW when collision occurred twice in the normal node and the selfish node became large.

From Fig. 8, in the case of UP 5, the P_d of 90% was obtained when the number of nodes was up to 7 for the ratio of 1:2. On the other hand, for the ratio of 2:1, the P_d of 90% was obtained only when the number of nodes was 5 or less. The reason is that collision is likely to occur because the CW is smaller than that of UP 2. That is, in an environment with a large number of nodes, it can be considered that it was impossible to distinguish between a selfish node and a normal node since collisions frequently occurred.

V. CONCLUSION

In this research, we have proposed and evaluated a detection method of a selfish node that illegally changed CW in a WBAN applying IEEE 802.15.6. As a result of computer simulations, the P_d became high when the ratio of the measurement

value at the first collision and the second collision was 1: 2, and the F_d became low when the rate was 2: 1. It was also found that the P_d decreased with the increase in the number of nodes. These results indicate that it is important to properly select the ratio of measured values according to the assumed illegal act and environment. As for the future work, we will evaluate the influence on a WBAN due to the existence of selfish nodes. In addition, we will also devise a method of removing detected selfish nodes.

REFERENCES

- [1] M. Chen, S. Gonzalez, A. Vasilakos, H. Cao, V. C. M. Leung, "Body Area Networks: A Survey. Mobile Networks and Applications," Mobile Networks and Applications, vol. 16, no. 2, pp. 171-193, Aug. 2010.
- [2] G. Acampora, D. J. Cook, P. Rashidi and A. V. Vasilakos, "A Survey on Ambient Intelligence in Healthcare," Proceedings of the IEEE, vol. 101, no. 12, pp. 2470-2494, Dec. 2013.
- [3] T. Hayajneh, G. Almashaqbeh, S. Ullah, A. V. Vasilakos, "A survey of wireless technologies coexistence in WBAN: analysis and open research issues," Wireless Networks, vol. 20, no. 8, pp. 2165-2199, May 2014.
- [4] J. Zhou, Z. Cao, X. Dong, X. Lin and A. V. Vasilakos, "Securing m-healthcare social networks: challenges, countermeasures and future directions," IEEE Wireless Communications, vol. 20, no. 4, pp. 12-21, Aug. 2013.
- [5] H. Cao, V. Leung, C. Chow and H. Chan, "Enabling technologies for wireless body area networks: A survey and outlook," IEEE Communications Magazine, vol. 47, no. 12, pp. 84-93, Dec. 2009.
- [6] J. M. L. P. Caldeira, J. J. P. C. Rodrigues and P. Lorenz, "Toward ubiquitous mobility solutions for body sensor networks on healthcare," IEEE Communications Magazine, vol. 50, no. 5, pp. 108-115, May 2012.
- [7] A. Boulis, D. Smith, D. Miniutti, L. Libman and Y. Tselishchev, "Challenges in body area networks for healthcare: the MAC," IEEE Communications Magazine, vol. 50, no. 5, pp. 100-106, May 2012.
- [8] T. Suzuki, H. Tanaka, S. Minami, H. Yamada and T. Miyata, "Wearable wireless vital monitoring technology for smart health care," in Proc. 2013 7th International Symposium on Medical Information and Communication Technology (ISMICT), Tokyo, 2013, pp. 1-4.
- [9] R. Cavallari, F. Martelli, R. Rosini, C. Buratti and R. Verdone, "A Survey on Wireless Body Area Networks: Technologies and Design Challenges," IEEE Communications Surveys & Tutorials, vol. 16, no. 3, pp. 1635-1657, Third Quarter 2014.
- [10] S. Movassaghi, M. Abolhasan, J. Lipman, D. Smith and A. Jamalipour, "Wireless Body Area Networks: A Survey," IEEE Communications Surveys & Tutorials, vol. 16, no. 3, pp. 1658-1686, Third Quarter 2014.
- [11] Wireless Medium Access Control (MAC) and Physical Layer (PHY) Specifications for Wireless Personal Area Networks (WPANs) used in or 12 around a body, IEEE Standard for Information technology - Telecommunications and information exchange between systems - Local and metropolitan area networks- Specific requirements: Part 15.6, 2012.
- [12] Smart Body Area Network (SmartBAN); Low Complexity Medium Access Control (MAC) for SmartBAN, ETSI TC Smart BAN TS 103 325 V1.1.1, 2015.
- [13] M. Raya, I. Aad, J.-P. Hubaux, and A. E. Fawal, "DOMINO: Detecting MAC Layer Greedy Behavior in IEEE 802.11 Hotspots," IEEE Transactions on Mobile Computing, vol. 5, no. 12, pp. 1691-1705, 2006.
- [14] P. Serrano, Albert Banchs, José Félix Kukiella "Detection of Malicious Parameter Configurations in 802.11e EDCA," Proceedings of GLOBE-COM '05, vol. 6, pp. 3295-3299, Dec. 2005.
- [15] P. Serrano, Member, IEEE, Albert Banchs, Member, IEEE, Valerio Targion, and José Félix Kukiella, "Detecting Selfish Configurations in 802.11 WLANs," IEEE Communications Letters (2010), 14(2), pp. 142-144, 2010.

Self-powered Wireless Urinary-incontinence Sensor System Detecting Urine Amount and Diaper Change Timing in Under 10 Minutes

Hiroya Sakamoto, Ami Tanaka, Ryota Suematsu, Yo Nakajima, and Takakuni Douseki

Department of Electronic and Computer Engineering

Ritsumeikan University

Kusatsu, Japan

a-tanaka@fc.ritsumei.ac.jp

Abstract— A self-powered wireless urinary-incontinence sensor system composed of a wireless sensor and a receiver has been developed that detects the amount of urine and the time for a diaper change. The wireless urinary-incontinence sensor, which consists of a urine-activated battery, an intermittent power-supply circuit with a storage capacitor, and a wireless transmitter, makes it possible to detect the number of urinations and the amount of urine from the spacing between the output signals. The urine-activated battery, which consists of two long flexible electrodes embedded in a diaper and placed under a piece of absorbent material with a trench structure, makes fast detection of less than 10 minutes possible. A prototype urinary-incontinence sensor system detected the amount of urine in a diaper from the spacing between the sensing signals with a resolution of 100 cm³ and detected the time for a diaper change 7 minutes after urinations.

Keywords— *urine-incontinence sensor; self-powered operation; wireless sensor; urine-activated battery; diaper change*

I. INTRODUCTION

Urinary incontinence is a problem that diminishes the quality of life not only of the person with the problem but also of a caregiver. The caregiver needs to change the diaper of an elderly person who requires nursing care every time an incident occurs. The medical treatment of urinary incontinence in elderly people who suffer from cognitive impairment or are bedridden requires the measurement of the number of incidents of incontinence per day and the amount of urine per incident [1]. However, due to the lack of nurses, it is difficult for these measurements to be made. Furthermore, even if a nurse is available, the frequent checks of patients' private parts can be an affront to their dignity. A wireless urinary-incontinence sensor automatically detects incontinence and informs a nurse. It eliminates unnecessary checking and allows a nurse to check and replace a patient's diaper only when the need arises. This reduces the workload of nurses and helps patients maintain their dignity.

We previously developed a self-powered wireless urinary-incontinence sensor system with a urine-activated battery [2]. The wireless sensor consists of a urine-activated battery, an intermittent-power-supply circuit with a storage capacitor, and

a wireless transmitter. When incontinence occurs, the sensor transmits ID signals intermittently, and the receiver receives the data and generates a notification signal, which becomes a sensing signal of incontinence. The sensor therefore provides continuous monitoring and the sensing signal makes a caregiver aware of each incident. However, it does not indicate when a diaper needs to be changed. To detect this, it is necessary to record the number of incidents and the amount of urine per incident. We also developed a self-powered wireless urinary-incontinence sensor system that is used for infant diapers and detects when a diaper needs to be changed from the spacing between the sensing signals [3]. However, the sensor needs one hour to detect the amount of urine and many experiments are required to determine the time for diaper change. This is because the time varies when the number of urinations and the volume of each differ even if the total amount of urine in the diaper is the same.

This paper describes a self-powered wireless sensor system with a nursing care diaper function that detects both the amount of urine per incident and the time for diaper change in less than 10 minutes. The system's urine-activated battery consists of two long flexible electrodes, one of activated carbon and the other of aluminum, and they are placed under a piece of absorbent material with a trench structure [4] in a diaper. The battery performs fast detection. A sensor in the diaper enables the time for a diaper change to be determined merely through simple experiments. We will first describe the structure of the urine-activated battery and its electrical characteristics. Next, the transmission capabilities of intermittent operation for the wireless sensor with the urine-activated battery are explained. Finally, we explain how the number of incidents, the amount of urine per incident, and the time for a diaper change are detected from the spacing between sensing signals.

II. RELATIONSHIP BETWEEN STRUCTURE OF DIAPER AND SPREAD OF URINE IN DIAPER

Figure 1 shows the structure of a piece of absorbent material with a trench [4] embedded in a nursing care diaper. When incontinence occurs, the urine flows along the trench toward the buttocks-side. The trench makes it possible to spread urine in the diaper quickly and evenly.

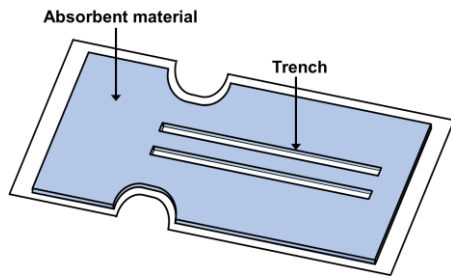
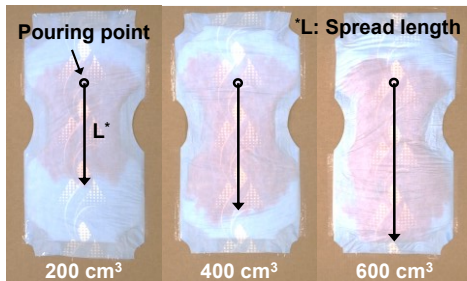
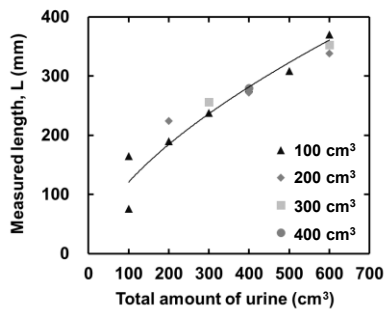


Fig. 1. Structure of absorbent material with trench embedded in diaper.

The spread length of urine in a disposable diaper for nursing care was investigated (Fig. 2). A unit volume of artificial urine (200 cm^3) was repeatedly poured onto a diaper until the total amount reached 600 cm^3 (Fig. 2a). The spread length of artificial urine toward the buttocks-side from the pouring point became longer. However, there was almost no change in the spread length toward the other direction. This is because the absorbent material has a trench toward the buttocks-side from the pouring point. The spread length (L) of artificial urine from the pouring point was measured. A unit volume of artificial urine (100 cm^3 , 200 cm^3 , 300 cm^3 , 400 cm^3) was repeatedly poured onto a diaper until the total amount reached 600 cm^3 . The graph (Fig. 2b) shows that, as the total amount of urine in the diaper increases, the spread length of urine becomes longer.



(a)

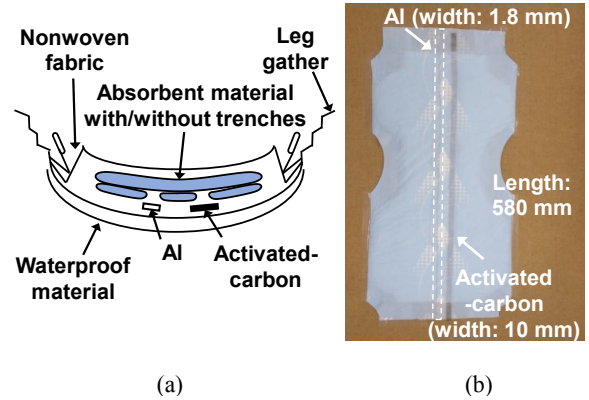


(b)

Fig. 2. Dependence of spread length on total amount of urine: (a) photographs of evaluated diaper and (b) measured spread length vs. total amount of urine.

III. URINE-ACTIVATED BATTERY THAT DETECTS AMOUNT OF URINE IN DIAPER

The diaper-shaped urine-activated battery (Fig. 3) in our system is composed of two pieces of absorbent materials and two long electrodes, all of which are embedded in a diaper. The lower piece of absorbent material has two trenches and the other has none. The electrodes are placed under the lower piece of the absorbent material with trenches (Fig. 3a). One electrode is made of activated carbon and the other one is made of Al. Both electrodes are 580 mm long and the widths are 10 mm for the activated-carbon electrode and 1.8 mm for the Al electrode (Fig. 3b).



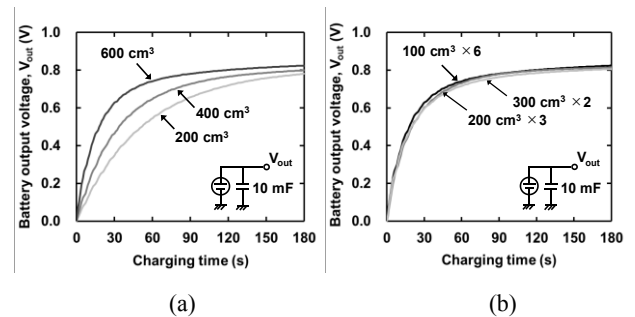
(a)

(b)

Fig. 3. Diaper-shaped urine-activated battery: (a) cross section and (b) photograph.

The charging characteristics of the batteries were measured. The output load capacitance was 10 mF. As the total amount of artificial urine in a diaper increased, the slope of the charging curve became steeper (Fig. 4a). The charging curves were the same when the total amount of artificial urine in a diaper was the same even though the unit volume of artificial urine varied (Fig. 4b).

Figure 5 shows the dependence of charging time of a capacitor on the total amount of artificial urine in a diaper. We evaluated the charging time until the battery output voltage reached 0.6 V. The charging time became shorter as the total amount of urine in a diaper increased. The charging time depended on the spread length of urine in a diaper.



(a)

(b)

Fig. 4. Charging characteristics of urine-activated batteries: (a) variation in total amount of urine and (b) variation in unit volume of urine.

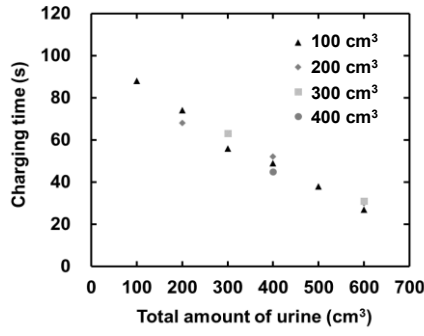


Fig. 5. Dependence of charging time on total amount of urine in diaper.

IV. EXPERIMENTS

To verify the effectiveness of our urinary-incontinence sensor system, we constructed a prototype system (Fig. 6). The system consists of a transmitter with a urine-activated battery and a removable sensor unit and a receiver. The sensor unit size was 26 mm × 25 mm × 6 mm (LWH).

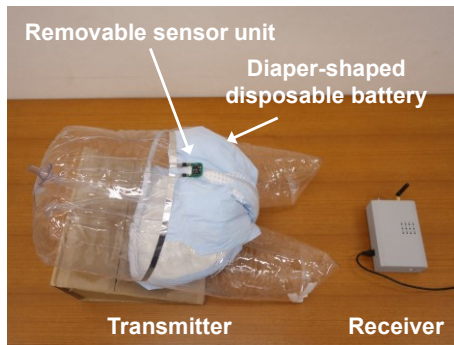


Fig. 6. Photograph of self-powered wireless urinary-incontinence sensor system with urine-activated battery.

Figure 7 shows a block diagram of our urinary-incontinence sensor system. It consists of a transmitter and a receiver. The transmitter consists of a urine-activated battery, a storage capacitor, an intermittent-power-supply circuit with a storage capacitor, and a wireless transmitter, and sends wireless signals intermittently in accordance with the charging time for the storage capacitor. The system makes it possible to determine the total amount of urine in a diaper from the spacing between the received sensing signals at the receiver.

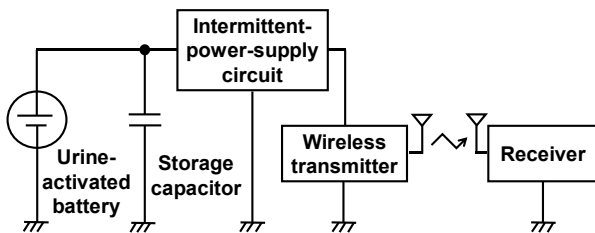
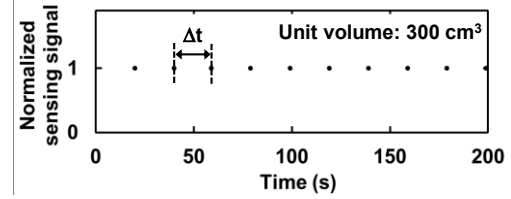
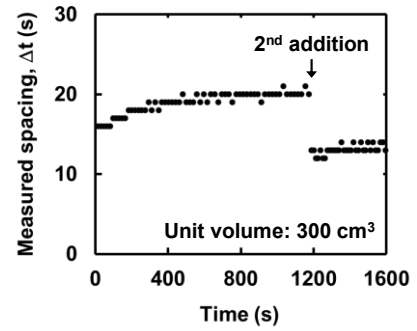


Fig. 7. Block diagram of self-powered wireless urinary-incontinence sensor system.

Figure 8a shows characteristics of received sensing signals when 300 cm³ of artificial urine was poured onto a diaper. Figure 8b shows characteristics of measured spacing between received sensing signals (Δt). The spacings gradually increased after pouring artificial urine onto a diaper. Around 7 minutes after pouring artificial urine, the spacings became constant. When artificial urine was poured for the second time, the spacing became shorter. This means the number of incidents.



(a)



(b)

Fig. 8. Characteristics of (a) received sensing signals, and (b) spacing between received sensing signals.

Figure 9 shows the method for detecting the calculation timing of the average spacing to determine the amount of urine in a diaper from spacing between received sensing signals. The calculation timing is detected when the result obtained in adding the offset time (t_{offset}) to the integrated value of the spacing between received sensing signals becomes at least 7 minutes. This is because the spacing becomes constant around 7 minutes after pouring artificial urine onto a diaper. Since the receiver does not know when urination occurs, the offset time is set. When the total amount of urine in a diaper was 100 cm³, the spacings between received sensing signals were more than 60 s and the time between occurrence of urination and the first time a sensing signal was received was around 150 s. Therefore, if the spacing of the first time is 60 s or more, we judge the total amount of urine to be 100 cm³ and set the offset time to 180 s. When the total amount of urine in a diaper was more than 100 cm³, we set the offset time to 65 s. The calculated average spacing (t) is given by

$$t = \frac{\sum_{k=0}^4 \Delta t_{n+k}}{5}. \quad (1)$$

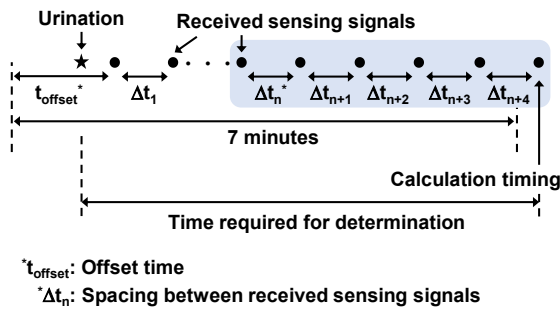


Fig. 9. Method for calculating timing of average spacing to determine amount of urine in diaper from spacing between received sensing signals.

Figure 10 shows the dependence of calculated average spacing on the total amount of urine in a diaper. As the total amount of urine in a diaper increases, the calculated average spacing becomes shorter. Therefore, the system detects the total amount of urine from the spacing. In addition, the amount of urine per incident is derived from the total amount of urine and the number of incidents. Table 1 shows the correspondence between the total amount of urine in a diaper and the spacing between received sensing signals.

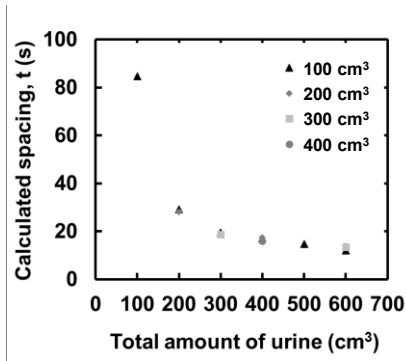


Fig. 10. Dependence of calculated average spacing on total amount of urine.

TABLE I. CORRESPONDENCE BETWEEN TOTAL AMOUNT OF URINE IN DIAPER AND SPACING BETWEEN RECEIVED SENSING SIGNALS

Total amount of urine	Spacing range
100 cm ³	60 s ≤ t
200 cm ³	23 s ≤ t < 60 s
300 cm ³	18 s ≤ t < 23 s
400 cm ³	16 s ≤ t < 18 s
500 cm ³	14 s ≤ t < 16 s
600 cm ³	t < 14 s

Table 2 shows the time required for determining the total amount of urine in a diaper after the occurrence of urination. Our system and our detection method make it possible to determine the amount of urine per incident to a resolution of 100 cm³, thus corresponding to cases when the diaper needs to be changed 7 minutes after the occurrence of urination.

TABLE II. TIME REQUIRED FOR DETERMINATION OF TOTAL AMOUNT OF URINE IN DIAPER AFTER OCCURRENCE OF URINATION

	Total amount of urine in diaper (cm ³)					
Unit volume of urine (cm ³)	100	200	300	400	500	600
100	394 s	390 s	366 s	391 s	382 s	383 s
200		395 s		393 s		397 s
300			403 s			390 s
400				396 s		

V. CONCLUSION

A self-powered wireless urinary-incontinence sensor system has been developed that is composed of a wireless sensor and a receiver. It determines when a diaper needs to be changed from the spacing between the sensing signals in less than 10 minutes. The wireless sensor scheme consists of a urine-activated battery comprising activated-carbon and aluminum electrodes under a piece of absorbent material with a trench structure in a diaper, an intermittent-power-supply circuit with a storage capacitor, and a wireless transmitter. It makes it possible to determine the amount of urine in a diaper to a resolution of 100 cm³, and thus when the diaper needs to be changed in 7 minutes. The next target of our research is a field test on subjects wearing a diaper with an embedded sensor.

ACKNOWLEDGMENT

This work was supported by JSPS KAKENHI Grant Number JP15K21504.

REFERENCES

- [1] Report of The Medical Information Network Distribution Service [Online]. Available at <http://minds.jcqhc.or.jp/n/med/4/med0015/G0000039/0001>
- [2] A. Tanaka and T. Douseki, "A Wireless Self-powered Urinary Incontinence Sensor Embedded in Disposable Diapers," 2013 7th International Symposium on Medical Information and Communication Technology (ISMICT), pp. 170-173, 2013
- [3] A. Tanaka, R. Suematsu, H. Sakamoto, and T. Douseki, "Self-powered Wireless Urinary-incontinence Sensor Determines Time for Diaper Change from Spacing Between Sensing Signals," Proceedings of IEEE SENSORS 2016 Conference, pp. 1721-1723, 2016.
- [4] Homepage of products introduction of nursing care diaper [Online]. Available at <https://www.hakujuji.co.jp/health/products/01/05.html>

Non-Laboratory-Based Risk Factors for Automated Heart Disease Detection

H. Mai¹, T. T. Pham^{*1,2}, D. N. Nguyen², E. Dutkiewicz²

¹ Garvan Medical Institute, NSW, Australia.

² Faculty of Engineering and IT, University of Technology Sydney, NSW, Australia.

Abstract—Developing a heart disease detection model using simple non-laboratory risk factors plays an important role in preventive care, especially for high risk subjects. The model allows physicians/epidemiologists to effectively diagnose a person as having heart disease. In this work, we aim to develop a non-invasive risk prediction model for automated heart disease detection that involves age, gender, rest blood pressure, maximum heart rate, and rest electrocardiography. We examine four public datasets from 1071 participants who were referred for a special X-ray of the heart's arteries (i.e., to see if they are narrowed or blocked). The subjects also undertook a physical examination and three non-invasive tests. To estimate the heart disease status, we apply a generalized linear model with regularization paths via coordinate descent. Even without laboratory-based data (e.g., serum cholesterol, fasting blood sugar), we observed a prediction accuracy as high as 72%, compared with 76% of other comprehensive models. This observation suggests that few non-invasive factors utilizing recent advances in data analytics can replace the current practices of heart disease risk assessment.

Index Terms—Heart disease, RBP, RestECG

I. INTRODUCTION

Heart diseases and conditions involving the heart and blood vessels (i.e., cardiovascular disease, CVD) are the most common ones leading to death. It has been reported that 17.7 million deaths from CVDs in 2015 accounted for approximately 31% of all deaths worldwide [1]. About half of that were due to coronary heart disease [1].

Early detection of heart disease and appropriate management are critical to people with heart disease [1]. One main reason is that most CVDs can be prevented by adjusting lifestyle (e.g., smoking, significant alcohol consumption, unhealthy diet, and physical inactivity). However, current practices to detect heart disease in population still have challenges in terms of expenditure and facility availability.

CVDs have been often diagnosed through several laboratory experiment results, e.g., blood tests, chest X-ray, or clinical assessments of electrocardiogram (ECG), echocardiogram. Recently, in a follow-up study cohort of 6186 people (over 21 years) [2], a non-laboratory-based model was shown comparable to a laboratory-based when predicting first-time fatal heart disease events. In the non-laboratory-based model, cholesterol was replaced by body-mass index. Another similar observation found in the LIPID study [3], non-laboratory-based risk factors were significantly associated with the risk of developing a recurrent heart disease

event [3]. However, these approaches still require “complicated” information such as diabetes and current hypertension treatment data as in the earlier work [2] or angina grade and myocardial infarction history as in the work [3]. We hypothesize that fewer non-laboratory-based risk factors such as age, gender, rest blood pressure, maximum heart rate, rest ECG ST-segment abnormality may also have comparable performance, especially in automated heart disease detection.

Simplifying risk assessment tool is a critical step for prevention strategies. Among cardiovascular deaths, 80% occur in developing countries where laboratory-based risk tools are costly and not practical because lack of facilities. Meanwhile, non-laboratory-based information is easier and less costly to collect. Moreover, simple analysis of data like short ECG measurements can be automatically implemented with nearly similar accuracy to manual clinical assessment. On the other hand, using a very large number of subjects, accurate probability models for CVD detection could be derived and applied universally. Early efforts [3]–[5] introduced probability algorithms built from several thousand patients. A recent study [6] reported clinical data alone are insufficient to predict the disease. Meanwhile, Hemingway et al., [7] proposed to use linked electronic medical records to increase the accuracy of coronary artery disease diagnostics. Our study, in line with the application of data science to health care, aim to propose a model for automated CVD detection using only five non-laboratory factors: age, gender, rest blood pressure (BP), maximum heart rate (MaxHR) achieved, rest ECG analysis.

The main contributions of this work are:

- We utilize a maximum collection size of a large well-known dataset for heart disease from multi-nation sites [4]. In the literature, due to clinical factors suffered from missing data across different hospitals, most related works on this dataset could only use one of the four databases of the dataset (i.e., Cleveland database [4]).
- We demonstrate that our proposed model includes fewer non-laboratory-based risk factors but performs comparably to models involving laboratory-based data inputs.

II. METHODS

A. Data Set

Our study used four public databases contributed by an international collaboration concerning heart disease diagnosis [4]. There are 303 instances from Cleveland Clinic Foundation, 294 from Hungarian Institute of Cardiology, 123 from

*: correspondence thuy.pham@uts.edu.au. Faculty of Engineering and IT, University of Technology Sydney, NSW, Australia

V.A. Medical Center (California, USA) and 200 instances from University Hospital (Switzerland) [4]. In general, 1071 participants who were referred for coronary angiography undertook a physical examination and three non-invasive tests. All participants had no history of myocardial infarction, valvular or cardiomyopathy disease. The class distribution of the predicted attribute among four hospitals is presented in Table I. In this work, towards an automated heart disease presence detection, we categorised them into two groups *Negative* (i.e., Class 0 in the dataset) and *Positive* (i.e., any of Class 1 to 4 in the dataset).

There are 13 risk factors provided in the dataset including laboratory-based and non-laboratory-based risk factors. Variables obtained from clinical test include chest-pain, serum cholesterol, resting blood pressure (in mm Hg) and fasting blood sugar (FBS). Whereas, non-invasive tests provide information about maximum heart rate (MHR), the slope of the peak exercise. Table II depicts the baseline characteristics of all 13 factors for 411 people who were diagnosed negative with CVDs and 509 patients who were positive. Patients with the disease appeared to be older, more likely to be men, and had a higher rest blood pressure, lower cholesterol than those in control group. People with positive CVDs also tend to have fasting blood sugar greater than 120 mg/dl. The index of all 13 selected variables was statistically different in two groups.

B. Generalized Linear Models with Regularization Paths via Coordinate Descent

To classify a subject has heart disease or not we use a generalized linear model (GLM) with convex penalties [8]. This is a binary classifier based on logistic regression (i.e., a quadratic approximation to the log-likelihood). There are three common penalties to generalize the model: l_1 (the Lasso), l_2 (ridge), and mixtures of the two (the elastic net) [8]. While the former does the shrinkage and variable selection at the same time, the latter may not select any subset of variables (i.e., may include all or none of them). These two approaches have different assumptions on the relationships between input and output data. For example, the ridge refers to a normal distribution for the coefficients of the linear transformation while the Lasso refers to the Laplace distribution. Thus, in this work, we compare both two models with different penalties: *Ridge* and *Lasso*. Let λ be the regularization parameter (i.e., control the weight of penalty).

C. Performance Metrics

The accuracy of proposed model in heart disease detection is evaluated as follows. Subjects who were labeled the same as annotation of *positive* are True Positives (TP). Subjects who were labeled as Positive but did not agree with the ground truth are False Positives (FP). Subjects who were labeled as Negative by the proposed method but were annotated as Positive are False Negatives (FN). The subject that was labeled as Negative by both are True Negative (TN).

The sensitivity was calculated as $\frac{TP}{TP+FN}$ and the specificity was calculated as $\frac{TN}{TN+FP}$.

III. RESULTS

1) *Fitting GLM models*: Fig. 1 visualizes the coefficients of fitted models using GLM approaches. In the figure, each variable is illustrated by a curve line against the l_1 -norm when varying λ values. The top axis represents the number of non-zero coefficients at the current λ (or can be referred to as degrees of freedom (df) for the Lasso).

2) *Model Selection with Cross-validation*: We implemented a ten-fold cross-validation using the misclassification error criterion. The grid of λ extends to a range of 100 values. Fig. 2 illustrates the cross-validation curve with the standard deviations (i.e., error bars). In the figure, two vertical dotted lines present two selected λ : λ_{min} (i.e., λ that gives the minimum error) and λ_{SE} (i.e., for one standard error range of the minimum error). These (λ_{min} , λ_{SE}) values, found through the cross-validation, are (0.03611, 0.1005) and (0.13598, 0.8741) for the Lasso-based and the Ridge regularization, respectively.

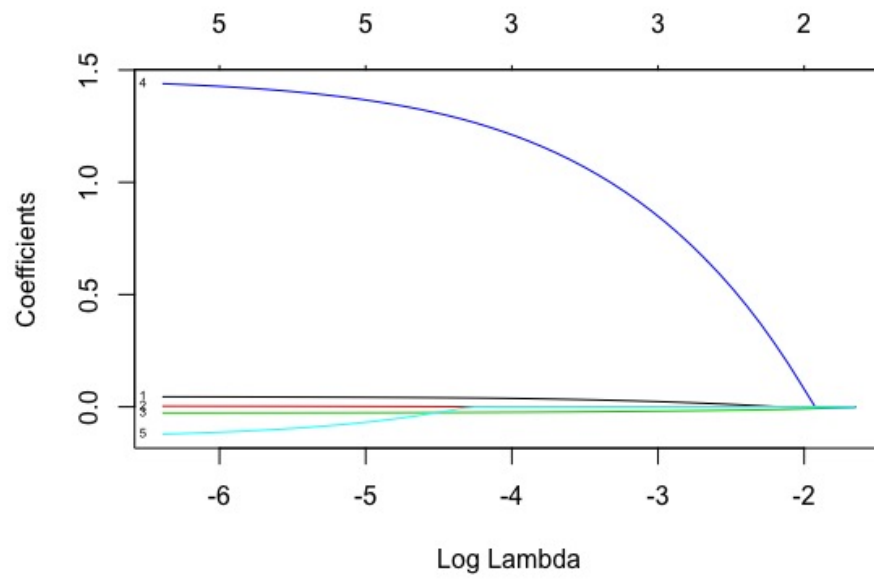
3) *Selected GLM models*: Table III lists the corresponding coefficients of fitted models at the best cross-validation parameter λ_{min} for five non-laboratory-based risk factors. We noticed that in the model using the Lasso regularization, the rest blood pressure and the abnormality of ST-T segment in ECG analysis do not play an important part. By contrast, in the model using the Ridge approach, these did contribute in the model.

Table IV depicts accuracy performance of two models during training period and hold-out test stage. We found that the performance of both models was consistent and greater than 70% through training and test sets.

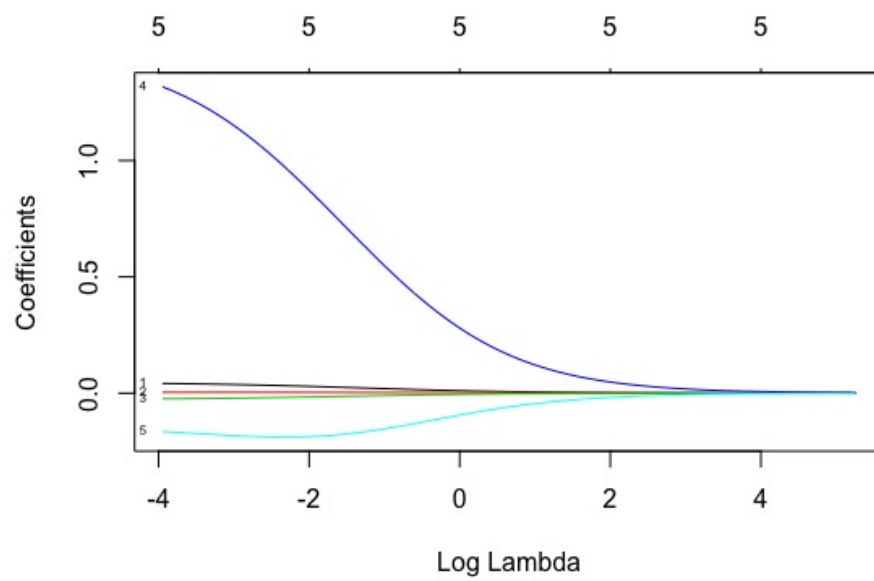
IV. DISCUSSION

In this work, we have examined the possibility of reducing the number of risk factors, especially those require costly and invasive laboratory-based results, to detect heart disease. We found that age, gender, rest blood pressure measurement, maximum heart rate, and the abnormality of ST segment in the rest ECG can be used to feed into a simple generalized linear model and achieved closely comparable accuracy as earlier works that utilized a more comprehensive input set. For example, authors of the well-known work [4] that included laboratory based data only yielded approximately a 77% classification accuracy (using a logistic regression approach). Furthermore, research advances in processing massive datasets may provide a useful real-time tool and massive information learning platform that cardiologists can assess an individual patient's risk for heart disease more accurately with less laboratory cost and faster. It is worth noting that the above ECG data used in our method can be obtained easily given the recent advances in wearable sensor for automated ECG analysis.

Relevancy of each component of the proposed information set has been long supported in clinical studies. Aging has been suggested one of the highest risk factors for CAD

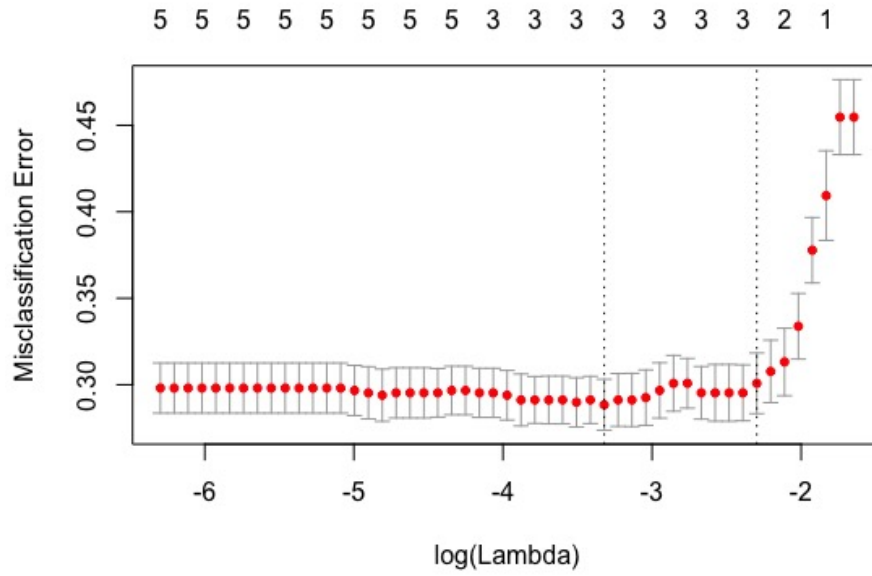


(a) Fitted GLM with Lasso penalty.

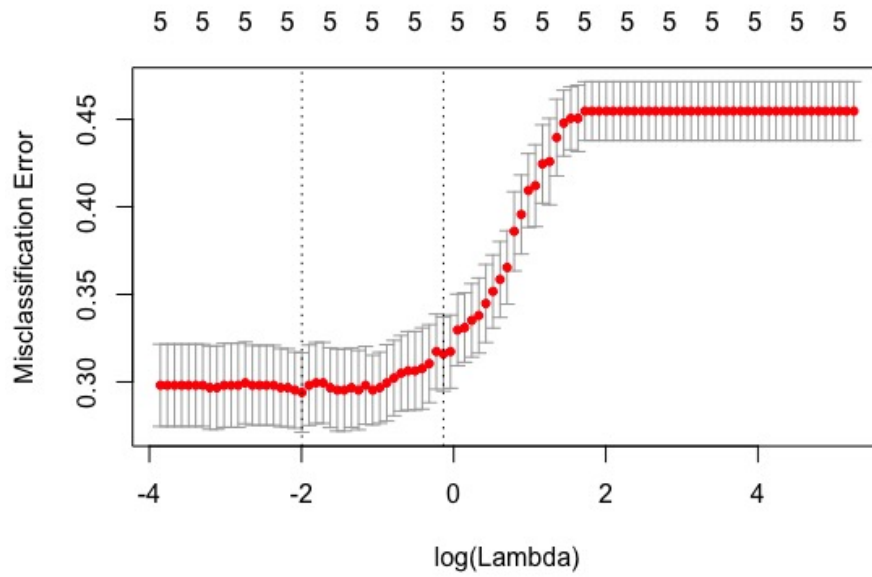


(b) Fitted GLM with ridge penalty.

Fig. 1. Fitted generalized linear models with regularization paths.



(a) Cross-validation for GLM with Lasso penalty.



(b) Cross-validation for GLM with ridge penalty.

Fig. 2. Cross-validation for generalized linear models (GLM) with different regularization paths. The top axis denotes the number of non-zero coefficients at a given λ . λ_{min} (λ_{SE}) are depicted by dotted lines. Error bars are upper and lower standard deviations.

TABLE I

MULTI-CLASS DISTRIBUTION (N PEOPLE) AND PREVALENCE % OF *Absence* = *Negative* OR *Presence* = *Positive* AMONG DATABASE LOCATIONS.

Database	Multi-Class (n people)					Total	Class Prevalance (%)	
	0	1	2	3	4		Negative	Positive
Cleveland	164	55	36	35	13	303	54.1%	45.9%
Hungarian	188	37	26	28	15	294	63.9%	36.1%
Switzerland	8	48	32	30	5	123	6.5%	93.5%
California	51	56	41	42	10	200	25.5%	74.5%

TABLE II

BASELINE CHARACTERISTICS OF 13 RISK FACTORS (THE WHOLE DATASET).

Factors		Class		P-value
		Negative	Positive	
		(n=411)	(n=509)	
Age		50.547 (9.4)	55.904 (8.7)	< 0.001
Sex	Men	267 (65 %)	459 (90.2 %)	< 0.001
	Women	144 (35 %)	50 (9.8 %)	
Chestpain (yes)	Typical	26 (6.3 %)	20 (3.9 %)	< 0.001
	Atypical	150 (36.5 %)	24 (4.7 %)	
	Non-agonal	131 (31.9 %)	73 (14.3 %)	
	Asymptomatic	104 (25.3 %)	392 (77.0 %)	
Rests blood pressure		129.9 (16.87)	133.979 (20.552)	0.002
Cholesterol		227.9 (75.8)	176.48(127.518)	< 0.001
Fasting blood sugar > 120mg/dl		44 (11.1 %)	94 (21.7 %)	< 0.001
RestECG	Normal	268 (0.652)	283 (0.558)	0.003
	Abnormal ST	61 (0.148)	118 (0.233)	
	LVHypertrophy	82 (0.2)	106 (0.209)	
Max heart rate		148.8 (23.6)	128.262 (24.02)	< 0.001
CPETAgina (yes)		55 (14.1 %)	282 (59.55 %)	< 0.001
Oldpeak		0.418 (0.716)	1.263 (1.197)	< 0.001
Slope		1.49 (0.62)	1.93 (0.56)	< 0.001
CA		0.279 (0.640)	1.132 (1.012)	< 0.001
Thal		3.99 (1.68)	5.92 (1.656)	< 0.001

TABLE III

COEFFICIENTS OF FITTED MODELS (AT THE BEST CROSS-VALIDATION PARAMETER λ_{min}) FOR FIVE NON-LABORATORY-BASED RISK FACTORS.

Risk factors	Coef. by Lasso ^a	Coef. by Ridge ^b
Age	0.029	0.029
RestBP	0	0.003
MaxHR	-0.021	-0.016
SexMale	0.998	0.871
Rest ECG normal-ST	0	-0.187

^a Coefficients estimated by GLM with Lasso regularization^b Coefficients estimated by GLM with Ridge regularization

ation) [12] a non-laboratory-based risk tool [13] has shown to have a very high correlation (N=47,466 people, cross-sectional collection from nine countries). More recently, non-laboratory Framingham score [14], which substitute BMI for lipids in FRS [11], was shown as the best performance among non-laboratory algorithms (internal validity only). However, these non-laboratory scores only eliminated blood-test based factors while maintain a larger number of inputs than our proposed model. Hence, using our approach, *Big data* based systems can be utilized for heart disease detection without laboratory-based values. This risk assessment approach is applicable to population where laboratory testing is not easily accessible (e.g., developing countries or regions with limited resources).

REFERENCES

- [1] World Health Organization, "Cardiovascular diseases (cvds)," May 2017.
- [2] Thomas A Gaziano, Cynthia R Young, Garrett Fitzmaurice, Sidney Atwood, and J Michael Gaziano, "Laboratory-based versus non-laboratory-based method for assessment of cardiovascular disease risk:

[5], [6], [9]. Authors of [9] showed the genetic relationship between aging and heart disease. Comparing with commonly used laboratory-based risk scores: Atherosclerotic Cardiovascular Disease (ASCVD) [10], Framingham Risk Score (FRS) [11], and SCORE (Systematic Coronary Risk Evalu-

TABLE IV

CONFUSION MATRIX AND STATISTICS WHEN USING FIVE NON-LABORATORY-BASED RISK FACTORS DURING TRAINING PERIOD AND HOLD-OUT TEST STAGE.

	Training Performance		Hold-out Test	
	Lasso	Ridge	Lasso	Ridge
Accuracy	0.7170	0.7060	0.7252	0.7405
95% CI	(0.6828, 0.7495)	(0.6715, 0.7389)	(0.6404, 0.7995)	(0.6566, 0.8131)
No Information Rate	0.5453	0.5453	0.5420	0.5420
P-Value [Acc > NIR]	< 0.0001	< 0.0001	< 0.0001	< 0.0001
Kappa	0.4227	0.4003	0.4392	0.4690
McNemar's Test P-Value	0.0017	0.0021	0.1336	0.0592
Sensitivity	0.7985	0.7884	0.8169	0.8451
Specificity	0.6193	0.6073	0.6167	0.6167
Pos Pred Value	0.7156	0.7065	0.7160	0.7229
Neg Pred Value	0.7193	0.7053	0.7400	0.7708
Prevalence	0.5453	0.5453	0.5420	0.5420
Detection Rate	0.4354	0.4299	0.4427	0.4580
Detection Prevalence	0.6085	0.6085	0.6183	0.6336
Balanced Accuracy	0.7089	0.6978	0.7168	0.7309

the NHANES I follow-up study cohort," *The Lancet*, vol. 371, no. 9616, pp. 923 – 931, 2008.

- [3] Jisheng Cui, Andrew Forbes, Adrienne Kirby, John Simes, and Andrew Tonkin, "Laboratory and non-laboratory-based risk prediction models for secondary prevention of cardiovascular disease: the lipid study," *European Journal of Cardiovascular Prevention & Rehabilitation*, vol. 16, no. 6, pp. 660–668, 2009.
- [4] Robert Detrano, Andras Janosi, Walter Steinbrunn, Matthias Pfisterer, Johann-Jakob Schmid, Sarbjit Sandhu, Kern H. Guppy, Stella Lee, and Victor Froelicher, "International application of a new probability algorithm for the diagnosis of coronary artery disease," *The American Journal of Cardiology*, vol. 64, no. 5, pp. 304 – 310, 1989.
- [5] George A Diamond and James S Forrester, "Analysis of probability as an aid in the clinical diagnosis of coronary-artery disease," *New England Journal of Medicine*, vol. 300, no. 24, pp. 1350–1358, 1979.
- [6] Frederick K Korley, Constantine Gatsonis, Bradley S Snyder, Richard T George, Thura Abd, Stefan L Zimmerman, Harold I Litt, and Judd E Hollander, "Clinical risk factors alone are inadequate for predicting significant coronary artery disease," *Journal of Cardiovascular Computed Tomography*, 2017.
- [7] Harry Hemingway, Gene S Feder, Natalie K Fitzpatrick, Spiros Denaxas, Anoop D Shah, and Adam D Timmis, "Using nationwide big data from linked electronic health records to help improve outcomes in cardiovascular diseases: 33 studies using methods from epidemiology, informatics, economics and social science in the clinical disease research using linked bespoke studies and electronic health records (caliber) programme," 2017.
- [8] Jerome Friedman, Trevor Hastie, and Rob Tibshirani, "Regularization paths for generalized linear models via coordinate descent," *Journal of Statistical Software, Articles*, vol. 33, no. 1, pp. 1–22, 2010.
- [9] Brian J. North and David A. Sinclair, "The intersection between aging and cardiovascular disease," *Circulation Research*, vol. 110, no. 8, pp. 1097–1108, 2012.
- [10] Paul Muntner, Lisandro D Colantonio, Mary Cushman, David C Goff, George Howard, Virginia J Howard, Brett Kissela, Emily B Levitan, Donald M Lloyd-Jones, and Monika M Safford, "Validation of the atherosclerotic cardiovascular disease pooled cohort risk equations," *Jama*, vol. 311, no. 14, pp. 1406–1415, 2014.
- [11] Keaven M Anderson, PW Wilson, Patricia M Odell, and William B Kannel, "An updated coronary risk profile. a statement for health professionals," *Circulation*, vol. 83, no. 1, pp. 356–362, 1991.
- [12] R.M. Conroy, K. Pyrl, A.P. Fitzgerald, S. Sans, A. Menotti, G. De Backer, D. De Bacquer, P. Ducimetire, P. Jousilahti, U. Keil, I. Njlstad, R.G. Oganov, T. Thomsen, H. Tunstall-Pedoe, A. Tverdal, H. Wedel, P. Whincup, L. Wilhelmsen, I.M. Graham, and, "Estimation of ten-year risk of fatal cardiovascular disease in europe: the score project," *European Heart Journal*, vol. 24, no. 11, pp. 987–1003, 2003.
- [13] Thomas A. Gaziano, Shafika Abrahams-Gessel, Sartaj Alam, Dewan Alam, Mohammed Ali, Gerald Bloomfield, Rodrigo M. Carrillo-Larco, Dorairaj Prabhakaran, Laura Gutierrez, Vilma Irazola, Naomi S. Levitt, J. Jaime Miranda, Antonio Bernabe-Ortiz, Ankur Pandya, Adolfo Rubinstein, Krisela Steyn, Denis Xavier, and Lijing L. Yan, "Comparison of nonblood-based and blood-based total cv risk scores in global populations," *Global Heart*, vol. 11, no. 1, pp. 37 – 46.e2, 2016, Investment in Global Health Research: A Public Private Partnership.
- [14] Jacob K Kariuki, Eileen M Stuart-Shor, Suzanne G Leveille, Philimon Gona, Jerry Cromwell, and Laura L Hayman, "Validation of the nonlaboratory-based framingham cardiovascular disease risk assessment algorithm in the atherosclerosis risk in communities dataset," *Journal of Cardiovascular Medicine*, vol. 18, no. 12, pp. 936–945, 2017.

PDMS-Embedded Conductive Fabric: A Simple Solution for Fabricating PDMS-Based Wearable Antennas with Robust Performance

Roy B. V. B. Simorangkir, Shilun Feng,
Abu Sadat Md. Sayem, Karu P. Esselle
School of Engineering
Macquarie University
Sydney, NSW 2109, Australia
Email: roy.basten@students.mq.edu.au

Yang Yang
School of Electrical and Data Engineering
University of Technology Sydney
Ultimo, Sydney, NSW 2007, Australia
Email: yang.yang.au@ieee.org

Abstract—A new and simple fabrication method to realize robust flexible wearable antennas by combining conductive fabric and polydimethylsiloxane (PDMS) is proposed. The conductive fabric acts as the conductive part of the antenna, while PDMS acts as the substrate as well as the encapsulation layers. The method takes advantage of the porous structure of the conductive fabric and the initial liquid form of PDMS to attain a significantly strong integration between the two, leading to a robust PDMS-based wearable antenna. A number of patch antennas have been designed, fabricated, and tested to validate the proposed concept and the results are presented, showing robust performance. The fabricated prototypes have a resonance frequency approximately at 2.46 GHz with a 10 dB return-loss bandwidth ranging from 3.3 to 5.7%.

I. INTRODUCTION

Polydimethylsiloxane (PDMS) has been considered one of the most promising materials for the realization of wearable antennas. The unique characteristics of PDMS, including extreme flexibility [1], acceptable loss and tunable relative permittivity [2], water resistance, transparency, temperature stability [3], and simple preparation [4], make it advantageous over its counterparts, such as textiles, paper, or any other polymers.

An issue in flexible antenna development using PDMS is, however, the inherent incompatibility of PDMS and metal. To achieve a strong adhesion between the PDMS and the antenna conductive parts which can stand extreme deformation and stress is therefore a challenging process. There have been a number of successful solutions to this issue, including substrate pretreatment through oxygen plasmas exposure [5], embedding carbon nanotube sheets [4], injecting liquid metal [6], and embedding silver nanowires (AgNWs) [7]. However, in general these approaches require a quite complex fabrication process.

In this paper, we present a simple, yet effective approach to overcome the aforementioned problems, allowing for a relatively easy realization of flexible and mechanically robust PDMS-based wearable antennas. In the following text, the proposed method is described. As concept demonstrations,

four inset-fed patch antennas have been fabricated and tested, validating the applicability of the proposed approach.

II. PROPOSED METHOD

The proposed solution is to utilize conductive fabric as the conductive parts of the antenna which then are embedded inside PDMS layers. Different to our work in [8], where the conductive fabric is simply adhered to the PDMS surface, this approach provides a stronger structural integration between the conductive and nonconductive parts of the antenna. That is due to the support from the PDMS-PDMS layers adhesion created through the pores of the fabric, which is much stronger than that of the PDMS and conductive fabric. As a result, this approach allows for a realization of PDMS-based antennas with a robust performance against very harsh operating conditions.

III. MATERIALS FOR REALIZATION

For the antenna conductive parts, i.e. the ground plane and patch, woven conductive fabrics are considered for their high and isotropic effective conductivity, compared to those of knitted conductive fabrics [9]. Multifilament entirely plated threads intertwine with each other in a one-to-one ratio between the vertical and horizontal directions, and the distance between the adjacent threads is very small, less than 0.04 mm, thus allowing a good resemblance to a solid metallic plate [10]. There are four different conductive fabrics from Marktek Inc. and Less EMF Inc. considered in this work, named CF I, II, III, and IV, respectively. The major differences between these fabrics are their thicknesses, the composition of metal coating on the threads, and the threads density, which lead to different effective conductivities, hence affecting the performance of the fabricated antenna.

To fabricate the PDMS layers, a Dow Corning Sylgard 184 silicone elastomer kit was employed. Firstly, the base and the curing agent of the kit were mixed at room temperature with a ratio of 10 to 1, followed by degassing the mixed solution in a vacuum desiccator to remove bubbles possibly formed during the mixing. Afterwards, the bubble-free solution

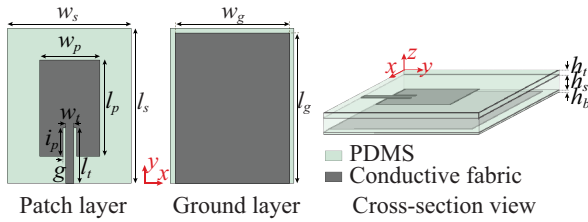


Fig. 1. Antennas designed for concept demonstration.

TABLE I
DETAILED DIMENSIONS OF PATCH ANTENNAS

Parameter	Antenna Dimension (mm)			
	CF I	CF II	CF III	CF IV
w_s	50.3	50.3	50.3	50.3
l_s	59.6	59.5	59.5	58.7
w_g	42.3	42.3	42.3	42.3
l_g	55.6	55.5	55.5	54.7
w_p	22.3	22.3	22.3	22.3
l_p	35.6	35.5	35.5	34.7
w_t	3	3	3	3
l_t	21	19	19	13.5
i_p	11	9	9	3.5
g	1	1	1	1
h_t	0.76	0.76	0.76	0.76
h_s	2.5	2.5	2.5	2.5
h_b	0.2	0.2	0.2	0.2

was tape-casted or poured into the target mold, to ensure the desired thickness of the PDMS layer. If necessary, the degassing process can be repeated to ensure that no air bubbles are left inside the solution. The last step was the curing of the solution that can be done at room temperature for 24 h or under an elevated temperature (65°C for 2 h) to expedite the polymerization.

IV. CONCEPT DEMONSTRATIONS

A. Antenna Configuration

To validate the applicability of the proposed approach for realization of flexible antennas, the combinations of PDMS and four conductive fabrics were applied to an inset-fed rectangular patch antenna design illustrated in Fig. 1. PDMS layers are used as the substrate and encapsulation that covers completely the antenna. For each combination, the antenna was optimized to have a fundamental-mode operation at ISM 2.45 GHz. Table I gives the dimensions of the final designs which were then fabricated through the process in [11], [12]. Four fabricated prototypes are shown in Fig. 2.

B. Measurements and Results

The RF performance of all prototypes were characterized, including input reflection coefficient ($|S_{11}|$) measurements using the Agilent PNA-X N5242A network analyzer, calibrated with an electronic calibration module N4691B from Keysight,

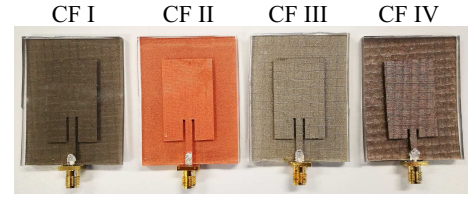


Fig. 2. Fabricated patch antennas.

TABLE II
SUMMARY OF THE PEAK GAINS AND EFFICIENCIES OF THE PROTOTYPES IN FREE SPACE

Antenna	Gain (dBi)		Eff.(%)	
	Sim.	Meas.	Sim.	Meas.
CF I	1.85	1.75	36.3	35.6
CF II	1.47	1.36	33.1	31.5
CF III	1.53	1.45	33.6	32.1
CF IV	-0.74	-0.82	20.1	19.7

and far-field measurements in the NSI700S-50 spherical near-field antenna range at the Australian Antenna Measurement Facility (AusAMF), Marsfield. As shown in Figs. 3(a)–(d), there is a good agreement between the measured $|S_{11}|$ results and those of the simulations. The fabricated prototypes have a resonance approximately at 2.46 GHz with a 10 return-loss bandwidth ranging from 3.3 to 5.7%. The minor differences between the simulated and measured results might be caused by fabrication error during the manual cutting of the fabric, especially CF IV whose edges easily suffered from fraying. When the antennas were bent around a plastic tube having a radius of 35 mm (see Fig. 4), the antennas remained functional despite slight shifts in their resonance frequencies, especially during bending along the E -plane of the antenna (see Figs. 3(a)–(d)). This is expected as it affects the main current path of the antenna. However, most importantly the conductive fabric remains intact inside the PDMS encapsulation. The desired boresight radiations are achieved from the far-field measurements as shown in simulations (see Figs. 5(a)–(d)). Further, the gains and efficiencies of all prototypes, measured at their resonance frequencies, are given in Table II, and they again agree well with the simulated results.

V. CONCLUSION

A simple yet effective approach for realizing flexible and mechanically robust wearable antennas has been presented. The proposed approach was validated by studying the performance of fabricated rectangular patch antennas. A good agreement is shown between the simulated and measured results, validating the proposed method.

REFERENCES

- [1] I. D. Johnston, D. K. McCluskey, C. K. L. Tan, and M. C. Tracey, "Mechanical characterization of bulk Sylgard 184 for microfluidics and microengineering," *J. Micromechanics and Microengineering*, vol. 24, no. 3, p. 035017, 2014.

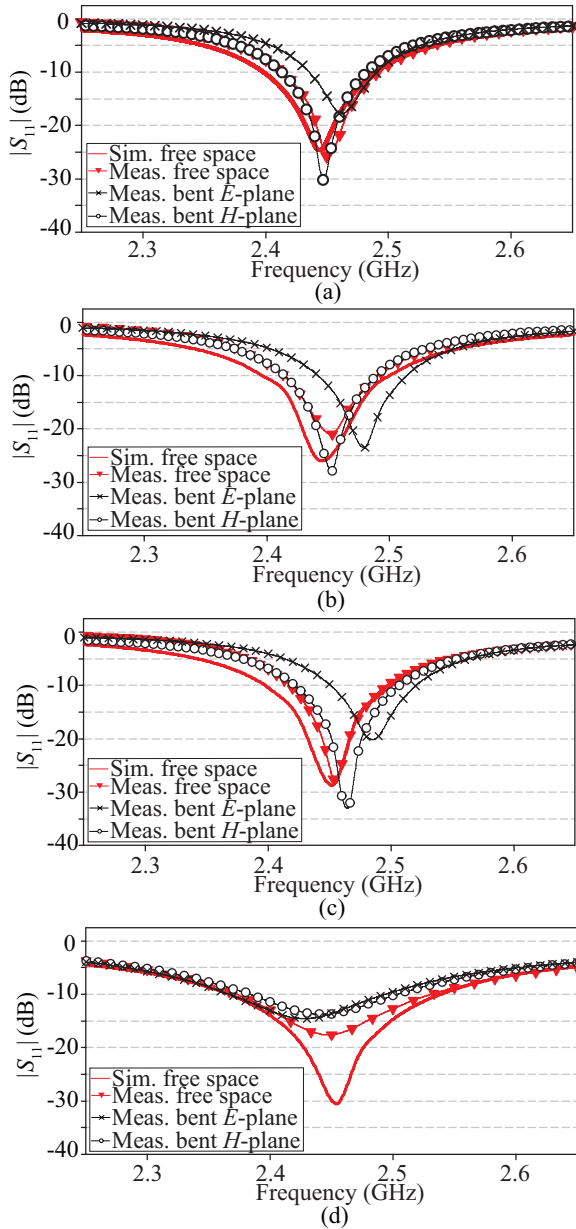


Fig. 3. Simulated and measured $|S_{11}|$ of the prototype with: (a) CF I, (b) CF II, (c) CF III, and (d) CF IV.

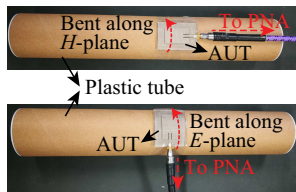


Fig. 4. Illustration of the antenna bending around the plastic tube.

- [2] S. Koulouridis, G. Kiziltas, Y. Zhou, D. J. Hansford, and J. L. Volakis, "Polymer-ceramic composites for microwave applications: Fabrication and performance assessment," *IEEE Trans. Microw. Theory Tech.*, vol. 54, no. 12, pp. 4202–4208, Dec 2006.
- [3] A. R. Colas, "Silicones: preparation, properties and performances," *Chimie Nouvelle, The Journal of the Societe Royale de Chimie*, pp.

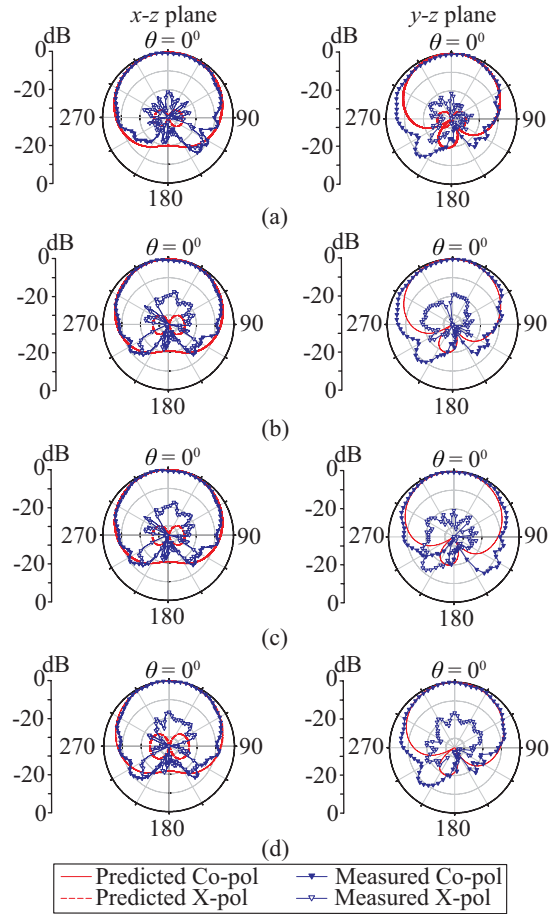


Fig. 5. Normalized simulated and measured radiation patterns of the prototype with: (a) CF I, (b) CF II, (c) CF III, and (d) CF IV.

- 847–852, 1990.
- [4] Y. Zhou, Y. Bayram, F. Du, L. Dai, and J. L. Volakis, "Polymer-carbon nanotube sheets for conformal load bearing antennas," *IEEE Trans. Antennas Propag.*, vol. 58, no. 7, pp. 2169–2175, July 2010.
- [5] P. Bodo and J.-E. Sundgren, "Titanium deposition onto ion-bombarded and plasma-treated polydimethylsiloxane: Surface modification, interface and adhesion," *Thin Solid Films*, vol. 136, no. 1, pp. 147–159, 1986.
- [6] G. J. Hayes, J. H. So, A. Qusba, M. D. Dickey, and G. Lazzi, "Flexible liquid metal alloy (EGaIn) microstrip patch antenna," *IEEE Trans. Antennas Propag.*, vol. 60, no. 5, pp. 2151–2156, May 2012.
- [7] G.-W. Huang, H.-M. Xiao, and S.-Y. Fu, "Wearable electronics of silver-nanowire/poly(dimethylsiloxane) nanocomposite for smart clothing," *Scientific Reports*, vol. 5, no. 2, p. 13971, 2015.
- [8] R. B. V. B. Simorangkir, Y. Yang, L. Matekovits, and K. P. Esselle, "Dual-band dual-mode textile antenna on PDMS substrate for body-centric communications," *IEEE Antennas Wireless Propag. Lett.*, vol. 16, pp. 677–680, 2017.
- [9] Y. Ouyang and W. J. Chappell, "High frequency properties of electro-textiles for wearable antenna applications," *IEEE Trans. Antennas Propag.*, vol. 56, no. 2, pp. 381–389, Feb 2008.
- [10] B. Ivisic, D. Bonefacic, and J. Bartolic, "Considerations on embroidered textile antennas for wearable applications," *IEEE Antennas Wireless Propag. Lett.*, vol. 12, pp. 1708–1711, 2013.
- [11] R. B. V. B. Simorangkir, Y. Yang, K. P. Esselle, and Y. Diao, "A varactor-tuned frequency-reconfigurable fabric antenna embedded in polymer: Assessment of suitability for wearable applications," in *2017 IEEE MTT-S International Microwave Symposium (IMS)*, June 2017, pp. 204–207.
- [12] R. B. V. B. Simorangkir, Y. Yang, K. P. Esselle, and B. A. Zeb, "A method to realize robust flexible electronically tunable antennas using polymer-embedded conductive fabric," *IEEE Trans. Antennas Propag.*, vol. 66, no. 1, pp. 50–58, Jan 2018.

Safety Consideration for Emerging Wireless Technologies - Evaluations of Temperature Rise in Eyes for RF Radiations up to 10 GHz

Yinliang Diao¹, Mengze Li^{2,3}, Weinong Sun¹, Sai Wing Leung¹, Yixin Cai³, Forest Zhu³, Yang Yang³

¹ Department of Electronic Engineering

City University of Hong Kong, Hong Kong

² Institute of Electromagnetics and Acoustics & Department of Electronic Science

Xiamen University, Xiamen, China

³ School of Electrical and Data Engineering

University of Technology Sydney, Sydney, Australia

yang.yang.au@ieee.org

Abstract—The study of temperature rise distribution in the human eye under plane electromagnetic wave exposure up to 10 GHz is presented in this paper. The effects of different frequencies and different blood perfusion rates of sclera to thermal calculations are investigated by finite difference method. The results reveal that the changes in the thermal parameter produce a maximum relative standard deviation of ~15% in the temperature rise in lens.

Keywords—electromagnetic safety; radio frequency; thermal parameter

I. INTRODUCTION

Due to the widespread use of wireless communication devices, there is an increasing concern of human safety issues related to Electromagnetic (EM) energy absorption in sensitive human organs [1]. Previous wireless technologies commonly use frequency band below 6 GHz, recently, there is a trend of adopting higher frequencies for wireless communications to support wider bandwidth, hence higher data transfer rate.

The human eyes, as a temperature-sensitive organ, have attracted many research attentions over the last decade. It has been shown that the formation of cataracts is related to acute radio frequency (RF) radiation [2]. It has also been summarized by international commission on non-ionizing radiation protection [3] that, under intense electromagnetic exposure, significant thermal damage would occur in sensitive tissues such as the eyes and the testis. Tissue heating effect in this frequency band, extending to 300 GHz, has been recognized by international standards as the basis for limiting the exposures.

Studies on the EM power absorption and temperature rise in human eyes have been investigated previously using numerical methods. In these numerical calculations, precise values of the EM and thermal parameters of human tissues are required. However, different datasets have revealed varied parameters, for example, the blood perfusion rate of sclera are different between [4] and [5]. The changes in thermal

parameters of human tissues will alter the heat transfer rate between eyeballs and surrounding tissues, hence affects the results of temperature calculations.

In addition, previous studies mainly focus on frequencies below 6 GHz, due to the limited spatial resolution of human models. In this study, with a refined human eye model, the effect of different blood perfusion rates of sclera on the thermal evaluations have been investigated for RF EM exposure up to 10 GHz.

II. MODELS AND METHODS

A. Human Head Model

Voxel human models have been widely used in previous dosimetry studies, but the spatial resolutions of these models are not fine enough for numerical EM calculations up to 10 GHz. In this paper, the generic eye model developed in [6] is adopted. This eye model is discretized to 0.25 mm resolution and then inserted into the Japanese head model [7], which is first resampled at 0.25 mm resolution, and hence forms a closed-eye human head model with spatial resolution of 0.25 mm.

B. Methods

Finite-difference time-domain (FDTD) method is adopted for the evaluations of SAR. The radiation source is a plane-wave with a power density of 100 W/m², radiates from the front of the head model. The SAR in different tissues of the head is calculated using following equation:

$$SAR = \frac{\sigma}{2\rho} |E|^2 \quad (1)$$

where σ , ρ are the conductivity and density of the tissue, and E is the peak value of the electric field strength. The calculated SAR are then used as heat sources for the evaluations of the temperature rise using steady-state bio-heat equation [7]:

$$\nabla \cdot (k \nabla \Delta T) - B \Delta T + \rho \cdot SAR = 0 \quad (2)$$

where k is the thermal conductivity ($\text{W}/(\text{m} \cdot ^\circ\text{C})$), the value of B is related to the blood perfusion rate ($\text{W}/(\text{m}^3 \cdot ^\circ\text{C})$), and ΔT is the steady-state temperature rise. The boundary condition is:

$$k \frac{\partial \Delta T}{\partial n} + H \Delta T = 0 \quad (3)$$

where $\partial \Delta T / \partial n$ is directional derivative of ΔT normal to the body surface, H is the convection coefficient, which is set to be $20 \text{ W}/(\text{m}^2 \cdot ^\circ\text{C})$ for the air-eye interface, and $8 \text{ W}/(\text{m}^2 \cdot ^\circ\text{C})$ for the air-skin interface.

The thermal parameters of the human tissue for the temperature rise calculation are mainly adopted from IT'IS dataset [5], and are listed in Table I. The blood perfusion rate of the sclera is found to be $2.48 \times 10^4 \text{ W}/(\text{m}^3 \cdot ^\circ\text{C})$ in [5], while an equivalent blood perfusion rate for compound retina/choroid/sclera tissue has been estimated to be $0.8 \times 10^5 \sim 1.6 \times 10^5 \text{ W}/(\text{m}^3 \cdot ^\circ\text{C})$ [4]. In this paper, in order to investigate the effect of the thermal parameters of sclera, different blood perfusion rates are adopted as shown in Table I.

III. RESULTS

The SAR values are first calculated using FDTD method; the temperature rise in human tissues are then calculated using finite difference method (FDM) taking the SAR as heat sources. Fig. 1 shows the temperature rise distributions inside the eye at some selected frequencies. As can be seen from Fig. 1, at higher frequencies, the hotspots of temperature rise tend to locate in the frontal part of the eyeball, due to the shallower penetration depth.

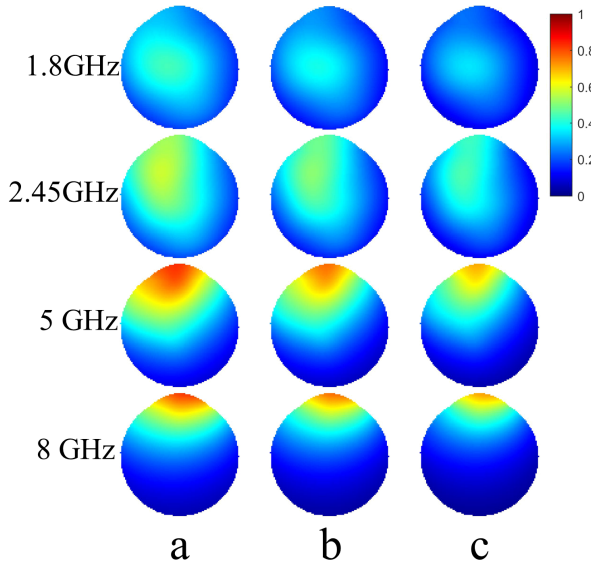


Fig. 1. Temperature rise distributions inside eyeball for different frequencies and blood perfusion rates of sclera: a: $B=2.48 \times 10^4 \text{ W}/(\text{m}^3 \cdot ^\circ\text{C})$, b: $B=0.8 \times 10^5 \text{ W}/(\text{m}^3 \cdot ^\circ\text{C})$, c: $B=1.6 \times 10^5 \text{ W}/(\text{m}^3 \cdot ^\circ\text{C})$.

Table II summarizes the maximum temperature rises in the lens. It can be seen that, as expected, higher blood perfusion of sclera increases the heat transfer rate between the eyeballs and

surrounding tissues, and then leads to lower temperature rise in lens.

TABLE I. THERMAL PARAMETERS OF EYE TISSUES

Tissue	Thermal conductivity k ($\text{W}/(\text{m} \cdot ^\circ\text{C})$)	Coefficient related to blood perfusion rate B ($\text{W}/(\text{m}^3 \cdot ^\circ\text{C})$)
Aqueous humour	0.59	0
Cornea	0.54	0
Iris	0.58	2.48×10^4
Lens	0.43	0
Sclera	0.58	A. 2.48×10^4 B. 0.8×10^5 C. 1.6×10^5
Vitreous humour	0.59	0

TABLE II. MAXIMUM TEMPERAUTRE RISE IN LENS

Frequency (GHz)	Maximum Temperature Rise in Lens ($^\circ\text{C}$)			
	$B=2.48 \times 10^4 \text{ W}/(\text{m}^3 \cdot ^\circ\text{C})$	$B=0.8 \times 10^5 \text{ W}/(\text{m}^3 \cdot ^\circ\text{C})$	$B=1.6 \times 10^5 \text{ W}/(\text{m}^3 \cdot ^\circ\text{C})$	Relative SD
0.9	0.36	0.31	0.26	15.1%
1.8	0.38	0.33	0.29	13.5%
2.45	0.57	0.51	0.45	12.2%
3	0.64	0.58	0.51	11.3%
4	0.65	0.58	0.51	12.2%
5	0.88	0.79	0.71	10.5%
5.8	0.82	0.75	0.67	10.1%
7	0.77	0.69	0.63	9.9%
8	0.67	0.61	0.55	10.0%
9	0.62	0.56	0.50	10.5%
10	0.61	0.55	0.49	10.7%

IV. DISCUSSIONS

A. Effect of resampling voxel head model

To validate the approach of resampling a low-resolution model for high resolution implementation, solutions obtained by using the same Japanese head model of 2 mm and 0.25 mm resolutions are compared. The calculated SARs are listed in Table III.

It is found that changes in the resolution would lead to differences in the peak local SARs between models of different spatial resolutions, but the averaged SARs are very close. This can be expected as the geometries of the resampled model are essentially the same as those of the original model, and resampling at a higher resolution does not alter the staircasing approximation of the physical boundaries of the original model. Similar findings have also been reported by [9], where the SARs for a 1.9 mm resolution model and the resampled model at 0.95 mm resolution have been compared.

TABLE III. COMPARISONS OF SAR VALUES FOR MODELS WITH DIFFERENT RESOLUTIONS

SAR Type	SAR Value (W/kg)	
	<i>Original model Resolution - 2 mm</i>	<i>Resampled model Resolution - 0.25 mm</i>
Eye averaged SAR	2.89 W/kg	2.93 W/kg
Cornea averaged SAR	3.92 W/kg	3.75 W/kg
Vitreous humour averaged SAR	2.90 W/kg	2.95 W/kg
Lens averaged SAR	2.14 W/kg	2.21 W/kg
Peak local SAR	25.08 W/kg	88.34 W/kg

B. Effect of blood perfusion rate of sclera

The effect of changing blood perfusion rate of sclera can be seen from Fig. 1 and Table II. In this study, the blood perfusion rate varies from 2.48×10^4 to 1.6×10^5 W/(m³·°C). As shown in Fig. 1, higher blood perfusion rate of sclera leads to lower temperature rises inside the eyeballs, and the relative standard deviations (SD) of temperature rises in lens are all within 15% at about 0.9 GHz.

V. CONCLUSION

In this paper, the study of temperature rise distribution in the human eyes under plane electromagnetic wave exposure is presented from baseband to 10 GHz. The results reveal that the changes in the thermal parameter produce a maximum relative standard deviation of 15% in the temperature rise in lens.

REFERENCES

- [1] B. Knave and others, "Electromagnetic fields and health outcomes.," Ann. Acad. Med. Singapore, vol. 30, no. 5, p. 489, 2001.
- [2] Z. Sienkiewicz, "Biological effects of electromagnetic fields and radiation.," *J. Radiol. Prot.*, vol. 18, no. 3, pp. 185–93, Sep. 1998.
- [3] ICNIRP-1998, "Guidelines for limiting exposure to time-varying electric, magnetic, and electro-magnetic fields (Up to 300 GHz)," *Health Phys.*, vol. 74, no. 4, pp. 494–522, 1998.
- [4] A. Hirata, S. Watanabe, O. Fujiwara, M. Kojima, K. Sasaki, and T. Shiozawa, "Temperature elevation in the eye of anatomically based human head models for plane-wave exposures.," *Phys. Med. Biol.*, vol. 52, no. 21, pp. 6389–99, Nov. 2007.
- [5] P. A. Hasgall, E. Neufeld, M. C. Gosselin, A. Klingenbock, A. and N. Kuster, IT'IS database for thermal and electromagnetic parameters of biological tissues version 2.5, 2014.
- [6] Y. Diao, S. W. Leung, K. H. Chan, W. Sun, Y. M. Siu, and R. Kong, "Detailed modelling of palpebral fissure and its influence on SAR and temperature rise in human eyes under GHz exposures," *Bioelectromagnetics*, vol. 37, no. 4, pp. 256–263, 2016.
- [7] T. Nagaoka, S. Watanabe, K. Sakurai, E. Kunieda, S. Watanabe, M. Taki, and Y. Yamanaka, "Development of realistic high-resolution whole-body voxel models of Japanese adult males and females of average height and weight, and application of models to radio-frequency electromagnetic-field dosimetry," *Phys. Med. Biol.*, vol. 49, no. 1, pp. 1–15, 2004.
- [8] H. H. Pennes, "Analysis of tissue and arterial blood temperatures in the resting human forearm," *J. Appl. Physiol.*, vol. 1, no. 2, pp. 93–122, 1948.
- [9] A. D. Tinniswood, C. M. Furse, and O. P. Gandhi, "Computations of SAR distributions for two anatomically based models of the human head using CAD files of commercial telephones and the parallelized FDTD code," *IEEE Trans. Antennas Propag.*, vol. 46, no. 6, pp. 829–833, 1998.

A design and implementation of an ambulatory electrocardiogram (ECG) acquisition circuit for emergency application

Jiewei Feng¹, Shahriar Hasan Shehab¹, Yang Yang², Nema C.Karmakar¹, Samir Gupta³

1. Department of Electrical and Computer Systems Engineering, Monash University

{jiewei.feng1, shahriar.shehab, nema.karmakar} @monash.edu,

2. School of Electrical and Data Engineering, University of Technology Sydney

yang.yang.au@ieee.org

3. Department of Marketing, Monash University

samir.gupta@monash.edu

Abstract—This paper presents the design and development of an ECG data acquisition circuit for emergency applications. The ECG signal extraction method and the design of the analogue front-end circuit are discussed. This design has been implemented in a printed circuit board (PCB), with comparable size to a 50 cent Australian coin. By applying the testing approach with this prototype, the output ECG trace quality is overall satisfactory with a clear display of QRS complex and certain robustness to motion artifacts.

Keywords—*Electrocardiogram(ECG); Motion Artifacts; Ambulatory ECG*

I. INTRODUCTION

According to the statistics by ST Vincent's Hospital, 25% of Australians have 3 or more risk factors for heart disease [1], which affects 1 in every 6 Australians, and causes 1 death in every 24 minutes [1]. Electrocardiogram (ECG) is a widely accepted tool for diagnosing and monitoring of heart disease [2]-[3]. An ECG is conventionally a medical test that monitors the electrical pulses generated from the heart muscle activity by using adhesive electrodes attached to the human body. The electrical activity is recorded and displayed in an electrocardiograph as a continuous waveform. As ECG has a regular pattern for a normal and healthy heart, any irregular heart rhythm or heart muscle damage can be reflected in the shape of the ECG signal, as a result of a change in the electrical activity of the heart. Therefore, heart problems could be diagnosed and monitored by analysing the pattern [1]-[2].

Although ECG is a widely used tool for health monitoring, there are some general problems with this medical test. Since the biological ECG signal from the human body is rather weak and susceptible to different types of noise, it generally suffers poor signal to noise ratio (SNR), especially due to the 50/60 Hz utility noise coupled by human body [4]. In the conventional ECG monitoring systems, the machine is too bulky for continuous everyday usage, and the cumbersome wires make the system inconvenient to use, even in a wearable Holter monitoring system [5].

To make ECG handy and comfortable for long-term monitoring, and to complement remote patient monitoring, ongoing research efforts have been put in the development of wearable ECG system and wireless body sensor network in the recent years. As a result, various convenient forms of ECG devices has evolved, some examples of which include Smart Vest [6], ECG monitoring shirt using dry electrodes with Planar-Fashionable Circuit Board (P-FCB) [5], contactless capacitive ECG monitoring system [7], and low power wireless ECG transducer employing amplitude modulation (AM) [8]. These developments of ECG system greatly enhance the convenience and the feasibility of continuous monitoring the health status of the end user.

Considering that ECG is one of the vital signals for an emergency patient with heart diseases, the applications of ECG can also be extended into ambulances and emergency department, these could provide opportunities for treatments to be planned and prepared before the patient arrives at the hospital [9]-[10]; as well as to facilitate the monitoring and diagnosis in the emergency department [11].

However, the application of ECG in the ambulance is still not highly developed in terms of system size, power consumption, multi-parameter functionality, and communication range. This work aims to develop a wireless ECG transducer for ambulance and emergency department. In this paper, the method for ECG signal extraction, and the design of a basic ECG signal acquisition circuitry are presented. The ECG circuit is comprised of 3 ECG electrode connections to form a Lead II configuration and noise cancelling with right leg drive. The susceptibility of ECG trace quality to motion artifacts has been highly reduced by this test approach and the developed ECG circuit. The rest of this paper is organised as follows: Section II presents circuit design and implementation, Section III explains the testing approach, Section IV discusses the results of testing and future plan, and the conclusion of this study comes in Section V.

II. CIRCUIT DESIGN AND IMPLEMENTATION

A. ECG Signals and System Diagram

The ECG transducer generates a signal stream with amplitude from $50\text{ }\mu\text{V}$ to 4 mV with frequency components concentrating at 0.5 to 100 Hz [4]. Considering that the ECG signal is too weak and subjected to a variety of noises, the system in Fig. 1 has been designed to obtain a clear ECG waveform. The circuit design of the developed ECG data acquisition system in Fig. 2 is discussed block by block as follows:

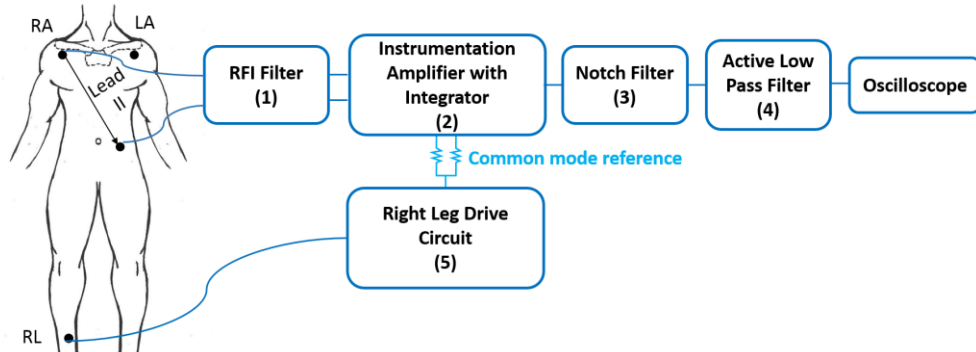


Fig. 1 Block diagram of the ECG acquisition circuit.

B. Circuit Design

1) Radio Frequency Interference (RFI) Filter

Apart from the significant $50/60\text{ Hz}$ utility noise, the ECG signal is often exposed to strong radio frequency (RF) fields from the electrosurgery machines. Those machines generate strong fields with frequency from 500 kHz to 3 MHz . To eliminate the RF interference, this design applied an R-C low pass filter at the inputs of the Differential Amplifier Module [12], and this RFI filter could also provide an input bias path

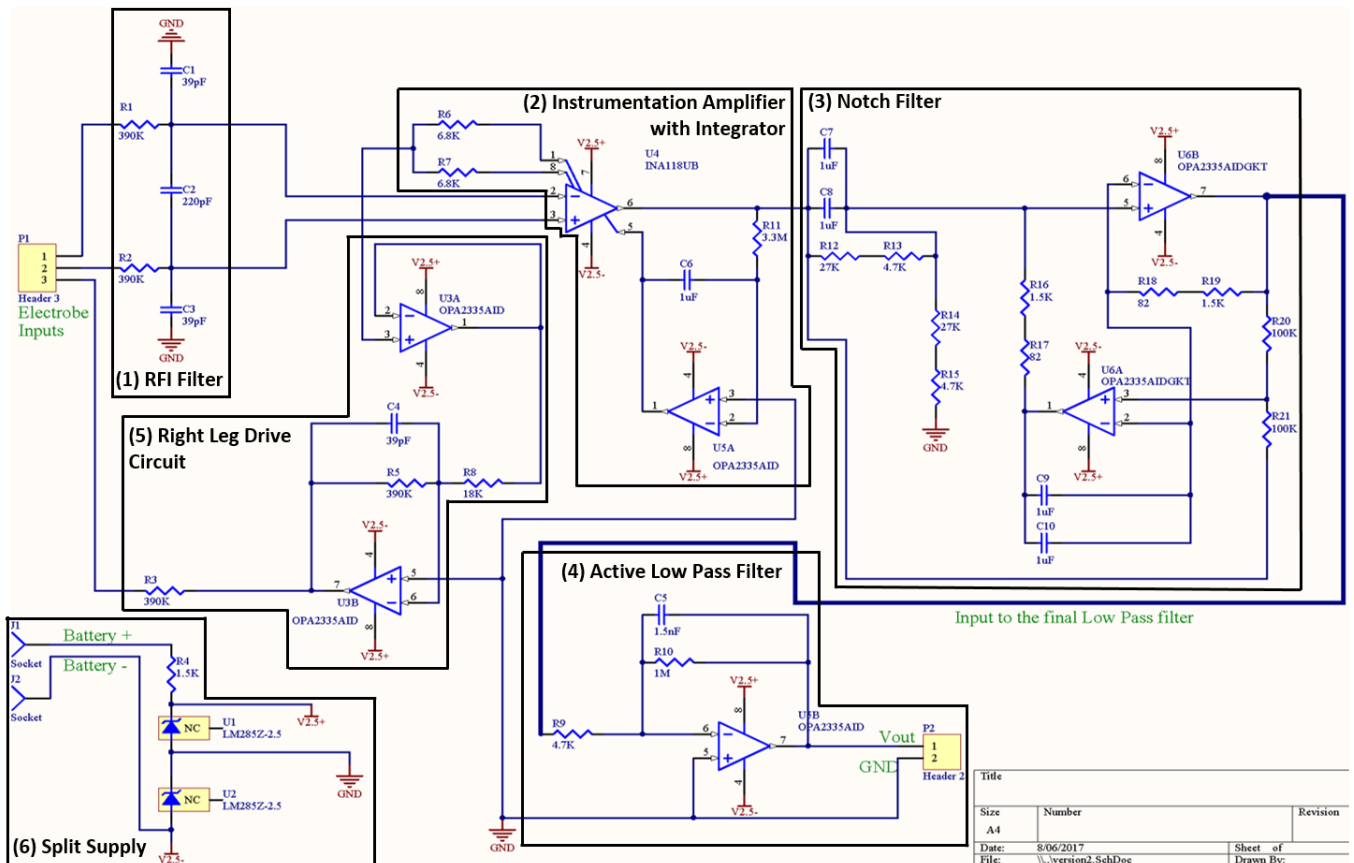


Fig. 2 Circuit diagram of the ECG analogue front-end.

for the Differential Amplifier INA118 [13].

As it can be seen from Fig. 2, R_1, R_2, C_1, C_2 and C_3 form a bridge circuit across the inputs of the differential amplifier. In order to avoid reducing the high Common Mode Rejection Ratio (CMRR), the time constant of R_1/C_1 and R_2/C_3 should be identical to keep the bridge balanced [4].

C_2 connects between two inputs of the differential amplifier, and it is effectively connected in parallel with C_1 and C_3 that are grounded in series. As C_2 has much higher capacitance than C_1 , it can significantly reduce any mismatch between the R-C filters formed at two input terminals [4].

Both differential and common mode signals would be the inputs of this filter. As these two types of signals will see different equivalent circuits, this results in two different bandwidths. Those are BW_{diff} for differential input signal, and BW_{cm} for common mode signal [4]. Suggested by [12], the cut-off frequency of the RFI filter shall not be lower than 100 Hz. These two bandwidths can be determined as stated in [4]:

$$BW_{diff} = \frac{1}{2\pi R(2C_2 + C_1)} \quad (1)$$

$$BW_{cm} = \frac{1}{2\pi RC_1} \quad (2)$$

2) Instrumentation Amplifier with Integrator

In order to extract the weak ECG signal with poor SNR, as well as to avoid amplifying noises, the differential amplifier plays a critical role in the ECG Signal Acquisition. The requirements for the differential amplifier are very high input impedance to minimise input current offset, very high CMRR to curb the common mode noise and increase SNR, low voltage offset drift to minimise unadjusted error, and low power consumption for battery operated systems [4], [6], [14].

The integrator circuit connects between the output and V_{ref} of the instrumentation amplifier. By forming a feedback loop with low output impedance in the difference amplifier of INA 118, it works equivalently as a high pass filter to remove the DC components (i.e. frequencies lower than 0.05Hz in this case), while preserving a good CMRR of the instrumentation amplifier [13], [15]-[16].

3) Notch Filter

Given that the 50 Hz noise from main AC supply is right in the middle of the ECG bandwidth (i.e. 0.05 – 100Hz) [12], a notch filter together with right-leg drive circuit is included to eliminate this in-band interference.

By considering the difficulty of implementing a single op-amp Twin-T notch filter in the physical circuit, a Fliege notch filter is used for this design. This configuration only requires 4 precision components rather than 6 in the Twin-T filter, and slight mismatches of components can be more tolerated. Another advantage of this filter is that the Q and the centre frequency can be adjusted independently to each other [17], where Q is defined as the ratio between the -3dB bandwidth and centre frequency [12].

High precision components are necessary for a deep notch at 50Hz, a 45 dB Notch Depth is achievable by using components with tolerances 1% or fewer [11], and the best

that could be hoped for is 40-50 dB with real-world components [17].

4) Active Low Pass Filter

The low pass filter in the final stage of the circuitry is to limit the signal bandwidth to 100 Hz, as well as to increase the overall voltage gain to around 1000; therefore, an active low pass filter was designed.

Given that the voltage gain from the differential amplifier module is around 5, a voltage gain of 200 from the low pass filter would be sufficient for amplifying the ECG signal. As a result, a readable ECG trace would be expected at the output of this low pass filter

5) Right Leg Drive Circuit

As human body can act as an antenna, environmental noise can be easily coupled into a human, it is especially so with the 50 Hz utility noise, which is normally larger than the ECG biological signal in the human body. Right Leg Drive circuitry was used in this design to apply an amplified and inverted common-mode noise that feeds back to human. This can compensate the current in the human body and drive the common-mode voltage to a low value [4], [18]. As for the design, the common-mode signal is extracted from average of the two input signals to the instrumentation amplifier, and that is the mid-point of gain resistors R_G in the instrumentation amplifier [13]-[14]. The output resistance R_{16} is used for limiting the drive current that is flowing into human body via the electrodes [4].

6) Split Supply

Indicated from Fig. 2, two micropower voltage reference diodes are used to form the split supply to power the circuit, where the virtual ground is extracted from the middle point of diodes connection. The current limiting resistor is designed to provide sufficient current to the circuit, while to prevent the diodes from being damaged.

C. Circuit Implementation

The circuit design in Fig. 2 has been implemented as a printed circuit board (PCB) prototype after the validation of simulation and breadboard prototype. Surface mount components are adopted in the PCB design to minimise the size of the prototype, with the battery holder mounted at the back of the PCB. This prototype is in a circular shape with a diameter of 32 mm. Its dimension is very similar to that of a 50 cent Australian coin, which has a diameter of 31.65 mm with the dodecagonal shape. Fig. 3 shows the comparison of dimensions of these two.

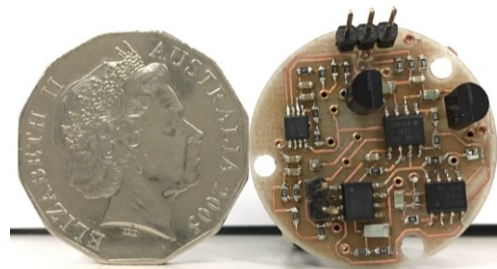


Fig. 3 Dimensions comparison between a 50 cents Australian coin and the ECG prototype

III. TEST APPROACH

A. Floating Electrodes

In this design, Ag/AgCl (floating) 3M™ Red Dot™ Electrodes will be used to pick up the electrical activities, which are generated from heart depolarisation and repolarisation. These conventional electrodes are not convenient for long duration application, as they may cause irritation and degradation of signal quality when the gel in the electrodes dries out after a long time usage [5]-[7]. However, considering the proposed application of this design is for a short-duration usage in ambulances/emergency applications, which demands consistent good trace quality, these floating electrode may be more suitable in this regard, as compared to the developed dry electrodes. This is due to that the electrical double layer formed by the metal-electrolyte interface is floated between the snap and gel sponge, rather than directly between metal and skin as in the dry electrodes; the noise associated with motion could be suppressed by a factor of 10, thus improving the stability [19]-[21].

B. Leads Configuration and Electrodes Placement

Indicated by Fig. 1, this design utilises a 3-lead configuration. In this configuration, the bipolar leads work in a similar fashion to a voltage meter to pick up the electrical signal generated from heart activities. As the main travel direction of the electrical signal is left, inferior and posterolateral [22], which is very similar to that of Lead II directional potential measurement, Lead II would be a good candidate to acquire the principle waves of ECG signal.

Suggested by [19], [23], the electrodes placed at the periphery of limbs (i.e. standard locations) would lead to the records being highly susceptible to muscle noise, even from a single finger movement. Placing electrodes at locations RA, LA and LL in Fig. 1 would be able to reduce the susceptibility to muscle noise, while providing a good quality of ECG trace as in the standard positions. Suggested by the name “Right leg drive”, the inverted feedback signal from the right leg drive circuit is returned to the human body via the electrode attached to location RL in Fig. 1.

C. Skin Preparation

The “barrier” layer Stratum Carenum is the outermost layer of skin. It stores dead cells and has high impedance (i.e. typically $50 \text{ k}\Omega/\text{cm}^2$), which is believed to be the major problem source for ECG signal quality. Skin deformation is the major source of motion artifacts, and this could cause a change of 5mV in the skin potential between the inside and outside of the “barrier” layer of the skin [20]. By applying fine sand paper with around 20 strokes, part of the Stratum Carenum will be removed, and this results in a reduction of this change in skin potential to a negligible level and a significant drop of skin impedance to less than $5 \text{ k}\Omega/\text{cm}^2$ [20], [24]. The drop of skin impedance also reduces the disturbance of 50 Hz utility interference, static electricity and conversion of common-mode voltage to differential voltage, where the last disturbance is due to the impedance variation in different locations of human body [20]. In this test, prior to placing

electrodes, 3M™ Red Dot™ Trace Prep was used by mild skin abrasion to reduce skin impedance and hence the disturbance.

IV. RESULTS AND DISCUSSION

A. Test results

Fig. 4 shows the prototype test result while the subject is standing. The principal components (i.e. P wave, QRS complex, and T wave) can be observed on the oscilloscope with negligible noise disturbance. This implies that the ECG signal extraction and noise filtering of the circuit are functioning properly; the $V_{\text{peak-peak}}$ of the QRS complex is measured to be 2.2 V, which implies sufficient amplification has been provided by the circuit.

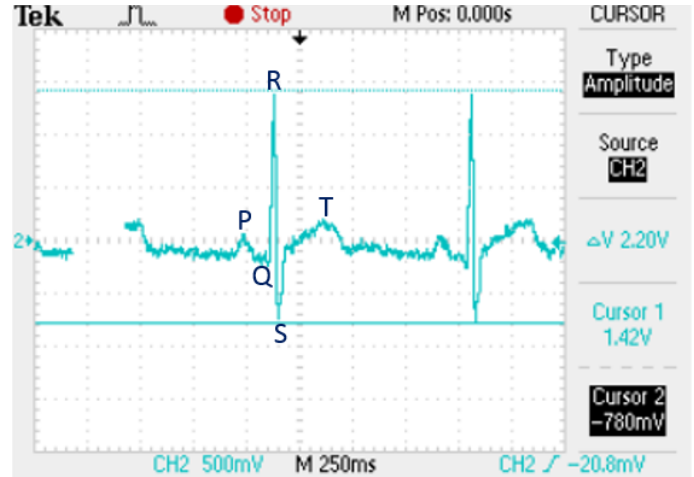


Fig. 4 Prototype test result while the subject is standing.

Fig. 5 show the sensitiveness of motion artifacts to the ECG trace quality. Fig. 5(a) shows the ECG waveform with finger motion, and only minor distortion to all the principle waves could be observed. Fig. 5(b) shows the ECG trace with walking motion, and it could be observed that P wave is totally masked, while QRS complex and T wave are still readable; the spurious peaks between the QRS complexes may be caused by the poor snap – crocodile clip connection. Therefore, it could be concluded that certain robustness has been obtained by the circuit prototype and test method.



Fig. 5 Prototype result with (a) finger movement (b) the subject walking.

B. Future plan

At this stage, the ECG circuit design has not yet been fully finalised. As discussed in the Test results section, the poor

snap-crocodile connection may hinder an accurate acquisition of ECG signal; snap type ECG cables with shielding layer will be utilised to replace the banana cable. Shield guarding circuitry will be adopted to the circuit design to further reduce the level of interference coupled to the circuit [25].

Fig. 6 shows the proposed system design for ambulance/emergency applications. The bottom layer consists of an Ag/AgCl (floating) electrode. This electrode and hence the whole system will be attached to the human body such that the lengths of wire connections to the rest two electrodes are minimised. The finalised ECG acquisition circuit will be placed in the middle layer, with batteries affixed to its backside. The top layer will be the microcontroller unit (MCU) for signal processing and data packaging, and a wireless module for transmitting the ECG signal in digital form. Through the medium of the built-in wireless receiver of consumer electronics (e.g. iPad, laptop, mobile phones), this digital signal can be plotted into real-time ECG trace via a graphical user interface (GUI). By this means, the real-time ECG signal could be monitored in a more flexible manner, as compared to utilising dedicated medical instruments (e.g. electrocardiography). This could facilitate monitoring the health status of patients, and hence prepare timely treatments in the emergency room and first aid in ambulances.

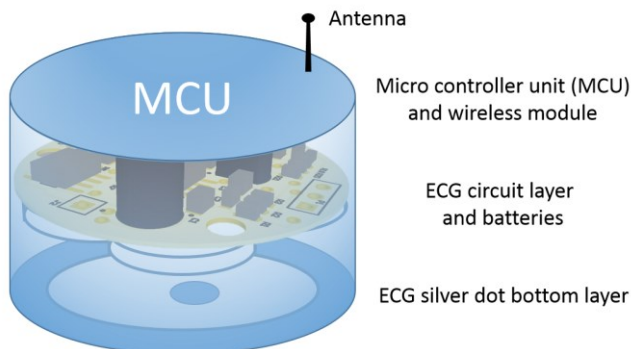


Fig. 6 Proposed ECG wireless transducer system design.

V. CONCLUSIONS

In this paper, the testing approach for reducing motion artifacts, and the design of a basic 3 lead ECG acquisition circuit have been presented. Satisfactory ECG trace quality has been obtained in the developed ECG prototype, and distortion by motion artifacts has been highly reduced. The circuit design has not yet been fully finalised at this stage, and this work will be expanded for ambulance/emergency applications with the proposed future plan.

ACKNOWLEDGMENT

This work was supported by the supervision and guidance from Dr Abdur Rahim, as well as resources from Monash University and Monash Microwave, Antennas, RFID and Sensors (MMARS) Laboratories.

REFERENCES

[1] "ECG," St Vincent's Hospital Heart Health, [Online]. Available: <https://svhhearthealth.com.au/Procedures/Tests/ECG>. [Accessed 20 03 2017].

[2] "ECG test," Better Health, 2 2017. [Online]. Available: <https://www.betterhealth.vic.gov.au/health/conditionsandtreatments/ecg-test>. [Accessed 20 03 2017].

[3] S. B. M. T. I. a. N. K. D. A. M. Jobayer, "Design and implementation of 3-lead ECG machine for rural modification," in 2015 International Conference on Electrical Engineering and Information Communication Technology (ICEEICT), Dhaka, 2015.

[4] Y. Li, X. Xu, Y. Liu and Y. Tian, "Analysis and Implement of ECG Front-End Signal Processing Circuit," in 2011 International Conference of Information Technology, Computer Engineering and Management Sciences, 2011.

[5] J. Yoo, J. Long Yan, J. Seulki Lee, J. Hyejung Kim and J. Hoi-Jun Yoo, "A Wearable ECG Acquisition System With Compact Planar-Fashionable Circuit Board-Based Shirt," IEEE Transactions on Information Technology in Biomedicine, vol. 13(6), pp. 897-902, 2017.

[6] P. Pandian, K. Mohanavelu, K. Safeer, T. Kotresh, D. Shakunthala, P. Gopal and V. Padaki, "Smart Vest: Wearable multi-parameter remote physiological monitoring system," Medical Engineering & Physics, vol. 30(4), pp. 466-477, 2008.

[7] E. Nemati, M. J. Deen and T. Mondal, "A wireless wearable ECG sensor for long-term applications," IEEE Communications Magazine, vol. 50(1), pp. 36-43, 2012.

[8] Y. Yang, X. Zhu, K. Ma, R. B. V. B. Simorangkir, N. Karmakar and K. P. Esselle, "Development of Wireless Transducer for Real-Time Remote Patient Monitoring," IEEE Sensors Journal, vol. 16, no. 12, pp. 4669-4670, Jun. 2016.

[9] C. Zywiets, V. Mertins, D. Assanelli and C. Malossi, "Digital ECG transmission from ambulance cars with application of the European Standard Communications Protocol SCP-ECG," in Computers in Cardiology 1994, 1994.

[10] K. Suma K V, K. Sandeep S, K. Vikram S, K. Hanjar and K. Sudharshan S M, "Cardiogenic shock monitoring system for ambulance," in 2015 International Conference on Advances in Computing, Communications and Informatics, 2015.

[11] N. C. Karmakar, Y. Yang and A. Rahim, "Microwave Sleep Apnoea Monitoring," Springer, Singapore, 2018, DOI: 10.1007/978-981-10-6901-7.

[12] J. E. I. I. & S. Carr, The technician's EMI handbook clues and solutions, Boston: Boston : Newnes , 2000 .

[13] "INA118 - Texas Instruments," 01 2016. [Online]. Available: <http://www.ti.com/lit/ds/symlink/ina118.pdf>. [Accessed 15 03 2017].

[14] M. W. Hann, "Ultra Low Power, 18 bit Precision ECG Data Acquisition System," 6 2013. [Online]. Available: <http://www.ti.com/lit/ug/slau516/slau516.pdf>. [Accessed 27 03 2017].

[15] Y. Yang, Radio Frequency-Based Wireless Monitoring of Sleep Apnoea Patient, Ph.D thesis, <http://arrow.monash.edu.au/hdl/1959.1/859040>.

[16] T. Kugelstadt, "Getting the most out of your instrumentation amplifier design," 2005. [Online]. Available: <http://www.ti.com/lit/an/slyt226/slyt226.pdf>. [Accessed 07 05 2017].

[17] B. Carter, "High-speed notch filters," Analog Applications Journal, pp. 19-25, 2006.

[18] A. Wong, A. Kong-Pang Pun, A. Yuan-Ting Zhang and A. Chiu-Sing Choy, "An ECG measurement IC using driven-right-leg circuit," in 2006 IEEE International Symposium on Circuits and Systems 2006, 2006.

[19] J. Webster, "Interference And Motion Artifact In Biopotentials," in IEEE 1977 Region Six Conference Record, 1977, 0 1977, pp.53-64, 1977.

[20] J. G. Webster, "Reducing Motion Artifacts and Interference in Biopotential Recording," IEEE Transactions on Biomedical Engineering, Vols. BME-31(12), pp. 823-826, 1984.

[21] H. Tam and J. G. Webster, "Minimizing Electrode Motion Artifact by Skin Abrasion," IEEE Transactions on Biomedical Engineering , Vols. Vol.BME-24(2), pp. 134-139 , March 1977.

[22] a. S. B. a. R. Stroobandt (Roland) and A. F. S. author., "The Normal ECG and the Frontal Plane QRS Axis," in ECG from basics to essentials : step by step, Chichester, West Sussex, UK ; Hoboken, NJ : Wiley Blackwell , 2015, pp. 58-59.

- [23] R. E. Mason and I. Likar, "A new system of multiple-lead exercise electrocardiography," *American heart journal*, vol. Vol.71, pp. 196-205, 1966.
- [24] C. D. Oster, "Proper Skin Prep Helps Ensure ECG Trace Quality," [Online]. Available: <http://multimedia.3m.com/mws/media/358372O/proper-skin-prep-ecg-trace-quality-white-paper.pdf>. [Accessed 03 05 2017].
- [25] A. P. C. A. G. A. C. MettingVanRijn, "High-quality recording of bioelectric events. Part 1. Interference reduction, theory and practice," 9 1990. [Online]. Available: https://www.biosemi.com/publications/pdf/Interference_reduction.pdf. [Accessed 16 05 2017].

Development of Novel Gold/PDMS Sensors for Medical Applications

Anindya Nag, Shilun Feng, Nasrin Afsarimanesh, Subhas Mukhopadhyay, *Fellow, IEEE* and Jürgen Kosel

Abstract—The paper presents the design and fabrication of novel gold/PDMS sensors using the sputtering method to use them for biomedical applications. The electrodes on the sensor patches were formed by placing a masked template containing the design over the PDMS. The sensor patches were flexible in nature with interdigitated electrodes formed on them. CTx-I, being one of the significant bone turnover biomarkers to determine the condition of the bones was tested at different concentrations to validate the functionality of the patches for this purpose. The results look promising to upgrade this idea into a fully-functionalized system for medical applications.

Keywords— Gold; PDMS; CTx-I; Flexible; Sputtering.

I. INTRODUCTION

The advancement in the sensing field has brought a big revolution in the quality of life of human beings [1]. In today's world, sensors are used in almost every field like domestic [2, 3], environmental [4, 5] and industrial sectors [6-8]. There has been a continuous demand to improve the quality and efficiency of the sensors since its intervention. Initially, the semi-conductive sensors [9] were a very popular choice due to their favorable operating conditions like the low cost of fabrication, linear response, high longevity and low input power. But still, there were some disadvantages like the limited range of operation, brittle nature and temperature dependence of the output which caused the researchers to opt for alternative approaches. With the innovation of sensors with flexible substrates [10, 11], a lot of problems related to the intransigence of the sensors were resolved, which increased their range of applications.

When the researchers were able to develop Microelectromechanical Systems (MEMS) based sensors [12], the cost of fabrication was reduced to a great extent. The problem of cost and ease of production of sensors were still into the picture, especially for the sensors which are used for day to day applications. Moreover, there are some sensors which have high efficiency in terms of sensitivity but are complex in nature and tough to fabricate, especially for unskilled workers. Thus, it is a state-of-art to develop sensors which have a low cost of fabrication and are simple in operation. This paper presents the design and fabrication of novel gold/PDMS sensors which were subsequently implemented for medical applications.

Anindya Nag, Shilun Feng, Nasrin Afsarimanesh and Prof. Subhas Mukhopadhyay are with Faculty of Science and Engineering, Macquarie University, Sydney, Australia. Prof. Jürgen Kosel is with Computer Electrical and Mathematical Sciences and Engineering Division, King Abdullah University of Science and Technology, Saudi Arabia. (Email: anindya1991@gmail.com)

With the flexible sensors in the picture, there are different materials, differing in terms of their electrical, mechanical and thermal properties are used for fabrication purposes. Some of the common materials used to develop the substrate part of the sensors are Polydimethylsiloxane (PDMS) [13], Polyethylene terephthalate (PET) [14], Polyethylene Naphthalate (PEN) [15] and Polyimide (PI) [16]. The selection of these materials mainly depends on the final dimension of the sensor patch and the applications they are being employed for. Among these, PDMS is the most advantages polymer due to its low-cost, non-toxicity and hydrophobicity. These advantages make it a popular choice to use to develop sensors for biomedical applications. Some of the common types of materials used to develop flexible sensors are Carbon Nanotubes (CNTs) [17], graphene [18], gold [19] and silver [20]. There have been prominent use [21-23] of gold nanoparticles compared to other materials due to their distinct advantages like high electrical conductivity, narrow size distribution, high aspect ratio and consistent size and shape. Another major advantage of using gold nanoparticles is their biocompatibility that includes non-toxicity and non-immunogenicity which increases the dynamicity in its applications [24]. The use of gold nanoparticles for sensing purposes is considered to be one of the standard applications.

For the electrode part of the sensor, there are different designs which have been used employed in the sensor structure for monitoring purposes. The operating principle differs as a result of the structural differences of the electrode parts. Interdigitated electrodes are one of the common types of electrodes which are largely exploited due to the advantages like minimized resonant frequency, increased effective capacitance and non-invasive nature. The interdigitated electrodes serve a great purpose for dielectric materials due to the ionic and faradic currents generated as a result of the interaction at the electrode-electrolyte interface leading to a highly sensitive response [25]. In this paper, we demonstrate the use of gold nanoparticles to develop interdigitated electrodes on the sensor patches.

Bio-medical sensing has been one of the major sectors for the applications of sensors in recent years [26-28]. Different kinds of sensors have been employed using wearable and non-wearable systems for ubiquitous monitoring of different parameters related to human health. Bio-medical biomarkers have been a significant part in this field of application, where the output of many chronic diseases can be monitored and cured at early stages by analyzing the information provided by them. This paper showcases the monitoring of one of the C-terminal Telopeptides which has been used to determine the risk of osteoporotic fractures [29]. Even though the current methodologies like Enzyme-linked Immunosorbent Assay

(ELISA) [30] and Dual-energy X-ray Absorptiometry (DEXA) [31] serve as gold standards for diagnosing the possibility of osteoporotic fractures by determining the bone densities, these processes have certain limitations like high equipment cost, highly time consuming method because of the high sample preparation time, and several steps need to complete the process of antibody binding, incubatory and spectrophotometric measurements [32]. So, a technique needs to be presented where the above-mentioned drawbacks can be addressed and rectified, keeping the efficiency and sensitivity of the working system constant. This paper highlights the proposal of a new system where the fabricated interdigitated sensors have been used to analyze the capability of the sensor to detect one of the C-Terminal biomarkers (CTx-I) at different concentrations.

The paper has been sub-divided into five sections. Followed by the introduction given in section one, the fabrication and working principle of the sensor patches are explained in sections two and three respectively. Then, the experimental set-up and results of the sensor patches for different CTx-I concentrations are shown in section four. The conclusion is given in the final section of the paper.

II. FABRICATION OF THE SENSOR PATCHES

The whole fabrication process was carried out in the laboratory at fixed temperature and humidity conditions. Figures 1(a) – 1(c) shows the schematic diagram of the fabrication process. PDMS (SYLGARD® 184, Silicon Elastomer Base) was formed by mixing the prepolymer and a curing agent at a ratio of 10:1 and cast on a petri dish as shown in Figure 1(a). The height of the cast PDMS was adjusted to around 1000 microns with a casting knife (SHEEN, 1117/1000 mm). This was followed by its desiccation for two hours to remove any trapped air bubbles in it. Then the PDMS was cured in the oven at 70°C for 2 hours to solidify the substrate. Then the sample was taken for sputtering of gold nanoparticles over it to form the electrodes. The sputtering was done using an EMITECH K550 machine with a pressure and current of 3×10^{-2} mbar and 25 mA respectively.

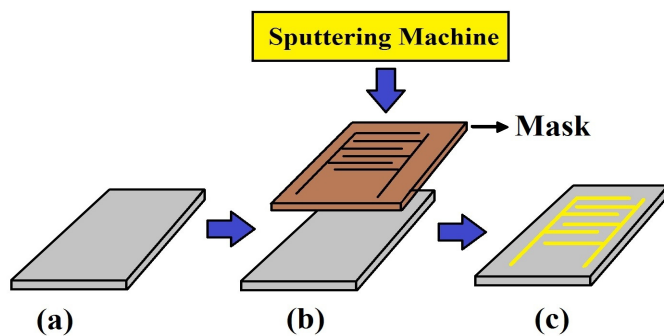


Figure 1: Schematic diagram of the fabrication process of the sensor patches. A layer of PDMS of fixed thickness was cast on a Petri dish (a). A template of the designed electrodes of specific dimensions was placed (b) top of the PDMS layer, followed by the sputtering of gold on it. The template was then removed to obtain the final product (c).

A mask was placed firmly over the PDMS substrate. The mask was made up of steel with the hollow part in it in the shape of the electrodes of the sensor patches. Steel was used as the mask due to its good adhesive nature with the PDMS. CREO Parametric 2.0 was used to design the electrodes for the mask with specified dimensions. The mask was placed properly over the PDMS substrate to nullify any gap between the former and the later, thus nullifying the shadow effect. The thickness of the sputtered gold was 100 nanometers. Followed by the sputtering of gold nanoparticles, the mask was taken off the substrate, leaving behind the electrode on the sensor. Figure 2 shows the final product of the fabrication process. It is seen that there was no shadow effect of the sputtering and the electrodes came off clean and perpendicular to the surface. Three pairs of interdigitated fingers were present each with a length and width of 10 mm and 2 mm respectively. The interdigital distance (d) between two consecutive electrodes is 100 microns. The total surface area of the sensing area is around 100 cm² with an area of 400 cm² of the total sensor.

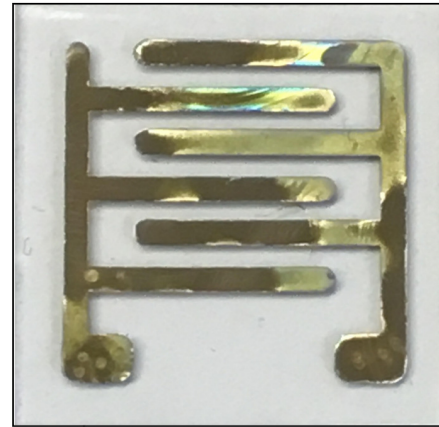


Figure 2: Final view of the fabricated sensor patch.

III. WORKING PRINCIPLE OF THE ELECTRODES

The electrodes of the developed sensor patches operate on capacitive principle as a result of their interdigitated shape. Figure 3 shows the schematic diagram of the working principle of these sensors. An electric field produced as a result of it a potential difference is applied to the two electrodes of the sensor. This field bulges from one electrode to another of opposite polarity due to its planar structure. When any material is kept in the proximity to the sensing area of the sensors, the electric fields penetrate the material while traveling from one electrode to another. This changes the characteristics of the field which is studied to analyze the attributes of the material. This technique has been largely used to study the properties of many dielectric materials in domestic [33, 34] and industrial [35, 36] applications. Out of the different methods used to study this field, Electrochemical Impedance Spectroscopy (EIS) [37] is one of the primary techniques employed to study the applications of interdigital sensors. Frequency Response Analysis (FRA) [38] is one common phenomenon in EIS where a frequency sweep over a fixed range is done to analyze the difference between the input

and the output signal. This output is monitored in terms of the effective impedance (Z) of the material.

Figure 3: Schematic diagram of the working principle of the electrodes.

IV. EXPERIMENTAL RESULTS

The experiments for the different CTx-I concentrations were conducted as per the experimental setup is shown in figure 4. The sensing area of the sensor was dipped inside the solution carefully to avoid any effect of the solution on the bonding pads of the sensor. The other end of the sensor was connected with IM 3536 HIOKI High tester via Kelvin probes to determine the response of the sensor for different concentrations. The High Tester was connected to a computer via a USB cable to collect the data in Microsoft Office Suite via automatic data acquisition system. An input of 1 V RMS with a frequency sweep of 500 Hz - 10 kHz was provided from the tester to the sensor. The frequency was considered from 500 Hz as the sensor patch did not respond properly for the preceding frequencies for the different solutions. An average of three readings from the tester was taken to ensure repeatability of the responses.

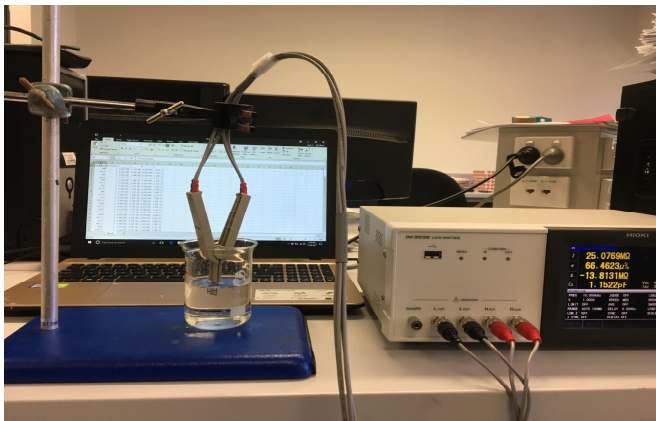


Figure 4: Experimental set-up depicting the placement of the sensing area of the sensor patch inside the solution. The bonding pads of the sensor are connected to the impedance analyzer via Kelvin probes to monitor the changes occurring as a result of the different concentrations of CTx-I.

The solutions were prepared by using CTx-I peptide as the solute and de-ionized water (Resistance: 18.2 M Ω) as the solvent. A series of dilution solutions were prepared to perform the experiments. Initially, a stock solution of 1000 ppm was prepared by mixing 1 gm of CTx-I to 1 L of de-

ionized water. This was used to prepare different concentrated solutions of 100 ppm, 50 ppm, 10 ppm, 1 ppm and 0.1 ppm for experimental purposes. Figures 5 and 6 show the response of the sensor patches for the CTx-I concentrations in terms of impedance (Z) and conductivity (S) with respect to the swept frequency range. It is seen from Figure 5 that the sensor was capable differentiating the CTx-I concentrations. The impedance values remain pretty much constant and do not change much with the variation in frequency.

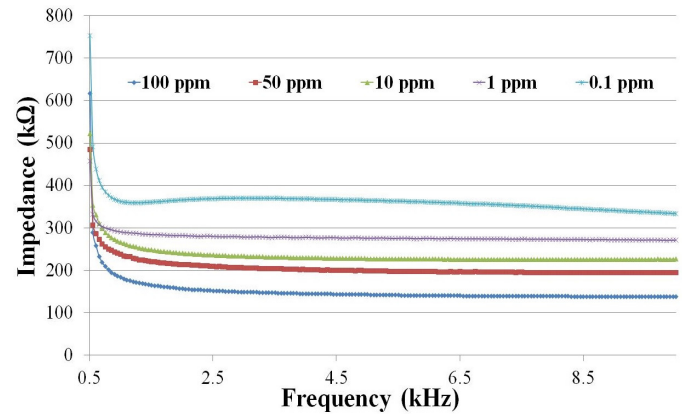


Figure 5: Response of the sensor patch for different CTx-I concentrations in terms of impedance vs. frequency.

The difference between the values took place due to the solution resistance occurring due to the ionic charge transfer between the solution and the electrodes of the sensor. The change in conductivity as a result of the CTx-I solutions are shown in Figure 6. It is seen that the conductivity values change symmetrically with the different concentrations. The decrease in conductivity values with different concentrations is evident from the increase in the impedance values from Figure 5.

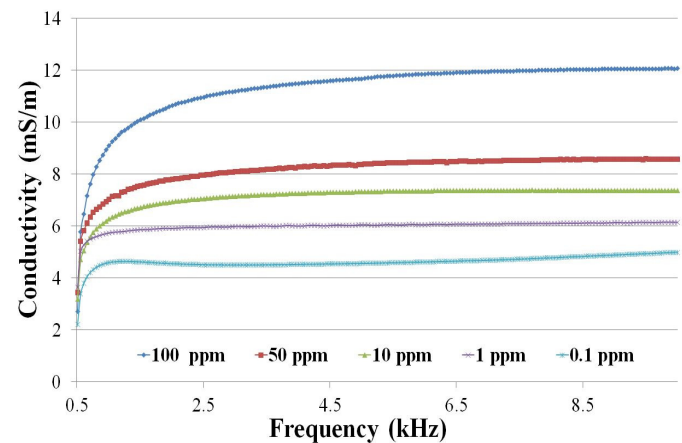


Figure 6: Response of the sensor patch for different CTx-I concentrations in terms of conductivity vs. frequency.

The sensitivity of the sensor patches was also obtained by determining the change in the conductivity values with respect to the control value at different concentrations. The control

value was obtained by measuring the conductivity of the de-ionized water. The change in sensitivity for different concentrations as shown in Figure 7 is obtained from the following equation:

$$\text{Sensitivity} = \frac{S_{\text{control}} - S_{\text{measured}}}{S_{\text{control}}} \quad (i)$$

where,

S_{control} is the conductivity value of the control solution (de-ionized water).

S_{measured} is the conductivity of different solutions.

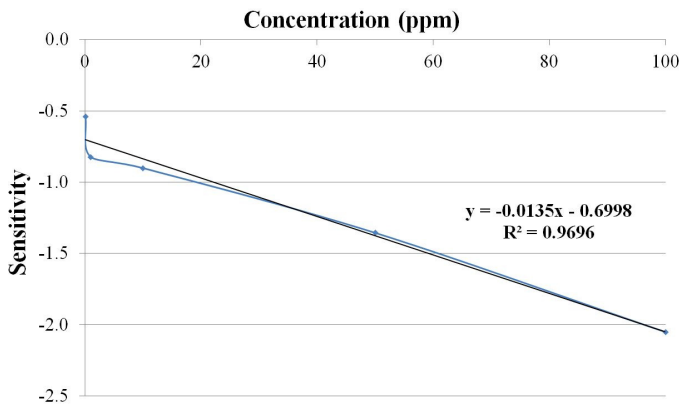


Figure 7: Sensitivity of the sensor patches for the tested CTx-I concentrations.

It is seen from Figure 7 that the sensitivity obtained from the sensor was 0.013, as evident from the slope of the graph. The linear fit plotted in the graph is very close to the experimental values as evident from the high coefficient of determination (R^2). The limit of detection (LOD) for these experimental solutions has been 0.1 ppm.

V. CONCLUSION

The paper showcases the fabrication and implementation of low-cost, novel gold/PDMS sensors. The sensors were developed using the sputtering technique having a mask containing the electrode design was placed over the substrate. The advantages of these sensors are its low-cost and easy fabrication process. The conductivity of the electrodes is also very high ($\sim 4 \times 10^6$ S/m). The sensor patches were also very flexible due to the nature of the substrate. The sensor patches were experimented with different CTx-I concentrations to employ them for osteoporotic applications. However, there are some issues that need to be addressed to optimize the use of these sensors for medical applications. The sensitivity of these sensors for any medical applications needs to be high. This can be achieved by two ways. The design, technique of fabrication or processed materials have to be altered to optimize the net electric field created between the electrodes of opposite polarity. The thickness of the electrodes can be changed to optimize the sensitivity. The individual passive elements of the sensor patch should also be determined to have a better understanding of the working circuitry. The

authors would address and rectify the above-mentioned points performing further experiments and report in the future work.

REFERENCES

- [1] A. Nag, and S. C. Mukhopadhyay, "Smart Home: Recognition of activities of elderly for 24/7; Coverage issues." pp. 480-489.
- [2] M. S. A. Rahman, S. C. Mukhopadhyay, and P.-L. Yu, "Novel Planar Interdigital Sensors," *Novel Sensors for Food Inspection: Modelling, Fabrication and Experimentation*, pp. 11-35: Springer, 2014.
- [3] M. S. A. Rahman, S. C. Mukhopadhyay, P.-L. Yu *et al.*, "Detection of bacterial endotoxin in food: New planar interdigital sensors based approach," *Journal of Food Engineering*, vol. 114, no. 3, pp. 346-360, 2013.
- [4] M. A. M. Yunus, S. Mukhopadhyay, and A. Punchihewa, "Application of independent component analysis for estimating nitrate contamination in natural water sources using planar electromagnetic sensor." pp. 538-543.
- [5] M. A. M. Yunus, G. R. Mendez, and S. C. Mukhopadhyay, "Development of a low cost system for nitrate and contamination detections in natural water supply based on a planar electromagnetic sensor." pp. 1-6.
- [6] A. I. Zia, S. Mukhopadhyay, I. Al-Bahadly *et al.*, "Introducing molecular selectivity in rapid impedimetric sensing of phthalates." pp. 838-843.
- [7] A. I. Zia, A. M. Syaifudin, S. Mukhopadhyay *et al.*, "Electrochemical impedance spectroscopy based MEMS sensors for phthalates detection in water and juices." p. 012026.
- [8] A. I. Zia, A. Mohd Syaifudin, S. Mukhopadhyay *et al.*, "Development of Electrochemical Impedance Spectroscopy based sensing system for DEHP detection." pp. 666-674.
- [9] S. M. Sze, *Semiconductor sensors*: Wiley New York, 1994.
- [10] A. Nag, S. C. Mukhopadhyay, and J. Kosel, "Wearable Flexible Sensors: A Review," *IEEE Sensors Journal*, 2017.
- [11] D. Vilela, A. Romeo, and S. Sánchez, "Flexible sensors for biomedical technology," *Lab on a Chip*, vol. 16, no. 3, pp. 402-408, 2016.
- [12] A. Wisitsoraat, V. Patthanasetakul, T. Lomas *et al.*, "Low cost thin film based piezoresistive MEMS tactile sensor," *Sensors and Actuators A: Physical*, vol. 139, no. 1, pp. 17-22, 2007.
- [13] S. Khan, L. Lorenzelli, and R. Dahiya, "Bendable piezoresistive sensors by screen printing MWCNT/PDMS composites on flexible substrates." pp. 1-4.
- [14] A. Nag, S. C. Mukhopadhyay, and J. Kosel, "Tactile Sensing From Laser-Ablated Metallized PET Films," *IEEE Sensors Journal*, vol. 17, no. 1, pp. 7-13, 2016.
- [15] R. Shabannia, and H. Abu-Hassan, "Vertically aligned ZnO nanorods synthesized using chemical bath deposition method on seed-layer ZnO/polyethylene naphthalate (PEN) substrates," *Materials Letters*, vol. 90, pp. 156-158, 2013.
- [16] A. Nag, S. C. Mukhopadhyay, and J. Kosel, "Sensing System for Salinity Testing Using Laser-induced Graphene Sensors," *Sensors and Actuators A: Physical*, 2017.
- [17] A. Nag, S. C. Mukhopadhyay, and J. Kosel, "Flexible carbon nanotube nanocomposite sensor for multiple physiological parameter monitoring," *Sensors and Actuators A: Physical*, vol. 251, pp. 148-155, 2016.
- [18] M. E. E. Alahi, A. Nag, S. C. Mukhopadhyay *et al.*, "A temperature-compensated graphene sensor for nitrate monitoring in real-time application," *Sensors and Actuators A: Physical*, vol. 269, pp. 79-90, 2018.
- [19] S. Gong, W. Schwalb, Y. Wang *et al.*, "A wearable and highly sensitive pressure sensor with ultrathin gold nanowires," *Nature Communications*, vol. 5, 2014.
- [20] J. Wang, J. Jiu, M. Nogi *et al.*, "A highly sensitive and flexible pressure sensor with electrodes and elastomeric interlayer containing silver nanowires," *Nanoscale*, vol. 7, no. 7, pp. 2926-2932, 2015.
- [21] A. Shiohara, J. Langer, L. Polavarapu *et al.*, "Solution processed polydimethylsiloxane/gold nanostar flexible substrates for

- plasmonic sensing," *Nanoscale*, vol. 6, no. 16, pp. 9817-9823, 2014.
- [22] C. Tasaltin, and F. Basarir, "Preparation of flexible VOC sensor based on carbon nanotubes and gold nanoparticles," *Sensors and Actuators B: Chemical*, vol. 194, pp. 173-179, 2014.
- [23] M. Segev-Bar, and H. Haick, "Flexible sensors based on nanoparticles," 2013.
- [24] R. Shukla, V. Bansal, M. Chaudhary *et al.*, "Biocompatibility of gold nanoparticles and their endocytotic fate inside the cellular compartment: a microscopic overview," *Langmuir*, vol. 21, no. 23, pp. 10644-10654, 2005.
- [25] R. Igreja, and C. Dias, "Analytical evaluation of the interdigital electrodes capacitance for a multi-layered structure," *Sensors and Actuators A: Physical*, vol. 112, no. 2, pp. 291-301, 2004.
- [26] S. Kruss, A. J. Hilmer, J. Zhang *et al.*, "Carbon nanotubes as optical biomedical sensors," *Advanced drug delivery reviews*, vol. 65, no. 15, pp. 1933-1950, 2013.
- [27] A. Chen, and S. Chatterjee, "Nanomaterials based electrochemical sensors for biomedical applications," *Chemical Society Reviews*, vol. 42, no. 12, pp. 5425-5438, 2013.
- [28] P. Roriz, O. Frazão, A. B. Lobo-Ribeiro *et al.*, "Review of fiber-optic pressure sensors for biomedical and biomechanical applications," *Journal of biomedical optics*, vol. 18, no. 5, pp. 050903-050903, 2013.
- [29] C. M. R. Barco, S. M. Arija, and M. R. Pérez, "Biochemical markers in osteoporosis: usefulness in clinical practice," *Reumatología Clínica (English Edition)*, vol. 8, no. 3, pp. 149-152, 2012.
- [30] S. Jabbar, J. Drury, J. N. Fordham *et al.*, "Osteoprotegerin, RANKL and bone turnover in postmenopausal osteoporosis," *Journal of clinical pathology*, vol. 64, no. 4, pp. 354-357, 2011.
- [31] C. Heiss, P. Govindarajan, G. Schlewitz *et al.*, "Induction of osteoporosis with its influence on osteoporotic determinants and their interrelationships in rats by DEXA," *Medical science monitor: international medical journal of experimental and clinical research*, vol. 18, no. 6, pp. BR199, 2012.
- [32] N. Afsarimanesh, S. C. Mukhopadhyay, and M. Kruger, "Molecularly Imprinted Polymer-Based Electrochemical Biosensor for Bone Loss Detection," *IEEE Transactions on Biomedical Engineering*, 2017.
- [33] A. Nag, A. I. Zia, X. Li *et al.*, "Novel Sensing Approach for LPG Leakage Detection: Part I—Operating Mechanism and Preliminary Results," *IEEE Sensors Journal*, vol. 16, no. 4, pp. 996-1003, 2016.
- [34] A. Nag, A. I. Zia, X. Li *et al.*, "Novel Sensing Approach for LPG Leakage Detection—Part II: Effects of Particle Size, Composition, and Coating Layer Thickness," *IEEE Sensors Journal*, vol. 16, no. 4, pp. 1088-1094, 2016.
- [35] M. S. A. Rahman, S. C. Mukhopadhyay, and P.-L. Yu, *Novel sensors for food inspection: Modelling, fabrication and experimentation*: Springer, 2014.
- [36] A. I. Zia, M. S. A. Rahman, S. C. Mukhopadhyay *et al.*, "Technique for rapid detection of phthalates in water and beverages," *Journal of Food Engineering*, vol. 116, no. 2, pp. 515-523, 2013.
- [37] E. Azzarello, E. Masi, and S. Mancuso, "Electrochemical impedance spectroscopy," *Plant Electrophysiology*, pp. 205-223: Springer, 2012.
- [38] M. Bagheri, M. S. Naderi, T. Blackburn *et al.*, "Frequency response analysis and short-circuit impedance measurement in detection of winding deformation within power transformers," *IEEE Electrical Insulation Magazine*, vol. 29, no. 3, pp. 33-40, 2013.

A Study on the Effect of Sports on Academic Stress using Wearable Galvanic Skin Response

Khalid Oweis, Hussam Quteishat
Electrical Engineering Department
American University of Madaba
Madaba, Jordan
k.owais@aum.edu.jo

Moudar Zgoul
Mechanical Engineering Department
American University of Madaba
Madaba, Jordan

Assal Haddad
Civil Engineering Department
American University of Madaba
Madaba, Jordan

Abstract— Wearable sensors have opened a new door for research to understand different human emotions and psychological states. This is the first study to employ wearable devices to measure the Galvanic Skin Response (GSR) of students. A set of Microsoft Band 2 was used to collect data from nineteen engineering students while attending the same class. The data was collected throughout a whole semester. Students were later divided into categories according to their weekly activity level. This activity level was determined by an online survey that the students filled out. One-Way Analysis of Variance was performed to assess differences between groups. Correlation Analysis was also performed to evaluate the correlations between groups. Findings of this work include significant intra-group differences. Significant correlations were also found between GSR values and activity level. Significant correlations were also found within the GSR values between the groups themselves.

Keywords— *GSR, Sports, Bio Data, Microsoft Band 2.*

I. INTRODUCTION

Physiological Sensor Analysis is a field of research that is growing [1, 2]. The last decade has shown greater accessibility to wearable devices. These devices are presently used for different purposes. Some of them are used in interactive applications; others are used to gather meaningful data for research purposes [3]. The advent of this technology has allowed the measurement of human stress by mainly two sensors: The first is the Galvanic Skin Response (GSR), which is also known as electro-dermal activity (EDA), psychogalvanic reflex, or skin conductance response. This sensor is used as a direct indicator of stress. The other is the Heart Rate Sensor and is used as a direct indicator of stress [4], and as an indirect indicator of stress through the analysis of its variability [1, 5, 6]. The GSR sensor measures the skin electric conductivity. Stress increases sweating, consequently, moisture causes the skin conductivity to increase [7, 8].

The stress that the students go through during their academic life is variable upon many factors; the first is the student himself / herself. This entails the lifestyle of the student, their academic ability, their eating habits, their gender, their emotional state, etc. Numerous studies have studied the stress of K-12 or higher education students through questionnaires. While surveys are considered a consistent method among the surveyed, their biggest drawback is that they are subjective and the outcomes depend mainly on the subject's reasoning and state at the type of surveys [9].

There are a number of studies that employed the GSR sensor to collect skin conductance values from students. These studies have encountered a number of shortcomings: First, these studies use a special type of GSR sensor. This sensor is a pair of electrodes that are either placed on the wrist or the fingers and is connected directly to a computer terminal or data acquisition device to log the data. An example of which is shown in Figure 1.



Fig. 1. Physiological data acquisition by using GSR sensor. Figure adopted from [10].

This method has the obvious disadvantage of not having the student in his natural learning mode of being in class. This results in the offset of the values of GSR due to the stress that is induced to students by connecting them to such machines. The second shortcoming is that this method will be hard to implement over a long period of time, or for a large number of classes due to its inflexibility.

This study is the first of its kind to use a wearable smartwatch to collect GSR signal values and other physiological values from students while there are sitting normally in their class with no attachments.

Currently, there is a plethora of consumer smart watches and bands. These devices function as fitness trackers and activity watchers. These bands/watches are manufactured by some of the biggest technology and sports companies like Samsung, Apple, Nike, Garmin, Fitbit, Jawbone, etc. However, the wearable devices that contain the GSR sensor are few; the first comes from Microsoft, which is the Microsoft Band 2. As of the writing of this article, this band has been discontinued. The other one is the Jawbone UP3 fitness tracker. Other wearable devices include the Embrace[®] watch and E4 Wristband[®] from Empatica Inc., the Basis Peak by Intel[®], which has also been discontinued and recalled for overheating, and the MAXREFDES73# from Maxim Integrated[®]. The limited availability and accessibility of wearable devices that embed the GSR sensor makes their use in education somewhat limited.

II. DATA ACQUISITION

Data was collected from 19 Civil Engineering students ($m=11$, $f=8$) at the American University of Madaba. The students are in their fourth and fifth level in civil engineering with age range (22-23). The students were asked to wear Microsoft Band 2 in a specific course only. This class was taught by one instructor only, who is one of the co-authors of this paper. This course would convene twice a week every Monday and Wednesday 11:30 AM – 12:45 PM in the same classroom. Students wore the bands every class session in all the classes throughout the semester. Each student would choose his specifically numbered band and wear it at the beginning of the class session, and then would take their bands off and return it to the research assistant at the end of the class. Data Collection started at the beginning of March 2017 and ended when the semester concluded at the end of May. The Final exam was held on June 10th.

Each Microsoft Band 2 was connected via Bluetooth to a separate Android phone with the Microsoft Band app installed. The GSR sensor readings of the Microsoft Band 2 cannot be accessed directly via the mobile application provided by Microsoft; they must be extracted using a specially developed mobile App. The data was logged by the “Companion for Microsoft Band” app. This app is available on the Google Play Store ®. This app logs all the sensors’ data of the band in a comma-separated variables (CSV) file that is stored locally on the phone. These phones that connected to the bands were not available to the students and were kept during class in a secure closet, in order for the students to keep their focus on the instructor. The frequency of the Band’s GSR sampling rate was 5 Hz.

Students were asked to fill out a survey at the beginning of the course to answer numerous questions. Some of which are the following:

- Date of Birth
- Gender
- Current Weight (Kgs)
- Height (Centimeters)
- Any diseases?
- How many times do you play sports per week?
- How many hours of study per week?

The results of the survey, particularly question No. (f), were used as a basis for this study. The distribution of students by their weekly activity level are shown in Table I.

TABLE I. STUDENT ACTIVITY LEVEL DISTRIBUTION

How many times do you play sports per week?	No. of Students
I do not / rarely play sports	3
Once	5
2 - 3 times	6
4 - 5 times	2
Every Day	2
Total	19

III. PRE-PROCESSING

Microsoft Band logs the GSR value as a resistance in Ohms. A higher GSR value indicates a more relaxed subject, whereas a lower GSR value indicates a more stressed subject. GSR is a subject-specific value and cannot be compared in its abstract value to other subjects’ values directly [11]. Consequently, the GSR values were normalized. The normalization technique was a modified one adopted from [12].

$$\text{Normalized GSR} = \frac{GSR_{max} - GSR_{current}}{GSR_{max}} \quad (1)$$

where GSR_{max} is the maximum value of GSR that the student has achieved during the entire semester. This value indicates the student’s resting state.

Noise was also encountered in the Data. The continuity of the contact between the band and the student’s skin affects the quality of the GSR signal. Some bands were somewhat larger than the wrists of some of the students and did not fit perfectly. This caused some noise in the signal and discontinuities in the readings. These gaps were accounted for and removed in pre-processing.

It is important to note that the stress of a person cannot be solely attributed to the class dynamics or content provided during the course. Numerous hidden factors might directly affect stress even more than the class itself but are hard to measure. Some of these factors could be related to the students’ emotional state. This emotional state could be strongly affected by their family, friends, love life, spirituality, financial situation, grades, sudden events, exercise, etc. [11].

IV. RESULTS AND DISCUSSION

Analysis of the results obtained based on data collected during a three-month period of the spring 2017 semester is presented in this research paper. The physiological data collected was mainly the students’ GSR response in a live classroom setting. Students were asked to fill out an online survey at the beginning of the semester. The survey’s outcome divided the students according to their weekly sports activity behavior into five different categories. Those categories are listed in Table I above. The investigation of One-Way ANOVA between means of groups and the correlations between the students’ normalized GSR response and those categories was performed in this research. The confidence interval that was considered was 95%, $p < 0.05$.

Table II shows the monthly average normalized GSR value of students’ vs their weekly Sports activity behavior.

TABLE II. AVERAGE MONTHLY GSR STUDENT ACTIVITY LEVEL DISTRIBUTION

Activity Level / Month	Mar	Apr	May	Grand Average
I do not / rarely play sports	0.87	0.92	0.91	0.91
Once	0.98	0.96	0.97	0.97
2 - 3 times	0.93	0.94	0.91	0.93
4 - 5 times	0.96	0.92	0.90	0.92
Every Day	0.29	0.73	0.95	0.48

Data shows that students who play sports Every Day had noticeably lower GSR values in the months of March and April than their peers. This result can be possibly attributed to extra sweat that might exist on their wrists due to their higher cardiac activity. The “Everyday” students group showed steady increase throughout the semester while other groups showed fluctuations in the same period. The increase of the average value of the everyday group in the month of May can be associated with lower activity level and more focus on studies. May is the last month of the semester and thus more study time is usually allocated by students during that month than activity time. This change is shown in Figure 2.

One-Way Analysis of Variance (ANOVA)

was performed to evaluate the differences between the groups. The number of data points that were collected from each group that was used in analysis is presented in Table III.

TABLE III. NO OF DATA POINTS PER GROUP

Sports Per Week	Symbol	N
I do not / rarely play sports	0	831
Once	1	1506
2 - 3 times	2.5	2178
4 - 5 times	4.5	1209
Every Day	7	986

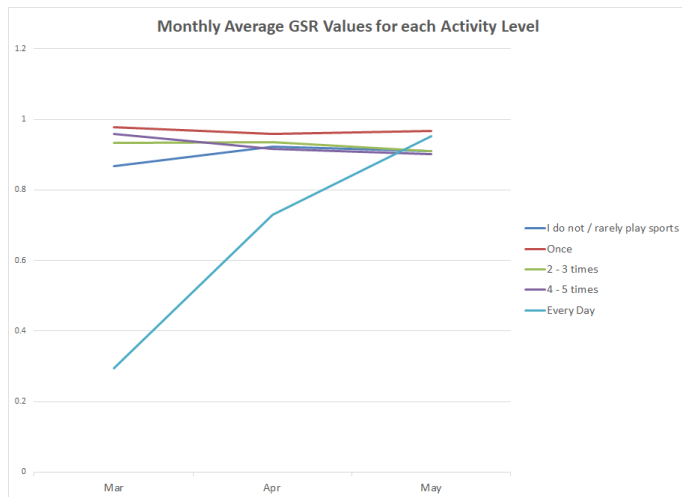


Fig. 2. Monthly Average GSR for each activity Level

The results that showed statistical significance ($p < 0.05$) are presented in Table IV.

TABLE IV. STATISTICALLY SIGNIFICANT DIFFERENCES BETWEEN MEANS OF GROUPS

Group 1 (I)	Group 2 (J)	Mean Difference (I-J)	Std. Error	Sig.
I do not Play	Once	-.0595*	0.00915	0.000
Once	2 - 3 times	.0407*	0.00710	0.000
Once	4 - 5 times	.0491*	0.00818	0.000
Every Day	I do not Play	-.4294*	0.00997	0.000
Every Day	Once	-.4889*	0.00867	0.000
Every Day	2 - 3 times	-.4482*	0.00813	0.000
Every Day	4 - 5 times	-.4398*	0.00909	0.000

The results shown in Table IV clearly show that the GSR levels are significantly different between most groups. Groups "Once" and "Every Day" were statistically different from all the other groups. Groups "I do not play", "2 - 3 times", and "4 - 5 times" were not statistically different from each other, but only from groups 1 and 7. This indicates that students who

play either every day or just once a week have statistically different stress levels than the rest of their peers. Figure 3 shows a plot of the estimated marginal means of the different groups.

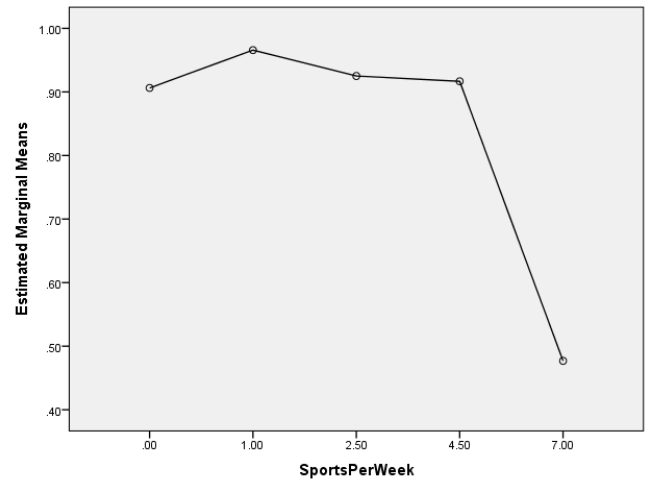


Fig. 3. Estimated Marginal Means of the Normalized GSR.

Figure 3 clearly shows that the students who play once a week have generally higher GSR value, an indication of a lower stress state. It also shows that students who play daily have lower GSR value, an indication of either higher stress level or an increased sweating state due to regular activity.

Furthermore, Correlation analysis was implemented to find correlations between the daily GSR values of students and their activity group. The first test that was performed was to find correlations between the students' resting state and their sports activity group. The daily maximum normalized GSR (GSRmax) indicates the resting state. A correlation coefficient $\rho = 0.27$ with statistical significance $p = 0.023$, < 0.05 was found between GSRmax and the activity group.

Figure 4 shows the grand average of students' resting State (GSRmax) vs their weekly sports activity level. Though the results are slightly comparable. The group of students who are most active (Every Day and 4-5 times/week) showed the lowest amount of resting GSR. This could also be attributed to several factors. First, the amount of sweat that could be on their wrists due to their activity level. In addition, it can be an attribute of this age group's regular physical activity. All other groups had higher resting state values.

Another correlation test was performed between the daily average GSR value and the activity group. A statistically significant correlation coefficient of $\rho = 0.4$ ($p = 0.000229 < 0.05$) was found between the activity behavior and the daily average GSR value. Further analysis was carried out to find the intra-groups correlation coefficient. These results are presented in Table V.

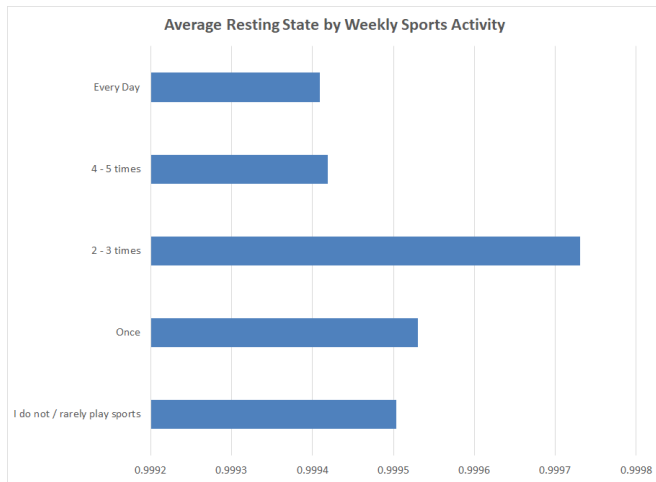


Fig. 4. Average of Resting State (GSR_{max}) vs Activity Level/Week

As can be inferred from Table V, none of the results was statistically significant. However, there were two sets of groups with reasonable correlation values and close to statistical significance. The first correlation was between the “Once” and “I do not Play” groups. The correlation coefficient $\rho = 0.48$ ($p = 0.072$). Figure 5 shows their daily average GSR values over time.

TABLE V. INTRA-GROUP CORRELATION ANALYSIS RESULTS

Group 1	Group 2	Correlation Coefficient ρ	Significance Level p
Once	I do not Play	0.48	0.072
Once	2-3 times	0.47	0.076
4-5 times	I do not Play	0.47	0.10
Everyday	I do not play	0.44	0.13

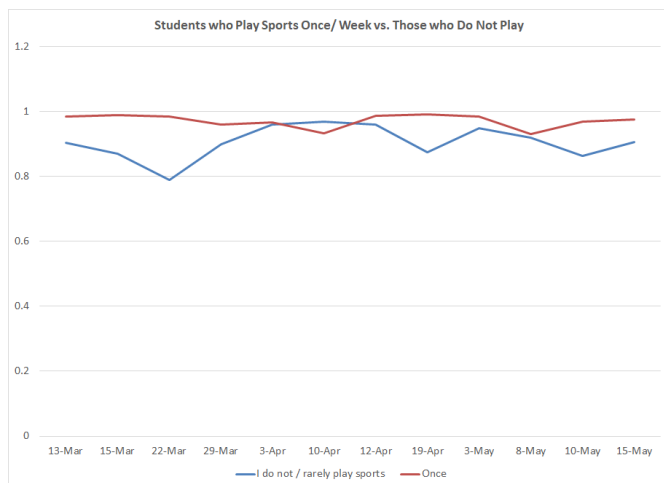


Fig. 5. Average GSR for groups “Once” and “I do not play” over Time

The other highest correlation was between the “Once” and “2-3 times / Week” groups. The correlation coefficient $\rho = 0.47$ ($p = 0.076$). Figure 6 shows their daily average GSR values over time. While there are other comparable correlation values between other sets of groups, their p-value is not significant and hence no valid argument can be inferred.

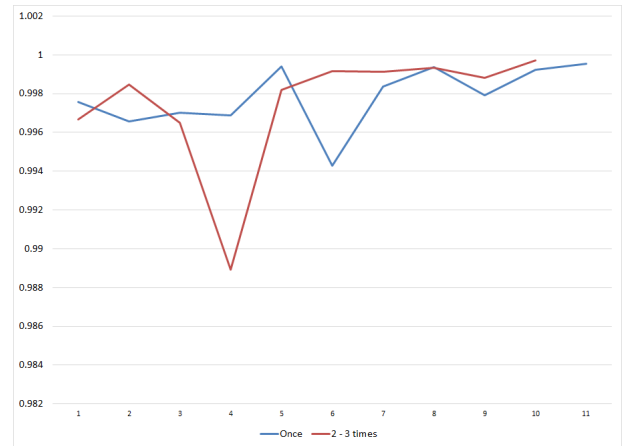


Fig. 6. Average GSR for groups “Once” and “2-3 Times” over Time

V. CONCLUSION

The galvanic Skin Response (GSR) of students under pre-set conditions/environment was measured over a whole semester. The purpose was to find statistical differences between students with different sports activity lifestyles and their stress levels. Several approaches were considered while conducting the research. Numerous results were statistically significant for the current data set.

It was found that those who play once a week and are in the low activity group, have statistically different GSR values from the students in all the other activity groups. It was also found that those who are in the highest activity group have also statistically different GSR values from all the other groups. Furthermore, a significant correlation between the GSR value and the activity level was found. However, there were no specific patterns that could be associated to any of the groups that could differentiate them.

Future work of collecting data from more students to build a substantial data set is needed. It is understandable that GSR data can be controlled by numerous measurable and immeasurable variables and is dependent on human behavior. While different students handle stress differently, some might share measurable characteristics in terms of biometrics that can measure the conductance levels of human skin.

ACKNOWLEDGMENT

The authors would like to thank Prof. Karim S. Numayr for his support during the proposal procedure of this project. The authors would also like to thank the American University of Madaba for providing the funding for this project. A great appreciation is owed to the students who volunteered for this project.

REFERENCES

- [1] McCraty R, Atkinson M, Tiller WA, Rein G, Watkins AD. The Effects of Emotions on Short-Term Power Spectrum Analysis of Heart Rate Variability. *The American Journal of Cardiology* (1995) 76, 14: 1089-1093.
- [2] Adinda van 't Klooster A, Collins N. An Emotion-Aware Interactive Concert System: A Case Study in Realtime Physiological Sensor Analysis. *Journal of New Music Research* (2017) : 1-9.
- [3] Lee VR, Drake J, Williamson K. Let's Get Physical: K-12 Students using Wearable Devices to Obtain and Learn about Data from Physical Activities. *TechTrends* (2015) 59, 4: 46-53.
- [4] Payne RL, Rick JT. Heart Rate as an Indicator of Stress in Surgeons and Anaesthetists. *Journal of Psychosomatic Research* (1986) 30, 4: 411-420.
- [5] Michels N, Sioen I, Clays E, De Buyzere M, Ahrens W, et al. Children's Heart Rate Variability as Stress Indicator: Association with Reported Stress and Cortisol. *Biological Psychology* (2013) 94, 2: 433-440.
- [6] McDuff, D., Gontarek, S. and Picard, R. Remote Measurement of Cognitive Stress Via Heart Rate Variability. (2014) 2957-2960.
- [7] Sysoev M, Sedlar U, Kos A, Pogacnik M. Stress-Sensors Classification and Stress-Analysis Algorithms Review/Pregled Senzorjev in Algoritmov Za Dolocanje Stopnje Stresa. *Elektrotehnikski Vestnik* (2014) 81, 5: 263.
- [8] Sharma N, Gedeon T. Objective Measures, Sensors and Computational Techniques for Stress Recognition and Classification: A Survey. *Computer Methods and Programs in Biomedicine* (2012) 108, 3: 1287-1301.
- [9] Perala, CH, Sterling, BS. Galvanic Skin Response as a Measure of Soldier Stress. (2007) .
- [10] Handri, S., Yajima, K., Nomura, S., Ogawa, N., Kurosawa, Y. and Fukumura, Y. Evaluation of Student's Physiological Response Towards E-Learning Courses Material by using GSR Sensor. *Computer and Information Science (ICIS)*, 2010 IEEE/ACIS 9th International Conference On (2010) 805-810.
- [11] Bakker, J., Pechenizkiy, M. and Sidorova, N. What's Your Current Stress Level? Detection of Stress Patterns from GSR Sensor Data. *Data Mining Workshops (ICDMW)*, 2011 IEEE 11th International Conference On (2011) 573-580.
- [12] Kanimozhi A, Raj VC. A Cognitive E-Learning System using Arousal Valence Emotional Model. *Journal of Theoretical and Applied Information Technology* (2015) 78, 3: 431.

Development of Printed Sensors for Shoe Sensing Applications

Anindya Nag, Shilun Feng, Subhas Mukhopadhyay, *Fellow, IEEE* and Jürgen Kosel

Abstract—The paper presents the design and implementation of a low-cost shoe sensing system using laser-induced graphene sensors. Commercial polymer films were laser-induced to photo-thermally form graphene, which was then used as electrodes on Kapton tapes to form sensor patches. Experiments were then conducted with these sensor prototypes to validate its functionality as pressure sensors to be used in shoe sensing system. Different weights were tested with the developed system to ensure the capability of these sensor patches to be used as pressure sensing. The results look promising to be a system for monitoring the movement of a person wearing a shoe containing these low-cost pressure sensors.

Keywords— *Graphene; Sensor; Laser writing; Pressure; Shoe sensing system;*

I. INTRODUCTION

The use of sensors to improve the quality of life has been one of the primary goals for researchers in the current world. After the introduction of sensors into the application world [1], one of the goals was to make the use of the sensors to improve the quality of life. This needed continuous improvement of the performance of the sensors based on their size, linear range, sensitivity, power consumption, etc. Today, researchers all over the world are trying to develop different kinds of sensors having optimized performance. One of the primary constraints on the fabrication of sensors is the cost of production. It is generally noted that even though the cost of each sensor commercially available in the market is low, the equipment required to fabricate the sensors is very low. This includes the required number of steps, cost of the raw materials, cost associated with the equipment processing the raw materials, etc. These constraints increase the overall cost of each sensor. The work on reducing the cost constraint is being dealt by the researchers all over the world by addressing the techniques and raw materials for production. This paper presents one of the techniques to generate highly efficient low-cost capacitive sensors.

The structure of the sensors has been changing with time. Due to the popularity of sensors with semi-conductive substrates, silicon sensors have been used to a large extent. Even though these sensors served a lot of applications, there were some disadvantages like the high raw material cost, high power consumption and brittle nature of the sensors associated with the sensors.

Anindya Nag, Shilun Feng, and Prof. Subhas Mukhopadhyay are with Faculty of Science and Engineering, Macquarie University, Sydney, Australia. Prof. Jürgen Kosel is with Computer Electrical and Mathematical Sciences and Engineering Division, King Abdullah University of Science and Technology, Saudi Arabia.

(Email: anindya1991@gmail.com)

For these reasons, alternating materials have been processed with to develop sensors better than the existing ones. Sensors with flexible materials are one popular choice [2] that is being developed nowadays for its distinct advantages over the rigid ones. Lower cost, smaller size, better electrical and mechanical properties, higher efficiency in terms of sensitivity are some of the attributes that the sensors with flexible substrates have an advantage over the rigid ones. Even though there are many materials that are used to develop the substrates of the flexible sensors, some of the common ones are the polymer materials like PDMS [3], PET [4], PI [5], PMMA [6], etc. The processing of these materials has been done in different ways to develop sensor prototypes for specific applications. For these substrate materials, different conductive materials like carbon [7], silver [8], gold [9], aluminum [10], etc. have been used to develop the electrodes of the sensor. Similarly, different processing techniques like photolithography [11], screen printing [12], laser cutting [13] have been utilized to develop the sensors. The use of a particular technique depends on the resolution of the electrode and substrate thickness of the final sensor prototype. This paper describes the use of laser writing technique on polymer films to develop the conductive material for the electrodes [14]. The use of laser processing method to develop flexible sensors has been advantageous over other processes in many ways like less sample preparation time, the absence of any clean room requirements, smooth cuts, and non-requirement of any post-processing steps. This paper provides a two-step process to develop graphene sensors by using the laser writing technique to photo-thermally convert a polymer film to develop graphene, which was then used as electrodes on a sensor patch for experimental purposes. The use of graphene has increased exponentially in the last decade or so [15] after its recognition to have excellent electrical, mechanical and thermal properties. Graphene, is an allotrope of carbon [16], has been largely used as electrodes in a sensor. Few of the major applications of graphene over the years have been its uses in micro-capacitors [17, 18], strain sensors [19, 20] and electrochemical sensors [21, 22]. The electrode of the sensor shown in this paper is an extension of strain sensor where an external pressure is applied by the sciatic area of the feet over the sensing area of the patch to analyze the functionality of the graphene sensors to be used in a shoe sensing system. The sensors were attached to the sole of a shoe along with the placement of the attached conditioning circuit placed on the top of the shoelaces. There has been extensive work done on the development of shoe sensing systems [23-25] in recent years. Scientists all over the world have tried different ways of developing shoe sensors for tackling different problems related to walking posture [26, 27], and gait analysis [23, 28-

30]. Among these vast topics covered by shoe sensors, one of the popular choices has been the use of pressure sensors in shoe sensing systems [31]. Pressure sensors have been placed on different regions [32, 33] of a shoe to determine the force exerted on that particular area while walking, running, etc. The use of shoe sensors has extensively covered different aspects till now. But there are certain disadvantages associated with these mentioned systems. Starting from the high fabrication cost of the systems, the developed systems are either very complex or require specialized condition and people to operate it. A simplified system is yet to be developed to date. The simplification of the system lies in the low cost of the processed raw materials to the simplified signal conditioning circuit to process the output of the sensor. The work described in this paper showcases the utilization of low-cost graphene sensor prototypes as pressure sensor patches to determine the walking of a person by analyzing the pressure exerted on the sensing area of the patch. This change in pressure while walking would be processed by a signal conditioning circuit and sent to the monitoring unit for further analysis.

II. FABRICATION OF THE SENSOR PATCHES

The fabrication process was carried out in the laboratory environment at constant temperature (25°C) and humidity (RH 50%) conditions. Low-cost commercial polymer films (Zibo Zhongnan Plastics Co., Ltd.) were considered as the raw material for developing the electrode material. Figure 1 shows the schematic diagram of the overall fabrication process. The laser writing is done on the PI films generated graphene according to the assigned design of the laser system. This conductive material was transferred to sticky tapes for using it as electrodes on a sensor patch. Figures 2(1) -2(4) shows individual steps of the fabrication process. The polymer film was attached to a glass substrate with biocompatible tapes (3M 810D Ruban Magique^{MC}) before placing it on the laser platform to restrict its movement during the laser induction process. Universal Laser Systems [34] was used to perform the laser induction process. Proper measurements were taken to exhaust the residual gases generated during the process. The optimization of the designed patterns was done by varying the given laser parameters. The designing of the electrodes was done on Coral DRAW, software that was integrated with the laser system. Three of the laser parameters, namely power (W), speed (m/min) and z-axis (mm) were varied to optimize the design of the electrodes.

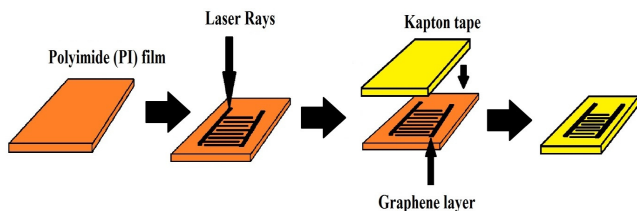


Figure 1: Schematic diagram of the fabrication steps of laser-induced graphene sensors.

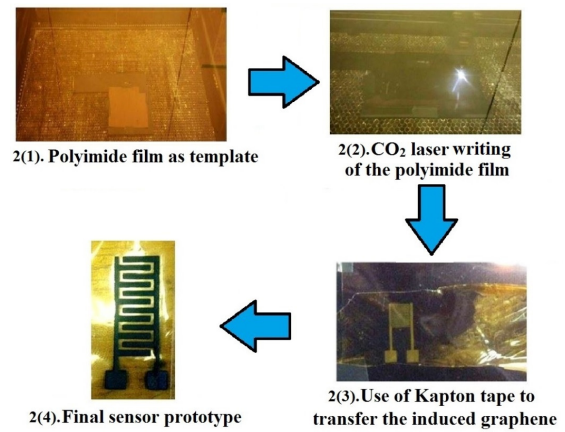


Figure 2: Individual steps for the fabrication of graphene sensor.

The power is defined as the amount of the energy of the laser exerted from the nozzle. Speed can be defined as the rate of movement of laser nozzle over the sample substrate. Z-axis defined the distance of the laser nozzle with the platform to adjust the focal point of the laser beam. The optimized parameters for this process were 9 W, 70 m/min, 1 mm. The laser induction process caused the breakage of the sp^3 hybridized C-C bonds of the PI film to form sp^2 hybridized C-C bonds in graphene. It is because graphene was generated in a power form, it would be really difficult to use it as electrodes in any sensor unless any stickiness was provided to hold the graphene. So, Kapton tapes were used for this purpose to transfer this graphene powder and use it as electrodes. Even though the commercial polymer films and Kapton tapes are of the same material (PI), there were two specific reasons for choosing the former material over the later one to develop the patches. The stickiness of the Kapton tapes would have tampered with the design and conductivity of the electrodes. The transfer of the graphene powder was done very carefully to preserve the design the electrodes. The Kapton tapes were placed over the graphene powder and manually pressed, starting from the sensing area of the sensor to the bonding pads. The conductivity and short-circuit tests were done before and after the transfer. The conductivity of the induced graphene was very high ($\sim 10^4$ S/m). The difference in conductivities between the induced and transferred graphene was less than 20 mS/m. The Kapton tapes with the transferred graphene were used as sensor patches for experimental purposes. The SEM images of the transferred graphene of one of the electrode fingers of its side and tip are shown in Figures 3 and 4 respectively. It is seen from the images that the electrode fingers of the transferred graphene came off smooth on the Kapton tapes. The edges of the electrodes were also perpendicular to the surface for which there was no requirement of any post-processing steps. The advantages of these developed patches are the high conductivity of the electrodes and the flexibility of the sensor patches. The electrical conductivity and bending diameter of the patches are $\sim 10^4$ S/m, and 6 mm respectively. Figure 5 shows the front and rear view of the final sensor patch. Six pairs of interdigitated fingers were present on the sensing area with an

interdigital gap of 200 microns. The sensing surface area was 96 mm² with a length of 500 microns and a width of 100 microns respectively.

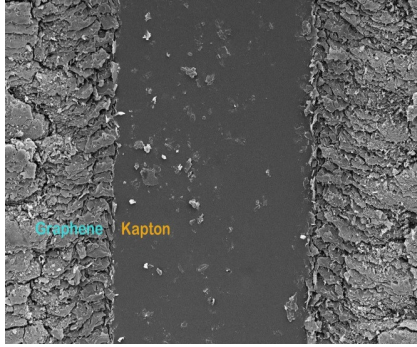


Figure 3: SEM image of top-view of the transferred graphene on Kapton tapes depicting the edges of the electrode fingers.

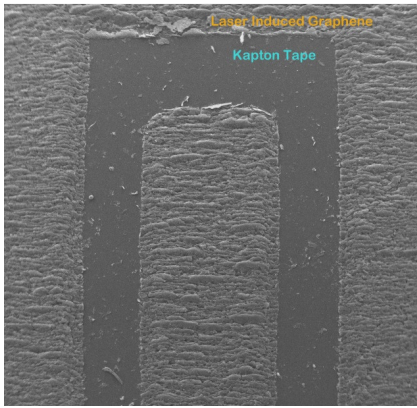


Figure 4: SEM image of top-view of the transferred graphene on Kapton tapes depicting one of the electrodes of the sensor.

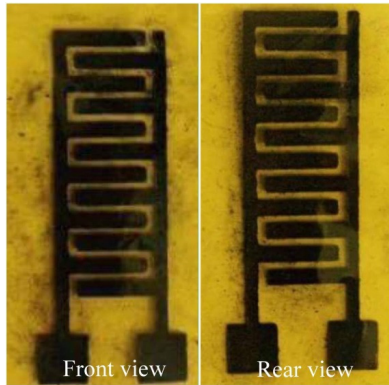


Figure 5: Front and rear view of the final fabricated sensor patch.

III. WORKING PRINCIPLE OF THE ELECTRODES

The electrodes of the developed sensor patches worked on the principle of deformation experienced by flexible sensors. Figure 6 shows the normal and expanded form of the sensor patch of which the latter is caused when a pressure is exerted on the patch. The deformation of the patch causes a change in

the resultant current flowing through the sensor when an electric field is applied to it.

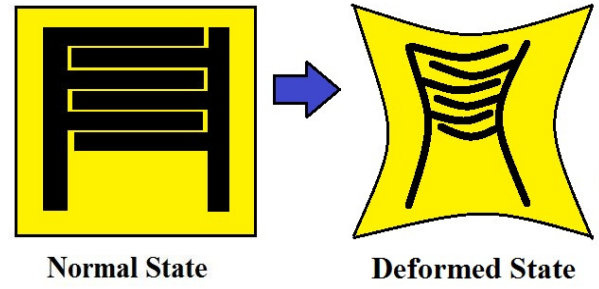


Figure 6: Schematic diagram depicting the change in structure from to normal to deformed state.

This change in current can be analyzed from schematic diagram shown in figure 7 [35]. It is seen from the figure that the R_{sense} and C_{sense} are the real (R) and imaginary (X) part of the impedance respectively. When any pressure is applied to the sensor patch, the resultant area (A) and interdigital distance (d) changes, thus changing the reactive response of the sensor. This change can be determined by the above equations:

$$V_{sense} = I_{in} * R_{series} \quad (1)$$

$$Z_{eq} = V_{in}/I_{in} = (V_{in}/V_{sense}) * R_{series} \quad (2)$$

$$X_{sense} = Z * \sin\phi \quad (3)$$

$$R_{sense} = Z * \cos\phi - R_{series} \quad (4)$$

$$\text{And, } X_{sense} = w * C_{sense} \quad (5)$$

$$\text{where, } C_{sense} = \frac{\epsilon_0 * \epsilon_r * A}{d} \quad (6)$$

where, V_{sense} is defined as the voltage across the series resistance.

Z_{eq} is the equivalent impedance.

V_{in} is the input voltage of the circuit.

ϕ is the phase angle between the input voltage and input current.

C_{sense} is the output capacitance in Farads, F.

ϵ_0 is the absolute permittivity ($\epsilon_0 = 8.854 * 10^{-12}$ F/m).

ϵ_r is the relative permittivity.

A is the effective area.

d is the effective interdigital distance between two consecutive electrodes.

The change in capacitance can be defined as the change caused due to the resultant area and interdigital distance.

$$\Delta C_{sense} = f(\Delta A, \Delta d) \quad (7)$$

$$\Delta X_{sense} = w * \Delta C_{sense} \quad (8)$$

where, ΔA and Δd are the resultant areas and interdigital distance caused due to the deformation.

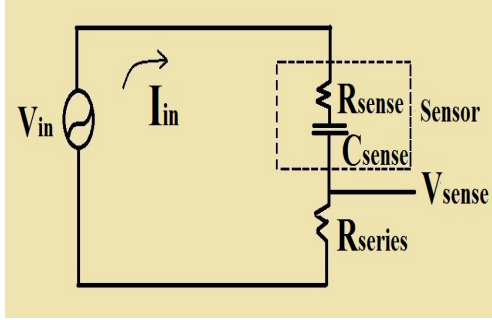


Figure 7: Schematic diagram of the electrical circuitry showing the change in current due to the change in output (sensed) impedance [35].

IV. EXPERIMENTAL RESULTS

Initially, the profiling of the sensor patch was done to determine the linearity of the sensor patches. This was done by testing the sensor patches with small weights to analyze the changes happening due to the deformation of the sensor patch in terms of resistance and voltage. This was followed by testing the sensor patches with an LCR meter.

a. Profiling of the sensor

The sensor patch was initially tested at different weights to determine its response in terms of voltage and resistance values. Figures 8 and 9 depict the response of the sensor towards different weights ranging from 1kg to 10kg.

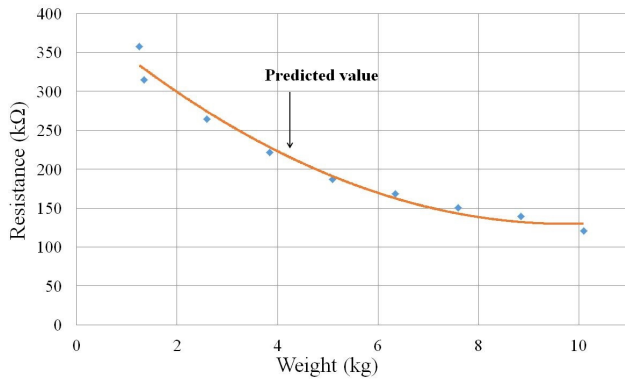


Figure 8: Response of the sensor patch to different weights in terms of resistance.

Even though it is known that the average weight of a person lies between 50 kg- 70kg, which states that the weight of a single foot would be approximately ± 25 kg, the limitation of the maximum weight to test the sensor was 10kg was because

of two reasons. Firstly, when a person walks, the weight of the whole leg (25 kg) is not on the sensor patch. The weight of the leg is distributed over the whole feet. And secondly, the idea to test the sensor with the weights is to validate the functionality towards pressure measurement. It is seen from figures 8 and 9 that the sensor is capable of responding in almost a linear way to different weights exerted on the sensing area of the patch. It is also seen from these two figures that the predicted value for the change in resistance and voltage readings of the sensor patches were very close to the actual values.

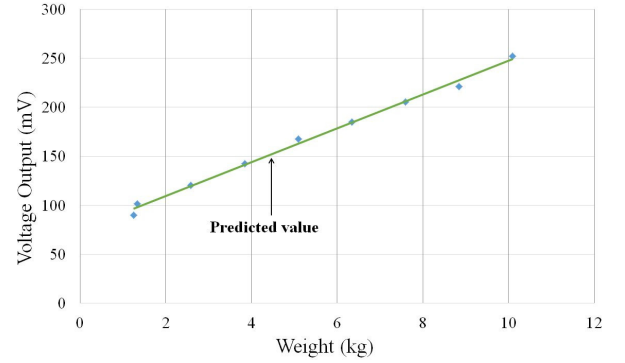


Figure 9: Response of the sensor patch to different weights in terms of voltage.

b. Experimental results with LCR meter

The sensor patch was tested with an LCR meter to validate its functionality for using it as a shoe sensing system. Due to the high conductivity of the electrodes, the sensor was capable of recognizing even pressures of small magnitude exerted on the sensing area of the patch. Figure 10 shows the connection of the LCR meter to the sensor. The change in impedance was analyzed by a HIOKI IM3536 High Precision Tester connected with Kelvin probes which in turn was connected to the bonding pads of the sensor patch. Due to the high flexibility of the patches, it was difficult to connect the Kelvin probes to the bonding pads. So, single-stranded flexible wires were connected to the bonding pads by a conductive carbon paint (BARE conductive® ELECTRIC PAINT), which in turn was connected to the Kelvin probes. A voltage of 1 Vrms was provided as an input to the sensor patch. The High Precision Tester was connected to a laptop via a USB cable to monitor the changes occurring with the exertion of pressure on the sensors in an alternative way. The data was collected in Microsoft Excel via automatic data acquisition algorithm. The experimental set-up is shown in figure 10. This figure shows the connection of the sensor patches to the High Precision Tester to the sensor patch. This was initially done to validate the functionality of the sensor patches to be used as pressure sensors in the shoe sensing system. Electrochemical Impedance Spectroscopy (EIS) was the algorithm associated with the High Precision Tester. EIS is a standard technique [36] used to characterize a material based on specific parameters. Among the different EIS technique available [37],

frequency response analyzer (FRA) [38] is one of the popular ways to characterize the material over the range of frequencies. This technique has been used for the characterization of different materials including human physiological parameters [39], food products [40], salinity testing [41] and tactile sensing [42]. The advantages of using this technique are its simple, non-invasive and single-sided testing [43]. Figures 11 and 12 show the responses of the sensor patches for the force exerted on the sensor patch in a slow and rapid motion respectively. Two situations, “a” and “b”, allocated for the two situations depicted in the figures represents the relaxed condition or pressure free condition and forced condition or the presence of the feet on the sensing patch condition respectively. The frequency values were swept between 2 kHz to 10 kHz to analyze the change in the reactance values. The sensor patch did not respond well to the frequencies below 2 kHz. One of the reasons for this behavior could be the connection of the Kelvin probes of the LCR meter to the single-stranded wires attached to bonding pads of the sensor patch. The reason for the decrease in reactance occurring due to the forced state can be attributed to the change in the dimensions of the sensor patch causing a change in C_{sense} (equation (6)) which as a result changes X_{sense} (equation (5)). It is seen from the figures that the sensor patch is capable of recognizing the two situations very distinctively. Repetitive movements were done for both the situations to ensure the repeatability of the response of the sensor patches.

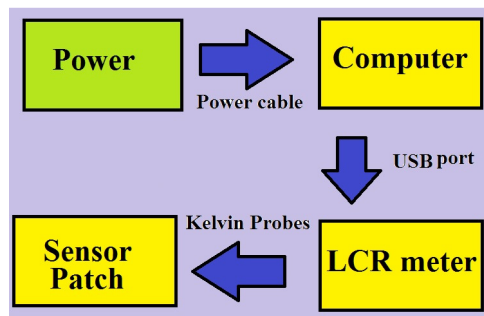


Figure 10: Schematic diagram depicting the process of data collection.

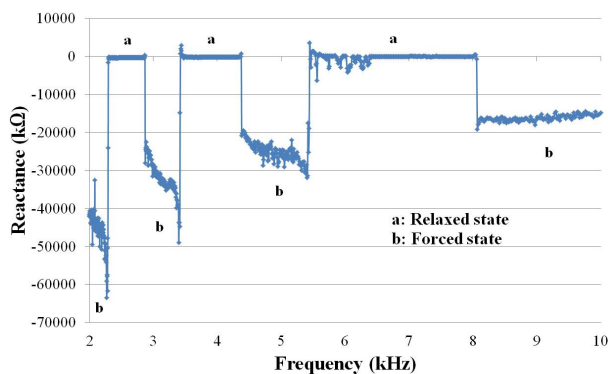


Figure 11: Response of the sensor patch in terms of reactance and frequency connected with the LCR meter with slow-motion expressed in the forced and relaxed state.

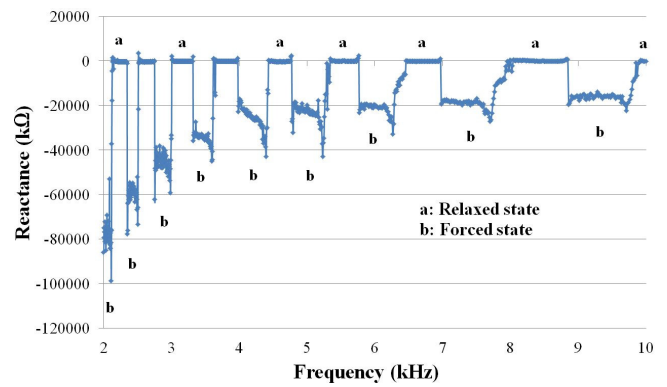


Figure 12: Response of the sensor patch in terms of reactance and frequency connected with the LCR meter with rapid motion expressed in the forced and relaxed state. is [7].

After testing the response of the sensor patches for repetitive cycles after in several experiments, they proved to be robust and sturdy in terms of wear and tear for this application. Also, the sensor patches had no memory effects in their responses after they were changed several times from one shoe to another while applying different amount of pressure.

V. CONCLUSION

This paper is an idealization of shoe sensing system with low-cost, laser-induced graphene sensors. The sensor patches were developed by using the electrodes formed by the photo-thermal conversion of the commercial polymer films. These sensor patches were then tested with the LCR meter to validate its functionality as pressure sensors which can be used for detection of movement for a shoe sensing system. However, there are some issues faced during the experimental procedures that should be rectified. Firstly, the range of sensor responses from the LCR meter in terms of reactance was not same during each cycle. This could be confusing for the monitoring unit once the reactance values for the forced state saturates to the values close to the relaxed state. Also, even though the sensor patches are very flexible in nature, there has to be testing done for their behavior and change in response with time. One of the ways is to implement a thresholding phenomenon for this purpose to clearly distinguish between the relaxed and the forced state. Secondly, even though the weight of different volunteers were tested with this system, all of them were perfectly normal having a proper walking posture. Thirdly, the use of LCR meter to validate this system should be replaced with an impedance analyzer embedded with a portable microcontroller based system to use it for real-time applications. The experiments with patients having an abnormal walking posture should be tried out to further validate this system. The rectification of these issues would be done and reported in near future work.

ACKNOWLEDGMENT

The authors would like to acknowledge King Abdullah University of Science and Technology (KAUST), Saudi Arabia to provide the research facilities to fabricate the sensor patches.

REFERENCES

- [1] S. M. Sze, *Semiconductor sensors*: Wiley New York, 1994.
- [2] A. Nag, S. C. Mukhopadhyay, and J. Kosel, "Wearable Flexible Sensors: A Review," *IEEE Sensors Journal*, 2017.
- [3] J.-H. Moon, D. H. Baek, Y. Y. Choi *et al.*, "Wearable polyimide-PDMS electrodes for intrabody communication," *Journal of Micromechanics and Microengineering*, vol. 20, no. 2, pp. 025032, 2010.
- [4] M.-x. Jing, C. Han, M. Li *et al.*, "High performance of carbon nanotubes/silver nanowires-PET hybrid flexible transparent conductive films via facile pressing-transfer technique," *Nanoscale research letters*, vol. 9, no. 1, pp. 1-7, 2014.
- [5] Y. Qin, Q. Peng, Y. Ding *et al.*, "Lightweight, superelastic, and mechanically flexible graphene/polyimide nanocomposite foam for strain sensor application," *ACS nano*, vol. 9, no. 9, pp. 8933-8941, 2015.
- [6] Y. Wang, R. Yang, Z. Shi *et al.*, "Super-elastic graphene ripples for flexible strain sensors," *ACS nano*, vol. 5, no. 5, pp. 3645-3650, 2011.
- [7] B. Natarajan, N. D. Orloff, R. Ashkar *et al.*, "Multiscale metrologies for process optimization of carbon nanotube polymer composites," *Carbon*, vol. 108, pp. 381-393, 2016.
- [8] S. Yao, and Y. Zhu, "Wearable multifunctional sensors using printed stretchable conductors made of silver nanowires," *Nanoscale*, vol. 6, no. 4, pp. 2345-2352, 2014.
- [9] S. Gong, W. Schwalb, Y. Wang *et al.*, "A wearable and highly sensitive pressure sensor with ultrathin gold nanowires," *Nature communications*, vol. 5, 2014.
- [10] W. Hu, S. N. Zhang, X. Niu *et al.*, "An aluminum nanoparticle-acrylate copolymer nanocomposite as a dielectric elastomer with a high dielectric constant," *Journal of Materials Chemistry C*, vol. 2, no. 9, pp. 1658-1666, 2014.
- [11] S. Khumpuang, H. Maekawa, and S. Hara, "Photolithography for minimal fab system," *IEEE Transactions on sensors and micromachines*, vol. 133, no. 9, pp. 272-277, 2013.
- [12] S. Khan, L. Lorenzelli, and R. S. Dahiya, "Bendable piezoresistive sensors by screen printing MWCNT/PDMS composites on flexible substrates," pp. 1-4.
- [13] X. Li, and S. Garner, "Laser cutting of flexible glass," p. ATu3L.1.
- [14] J. Lin, Z. Peng, Y. Liu *et al.*, "Laser-induced porous graphene films from commercial polymers," *Nature communications*, vol. 5, 2014.
- [15] A. K. Geim, and K. S. Novoselov, "The rise of graphene," *Nature Materials*, vol. 6, no. 3, pp. 183-191, 2007.
- [16] W.-W. Liu, S.-P. Chai, A. R. Mohamed *et al.*, "Synthesis and characterization of graphene and carbon nanotubes: A review on the past and recent developments," *Journal of Industrial and Engineering Chemistry*, vol. 20, no. 4, pp. 1171-1185, 2014.
- [17] Z. Peng, R. Ye, J. A. Mann *et al.*, "Flexible boron-doped laser-induced graphene microsupercapacitors," *ACS nano*, vol. 9, no. 6, pp. 5868-5875, 2015.
- [18] H.-P. Cong, X.-C. Ren, P. Wang *et al.*, "Flexible graphene-polyaniline composite paper for high-performance supercapacitor," *Energy & Environmental Science*, vol. 6, no. 4, pp. 1185-1191, 2013.
- [19] Y. Wang, L. Wang, T. Yang *et al.*, "Wearable and highly sensitive graphene strain sensors for human motion monitoring," *Advanced Functional Materials*, vol. 24, no. 29, pp. 4666-4670, 2014.
- [20] S.-H. Bae, Y. Lee, B. K. Sharma *et al.*, "Graphene-based transparent strain sensor," *Carbon*, vol. 51, pp. 236-242, 2013.
- [21] A. T. Lawal, "Synthesis and utilisation of graphene for fabrication of electrochemical sensors," *Talanta*, vol. 131, pp. 424-443, 2015.
- [22] S. Wu, Q. He, C. Tan *et al.*, "Graphene-based electrochemical sensors," *Small*, vol. 9, no. 8, pp. 1160-1172, 2013.
- [23] S. J. M. Bamberg, A. Y. Benbasat, D. M. Scarborough *et al.*, "Gait analysis using a shoe-integrated wireless sensor system," *IEEE Transactions on Information Technology in Biomedicine*, vol. 12, no. 4, pp. 413-423, 2008.
- [24] E. S. Sazonov, G. Fulk, J. Hill *et al.*, "Monitoring of posture allocations and activities by a shoe-based wearable sensor," *Biomedical Engineering, IEEE Transactions on*, vol. 58, no. 4, pp. 983-990, 2011.
- [25] C. E. Judy, L. D. Galuppo, J. R. Snyder *et al.*, "Evaluation of an in-shoe pressure measurement system in horses," *American journal of veterinary research*, vol. 62, no. 1, pp. 23-28, 2001.
- [26] H. Jonely, J.-M. Brismée, P. S. Sizer *et al.*, "Relationships between clinical measures of static foot posture and plantar pressure during static standing and walking," *Clinical Biomechanics*, vol. 26, no. 8, pp. 873-879, 2011.
- [27] S. Yang, and Q. Li, "Inertial sensor-based methods in walking speed estimation: A systematic review," *Sensors*, vol. 12, no. 5, pp. 6102-6116, 2012.
- [28] A. Y. Benbasat, S. J. Morris, and J. A. Paradiso, "A wireless modular sensor architecture and its application in on-shoe gait analysis," pp. 1086-1091.
- [29] M. Gabel, R. Gilad-Bachrach, E. Renshaw *et al.*, "Full body gait analysis with Kinect," pp. 1964-1967.
- [30] B. Mariani, M. C. Jimenez, F. J. Vingerhoets *et al.*, "On-shoe wearable sensors for gait and turning assessment of patients with Parkinson's disease," *Biomedical Engineering, IEEE Transactions on*, vol. 60, no. 1, pp. 155-158, 2013.
- [31] K. F. Lei, K.-F. Lee, and M.-Y. Lee, "Development of a flexible PDMS capacitive pressure sensor for plantar pressure measurement," *Microelectronic Engineering*, vol. 99, pp. 1-5, 2012.
- [32] "Shoe Insole Sensor measuring pressure," <https://www.2mel.nl/technology-incubation/shoe-insole-sensor-pressure-shear-force-9dof/>. Last accessed on 01.02.2018.
- [33] S. Sungkarat, B. E. Fisher, and A. Kovindha, "Efficacy of an insole shoe wedge and augmented pressure sensor for gait training in individuals with stroke: a randomized controlled trial," *Clinical rehabilitation*, vol. 25, no. 4, pp. 360-369, 2011.
- [34] "Universal Laser Systems," <https://www.ulsinc.com/resources/laser-safety>. Last accessed on 01.02.2018.
- [35] A. Nag, A. I. Zia, X. Li *et al.*, "Novel Sensing Approach for LPG Leakage Detection: Part I—Operating Mechanism and Preliminary Results," *IEEE Sensors Journal*, vol. 16, no. 4, pp. 996-1003, 2016.
- [36] M. E. Orazem, and B. Tribollet, *Electrochemical impedance spectroscopy*: John Wiley & Sons, 2011.
- [37] J. R. Macdonald, and E. Barsoukov, "Impedance spectroscopy: theory, experiment, and applications," *History*, vol. 1, no. 8, 2005.
- [38] M. Ordóñez, M. O. Sonnaillon, J. E. Quaiçoe *et al.*, "An embedded frequency response analyzer for fuel cell monitoring and characterization," *IEEE Transactions on Industrial Electronics*, vol. 57, no. 6, pp. 1925-1934, 2010.
- [39] A. Nag, S. C. Mukhopadhyay, and J. Kosel, "Flexible carbon nanotube nanocomposite sensor for multiple physiological parameter monitoring," *Sensors and Actuators A: Physical*, vol. 251, pp. 148-155, 2016.
- [40] S. C. Mukhopadhyay, and C. P. Gooneratne, "A novel planar-type biosensor for noninvasive meat inspection," *Sensors Journal, IEEE*, vol. 7, no. 9, pp. 1340-1346, 2007.
- [41] A. Nag, S. C. Mukhopadhyay, and J. Kosel, "Sensing System for Salinity Testing Using Laser-induced Graphene Sensors," *Sensors and Actuators A: Physical*, 2017.
- [42] A. Nag, S. C. Mukhopadhyay, and J. Kosel, "Tactile Sensing From Laser-Ablated Metallized PET Films," *IEEE Sensors Journal*, vol. 17, no. 1, pp. 7-13, 2016.
- [43] E. Azzarello, E. Masi, and S. Mancuso, "Electrochemical impedance spectroscopy," *Plant Electrophysiology*, pp. 205-223: Springer, 2012.

A Network Simulator to Develop Wireless Networking Protocols Suited for Vital Information Collection from a Group of Exercisers

Hirofumi Ogura⁽¹⁾, Takuma Hamagami⁽²⁾, Ryusuke Miyamoto⁽³⁾, Hiroyuki Yomo⁽⁴⁾, Shinsuke Hara⁽¹⁾

(1) Graduate School of Engineering, Osaka City University,

Email: {ogura@c., hara@}info.eng.osaka-cu.ac.jp

(2) Oki Electric Industry Co., Ltd.,

Email: hamagami523@oki.com

(3) School of Science and Technology, Meiji University,

Email: miya@cs.meiji.ac.jp

(4) Graduate School of Engineering Science, Kansai University,

Email: yomo@kansai-u.ac.jp

Abstract—To develop a wireless networking protocol suited for real-time vital information collection from a group of exercisers, it is mandatory to compare the performances among different protocol candidates by experiments using a group of subjects as a matter of course. However, fair comparison is almost impossible because the experiments have no repeatability.

In this paper, we propose a software network simulator to fairly compare the performances of different networking protocols. The simulator is composed of two unique functions such as mobility model and channel model, both of which were developed through real experiments using a group of subjects. The mobility model outputs data sets for the time-series of locations of persons during different kinds of sports and exercises, and the channel model determines the channel characteristics between persons taking into consideration the transmission power, antenna pattern and blocking by other persons. We demonstrate by the simulator the performance of a wireless networking protocol using different types of antennas for the case of football game.

I. INTRODUCTION

In the field of school education, promotion of health and prevention of disease/injury are essential for schoolchildren during physical training and after-school sports club activities. On the other hand, in the field of sports, training according to athletes' scientific evidence such as vital and physical signs has proven to be effective. These health promotion, disease/injury prevention and evidence-based physical training can be realized by a real-time vital information monitoring system for a group of exercisers [1].

Wireless networking protocol plays an important role in making the real-time vital information monitoring system more reliable. To develop the best-suited wireless networking protocol, performance comparison among several protocol candidates by experiments using subjects is required as a matter of course, however, fair comparison is impossible because real experiments have no repeatability; we have to separately evaluate the performances of different protocols in different experiments.

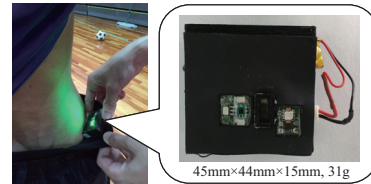


Fig. 1. A photo of the wireless vital sensor node.

To fairly compare the performances of different wireless networking protocols using the same locations and motions of persons and the same channel conditions among them, we have constructed a software network simulator. The network simulator is supported on two unique functions such as mobility model and channel model, both of which are obtained by real experiments using a group of subjects. In this paper, we present the structure of the network simulator and demonstrate by the simulator the performance of a wireless networking protocol using different types of antennas for the case of football game.

II. SYSTEM MODEL AND WIRELESS NETWORKING

We have developed a wireless vital sensor node (WSN) which can sense heart rate (HR), energy expenditure (EE) and core body temperature (CBT), and transmit the sensed data by wireless. The transceiver of the WSN is compliant with the ARIB T-108 standard of Japan which transmits signal in the 920MHz band with transmission power of 20mW and information data rate of 100kbps [2]. Figure 1 shows a photo of the developed WSN. We put the WSNs to the back waist positions of persons in a group, and a data collection node (DCN) monitors the vital information in real-time, which are collected by a networking protocol from all the persons during a sports game or an exercise in an open field. We developed a similar system where several data forwarding nodes are placed around the field, but we do not take the approach this time; without data forwarding nodes, our new system can collect vital information from all the persons by multi-hop manner,

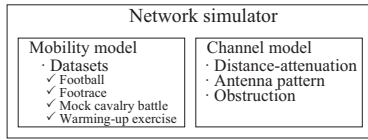


Fig. 2. Structure of the network simulator.

namely, through WSNs. Therefore, our target is to develop a reliable wireless multi-hop networking protocol suited for a variety of sports games and exercises.

III. STRUCTURE OF NETWORK SIMULATOR

Figure 2 shows the structure of the network simulator, which works on MATLAB. The mobility model stores data sets to give the time-series of the locations of persons during different kinds of sports games and exercises. The data sets are generated by applying personal identification then location tracking for the moving images [3], [4] which are obtained by experiments using a group of subjects. Even if the time-series of the locations of persons are given, the channel characteristics between persons are still unknown, so the channel model calculates the received power between transmitter and receiver nodes taking the channel and node characteristics into consideration.

A. Mobility Model

To make the wireless networking protocol reliable in the realistic applications, the mobility model data sets, which are used to evaluate the protocols, should include the motions and locations of persons with a variety of mobility. Therefore, we listed four different kinds of sports games and exercise in total, such as football, footrace, mock cavalry battle and warming-up exercise. Football game gives a mixture of low mobility and high mobility; in a football game, two team players tend to face each other spreading over the entire field. Some players show low mobility but suddenly change their directions, and other players show high mobility, chasing the ball. Footrace game gives high mobility; in a footrace game, runners show high and not-coordinated mobility. Mock cavalry battle game gives coordinated mobility; four players move forming a group. Finally, warming-up exercise gives low mobility with high density over the entire field.

To generate the mobility model data sets, we conducted video recording experiments. The experiments took place in a gymnasium where several tens of subjects performed the four kinds of sports games and exercise. As shown in Fig. 3 (a), we placed eight video camera around the floor, and recorded the sports games and exercise, where each person had his own identifier (ID) of a distinct combination of color and number of training bib. From the recorded image, each person was identified using his ID, and then his location was tracked by using his trajectories.

In this paper, we focus our attention on the performance evaluation using the simulator for football game. The football field size in the gymnasium was 57m×46m and the video recording frame rate was 30 frames per second, so the $[x, y]$ -locations of players were estimated in the area of 57m×46m

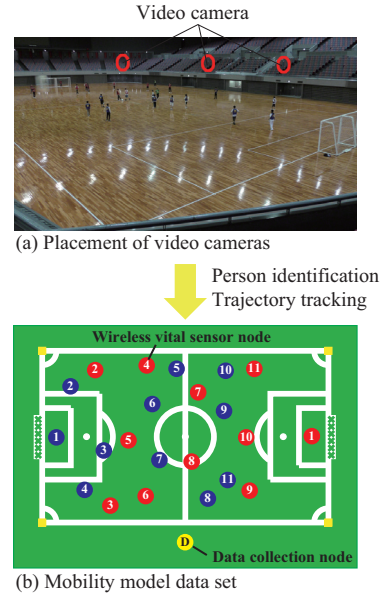


Fig. 3. Generation of the time-series of the locations of persons.

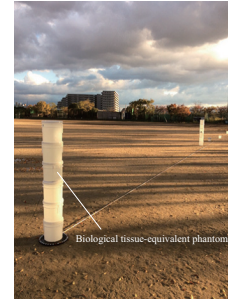


Fig. 4. A photo of the biological tissue-equivalent phantom.

with time interval of 1/30 seconds. However, the size was small as compared to the normal size of football field, so to make the size satisfy the international match standard, the estimated locations were enlarged to around 1.76 times (101.58m×81.18m), resulting in the time interval of 1/17 seconds. Fig. 3 (b) shows an example of data set output for the case of football game.

B. Channel Model

The channel characteristics between two persons, namely, two WSNs, depend on the frequency band, type of antenna giving a different radiation pattern, and signal transmission situation with or without obstacles around the channel. To keep the repeatability of experiment, we conducted experiments using liquid-type biological tissue-equivalent phantoms instead of human subjects in the outdoor playground of Osaka City University. As shown in Fig. 4, the phantom was composed of six-tiered buckets, where each bucket was made of polyethylene and contained salt solution. Note that the relative permittivity of polyethylene is 2.3, and the concentration in the solution was set to 0.18 weight% to make the electric characteristics of the phantom (relative permittivity (ϵ_r)=55.96

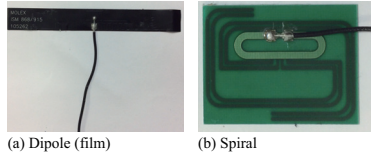
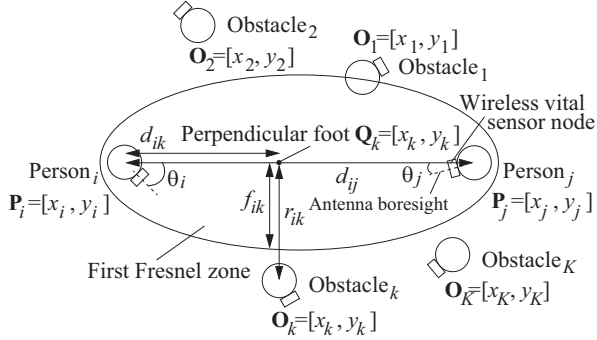


Fig. 5. Photos of the antennas.

Fig. 6. A situation where node_i is transmitting a signal to node_j.

and conductivity (σ)=0.97) closer to those of human body (ϵ_r =77.98 and σ =0.51). Table I lists the specifications of the phantom simulating an adult subject.

TABLE I
SPECIFICATIONS OF THE PHANTOM.

Length of circumference [cm]	78
Radius [cm]	12.7
Height [cm]	174
Antenna height [cm]	90

We discuss the channel models for two types of antennas; one is a dipole antenna made of film and the other is a spiral antenna, which are shown in Fig. 5. The spiral antenna was small enough to be put into the case of the WSN, but the dipole antenna was too large, so we folded both ends of the dipole antenna. In the following, we discuss the wireless propagation characteristics for the spiral antenna (in the node case), dipole antenna (folded in the node case) and dipole antenna (unfolded out of the node case).

Figure 6 shows a situation where the node of Person_i is transmitting a signal to that of Person_j while being surrounded by K obstacles. Defining the locations of Person_i, Person_j and Obstacle_k ($k = 1, 2, \dots, K$) as $\mathbf{P}_i = [x_i, y_i]$, $\mathbf{P}_j = [x_j, y_j]$ and $\mathbf{O}_k = [x_k, y_k]$, respectively, and the angle between the antenna boresight at \mathbf{P}_i (\mathbf{P}_j) and the line through \mathbf{P}_i and \mathbf{P}_j (direct path between \mathbf{P}_i and \mathbf{P}_j) as θ_i (θ_j), the received power at \mathbf{P}_j is written as

$$\mathbf{P}_j = D(\mathbf{P}_i, \mathbf{P}_j) + A(\theta_i) + A(\theta_j) + \sum_{k=1}^K B(\mathbf{O}_k, \mathbf{P}_i, \mathbf{P}_j) \quad (1)$$

where $D(\mathbf{P}_i, \mathbf{P}_j)$, $A(\theta_i)$ and $B(\mathbf{O}_k, \mathbf{P}_i, \mathbf{P}_j)$ denote the distance-attenuation, antenna pattern and obstruction factors, respectively. We characterized these three factors according to the experimental results.

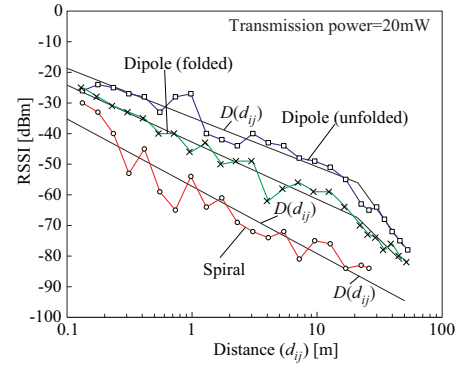


Fig. 7. Distance-attenuation characteristics.

One may think that we should add one more probabilistic term to (1) showing fading factor, but to simplify the model, we omit it in this paper.

1) *Distance-attenuation characteristic*: We measured the distance-attenuation characteristics setting $\theta_i = 0$ and $\theta_j = 0$ with no obstacles. Figure 7 shows the received signal strength indicator (RSSI), namely, the received power against the distance between \mathbf{P}_i and \mathbf{P}_j , which is given by

$$d_{ij} = \|\mathbf{P}_i - \mathbf{P}_j\|. \quad (2)$$

Note that the RSSI was averaged over the results obtained by four-time measurements.

Since metal devices and circuits in the node case cause antenna mismatch, significantly large losses of more than 5dB are observed for the folded dipole and spiral antennas, as compared to the unfolded dipole antenna. The characteristics by the dipole antennas, which transmit and receive linearly-polarized signal, can be well described by the two-path ground-reflection model [5]; the direct wave and reflected wave interfere each other, so some notches and a break point which is denoted by δ_{th} are observed in each characteristic. On the other hand, for the spiral antenna which transmits and receives right (or left) circularly polarized signal, its polarization changes from right to left (left to right) when it is reflected by the ground, so the receiver node can receive the direct signal with no reflected interference.

Taking into consideration that the distance-attenuation model should be as simple as possible, from the experimental results, we finally modeled the distance-attenuation characteristic as

$$D(\mathbf{P}_i, \mathbf{P}_j) = D(d_{ij}) = \begin{cases} \alpha_1 d_{ij} + \beta_1 \text{ [dBm]} & (0 \leq d_{ij} \leq \delta_{th}) \\ \alpha_2 d_{ij} + \beta_2 \text{ [dBm]} & (\delta_{th} < d_{ij}) \end{cases} \quad (3)$$

where α_1 , α_2 , β_1 , β_2 and δ_{th} are the parameters. The values of the parameters are listed in Table II.

2) *Antenna pattern characteristic*: Figure 8 shows the antenna pattern characteristic, which was also measured in the outdoor playground of Osaka City University. The main lobe of the folded dipole antenna is slightly broader than that of

TABLE II
VALUES OF THE PARAMETERS [DBM].

	α_1	α_2	β_1	β_2	δ_{th}
Dipole (unfolded)	-1.58	-4.21	-35.03	0.614	22.06
Dipole (folded)	-1.84	-3.00	-42.82	-27.15	22.06
Spiral	-2.17		-57.24		

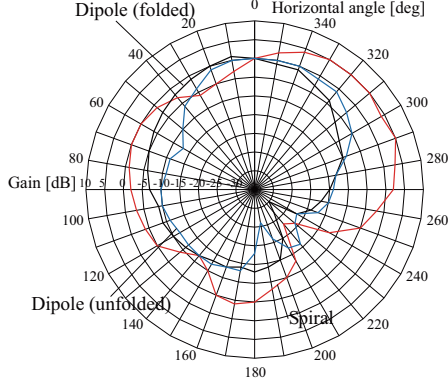


Fig. 8. Antenna pattern characteristics.

the unfolded dipole antenna, and that of the spiral antenna is broader than those of the dipole antennas.

We finally modeled $A(\theta_i)$ and $A(\theta_j)$ as not an equation but the obtained data in Fig. 8.

3) *Obstruction characteristic*: First of all, as shown in Fig. 6, assuming the perpendicular foot of \mathbf{O}_k on the direct path between \mathbf{P}_i and \mathbf{P}_j as \mathbf{Q}_k , we define its distance from \mathbf{P}_i and its distance from \mathbf{O}_k respectively as d_{ik} and r_{ik} :

$$d_{ik} = \|\mathbf{Q}_k - \mathbf{P}_i\| \quad (4)$$

$$r_{ik} = \|\mathbf{Q}_k - \mathbf{O}_i\|. \quad (5)$$

Furthermore, we define the radius of the first Fresnel zone at \mathbf{Q}_k as f_{ik} :

$$f_{ik} = \sqrt{\lambda \frac{d_{ik}(d_{ij} - d_{ik})}{d_{ij}}} \quad (6)$$

where λ denotes the wavelength of the wireless signal [5].

We measured the obstruction characteristics setting $\theta_i = 0$ and $\theta_j = 0$ with one obstacle. Figure 9 shows the gain against r_{ik} normalized by f_{ik} . We can see from the figure that the obstacle gives a large loss when it is in the first Fresnel zone whereas it gives almost no loss when it is out of the zone. From the experimental result, we finally approximated the gain *per obstacle* as

$$B(\mathbf{O}_k, \mathbf{P}_i, \mathbf{P}_j) = D(r_{ik}, f_{ik}) = \begin{cases} -4 \text{ [dB]} & (0 \leq r_{ik}/f_{ik} \leq 1) \\ 0 \text{ [dB]} & (1 < r_{ik}/f_{ik}) \end{cases} \quad (7)$$

Note that the model gives much larger losses as compared to the measured values. Therefore, the network simulator evaluates a worst-case performance for wireless networking protocol.

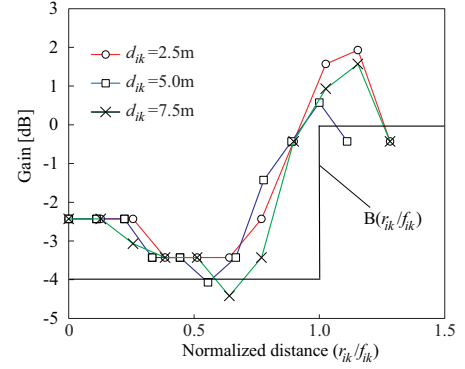


Fig. 9. Obstruction characteristics.

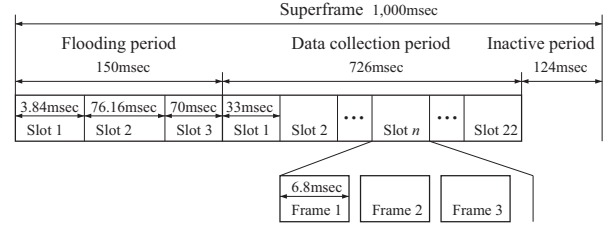


Fig. 10. Structure of superframe.

IV. PERFORMANCE EVALUATION USING THE NETWORK SIMULATOR

Now that we have completed the network simulator, in this section, we will evaluate the performance of a wireless networking protocol using the simulator. To achieve reliable vital information collection, we have designed a wireless networking protocol limiting the number of hops, which employs flooding for parent node selection period whereas time division multiple access (TDMA) for vital information collection period to guarantee no frame collision. In the following, we will investigate the effect of antenna on the performance for the flooding/TDMA protocol for the networking system which is composed of one DCN and twenty two WSNs.

A. Outline of the Flooding/TDMA Protocol

Figure 10 shows the structure of the superframe. Each superframe is initiated by a beacon broadcast by the DCN.

In the flooding period, when any WSN receives a beacon broadcast by the DCN or any other WSN, it can re-broadcast a beacon showing its own node ID and its own hop count. The maximum number of hops is limited to three in this paper, so the flooding period is divided into three slots. In addition, every time when a WSN receives multiple beacons from other WSNs within a certain period, it measures the RSSI for each received beacon, and it memorizes the node ID which gives the largest RSSI as its parent node.

On the other hand, for football game, the data collection period is divided into 22 slots. In the network association process, the DCN has assigned unique numbers to all WSNs, which correspond to the frame numbers in the data collection period. Therefore, each slot has been assigned to a distinct

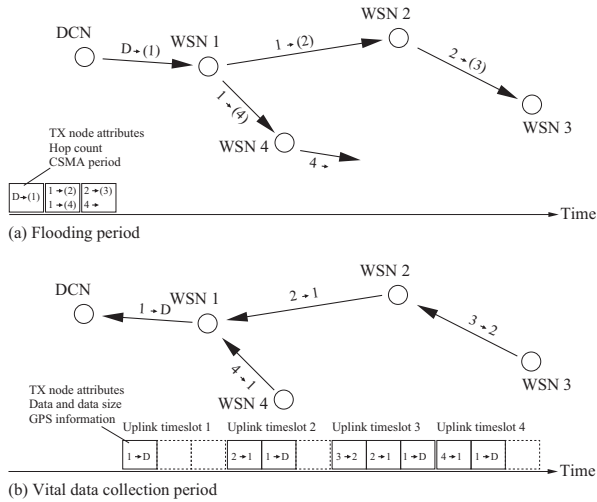


Fig. 11. Flooding and data collection (TDMA) periods.

TABLE III
SPECIFICATIONS OF COMPUTER SIMULATION.

System model	
Transmission power	13dBm
Noise power	-111.4dBm
Frequency band	920MHz
Data transmission rate	100kbps
Modulation/demodulation	NCFSK
MAC	CSMA
Networking	Flooding/TDMA
Maximum number of hops allowed	3
Beacon length	48Bytes
Frame length	85Bytes
Mobility model	
Type	Football game
Field size	101.58m×81.18m
Location update time	1/17seconds
Channel model	
Distance-attenuation	Eq.(3) and Table II
Antenna pattern	Figure 8
Obstruction	Eq.(7)

WSN, in other words, the n th slot ($n = 1, 2, \dots, 22$) has been assigned to the WSN with ID of n , which is referred to as “a slot owner.” In each slot, frame transmission is initiated only by its slot owner, and a transmitter node unicasts a frame to its parent node. Figure 11 shows examples of the flooding and data collection periods.

B. Evaluation Result

Table III shows the specifications of computer simulation using the network simulator, and Fig. 12 shows the evaluation result. As compared to the unfolded dipole antenna, the folded dipole antenna has a slightly broader main lobe but gives a larger transmission power loss, so its data collection rate (DCR) is lower; the DCR of the folded dipole antenna=0.854 whereas that of the unfolded dipole antenna=0.965. On the other hand, as compared to the dipole antennas, the spiral antenna has a much broader main lobe but gives a much larger transmission power loss, so its DCR is much lower; the DCR of the spiral antenna=0.407.

Around 5% of data are still lost even for the unfolded dipole antenna giving the highest DCR. Even when a WSN selects

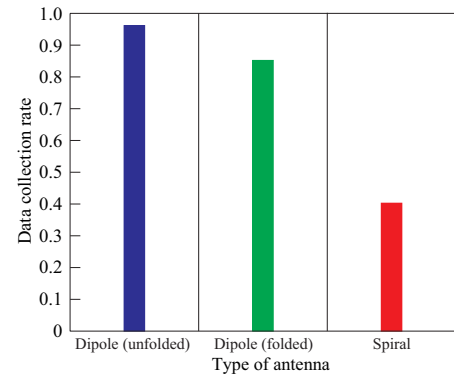


Fig. 12. Data collection rate.

another WSN with the largest RSSI, namely, a closer WSN as its parent node, if the parent WSN changes its direction during 1,000msec-period, the frame from the WSN cannot reach its parent WSN any more, since the antenna pattern is not omnidirectional.

V. CONCLUSIONS

In this paper, we have presented the design and construction of a software network simulator for real-time vital information from a group exercisers, and have demonstrated the performance of a flooding/TDMA protocol using different types of antennas for a football game scenario. The computer simulation results on the effect of antenna type have revealed that, since the tiny node case gives the installed antenna a directivity, selection of parent node is a fatal problem for networking exercisers. Using the developed network simulator, we also have evaluated the performance of a multi-channel flooding-type networking protocol for the same purpose. Its detail is shown in [6].

ACKNOWLEDGMENT

The research was supported by the Research and Development of Innovative Network Technologies to Create the Future, the Commissioned Research of National Institute of Information and Communications Technology (NICT) of Japan.

REFERENCES

- [1] S. Hara, H. Yomo, R. Miyamoto, Y. Kawamoto, H. Okuhata, T. Kawabata, and H. Nakamura, “Challenges in real-time vital signs monitoring for persons during exercises,” *International Journal of Wireless Information Networks*, pp. 1–18, 2017.
- [2] Association of Radio Industries and Businesses, *ARIB STD -T108, version 1.0*, 2011.
- [3] R. Miyamoto and T. Oki, “Soccer player detection with only color features selected using informed haar-like features,” *Concepts for Intelligent Vision Systems*, pp. 1751–1760, 2016.
- [4] H. Yokokawa, T. Oki, and R. Miyamoto, “Feasibility Study of a Simple Tracking Scheme for Multiple Objects Based on Target Motions,” *Proc. 2017 International Workshop on Smart Info-Media Systems in Asia (SISA)*, pp. 293–298, 2017.
- [5] T.S. Rappaport, *Wireless Communications Principles and Practice*, Prentice Hall, 1996.
- [6] S. Yamaguchi, A. Niino, H. Ogura, R. Miyamoto, T. Kawabata, H. Yomo, and S. Hara, “Applying Multi-channel Flooding to Vital Data Monitoring of a Large Number of Exercisers: Mobility and Link Modeling and Performance Evaluation,” *submitted for ISMICT 2018, Sydney, Australia, 26-28 Mar. 2018*.

A Non-Linear Tensor Tracking Algorithm for Analysis of Incomplete Multi-Channel EEG Data

Nguyen Linh-Trung¹, Truong Minh-Chinh^{1,2}, Viet-Dung Nguyen^{1,3}, Karim Abed-Meraim⁴

¹ AVITECH Institute, University of Engineering and Technology, Vietnam National University, Hanoi, Vietnam

² Department of Physics, Hue University of Education, Hue, Vietnam

³ L2S Laboratory, CentraleSupélec, University Paris-Saclay, Gif-sur-Yvette, France

⁴ PRISME Laboratory, University of Orléans, Orléans, France

Abstract—Tensor decomposition is a popular tool to analyse and process data which can be represented by a higher-order tensor structure. In this paper, we consider tensor tracking in challenging situations where the observed data are streaming and incomplete. Specifically, we proposed a non-linear formulation of the PETRELS cost function and based on which we proposed NL-PETRELS subspace and tensor tracking algorithms. The non-linear function allows us to improve the convergence rate. We also illustrated the use of our proposed tensor tracking for incomplete multi-channel electroencephalogram (EEG) data in a real-life experiment in which the data can be represented by a third-order tensor.

I. INTRODUCTION

Tensor decomposition is a popular tool to analyse and process data which can be represented by a higher-order tensor structure [1], [2]. In this paper, we are interested in using tensor decomposition in challenging situations where observed data are either *streaming* [3], [4] and/or *incomplete* [5]–[7].

Incomplete (missing, partial) observation of data occurs when we passively acquire the data partially, or when it is difficult or impossible to acquire all information. It also occurs when we actively schedule to acquire only a certain fraction of data, because of limitation in power consumption, storage and/or computational complexity. In such cases, the percentage of observed data can be moderate to very low, making classical processing approaches difficult to handle. Moreover, when data are of streaming (online) nature, processing them often requires fast updating instead of recalculating from the beginning due to time constraints.

In this paper, we are also interested in the use of tensor decomposition for a special type of data—electroencephalography (EEG). EEG records the electrical activity of the brain via electrodes adhered to the scalp [8]. EEG is used for diagnosis and treatment of various brain disorders, for example localizing the lesion in the brain that causes an epileptic seizure. Tensor decomposition has been shown to successfully represent and analyse EEG signals [9]–[12]. The reason for the success is that EEG signals are multi-dimensional while tensors provide a natural representation of multi-dimensional signals. Each single-channel EEG signal (i.e., recorded from one electrode) is a record in time of the brain activity, and thus provides a dimension of time. Each EEG record includes recordings from all electrodes, which is a multi-channel EEG signal, and hence has two dimensions of time and space. We often analyse each

single-channel EEG signal in the joint time-frequency domain, thus adding an extra dimension of frequency. In special situations, there could be even 7 dimensions: time, frequency, space, trial, condition, subject and group [10]. Tensor decomposition reveals interactions among multiple dimensions, improving the quality and interpretation of the analysis. Other reasons for using tensor decomposition is to exploit its uniqueness, versatile representation and superior performance [12].

Incomplete observation of EEG signals can occur as well, when for example electrodes become loose or disconnected during the recording process. This is due to difficulty of keeping the head fixed (e.g., EEG recording for children) or reduced quality of conductive gels when the recording is done in a long time (e.g., 24-hour monitoring). In such cases, signals recorded from one or several electrodes do not correctly describe the electrical activity of the brain and thus can be discarded, making the observed data incomplete.

Most existing methods for EEG analysis by tensor decomposition are based on batch processing [10], [13] (i.e., data are stored and processed offline). However, when data are of streaming nature like EEG signals in long recordings, adaptive processing is more suitable. This is due to the fact that processing such kinds of data often requires fast updating instead of recalculating from the beginning or processing the whole data as batch method, because of time and storage constraints. To the best of our knowledge, tensor tracking from streaming EEG data has only been considered in [14]. However, the situation of incomplete data was not taken into account.

In this paper, we aim to improve on existing tensor tracking algorithms from incomplete tensors and to apply such an improvement to multi-channel EEG analysis. While there are different models of tensor decomposition, we focus here Parallel Factor (PARAFAC) decomposition. This is inspired by our two recent works. The first one is on adaptive PARAFAC tracking [6], which combines the Parallel Subspace Estimation and Tracking by Recursive Least Squares (PETRELS) algorithm proposed by Chi *et al.* [15] for subspace tracking and the adaptive PARAFAC decomposition algorithm proposed by Nion and Sidiropoulos [3] for streaming third-order tensors. The second one is on a new formulation of PETRELS cost function, which we will provide details in a subsequent publication for subspace tracking from incomplete data.

The contributions are three-fold. First, we propose a nonlinear formulation of the PETRELS cost function. The resulting nonlinear subspace tracking algorithm, referred to as NL-PETRELS, can converge faster than PETRELS while achieving a similar performance. Second, by replacing the subspace tracking step in our adaptive PARAFAC decomposition [6] with NL-PETRELS, we propose a non-linear tensor tracking algorithm for incomplete data. Third, we show how our tensor tracking algorithm can be used to track incomplete multi-channel EEG data.

Notations: Calligraphic letters are used for tensors. Boldface uppercase, boldface lowercase, and lowercase denote matrices, (row and column) vectors, and scalars respectively. Operators \otimes , \odot , $*$, \circ , $(\cdot)^T$ and $(\cdot)^\#$ denote the Kronecker product, the Khatri-Rao product, the Hadamard product (element-wise matrix product), and the outer product, the transpose and the pseudo-inverse, respectively.

II. PROPOSED ALGORITHMS FOR INCOMPLETE DATA

A. Non-linear subspace tracking from incomplete data

Consider the standard linear data model [15] of $\mathbf{r}(t) \in \mathbb{R}^n$, given by

$$\mathbf{r}(t) = \mathbf{D}\mathbf{s}(t) + \mathbf{n}(t), \quad (1)$$

where $\mathbf{D} \in \mathbb{R}^{n \times p}$ is the system matrix of full column rank, $\mathbf{s}(t) \in \mathbb{R}^p$ is the signal vector randomly distributed according to the Gaussian distribution with zero mean and unit variance, and $\mathbf{n}(t) \in \mathbb{R}^n$ is the noise vector distributed according to the Gaussian distribution with zero mean and variance σ^2 .

A partial observation of $\mathbf{r}(t)$ is given by

$$\mathbf{y}(t) = \mathbf{p}(t) * \mathbf{r}(t), \quad (2)$$

where $\mathbf{p}(t) = [p_1(t), p_2(t), \dots, p_n(t)]^T$ is the mask vector; that is, $p_i(t) = 1$ if the i -th entry of $\mathbf{r}(t)$ is observed, and $p_i(t) = 0$ otherwise.

Our purpose is to estimate a principal subspace \mathbf{W} of \mathbf{D} , given that the data were incompletely acquired according to (2). To do so, we first propose the following general non-linear cost function for subspace tracking in the situation of incomplete data:

$$J(\mathbf{W}) = \sum_{i=t-L+1}^t \beta^{t-i} \|\mathbf{P}(i)[\mathbf{y}(i) - \mathbf{W}g((\mathbf{P}(i)\mathbf{W})^\# \mathbf{y}(i))]\|^2, \quad (3)$$

where L is the length of a window applied to the signal, β is known as the forgetting factor with $0 < \beta \leq 1$, $\mathbf{P}(t) = \text{diag}(\mathbf{p}(t))$, and $g(x)$ is a non-linear function.

We have the following observations:

- If $g(x) = x$, we obtain a linear cost function. Specifically, the cost function in (3) corresponds to the exponential-window cost function when $L \rightarrow \infty$, and to the sliding-window cost function when $\beta = 1$. Moreover, for complete data (i.e., $\mathbf{P}(i) = \mathbf{I}$ for all i), (3) becomes the well-known projection approximation subspace tracking (PAST) cost function [16].

- In general, $g(x)$ can be any non-linear function whose specific form depends on the application at hand. For example, in this paper, we use $g(x) = \tanh(x)$ for subspace and tensor tracking, aimed at accelerating the convergence rate. We also note that (3) is essentially compatible with non-linear principal component analysis (PCA) investigated in [17], [18] for complete data.

In this paper, we present the proposed NL-PETRELS subspace tracking algorithm, only for the case of exponential-window cost function. Accordingly, (3) is rewritten as

$$J_{\text{EW}}(\mathbf{W}) = \sum_{i=1}^t \beta^{t-i} \|\mathbf{P}(i)[\mathbf{y}(i) - \mathbf{W}g((\mathbf{P}(i)\mathbf{W})^\# \mathbf{y}(i))]\|^2. \quad (4)$$

Following the derivation from [15] and [17], the proposed algorithm can be summarised as in Algorithm 1.

The main difference, compared to PETRELS, comes from the non-linear step at line 3 in estimating $\mathbf{a}(t)$ under the condition that the number of non-zero percentage (NNZP) is less than a certain threshold (ϵ_0), which is always relative small and determined by the experiment. For example, it will be set to be less than 10% in total observation in our simulation. Otherwise, the algorithm essentially corresponds to PETRELS.

B. Non-linear PARAFAC tracking from incomplete tensors

In this section, we generalize NL-PETRELS for adaptive tensor tracking of third-order tensors, following the PARAFAC decomposition model. A third-order tensor $\mathcal{X} \in \mathbb{R}^{I \times J \times K}$ can be decomposed according to the PARAFAC model as [1]

$$\mathcal{X} = \sum_{r=1}^R \mathbf{a}_r \circ \mathbf{b}_r \circ \mathbf{c}_r, \quad (5)$$

Algorithm 1: Nonlinear PETRELS (NL-PETRELS)

Initialization: Random $\mathbf{W}(0) \in \mathbb{R}^{n \times p}$, $\mathbf{R}_m^{-1}(0) = \mathbf{I}_p$

```

1 for  $t = 1 : T$  do
2   if  $\text{NNZP} \leq \epsilon_0$  then
3      $\mathbf{a}(t) = g((\mathbf{P}(t)\mathbf{W}(t-1))^\# \mathbf{y}(t))$ 
4   end
5   else
6      $\mathbf{a}(t) = (\mathbf{P}(t)\mathbf{W}(t-1))^\# \mathbf{y}(t)$ 
7   end
8 end
9 for  $m = 1 : n$  do
10   $\alpha_m(t) = 1 + \beta^{-1} \mathbf{a}^T(t) \mathbf{R}_m^{-1}(t-1) \mathbf{a}(t)$ 
11   $\mathbf{u}_m(t) = \beta^{-1} \mathbf{R}_m^{-1}(t-1) \mathbf{a}(t)$ 
12   $\mathbf{R}_m^{-1}(t) =$ 
13     $\beta^{-1} \mathbf{R}_m^{-1}(t-1) - p_m(t) \alpha_m^{-1}(t) \mathbf{u}_m(t) \mathbf{u}_m^T(t)$ 
14   $\mathbf{w}_m(t) = \mathbf{w}_m(t-1) + [y_m(t) - p_m(t) \mathbf{a}(t) \mathbf{w}_m(t-1)] \mathbf{R}_m^{-1}(t) \mathbf{a}(t)$ 
15 end
```

which is sum of R rank-one tensors¹. Always, (5) is only an approximate tensor in a noisy environment, that is,

$$\mathcal{X} = \sum_{r=1}^R \mathbf{a}_r \circ \mathbf{b}_r \circ \mathbf{c}_r + \mathcal{N}, \quad (6)$$

where \mathcal{N} is a noise tensor. By grouping $\mathbf{A} = [\mathbf{a}_1 \dots \mathbf{a}_R] \in \mathbb{R}^{I \times R}$, $\mathbf{B} = [\mathbf{b}_1 \dots \mathbf{b}_R] \in \mathbb{R}^{J \times R}$, and $\mathbf{C} = [\mathbf{c}_1 \dots \mathbf{c}_R] \in \mathbb{R}^{K \times R}$, (6) can be rewritten in matrix form² as

$$\mathbf{X} = (\mathbf{A} \odot \mathbf{C}) \mathbf{B}^T + \mathbf{N}. \quad (7)$$

Thus, given a noisy data tensor \mathcal{X} , PARAFAC decomposition tries to perform R -rank best approximation in the least squares sense, that is,

$$\phi(\mathbf{A}, \mathbf{B}, \mathbf{C}) = \|\mathbf{X} - (\mathbf{A} \odot \mathbf{C}) \mathbf{B}^T\|_F \quad (8)$$

When the data are incomplete, (8) becomes

$$\phi_M(\mathbf{A}, \mathbf{B}, \mathbf{C}) = \|\mathbf{M} * (\mathbf{X} - (\mathbf{A} \odot \mathbf{C}) \mathbf{B}^T)\|_F^2, \quad (9)$$

where \mathbf{M} is a mask matrix, defined as

$$\mathbf{M}(i, j) = \begin{cases} 1, & \text{if } \mathbf{X}(i, j) \text{ was observed,} \\ 0, & \text{otherwise.} \end{cases} \quad (10)$$

In batch processing, the three dimensions of the tensor are constants. In adaptive processing, we are interested in this paper third-order tensors which have one dimension growing in time while the other two dimensions remain constant, e.g., $\mathcal{X}(t) \in \mathbb{R}^{I \times J(t) \times K}$, as shown at the top of Fig. 1.

Using the matrix representation in (7) and in the noiseless case, we have the following PARAFAC decompositions at two successive time instants $t-1$ and t :

$$\mathbf{X}(t-1) = [\mathbf{A}(t-1) \odot \mathbf{C}(t-1)] \mathbf{B}^T(t-1) \quad (11a)$$

$$\mathbf{X}(t) = [\mathbf{A}(t) \odot \mathbf{C}(t)] \mathbf{B}^T(t). \quad (11b)$$

Thus,

$$\mathbf{X}(t) = [\mathbf{X}(t-1) \quad \mathbf{x}(t)], \quad (12)$$

where $\mathbf{x}(t)$ is the vectorised representation of a new slice (see the bottom of Fig. 1):

$$\mathbf{x}(t) = [\mathbf{A}(t) \odot \mathbf{C}(t)] \mathbf{b}^T(t) = \mathbf{H}(t) \mathbf{b}^T(t), \quad (13)$$

where $\mathbf{b}^T(t)$ is the t -th column of $\mathbf{B}^T(t)$.

Consider the following exponentially weighted least-square cost function:

$$\Psi_{\mathbf{P}(t)}(t) = \sum_{i=1}^t \beta^{t-i} \|\mathbf{P}(i)[\mathbf{x}(i) - \mathbf{H}(t) \mathbf{b}^T(i)]\|^2. \quad (14)$$

Estimating the loading matrices of the adaptive PARAFAC model of (18) corresponds to

$$\underset{\mathbf{H}(t), \mathbf{B}(t)}{\text{minimize}} \Psi_{\mathbf{P}(t)}(t) \quad (15)$$

$$\text{subject to } \mathbf{H}(t) = \mathbf{A}(t) \odot \mathbf{C}(t). \quad (16)$$

¹A rank-one tensor is defined as $\mathbf{a}_r \circ \mathbf{b}_r \circ \mathbf{c}_r$.

²Other matrix forms are possible.

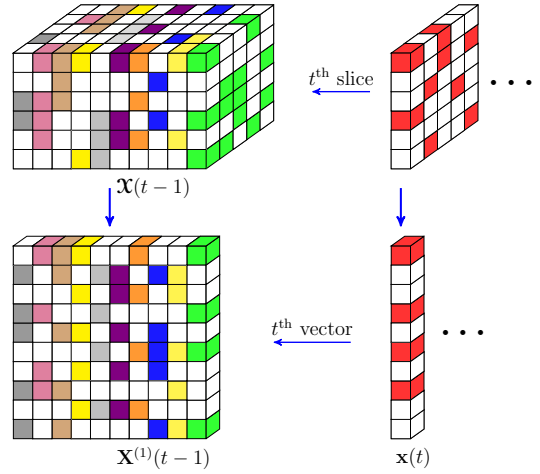


Fig. 1. Adaptive third-order tensor model for incomplete data and its equivalent matrix form.

We also adopt the following assumptions from [6]:

- The loading matrices \mathbf{A} and \mathbf{C} are unknown but follow slowly time-varying models, i.e., $\mathbf{A}(t) \simeq \mathbf{A}(t-1)$ and $\mathbf{C}(t) \simeq \mathbf{C}(t-1)$. As a consequence, since $\mathbf{H}(t) \simeq \mathbf{H}(t-1)$, we obtain

$$\mathbf{B}^T(t) \simeq [\mathbf{B}^T(t-1), \mathbf{b}^T(t)], \quad (17)$$

which allows us to estimate $\mathbf{B}(t)$ in a simple manner. Specifically, instead of updating the whole $\mathbf{B}(t)$ at each time instant, we only need to estimate the row vector $\mathbf{b}(t)$ and augment it to $\mathbf{B}(t-1)$ to obtain $\mathbf{B}(t)$. In the other words, $\mathbf{B}(t)$ has time-shift structure.

- The tensor rank, R , is constant and known in advanced. Moreover, the uniqueness property of the new tensor is satisfied when a new data slice is added to the old tensor.

In the situation of incomplete data, $\mathbf{x}(t)$ is replaced by

$$\tilde{\mathbf{x}}(t) = \mathbf{p}(t) * \mathbf{x}(t), \quad (18)$$

where $\mathbf{p}(t)$ is defined in (2).

Observe that given $\mathbf{b}^T(t)$, estimating $\mathbf{H}(t)$ from incomplete observation $\tilde{\mathbf{x}}(t)$ is a least-squares problem. This procedure is known as alternating least-squares (ALS) minimization which is used extensively in the tensor literature. We also use this approach to develop our tensor tracking algorithm, which is summarised in Algorithm 2.

Given $\mathbf{H}(t-1)$, we can estimate $\mathbf{H}(t)$ by first setting

$$\mathbf{b}^T = g((\mathbf{P}(t) \mathbf{H}(t-1))^{\#} \tilde{\mathbf{x}}(t)), \quad (19)$$

at line 3 in Algorithm 1 of our proposed NL-PETRELS algorithm, then obtaining $\mathbf{H}(t)$ as the output of the algorithm.

To extract $\mathbf{A}(t)$ and $\mathbf{C}(t)$ from $\mathbf{H}(t)$, we use the bi-SVD method as in [6]:

$$\mathbf{a}_i(t) = \mathbf{H}_i^T(t) \mathbf{c}_i(t-1), \quad (20)$$

$$\mathbf{c}_i(t) = \frac{\mathbf{H}_i(t) \mathbf{a}_i(t)}{\|\mathbf{H}_i(t) \mathbf{a}_i(t)\|}, \quad (21)$$

with $i = 1, \dots, R$. Note that each column of $\mathbf{H}(t)$ is the result of vectorising rank-1 matrix: $\mathbf{H}_i(t) = \text{unvec}(\mathbf{a}_i(t) \otimes \mathbf{c}_i(t))$. Thus, estimating vectors $\mathbf{c}_i(t)$ and $\mathbf{a}_i(t)$ corresponds to extract the principal left singular vector and the conjugate of the principal right singular vector of matrix $\mathbf{H}_i(t)$.

Finally, we re-estimate $\mathbf{b}^T(t)$ as

$$\mathbf{b}^T(t) = [\mathbf{P}(t)(\mathbf{A}(t) \odot \mathbf{C}(t))]^\# \tilde{\mathbf{x}}(t). \quad (22)$$

We note that when NNZP is small, computing $[\mathbf{P}(t)(\mathbf{A}(t) \odot \mathbf{C}(t))]^\#$ is fast because only non-zero rows of $\mathbf{H}(t)$ are used in the computation.

III. EXPERIMENTS

In this section, we present selected experiments to illustrate the effectiveness of proposed algorithms. First, we assess tracking performance of the NL-PETRELS subspace tracking algorithm, using simulated data. Then, we illustrate how the NL-PETRELS-based PARAFAC tracking algorithm can be applied to real EEG data [19].

A. NL-PETRELS subspace tracking

To assess the accuracy of subspace estimation, we use (2) to generate simulated data and the following least-squares performance index [20]:

$$\text{SEP}(t) = \frac{\text{tr}\{\mathbf{W}_i^H(t)[\mathbf{I} - \mathbf{W}_{\text{ex}}(t)\mathbf{W}_{\text{ex}}^H(t)]\mathbf{W}_i(t)\}}{\text{tr}\{\mathbf{W}_i^H(t)(\mathbf{W}_{\text{ex}}(t)\mathbf{W}_{\text{ex}}^H(t))\mathbf{W}_i(t)\}}, \quad (23)$$

where \mathbf{W}_i is the estimated subspace at the i -th run, and \mathbf{W}_{ex} is the exact subspace weight matrix computed by orthogonalising \mathbf{A} . The result is shown in Fig. 2.

We also assess performance through matrix completion example [15], as shown in Fig. 3. The MATLAB implementation of this experiment is downloaded from the web page of the first author. To assess convergence rate, we modify the codes to generate a sudden change of subspace at time instant 10,000. Moreover, a noise level at 10^{-3} is added. In this experiment, normalized subspace error is used as performance index. For more details, we refer the reader to [15].

Parameters in both experiments are summarised in Table I. NNZP = 0.1 corresponds to only 10% observation data

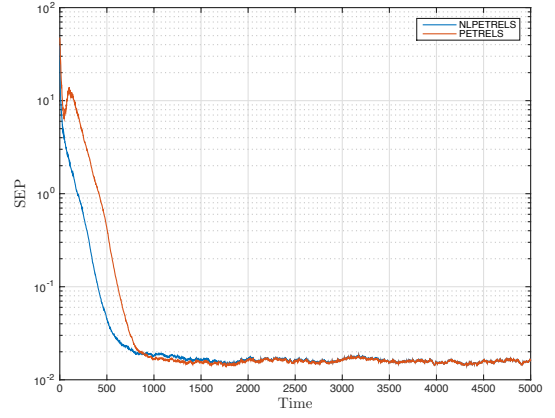


Fig. 2. NL-PETRELS subspace tracking performance.

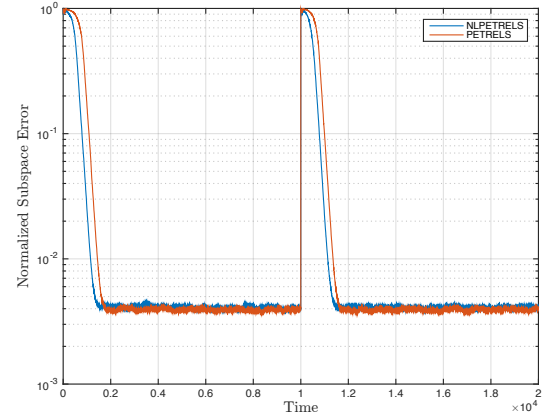


Fig. 3. Adaptive subspace tracking performance.

TABLE I
EXPERIMENTAL PARAMETERS

n	p	T	NNZP
500	10	5000/20000	0.1

Algorithm 2: NL-PETRELS-based PARAFAC tracking

Initialization: $\mathbf{H}(0), \mathbf{R}_m^{-1}(0) = \mathbf{I}_R, \mathbf{A}(0), \mathbf{B}(0), \mathbf{C}(0)$

```

1 for  $t = 1 : T$  do
2    $[\mathbf{H}(t), \mathbf{R}_m^{-1}(t), \mathbf{b}^T(t)] =$ 
   NL-PETRELS( $\tilde{\mathbf{x}}(t), \mathbf{H}(t-1), \mathbf{R}_m^{-1}(t-1)$ )
3   for  $i = 1 : R$  do
4      $\mathbf{a}_i(t) = \mathbf{H}_i^T(t)\mathbf{c}_i(t-1)$ 
5      $\mathbf{c}_i(t) = \frac{\mathbf{H}_i(t)\mathbf{a}_i(t)}{\|\mathbf{H}_i(t)\mathbf{a}_i(t)\|}$ 
6   end
7    $\mathbf{b}^T(t) = [\mathbf{P}(t)(\mathbf{A}(t) \odot \mathbf{C}(t))]^\# \tilde{\mathbf{x}}(t)$ 
8 end

```

used. We used default parameters of PETRELS to have fair comparison in both experiments.

We can see that in both experiments, when PETRELS and NL-PETRELS converge, they have the same performance. However, NL-PETRELS outperformed PETRELS in terms of convergence rate (first 1,000 samples in the first experiment, and 2,000 samples in the second one) and in presence of sudden change of subspace.

For non-linear characterization of the NL-PETRELS subspace tracking algorithm, as discussed in [18, Chapter 12], minimizing the non-linear cost function in (4) does not provide a smaller least mean square error than its linear version. This characterization also keeps in the situation of incomplete data and was confirmed by our experiments.

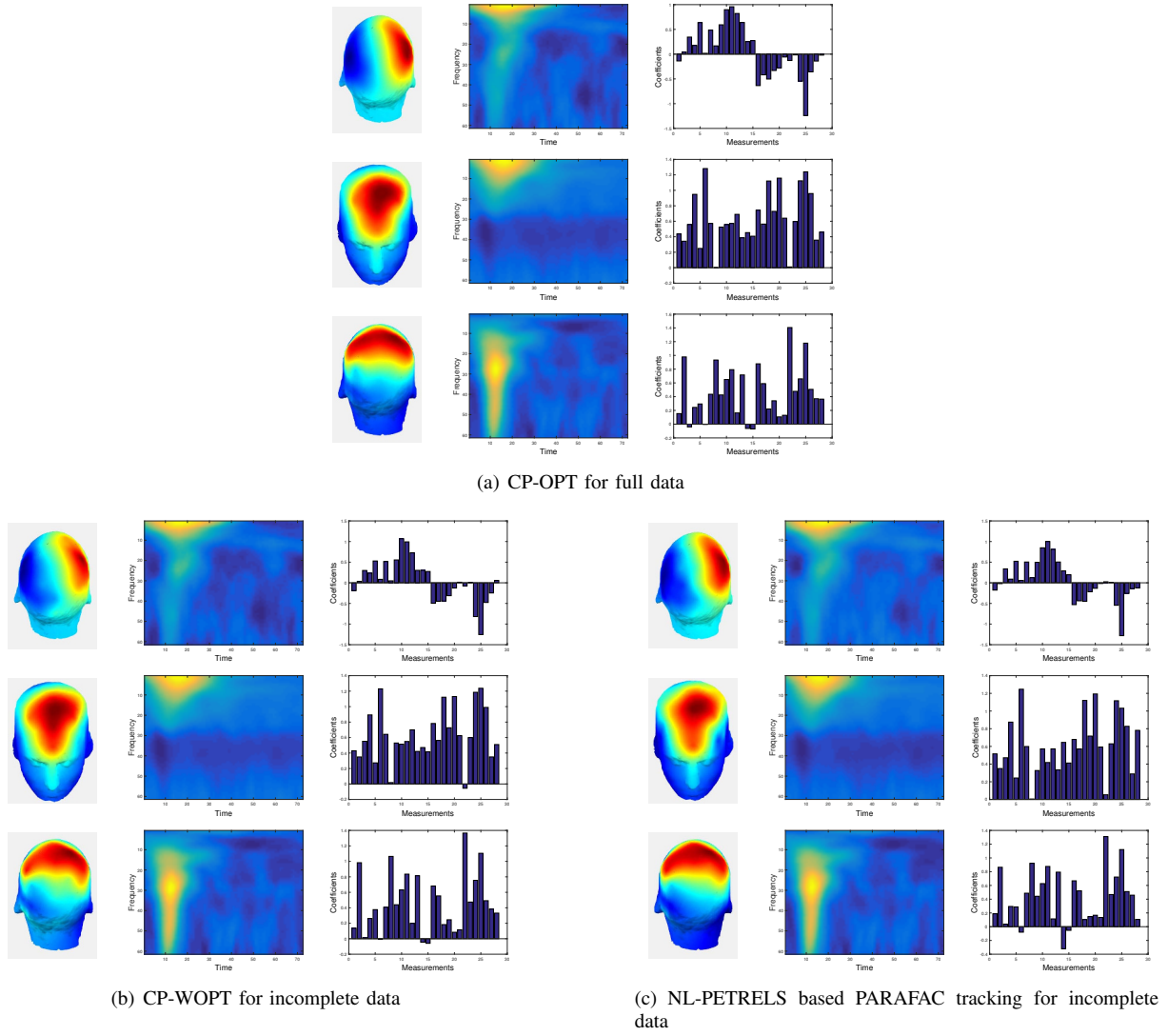


Fig. 4. Estimates of loading matrices **A**, **B**, **C** using CP-WOPT and our proposed NL-PETRELS PARAFAC tracking.

B. NL-PETRELS based PARAFAC tracking from incomplete EEG data

We use the EEG dataset provided in [19], which records gamma activation during proprioceptive stimuli of left and right hands. The dataset includes 28 measurements of 14 subjects. For each subject, left and right hands are stimulated and recorded by 64 EEG channels.

The EEG data are represented by a tensor of three dimensions: *channel* \times *time-frequency* \times *measurement*. To create the time-frequency image from the EEG signal in each channel, the continuous wavelet transform was used [19]. This time-frequency matrix is then vectorised to form a vector of length 4392. Therefore, the size of the tensor is: $64 \times 4392 \times 28$.

We compare our NL-PETRELS-based PARAFAC tracking algorithm with the CP-WOPT algorithm in [21]. CP-WOPT is a batch algorithm for incomplete data. Accordingly, we process the data in a similar manner. The tensor is centered (demeaned) across the channels. The rank of the tensor is $R = 3$. To

create the situation of incomplete data, for each measurement, data from randomly selected 20 channels are discarded. Different from CP-WOPT is the ability to deal with streaming data of our proposed algorithm. The implementation of this experiment used several MATLAB toolboxes: Tensor [22], Poblano [23], and EEGLAB [24].

The adaptivity is done along the second dimension (time-frequency), as if each EEG time-frequency image is vectorised and the resulting vector of data is being streamed. To initialize our algorithm, we run CP-WOPT with the first 1500 slices, i.e., tensor with size of $64 \times 1500 \times 28$. This is known as batch initialization [3] and is necessary to make algorithm converge. We have experimentally observed that random initialization may cause algorithm diverge for the EEG data.

The results are given in Fig. 4. Three rows in each sub-figure correspond to three PARAFAC components ($R = 3$), i.e. the first, second and third columns of the loading matrices. In each row, the 3-dimensional head, the time-frequency representation

and the bar plot correspond to the i -th vectors of the loading matrices **A**, **B** and **C** respectively, $i = 1, 2, 3$. Fig. 4 illustrates the estimation of the loading matrices **A**, **B**, **C**, using CP-WOPT in (a) for full data and (b) for incomplete data and (c) using our proposed NL-PETRELS PARAFAC tracking for incomplete data, showing that our algorithm can track the loading matrices successfully.

In our experiment, for illustration purposes, the way we created the EEG tensor is offline, that is applying the continuous wavelet transform for the whole duration of the EEG signal in each channel and performed the tracking as if we gradually received data from this whole time-frequency vector. In practice, it would be more appropriate to perform the wavelet transform in real-time [25]–[28], as the time samples of an EEG signal is being recorded.

IV. CONCLUSION

In the context of using tensor decomposition in challenging situations where the observed data are streaming and incomplete, we have proposed a non-linear formulation of the PETRELS cost function and based on which we proposed NL-PETRELS subspace and tensor tracking algorithms. While the performance of the NL-PETRELS subspace tracking algorithm was investigated and shown to be better than PETRELS in terms of convergence rate, the NL-PETRELS based PARAFAC tracking algorithm was illustrated for tracking multi-channel incomplete EEG data, represented by a tensor of three dimensions: channel \times vectorised time-frequency \times measurement. The algorithm successfully tracked the data even when data from 20 out of 64 channels were missing. Investigation on the performance of the proposed tensor tracking algorithm by itself and with respect to the presented type of EEG tensor is necessary, as well as on different types of EEG tensors.

ACKNOWLEDGMENT

This research is funded by Vietnam National Foundation for Science and Technology Development (NAFOSTED) under grant number 102.02-2015.32.

REFERENCES

- [1] T. G. Kolda and B. W. Bader, "Tensor decompositions and applications," *SIAM Review*, vol. 51, no. 3, pp. 455–500, 2009.
- [2] A. Cichocki, D. Mandic, L. De Lathauwer, G. Zhou, Q. Zhao, C. Caiafa, and H. A. Phan, "Tensor decompositions for signal processing applications: From two-way to multiway component analysis," *IEEE Signal Processing Magazine*, vol. 32, no. 2, pp. 145–163, 2015.
- [3] D. Nion and N. D. Sidiropoulos, "Adaptive algorithms to track the PARAFAC decomposition of a third-order tensor," *IEEE Transactions on Signal Processing*, vol. 57, no. 6, pp. 2299–2310, 2009.
- [4] V.-D. Nguyen, K. Abed-Meraim, and N. Linh-Trung, "Second-order optimization based adaptive PARAFAC decomposition of three-way tensors," *Digital Signal Processing*, vol. 63, pp. 100–111, Apr. 2017.
- [5] M. Mardani, G. Mateos, and G. B. Giannakis, "Subspace learning and imputation for streaming big data matrices and tensors," *IEEE Transactions on Signal Processing*, vol. 63, no. 10, pp. 2663–2677, 2015.
- [6] T. Minh-Chinh, V.-D. Nguyen, N. Linh-Trung, and K. Abed-Meraim, "Adaptive PARAFAC decomposition for third-order tensor completion," in *6th IEEE International Conference on Communications and Electronics (ICCE)*, Jul. 2016, pp. 297–301.
- [7] H. Kasai, "Online low-rank tensor subspace tracking from incomplete data by CP decomposition using recursive least squares," in *IEEE International Conference on Acoustics, Speech and Signal Processing (ICASSP)*, 2016, pp. 2519–2523.
- [8] L. Sörnmo and P. Laguna, *Bioelectrical Signal Processing in Cardiac and Neurological Applications*. Academic Press, 2005.
- [9] E. Acar, C. Aykut-Bingol, H. Bingol, R. Bro, and B. Yener, "Multiway analysis of epilepsy tensors," *Bioinformatics*, vol. 23, no. 13, pp. i10–i18, 2007.
- [10] F. Cong, Q.-H. Lin, L.-D. Kuang, X.-F. Gong, P. Astikainen, and T. Ristaniemi, "Tensor decomposition of EEG signals: A brief review," *Journal of Neuroscience Methods*, vol. 248, pp. 59–69, 2015.
- [11] B. Hunyadi, P. Dupont, W. Van Paesschen, and S. Van Huffel, "Tensor decompositions and data fusion in epileptic electroencephalography and functional magnetic resonance imaging data," *Wiley Interdisciplinary Reviews: Data Mining and Knowledge Discovery*, vol. 7, no. 1, 2017.
- [12] A. Cichocki, "Tensors decompositions: New concepts for brain data analysis?" *Journal of Control Measurement, and System Integration*, vol. 7, pp. 507–517, 2011.
- [13] V. D. Nguyen, K. Abed-Meraim, and N. Linh-Trung, "Fast tensor decompositions for big data processing," in *International Conference on Advanced Technologies for Communications*, Oct. 2016, pp. 215–221.
- [14] A. Fotouhi, E. Eqlimi, and B. Makkiabadi, "Evaluation of adaptive PARAFAC algorithms for tracking of simulated moving brain sources," in *37th Annual International Conference of the IEEE Engineering in Medicine and Biology Society (EMBC)*, Aug. 2015, pp. 3819–3822.
- [15] Y. Chi, Y. C. Eldar, and R. Calderbank, "PETRELS: Parallel subspace estimation and tracking by recursive least squares from partial observations," *IEEE Transactions on Signal Processing*, vol. 61, no. 23, pp. 5947–5959, Dec. 2013.
- [16] B. Yang, "Projection approximation subspace tracking," *IEEE Transactions on Signal Processing*, vol. 43, no. 1, pp. 95–107, 1995.
- [17] J. Karhunen and J. Joutsensalo, "Representation and separation of signals using nonlinear PCA type learning," *Neural Networks*, vol. 7, no. 1, pp. 113–127, 1994.
- [18] A. Hyvärinen, J. Karhunen, and E. Oja, *Independent Component Analysis*. John Wiley & Sons, 2004, vol. 46.
- [19] M. Mørup, L. K. Hansen, and S. M. Arnfred, "ERPWAVELAB: A toolbox for multi-channel analysis of timefrequency transformed event related potentials," *Journal of Neuroscience Methods*, vol. 161, no. 2, pp. 361–368, 2007.
- [20] V.-D. Nguyen, K. Abed-Meraim, N. Linh-Trung, and R. Weber, "Generalized minimum noise subspace for array processing," *IEEE Transactions on Signal Processing*, vol. 65, no. 14, pp. 3789–3802, Jul. 2017.
- [21] E. Acar, D. M. Dunlavy, T. G. Kolda, and M. Mørup, "Scalable tensor factorizations for incomplete data," *Chemometrics and Intelligent Laboratory Systems*, vol. 106, no. 1, pp. 41–56, 2011, multiway and Multiset Data Analysis.
- [22] B. W. Bader, T. G. Kolda *et al.*, "MATLAB tensor toolbox version 2.6," Feb. 2015. [Online]. Available: <http://www.sandia.gov/~tgkolda/TensorToolbox/>
- [23] D. M. Dunlavy, T. G. Kolda, and E. Acar, "Poblano v1.0: A MATLAB toolbox for gradient-based optimization," Sandia National Laboratories, Tech. Rep. SAND2010-1422, 2010.
- [24] A. Delorme and S. Makeig, "EEGLAB: An open source toolbox for analysis of single-trial EEG dynamics including independent component analysis," *J. Neuroscience Methods*, vol. 134, no. 1, pp. 9–21, 2004.
- [25] K. McGill and C. Taswell, "Length-preserving wavelet transform algorithms for zero-padded and linearly-extended signals," *preprint, Rehabilitation R&D Center, VA Medical Center, Palo Alto, CA*, 1992.
- [26] M. Vishwanath, "The recursive pyramid algorithm for the discrete wavelet transform," *IEEE Transactions on Signal Processing*, vol. 42, no. 3, pp. 673–676, 1994.
- [27] H. O. Mota, F. H. Vasconcelos, and R. M. da Silva, "Real-time wavelet transform algorithms for the processing of continuous streams of data," in *IEEE International Workshop on Intelligent Signal Processing*. IEEE, 2005, pp. 346–351.
- [28] P. Rajmic and J. Vlach, "Real-time audio processing via segmented wavelet transform," in *International Conference on Digital Audio Effects (DAFx-07)*, 2007.

PPG based Respiration Signal Estimation using VMD-PCA

Hangyang Ye, Jin Zhu

College of Electronics and Information Engineering
Tongji University
Shanghai, China

2015_yehangyang@tongji.edu.cn, zhujin@tongji.edu.cn

Yongqiang Cheng

SoECS
University of Hull
Hull, HU6 7RX, UK
y.cheng@hull.ac.uk

Abstract—The photoplethysmography(PPG) waveform is a pulsatile physiological waveform reflecting the blood volume changes attributed to cardiac synchronous activities, and with the lower frequency waveform components attributed to respiration, sympathetic nervous system activities and thermoregulation. Therefore, PPG waveforms are commonly used as non-invasive approach to extract cardiorespiratory signals such as heartbeat and respiration rate. The existing methods either only estimate the respiration rate or sensitive to noises. In this paper, an algorithm based on variational mode decomposition with principal component analysis (VMD-PCA) is proposed as a novel approach to both recover the respiration signal (RS) and estimate respiration rate (RR) from PPG signal. Some 80 PPG samples from the MIMIC database (Physionet ATM data bank) are used to validate the performance of our algorithm. The results are examined with respect to the capnograph-based respiration signal as the ground truth. The performance measurement matrix is composed of mean normalized root mean square deviation (NRMSD), magnitude squared coherence (MSC) and Pearson's correlation coefficient (PCC) with values of 0.434, 0.382 and 0.209 respectively. The proposed method has also achieved 6.67 and 3.34 times faster than EEMD-PCA and EWT-PCA algorithms respectively.

Keywords—Variational mode decomposition, Respiration rate, non-invasive technology, PPG

I. INTRODUCTION

The photoplethysmography (PPG) signal is a non-invasive technique which has been widely used to monitor clinic information. Recently, low cost, non-invasive PPG sensor empowered portable wearable devices have sprung up prosperously. In addition to heartbeat information controlled by heart activities, the respiration information carried in the PPG signal has also drawn great interests among researchers for their potential of real-time measurement and cardiorespiratory diseases diagnosis.^{[1][2][3]} To extract the respiration signal accurately and fast from PPG signal simultaneously along with other vital signals, digital filtering^{[4][5][6]}, wavelet transform^{[7][8][9]}, time domain analysis^{[10][11][12]}, time-frequency analysis^{[13][14]} were reported in literatures. Most algorithms require heavy computational resources and this becomes inevitable challenges when adopting the algorithms on the resource constraint wearable devices.

Huang et al have proposed a direct time data series method, the empirical mode decomposition (EMD) on decomposing PPG into several Intrinsic Mode Functions (IMFs)^[15]. The EMD not only calculated the respiration rate but also estimated the respiration signal during the process. However, the performances are degraded in the presence of noise.^[16]

Wu and Huang et al proposed the Ensemble Empirical Mode Decomposition(EEMD) to overcome disadvantages of EMD like mode overlap and noise-sensitive.^[17] But EEMD is a stationary recursive decomposition approach. J. Gilles proposed Empirical Wavelet Transform (EWT) to avoid mode overlap.^[19] However, it was lack of theoretical analytics. K. Dragomiretskiy proposed Variational Mode Decomposition (VMD) with theoretical proof which is a non-recursion decomposition, overcomes mode overlap, and reduces computational cost and maintains good robustness.

In this paper, we introduced a new approach for estimating simultaneously the RS and RR from PPG signal based on VMD with principal component analysis (VMD-PCA). Compared to EEMD-PCA^{[17][18]} and EWT-PCA, VMD-PCA has achieved as superiorly as others in respect to metrics NRMSD, MSC and PCC with much less computational cost required.

The paper is organized as follows. Section II introduces data source and adaptive signal decomposition methods. Section III defines the comparison matrix used in this work. Section IV presents the results and the paper is concluded in Section V.

II. DATA SOURCE AND METHODOLOGY

A. Data

The MIMIC database contains 72 subjects with over 100 samples for each. Each sample was composed of three ECG signals sampled at 500 Hz, and PPG signal, capnograph-based respiration signal each sampled at 125 Hz.^[22] In this study, we extract 80 epochs of simultaneous PPG signal and respiration signal with 160s (20000 sample points) each from the MIMIC database to evaluate the performance of our proposed algorithm in respect to three existing adaptive signal decomposition methods.

B. Adaptive signal decomposition methods

The EEMD, EWT and VMD are three well-known adaptive signal decomposition methods that can decompose original time

series signals into combinations of Intrinsic Mode Functions (IMFs) as principal modes and residual ones. Each of IMF represents a specific physical or artificial signal. A process time series $e(t)$ can be described as

$$e(t) = \sum_{i=1}^N u_i(t) + r(t) \quad (1)$$

where $u_i(t)$ is an IMF, $i = 1, 2, 3 \dots N$, N is the number of IMFs and $r(t)$ is residual.^[20]

The EEMD develop process can be summarized as below: (1) add white noise series to the targeted data; (2) decompose the data with added white noise into IMFs; (3) repeat (1) and (2), but with different white noise series added at each time; (4) obtain the (ensemble) means of corresponding IMFs of the decompositions as the final result.^[17]

Compared with EMD, the added white noise series in EEMD cancel each other, and the mean IMFs stays within the natural dyadic filter windows, significantly reducing the chance of mode overlap and preserving the dyadic property.^{[16][17]}

The EWT algorithm was developed to extract the principle modes based on segmentation of Fourier spectrum. The main idea is to build a wavelet filter bank based on Fourier supports detected from the information contained in the processed signal spectrum, such as detecting the local maxima.

The EWT approach gives a more consistent decomposition while, generally, the EMD exhibits too many modes, which are sometimes really difficult to interpret. Another advantage of the EWT compared to the EMD is that people can adapt the classic wavelet formalism to understand it.^[19]

The VMD algorithm decomposes a signal into an ensemble of band-limited IMFs. Comparing to existing decomposition models, VMD refrain from modeling the individual modes as signals with explicit IMFs.^[25]

C. Decompose PPG signal

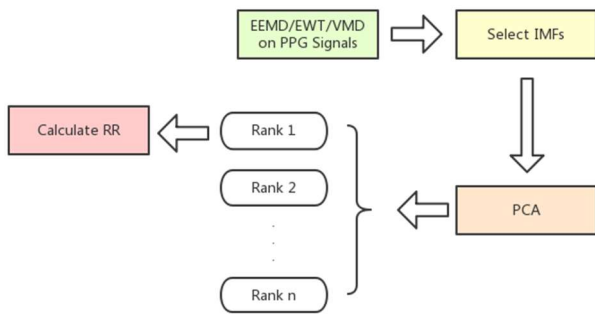


Fig. 1. Overview of RR extraction method

The overview of RS estimation method is illustrated in Fig. 1. The processes can be generally divided into four steps: (1) Decompose PPG signal. (2) Select intrinsic mode functions (IMFs) according to frequency. (3) Apply PCA on the selected IMFs and obtain RS. (4) Calculate RR according to the first principal component (PC). The details of those four steps are described below.

1) Apply time series decompositions

Three decompositions, EEMD, EWT and VMD have been implemented in many fields of application, e.g. medical, mechanics, and geophysics.^[20] PPG signal can be decomposed into several IMFs by applying EEMD, EWT, VMD separately. The source code of these three methods were available.^{[21][23][24]} These IMFs demonstrate the physical meaning to the greatest extent possible.

2) Select candidate IMFs

After executing decompositions and obtaining IMFs, artifacts and noisy IMFs could be identified by frequency ranges and filtered out. Specifically, PPG signal consists of cardiac activities in frequency (1-2 Hz) and respiration signal in frequency (0.2-0.4 Hz). Apply fast Fourier transform (FFT) on each IMF and calculate the dominant frequency. IMFs with a frequency higher than 0.8 Hz were dropped as noise and the rest of IMFs with a frequency lower than 0.8 Hz were selected for further processing.

3) Apply PCA on the selected IMFs

PCA uses an orthogonal transformation to convert a set of observations of possibly correlated variables into a set of values of linearly uncorrelated variables called principal components. This transformation is defined in such a way that the first principal component has the largest possible variance.

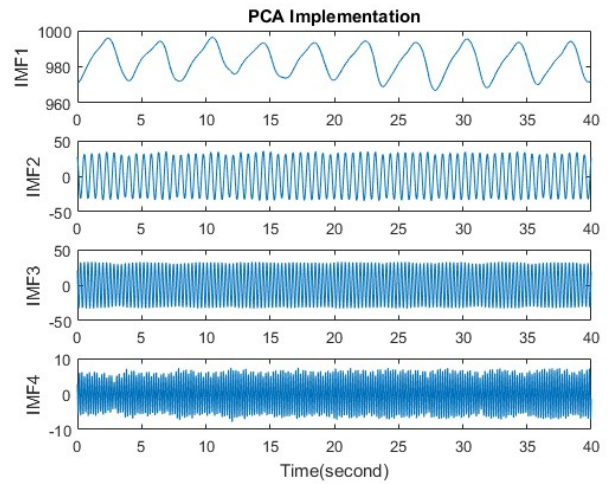


Fig. 2. Applying PCA on candidate IMFs

We constituted data set as below:

$$X = [IMF_1^T, IMF_2^T, IMF_3^T, \dots, IMF_N^T] \quad (2)$$

where IMF_N is 1×20000 dimensional matrix derived from signal decomposition. By applying PCA, X was converted into a new matrix Y ordered by descent of feature values. The larger feature value is, the more the IMF dominates X . Hence the first column of Y was selected as the estimation RS. Each column of Y was drawn sequentially in Fig. 2.

4) Calculate RR

The frequency of respiratory rate (f_{RR}) can be calculated by applying FFT on the estimated RS. f_{RR} was converted to RR by

Eq. (3). Reference RR was calculated from capnograph-based respiration signal in the same way.

$$RR = f_{RR} * 60(breaths/min) \quad (3)$$

III. PERFORMANCE ANALYSIS

We calculated Magnitude Squared Coherence (MSC), Pearson's Correlation Coefficient (PCC) and Normalized Root Mean Square Deviation (NRMSD) of VMD-PCA based on RS with reference respiration signal, details of these metrics are as below:

MSC is a statistic indicator used to examine the relation between two signals in the frequency domain. The Coherence between the reference respiration signal $r(t)$ and estimated RS $e(t)$ from PPG is calculated as follows:

$$C_{re}(f) = \frac{|P_{re}(f)|^2}{P_{rr}(f)P_{ee}(f)} \quad (4)$$

Where $P_{re}(f)$ is the Cross-spectral density between $r(t)$ and $e(t)$, $P_{rr}(f)$ and $P_{ee}(f)$ are the spectral density of the $r(t)$ and $e(t)$ respectively. Values of MSC will always satisfy $0 \leq C_{re} \leq 1$. For an ideal constant parameter linear correlation between $r(t)$ and estimated RS $e(t)$, the coherence will be equal to one.

PCC is a number that quantifies the linear correlation between two variables X and Y. It has a value between +1 and -1, where 1 is a total positive linear correlation, 0 means no linear correlation, and -1 is a total negative linear correlation. PCC is defined as:

$$\rho_{re} = \frac{Cov(r,e)}{\sigma_r \sigma_e} \quad (5)$$

Where, $Cov(r,e)$ represent the covariance of $r(t)$ and $e(t)$, σ_r and σ_e are the standard deviation of $r(t)$ and $e(t)$ respectively. [26][27][28]

NRMSD is a frequently used metric of differences between values (sample and population values) predicted by a model or an estimator and the values actually observed. The equation for estimating NRMSD is given below:

$$NRMSD = \sqrt{\frac{\sum_{t=1}^n (e(t) - r(t))^2}{n}} \quad (6)$$

where r_{max} is the maximum of reference signal and r_{min} is the minimum of reference signal.

IV. RESULT AND DISCUSSION

The estimated RS from the same PPG signal by EEMD-PCA, EWT-PCA, VMD-PCA respectively is shown in Fig. 3 together with original PPG signal and capnograph based respiration signal. It's obvious that each estimated RSs are analogous to the reference respiration signal to some extent.

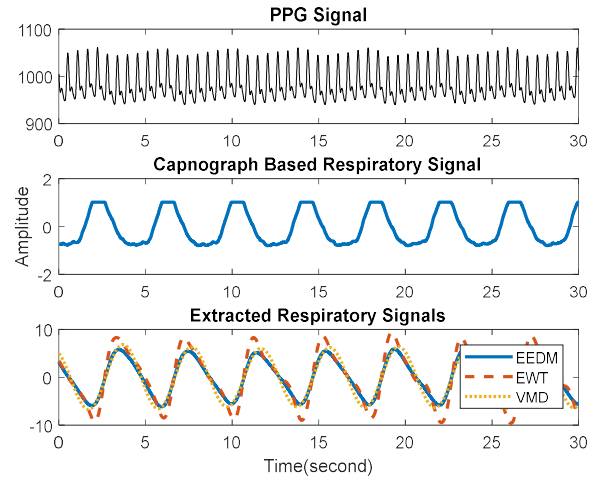


Fig. 3. PPG signal, Capnograph based respiratory signal and estimated RS by EEMD-PCA, EWT-PCA, VMD-PCA.

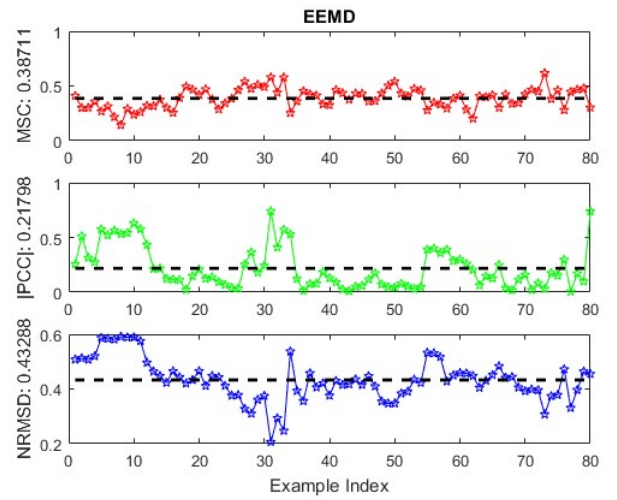


Fig. 4. MSC, |PCC|, NRMSD value of EEMD-PCA

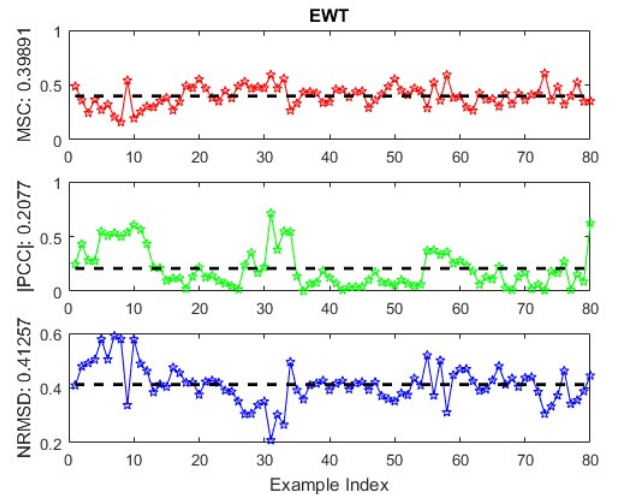


Fig. 5. MSC, |PCC|, NRMSD value of EWT-PCA

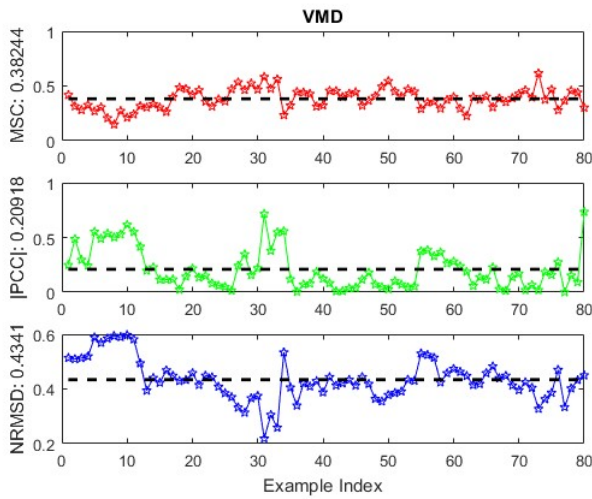


Fig. 6. MSC, |PCC|, NRMSD value of VMD-PCA

A. RS estimation performance

Each value of MSC, PCC, NRMSD between estimated RS and reference RS were plotted in Fig. 4, Fig. 5, Fig. 6. There was consistency in decomposition ability for each method.

TABLE 1. THE MEAN VALUE OF MSC, |PCC|, NRMSD

Method	MSC	PCC	NRMSD
EEMD-PCA	0.387	0.217	0.433
EWT-PCA	0.399	0.208	0.413
VMD-PCA	0.392	0.213	0.434

The results shown in Table 1 indicate that EEMD-PCA, EWT-PCA, and VMD-PCA all have achieved a similar level performance in terms of the measurement index where EWT-PCA performs the best in respect to MSC and NRMSD, and EEMD-PCA has the highest |PCC| value. Although VMD-PCA is not ranked as the highest in the indicators, the mean values of each metrics have illustrated that VMD-PCA presents as good decomposition ability as others.

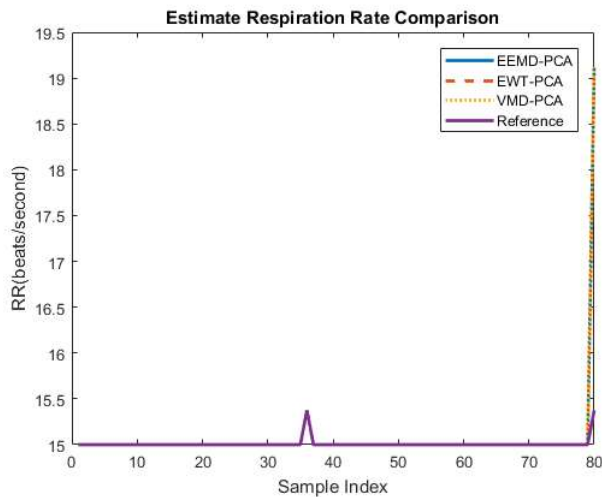


Fig. 7. Respiration rate results

B. RR estimation performance

The RR calculated from estimated RS extracted by EEMD-PCA, EWT-PCA, VMD-PCA were depicted in Fig. 7 along with the reference RR. All algorithms have achieved a similarly high accuracy rate. The estimated RR graphs are mostly overlapped with the reference one, with deviations 0.00390630, 0.00390598 and 0.00390625 respectively.

C. Computational cost

The data processing platform has been carried out on a Windows 10 64 bits desktop PC with Intel(R) Core(TM) i5-4570 CPU @ 3.20GHz. 8.00GB (7.88 GB Available) RAM. Table 2 has listed the time consumed by each method to process the 80 samples with 160s length each. VMD-PCA took roughly 1/3 of the time used by EWT-PCA and 1/6 that of EEMD-PCA. As for the wearable device, the duration of input could be reduced from 160s to 30s or even shorter when the VMD-PCA algorithm is implemented. Hence the process time to report the first respiration becomes roughly 10 seconds. Furthermore, the computation can be off load to tablet or cloud server such as the Verity device^[29] to balance the performance and power consumption.

TABLE 2. TIME CONSUMPTION OF EACH METHOD

Method	Total Time (80 samples)	Time (1 sample)
EEMD-PCA	30209.714s	377.621s
EWT-PCA	15121.785s	189.022s
VMD-PCA	4527.807s	56.597s

V. CONCLUSION

In this paper, we have derived a novel algorithm VMD-PCA for estimating RS and RR simultaneously whilst existing methods only extract RR from PPG signal but not RS. In addition to achieving high accuracy, VMD-PCA is 6.67 times faster than EEMD-PCA and 3.34 times faster than EWT-PCA. This advantage has made VMD-PCA suitable for portable and wearable devices.

Future work will be applying the algorithm to other cardiovascular or cardiorespiratory signals, such as ECG and pulmonary sound analysis, particularly with a focus on the wearable device based cardiac disease diagnosis.

ACKNOWLEDGMENT

This work was supported in part by iMonSys Ltd., U.K.

REFERENCES

- [1] Harishchandra Dubey, Nicholas Constant, Kunal Mankodiya, "RESPIRE: A Spectral Kurtosis-based Method to Extract Respiration Rate from Wearable PPG Signals," *Connected Health: Applications, Systems and Engineering Technologies*, Philadelphia PA USA, Jul. 2017, pp. 84-89.
- [2] Jin Li, Jie Jin, Xiang Chen, Weixin Sun, Ping Guo, "Comparison of respiratory-induced variations in photoplethysmographic signals," *Physiological measurement*, Vol. 31, No. 3, pp. 415-425, 2010.
- [3] Lena Nilsson, Anders Johansson, Sigga Kalman, "Monitoring of respiratory rate in postoperative care using a new photoplethysmographic technique," *Journal of Clinical Monitoring and Computing*, Vol. 16, No. 4, pp. 309-315, May. 2000.
- [4] K. Nakajima, T. Tamura*, T. Ohta, H. Miike, P. A. Oberg, "Photoplethysmographic measurement of heart and respiratory rates using

- digital filters," Engineering in Medicine and Biology Society, 1993. Proceedings of the 15th Annual International Conference of the IEEE, pp. 1006-1007, Oct. 1993.
- [5] Mitsuhiro Ogawa, Toshiyo Tamura, "Monitoring of heart and respiratory signals with PPG in bathing," Engineering in Medicine and Biology, IEEE, pp. 788, Oct. 1999.
- [6] Parastoo Dehkordi, Ainara Garde, Behnam Molavi, Christian L. Petersen, J. Mark Ansermino, "Estimating Instantaneous Respiratory Rate from the Photoplethysmogram," Engineering in Medicine and Biology Society, 37th Annual International Conference of the IEEE, Milan Italy, 2015, pp. 6150-6153.
- [7] John Allen, "Photoplethysmography and its application in clinical physiological measurement," IOP Publishing, Physiological Measurement, Vol. 28, pp. R1-R39, Feb. 2007.
- [8] Alistair E W Johnson, Sharath R Cholleti, Timothy G Buchman, Gari D Clifford, "Improved Respiration Rate Estimation Using a Kalman Filter and Wavelet Cross-Coherence," Computing in Cardiology Conference, Zaragoza Spain, Sept. 2013, pp. 791-794.
- [9] J. C. Cobos, M. Abderrahim, "Measuring Heart and Breath Rates by Image Photoplethysmography using Wavelets Technique," IEEE Latin America Transactions, Vol. 15, No. 10, Oct. 2017.
- [10] J. Lázaro, E. Gil, R. Bailón, and P. Laguna, "Deriving respiration from the pulse photoplethysmographic signal," Computing in Cardiology, Hangzhou China 2011, pp. 713-716.
- [11] J. Lázaro, E. Gil, R. Bailón, A. Mincholé, P. Laguna, "Deriving respiration from photoplethysmographic pulse width," Medical & Biological Engineering & Computing, Vol. 51, No. 1-2, pp. 233-242, Feb. 2013.
- [12] Xiaofeng Yang, Guanghao Sun, Koichiro Ishibashi, "Non-contact Acquisition of Respiration and Heart Rates Using Doppler Radar with Time Domain Peak-detection Algorithm," Engineering in Medicine and Biology Society, 39th Annual International Conference of the IEEE, Seogwipo, South Korea, Jul. 2017, pp. 2847-2850.
- [13] Ki H. Chon, Shishir Dash, Kihwan Ju, "Estimation of Respiratory Rate From Photoplethysmogram Data Using Time-Frequency Spectral Estimation," IEEE Transactions on Biomedical Engineering, Vol. 56, No. 8, pp. 2054-2063, Aug. 2009.
- [14] Shishir Dash, Kirk H. Shelley, David G. Silverman, Ki H. Chon*, "Estimation of respiratory rate from ECG, photoplethysmogram, and piezoelectric pulse transducer signals: a comparative study of time-frequency methods," IEEE Transactions on Biomedical Engineering, Vol. 57, No. 5, pp. 1099-1107, May. 2010.
- [15] K. Venu Madhav, M. Raghu Ram, E. Hari Krishna, Nagarjuna Reddy Komalla, K. Ashoka Reddy, "Estimation of Respiration Rate from ECG, BP and PPG signals using Empirical Mode Decomposition," Instrumentation and Measurement Technology Conference, Binjiang China, May. 2011.
- [16] Huang Jian, Hu Xiao'guang, Gong Yu'nan, Yang Fan, "Machinery fault diagnosis expert system for high voltage circuit breaker," Electric Machines And Control, Vol. 15, No. 10, pp. 43-49, Oct. 2011.
- [17] Zhao'hua Wu, Norden E. Huang, "Ensemble empirical mode decomposition: a noise-assisted data analysis method," Advances in Adaptive Data Analysis, Vol. 1, No. 1, pp. 1-14, Jan. 2009.
- [18] Mohammad Abdul Motin, Chandan Kumar Karmakar, Marimuthu Palaniswami, "An EEMD-PCA Approach to Extract Heart Rate, Respiratory Rate and Respiratory Activity from PPG Signal," IEEE, Engineering in Medicine and Biology Society, Oct. 2016.
- [19] Jérôme Gilles, "Empirical Wavelet Transform," IEEE Transactions on Signal Processing, Vol. 61, No. 16, pp. 3999-4010, Aug. 2013.
- [20] Awang N. I. Wardana, "A Comparative Study of EMD, EWT and VMD for Detecting the Oscillation in Control Loop," IEEE, International Seminar on Application for Technology of Information and Communication, pp. 58-63, Aug. 2016.
- [21] Fast EMD/EEMD Code package. URL: <http://rcada.nyu.edu.tw/research1.htm>
- [22] The MIMIC Database. URL: <https://www.physionet.org/physiobank/database/mimicdb/>
- [23] Empirical Wavelet Transforms Code package. URL: https://cn.mathworks.com/matlabcentral/fileexchange/42141-empirical-wavelet-transforms?s_tid=srchtitle
- [24] Variational Mode Decomposition Code package. URL: https://cn.mathworks.com/matlabcentral/fileexchange/44765-variational-mode-decomposition?s_tid=srchtitle
- [25] Konstantin Dragomiretskiy, Dominique Zosso, "Variational Mode Decomposition," IEEE Transactions on Signal Processing, Vol. 62, No. 3, Feb. 2014.
- [26] Francis Galton, "Regression towards mediocrity in hereditary stature," Journal of the Anthropological Institute of Great Britain and Ireland, Vol. 15, pp. 246-263. 1886.
- [27] Karl Pearson, "Note on regression and inheritance in the case of two parents," Proceedings of the Royal Society of London, Vol. 58, pp. 240-242. Jun. 1895.
- [28] Stephen M. Stigler, "Francis Galton's Account of the Invention of Correlation," Statistical Science, Vol. 4, No. 2, pp. 73-79, 1989.
- [29] Yongqiang Cheng, Ping Jiang, and Yonghong Peng. "Increasing big data front end processing efficiency via locality sensitive Bloom filter for elderly healthcare." In computational intelligence in big data (CIBD), 2014 IEEE symposium on, pp. 1-8. IEEE, 2014.

SAM Smart Asthma Monitoring: Focus on Air Quality Data and Internet of Things (IoT)

Nikita Isaac, Naveenaa Sampath and Valerie Gay

*Faculty of Engineering and IT
University of Technology Sydney
Broadway NSW 2007, Australia
Email: Valerie.Gay@uts.edu.au*

Abstract— Nowadays, mobile technologies and in particular the Internet of Things (IoT), data and machine learning technologies can have a positive impact on the way we manage our health. This paper focuses on Asthma, a condition that affects 10% of Australians. This research collects and analyses data about air quality using New South Wales regional area data and data obtained from our faculty smart building (UTS building 11). Based on a persons location and travel plans, we analyze the Air Quality Index (AQI) and provide a personalized and localized feedback to individuals living with asthma and help them manage their condition better.

Keywords— *Asthma monitoring; mobile technology; wearable technology; machine learning; data analysis; personalised feedback;*

I. INTRODUCTION

According to The Global Asthma Report 2014, more than 334 million people have asthma worldwide [1]. In Australia, approximately 10% of the population suffers from the disease [2]. For many people living with asthma, the onset of symptoms is a direct result of environmental factors, or factors relating to the individual's physical condition. In the United States, asthma has seen an increased prevalence of asthma in all ages, from 7.3% (20.3 million people) to 8.2% (24.6 million people) over the last decade [3]. In the United States, asthma is the most common chronic disease among youth [4] and carries an economic burden of \$56 billion [5]. According to the Australian Bureau of Statistics (ABS), Asthma affects approximately 2.3 million people in Australia with \$655 million spent on asthma in 2008-2009; or approximately 0.9% of all direct health spending on diseases [6].

As the prevalence of asthma is increasing, and with no known cure, there needs to be further research into how the disease can be managed and controlled more effectively. Studies have shown that there are several environmental and physical triggers to asthma. The environmental factors that are known to trigger or exacerbate asthma symptoms are extreme temperatures, extreme humidity or dryness, air pollution, pollen, smoke, and mould [7,8]. However, the effect of these environmental factors varies on a per patient basis. There is also a relationship between physical activity and asthma that can impact daily living [9]. Cardiorespiratory performance of asthmatic patients is suboptimal, but medically supervised physical activity can produce beneficial results for those who have asthma. Insufficient sleep and poor sleep hygiene can lead to increased asthma symptoms the following day, and Asthma also affects sleep [10].

The top factors contributing to asthma susceptibility were factors based on physical activity and work stress [11] [10]. Some popular examples of wearable fitness tracking devices are Fitbit, Garmin, and Jawbone. Data can also be tracked directly within a smartphone, such as the GPS location and manual input, and aggregated with additional data such as weather forecast. Web pages such as www.weatherzone.com.au allow for developers to access these attributes via their API. The increased adoption of wearable fitness tracking devices acquires the subsequent metadata to assist asthma sufferers proactively manage their condition.

Air Quality Index (AQI) is the term used by the authorities to express recent air quality and to provide a prediction of air quality. Using environmental data available on the cloud, wearable fitness tracking devices, building sensory equipment, peak flow meter data, and location-specific information, our architecture presents how asthma can be monitored with tailored feedback and up-to-date asthma management plan for individuals and empower asthma sufferers by giving them relevant information when needed.

The Internet of Things (IoT) has enabled buildings and homes to be more connected [12]. At UTS building 11, building sensors are typically used to determine occupancy levels and energy efficiency [12]. Some of the indoor building conditions such as oxygen levels, smoke detection, temperature, humidity and levels of indoor air pollutants can be obtained from these building sensors, which have a direct influence on asthma [13]. Building sensors can be useful in assessing exposure and identifying environments that are causing asthma attacks both short and long-term.

There are two types of asthma such as asthma caused by allergens, and asthma caused by air quality, stress, physical activity and weather conditions [2]. Air quality is one of the triggers of asthma that is caused due to the presence of air pollutants in the air. However, some asthma patients have varying levels of tolerance to the triggers mentioned above [3] [4]. Elevated levels of Ozone (O₃), PM_{2.5}, and PM₁₀ also cause long-lasting lung diseases in people living with asthma [5]. Web pages such as www.environment.nsw.gov.au provide expected air quality for the regional areas of NSW. In Australia, bushfires instigate an adverse impact on air quality. Air quality is typically elevated in the presence of smoke and particulate materials. This is the reason asthma sufferers need attention while they are outdoor [11]. Various surveys and studies are conducted through social media such as Facebook, Twitter to investigate the degree of people living with asthma in Australia [8]. With the help of the

analysed data, about 75% of asthma patients are shown using broadcasting forewarns to change their outdoor activities [9].

The sensors are embedded within electronic devices to detect the air quality, humidity and weather, thereby alerting the users whether to stay indoors or outdoors [31]. There are also sensors that detect the number of times inhalers are used by the patients, therefore keeping track of their inhaler usage. The Smart Peak Flow device is a recently developed device for smartphones that has a propeller that rotates when the user blows and connects the reading with the smartphone application [28]. AQI indications on smartphones are on research, but the other applications such as smart peak flow are high in use. The mobile interfaces have been developed to connect Global System for Mobile communications (GSM) with the cell identities of the users to show the pollution reports to the users [29,30].

There are currently some asthma management smartphone apps available, including AsthmaMD, which allow users to manage their asthma and record vital information including medication, action plans and reminder systems [14]. Many of these apps require the manual input of data, such as peak flow measurements, height, weight, and age, then predict the risk of acute asthma symptoms occurring based on this data [15,16,17].

There are a considerable amount of projects that currently focus on asthma management. However, these plans focus on providing notifications to the users using sensors that can only function efficiently in a regulated environment. If the individual is present in a pervasive environment, their performances are limited, and air quality is overlooked in these asthma management applications (For instance, Propeller – Measures inhaler usage, Asthma Buddy – Traces variations in symptoms).

In this paper, we propose an architecture for smart asthma management. It collects data using Microsoft Excel and analyses data using MATLAB, thereby gives feedback to provide localized and personalised smart asthma monitoring.

In section 1, the paper presents a Smart Asthma Monitoring (SAM) architecture. In Section 2, it discusses the data collected from multiple sources and their aggregation. In Section 3, it focuses on the data analysis and section 4 on the feedback. The conclusion summarises our focus on using the personalised feedbacks to make the necessary changes such as while the individuals are in the indoor environment. The paper is based on our current research work on air quality in the NSW regional areas, UTS building 11 and mobile personalised health monitoring.

II. ARCHITECTURE

Our proposed architecture for SAM is presented in figure 1. It uses an App and cloud services to collect and aggregate the data relevant to the individual, analyse the data using both machine learning and health professional expertise and provide personalised feedback. The feedback includes reminders such as regular medications, upcoming sports activity. The feedback also includes localized information about asthma triggers such as pollution levels and shows the

high-risk locations that have triggered asthma attacks for them or even people like them. These feedbacks make it easier for users to keep track of their asthma. The architecture could warn hospital of the need for extra hospital beds; it could even deliver the medicine, pre-emptively change the medication and act on the smart environment (close car windows and start the air purifier).

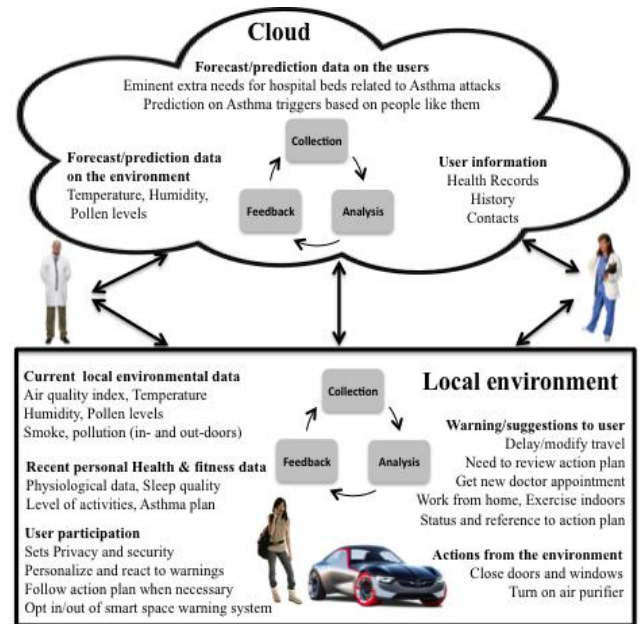


Fig. 1. Smart Asthma Monitoring Architecture

III. COLLECTION AND AGGREGATION

By embedding the air quality sensors with computing software such as MATLAB, IoT technology enhances the accuracy and efficiency by providing feedback to the individuals through smart devices based on the analysed data. This allows to connect and interact with the data.

Microsoft Excel spreadsheets are considered beneficial for data collection, especially when the collected data is used for data analysis. Excel as a data collection tool can retrieve definite information regardless of user interference. Data collection and storage is done certainly where the data cleaning is more accessible in excel compared to other data collection tools [23].

The indoor environment settings such as Oxygen (O₂), Carbon dioxide (CO₂), Hydrocarbons (HO), dust particles and air pollutants are attained from the building sensors of UTS building 11 that help with indicating the conditions that should be avoided for people living with asthma. The outdoor AQI in New South Wales (NSW) is composed of O₃, Nitrogen dioxide (NO₂), Visibility (NEPH), Carbon monoxide (CO), Sulphur dioxide (SO₂), PM_{2.5} and PM₁₀ [25] which are obtained from the sensors installed by NSW Office of Environment and Heritage.

Data collection is done using Microsoft Excel for a user-specified period. For the outdoor environment, the data is collected between the time specified by user. The user can select the location for which they require the personalised feedbacks. The users can also select the time frame and exact time for which they require the personalised feedbacks. The sensors collected the data continuously and based upon the data collection through Microsoft excel. Upon the user's selection of the date, time and location, MATLAB analysis the data and accordingly the feedbacks are provided to the users.

For instance, if 4.00 PM to 5.00 PM is selected since it is the peak time involving heavy transports and a substantial number of people are travelling outdoors, the same time and dates can be followed for the indoor environment and case study as well.

1. The data collected for outdoor environment is gathered from the website <http://www.environment.nsw.gov.au/>
2. The data collected for indoor environment is inferred from the website <https://eif-research.feit.uts.edu.au/>, where the data is obtained from the building sensors of UTS building 11.

Data cleaning is not necessary for the outdoor environment. However, for the indoor environment, a huge volume of data is recorded from the sensors. Therefore, the excel functions such as $\text{=max}(x:y)$ and $\text{=min}(x:y)$ are used for data cleaning. For the indoor environment, the data that is obtained from the sensors are raw data except for air pollutants and hence they are standardized to parts per million (ppm) for CO₂, HO, and percentages for O₂.

On a typical day, SAM collects the air quality data from the indoor, outdoor environment and the location of travel, to provide personalised feedback to the individuals. The user controls the feedbacks of the location. That is, for instance if the user wants to obtain feedback on air quality from Randwick to Rozelle, she can get that required feedback. The user is in control of the data she wants to collect locally and whether she wishes to share it or not and with whom. She can enter data manually and annotate a reading by adding comments and contextual information, such as extra-performed activities. SAM can also obtain data from sensors and wearable around the user and in the cloud.

Quality of the data obtained from the various sources may not always be accurate and reliable. It is therefore important to tag the data collected and take the data quality into account when deciding. The required quality and source of the data are dependent on the individual patient's susceptibility. Once a patient has developed a historical data pattern, this can be used to determine the quality of the attribute relative to that person.

IV. DATA ANALYSIS

Previously, AQI has been calculated mathematically, which is currently replaced by data analysis practices [22]. The data analysis is done using MATLAB, which analyses the collected data from outdoor regional areas of NSW and the indoor UTS buildings that are embedded to provide the personalized feedback to the individuals. MATLAB is a mathematical, analytical software that can handle processing of real-time data using microcontrollers such as Arduino UNO and electronic sensors. Data analysis with MATLAB software is efficient since excel can be read into MATLAB and Matlab handles a high volume of data with lesser delay [24].

Data analysis is done using MATLAB. The data from Microsoft excel are read into MATLAB using the function `"aqi=xlsread('Excel_filename','sheet_number')"`. For instance, to read the AQI data of Randwick region, the following function is used, `Randwick=xlsread('Excel_filename','sheet_number','cell_number')`;

Upon data analysis, IoT helps the users directly connect with the environment they belong in and provides personalized feedback on the air quality in their location. The users can select their means of storage, whether on their mobile devices or on the cloud. Depending on the history of storage, feedbacks can regularly be provided.

In addition to that, various other conditional functions are used to compare the collected data to the threshold levels. In case of the indoor environment, there are different conditions for different elements which are detailed in the results section. Based on the analysis, some of the outdoor regions have frequently been identified to have an elevated AQI level. While some outdoor regions are marked safe for most of the time. The cases are detailed in the result section.

Table I

AQI	Personalised feedback
0 - 33	Very Safe to travel Outdoor
34 - 64	Safe to travel Outdoor
65 - 99	Sensitive people advised staying indoors
100 - 149	Poor air quality. Sensitive people highly advised to stay indoors
150-199	Warning levels of air quality. Sensitive people must stay indoor
200	Hazardous levels of air quality. Sensitive people must avoid outdoor activities

a. Conditions for outdoor air quality analysis

The air quality analysis for the outdoor environment is done based on the above conditions. For an outdoor location showing the air quality index obtained from the website NSW Office of environment and heritage, the above feedbacks will be provided to the users upon their selection of location.

Table II

Indoor elements	Quantity present indoor	Personalised feedback
Carbon dioxide	380 ppm to 398 ppm	Ventilation is required.
	399 ppm and above	Immediate ventilation required.
	360 ppm and below	The area is well-ventilated.
Hydrocarbons	35ppm to 399ppm	People sensitive to CO concentration need attention
	400ppm and above	Dangerous levels of carbon monoxide.
	10ppm to 15 ppm	Concentration is safe
	0 to 9ppm	Concentration is safest.
Oxygen	Below 21%	Area requires ventilation
	21% and above	Area is properly ventilated
Air pollutants	0.8 to 1.0	Air is clean.
	Below 0.8	Dangerous gases may be present.
	Above 1.0	Air is clean, but a negligible amount of pollutants may be present.
Dust Particles	0.1 and Below	No dust particles are present
	Above 0.1	Dust particles are present. Area needs attention.

b. Conditions for indoor air quality analysis

The above table consists of the data analysis conditions for the indoor environment. For analyzing the air quality of indoor environment, we selected the location ES_B_08_422_7BDC. The area is selected as many students use the area for studying, and there are various labs and staff rooms in that location. There are various sensors at various levels at UTS building 11. For instance, ES_A_13_276_7C44 location has dust particles detecting sensors to distinguish the clean air and dust particles such as cigarette smokes.

If the user chooses to store data, depending upon selection data can be stored locally on the mobile device, on the cloud or on a server chosen by the user. The user opts for this storage option to get more intelligent feedbacks based on his long-term history and possibly comparing it to other citizens with similar conditions. Some users will accept that to get better insights while others will opt for less feedback and keep their data private.

These outdoor AQI feedbacks when provided to the hospitals and government health experts, they can arrange the

hospitalization facilities and medical treatments in that location if suddenly a high AQI break-out is prominent.

Users may also opt for his clinicians to get access to their data and decide, for example, that there is a need to adjust their asthma plan. This option gives clinicians an overall view of their patient health and fitness data. This enables them making a more precise and personalised valuation. This could also allow the hospital to estimate how many hospital beds they need to reserve for victims of an asthma attack.

Once the data is aggregated, it is filtered it into standard data sets with the required attributes for the individual. The rule-based engine, which is effectively a decision-making tree performs classification of the data. With that data, we can anticipate the likelihood of a flare up and inform the user accordingly.

On the cloud, machine learning methods are used to classify the collective data into sub-sections based on rule engine's inbuilt decision-making criteria. Machine learning can not only help classify asthma factors and management but also can be used in understanding more factors that may trigger an asthma attack, the level of influence it may have on the patient and the relationship between these factors and emergency department visits. Classification and Regression Trees (CART) is a tree building technique and is used in generating clinical decision rules [18].

An important aspect of SAM is that health professionals are not left out of the system. They are important players in the data analysis and the personalized feedback provided to the system and to its users.

V. FEEDBACK

For the feedback, we opted a user-centred approach where the user is in control of the way the data is presented to him. Triggers are personalized to the user and the app provides a threshold for triggering an alert. For example, the app would alert a user when the air quality deteriorates and raise the alarm if it gets hazardous. The user can either see the data in real-time, or just get a notification or nudge when necessary or even get a phone call from his doctor if he needs to do something. Users can opt for a nudge when needed and an automatic reaction from his smart space when possible (automatic closing/opening of doors and windows at home or in the car, adjustment of the air conditioning. They can select to have real-time analysis and get warnings and references to their asthma plan based on their personal threshold levels on several parameters (including pollen and pollution level, peak flow readings). Users may also be contacted by their clinicians to make an appointment or to adjust their asthma plan. Based on calendar information that contains the place and activities the user is planning to go to, they may also receive some advice to change plans (e.g.: work from home, exercise indoor) based on the location's current and forecasted data.

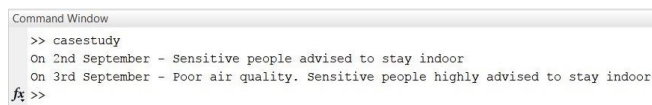
The regions that more regularly show elevated pollution levels are Chullora, Randwick, Macquarie Park, Camden, Bringelly, Richmond, Campbelltown, Muswellbrook, and Illawarra region. The regions that are always safe to stay outdoor are a Lower hunter (Wallsend, Newcastle, and Beresfield), Central Tablelands (Bathurst), North-west (Tamworth) and South-West slopes (Albury, Wagga Wagga North) and Singleton. It can also be observed that, with the

increase in temperature, the air quality index is also increasing. Therefore, the air quality index is higher on sunny days when compared to the other days. This feedback depends on the days and time. IOT allows its servers to remotely and locally store the information, thereby providing a record of their routine activities.

The feedback also addresses one of the challenges: to identify the data that is important for a user. Part of the feedback from the data analysis can be to change the data collection (quality- or quantity- wise) based on previous flare-ups or patients like the users.

SAM can provide personalized feedback to the individuals suffering from asthma based on their location and area of travel. IoT when embedded with the smart devices of the users can direct the feedbacks whether the users should stay indoors, travel outdoor or avoid direct exposure.

Case study is considered at the same time from the location Randwick to Rozelle. Upon their corresponding AQI the following feedbacks are provided. The air quality feedback for asthma plan are provided in the following MATLAB output,



```

Command Window
>> casestudy
On 2nd September - Sensitive people advised to stay indoor
On 3rd September - Poor air quality. Sensitive people highly advised to stay indoor
fx >>

```

Fig. 2. MATLAB output displaying personalised feedback

SAM uses the results of the data analysis and the help of health professionals to update the individual's asthma management plan or determine whether the user needs to take any action to address their asthma. SAM users do not need to refer to their asthma plan all the time manually; if they opt for it, the app will update them when they need to act.

VI. DISCUSSION AND CONCLUSIONS

This paper portrayed our vision of how life can be improved for asthma sufferers through the development of a personalized smart asthma monitoring with a focus on air quality analysis. The portrayal is based on the collected data samples and their analysis.

We aim to make life easier for those who suffer from asthma by creating tailored feedback and personalized up-to-date asthma management plans using readily available data and machine learning. Today, as an asthma sufferer, people carry around multiple medications, inhaler spacer and sensors like a peak flow meter and it is hard to keep track of everything. Our proposed architecture uses an App and cloud services to collect and aggregate the data relevant to the individual, analyze the data and provide timely and personalized feedback. In the near future, it could even deliver the medicine, pre-emptively change the medication and act in the smart environment.

The personalised feedbacks can be based on the individuals' location of travel. The feedbacks which can either be suggestions or warnings to the individuals can advise them to stay indoors based on the AQI level, advice the individuals to close their windshields while travelling through the AQI elevated locations or provide the indoor ventilation levels and air quality levels in UTS building 11.

Several areas require further research such as using mathematical methods for data cleaning. The areas that do not require further implementation include collection of data in software, since they do not focus on real-time feedback. The future scope of the project includes, using various data technologies such big data technologies and machine learning. Therefore, real-time data can be processed and analysed to provide contemporary feedback to the individuals suffering from asthma. This development of asthma plans when embedded with smart systems such as smart home, smart transport and smart intelligent systems can provide a greater benefit for the asthma sufferers, thereby enabling them to lead a healthier life.

SAM reminds asthma sufferers to take regular medications and informs asthma triggers such as high pollen count depending upon the locations. This makes asthma management easier, smarter and the technology is here today. This could decrease unnecessary visit to the emergency department, as most of hospital visits are preventable with better asthma management. SAM empowers asthma sufferers with their routine activities and helps health professionals to monitor and control asthma in an informed way.

REFERENCES

- [1] The Global Asthma Network. (2014). The Global Asthma Report. Auckland, New Zealand.
- [2] Statistics - An Asthma Australia site. (2016). Asthmaaustralia.org.au. Retrieved 25 February 2017, from <http://www.asthmaaustralia.org.au/national/about-asthma/what-is-asthma/statistics>
- [3] Centers for Disease Control and Prevention. Vital signs: asthma prevalence, disease characteristics, and self-management education - United States 2001-2009. Morb Mortal Wkly Rep Surveill Summ. 2011; 60(17):546-52.
- [4] World Health Organization. Asthma Fact Sheet. 2011. Report No.: N307.
- [5] Cleland, J. C., Jan, Ryan, Dermot. (2007). A qualitative study of the attitudes of patients and staff to the use of mobile phone technology for recording and gathering asthma data. Journal of Telemedicine and Telecare, 13, 85-89.
- [6] Profiles of Health, Australia, 2011-13. (2016). Abs.gov.au. Retrieved 25 February 2017, from <http://www.abs.gov.au/ausstats/abs@.nsf/Lookup/4338.0main+features152011-13>
- [7] CDC - Asthma - Common Asthma Triggers. (2012). Cdc.gov. Retrieved 25 February 2017, from <http://www.cdc.gov/asthma/triggers.html>
- [8] Stark, P. C., Ryan, L. M., McDonald, J. L., & Burge, H. A. (1997). Using meteorologic data to predict daily ragweed pollen levels. Aerobiologia, 13(3), 177. DOI= <http://doi:10.1007/bf02694505>
- [9] Clark, C. J., & Cochrane, L. M. (1999). Physical activity and asthma. Current Opinion in Pulmonary Medicine, 5(1), 68.

- [10] [Meltzer, L. J., Ullrich, M., & Szefer, S. J. (2014). Sleep Duration, Sleep Hygiene, and Insomnia in Adolescents with Asthma. *The Journal of Allergy and Clinical Immunology. In Practice*, 2(5), 562–569. DOI=<http://doi.org/10.1016/j.jaip.2014.02.005>
- [11] Tang, M., Agrawal, P., & Jain, R. (2015). Habits vs Environment: What Really Causes Asthma? , 1-5. DOI=<http://doi:10.1145/2786451.2786481>
- [12] Kriksciuniene, D. P., Thomas; Kucera, Adam; Sakalauskas, Virgilijus. (2014). Data Analysis in the Intelligent Building Environment. *International Journal of Computer Science and Applications*, 11(1), 1-17.
- [13] Castellsague, J., Sunyer, J., Sáez, M., & Antó, J. M. (1995). Short-term association between air pollution and emergency room visits for asthma in Barcelona. *Thorax*, 50(10), 1051-1056. <http://doi:10.1136/thx.50.10.1051>
- [14] Asthma Control iPhone App | AsthmaMD. Asthmam.org, 2016. Retrieved 25 February 2017, from <http://www.asthmamd.org/>
- [15] Mack, H. (2016). Sparo Labs gets FDA nod for its app-connected lung function monitor, Wing. *MobiHealthNews*. Retrieved 25 February 2017, from <http://www.mobihealthnews.com/content/sparo-labs-gets-fda-nod-its-app-connected-lung-function-monitor-wing>
- [16] Ra, H.-K., Stankovic, J. A., Salekin, A., Yoon, H. J., Kim, J., Nirjon, S., . . . Son, S. H. (2015). Asthma Guide: An Ecosystem for Asthma Monitoring and Advice. 451-452.<http://doi:10.1145/2809695.2817849>
- [17] Sofuoglu, S. C. (2008). Application of artificial neural networks to predict prevalence of building-related symptoms in office buildings. *Building and Environment*, 43(6), 1121-1126. <http://dx.doi.org/10.1016/j.buildenv.2007.03.003>
- [18] Lewis, R. J. (2000). An introduction to classification and regression tree (CART) analysis. Paper presented at the Annual Meeting of the Society for Academic Emergency Medicine, San Francisco, California
- [19] Gordon, L. (2013). Using Classification and Regression Trees (CART) in SAS® Enterprise Miner™ For Applications in Public Health. University of Kentucky, Lexington, KY.
- [20] How many people have an asthma action plan? (AIHW). Aihw.gov.au, 2016. <http://www.aihw.gov.au/asthma/action-plan/>.
- [21] The National Asthma Council Australia. NationalAsthma.org.au, 2016. Retrieved 8 October 2016, from <https://www.nationalasthma.org.au/living-with-asthma/asthma-action-plans>
- [22] E. Jaraúta-Bragulat, C. Hervada-Sala, and J. J. Egozcue, "Air Quality Index Revisited from a Compositional Point of View," *Mathematical Geosciences*, vol. 48, no. 5, pp. 581-593, 2016.
- [23] [13] R. D. Ainsbury *et al.*, "Method and apparatus for performing data collection, interpretation and analysis, in an information platform," ed: Google Patents, 2000.
- [24] [14] W. Menke, *Geophysical data analysis: discrete inverse theory: MATLAB edition*. Academic press, 2012.
- [25] N. G. O. o. E. Heritage. (2016, 10/13). *Air Quality Index values*. Available: <http://www.environment.nsw.gov.au/aqms/aqitable.htm>
- [26] E. R. D. Interface. (n.d, 13/10). *EIF Wiki*. Available: <https://eif-wiki.feit.uts.edu.au/>
- [27] CAMA, J. 1998. Combination inhaler and peak flow rate meter. Google Patents.
- [28] HUNTER, G. W., XU, J. C., BIAGGI-LABIOSA, A., LASKOWSKI, D., DUTTA, P., MONDAL, S., WARD, B., MAKEL, D., LIU, C. & CHANG, C. 2011. Smart sensor systems for human health breath monitoring applications. *Journal of breath research*, 5, 037111.
- [29] KANJO, E., BACON, J., ROBERTS, D. & LANDSHOFF, P. 2009. MobSens: Making smart phones smarter. *IEEE Pervasive Computing*, 8.
- [30] MCKENNA, M. 2013. The new age of medical monitoring. *Scientific American*, 308, 16-17.

APPENDIX

Available upon demand

Secured Cancer Care and Cloud Services in IoT/WSN Based Medical Systems

Adeniyi Onasanya
Department of Computer Science
University of Regina
 onasanya@uregina.ca

Maher Elshakankiri
Department of Computer Science
University of Regina
 Maher.Elshakankiri@uregina.ca

Abstract—In recent years, the Internet of Things (IoT) has constituted a driving force of modern technological advancement, and it has become increasingly common as its impacts are seen in a variety of application domains, including healthcare. IoT is characterized by the interconnectivity of smart sensors, objects, devices, data, and applications. With the unprecedented use of IoT in industrial, commercial and domestic, it becomes very imperative to harness the benefits and functionalities associated with the IoT technology in (re)assessing the provision and positioning of healthcare to ensure efficient and improved healthcare delivery. In this research, we are focusing on two important services in healthcare systems, which are cancer care services and business analytics/cloud services. These services incorporate the implementation of an IoT that provides solution and framework for analyzing health data gathered from IoT through various sensor networks and other smart devices in order to improve healthcare delivery and to help health care providers in their decision-making process for enhanced and efficient cancer treatment. In addition, we discuss the wireless sensor network (WSN), WSN routing and data transmission in the healthcare environment. Finally, some operational challenges and security issues with IoT-based healthcare system are discussed.

Index Terms—IoT, smart health care system, (wireless) sensor network, cancer care services, cloud services, business analytics

I. INTRODUCTION

Internet of things (IoT) technology presents promising technological, economic, and social benefits to the evolution of data communications and networking facilities due to the advanced connectivity of devices, systems, and services beyond machine-to-machine (M2M) communications. Interestingly, the IoT technology has contributed to and supported a wide range of services and applications, such as smart cities, waste management, home automation, transportation systems, and healthcare. It is also fuelling the development of “smart connected things” – televisions, thermostats, medical devices, cars, wearable technology - clothing and devices [7].

This research considers two of the various services that are pertinent to healthcare delivery. Specifically, it is intended to propose the application and implementation of IoT technology in cancer care health delivery in the context of cancer care services along with the incorporation of business analytics and cloud services for cancer care treatments and diagnoses. The combination of these services proffers solution and framework for analyzing health data gathered from IoT through various sensor networks and other smart connected devices to help

healthcare providers to turn a stream of data into actionable insights and evidence-based healthcare decision making about the health conditions of patients using appropriate analytics tools to improve and enhance cancer treatments.

A. Motivation and Related Work

The motivation for this research work has been triggered by the desire to improve the cancer care in healthcare delivery. Hence, this has prompted the need to (re)assess the provision and positioning of healthcare services to harness the benefits associated with the use of IoT technology. This relatively new trend in IoT technology will suffice in ensuring interconnectivity and interoperability among the health centres, clinics, and hospitals in various regions through network design that will facilitate health region-wide communications. As a result, it is argued that the use of IoT initiative will offer huge benefits such as increased workforce productivity, overall cost savings, enhanced Return on Investment (ROI), improved and new business models [12], and improved collaboration with health practitioners and patients in every service of healthcare delivery. It is also argued that by 2019, about 87% of healthcare organizations would have adopted IoT technology with about 76% in the healthcare industry [16]. The widespread application of IoT in healthcare domain has been successfully applied in a variety of services, including cancer care & business analytics/cloud services [8], medical system (such as clinical care – drug labelling and administration, blood transfusion, real-time ECG monitoring, etc.) [7], [10], health and wellness monitoring, remote monitoring system [11], rehabilitation system [3], operational services system [2], [4], emergency services system [4], [9], just to mention a few. In the course of this research work, we found that most of the papers only mentioned some of the services listed above but none on the application of IoT in cancer care services until a brief version of our initial work [8] has been published. In essence, we have incorporated lots of details and proposed new frameworks, components, and benefits not previously covered in the implementation of IoT and cloud services in cancer care services in this research.

B. Background of Smart Healthcare System

Adoption of IoT based healthcare systems in all the operations of health industry will facilitate enhanced diag-

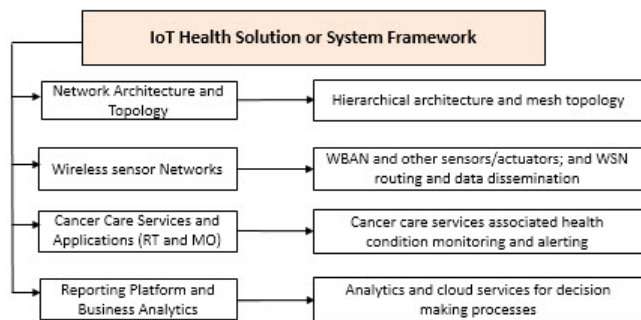


Fig. 1. IoT Health Solution/System Framework.

noses/treatments and monitoring, automatic infirmity and condition detecting and sensing, community health care, location-based health care, rehabilitation, surgery and recovery, imaging services, etc. The IoT devices will be used for communicating between patients and those in the circle of care, and for sharing and interconnecting healthcare network resources into the network as related to the delivery of IoT-based smart healthcare system. The healthcare resources include physicians, doctors, oncologists, health providers, nurses, other health personnel in the circle of care, patients, caregivers, human resources, ambulances, emergency units, medical devices, hospital sites, clinics, community health centres, workstation servers, smart devices or connected things (e.g. tablets), sensors, etc. This interconnection of resources can be achieved through various network industry communication standards such as wireless (short, medium and long), Ethernet with transmission control protocol/internet protocol (TCP/IP), unique identifier (UID) based identification, and GPS-based location technologies.

The remainder of the paper is organized as follows. Section II discusses the framework for IoT solution. Section III provides the methodology and analysis of the network, which includes design basics and hierarchical architecture based on the core, distribution, and access layouts, respectively. Also discussed is the WSN, its routing and data dissemination in the healthcare environment. Section IV presents the network design solutions for healthcare services using mesh hierarchical topology. Lastly, Section V discusses the concluding remarks and recommendations for future research.

II. IOT BASED HEALTHCARE SYSTEM FRAMEWORK

Fig. 1 represents an IoT based healthcare system framework for the proposed network that shows the interdependencies of various components that are impacted by the network design methodology. The framework captures some features and approaches to be adopted in presenting the design solution. It also defines the way we integrate, interface, network and transmit the network resources produced by those connected devices from one node to another within the system.

III. NETWORK METHODOLOGY AND ANALYSIS

A. Network Design Basics and Hierarchical Architecture

It should be noted that the success of any network design is crucial to its implementation. This is why we have paid a close

attention to the network design to ensure flaws are eradicated, especially to project of this nature, in terms of the organization size and the number of healthcare network resources that are interconnected. Though, it might be difficult to design a network that is nearly 100 percent reliable. However, we have thoroughly determined the requirements (i.e. technical and non-technical) in the design of the smart healthcare system in order to decide what is considered a good design, thereby avoiding over complication of the network design.

In addition, two categories of network architecture are considered, namely, *flat architecture* and *hierarchical architecture*, but the focus here is on the hierarchical architecture. Hierarchical architecture is easier to manage and expand, and any inherent issues are more quickly solved with little or no disruption to operation. Typically, hierarchical architecture divides the network into three discrete layers: (1) Core Layout; (2) Distribution Layout; and (3) Access Layout. Each of these layers provides specific functions that define its role within the overall network, thereby resulting in a network that provides modularity with the design goals of scalability (i.e. to meet the demands for additional services), supportability, availability, performance, redundancy, maintainability, security, tolerance, and manageability [5]. The access layer interfaces and controls the end devices (such as sensors, actuators, and IoT connected/smart devices) and the rest of network resources that communicate on the network.

B. Wireless Sensor Networks

The combination of the Internet, network communications, information technology, and engineering advances have made provision for a new generation of inexpensive sensors and actuators, which are capable of achieving a high order of spatial and temporal resolution and accuracy. Currently, network sensor systems are seen as an important component of the IoT technology, which has experienced rapid growth in various applications [12], [14]. According to [12], a sensor network is an infrastructure comprising of sensing (measuring), computing, and communication elements that gives an administrator the ability to instrument, observe, and react to events and phenomena in a specified environment, where the environment can be viewed as physical world, biological system, or an information technology system. The technology embedded in sensors constitutes a broad range of applications in health care, agriculture, energy, food safety, production processing, quality of life, and many other fields. All these applications involve sensing, collecting, and sharing data.

C. WSN Routing and Data Dissemination in Healthcare

Predominantly, the use of wireless/smart sensors and connected devices plays a major part of IoT implementation. These devices are deployed for all the services (with a few exceptions) as they will be strategically attached to or implanted within human body or placed in a specific area to monitor patient under surveillance, treatment or diagnosis in order to collect objective measures/data. Once deployed, the

sensor nodes form an autonomous wireless ad hoc network which is attached to the main network.

As the application of WSNs becomes apparently useful for various services in healthcare setting, data and information from sensors are being transmitted and routed within the networks from one site to another, then to the data center site through cloud services (as will be discussed in business analytics and cloud services section). In data dissemination through WSN, some characteristics have to be addressed such as routing protocols from one source to another. This is necessary to adopt appropriate routing strategy in WSNs that is capable of managing the trade-off between optimality and efficiency to ensure computation and communication capabilities [12]. In WSN routing, four strategies are proposed, namely: *at network*, *structure on the network*, *data-centric network*, and *location network*. But in this research, we consider the location-based routing since it cuts across different locations where the position of the node within the geographical coverage of the network is relevant to query issued by the source node. This ensures cost effective routing approach geographically due to its low overhead and localized interaction [12], and it offers the possibility of including several routing algorithms for data dissemination. The geographical WSN routing and data transmission from WSNs in a clinical setting is illustrated in Fig. 2, where each node of the sensor forwards data to the destination located at the data center within the network.

D. Proposed IoT-Based Healthcare Services and Applications

In the design of network, there is a variety of network topologies for network communication. Since the desire is to identify the best solution that meets the needs of a smart healthcare system, a full mesh topology is proposed. In this, every node in the network has a connection to each of the other nodes (i.e. all nodes cooperate in the distribution of data thus allowing for most transmissions to be distributed, even if one of the connections goes down) [5]. The proposed IoT-based healthcare system comprises of services and an array of applications and conditions to patients administered by those in the circle of care. There exists an association between the services and applications/conditions for managing different types of diseases/infirmities, along with the broad categories of disease or infirmity conditions, as summarized in Fig. 3. The architectures for both services are discussed subsequently.

IV. NETWORK DESIGN SOLUTIONS FOR SERVICES

1) *Cancer Care Services*: Essentially, cancer care services comprise of two sub-services associated with the diagnosis and treatment of cancer, namely, chemotherapy and radiotherapy. The chemotherapy is associated with medical oncology (MO) while the radiotherapy (RT) is associated with radiation oncology (RO). The use of smart devices and wireless sensors can be applied towards improving the quality of cancer care services and patient care by seamless and secure integration of those devices in medical oncology and radiation oncology procedures. This is argued in [15] that patient care (i.e.

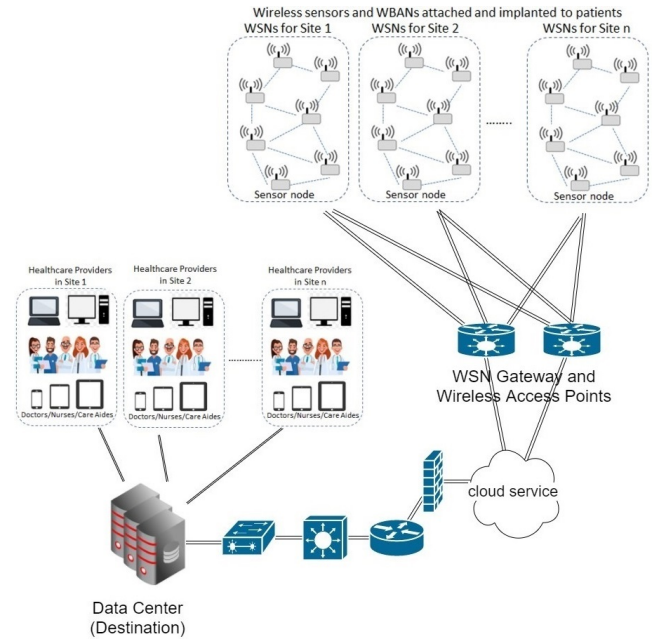


Fig. 2. WSN Routing and Data Transmission

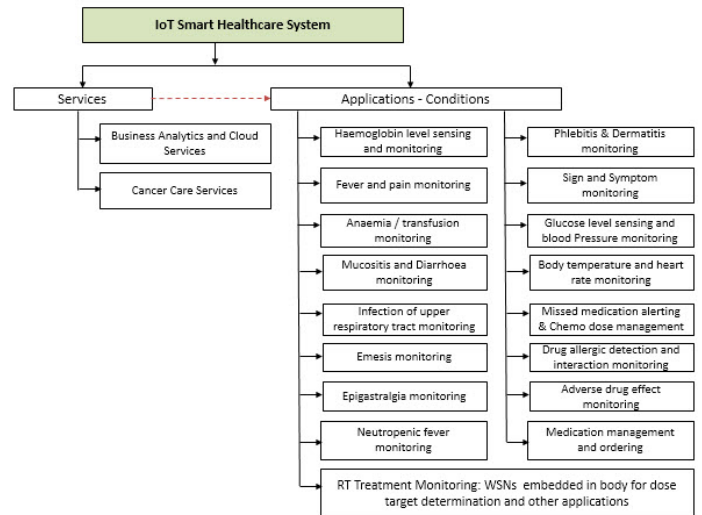


Fig. 3. IoT Health Care Services and Applications/Conditions.

monitoring, alerting, and following-up) for cancer patients undergoing chemotherapy can safely be moved into the home.

As pointed out in [8], attaching and embedding WSNs and smart devices to patients can enhance cancer treatments by allowing health practitioners/nurses to monitor and be alerted of any changes, complications, problems, signs, symptoms, adverse effects, allergies, pains, infections, toxic effects, neutropenic fever occurrences, missed medications, haemoglobin level issues, drug allergic detection, drug interaction, phlebitis, dermatitis, mucositis, diarrhoea, infection of upper respiratory tract, emesis, epigastralgia, neutropenic fever, etc. These issues can automatically be detected, subdued, and blocked, thereby influencing patient care and attention related to patient treatment and enforcing what controls to put in place to circumvent those changes, issues, effects, and symptoms.

Although, [1] claims that no perfect methodology for identifying the magnitude of the adverse effects and issues of chemotherapy, but as alluded by [8], the MO cancer care services can incorporate smart devices that provide assistance to cancer patients in the event of any issues/complications through process automation, remote monitoring, and alert communication. In essence, the IoT technologies through WSNs/smart devices can be programmed at certain level of precision to determine fairly reasonable magnitude deemed fit for the adverse effects of those characteristics on the body. With this innovation, the level of care to patients undergoing such issues can be monitored as shown in Fig. 3.

On the other hand, the implementation of IoT and WSN devices in radiation oncology treatment or radiotherapy is different because of the manner the prescription doses are being administered to patients. Though the use of IoT connected devices can be applied as depicted in Fig. 4. Generally, prior to the DICOM communicating with the various pieces of software, a sequence of steps for the RT treatment starts with the generation of treatment plans in *EclipseTM* by associating related files, namely computed tomography (CT) files, radiotherapy (RT) structure files and dose-volume as applicable to commercial treatment planning system, *EclipseTM* with DICOM as interface [6]. This leads to the determination of prescription doses or final dose calculation for the targets or disease sites and the dose volume constraints for organ at risk (OAR). This is followed by the uploading of plan DICOM files back to Eclipse and recalculating the dose and dose volume history (DVHs), then finally doing the evaluation on Eclipse and also conducting patient QA for dosimetric analysis of internal anatomy because emphasis should be placed on the accurate definition for the targets to ensure precision of protons radiotherapy prior to administering of the doses to patients [6]. Having discussed above, we have to admit that the use of inherent smart devices and wireless sensor networks could help achieve intended results for patient treatment. Therefore, the use of IoT technology can be beneficial for administering radiotherapy to patients as it could help improve the margin, preciseness, and accuracy of the radiotherapy doses to ensure they hit the targets/disease sites thereby eliminating geometric uncertainties in setup, patient motion, and patient changes. In this case, WSNs or IoT devices can be implanted or embedded close to the targets, and this will ensure the doses from the linear accelerator do not miss their targets. WSNs are perceived to be useful in achieving better treatment planning results toward appropriate prescription doses.

From Fig. 4, the Health Level-7 (HL7) connectivity utilizes XML technology for interoperating two or more systems for data definition and message exchanging, sharing and reusing within and between lab centres and clinics. On the other hand, the Digital Imaging and Communications in Medicine (DICOM) connectivity communicates with the various pieces of software for transmission of diagnostic images while the embedded systems, such as Laboratory Interface System (LIS), Pathology Interface System (PIS) and Radiology Interface System (RIS), serve as access points for the healthcare

providers to access patient information relating to lab results, malignancy or abnormal (pathology) results, and radiology results. In wrapping up, all these systems along with the pharmacy, medical oncology, and radiation oncology servers allow access to comprehensive patient chart information from any device (workstations, tablets, etc.) either at the clinical environment or via remote VPN access from outside the clinic(s). The underlying technologies being considered include: Bluetooth Low Energy (BT-LE), Near Field Communication (NFC), Radio Frequency Identification (RFID), and 6LoWPAN/WiFi/ZigBee [8]. Fig. 4 illustrates the network architecture for the proposed cancer care services.

2) *Business Analytics and Cloud Services*: With the growing rate of patient data generated by means of the wireless sensor networks (i.e. WBANs, wearables, smart devices, and embedded systems), data, queries and physical characteristics as observed from these devices and equipment are gathered and collected for researching, analyzing and reporting purposes; gaining intelligence; formulating insights; streamlining operations; and gaining competitive business advantage.

The incorporation of business analytics and cloud services to cancer care services ensures availability and accessibility of patient data being streamed from various sources on a real-time and continuous basis. This, in turn, enables the ever-increasing data to be managed and shared across the healthcare network systems upon deployment into the cloud. Obviously, streams of data are relayed and generated about patients and for some medical devices (through sensors and other connected devices) as related to the patients. These data, in form of multimedia, textual and visual formats, are transmitted through the cloud services to remote servers (data center). As a result, the volume, velocity, and variety of health data and information of patients have continually increased significantly, which puts challenges for analysis and interpretation of data for decision-making purposes using appropriate analytical tools [8].

This architecture also offers reporting capabilities for immediate dashboards that facilitate treatment decisions as we will be able to discover patterns from all the data from various services in order to analyze the quality of care and risk, disease and epidemic pattern, patient/facility monitoring and optimization, etc. This, indeed, will be beneficial to healthcare providers to turn a stream of data into actionable insights and evidence-based healthcare decisions about the health conditions of patients, and also for helping the clinical experts and research groups to keep up to date with the latest trends and breakthroughs in clinical oncology practices. The architecture uses the Picture Archiving Communication System (PACS), which comprises of secure computer systems for storage, retrieval, and display of diagnostic images such as X-rays, CT scans, Magnetic Resonance Imaging (MRIs), etc. The PACS constitutes an important component, where the diagnostic images are being retrieved and accessed through the business analytics and cloud services as made available on the cloud. In view of this, we have proposed an appropriate strategy to gather and analyze data as collected across the network fabric and communications infrastructure through

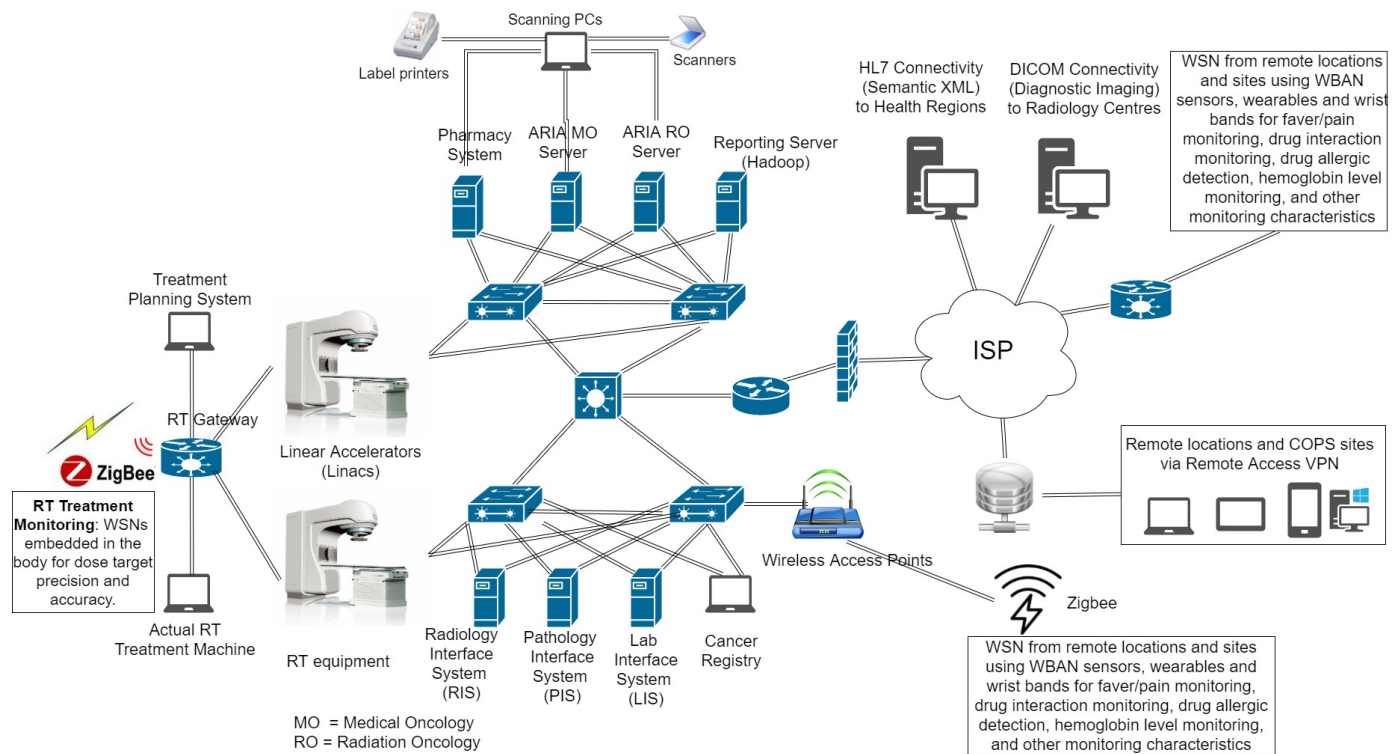


Fig. 4. Cancer Care Services Network Architecture.

secure transmissions from one end to the other. The details of the network architecture for the business analytics/cloud services are as depicted in Fig. 5, where the initial figure in [8] has been modified to include PACS component.

3) *Hadoop Deployment in Business Analytics and Cloud Services*: Based on the huge volume of data involved for those services, the Hadoop cluster or framework is viewed as an ideal solution for processing and solving the workloads associated with massive amounts of data storage, which ensure transformations between source systems and data warehouses. Hadoop cluster is used for predictive analytics through its own machine learning and data mining capabilities. With Hadoop cluster, crucial single point(s) of failure that could bring down the entire Hadoop cluster can be eliminated, and it makes provision for data to be normally triple replicated to ensure availability in the event of failures and disasters [10]. Other benefits of Hadoop include its low response time and real time alert capability. In summary, Hadoop is considered for the following features and characteristics, as follows [13]: *data value; schema; workload; data sources; availability; security; and scalability*. The NoSQL databases and Hadoop cluster components are suggested for the business analytics and cloud services basically for conducting disease, genomics and epidemic pattern research; patient-disease tracking and monitoring; patient sentiment analysis; risk and quality of care analysis; etc. (as shown in Fig. 5).

A. Operational Challenges and Security Issues

In [8], we have outlined the analysis of the operational challenges and security issues to cancer care services based

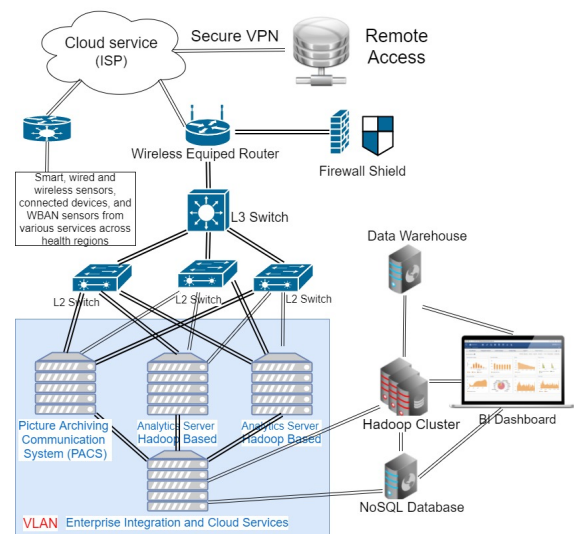


Fig. 5. Business Analytics and Cloud Services Network Architecture [8].

on IoT, which we will suggest to the reader to read it though additional information is provided here. While using business analytics on patient data, the issues of confidentiality and privacy have been a concern without exposing the patient demographic information to the research group and business experts. As a result, we will ultimately ensure that patient-sensitive information is protected and encrypted as this may be a major threat and barrier in realizing the potential benefits of business analytics services in healthcare environment, which could deter business improvements, if not addressed.

Since there are various nodes, wireless devices and sensors in the proposed solutions, then we have to ensure that those devices conform to industry standard (i.e. meeting the service- and operational-level agreements) that guarantee reliability and security. In addition, the reliability of the network system is very paramount especially due to the nature of the healthcare environment coupled with the sensitivity of patient information/data. This is one of the reasons why mesh topology is proposed, especially at the distribution layer such that every data transmitted from the source is accepted at the destination within a reasonable time. It is also to ensure high availability with minimal equipment failure and human intervention.

B. Securing IoT Services and Devices

Knowing that the security of patient medical data cannot be underestimated and jeopardized, then it becomes imperative to talk about securing the various devices and services being made available during the design of the IoT based medical system in order to avoid leakage of patient information. Hence, some feasible security mechanisms as related to this research include but not limited to: *security for communication in IoT*. For the communication in IoT devices from one layer to another in the network architecture, the three layouts: core, distribution, and access, should be an utmost consideration in terms of security and protection due to the nature of the healthcare environment; *security approaches or mechanisms for WSN, smart connected and remote (RFID) devices*. It is equally paramount to ensure security mechanisms for the WSNs that characterize the IoT solution through securing the routing protocols to prevent attacks that could affect the entire network. In addition, the security mechanisms can be extended to prevent illegal node access, while at the same introduce trust management and distribution mechanism for the WSN routing for data privacy and location privacy of patients within and outside the clinical environment, more so that a large number of nodes is required coupled with the generation/dissemination of a large amount of data; *security for IPv6 (6LoWPAN)*. The use of low power consumption devices and sensors should be considered especially with long-term device or sensory operation coupled with the involvement of human lives (as for devices that are embedded in the human body or with contact with the human body). This will certainly mandate the use of low power IPv6 architecture in the design of the IoT based solution with low power consumption for secured integration; and *security, privacy, and encryption of actuators/sensors, remote devices are equally important*.

V. CONCLUSIONS AND FUTURE WORK

We have proposed the implementation of the IoT based medical system, with reference to cancer care services and business analytics/cloud services, for enhanced treatment, diagnosis, and monitoring of cancer patients. The healthcare solution has been accomplished through the use of WSNs and smart connected devices. This is because WSN plays an important role that allows a number of spatially distributed autonomous sensors to be linked to the network fabric based

on geographical routing from source to destination, which facilitate data transmission/exchange. We have also delved into business analytics/cloud services that ensure the availability of patient data stream for actionable insights and evidence-based healthcare decisions. Also addressed are the operational and security challenges associated with the deployment of IoT based medical system due to the nature of the environment and the sensitivity of patient information. This is necessary prior to the go-live phase of the IoT based solution implementation to avoid failure to the entire system and breach of patient data.

In wrapping up, it is worth mentioning that there are various services being delivered in healthcare settings but we have only covered the cancer care and business analytics/cloud services. Hence, we will be considering and integrating more services in our future research work in the same research domain.

REFERENCES

- [1] Baena-Canada, J. M., Estalella-Mendoza, S., Rosado-Varela, P., Exposito-Alvarez, I., Gonzalez-Guerrero, M., Diaz-Blanco, M. C., Cortes-Carmona, C., Ramirez-Daffos, P., Arriola-Arellano, E., Rueda-Ramos, A., Solana-Grimaldi, L., Benitez-Rodriguez, E.: Use of health-care services during chemotherapy for breast cancer. *European Journal of Cancer*, 48, 3328–3334, (2012).
- [2] Dineshkumar, P., SenthilKumar, R., Sujatha, K., Ponmagal, R. S., Rajavarman, V. N.: Big Data Analytics of IoT based Health care monitoring system. *IEEE Uttar Pradesh Section International Conference on Electrical, Computer & Electronics Engineering*, 55–60, (2016).
- [3] Fan, Y. J., Yin, YH., Xu, LD., Zeng, Y., Wu, F.: IoT-Based Smart Rehabilitation System. *IEEE Transactions on Industrial Informatics*, 10(2), 1568–1577, (2014).
- [4] Lakkis, S., Elshakankiri, M.: IoT based Emergency and Operational Services in Medical Care Systems, 13th CTTE/CMI Conf. on Internet of Things – Business Models, Users, & Networks, Denmark (2017).
- [5] Lewis, W: LAN Switching and Wireless. *CCNA Exploration Companion Guide*. Cisco Press, Indianapolis, Indiana, USA, (2009).
- [6] Liu, W.: Robustness Quantification and Worst-Case Robust Optimization in Intensity-Modulated Proton Therapy. In Rath, A.K., Sahoo N. (eds.), *Particle Radiotherapy: Emerging Technology for Treatment of Cancer*, Springer India, 139–155, (2016).
- [7] Lu, D., Liu, T.: The Application of IoT in Medical System. *IEEE Intl. Symposium on IT in Medicine and Education*, (1), 272–275, (2011).
- [8] Onasanya, A., Elshakankiri, M.: IoT Implementation for Cancer Care & Business Analytics/Cloud Services. In *Proc. of the 10th IEEE/ACM International Conference on Utility & Cloud Computing (UCC 2017)*, 205–206, Austin, TX, (2017). <https://doi.org/10.1145/3147213.3149217>
- [9] Rahmani, A., Thanigaivelan, N. K., Gia, T. N., Granados, J., Negash, B., Liljeberg, P. & Tenhunen, H.: Smart e-Health Gateway: Bringing intelligence to Internet-of-Things based ubiquitous healthcare systems. *12th Annual IEEE Consumer Communications and Networking Conference (CCNC)*, 826–834, (2015).
- [10] Riazul Islam, S. M., Kwak, D., Kabir, H., Hossain, M., Kwak, K.S.: The IoT for Health Care: A Comprehensive Survey. *IEEE Access*, 3, 678–708, (2015).
- [11] Satija, U., Ramkumar, B., Sabarimalai Manikandan, M.: Real-Time Signal Quality-Aware ECG Telemetry System for IoT-Based Health Care Monitoring. *IEEE Internet of Things Journal*, 4(3), pp.815–823, (2017).
- [12] Sohraby, K., Minoli, D., Znati, T.: *Wireless Sensor Networks: Technology, Protocols, & Applications*, John Wiley & Sons Inc., NJ, (2007).
- [13] Stackowiak, R., Licht, A., Mantha, V., Nagode, L.: *Big Data and The IoT. Enterprise Information Architecture for A New Age*, Apress, Ontario, (2015).
- [14] A Wireless Sensor Networks Bibliography. Autonomous Networks Research Group. <http://ceng.usc.edu/~anrg/SensorNetBib.html#0103>. Retrieved on May 25, 2017.
- [15] IoT project for home cancer care. <http://wireless.electronicspecifier.com/around-the-industry/internet-of-things-project-for-home-cancer-care>. Retrieved on June 5, 2017.
- [16] State of IoT Healthcare by Aruba, an HP Enterprise company. <http://www.arubanetworks.com/iot>. Retrieved on May 25, 2017.

Joint PHY-MAC Realistic Performance Evaluation of Body-to-Body Communication in IEEE 802.15.6 and SmartBAN

Rida Khan, Muhammad Mahtab Alam
 Thomas Johann Seebeck Department of Electronics
 Tallinn University of Technology
 Tallinn, Estonia
 Email: {rikhan, muhammad.alam}@ttu.ee

Abstract—This paper presents the joint physical-medium access control (PHY-MAC) performance analysis of inter-BAN communication systems using realistic body-to-body (B2B) wireless channel model in IEEE 802.15.6 and smartBAN standards. The time-varying distances for the space-time B2B link variations are generated by real-time motion capture traces which are then introduced into already established B2B wireless channel model to give the actual path-loss values in dynamic environments. The SNR (Signal to Noise Ratio), BER (Bit Error Rate) and PER (Packet Error Rate) computations are briefly discussed to give an overview of the radio link modeling employed in the simulations. Using the mobility and the proposed radio link models, a more tangible performance assessment of B2B systems with IEEE 802.15.6 and SmartBAN specifications is achieved. Consequently, transmission power, packet length and data rate variations are investigated and the obtained results of packet reception rate (PRR) identify “head” as the best position to place the coordinator nodes for B2B communication.

Keywords—WBANs; inter-BAN; mobility modeling; radio link modeling; IEEE 802.15.6; SmartBAN; PRR.

I. INTRODUCTION

Wireless body area networks (WBANs) refer to a network of sensors (and/or actuators) placed on, inside or around the human body in order to serve a variety of emerging applications [1]. WBANs not only offer a wide scope of research and development but also represent a new generation of personal area networks, with their own unique set of challenges for implementation. The vital issues encountered by WBAN technology include the mobility of WBAN nodes, reliable low power operation, security and privacy of WBAN data and coexistence of multiple WBANs in the same environment [2]. WBANs have different types of communication scenarios based on the relative positions of WBAN nodes. The placement of communicating BAN nodes on multiple bodies is attributed to body-to-body Networks (BBNs) [3]. BBNs provide innovative solutions for a wide range of applications such as remote health care, precision monitoring of athletes, search and rescue operations in disastrous situations and coordination of soldiers on a battlefield [3].

Most of the efforts in channel characterization of WBANs have been dedicated to on-body communications and the contribution of research efforts in body-to-body (B2B) channel

modeling is quite limited. Nonetheless, many noteworthy contributions exist in the literature which attempt to discuss B2B channel characteristics [4]–[6]. But these channel models assume very limited mobility scenarios and for the realistic performance evaluation of BBNs on the higher layers such as medium access control (MAC) and network, accurate mobility and radio link modeling should be taken into account. A comprehensive analysis of the MAC layer performance evaluation is presented in [7] for on-body communication scenario, after measuring the channel characteristics when the nodes are placed on a walking subject. The notion of integrating realistic mobility traces with IEEE 802.15.6 channel models for accurate performance analysis of on-body communication at the MAC layer was proposed in [8]. Considering other co-located WBAN signals as interference and jointly exploiting on-body and B2B realistic channel models, a comprehensive MAC level performance analysis of intra-BAN communication is given in [9], [10]. However, to the best of our knowledge, no research work has been dedicated so far to study the joint physical-MAC (PHY-MAC) layer performance evaluation of inter-BAN communication systems under realistic/unrestricted mobility scenarios.

This research work is focused on the joint PHY-MAC performance assessment of B2B communication over a dedicated frequency channel with realistic channel models, using IEEE 802.15.6 and smartBAN standards specifications. The primary contributions of this paper include the identification of suitable positions to place the BAN coordinators for B2B communication and the examination of appropriate transmission power levels under different packet sizes and data rates. With the help of real time motion capture data, mobility traces are generated for multiple co-located BANs which provide dynamic distances with space-time variations. These dynamic distances serve to provide the realistic path-losses for B2B links under various mobility profiles (e.g., walking, running, standing etc.) using the B2B channel model derived by the real time measurement campaign. Subsequently, a detailed radio link modeling, based on the B2B channel characteristics, is implemented in which signal to noise ratio (SNR), bit error rate (BER) and packet error rate (PER) are computed using

the generated path-losses. The performance is examined in terms of packet reception rate (PRR) and the PHY-MAC layer specifications of both IEEE 802.15.6 as well as SmartBAN are considered in this context. A thorough investigation of PRR reveals that the relative coordinator nodes position is crucial for reliable data transmission over B2B links under real time dynamic environments.

The rest of the paper is arranged in the following way: section II elaborates the system model whereas IEEE 802.15.6 and smartBAN PHY-MAC layer parameters are described in section III. In section IV, the simulation results are presented and discussed while section V gives the concluding remarks.

II. SYSTEM MODEL

This section explains the underlying system model used in performance evaluation, as given:

A. B2B Channel Model

We use B2B channel model derived in [11], [12], using real time measurement campaigns under restricted mobility scenarios. This channel model provides channel gain, long term (LT) and short term (ST) fading components to estimate the path-loss values and the channel characteristics are a function of inter-body distance (d) and mutual body orientation (α) for various inter-BAN links. These links include head-to-head, belt-to-belt, wrist-to-wrist, head-to-belt, head-to-wrist, belt-to-wrist and vice versa, as depicted in Fig. 1, and are in-line with the links investigated in [11], [12]. In this model, shadowing effects by the bodies are primarily dealt with the distance and orientation-dependent channel gain, LT effects caused by the environment are represented by LT fading and ST fading is the outcome of the constructive and destructive interference resulting from multi-path propagation. According to [11], the distance (d) and orientation (α) dependent channel gain can be stated in dB as

$$G(d, \alpha) = G_0(\alpha) - 10n(\alpha)\log_{10}\left(\frac{d}{d_0}\right), \quad (1)$$

where n corresponds to the path-loss exponent and G_0 represents the gain at the reference distance d_0 , equal to 1m. $G_0(\alpha)$ and $n(\alpha)$ show different characteristics for various links between the relative node positions over different BANs. For example, n and G_0 do not exhibit mutual orientation dependence for head-to-head links between two different BANs so, distance-based channel gain can be calculated with the fixed values of n and G_0 . But mutual orientation α is crucial in determining n and G_0 values for other links mentioned previously. Further information about $G_0(\alpha)$ and $n(\alpha)$ calculations for obtaining the channel gains corresponding to other links can be found in [11]. The LT fading component in dB scale can be characterized with a zero-mean normal distribution [11] as

$$f(z_{LT}) = \frac{1}{\sigma_{LT}\sqrt{2\pi}} \exp\left(\frac{-z_{LT}^2}{2\sigma_{LT}^2}\right), \quad (2)$$

where z_{LT} is the LT fading component in dB and σ_{LT} is the standard deviation, whose values for different B2B links

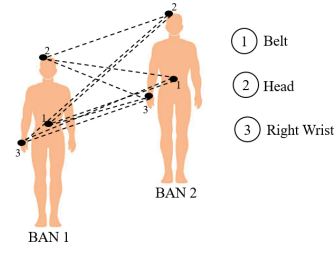


Fig. 1: B2B Channels.

are indicated in [11, Tab. 5]. The ST fading envelope can be typically represented by Rice distribution [11], [12], as given

$$f(z_{ST}) = \frac{z_{ST}}{\sigma^2} \exp\left(\frac{-z_{ST}^2 - A^2}{2\sigma^2}\right) I_0\left(\frac{z_{ST}A}{\sigma^2}\right), \quad (3)$$

where z_{ST} is the ST fading envelope, A is the non-centrality parameter and σ represents the scale parameter. Rice K -factor, the power ratio between the direct path and the multi-paths, is given as $K = \frac{A^2}{2\sigma^2}$. The characteristics of head-to-head links again do not show mutual orientation-dependence in estimating A and σ values whereas for other links, A and σ values are mainly described by mutual orientation α [11], [12]. A comprehensive discussion of ST fading properties for other B2B links is presented in [11], [12].

B. Realistic Mobility Modeling

The space-time variations of wireless links under unrestricted mobility are often not fully considered while developing path-loss models using measurement campaigns [8]. The B2B channel model proposed in [11], [12] assumes restricted mobility scenarios (close and far crossing and parallel walking) and can be enhanced to give more practical inter-BAN performance by the integration of dynamic distances with unrestricted mobility. This can be accomplished by exploiting real-time body motion capture traces which include various mobility scenarios (walking, running, sitting, exercising etc.) [8]. This real-time motion capture data when combined with geometrical transformation and analysis methods helps in actual performance evaluation of BANs and BBNs. The details of the entire process for intra-BAN communication are illustrated in [8], [10] but the major changes in algorithm to modify it for B2B communication are mentioned as

- The determined body constructed by motion capture traces is replicated in multiple human bodies for simulating dynamic inter-BAN links.
- The impact of body shadowing is mainly considered in the distance and orientation-dependent channel gain for the links between various relative node positions, as discussed in sub-section II-A, so, it is not important to characterize such links as LOS or NLOS. But wrist-related channels can be line of sight (LOS) or non-line of sight (NLOS) for the same body orientation because for the same α , the two nodes may either be shadowed or not by the torso [11], [12]. Therefore, geometrical analysis is

applied to ensure the accuracy of link types in inter-BAN wrist-related channels. In this case, the intersection of the link with single or multiple human body torso cylinders declares the given B2B link as NLOS for the wrist-related channels.

- Space-time varying inter-BAN links and mobility traces are generated to give the appropriate dynamic distances for the B2B channels mentioned in sub-section II-A. The mutual orientation between two separate BANs is taken the same throughout the mobility trace duration since a coordinated movement scenario is simulated in this paper and the variations in α are within a range of 10° . Furthermore, the classification of dynamic link types as LOS or NLOS is performed for B2B wrist-related channels.

After obtaining the dynamic distances and link types for the given inter-BAN scenario, the channel behavior is accurately modeled with unrestricted mobility. The inter-BAN dynamic distances and mutual orientation are used to obtain channel gain values while ST fading parameters for different links are a function of mutual orientation only. The channel gain, LT fading and ST fading for wrist-related channels are computed differently for LOS and NLOS link types so, the knowledge of dynamic link types is important in this context. It should be noted that mobility modeling provides higher and more accurate space-time variations which help in estimating more accurate path-loss results in comparison to the restricted mobility based channel models [8], [10] for B2B channels. Subsequently, the obtained path-loss values are utilized in radio link modeling to calculate the SNR, BER and PER. The entire system model with mobility modeling, B2B channel modeling and radio link modeling is illustrated in Fig. 2.

C. Radio Link Modeling

The realistic mobility modeling of inter-BAN communication and the resultant space-time varying channels are followed by the significance of accurate radio link modeling, which

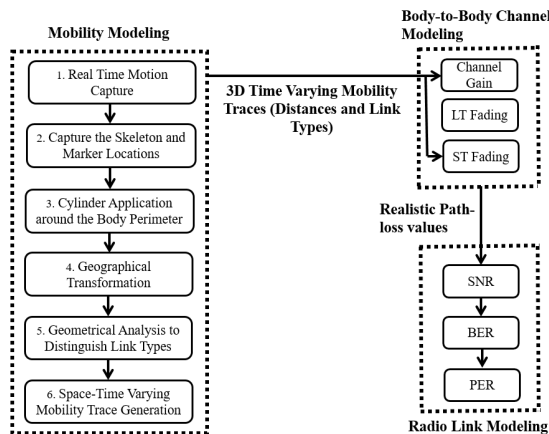


Fig. 2: Mobility, channel and radio link modeling for B2B communication.

includes SNR, BER and PER evaluation. The PER estimation using threshold based method is not an accurate approach [8], so an extensive approach and a practical method is presented in this sub-section to calculate PER for B2B links. The SNR between the two nodes i and j on two different BANs over the time index t can be written as

$$SNR_{i,j,t}^{dB} = P_{Tx}^{dBm} + PL_{i,j,t}^{dB} - P_N^{dBm}, \quad (4)$$

where P_{Tx} is the transmit power, P_N is the noise power and $PL_{i,j,t}^{dB}$ is the path-loss between i and j over the time t .

The exact formulation of the energy per bit to noise power spectral density ratio E_b/N_0 and BER is done depending upon the frequency and exact data rate at the physical layer. According to IEEE 802.15.6 physical layer specifications, differential binary phase shift keying (DBPSK) modulation is used for low data rates and differential quadrature phase shift keying (DQPSK) modulation is employed for high data rates at 2.45 GHz frequency [1]. The value of E_b/N_0 in dB, based on the current $SNR_{i,j,t}^{dB}$, bandwidth BW in Hz and data rate R in bps can be written as

$$E_b/N_0[dB] = SNR_{i,j,t}^{dB} + 10\log_{10}\left(\frac{BW}{R}\right), \quad (5)$$

Since Rice type ST fading is assumed in the channel model, therefore the corresponding DBPSK BER for low data rate between the inter-BAN links i and j over the time t can be calculated as

$$BER_{i,j,t}^{DBPSK} = \frac{K+1}{2(1+K+\Gamma)} \exp\left(-\frac{K\Gamma}{1+K+\Gamma}\right). \quad (6)$$

where Γ is the average SNR given as $\Gamma = E\{z_{ST}^2\} \frac{E_b}{N_0}$ [13]. The DQPSK BER expression for high data rate is derived using the Rice density equation as a function of instantaneous SNR γ_b and the DQPSK additive white Gaussian noise (AWGN) error equation which are respectively written as

$$p(\gamma_b) = \frac{K+1}{\Gamma} \exp\left(-\frac{\gamma_b(K+1) + K\Gamma}{\Gamma}\right) I_0\left(\sqrt{\frac{4(K+1)K\gamma_b}{\Gamma}}\right), \quad (7)$$

$$P_e(\gamma_b) = Q\left(\sqrt{1.112\gamma_b}\right). \quad (8)$$

Substituting $p(\gamma_b)$ and $P_e(\gamma_b)$ into the average error probability expression $P_e = \int_0^\infty P_e(\gamma_b)p(\gamma_b)d(\gamma_b)$ [13] and integrating using the Chernoff bound for Gaussian Q-function $Q(\gamma_b) \leq \frac{1}{2}\exp^{-\frac{\gamma_b^2}{2}}$ [14], the upper bound on the respective DQPSK BER for high data rate between the inter-BAN links i and j over the time t can be described as

$$BER_{i,j,t}^{DQPSK} \leq \frac{\Gamma}{2(1+K+0.556\Gamma)} \left(\frac{K+1}{\Gamma}\right) \exp\left(-K + \frac{K(K+1)}{1+K+0.556\Gamma}\right). \quad (9)$$

The smartBAN standard defines the usage of Gaussian minimum shift keying (GMSK) with the bandwidth-bit period product (BT) of 0.5 and modulation index (h) of 0.5 as the key modulation technique at the physical layer [15]. The upper bound on GMSK BER under Rice fading is acquired using the procedure discussed above and taking $P_e(\gamma_b)$ as

$$P_e(\gamma_b) = Q\left(\sqrt{2\epsilon\gamma_b}\right), \quad (10)$$

where ϵ is the GMSK constant and for BT of 0.5 is equal to 0.79 [16]. The upper bound on the corresponding GMSK BER between the given B2B links i and j over the time t is therefore mentioned as

$$BER_{i,j,t}^{GMSK} \leq \frac{\Gamma}{2(1 + K + 0.79\Gamma)} \left(\frac{K + 1}{\Gamma} \right) \exp\left(-K + \frac{K(K + 1)}{1 + K + 0.79\Gamma}\right). \quad (11)$$

Consequently, the PER is computed based on the packet length N in bits and the adequate $BER_{i,j,t}$ expression as

$$PER_{i,j,t} = 1 - (1 - BER_{i,j,t})^N. \quad (12)$$

Finally, the obtained PER values which are based on the dynamic space-time dependent channel measurements and the accurate radio link modeling, are given to the high level packet-oriented simulation environment for the MAC layer performance evaluation.

III. PHY/MAC LAYER PARAMETERS

In this work, the joint PHY-MAC layer performance evaluation in terms of both IEEE 802.15.6 and smartBAN standards is performed. Therefore, this section highlights the physical and the MAC layer specifications of IEEE 802.15.6 and smartBAN used in the PRR simulations.

A. IEEE 802.15.6 PHY/MAC Layer

We consider time division multiple access (TDMA)-based scheduled access mechanism with beacon-enabled superframe format [1] since the priority is the investigation of the impact of accurate channel modeling on MAC layer performance. The variable-length MAC frame body is appended with MAC frame header and frame check sequence (FCS) to form physical layer service data unit (PSDU), which is spread using the spreading factor determined by the data rate. The resulting PSDU is added with physical layer convergence protocol (PLCP) preamble for timing synchronization, channel offset recovery and packet detection and with PLCP header for conveying information about the physical and MAC parameters required at the receiver side. The PLCP header spreading is additionally done and the combination of PLCP preamble, PLCP header and PSDU forms a physical layer protocol data unit (PPDU) which represents the information transmitted through the propagation medium [17]. Guard duration is used to separate PPDU's sent by different BBN nodes in different time slots. The additional information on guard duration formulation using the synchronization interval, inter-frame spacing and turnaround time, as well as the maximum

packet transmission duration and packet size calculations can be found in [1], [17].

B. SmartBAN PHY/MAC Layer

Again TDMA-based scheduled access method is used in this context and each time slot comprises of data frame transmission and ACK frame transmission periods separated by inter-frame spacing. Each BBN node transmits its data in data frame transmission period while the receiving node shall send an ACK frame (successful transmission) or a NACK frame (unsuccessful transmission) in the ACK frame transmission time which is ended with inter-frame spacing at the end of the slot [18].

On the MAC layer, a 56 bit MAC header and 16 bit frame parity are added to the MAC frame body to generate MAC protocol data unit (MPDU). Since we assume uncoded data transmissions for both IEEE 802.15.6 and smartBAN, MPDU will be the same as PSDU. The PSDU is further appended with 16 bit PLCP preamble and 40 bit PLCP header fields to create a PPDU structure [15]. A complete discussion on the smartBAN physical and MAC layer specifications and parameters can be explored in [15], [18].

IV. JOINT PHY-MAC PERFORMANCE RESULTS

This sections presents a thorough analysis of the results obtained using the system model and PHY/MAC layer parameters discussed in Section II and III respectively.

A. Simulation Setup

We assume three different BANs with one of them being the leader (BAN1) and the rest two being the followers (BAN2 and BAN3), receiving information from their leader for the coordinated movements over a dedicated frequency channel. Note that a separate frequency channel is used for on-body communication within each BAN and here different coordinator node positions for inter-BAN communication are investigated. The mobility scenarios considered in the simulations include walking, running, sitting and standing and therefore, represent the primary movements made in the mission critical operations and precise monitoring during sports activities. The node positions for all the BANs examined in simulations consist of head (H), belt (B) and right wrist (W). Each coordinator node on the leader BAN sends its information to all the other coordinator nodes placed on the follower BANs in its assigned time slot with an objective to identify the best coordinator

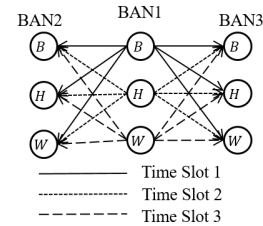


Fig. 3: TDMA for B2B communication.

location, as shown in Fig. 3. For IEEE 802.15.6 standard, MAC payload sizes of 16, 128 and 256 bytes as well as both low data rate (LDR, 121.4 kbps) and high data rate (HDR, 971.4 kbps) are considered. Whereas smartBAN assumes a data rate of 1000 kbps for all payload sizes [15] and with no data transmission repetition, MAC payload sizes of 16, 128 and 250 bytes are taken.

B. Simulation Results

The main purpose of this work is the investigation of the suitable coordinator nodes positions in inter-BAN communication using PRR as the performance criteria. For this purpose, statistical results including mean, standard deviation and correlation coefficient of path-losses corresponding to different transmitter-receiver location combinations are listed in Table I. The results are demonstrated for the running scenario since it involves the highest level of mobility. It can be seen that for every transmitter node location, the mean path-loss values are the minimum when the receiver node is placed on head. Moreover, the positioning of the transmitter node on head also results in the reduction of mean path-loss values as compared to the other coordinator positions. Furthermore, the high correlation coefficient values indicate

TABLE I: Statistical Analysis of the Channel Model with Mobility Modeling (Running Scenario)

Link Type	Mean	Standard Deviation	Correlation Coefficient
Belt-to-Belt	59.25	3.18	0.23
Belt-to-Head	54.50	2.94	0.17
Belt-to-Wrist	71.36	3.97	0.20
Head-to-Belt	54.35	2.90	0.14
Head-to-Head	42.15	2.72	0.17
Head-to-Wrist	66.41	17.09	0.67
Wrist-to-Belt	74.65	3.91	0.20
Wrist-to-Head	63.90	13.92	0.55
Wrist-to-Wrist	60.83	3.37	0.25

that the unrestricted mobility-based path-loss model keeps the track of high mobility and temporal variations for B2B links as well, in the same manner as indicated in [8] for on-body links. It is also noticeable that the statistical values are not very different when the transmitter and the receiver node positions are interchanged. Using these observations as the basis, the MAC level performance results are further narrowed down to the links which include head as the receiver node position since these links assume comparatively lesser mean path-losses.

Fig. 4, Fig. 5 and Fig. 6 summarize the PRR results of belt-to-head, head-to-head and wrist-to-head links respectively for different transmission power levels using IEEE 802.15.6 specifications. It is quite obvious that head-to-head links outperform all the other links while wrist-to-head links give the worst performance. The PRR values degrade for all link types if the packet size and the data rate are increased. For belt-to-head links, the acceptable performance of equal or above 90 percent PRR is achieved only when 16 byte payload is sent with LDR at any given transmission power level. 128 byte payload also gives adequate performance when transmitted at higher power levels with LDR. But for head-to-head links, the PRR performance is considerably improved in comparison to the belt-to-head links. For LDR, the transmission of different payload sizes is permissible even at the lower transmission power levels. High transmission power and small payload size should be used when data is transmitted at the high rate. For wrist-to-head links, a PRR above 90 percent is achieved only at the higher transmission power levels with lower payload sizes and data rate.

Finally, the PRR performance evaluation of smartBAN is shown in Fig. 7 for the above mentioned link types. Head-to-head links again give the best results among all the link types with smartBAN specifications as well. Data can be sent with all payload sizes at almost all transmission power levels over head-to-head links. For belt-to-head links, payload of 16 bytes can be transmitted at the transmission power level of above -5dB while the payload size of 128 bytes requires higher

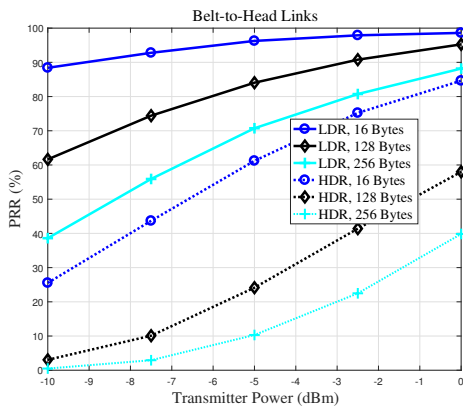


Fig. 4: PRR versus transmission power level results for belt-to-head links in BBN, $N = 16, 128$ and 256 bytes, LDR (121.4 kbps) and HDR (971.4 kbps).

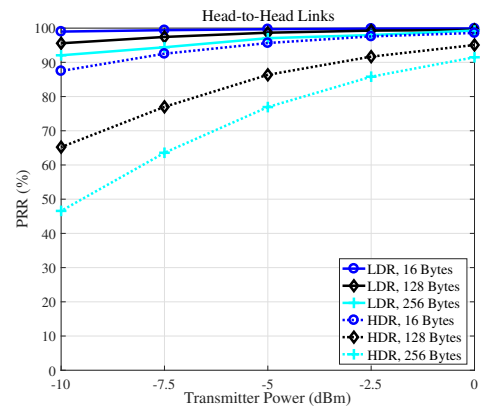


Fig. 5: PRR versus transmission power level results for head-to-head links in BBN, $N = 16, 128$ and 256 bytes, LDR (121.4 kbps) and HDR (971.4 kbps).

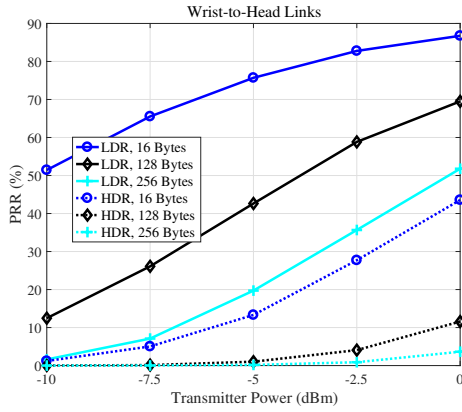


Fig. 6: PRR versus transmission power level results for wrist-to-head links in BBN, $N = 16, 128$ and 256 bytes, LDR (121.4 kbps) and HDR (971.4 kbps).

transmission power levels. Finally, wrist-to-head links do not contribute to any transmission with acceptable performance for any payload size or transmission power and might require encoded or repetitive transmissions.

V. CONCLUSION

Recently developed channel models through measurement campaigns are integrated into realistic mobility and radio link modeling and the joint PHY-MAC performance evaluation of B2B communication for IEEE 802.15.6 and smartBAN standards specifications is performed. The usage of mobility modeling facilitates more accurate performance analysis of time-varying inter-BAN links. The presented results indicate that the placement of coordinators on the head significantly reduces the required transmission power levels for inter-BAN communication, even at high data rate and payload sizes.

ACKNOWLEDGMENT

This research was supported by the Estonian Research Council through the Institutional Research Project IUT19-11, and by the Horizon 2020 ERA-chair Grant Cognitive Electronics COEL H2020-WIDESPREAD-2014-2 (Agreement number: 668995; project TTU code VFP15051).

REFERENCES

- [1] A. Astrin et al., "IEEE Standard for Local and Metropolitan Area Networks Part 15.6: Wireless Body Area Networks: IEEE Std. 802.15.6-2012," February 2012.
- [2] S. Movassaghi, M. Abolhasan, J. Lipman, D. Smith, and A. Jamalipour, "Wireless Body Area Networks: A Survey," *IEEE Commun. Surveys and Tutorials*, vol. 16, no. 3, pp. 1658-1686, Jan. 2014.
- [3] M. M. Alam and E.B. Hamida, "Surveying Wearable Human Assistive Technology for Life and Safety Critical Applications: Standards, Challenges and Opportunities," *Sensors*, vol. 14, no. 5, pp. 9153-9209, 2014.
- [4] S. L. Cotton and W. G. Scanlon, "Channel Characterization for Single- and Multiple-Antenna Wearable Systems Used for Indoor Body-to-Body Communications," *IEEE Trans. on Antennas Propag.*, vol. 57, no. 4, pp. 280-290, Apr. 2009.
- [5] Y. Wang, I. B. Bonev, J. O. Nielsen, I. Z. Kovacs, and G. F. Pedersen, "Characterization of the Indoor Multi antenna Body-to-Body Radio Channel," *IEEE Trans. on Antennas and Propag.*, vol. 57, no. 4, pp. 972-979, 2009.

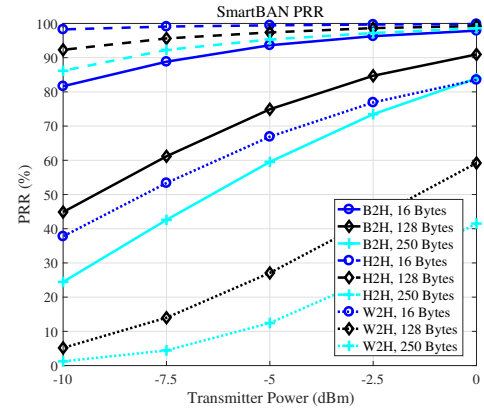


Fig. 7: PRR versus transmission power level results for smartBAN, $N = 16, 128$ and 250 bytes, belt-to-head (B2H), head-to-head (H2H) and wrist-to-head (W2H) links.

- [6] N. Bhargav, S. L. Cotton, and D. B. Smith, "An Experimental-Based Analysis of Inter-BAN Co-Channel Interference Using the κ - μ Fading Model," *IEEE Trans. on Antennas and Propag.*, vol. 65, no. 2, pp. 983-988, Dec. 2016.
- [7] R. Rosini, F. Martelli, M. Maman, R. D'Errico, C. Buratti, and R. Verdone, "On-body area networks: from channel measurements to MAC layer performance evaluation," in *Proc. 18th European Wireless Conference*, Poznan, Poland, April 2012.
- [8] M. M. Alam and E. B. Hamida, "Towards Accurate Mobility and Radio Link Modeling for IEEE 802.15.6 Wearable Body Sensor Networks," in *Proc. 10th WiMob Conference*, Oct. 2014, pp. 298-305.
- [9] M. Maman, F. Mani, B. Denis, and R. D'Errico, "Evaluation of multiple coexisting Body Area Networks based on realistic on-body and body-to-body channel models," in *Proc. 10th Int. Symp. on Medical Info. and Commun. Tech.*, Mar. 2016, pp. 1-5.
- [10] M. M. Alam, E. B. Hamida, D. B. Arbia, M. Maman, F. Mani, B. Denis, and R. D'Errico, "Realistic Simulation for Body Area and Body-To-Body Networks," *Sensors*, vol. 16, no. 4, art. 561, 2016.
- [11] F. Mani and R. D'Errico, "A Spatially Aware Channel Model for Body-to-Body Communications," *IEEE Trans. on Antennas and Propag.*, vol. 64, no. 8, pp. 3611-3618, Aug. 2016.
- [12] F. Mani and R. D'Errico, "Short term fading spatial dependence in indoor body-to-body communications," in *Proc. IEEE 26th Annual Int. Symp. on Pers. Indoor and Mobile Radio Commun. (PIMRC)*, Aug. 2015, pp. 171-175.
- [13] F. Ziong, "Digital Modulation Techniques." Artech House Inc., 2006, p. 553-559.
- [14] S. H. Chang, P. C. Cosman, and L. B. Milstein "Chernoff-Type Bounds for the Gaussian Error Function," *IEEE Trans. on Commun.*, vol. 59, no. 11, pp. 2939-2944, Nov. 2012.
- [15] W. H. Chin, H. Tanaka, T. Nakanishi, T. Paso, and M. Hamalainen, "An Overview of ETSI TC SmartBAN's Ultra Low Power Physical Layer," in *Proc. IEEE 9th Int. Symp. on Medical Info. and Commun. Tech.*, Mar. 2015, pp. 6-9.
- [16] R. Anane, M. Bouallegue, K. Raoof, and R. Bouallegue, "Achieving Energy Efficient and Reliable Communication in WSN with Coded GMSK System under various Channel Conditions," in *Proc. IEEE Int. Conf. on Wireless Comm. and Mobile Computing.*, Aug. 2015, pp. 769-775.
- [17] M. M. Alam and E. B. Hamida, "Strategies for Optimal MAC Parameters Tuning in IEEE 802.15.6 Wearable Wireless Sensor Networks," *Journal of Medical Systems*, vol. 39, no. 9, pp. 106-120, Aug. 2015.
- [18] T. Paso, H. Tanaka, M. Hamalainen, W. H. Chin, R. Matsuo, S. Subramani, and J. Haapola, "An Overview of ETSI TC SmartBAN MAC Protocol," in *Proc. IEEE 9th Int. Symp. on Medical Info. and Commun. Tech.*, Mar. 2015, pp. 10-14.

Performance Comparison between ETSI SmartBAN and Bluetooth

Andrea D'Souza¹, Harri Viittala², Matti Hämäläinen², Lorenzo Mucchi¹

¹Department of Information Engineering, University of Florence, Florence, Italy
matrea3@gmail.com, lorenzo.mucchi@unifi.it

²Centre for Wireless Communications
University of Oulu, Oulu, Finland
harri.viittala@gmail.com, matti.hamalainen@oulu.fi

Abstract—This paper introduces the comparative performance analysis between ETSI SmartBAN and Bluetooth low energy (BLE) in the interfered additive white Gaussian noise (AWGN) channel as well as in multipath fading channel. Both technologies are possible solutions for wireless body area networks (WBAN) to implement services like delivering the vital signs data of an individual. The results show how the SmartBAN can outperform BLE in both AWGN and fading channel. In addition, SmartBAN can take advantages of repetition and coding features, which are not present in BLE to increase its performance even more.

Keywords—bluetooth low energy, interference; multipath; bit error rate; frame error rate.

I. INTRODUCTION

The use of wireless body area network (WBAN) is one way to convey further a vital sign information measured from a human body. This procedure is a modern way towards personalized healthcare and remote health monitoring. If a patient can be remotely monitored and the health-related information is possible to ubiquitously access by healthcare professionals, patients can be, e.g., discharged earlier from hospitals thus reducing medics workload and reduce costs.

In 2013, the European Telecommunications Standards Institute (ETSI) initiated a work towards smart body area networks under the technical committee (TC) SmartBAN. The focus of SmartBAN is to develop a low-power technology to be used in wireless devices for wearable and implantable devices. The SmartBAN utilization areas include health & wellness, training, personalized medicine and safety applications. [1]

So far, TC SmartBAN has released three standards [2]-[4]. In addition, technical report describing the radio environment at hospital is released [5].

The objective of this paper is to compare the SmartBAN technology with another low power technology useable in wireless medical application, namely Bluetooth low energy (BLE) standard [12]. Both standards have low power consumption and are operating at the 2.4 GHz ISM (Industrial, Science and Medical) band. BLE is one of the most used standards nowadays for wireless short-range communications.

The paper is organized as follows: Section II provides description of Bluetooth low energy and of the main characteristics of its physical layer. In Section III, simulation models of the SmartBAN and BLE used in the study are given. In Sec. IV, the simulation results are shown and discussed. The conclusions are given in Sec. V.

II. OVERVIEW OF BLETOOTH LOW ENERGY STANDARD

The concept of low energy in Bluetooth has been introduced in 2010 with the Bluetooth 4.0 standard but has been proved that the two technologies (Bluetooth and BLE) are not interchangeable. [14]

The BLE is developed to improve the Bluetooth performance in regards of energy consumption, to reduce the costs and for less complexity respect to the original Bluetooth technology [13]. BLE design is similar in respect to the typical Bluetooth (BT) with very few differences at physical layer (PHY) level. In this study, a BLE PHY model following the specification from [12] is developed. The model, with modulation and frequency hopping features, is verified with the standard Bluetooth PHY model designed by Mathworks [14].

The operating frequency band of the BLE is between 2402 MHz and 2480 MHz. Instead of the 79 channels of 1 MHz in the BT, BLE is characterized by 40 channels with 2 MHz spacing. The 40 BLE channels are shown in Figure 1. [15] The three highlighted channels are named advertising channels used mainly for highlight own presence or discovering devices. Advertising channels are channels 37, 38 and 39, decentralized respectively in the following frequencies 2402, 2426 and 2480 MHz. The other 37 channels are used to transfer data between devices, and they are named data channels. [16]

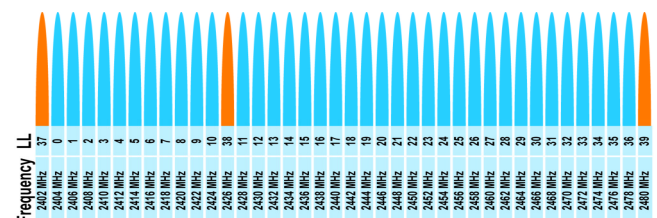


Figure 1. Bluetooth Low Energy Frequency Channels.

One of the main points of the BLE and BT technologies is the use of frequency hopping mechanism. In BLE, an adaptive frequency hopping mechanism is used in data channels to prevent multipath fading or channels interference [17]. In the simulator, the frequency hopping code is implemented according to [12].

Another specification of the physical layer of BLE is the modulation, which is Gaussian Frequency Shift Keying (GFSK), so the data pulses are first filtered in a Gaussian filter and then after are FSK modulated with a modulation index in the range [0.45 - 0.55]. A transmission rate is 1 Mbps with 1 bit per symbol [12].

III. SIMULATION MODEL

In this section, the simulation models used in the study are presented.

A. SmartBAN simulator

ETSI SmartBAN PHY model is based on the overall system description presented in [6] and physical layer definitions from [2][7]. Radio channel model is based on the on-on-body channel model CM3 by the IEEE [8]. In addition, realistic, measurement based co-channel interference as introduced in [5][9] is used in the simulations. The performance of SmartBAN system in interfered fading channel is presented in [10] and [11], but the comparative analysis between SmartBAN and any other competing technology has not been published yet. This paper is fulfilling this gap by comparing SmartBAN and BLE bit-error-rate (BER) performances in AWGN and fading channels. The SmartBAN simulator is based on the simulator presented in [19], and it is illustrated in Figure 2. The data bits $b[k]$ are encoded with the BCH (127,113) encoder followed by GFSK modulator with the modulation index (h) of 0.5 and bandwidth-time product (BT) of 0.5. The PHY layer protocol data unit (PPDU) is repeated one, two or four times according to [2]. The received signal $r(t)$ is

$$r(t) = s(t) * h(t) + i(t) + n(t), \quad (1)$$

where $*$ denotes the convolutional operator, $h(t)$ is the fading channel, $i(t)$ is the interference process and $n(t)$ is the additive white Gaussian noise (AWGN) with zero mean and variance σ_n . Different interference models are introduced in [19]. These interference models are based on the measurement campaigns carrier out in the real hospital environment [5]. The received PPDU are combined by using the equal gain combining (EGC) method. The demodulator applies a correlator followed by a maximum-likelihood sequence detector (MLSD).

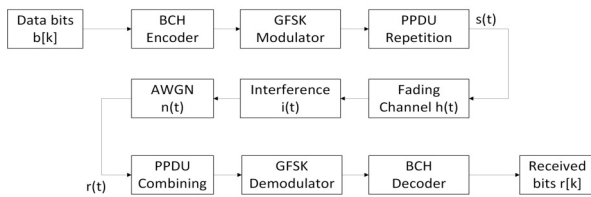


Figure 2. SmartBAN simulator.

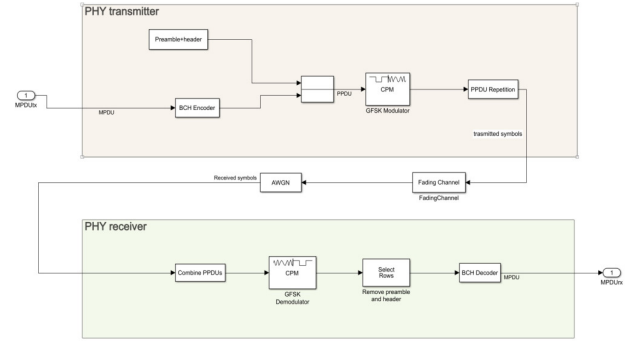


Figure 3. Physical layer of SmartBAN. Implementation in SmartBAN simulator.

For a fair comparison between the SmartBAN and BLE a single system simulator has been developed using Matlab® with Simulink®. The PHY simulation models for SmartBAN and BLE are represented in Figure 3 and Figure 4, respectively, in more details.

B. BLE simulator

The BLE PHY in Figure 4 on the transmitter part is designed to assemble packets of 62500 bits at a speed of 1 Mbps. Those packets are sent to a GFSK modulator implemented with a frequency hopping mechanism. The GFSK modulator uses modulation index of 0.5, bandwidth-time product of 0.5, 100 samples per symbol and a pulse length of one bit per symbol.

A fundamental part of the PHY in BLE simulator is the frequency hopping mechanism, where the frequency is changed following a random pattern to reduce interference. The radio channel set is composed by 40 different channel realizations. The frequency hopping code implemented is shown in Figure 5. A random data channel between 0 and 36 is selected so that no overlapping channel is present. The hop rate used in the simulator is 1600 Hz.

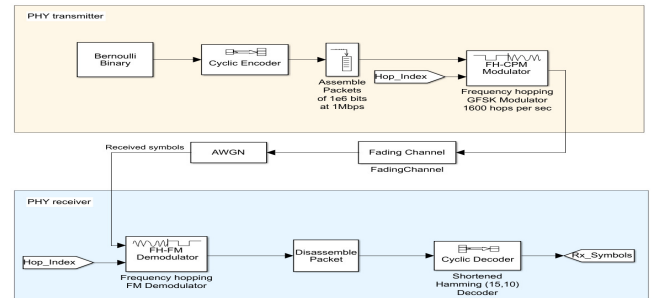


Figure 4. Physical layer of the Bluetooth low energy. Implementation in SmartBAN simulator.

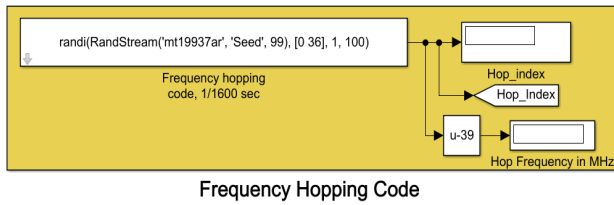


Figure 5. Frequency hopping mechanism in BLE.

The modulated signal propagates through the fading channel and an additive white Gaussian noise (AWGN) block. The received signal is demodulated in a FH-FM demodulator characterized by a frequency separation of 10 Hz and 100 samples per symbol.

For validation of the designed BLE PHY, a performance comparison with the theoretical curve GFSK was done. The GFSK modulator parameters are set as $BT = 0.5$ and $h = 0.5$ for the comparison.

The results of the comparison are given in Figure 6. The performance of the BLE is slightly worse than the theoretical one, as expected. The gap between the BER curves is acceptable and the result validates the design of the BLE PHY that will be used for the comparison with SmartBAN in this paper.

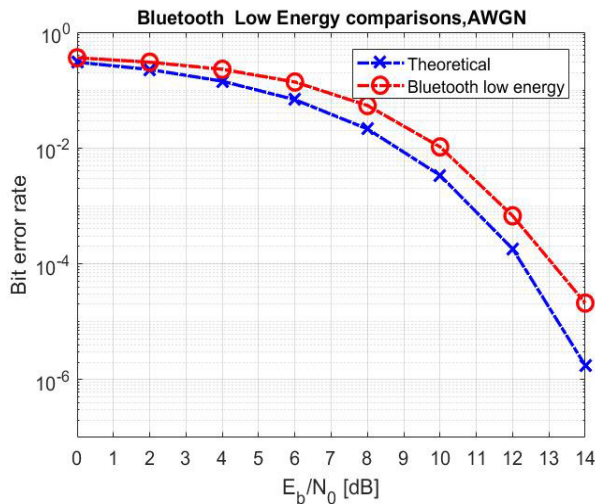


Figure 6. Comparison between BLE and the theoretical curve with GFSK with AWGN channel.

A summary of the main parameters of the PHYs are presented in Table 1. The main difference between SmartBAN and BLE is that the former implements PHY Protocol Data Unit (PPDU) repetition while the BLE does not.

In both cases, the modulated signals pass through a fading and a AWGN channel. The fading channel model used in the analysis is the IEEE 802.15.6 body surface to body surface model CM3 (Scenario S4 & S5) for 2.4 GHz [18]. The measurement for modelling the fading channel were carried out in a hospital and mainly models a link between a coordinator situated in the middle of a human torso and different locations on the body. The channel model

for flat small fading is described by a Ricean distribution with parameters described in [10]. In the simulations, the noise variance in AWGN channel is changed to define the required E_b/N_0 at the receiver.

TABLE 1. SMARTBAN AND BLE 2.4 GHz PHYS

PARAMETER	SmartBAN	BLE
Operating frequency [MHz]	2401-2481	2402-2480
Channel bandwidth [MHz]	2	2
Number of channels	40	40
Repetition/spreading	2x or 4x, Entire PPDU	No repetition
Modulation	GFSK ($BT=0.5$, $h=0.5$)	GFSK ($BT=0.5$, $h=0.5$)
Symbol rate [Mbps]	1	1
Receiver type	coherent	non-coherent

IV. SIMULATION RESULTS

A. Simulation parameters

The parameters used in the SmartBAN and BLE simulations are summarized in Table 2 and Table 3, respectively. More details about the SmartBAN simulator can be found from [10].

TABLE 2. SMARTBAN SIMULATION PARAMETERS

Parameter	Value(s)
PPDU repetition	1
Retransmission	no
MAC frame body	50, 250, 500, 1000
Samples for GFSK symbol	20
Pulse length of GFSK	1
Traceback depth of GFSK demodulator	10
Distance [cm]	45

TABLE 3. BLE SIMULATION PARAMETERS

Parameter	Value(s)
Repetition	Not present
Retransmission	Not available
Sample for GFSK symbol	100
Pulse length of GFSK	1
Traceback depth of GFSK demodulator	10
Distance [cm]	45

The performances are evaluated using a bit error rate (BER) as well as frame error rate (FER). BER represents the number of bit errors divided by the total number of transferred bits. The FER is the number of corrupted frames divided by the total number of transmitted frames.

B. Results in AWGN channel

A first approach to evaluate the performances of BLE and SmartBAN has been made only in a AWGN channel to see how the BER changes with different values of energy per bit to the spectral noise density ratio (E_b/N_0). The results comparing the BERs of these two technologies are shown in Figure 6.

In Figure 6, the SmartBAN curve is drawn by using the PPDU repetition of 1, being the worst BER curve from an analysis, as seen in a previous analysis on SmartBAN in [10].

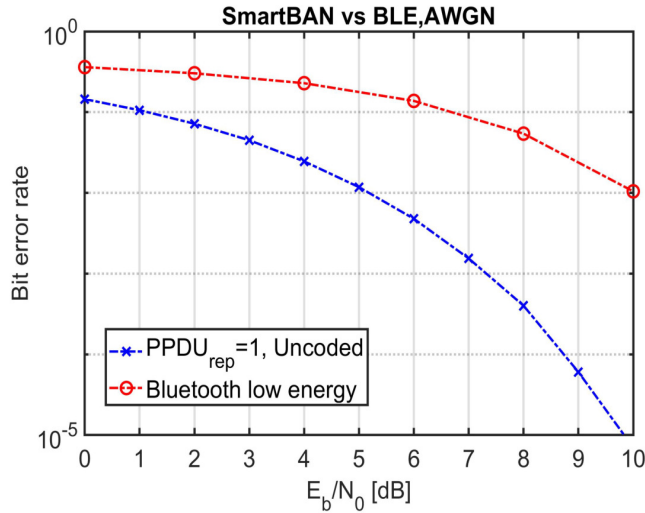


Figure 6. BER performance in the AWGN for SmartBAN and BLE.

The SmartBAN always show a better performance in terms of BER. BLE starts with 0.364 and the SmartBAN at 0.18 at $E_b/N_0 = 0$ dB. Increasing E_b/N_0 , the performance of the SmartBAN increases drastically reaching a BER of 10^{-5} with a $E_b/N_0 = 7.5$ dB, BLE requires much higher E_b/N_0 for the same performance.

C. Results in fading channel

The channel model is described in the IEEE 802.15.6 CM3. For the SmartBAN system, different MAC frame sizes have been used: 50, 250, 500 and 1000 octets with a PPDU repetition of 1 since it represents the worst-case scenario for SmartBAN [10]. For the BLE, BER and FER needed for the comparison are derived. The MAC layer is not going to affect the performance in the PHY comparison between these two technologies and it is not modeled into the simulator.

In Figure 7, a performance comparison between SmartBAN and BLE is given and shows the BER performance comparison between SmartBAN and BLE: even with fading channel the SmartBAN works better than the BLE, even with the lowest MAC frame size. Anyway, it can be highlighted the difference of performance is less accentuated than the previous case with the presence of only AWGN.

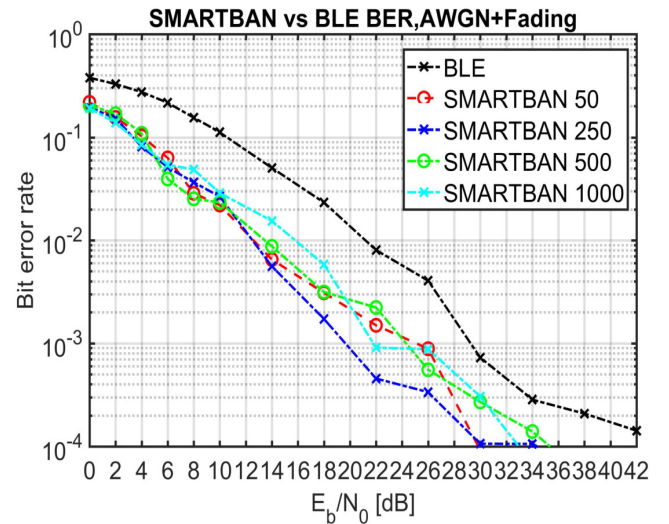


Figure 7. BER performance in the fading channel SmartBAN vs BLE.

In Figure 8, the FER comparison between BLE and SmartBAN in fading channel is given. In this case, the performance of the two standards is almost the same and from this point of view, the two technologies can be considered to work similarly. Neither the repetition nor the encoding has been chosen for the SmartBAN to make a fair comparison with BLE, in this case. Adding repetition and encoding to SmartBAN surely lead to a FER curve below the BLE one.

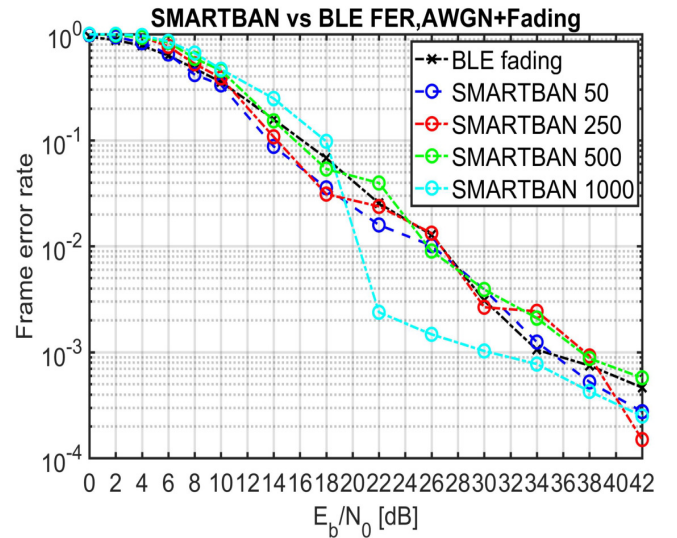


Figure 8. FER performance in the fading channel SmartBAN vs BLE.

V. CONCLUSIONS

This paper introduced the simulation results of the performance of SmartBAN technology compared with the BLE technology.

During the studies, a simulation environment using MATLAB software has been developed. By analyzing BER and FER results, it is possible to determine the performance of SmartBAN and BLE. For SmartBAN, the worst case

scenario selected from the previously published results has been chosen. For BLE, the standard does not present encoding and repetition, so for a fair comparison, also SmartBAN performance was analyzed without. Concerning the BER performance, with no doubt, the SmartBAN standard for healthcare applications performs better than BLE. In terms of FER, the two technologies showed similar performance.

Future work will include a comparison with the new technology of BLE version 5.0, which presents encoding and a comparison between the technologies considering also the interference models used in the SmartBAN standard.

ACKNOWLEDGMENT

Authors would like to thank members of ETSI TC SmartBAN for fruitful discussions and co-operation.

REFERENCES

- [1] <http://www.etsi.org/technologies-clusters/technologies/smart-body-area-networks>
- [2] ETSI, Smart Body Area Network (SmartBAN); Enhanced Ultra-Low Power Physical Layer. ETSI TS 103 326.
- [3] ETSI, Smart Body Area Network (SmartBAN); Low Complexity Medium Access Control (MAC) for SmartBAN. ETSI TS 103 325.
- [4] ETSI, Smart Body Area Networks (SmartBAN) Unified data representation formats, semantic and open data model. ETSI TS 103 378.
- [5] ETSI, Smart Body Area Network (SmartBan); Measurements and modelling of SmartBAN Radio Frequency (RF) environment. ETSI TR 103 395.
- [6] M. Hämäläinen, T. Paso, L. Mucchi, M. Girod-Genet, J. Farserotu, H. Tanaka, W.H. Chin, L. Nachabe, "ETSI TC SmartBAN: Overview of the Wireless Body Area Network Standard", The 9th International Symposium on Medical Information and Communication Technology (ISMICT2015), 24-26.3.2015, Kamakura, Japan.
- [7] W.H. Chin, H. Tanaka, T. Nakanishi, T. Paso, M. Hämäläinen, "An Overview of ETSI TC SmartBAN's Ultra Lower Power Physical Layer", The 9th International Symposium on Medical Information and Communication Technology (ISMICT2015), 24-26.3.2015, Kamakura, Japan.
- [8] K. Y. Yazdandoost, K. Sayrafian-Pour, "Channel model for body area network (BAN)", Apr. 2009.
- [9] M.H. Virk, R. Vuoltoniemi, M. Hämäläinen, J. Iinatti, J-P. Mäkelä, "Stochastic Spectral Occupancy Modeling: A Body Area Network Perspective in ISM Band", The 9th International Symposium on Medical Information and Communication Technology (ISMICT2015), 24-26.3.2015, Kamakura, Japan.
- [10] H. Viitala, L. Mucchi, M. Hämäläinen, T. Paso: "ETSI SmartBAN System Performance and Coexistence Verification for Healthcare", IEEE Access, Dec. 2017, Volume: 5, Issue: 1, pp: 8175-8182. DOI: 10.1109/ACCESS.2017.2697502.
- [11] H. Viitala, L. Mucchi, M. Hämäläinen, "Performance of the ETSI SmartBAN System in the Interfered IEEE 802.15.6 Channel", the 11th International Symposium on Medical Information and Communication Technology (ISMICT2017), 6-8.2.2017, Lisbon, Portugal.
- [12] Bluetooth Specification version 4.2, The Bluetooth Special Interest Group, Kirkland, WA, USA, 2013. P 2565
- [13] K. Mikhaylov et.al., "Performance analysis and comparison of Bluetooth Low Energy with IEEE 802.15.4 and SimplicTI," J. Sens. Actuator Networks, vol. 2, no. 3, pp. 589-613, Aug. 2013.
- [14] Mikhaylov, K., & Tervonen, J. (2013, November). Multihop data transfer service for Bluetooth Low Energy. In ITS Telecommunications (ITST), 2013 13th International Conference on (pp. 319-324). IEEE.
- [15] BLE CHANNELS FIGURE <http://www.rfwireless-world.com/Tutorials/Bluetooth-Smart-Bluetooth-Low-Energy-BLE-tutorial.html>
- [16] Jia Liu, Canfeng Chen, and Yan Ma, "Modeling Neighbor Discovery in Bluetooth Low Energy Networks"
- [17] Carles Gomez, I. Joaquim Oller, and Josep Paradells, "Overview and Evaluation of Bluetooth Low Energy: An Emerging Low-Power Wireless Technology"
- [18] K.Y. Yazdandoost and K. Sayrafian-Pour, "Channel Model for BodyArea Network (BAN)," IEEE P802.15 Wireless Personal Area Networks, Tech.Rep. IEEE P802.15-08-780-09-0006, April, 2009.
- [19] Specialist Task Force 511: SmartBAN Performance and Coexistence Evaluation, accessed on Apr. 28, 2017. [Online]. Available: <https://portal.etsi.org/STF/stfs/STFHomePages/STF511>.

A New Optimal Relay Selection Strategy for the Coincident Multi-user Access

Jiajia Mei¹, Jie Zeng², Bei Liu², Xin Su², Chang Wang¹, Qi Liu³, and Shihai Shao¹

¹ National Key Laboratory of Science and Technology on Communications
University of Electronic Science and Technology of China, Chengdu, China

² Tsinghua National Laboratory for Information Science and Technology
Research Institute of Information Technology, Tsinghua University, Beijing, China

³ China Unicom

Email: suxin@tsinghua.edu.cn

Abstract—Non-orthogonal multiple access (NOMA) has been recognized as one of the promising multiple access technologies to provide higher spectral efficiency and system capacity to address several challenges in the fifth generation (5G) wireless systems. Telemedicine in the process of being greatly advanced by the high-reliable communication in future 5G wireless systems. This paper proposed a novel optimal relay selection (RS) strategy for the cooperative NOMA to achieve the minimum outage probability, which means that the number of retransmissions in hybrid automatic repeat request (HARQ) is decreased and hence indirectly reduce the communication latency. Small latency ensures the validity of medical data, thereby improving the quality of service (QoS) in medical communications. In addition, compared to another optimal relay selection, namely two-stage strategy, the proposed enhanced max-min RS has a lower computational complexity and lower storage overhead. The proposed enhanced max-min RS strategy can reduce almost 43% storage overhead and 95% latency caused by selection strategy in the cooperative RS-NOMA system used for wireless medical communications.

Index Terms—Cooperative NOMA, medical communications, quality of service (QoS), relay selection.

I. INTRODUCTION

As the 5G era approaches, large-scale medical internet of things (IoT) ecosystem will cover millions or billions of low-power, low bit rate network medical and health monitoring devices, clinical wearable devices and remote sensors [1]. This will make the diagnosis and treatment more scientific, the distance not to be the matter and the rescue more timely. NOMA was recognized as one of the promising multiple access technologies to provide higher spectral efficiency and system capacity to address several challenges in the 5G wireless systems [2] [3]. Using NOMA technique in 5G wireless systems for medical communication may be a promising trend. Improving the wireless communication reliability of NOMA system in 5G scenarios to ensure the correctness or validity of medical data becomes a problem to be solved [4]. The issue to be considered in this paper is to improve the QoS of medical communications in NOMA system. We discuss the relay selection strategy in cooperative RS-NOMA system for improving the QoS of the medical communications in remote locations.

This work was supported by the China's 863 Project (No. 2015AA01A706), the National S&T Major Project (No. 2016ZX03001017), Science and Technology Program of Beijing (No. D17110006317002), and Ministry of Education-China Mobile Research Fund (No. MCM20160105).

So far, researchers have paid some effort in cooperative NOMA system to improve the QoS of communications. The authors in [5] select near users with strong channel gain to be relays for cooperative communication to increase its reliability. In addition, dedicated relay has also been considered in NOMA system. In [6], an amplify-and-forward (AF) relay was used to reduce the outage probability for cooperative NOMA system. And the authors of [7] utilized a buffer-assisted relay to improve the throughput for the adaptive transmission in cooperative NOMA system. The issue of relay selection in cooperative NOMA system is proposed in [8], in which authors proposed an optimal relay selection strategy and compared it with the conventional strategy that used to be applied in conventional orthogonal multiple access (OMA). These techniques are proposed to improve the QoS of users in cooperative NOMA system, which can be applied to medical communications to ensure the communication reliability in future 5G wireless systems.

This paper proposes a new optimal relay selection strategy, namely the enhanced max-min RS strategy, for cooperative RS-NOMA system. Compared to another optimal relay selection strategy in [8], the proposed enhanced max-min RS strategy has a lower computational complexity and its storage overhead is smaller. The enhancement of the proposed RS strategy is that it weighted each channel according to the targeted data rates (TDR) of users before taking the max-min value compared with the conventional max-min RS strategy. Closed form expression of the outage probability reached by the enhanced max-min RS strategy is derived and compared with that of other strategies, which indicates that the enhanced max-min RS scheme can get the maximum diversity gain of relays. In addition, we theoretical proof that the outage probability reached by the enhanced max-min RS strategy is also optimal. Then, the simulation results also indicate that not only the enhanced max-min RS can obtain the optimal outage performance, but also the time consumption of it is only 5% of the another optimal relay selection.

Utilizing this relay selection in cooperative RS-NOMA system can achieve the optimal outage probability, which means that the number of retransmissions in hybrid automatic repeat request (HARQ) is decreased and hence communication latency is indirectly reduced. Small latency can ensure the validity of medical data, which means it can improve

the quality of service (QoS) in medical communication. In addition, the smaller storage overhead of the proposed enhanced max-min relay selection strategy will bring the cost reduction in the practical deployment for cooperative NOMA system compared with the another outage-optimal relay selection. Generally, the proposed enhanced max-min RS scheme is especially suitable for video guided surgery on mobile ambulances, since it will choose to switch to the best relay in real time to communicate based on the changes of channels. Certainly, the proposed enhanced max-min RS scheme is also suitable for medical emergency rescue in remote areas, because it can guide patient, family or medical robots to urgently deal with the injury so as not to miss the optimal treatment time by its cooperative communication.

The rest of this paper is organized as follows: In Section II, we introduce the system model of cooperative RS-NOMA and give the methods of three relay selection strategies. The outage performance of these relay selection strategies is analyzed in Section III. Section IV shows the simulation results of these relay selection strategies. Finally, we make a conclusion in Section V.

II. SYSTEM MODEL

In this paper, we consider a downlink cooperative NOMA system with 2 users superimposed together to transmit with N relays. Each node is only equipped with a signal antenna and there is no direct connection between the base station (BS) and users. We can divide the communication process into two stages: the BS transmits the superimposed signal to a relay and the relay decodes and forward (DF) the signal to users. How to select the relay from N relays for improving the quality of service (QoS) of systems becomes the main points to be discussed. Fig. 1 shows the system of the cooperative RS-NOMA system.

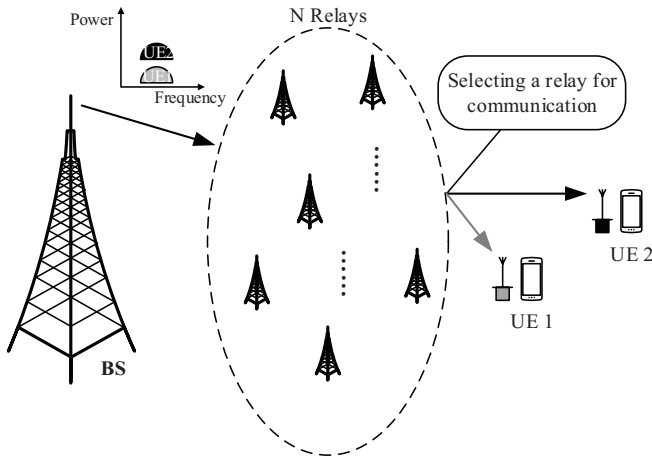


Fig. 1. The system model of cooperative RS-NOMA.

During the first stage, the signals to user 1 and user 2 are superimposed to a mixture, $(\alpha_1 x_1 + \alpha_2 x_2)$, where x_i denotes the signal that needs to be transmitted to user i , α_i denotes the power allocation factor and $\alpha_1^2 + \alpha_2^2 = 1$. The BS will transmit the mixture to the n th relay, and the observation of the n th relay is

$$y_n^r = h_n(\alpha_1 x_1 + \alpha_2 x_2) + w_n^r, \quad 1 \leq n \leq N, \quad (1)$$

where h_n denotes the channel gains from the BS to the n th relay, and w_n^r is the corresponding additive Gaussian noise.

Without loss of generality, we assume that relays decode user 1 first, and then eliminate it from their observations by the successive interference cancellation (SIC) technique [9]. Conditions of the n th relay to decode the two signals are

$$\frac{1}{2} \log \left(1 + \frac{|h_n|^2 \alpha_1^2}{|h_n|^2 \alpha_2^2 + 1/\rho} \right) \geq R_1, \quad \frac{1}{2} \log (1 + \rho |h_n|^2 \alpha_2^2) \geq R_2, \quad (2)$$

where ρ denotes the transmit signal to noise ratio (SNR) and R_i denotes the TDR for user i .

During the second stage, we assume that the n th relay can decode the two signals and their own transmitted power is not changed. Thus, user i observes

$$y_{n,i}^u = g_{n,i}(\alpha_1 x_1 + \alpha_2 x_2) + w_{n,i}^u, \quad i \in \{1, 2\}, \quad (3)$$

where $g_{n,i}$ denotes the channel gains from the n th relay to the user i , and $w_{n,i}^u$ is the corresponding additive Gaussian noise in this channel. Therefore, user 1 decodes its own information with the signal to interference plus noise ratio (SINR),

$$SINR = \frac{|g_{n,1}|^2 \alpha_1^2}{|g_{n,1}|^2 \alpha_2^2 + 1/\rho}. \quad (4)$$

User 2 needs to decode user 1 first to remove the signal of user 1 from the mixture by the SIC technique. Then, user 2 can decode its own signal with $SINR = \rho |g_{n,2}|^2 \alpha_2^2$. The condition of user 2 that can decode the user 1 successfully is

$$\frac{1}{2} \log \left(1 + \frac{|g_{n,2}|^2 \alpha_1^2}{|g_{n,2}|^2 \alpha_2^2 + 1/\rho} \right) \geq R_1. \quad (5)$$

Note that the fixed power allocation between user 1 and user 2 is utilized in this model. Optimizing power allocation factors can further obtain a performance improvement of cooperative RS-NOMA system, which is out of range of this paper. Next, we will give several strategies of relay selection in cooperative RS-NOMA system.

A. Relay Selection Strategies

1) The Conventional Max-Min RS [10]:

$$n^* = \arg \max_n \{ \min \{ |h_n|^2, |g_{n,1}|^2, |g_{n,2}|^2 \}, n \in S \}, \quad (6)$$

where S denotes the set of the N relays. The criterion of this RS strategy is that selecting a relay with the maximum $\min \{ |h_n|^2, |g_{n,1}|^2, |g_{n,2}|^2 \}$.

2) The Two-Stage RS [8]:

This first stage of the RS strategy is to ensure that the TDR of user 1 is realized, i.e., selecting relays to meet the following conditions:

$$S_r = \left\{ n \mid \begin{aligned} & \frac{1}{2} \log \left(1 + \frac{|h_n|^2 \alpha_1^2}{|h_n|^2 \alpha_2^2 + 1/\rho} \right) \geq R_1, \frac{1}{2} \log \left(1 + \frac{|g_{n,1}|^2 \alpha_1^2}{|g_{n,1}|^2 \alpha_2^2 + 1/\rho} \right) \geq R_1, \\ & \frac{1}{2} \log \left(1 + \frac{|g_{n,2}|^2 \alpha_1^2}{|g_{n,2}|^2 \alpha_2^2 + 1/\rho} \right) \geq R_1, n \in S \end{aligned} \right\}. \quad (7)$$

After the first stage, all the relays selected in S_r can demodulate x_1 by treating x_2 as noise. Then, the second stage of the two-stage RS strategy selects a relay in S_r to maximize the data rate of user 2, i.e.

$$n^* = \arg \max_{n \in S_r} \left\{ \min \left\{ \frac{1}{2} \log (1 + \rho |h_n|^2 \alpha_2^2), \frac{1}{2} \log (1 + \rho |g_{n,2}|^2 \alpha_2^2) \right\} \right\}. \quad (8)$$

3) *The Enhanced Max-Min RS*: Note that $\xi_1 = \frac{2^{2R_1}-1}{\rho(\alpha_1^2-(2^{2R_1}-1)\alpha_2^2)}$ and $\xi_2 = \frac{2^{2R_2}-1}{\rho\alpha_2^2}$ denote the values of $|h|^2$ corresponding to the TDRs of user 1 and user 2, respectively. The enhanced max-min RS strategy uses a weighted coefficient method. Since all the signals need to be decoded at the relay and the user 2's receiver but the receiver of user 1 only needs to decode its own signal, we utilize the ξ_1 and ξ_2 as the corresponding weighted coefficients to make each channel fairness. The enhanced max-min RS can be described as follows:

$$n^* = \arg \max_n \{ \min \{ \xi_1 |h_n|^2, \xi_2 |g_{n,1}|^2, \xi_1 |g_{n,2}|^2 \}, n \in S \}. \quad (9)$$

III. PERFORMANCE ANALYSIS

In this Section, we illustrate the outage probability reached by the enhanced max-min RS scheme. Firstly, under the condition of that the relay selection strategies select the n th relay to transmit the signal, the outage probability of the system can be given by

$$P_{out} = 1 - P \left\{ \begin{array}{l} |h_n|^2 \geq \max(\xi_1, \xi_2), |g_{n,1}|^2 \geq \xi_1, \\ |g_{n,2}|^2 \geq \max(\xi_1, \xi_2) \end{array} \right\}, \quad (10)$$

where the event $\{|h_n|^2 \geq \max(\xi_1, \xi_2)\}$ denotes that the two users are not in outage at the n th relay, and the event $\{|g_{n,1}|^2 \geq \xi_1\}$ denotes that outage is not occurred at user 1, in which the data of user 2 is not necessary to be decoded. Similarly, the event $|g_{n,2}|^2 \geq \max(\xi_1, \xi_2)$ denotes that the two users are not in outage at user 2, in which the signal of user 1 is necessary to be decoded to remove from the mixture by SIC and then user 2 can decode its own message.

A. Enhanced Max-Min Relay Selection Outage Probability

Note that $O_1 = \left\{ \arg \max_{n^* \in S} \{ \min \{ \xi_1 |h_n|^2, \xi_2 |g_{n,1}|^2, \xi_1 |g_{n,2}|^2 \} \} \right\}$ denotes the event that the relay n^* is selected by the enhanced max-min strategy. Thus, by using the equation (10), the system outage probability is

$$P_{out}^1 = 1 - \left(P \left\{ \begin{array}{l} |g_{n^*,2}|^2 \geq \max(\xi_1, \xi_2), \\ |g_{n^*,1}|^2 \geq \xi_1, \\ |h_{n^*}|^2 \geq \max(\xi_1, \xi_2) \end{array} \right\} | O_1 \right) P(O_1). \quad (11)$$

Note that $Y_n = \min \{ \xi_1 |h_n|^2, \xi_2 |g_{n,1}|^2, \xi_1 |g_{n,2}|^2 \}$, and all of channels are Rayleigh fading channels and they are independent and identically distributed. Assume that the probability density function (PDF) of arbitrary channel $|h|^2$ is $f(x) = \frac{1}{\sigma^2} e^{-\frac{x}{\sigma^2}}$ [11]. Then, the cumulative distribution function (CDF) of Y_n is given by

$$\begin{aligned} F_{Y_n}(x) &= P(\min \{ \xi_1 |h_n|^2, \xi_2 |g_{n,1}|^2, \xi_1 |g_{n,2}|^2 \} \leq x) \\ &= 1 - P(\min \{ \xi_1 |h_n|^2, \xi_2 |g_{n,1}|^2, \xi_1 |g_{n,2}|^2 \} > x) \\ &= 1 - P(\xi_1 |h_n|^2 > x) P(\xi_2 |g_{n,1}|^2 > x) P(\xi_1 |g_{n,2}|^2 > x) \\ &= 1 - \left(e^{-\frac{x}{\sigma^2 \xi_1}} \right) \left(e^{-\frac{x}{\sigma^2 \xi_2}} \right) \left(e^{-\frac{x}{\sigma^2 \xi_1}} \right) \\ &= 1 - e^{-\left(\frac{2x}{\sigma^2 \xi_1} + \frac{x}{\sigma^2 \xi_2} \right)}. \end{aligned} \quad (12)$$

Then, note that $Y_{n^*} = \max \{ Y_1, Y_2, \dots, Y_N \}$, the CDF of Y_{n^*} can be given by

$$\begin{aligned} F_{Y_{n^*}}(x) &= P(Y_{n^*} \leq x) = \prod_{n=1}^N P(Y_n \leq x) \\ &= \left(1 - e^{-\left(\frac{2x}{\sigma^2 \xi_1} + \frac{x}{\sigma^2 \xi_2} \right)} \right)^N. \end{aligned} \quad (13)$$

We decode the user 1 first, there are relations $R_1 \leq R_2$ and $\xi_1 \leq \xi_2$, generally. Therefore, the outage probability of system can be calculated as follows:

$$\begin{aligned} P_{out}^1 &= 1 - \left(P \left\{ \begin{array}{l} |g_{n^*,2}|^2 \geq \max(\xi_1, \xi_2), \\ |g_{n^*,1}|^2 \geq \xi_1, \\ |h_{n^*}|^2 \geq \max(\xi_1, \xi_2) \end{array} \right\} | O_1 \right) P(O_1) \\ &= 1 - \left(\arg \max_n \{ \min \{ \xi_1 |h_n|^2, \xi_2 |g_{n,1}|^2, \xi_1 |g_{n,2}|^2 \}, \right. \\ &\quad \left. P \{ |g_{n^*,2}|^2 \geq \xi_2, |g_{n^*,1}|^2 \geq \xi_1, |h_{n^*}|^2 \geq \xi_2 \}, n \in S \} \right) \\ &= 1 - \left(\arg \max_n \{ \min \{ \xi_1 |h_n|^2, \xi_2 |g_{n,1}|^2, \xi_1 |g_{n,2}|^2 \}, \right. \\ &\quad \left. P \{ \xi_1 |h_{n^*}|^2 \geq \xi_1 \xi_2, \xi_2 |g_{n^*,1}|^2 \geq \xi_1 \xi_2, \xi_1 |g_{n^*,2}|^2 \geq \xi_1 \xi_2 \} \right) \\ &= 1 - P(\max \{ \min \{ \xi_1 |h_n|^2, \xi_2 |g_{n,1}|^2, \xi_1 |g_{n,2}|^2 \} \geq \xi_1 \xi_2) \\ &= 1 - P(Y_{n^*} \geq \xi_1 \xi_2) = P(Y_{n^*} \leq \xi_1 \xi_2) = \left(1 - e^{-\left(\frac{2\xi_2 + \xi_1}{\sigma^2} \right)} \right)^N. \end{aligned} \quad (14)$$

B. Conventional Max-Min Relay Selection Outage Probability

Note that $O_2 = \left\{ \arg \max_{n^* \in S} \{ \min \{ |h_n|^2, |g_{n,1}|^2, |g_{n,2}|^2 \} \} \right\}$ denotes the event that the relay n^* is selected by the conventional max-min strategy. Similarly, the outage probability can be described as

$$P_{out}^2 = 1 - \left(P \left\{ \begin{array}{l} |g_{n^*,2}|^2 \geq \max(\xi_1, \xi_2), \\ |g_{n^*,1}|^2 \geq \xi_1, \\ |h_{n^*}|^2 \geq \max(\xi_1, \xi_2) \end{array} \right\} | O_2 \right) P(O_2). \quad (15)$$

We note that $X_n = \min \{ |h_n|^2, |g_{n,1}|^2, |g_{n,2}|^2 \}$ and $X_{n^*} = \max \{ X_1, X_2, \dots, X_N \}$. Similarly, we can get the corresponding CDF as follows:

$$\begin{aligned} F_{X_n}(x) &= P(\min \{ |h_n|^2, |g_{n,1}|^2, |g_{n,2}|^2 \} \leq x) \\ &= 1 - \left(e^{-\frac{x}{\sigma^2}} \right)^3 = 1 - e^{-\frac{3x}{\sigma^2}}, \end{aligned} \quad (16)$$

$$\begin{aligned} F_{X_{n^*}}(x) &= P(X_{n^*} \leq x) = \prod_{n=1}^N P(X_n \leq x) \\ &= \left(\int_0^x \frac{3}{\sigma^2} e^{-\frac{3t}{\sigma^2}} dt \right)^N = \left(1 - e^{-\frac{3x}{\sigma^2}} \right)^N. \end{aligned} \quad (17)$$

By using equation (17), we can calculate the system outage probability reached by the conventional max-min RS by

$$\begin{aligned} P_{out}^2 &= 1 - P \left(\arg \max_n \{ \min \{ |h_n|^2, |g_{n,1}|^2, |g_{n,2}|^2 \}, n \in S \} \right. \\ &\quad \left. \max \{ \min \{ |h_n|^2, |g_{n,1}|^2, |g_{n,2}|^2 \} \} \geq \xi_2 \cup \right. \\ &\quad \left. \{ \xi_1 \leq |g_{n,1}|^2 < \xi_2, |h_n|^2 \geq \xi_2, |g_{n,2}|^2 \geq \xi_2 \} \right) \\ &= \left(1 - e^{-\frac{3\xi_2}{\sigma^2}} \right)^N - \left(e^{-\frac{2\xi_2 + \xi_1}{\sigma^2}} - e^{-\frac{3\xi_2}{\sigma^2}} \right)^N. \end{aligned} \quad (18)$$

C. Comparing the Enhanced Max-Min strategy with the Two-Stage strategy

It can be seen in [8], where given the value $\sigma^2 = 1$, that the outage probability reached by the two-stage RS strategy is

$$P_{out}^3 = \sum_{l=0}^N \binom{N}{l} (F(2R_2))^l e^{-3l\xi_1} [1 - e^{-3\xi_1}]^{N-l}, \quad (19)$$

where $F(x) = e^{2\xi_1} \left(e^{-2\xi_1} - e^{-\frac{2(2^x-1)}{\rho\alpha_2^2}} \right)$. By utilizing $\xi_2 = \frac{2^{2R_2}-1}{\rho\alpha_2^2}$, we can obtain the overall outage probability by

$$\begin{aligned} P_{out}^3 &= \sum_{l=0}^N \binom{N}{l} \left(1 - e^{2(\xi_1 - \xi_2)} \right)^l e^{-3l\xi_1} \left[1 - e^{-3\xi_1} \right]^{N-l} \\ &= \sum_{l=0}^N \binom{N}{l} \left(e^{-3\xi_1} - e^{-\xi_1 - 2\xi_2} \right)^l \left[1 - e^{-3\xi_1} \right]^{N-l} \\ &= \left[\left(e^{-3\xi_1} - e^{-\xi_1 - 2\xi_2} \right) + \left(1 - e^{-3\xi_1} \right) \right]^N \\ &= \left(1 - e^{-(\xi_1 + 2\xi_2)} \right)^N = P_{out}^1 \end{aligned} \quad (20)$$

Since the authors in [8] proved that this two-stage strategy is an optimal method to minimize the overall outage probability, equation (20) indicates that the enhanced max-min strategy is also an optimal relay selection strategy. Furthermore, we can compare the two optimal relay selection strategies in term of their selection complexity.

TABLE I. Computational complexity of the two strategies

Strategy	Numbers of Multiplications	Numbers of Additions
Enhanced Max-Min	$O(3N)$	$O(3N)$
Two-Stage	$O(20N)$	$O(14N)$

1) *Computational complexity*: From section II, we can see that the difference in computation between the two optimal strategies is large. Table I shows their numbers of multiplications and additions in computation specifically, where N denotes the account of relays. It is quite obvious that the proposed enhanced max-min RS is better than the other optimal relay selection strategy in term of computational complexity.

2) *Storage overhead*: During the selection process of the two-stage RS strategy, we need to store the gains of all the channels first. Then the values which meet the three conditions in the first stage also need to be saved. At last, the minimum of the two data rates in second stage need to be saved for maximizing it to get the relay n^* . So the storage overhead of the two-stage RS is $O(3N + 3N + N) = O(7N)$. For the proposed enhanced max-min RS strategy, except for storing the gains of all the channels, we need to store the values of $\min\{\xi_1|h_n|^2, \xi_2|g_{n,1}|^2, \xi_1|g_{n,2}|^2\}$. Thus, the storage overhead of the enhanced max-min RS is $O(3N + N) = O(4N)$.

IV. NUMERICAL RESULTS

The outage performance of the cooperative RS-NOMA system with the above several RS strategies is evaluated by simulating in this Section. Firstly, the outage probabilities of the cooperative RS-NOMA with the three mentioned relay selection strategies are compared in Fig. 2. We can see that the two optimal relay selection strategies achieve the same outage performance, both outperform the conventional max-min RS strategy. Fig. 3 shows the storage overhead and the time consumption of the two optimal relay selection strategies, which is achieved when $N = 100$ and the time consumption is obtained by MATLAB in Windows 10 with

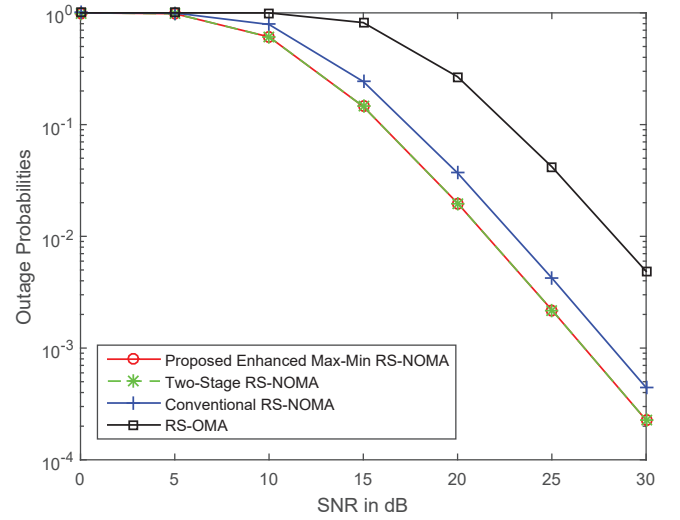


Fig. 2. The outage probabilities of cooperative RS-OMA and RS-NOMA with different RS strategies. $R_1 = 0.5$ BPCU, $R_2 = 2$ BPCU, $\alpha_2^2 = 1/4$, $N = 2$, and $\sigma^2 = 10$.

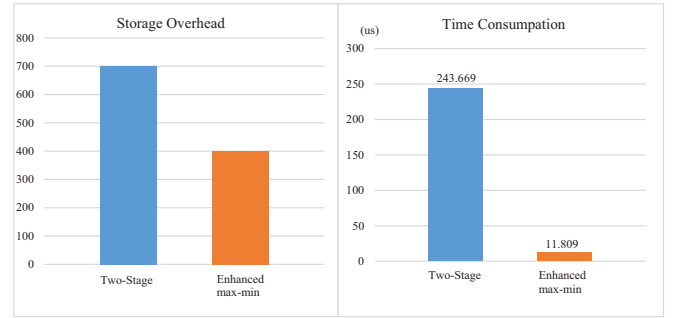


Fig. 3. Storage overhead and time consumption of the two optimal strategies.

the Intel(R) Core(TM)2 Quad CPU Q9300. We can draw that the proposed enhanced max-min RS can reduce almost 43% storage overhead and 95% latency caused by selection strategy compared with another optimal relay selection. In addition, the performance of cooperative RS-OMA is also evaluated in the simulations. For the relay selection strategy of OMA system, we use the conventional max-min criterion. As can be seen from Fig. 2, the cooperative RS-NOMA system can efficiently improve the outage performance, which means that using NOMA technique can achieve a significant gain in term of the reception reliability compared with using OMA technique with the same relay selection. Cooperative RS-NOMA system can obtain this performance gain because it can serve the two users simultaneously, whereas RS-OMA system needs twice resources, such as bandwidth or time slots, to serve them.

Furthermore, we simulated the outage performance under the different N and σ^2 , where N denotes the number of relays to select and σ^2 denotes the Rayleigh fading channels parameter, which is described specifically in Section III. From Fig. 4 we can see that the outage performance with $N = 5$ is better than that with $N = 2$, especially in high SNR. The reason is that these RS strategies can obtain the

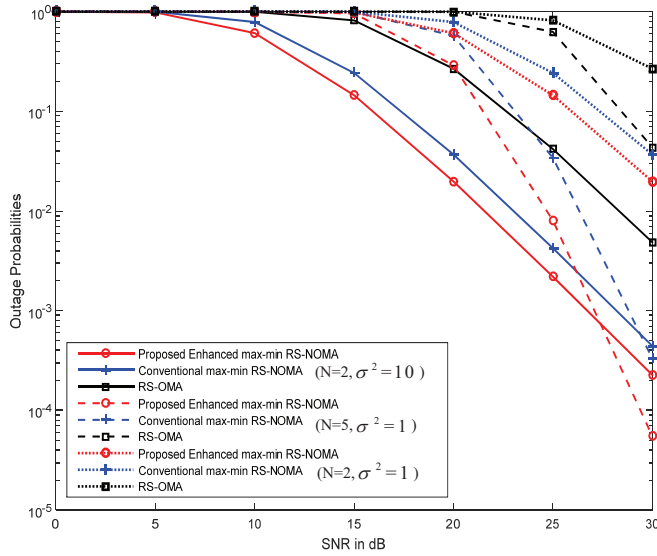


Fig. 4. The impact of N and σ^2 on outage performance for different relay selections.

diversity gain of the N relays. In addition, the enhanced max-min RS-NOMA scheme has higher SNR gains when N is larger compared with the conventional max-min RS-NOMA scheme and the RS-OMA scheme. By comparing the curves of these relay selections with different σ^2 , we know that the outage performance is better when $\sigma^2 = 10$, especially the outage performance gain is larger in low SNR. This is because the bigger of the σ^2 , the better of the channel ($E(|h|^2) = \sigma^2$). Finally, compared the dash with solid line in Fig. 4, we can achieve a lower outage probability by adding the number of relays to select when channel is worse ($\sigma^2 = 1$).

V. CONCLUSIONS

We proposed and analyzed the enhanced max-min RS strategy for cooperative RS-NOMA system in this paper. Analytical results and simulation results both demonstrated that the enhanced max-min RS strategy can obtain not only the optimal outage performance, but also the maximum diversity gain of the N relays. This makes the relay selection well suited for mobile ambulance video guided surgery communications because it will choose to switch to the best relay in real time to ensure the QoS of medical communications. Compared to another optimal relay selection, the enhanced max-min scheme has a lower computational complexity and its storage overhead is smaller. The proposed enhanced max-min RS can reduce almost 43% storage overhead and 95% latency caused by selection strategy compared with another optimal relay selection. Then, smaller latency in cooperative RS-NOMA system could be guaranteed by using this enhanced max-min RS scheme. Smaller latency can make the medical communication more reliable, since the timeliness of some medical data is very short, such as real-time blood pressure for heart diseases.

REFERENCES

[1] W. D. de Mattos and P. R. L. Gondim, "M-Health Solutions Using 5G Networks and M2M Communications," *IT Professional*, vol. 18, no.3, pp.24-29, May. 2016.

[2] A. Benjebbour, Y. Saito, Y. Kishiyama, et al., "Concept and Practical Considerations of Non-orthogonal Multiple Access (NOMA) for Future Radio Access," *Proc. IEEE Intelligent Signal Processing and Communications Systems (ISPACS)*, Naha, 2013, pp.770-774.

[3] L. Dai, B. Wang, Y. Yuan, et al., "Non-orthogonal multiple access for 5G: Solutions, challenges, opportunities, and future research trends," *IEEE Commun. Mag.*, vol. 53, no. 9, pp. 74-81, Sept. 2015.

[4] D. K. Rout, and S. Das. "Reliable communication in UWB body area networks using multiple hybrid relays," *Wireless Networks*, 2016: 1-16.

[5] Z. Ding, M. Peng and H. V. Poor, "Cooperative Non-Orthogonal Multiple Access in 5G Systems," *IEEE Commun. Lett.*, vol. 19, no. 8, pp. 1462-1465, Aug. 2015.

[6] X. Liang, Y. Wu, D. W. K. Ng, et al., "Outage Performance for Cooperative NOMA Transmission with an AF Relay," *IEEE Commun. Lett.*, vol. 21, no.11, pp.2428-2431, Nov. 2017.

[7] S. Luo and K. C. Teh, "Adaptive Transmission for Cooperative NOMA System with Buffer-Aided Relaying," *IEEE Commun. Lett.*, vol. 21, no. 4, pp. 937-940, Apr. 2017.

[8] Z. Ding, H. Dai and H. V. Poor, "Relay Selection for Cooperative NOMA," *IEEE Wireless Commun. Lett.*, vol. 5, no. 4, pp. 416-419, Aug. 2016.

[9] F.-L. Luo, C. Zhang, *Signal Processing for 5G: Algorithms and Implementations*, Wiley-IEEE Press, pp. 143-168, 2016.

[10] Y. Jing and H. Jafarkhani, "Single and multiple relay selection schemes and their achievable diversity orders," *IEEE Trans. Wireless Commun.*, vol. 8, no. 3, pp. 1414-1423, Mar. 2009.

[11] D. Tse, P. Viswanath, *Fundamentals of Wireless Communication*, Cambridge University Press, Cambridge, 2005.

Impact of the Sternotomy Wires and Aortic Valve Implant on the On-Body UWB Radio Channels

Mariella Särestöniemi, Timo Kumpuniemi,
Matti Hämäläinen, Jari Iinatti
Centre for Wireless Communications (CWC)
University of Oulu
Oulu, Finland
givenname.familyname@oulu.fi

Carlos Pomalaza-Raéz
Department of Electrical and Computer Engineering
Purdue University
Fort Wayne, Indiana, USA
cpomalaz@purdue.edu

Abstract—In this paper, the impact of the sternotomy wires and aortic valve implant on the ultra wideband (UWB) channel characteristics is studied. The evaluations are performed by calculations, measurement data analysis, and power flow simulations. The aim is to show that implants, which consist of steel, titanium, and other highly conductive materials, do have clear effect on the signal propagation even inside the tissues. This impact should be taken into account when using in-body or on-body communications devices, such as capsule endoscopes, etc.

Keywords—aortic valve implant; radio channel; signal propagation; sternotomy closure wires; WBAN

I. INTRODUCTION

Wireless body area network (WBAN) channel characteristics have been under an intensive study during the recent years. Several channel models, measurement campaigns and propagation simulations have been realized to get deeper understanding of the channel propagation in the vicinity or even inside a human body [1-10].

Medical implants, such as pace makers, valve implants, etc. bring their own challenge on this field. Many of the implants may contain steel, titanium alloy, tungsten, and other highly conductive materials and thus will have clear effect on the channel characteristics in the vicinity where they are located. Furthermore, medical wires, staples, and bands, which are used for the closure after the operation [11], can have significant impact since usually they are located close to the skin and hence close to the on-body antennas and sensor nodes.

There are just a few studies on the impact of the medical implants on the channel characteristics [6-8]. The main challenge in this type of studies is the difficulty to obtain measurement data. Although the WBAN channel characteristics can be investigated through electromagnetic propagation simulations, which are based on, for instance, Finite Difference Time Domain (FDTD), Finite Integration Technique (FIT) or Finite Element Method (FEM) [9, 10], at some phase the results should be verified with the real measurement data.

The impact of a titanium based aortic valve implant on the ultra wideband (UWB) channel characteristics has been reported in [6-8]. The studies in [6-7] included measurement data where one of the volunteers has an aortic valve implant. The main

result of the previous work is that the titanium based aortic valve has an impact on the channel characteristics depending on the locations of the on-body antennas. Reference [8] applies this scenario in the FEM-based 3D simulator studying the impact of the aortic valve on different locations of the antennas as well as the impact of the depth of the valve.

To our best knowledge, there are no published studies on the impact of the post-surgery medical wires on the UWB on-body channel propagation. However, it is essential to understand their impact on the channel characteristics since these kinds of impacts have to be taken into account when using any in-body or on-body device, for instance endoscopy capsules or wearables.

The main contribution of this paper is to show the impact of the sternum closure wires on the propagation of UWB signals. The study is performed by calculations, measurement data analysis and FIT-based power flow simulations. Three different on-body antennas using two different separation distances are considered. In this study, the impact of the titanium based aortic valve on the channel characteristics has also been reported.

This paper is organized as follows: Section II presents the setups used in the simulations and measurement campaign. Section III presents the results of the power flow simulations. Calculations for propagation times are presented in Section IV. Measurement results are presented and discussed in Section V. Summary and Conclusions are given in Section VI.

II. SIMULATION AND MEASUREMENT SETUP

A. Antennas

In this study, we used three different antennas designed for on-body communication: loop and dipole antennas designed at CWC [12], and commercial SkyCross antennas [13]. The antennas were located on the chest asymmetrically respect to the sternum: i.e., one antenna was on the middle of the sternum and the other on the left side of the chest. Two antenna separation distance cases were studied: 6.5 cm and 15 cm. Figure 1 illustrates the location of the antennas respect to the sternum, heart and the sternotomy wires. Figure 2 presents the location of the aortic valve in the heart. For an antenna separation distance 6.5 cm, we studied also the case when the antenna is on the right

side of the chest. Between the antenna and the human body, there was a 4 mm rohacell piece to improve antenna efficiency.

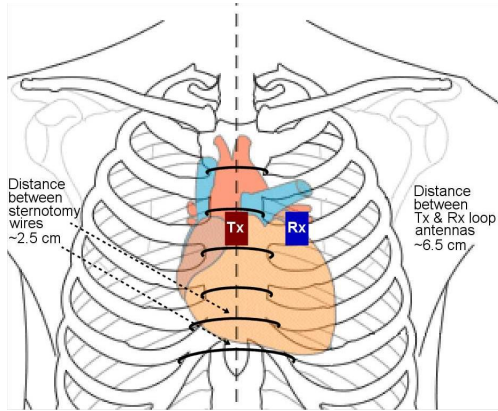


Figure 1. Location of the antennas on the chest for left side case.

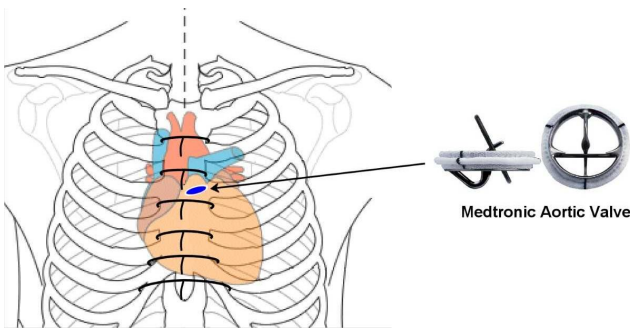


Figure 2. Location of the aortic valve in the heart.

B. Simulator

We studied the propagation inside the human body using the CST MicroWaveStudio (MWS) [14] simulation software with an extension of BiModel library. An anatomical voxel model Tom was chosen for our simulations. A simplified version of an aortic valve implant was modelled according to the figures and information provided by Medtronic in [15], and included it in the heart of the voxel model. The picture of a Medtronic's valve is found in Figure 2 [15]. The aim of the simulations was to model the power flow inside the human body to find the possible reflections and diffractions from the sternotomy wires and the aortic valve.

C. Measurements

The measurements were conducted in an anechoic chamber. Two sets of measurements were taken. In the first measurement set, the frequency bandwidth was 2-8 GHz and the antenna distance was $d_A = 6.5$ cm. Volunteers A (with implant) and B (without implant) participated into this measurement. In the second measurement set, in which the volunteers A and C (without implant) participated, the frequency bandwidth was 3.1-10.6 GHz and $d_A = 15$ cm. In both measurements, the number of frequency points per sweep was set to 1601. The measurements were conducted in a frequency domain to obtain channel's frequency responses (S_{21} parameters,) which were later transformed into time domain in Matlab using Inverse Fast Fourier Transform (IFFT) to get impulse response (IR). Since the channel data is stored in the frequency domain, it will be

possible to study impulse responses for different bandwidths as the IFFT can be performed to the selected bandwidth.

D. Volunteers

Three male volunteers assisted in the measurements. The sizes of the volunteers are summarized in Table I. One of them has a titanium alloy based aortic valve implant (illustrated in Figure 2.) This subject also has medical wires in his sternum used in the sternum closure after the valve operations. The medical wires are made from steel and there are altogether six wires as shown in Figure 1.

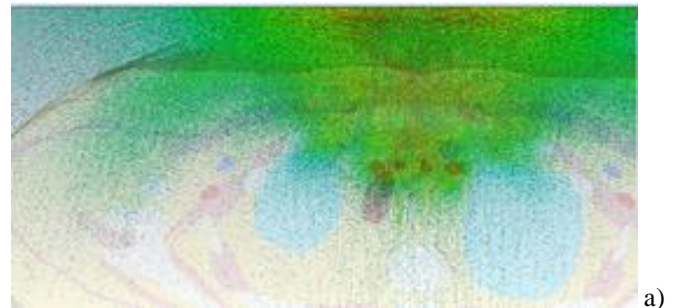
III. POWER FLOW SIMULATIONS

First, the propagation inside the human body with an aortic valve implant was studied by simulating the power flow around the chest area. For this first scenario, we did not include yet the metallic wires in the model since we preferred to see the pure impact of the aortic valve. For the comparison, the propagation flow was simulated for the voxel model without the implant as well.

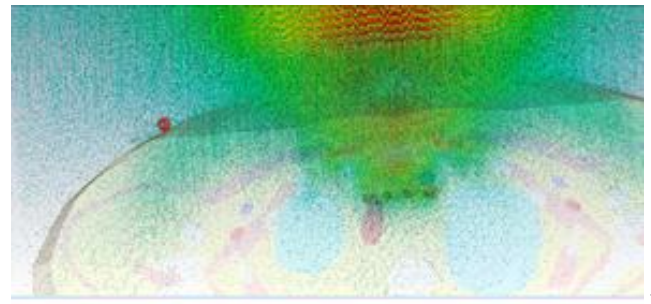
Figures 3a ja 3b show the power flows with and without implant, respectively. We can observe that the implant has a clear effect on the propagation flow: the power flow is different in terms of spreading and intensity if the valve and wires are included in the model since there are several reflections from the titanium alloy torus ring, as well as from the steel wires.

Table I Information about the volunteers.

	A(with implant)	B (no implant)	C (no implant)
Height	170 cm	181 cm	173 cm
Weight	62 kg	76 kg	75 kg
Age	61	22	27

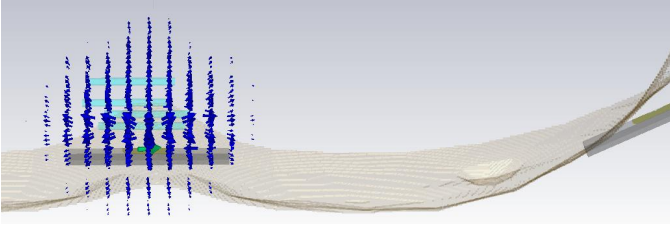


a)



b)

Figure 3a and 3b. Simulated power flow for the voxel model a) with a valve implant and b) without a valve implant.



Figures 4. Reflections from the sternotomy wires.

Furthermore, the power flow study is repeated for the model with metallic wires used for sternum closure (Figure 4.) In this case, the valve implant is not included in the model. From the propagation flow figure, one can note reflections from metal wires towards RX-antenna.

IV. PROPAGATION TIME CALCULATIONS

According to the propagation flows, there are several reflected propagation paths from the valve implant and sternotomy wires. Different paths go through different tissues and with different propagation times. Just some of the reflected signals arrive with power level high enough to be recognized in the RX-antenna. In this section, we calculate propagation time for signals reflecting from the valve and the sternotomy wires.

When calculating the reflection from the wire, we assume straightest reflection path, which is assumed to be the strongest one, from the wire towards RX-antenna. Basically, this signal would go through muscle, fat and skin tissues.

When we calculate the impact of the aortic valve on the channel characteristics, we also assume reflection from the valve or the surrounding torus ring towards RX. This signal would travel through all the tissues: heart, lung, bone, muscle, fat and skin. Next, we will calculate the assumed arrival time for the peaks due to the wires and the peaks due to the valve. The velocity of the propagation signal in the i^{th} tissue is calculated as

$$v_{i,f} = \frac{c}{\sqrt{\epsilon_{i,f}}}, \quad (1)$$

where $\epsilon_{i,f}$ is the relative permittivity of a tissue at frequency f . The relative permittivity may change significantly with the frequency depending on the tissue. Once we know the velocity, we can easily calculate the propagation time in each of the tissues having a length of d_i using

$$t_{i,f} = \frac{d_i}{v_{i,f}}, \quad (2)$$

which are then summed up to obtain overall propagation time.

We made our assumptions of the d_i based on the dimensions of the voxel model and information obtained from the anatomy references [11]. Parameter d consist of the signal path going directly from TX-antenna to the valve $d_{\text{TX-V}}$ and then the reflected path from valve to RX $d_{\text{V-RX}}$. In general, these distances are just assumptions since human bodies have different dimensions.

Table II. Relative permittivity (ϵ) and depth of different tissues in the study cases (d/i deflated/inflated).

	<i>Skin</i>	<i>Bone</i>	<i>Fat</i>	<i>Muscle</i>	<i>Heart</i>	<i>Lung (d/i)</i>
ϵ , 2 GHz	38.6	11.7	11.0	53.3	55.8	21/49
ϵ , 3 GHz	31.3	11.0	10.7	52.1	53.7	20/47
ϵ , 8 GHz	33.2	8.8	9.3	45.5	45.4	17/41
ϵ , 10GHz	37.5	8.12	8.8	42.8	42.2	16/38
$d_{\text{TX-w}}$ as $d_{\text{TX,RX}}=6.5$ cm, 15 cm	0.005 m	-	0.005 m	-	-	-
$d_{\text{w-RX}}$ as $d_{\text{TX,RX}}=6.5$ cm	0.005 m	-	0.01 m	0.045 m	-	-
$d_{\text{TX-v}}$ as $d_{\text{TX,RX}}=6.5$ cm, 15 cm	0.005 m	0.01 m	0.005 m	0.01 m	0.03 m	-
$d_{\text{v-RX}}$ as $d_{\text{TX,RX}}=6.5$ cm	0.005 m	0.01 m	0.005 m	0.001 m	0.02 m	0.025 m
$d_{\text{w-RX}}$ as $d_{\text{TX,RX}}=15$ cm	0.005 m	-	0.05 m	0.085 m	-	-
$d_{\text{v-RX}}$ as $d_{\text{TX,RX}}=15$ cm	0.005 m	0.01 m	0.015 m	0.02 m	0.02 m	0.08 m

Table III. Propagation time of the reflected signal

Antenna distance $d_{\text{A_tot}}$	6.5 cm [2-8 GHz]	15.0 cm [3-10 GHz]
Time [s]		
$t_{\text{TX-w}}$	1.5e-10	1.4e-10
$t_{\text{w-RX}}$	1.2e-9	2.4e-9
$t_{\text{total_wire}}$	1.3 e-9	2.5e-9
$t_{\text{TX-v}}$	1.2e-9	1.1e-9
$t_{\text{v-RX}}$	1.4e-9	2.9e-9
$t_{\text{total_valve}}$	2.6e-9	4.0e-9

The dimensions and relative permittivity of corresponding tissues at different frequencies are obtained from [16] and summarized in Table II. Permittivity values for 2, 3, 8, ja 10 GHz are presented to show the variation of the permittivity values within the studied frequency ranges. When we calculate the velocity in each tissue, we use the permittivity averaged over the frequency range used in the measurements.

V. MEASUREMENT RESULTS

A. Antenna distance 6.5 cm

At first we study the channel impulse responses obtained using the SkyCross antenna in the measurements with the volunteer having an implant. Figure 4a illustrates all 100 impulse response samples obtained in the measurements when the antenna was on the left side of the body. For comparison, the impulse responses with the reference volunteer (non-implant)

are shown in Fig. 4b. The variation between the samples are due to the small unintentional movements of the volunteer during the measurement. For both cases, the main peak arrives at same time, approximately 0.5 ns. This is the line-of-sight propagation peak. At time instant 1 ns arrives the second peak for both cases, assumed the signal propagation through creeping waves.

A rough comparison between the impulse responses presented in Fig 4a and Fig 4b show that there are more peaks at significant signal level in the channel impulse responses of the volunteer with an aortic valve implant. According to the calculations presented in Table III, the peaks due to the metallic wires in the sternum should arrive at the time of approximately 1.3 ns. Some variation is seen in the timing and strength of the peaks because there are several wires and also breathing has impact on this. In Figure 4a, the peaks due to the metallic wires can clearly be seen around 1.3 ns. Instead, in the channel IR of the reference person, there is no clear peak at this time set.

According to Table III, the peaks due to the aortic valve should be seen at the time instant of 2.6 ns. With SkyCross antenna, the implanted volunteer has a peak around 2.3 ns in the measurement, when the RX-antenna is on the left side and 2.5 ns in the measurements, when the RX-antenna is on the right side. Since the valve is located slightly on the left side of the body center, the reflected signal has to propagate longer distance within the tissues on the right-side measurements, which explains the difference between the timing and attenuation differences in left and right side cases. The level of the peak is relatively low compared to the main peak since the attenuation of the signal within the body tissues is high. Since the valve is moving with the heartbeat, also the reflection angle is changing periodically and thus the arrival timing is changing. This explains the differences between timing of the samples.

Next we study the impulse responses obtained in the measurements with the loop antenna on the volunteer with an aortic valve implant. Both left side and right side cases were studied and the results were shown in Figure 6a and 6b. Similar tendencies can be found as with SkyCross antenna: Peaks due to the metallic wires in the sternum can be found approximately at the time instant of 1.2 ns. Furthermore, the peaks due to the aortic valve implant at the time instant of 2 ns.

B. Antenna distance 15 cm

Next, we study the measurement results for left-side case where the distance between the antennas is 15 cm. The impulse responses for all 100 samples are plotted for loop and dipole antennas in implant and non-implant cases in Figures 7a and 7b, respectively. Additionally, the average of the impulse responses are included in the figures.

According to the calculations presented in Table III, the signal paths due to the reflection from the metallic wires should arrive approximately at the time instant 2.6 ns. From the Figure 7a, we can see clear peaks arriving at this time instant. For some IR samples, the peaks around 2-2.6 ns are clearly higher. However, the average curve shows only a small peak at 2.6 ns since the arriving peaks are not aligned, which may affect destructively on the peaks of the averaged IR.

Finally, the reflections from the aortic valve are evaluated. Table III shows that the signal paths reflected from the valve should arrive approximately at time instant 4.0 ns. When looking at the averaged impulse response (black dashed line) in Figure 8a, there is no peak visible in the impulse response. Instead, when we study the single impulse responses more precisely, we can notice very low peaks in some of the IR samples. This is due to the fact that aortic valve is moving and hence causing variations in the reflections. Due to the strong attenuation of the signal within the tissues, the level of the peak is very low as the antenna distance is 15 cm. When studying the averaged channel IR (blue solid line) of the reference volunteer, we see also several peaks but those at the considered time instant are almost at noise level. These results are valid both for loop and dipole antennas.

VI. SUMMARY AND DISCUSSION

In this paper, we have examined the impact of the sternotomy wires and aortic valve implant on the UWB channel characteristics. The evaluations are performed by calculations, measurement data analysis, and FIT-based power flow simulations. In the measurements, we used three different antennas designed for on-body and off-body communications.

From the results it was found that the sternotomy wires and the aortic valve implant have an impact on the channel characteristics. The impact depends on the nature of the antennas and their location. Even with the on-body antennas, the impact can clearly be seen in the measurement results: there are peaks at time instances that correspond to the expected propagation delay from the sternotomy wires and the aortic valve implant. In the calculation of the expected propagation delay, the propagation velocities in different tissues on the propagation path has been taken into account. Naturally, the individual differences may cause strong variation in the results. Furthermore, the impact is also assumed to be clearly more significant if in-body antennas were used instead of on-body antennas.

Previously the impact of the sternotomy wires has not been investigated and, hence, the results presented in this paper provide a first insight to this aspect. The medical wires can be considered as a type of medical implant since they are non-biological material and normally stay in the body after the operation for the rest of patient's life. Many of them are close to the skin and hence can have a significant impact on the channel characteristics. This has to be taken into account if using any in-body or on-body communication devices, for instance endoscopy capsules, etc., since additional peaks in the channel impulse response may cause interference. Besides, knowledge about the impact of the wires would allow to better locate Rx and Tx antennas for communications with in-body implants avoiding that interference.

ACKNOWLEDGMENT

We would like to thank all the volunteers who participated in the experimental measurements. We would also like to thank Dr. Richard Kovacs, Clinical Director of the Krannert Institute of Cardiology, at Indiana University, USA, for his help in gathering technical information about the nature of sternotomy wires and Medtronic aortic valve, and to the Medtronic engineers, who

participated in the process of locating this information. We also like to thank our internal Wireless In-body Communications (WiB) project for funding.

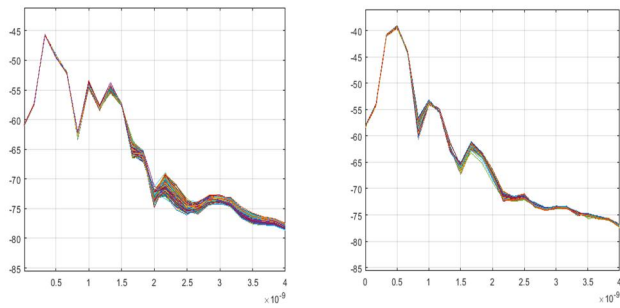


Figure 4. SkyCross antenna IRs a) with implant, and b) without implant in the left side case

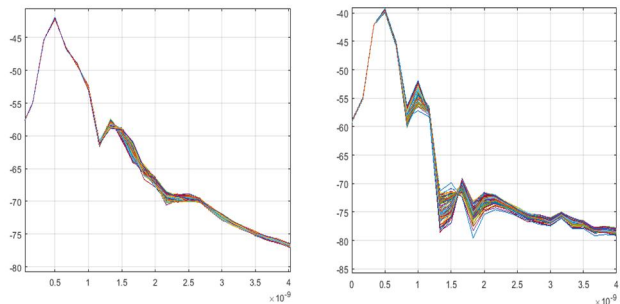


Figure 5. SkyCross antenna IRs a) with implant, and b) without implant in the right side case.

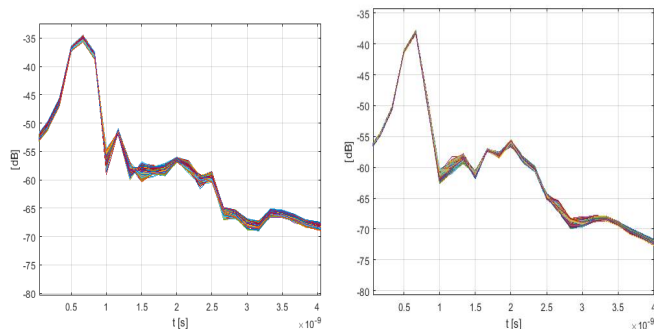


Figure 6. Loop antenna IRs a) at left side measurements and b) right hand measurements

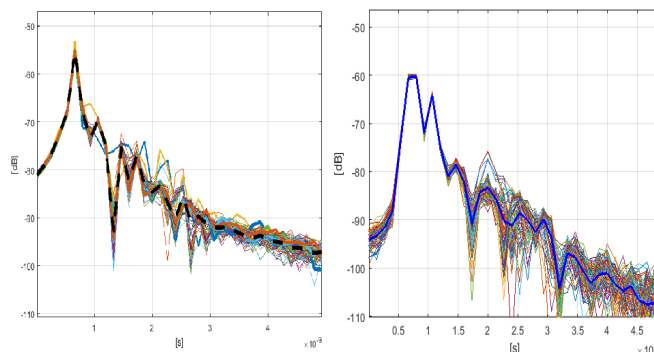


Figure 7. Loop antenna IRs a) with the implant and b) without the implant.

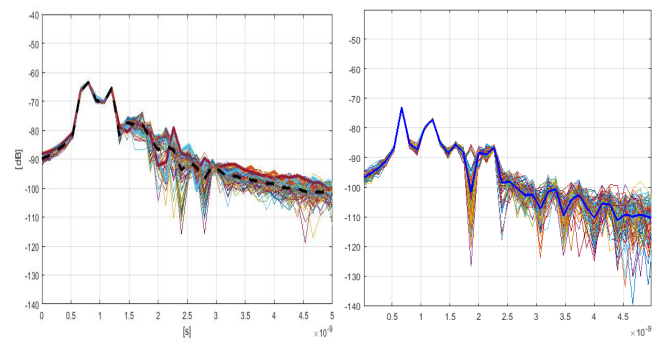


Figure 8. Dipole antenna IRs a) with the implant and b) without the implant.

REFERENCES

- [1] S. Cotton, R. D'Errico, C. Oestges, "A Review of Radio Channel Models for Body Centric Communications," *Radio Sci*, Jun, 2014. doi: 10.1002/2013RS005319.
- [2] X. Yang, M. Fang, A. Ren, Z. Zhang, Q. Abbasi, A. Alomainy, K. Mehran, "Reverse Recognition of Body Postures using On-Body Radio Channel Characteristics," *IET Microwaves, Ant., and Prog.*, 2017.
- [3] I. Dove, "Analysis of Radio Propagation Inside the Human Body for in-Body Localization Purposes", University of Twente, Netherland, Aug. 2014.
- [4] T. Kumpulniemi, M. Hämäläinen, K. Y. Yazdandoost, J. Iinatti, "Human Body Shadowing Effect on Dynamic UWB On-Body Radio Channels," *IEEE Antennas and Wireless Propagation Letters*, Vol 16, 2017.
- [5] T. Kumpulniemi, M. Hämäläinen, K. Y. Yazdandoost, J. Iinatti, "Categorized UWB On-Body Radio Channel Modeling for WBANs," *Progress in Electromagnetic Research B*, Vol. 67, 2016.
- [6] A. Taparugssanagorn, C. Pomalaza-Ráez, A. Isola, R. Tesi, M. Hämäläinen, J. Iinatti, "Preliminary UWB Channel Study for Wireless Body Area Networks in Medical Applications" in *International Journal of Ultra Wideband Communications and Systems*, InderScience Publishers, vol. 2, no. 1, pp. 14-22, 2011.
- [7] A. Taparugssanagorn, C. Pomalaza-Ráez, A. Isola, R. Tesi, M. Hämäläinen, J. Iinatti, "UWB Channel Modeling for Wireless Body Area Networks in Medical Applications," *Applied Sciences in Biomedical and Communication Technologies (ISABEL)*, 2009.
- [8] W.-B. Yang, K. Sayrafian-Pour, J. Hagedorn, J. Terrill, K.Y. Yazdandoost, A. Taparugssanagorn, M. Hämäläinen, J. Iinatti, "Impact of an Aortic Valve Implant on Body Surface UWB Propagation: A Preliminary Study", *Proc. the 5th International Symposium on Medical Information and Communication Technology*, 2011.
- [9] M. Särestöniemi, M. Hämäläinen, J. Iinatti, "An Overview of Electromagnetic Propagation Based Channel Modeling Techniques for Wireless Body Area Network Applications," *IEEE Access*, 2017.
- [10] A. Pellegrini et al, "Antennas and Propagation for Body-Centric Wireless Communications at mm-wave Frequencies: A Review," *IEEE Antennas Propagation Mag.*, Vol. 55, 2013.
- [11] A. Elfström, A. Grunditz, "Evaluation of Sternum Closure Techniques Using Finite Element Analysis," Master Thesis, in *Medical Engineering*, The Royal Institute of Technology, Sweden, 2013.
- [12] T. Tuovinen, K. Yekeh Yazdandoost, J. Iinatti, "Comparison of the Performance of Two Different UWB Antennas for the use in WBAN On-Body Communications," *6th Europ. Conf. Antennas and Propagation (EUCAP)*, 2012.
- [13] SkyCross Antenna Product, www.skycross.com
- [14] CST Microwave Studio, [Online]. Available: <http://www.cst.com>.
- [15] Medtronic aortic valve, [URL:http://www.15tronic.com/us-en/healthcare-professionals/products/cardiovascular/heart-valves-surgical.html](http://www.15tronic.com/us-en/healthcare-professionals/products/cardiovascular/heart-valves-surgical.html)
- [16] <https://www.itis.ethz.ch/virtual-population/tissue-properties/database/dielectric-properties/>

Simulation-based Body Motion Classifier using Radio Channel Characteristics

Minseok Kim, Yuki Ichikawa,

Graduate School of Science and Technology, Niigata University, Niigata, Japan

Email: mskim@ieee.org

Abstract—Human motion classification is emerging technology which can improve healthcare system and to realize context-aware body area network (BAN). This paper focused the fact that the radio channel characteristics between sensor devices and coordinator may have stronger potential for motion classification than the conventional methods using accelerometer and the video sensor. Due to extremely large variety of possible combination of the channel components it is actually very difficult to obtain the accurate motion classifier based on measurement. Therefore, this study proposed a simulation-based classifier that is generated by large amount of data from the combination of individual channel components in computer simulation. This paper presented the current development that included only the free-space path loss variation by body motion. The automatic motion classification for 6 motion scenarios by using the radio channel between four sensor devices and coordinator was evaluated. From the results, it was seen that the method using radio channel entirely outperforms the method using acceleration, particularly in static motion scenarios.

Index Terms—motion classification, radio channel, acceleration, machine learning, decision tree

I. INTRODUCTION

Facing with the problems of declining birthrates, aging society, and shrinking population, the information communication technology (ICT) for medical healthcare applications is emerging, and thus the body area network (BAN) that connects wireless devices around the human body has attracted considerable attention. IEEE 802.15.6 standardization for BAN was established in 2012 [1]. The BAN is a short range wireless sensor network in the vicinity of humans; the applications include medical and healthcare services and consumer electronics. In medical and healthcare applications, various wireless sensor devices are implanted within the human body or attached to the body surface, and a coordinate node collects the vital information from sensor devices. The collected vital data of patients or elderly people from BAN is transferred to remote healthcare services and can significantly improve healthcare system.

This work challenges an accurate human motion identification using a radio channel characteristics in BAN as an innovative BAN application. Human motion identification can offer significant functions in various healthcare applications such as fall detection of elderly people, watching children, the disabled care, analysis/diagnosis of lifestyle, elucidation of the pathogenesis. Furthermore, context-aware control of power consumption and data traffic, and thus can improve

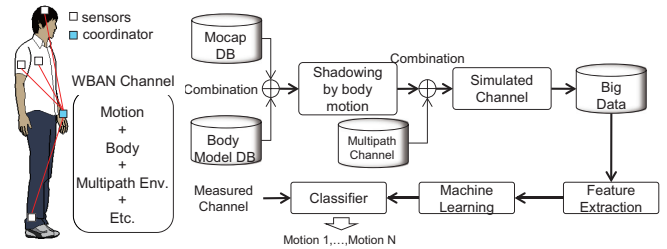


Fig. 1. Simulation-based body motion classifier.

the efficiency of the wireless network. For human motion identification, the several techniques using accelerometer and the video sensor have often been developed, but further improvement of the classification accuracy and extension of the use cases is necessary to widely use it in various healthcare applications [2]–[6].

This study aims at developing an accurate motion classification method by using the radio channel between the coordinator and multiple sensor devices. As discussed in many previous studies [7]–[9], the BAN channel response between the transmitter and receiver is inevitably influenced by the body, which causes different propagation mechanisms from those of conventional wireless systems. In general, many interconnected channel components such as body motion/posture, physique, sensor position, antenna characteristics and multipath propagation affect the channel characteristics in the measured channel response, and thus, it is very difficult to distinguish each component clearly to describe the propagation mechanisms [7]. Moreover, the BAN channel is usually not stationary due to body movement and daily changes in human environments. As the BAN system operates under time-varying conditions depending on human activities in which the whole body or part of the body is in movement, it can be subject to time-varying channel fading [8], [9].

As described above, the BAN channel property is disadvantageous from the viewpoint of wireless data transmission, but it may have stronger potential for motion classification than the conventional methods using accelerometer and video sensor. By using the radio channels collected in various motions, machine learning techniques can produce an accurate motion classifier. However, because there are extremely large variety of possible combination of the channel components described

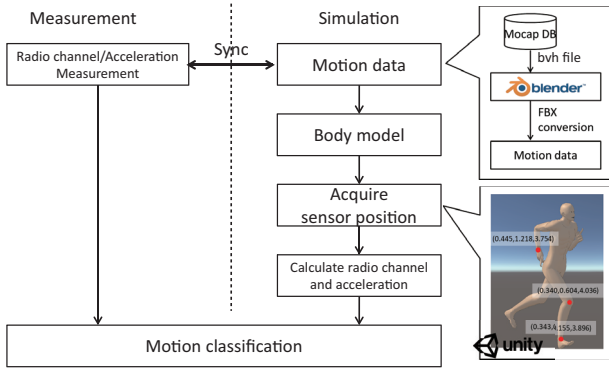


Fig. 2. Flowchart of motion simulation

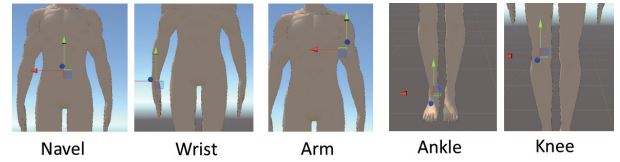
above, it is actually very difficult to obtain the accurate motion classifier based only on measurement. Therefore, in this study, a simulation-based classifier that is generated by large amount of data from the combination of individual channel components in computer simulation is proposed. Fig.1 shows the framework of this study. By increasing the number of training data, the accuracy of the classifier can be improved.

In our previous work [10], we experimentally compared the classification performance of two methods using radio channel and acceleration in terms of eight body motion scenarios. The radio channels were simulataneously measured between coordinators attached to Navel and four sensor devices attached to Arm, Wrist, Thigh, and Ankle, and the three-axis acceleration was also measured at the same time. From measured data seven time-domain features are extracted and the classifier was obtained by decision tree algorithm. We demonstrated that using radio channel is more advantageous than using accelerometer especially for static motion/posture. However, as long as the radio channel is a combination of various channel components, the performance is usually determined by the specific condition of the measurement.

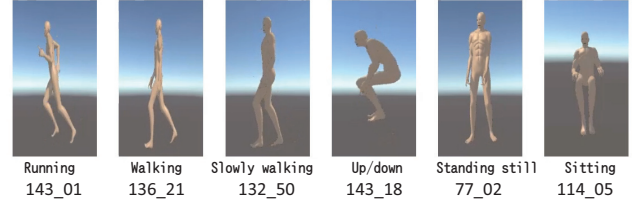
This paper describes the initial development of the computer simulation environment to generate radio channel by body movement using motion capture database, and presents preliminary results.

II. DEVELOPED SIMULATION ENVIRONMENT

In our initial development, the radio channel depends only on the distance between the sensor device and the coordinator, namely free-space path loss is only considered, but body shadowing and multipath propagation are not included. As a body motion emulation tool, Unity, a cross-platform game engine developed by Unity technologies is employed. As shown in Fig.2, the time series of the coordinates of the sensors and the coordinator at every sampling interval were measured in the software. By calculating the distance between the sensor and the coordinator, the temporal variation of channel path gain and three-axis acceleration are obtained. Using the same parameters of the previous measurement for comparison purpose, the carrier frequency, sampling interval and transmit power are chosen by 2.4 GHz, 40 ms and 2.5 dBm.



(a) Node positions



(b) Body motion scenarios with the motion id number of CMU mocap DB

Fig. 3. Simulation model

As shown in Fig.3(a), it is assumed that the sensor devices are attached to Arm, Wrist, Knee, and Ankle, and the coordinator is attached to Navel. In order to act the body in Unity, the free motion capture database developed by Carnegie Mellon University (CMU). The motion capture database includes more than 2,500 motion data which were captured by Vicon motion capture system consisting of 12 infrared MX-40 cameras in a working volume of approximately 3 m × 8 m.

In this study, six motion scenarios of Running, Walking, SlowWalking, Updn, Standing, and Sitting are selected as shown in Fig.3(b). For precise evaluation of the proposed simulation-based method with measurement, the body motion should be captured simultaneously with radio channel and acceleration. However, in this work, appropriate motion data from CMU motion capture database for convenience's sake. Each data has a different length, but the length was adjusted to that of longest data of Updn repeating each original.

III. DATA PROCESSING

In this study, we employ time-domain processing using the received signal strength (RSS) which is one of narrowband channel characteristics. The RSS is obtained by the Friis formula as

$$P_r = \left(\frac{\lambda}{4\pi d} \right)^2 P_t \quad (1)$$

where λ , d and P_t denote the wavelength, the distance between the sensor and the coordinator, and transmit power, respectively, and the antenna gain is assumed to be unit (isotropic radiation). In addition, we used a combined acceleration (ACC) that is

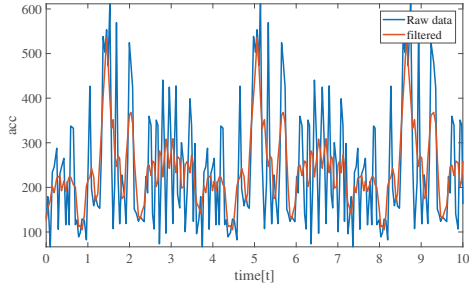


Fig. 4. Noise filtering (Running@Arm)

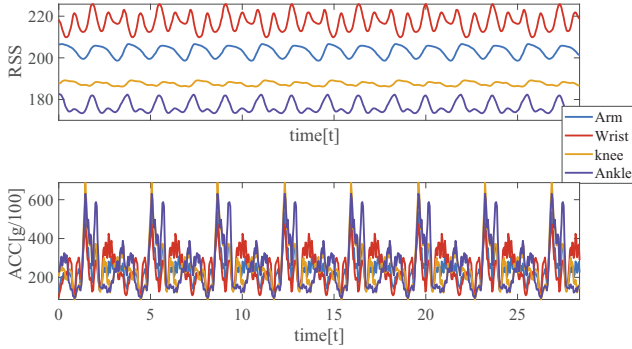


Fig. 5. Filtered signal example; Running.

calculated by

$$A_r = \sqrt{a_x^2 + a_y^2 + a_z^2} \quad (2)$$

where a_x , a_y and a_z denote the acceleration along x , y and z axes in $[g/100]$, respectively. The gravitational acceleration $g = 9.8 \text{ m/s}^2$.

The following subsections briefly describe the data processing procedure from the preprocessing to the motion classification.

A. Pre-processing

The temporal variation of the RSS and ACC usually include trivial fluctuation from any possible involuntary movement irrelevant to the body motion. The high frequency component can be cut off by moving average filter in time domain as shown in Fig.4 for Running where the window size was set by $N = 5$ so as the cutoff frequency to be 5 Hz. As an example, the signal after preprocessing is presented in Fig. 5.

B. Feature Extraction

From the filtered temporal variation of the RSS and ACC of four sensors in preprocessing, the features are calculated at every sample sliding the window with the length of M where the length was set by $M = 6$ (240 ms) as in [11]. Some features in time domain such as mean value, variance, level change, mean value slope, square integral, root-mean-square,

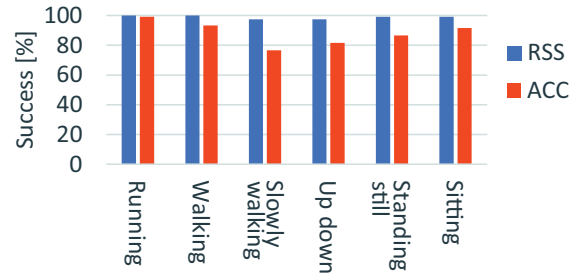


Fig. 6. Classification performance comparison

and range were evaluated in previous study, from correlation-based feature selection it was concluded that the following feature set is the best combination for the highest performance.

$$\text{Mean value : MV} = \frac{1}{N} \sum_{n=1}^N Z_n, \quad (3)$$

$$\text{Level change : LC} = \frac{1}{N-1} \sum_{n=1}^{N-1} |Z_{n+1} - Z_n| \quad (4)$$

where Z is replaced by the RSS and ACC for feature calculation.

C. Machine Learning Algorithm

The decision tree machine learning algorithm was employed to generate a motion classifier. In this study, the C4.5 based decision tree algorithm was used for classifier generation and validation. This algorithm was developed in J48 and included in WEKA machine learning package [12]. We choose the decision tree algorithm because it offers comprehensive visualization of the classification mechanism. The whole data is separated into 10 equal-length data segments for 9 training data sets and 1 test data sets. By cross-validation with these 10 data segments exchanging the test data set, the evaluations for 10 test data sets in total were performed.

IV. MOTION CLASSIFICATION RESULTS

The performance comparison of the decision tree classifiers generated by using RSS and ACC is presented in Fig.6. It is seen that the success rates of the two methods using RSS and ACC are approximately 99 % and 88 %, respectively, and the method using RSS entirely outperforms that using ACC. As a more insightful result, the confusion matrices are presented in Tables I and II where the row denotes the class label of the test data and the column indicates the correctly decided class label. From these results, it can be seen that while the error of the classification by ACC increases in static motion scenarios such as SlowWalking, Standing, and Sitting, the classification by RSS has no significant error increment.

The reason is thought that the ACC is not significantly changed in the static motion but the RSS at each link differ from one another depending on the transmission distance. In near future, we will consider body shadowing, multipath

propagation, antenna effects and so on in this simulation framework, then an accurate classifier is expected to be produced by more realistic RSS data.

V. SUMMARY

This paper presented a preliminary result of the simulation-based body motion classifier which aims to improve the accuracy by using large amount of data from the combination of individual channel components in computer simulation. The channel component included in the current development is only the free-space path loss variation by body motion that is obtained by a motion software Unity with a motion data from the CMU motion capture database. Assuming that the sensor devices are attached to Arm, Wrist, Knee, and Ankle, and the coordinator is attached to Navel, the automatic classification for 6 motion scenarios of Running, Walking, SlowWalking, Updn, Standing, and Sitting was evaluated where the classifier was generated by decision tree machine learning algorithm. The results showed that the method using RSS entirely outperforms the method using ACC, particularly in static motion scenarios, which is consistent with our previous measurement results.

ACKNOWLEDGEMENT

The motion data used in this paper was obtained from mocap.cs.cmu.edu. The database was created with funding from NSF EIA-0196217.

REFERENCES

- [1] A. Astrin, "IEEE Standard for Local and metropolitan area networks part 15.6: Wireless Body Area Networks: IEEE Std 802.15.6-2012," (The document is available at IEEE Xplore).
- [2] D. P. Tobon, T. H. Falk, M. Maier, "Context Awareness In WBANS: A Survey On Medical And Non-Medical Applications," *IEEE Wireless Communications*, pp. 30–37, Aug. 2013.
- [3] B. Liu, Z. YAN, C. W. CHEN, "MAC Protocol In Wireless Body Area Networks for E-Health: Challenge And a Context-Aware Design," *IEEE Wireless Communications*, pp. 64–72, Aug. 2013.
- [4] S. F. Heaney, W. G. Scanlon, E. Garcia-Palacios, S. L. Cotton, "Fading Characterization for Context Aware Body Area Networks (CABAN) in Interactive Smart Environments," *Proc. 2010 Loughborough Antennas & Propagation Conference*, Nov. 2010.
- [5] F. Casamassima, E. Farella, L. Benini, "Context aware power management for motion-sensing body area network nodes," *Proc. The conference on Design, Automation & Test in Europe*, Mar. 2014.
- [6] S. Archasantisuk, T. Aoyagi, M. Kim, and J. Takada, "Transmission Power Control in WBAN Using the Context-Specific Temporal Correlation Model," *Proc. The 27th Annual IEEE International Symposium on Personal, Indoor and Mobile Radio Communications (PIMRC2016)*, Sept. 2016.
- [7] K. Yazdandoost, "Channel Model for Body Area Networks (BAN)," IEEE 15-08-0780-12-0006, 2010 (Web document is available at <https://mentor.ieee.org/802.15/dcn/08/15-08-0780-12-0006-tg6-channel-model.pdf>).
- [8] M. Kim, J. Takada, "Statistical Model of 4.5 GHz Narrowband On-Body Propagation Channel with Specific Actions," *IEEE Antennas Wireless Propag. Lett.*, pp. 1263–1267, 2009.
- [9] M. Kim, and J. Takada, "Characterization of Wireless On-Body Channel Under Specific Action Scenarios at Sub-GHz Bands," *IEEE Trans. Antennas Propag.*, Vol.60, No.11, pp. 5364–5372, Nov. 2012.
- [10] Y. Ichikawa, M. Kim, "An Investigation of Body Motion Identification Method using Radio Channel Characteristics for BAN Context-Aware Communications," *IEICE Technical Report*, MICT2016-74, Jan. 2017 (in Japanese).

TABLE I
CONFUSION MATRIX OF THE METHOD USING RADIO CHANNEL

Running	Walking	Slow Walking	Updn	Standing	Sitting	classified as
651	0	0	0	0	0	Running
4	644	0	3	0	0	Walking
0	0	649	0	2	0	SlowWalking
0	7	0	643	0	1	Updn
0	0	0	0	651	0	Standing
0	0	0	0	0	651	Sitting

TABLE II
CONFUSION MATRIX OF THE METHOD USING ACCELERATION

Running	Walking	Slow Walking	Updn	Standing	Sitting	classified as
651	0	0	0	0	0	Running
4	631	0	10	5	1	Walking
0	2	459	46	80	64	SlowWalking
0	24	35	480	71	41	Updn
0	5	86	54	438	68	Standing
0	5	54	25	55	512	Sitting

- [11] S. Archasantisuk, T. Aoyagi, T. Uusitupa, M. Kim, J. Takada, "Human Motion Classification Using Radio Signal Strength in WBAN," *IEICE Trans. Commun.*, Vol.E99-B, No.3, pp. 592-601, Mar. 2016.
- [12] "WEKA documentation," [Online]. Available: <http://www.cs.waikato.ac.nz/ml/weka>

Evaluating Contemporary Physical Activity Self-Monitoring Technology Performance

Reem Altamimi and Geoff Skinner

School of Electrical Engineering and Computing
The University of Newcastle
Newcastle, Australia
Reem.Altamimi@uon.edu.au
Geoff.Skinner@newcastle.edu.au

Abstract—Encouraging physical activity is becoming an increasingly relevant issue in modern society. Studies have shown that being involved in regular physical activity is essential for individuals' physical, mental and social development. The field of Information and Communication Technology (ICT) has been applied in several areas of research. One of the main domains that utilize the applications of ICT is the health domain. The definition of eHealth has appeared in the literature describing this integrated area of research. Health technologies have been increasingly utilized in physical activity promotion and intervention. Physical Activity Self-Monitoring Technologies (PAMTs) are a popular example of such technologies. New wearable activity monitoring technologies, such as fitness bracelets that track everyday activity, provide a technological solution for promoting active lifestyles. This research presents a pilot test that makes a valuable contribution within the area of valid and accurate trackers in terms of distance walked, using a treadmill walking activity, and a manual counting of steps, taken in a stair climbing activity. This study might assist other researchers in their choice of reliable equipment to use in research that involves reliable and accurate distance and steps calculations.

Keywords— *Activity Trackers; eHealth; Fitbit; Jawbone; Physical Activity Monitoring Technologies.*

I. INTRODUCTION

Physical activity is an important issue that has previously been considered [1] [2]. The first Surgeon General's Report on physical activity and health, highlighted the importance of regular physical activity for all ages including males and females [1]. Physical activity is associated with positive effects on individuals' body systems, such as the musculoskeletal, cardiovascular, respiratory and immune systems. Regular participation in physical activity has been found to reduce the risk of many diseases, improve physiological and psychological functions, and is also associated with lower mortality rates [1]. It has been demonstrated that participating in regular, moderate-to-vigorous physical activity benefits people of all ages. Exercise contributes in a positive way to both physical development and general health, while providing additional benefits for mental health [1] [3]. Physical activity supports the maintenance of healthy bones, muscles and joints, as well as helping to manage weight and reduce fat. Positive

effects of exercise include: reduced levels of depression, improved mood, and enhanced cardiovascular and musculoskeletal function [1]. Increased physical activity reduces the risk of specific diseases such as: heart disease, high blood pressure, colon cancer and diabetes, while lower levels of physical activity contribute to the likelihood of obesity. Therefore, health institutions such as: the ACSM, the CDC, the AHA, the PCPFS, and the NIH, have all recommended regular participation in physical activity [1]. One main factor that contributes to a healthy and active life-style, is ensuring adherence to their daily recommendations for physical activity.

Information and Communication Technology (ICT) is a large and rapidly changing field of study that relates to the technologies used to manage information and support communication. ICT innovations have been adopted in different contexts and used in many sectors because of their creative potential and positive implications. Technology-based interventions have become widely used for health promotion [4]. The term eHealth has been extensively mentioned in the scientific literature. Researchers have identified the "Health" and "Technology" as a two general themes in most published definitions of the term eHealth [5]. All definitions of eHealth consider technology as a tool to increase, serve, assist or improve user activities in health care [5]. Research supports the use of health ICTs in physical activity interventions [6]. Technology has the potential to play a significant role in contributing to physical activity and influencing exercise behaviors. Indeed there is a notable trend for using technology to help promote physical health [7] [8] [9] [10]. A number of new technologies have been employed within this context, including desktop computer systems, mobile applications, monitoring devices, computer games and exergaming technologies [8] [9] [10].

Different technologies have been used for physical activity promotion such as Physical Activity Self-Monitoring Technologies (PAMTs) [11]. PAMTs refer to the technology that is used for the purpose of tracking a user's physical movement, and measuring objective data related to such movement. Wearable PAMT devices have the ability to monitor and measure users' daily physical activity data [12]. This ability draws researchers' attention towards the use of these tools in different applications, especially within a health

Reem Altamimi is a research student with the University of Newcastle, NSW, Australia, and is employed and sponsored by Taibah University, Madinah, Saudi Arabia.

context [13]. PAMTs have a range of types, mechanisms and capabilities. They are also varied in their way of attachment to an individual's body (that is, waist-clips, wrist-bands, or applications installed on a user's mobile or tablet device). In addition, PAMTs have the ability to measure different components of physical activity, such as duration, frequency, and intensity of physical activity. Three main measurements have been widely investigated in the literature of PAMT. Step count is one of the most common measurements in quantifying levels of physical activity [14]. PAMTs are able to calculate the number of steps a person performs during his/her physical movements. Distance travelled is another measurement that is recorded by many PAMTs. Energy expenditure is a further measurement estimated by many types of physical activity monitors. Previous studies have used these parameters to examine the accuracy, validity and reliability of these monitoring devices [15] [16] [17] [18] [19] [20].

As part of the research agenda in active living technology adaption and use, this research found a growing diversity of physical activity monitoring technologies on the market. Based on the primary aim to integrate PAMT with ICT into our Active Living Technology framework, the issue of choosing the most appropriate contemporary activity tracking technology was raised. Therefore, a small pilot study was conducted in order to test the most popular PAMTs and find the one that is best suited for integration into the active living technology application. We specifically looked at features such as the accuracy of recording, validity and reliability, ease of use and applicability in everyday lives. This paper is organized as follows: Section 2 provides a specific review of the previous literature on related work in the assessment of PAMTs. Section 3 introduces the three stages of the pilot study that aims to validate a number of contemporary PAMTs. Section 4 details the third stage of the experiment including the methods, data analysis, results, findings, and limitations. The last section of this paper summarizes this pilot investigation.

II. RELATED WORKS

In the last few years, many researchers have started to investigate, evaluate, and assess the contemporary wearable PAMTs [12] [13] [15] [21]. This work has been varied, based on the technology used and the aspect specifically investigated. According to the Fitabase Library, since 2012, over 400 publications have used Fitbit monitors in research [22]. Much of the literature has investigated the accuracy of different PAMTs for measuring step count, distance walked and/or energy expenditure [12] [23]. Researchers have examined the validity and reliability of popular physical activity monitors based on experimental data [15]. Research using different types of physical activity trackers concurrently, during the same activity, has also been conducted in order to compare the output results [24] [25] [26].

In 2013, a study examined the reliability and validity of Fitbit and Fitbit Ultra trackers for recording step counts and energy expenditure. Twenty three adult participants completed a session of treadmill walking, jogging and stair-stepping while wearing six trackers, including two Actical accelerometers, two Fitbits and two Fitbit Ultras as well as an indirect calorimetry device. The results showed that both the Fitbit and the Fitbit

Ultra trackers are valid and reliable when estimating the step count and energy expenditure when walking and jogging and where no incline is combined [18]. Similarly, another study in 2013, reported that the most accurate steps recorded, with the smallest margin of error (equal to 1%), was Fitbit, compared to other popular market activity monitoring technologies (Nike+ bands, iPhone Move app and Pedometers) [12]. Fitbit One has been shown to be valid and reliable in recording step count while walking on a treadmill. However, the Fitbit One monitor was inaccurate in calculating the distance travelled [15].

In 2014, researchers investigated the validity of a Fitbit Zip tracker which was used as a physical activity monitor in free-living settings. Participants wore three waist-based trackers over seven days including a Fitbit Zip, an ActiGraph accelerometer and a Yamax pedometer. Comparing the results of the three trackers, the findings showed a significant correlation between the Fitbit Zip measurement of steps per day and both the accelerometer and the pedometer. While there was no significant difference between the Fitbit Zip and the Yamax pedometer in step counts per day, the Fitbit Zip recorded significantly more steps per day compared to the ActiGraph accelerometer. The study concluded that the Fitbit Zip is valid, and as such it was recommended for measuring physical activity in free-living settings [19]. Another pilot study in the same year, reported that the Fitbit Ultra and the ActiGraph™ GT1M had a strong agreement regarding step measurements while walking at slow and brisk speeds on a treadmill [23].

A study in 2015 also investigated the validity and the reliability of PAMTs. Twenty three adults participated in a treadmill trial, including slow, moderate and brisk walking, and jogging, while wearing three Fitbit One devices on their hips, and two Fitbit Flex devices on their wrist. The researchers focused on the Fitbit estimation of step count and energy expenditure. These estimated measurements were compared to the observed manual step count and the indirect calorimetry measurement of energy expenditure. Their results showed that both the Fitbit One and the Flex recorded a reliable estimation of the step count and energy expenditure during walking and jogging activities. However, the Fitbit One hip tracker performed better than the Fitbit Flex wrist tracker [20]. Furthermore, it has been found that Fitbit Ultra trackers have good inter-device reliability when measuring steps over different time units (minutes, hours, and days), especially in the day time in a free-living condition [27]. Another study, published in the same year, determined the accuracy of the recent popular wearable activity trackers based on the closeness of the measured values to the positive controls. For example, in measuring the accuracy of the step count value, the positive control was the observer manual count of steps. This study revealed that the highest accurate tracker was the MisFit Shine (99.1%) and that the least accurate tracker was the Samsung Gear 2 (79.8%), while the other fitness trackers and smart watches were relatively accurate [28]. A further study in 2015 demonstrated the validity of a number of PAMTs for step measurements in free-living conditions, with particularly the Fitbit One, Fitbit Zip and Withings Pulse achieving the highest performance [29]. The Fitbit Zip also showed the highest

validity and reliability of step counting in both laboratory and free-living conditions [30].

In 2016, a study investigated the accuracy of different PAMTs in measuring steps and distance during level, upstairs, and downstairs walking in healthy adults [31]. While most of the tested PAMTs were valid in their step count for ground level walking, they underestimated step count and overestimated distance recordings for both upstairs and downstairs walking [31]. Furthermore, another research found that both Fitbit Charge and Fitbit One showed different step recordings to the Actigraph GT3X monitor, however, all three monitoring devices revealed similar results in their recordings of moderate to vigorous physical activity [32].

Recently, a study published in 2017, investigated the validity of ten PAMTs in their step recordings. This study reported that the Fitbit Zip and Withings Pulse were the most accurate step recorders under the conditions of: treadmill, over-ground, and 24-hour free-living [33]. Another research found significant reliability between Fitbit devices in free-living conditions, as they had recorded similar monitoring results regardless of wear-location [34]. A further study, in its investigation of intra- and inter-monitor reliability for a number of PAMTs (Fitbit One, Zip, Flex, and Jawbone UP24), demonstrated that they had provided reliable recordings of physical activity in laboratory conditions. However, their reliability was found to decrease in free-living conditions [35]. Furthermore, it has been reported that the Fitbit Charge is valid for recording distance walked, while walking on a treadmill, at three different speeds - including 2.5mph, 4.5mph, or 6mph [36].

Many studies have reported on the validity and reliability of different PAMTs. A systematic review, which examined an assessment of Fitbit trackers, reported that the validity and the inter-device reliability of certain Fitbit models in their step measurements, were generally high. However, not all of the Fitbit models were tested and investigated [37]. Based on our knowledge and on this systematic review, published in 2015 [37], we established that there was no published literature on the validity and reliability of the Fitbit Surge and the Jawbone UP3 trackers at that time. We used these two tracker bands in an experiment that focused on the validity and reliability for recording the distance walked and steps taken. This experiment was conducted in 2015. However, while preparing this paper, we found a number of studies that have recently been published in the field of validating the Fitbit Surge [38] [39] [40]. Their validation includes the recording of sleep stages [38]; energy expenditure [39]; step count [40]; heart rate and energy expenditure [41]; steps, distance and heart rate [42]. Other recent studies have also included the Fitbit Surge and the Jawbone UP3 in their selection of tested devices, for the purpose of assessing the accuracy of these devices [43], and the consistency of their recordings [44].

III. EVALUATION OF THE CONTEMPORARY PHYSICAL ACTIVITY SELF-MONITORING TECHNOLOGY

This research assessed a number of the currently available physical activity monitors: Fitbit One, Fitbit Flex, Fitbit Surge, Jawbone UP, Jawbone UP3, and the Health iPhone application

for recording steps taken and distance travelled. This assessment was conducted over three testing stages. In Stage 1, the aim was to review the feasibility and applicability of the devices in real life settings. A further aim of this stage was to find the right type of physical activity to monitor in Stage 2, in order to ascertain the most accurate and reliable tracking device. In Stage 2, a structured walking activity was conducted in a controlled environment for the purpose of validating three types of physical activity monitoring technologies, including a waist-clip, a wrist-band and mobile application monitors. The investigations of both Stage 1 and Stage 2 were conducted in 2015 and published in 2016 [45] [46]. Based on the findings of the second stage, it was found that the Jawbone and Fitbit trackers recorded the most accurate results. Therefore, the final stage presented in this paper, aimed to select from the most recently released wristbands of the Jawbone and Fitbit brands at that time, the Fitbit Surge and the Jawbone UP3. We used these two bands in an experiment that focused on validating their accuracy and reliability in recording the two measurements of: the distance walked and the steps taken.

Validity refers to the ability of an instrument to measure what it is supposed to measure and to perform what it is designed to perform [47]. Measuring the validity of a device involves a process of collecting and analyzing its data to assess its accuracy [47]. On the other hand, assessing the reliability of a device refers to the ability of an instrument to consistently measure what it is intended to measure [47]. Reliability can refer to the precision of the instrument used. Precision and accuracy are incomplete and inaccurate synonyms for reliability and validity. However, this is not true in cases where we know the true value [48]. Therefore, within the context of this pilot study, the accuracy of the physical activity self-monitoring technology, refers to how its recordings were closest to the true value of steps taken (measured through manual counting) and distance travelled (measured through treadmill). Furthermore, the reliability of the physical activity self-monitoring technology, refers to the capacity of the trackers to provide the most consistent recordings of steps and distance walked each time the activity was repeated.

IV. VALIDATION OF THE WRIST-BANDS IN A CONTROLLED ENVIRONMENT

The research question that guided this stage was:

Which is the most accurate and reliable physical activity tracking wristband (Fitbit Surge or Jawbone UP3) that most accurately records distance walked and steps counted?

The Fitbit Surge and the Jawbone UP3, track users' physical workouts. Furthermore the devices incorporate an 'easy to use' app where users can monitor their daily activities as well as view their past historical activities. These devices have many tracking features, such as heart rate, number of steps, distance walked and calories burned. In this study, the devices' reliability to record a specific distance walked through the activity of treadmill walking (500 m), and a specific count of steps taken through the activity of stair climbing (51 stairs), were investigated.

The Fitbit Surge is a kind of wearable tracking technology that is worn on an individual's wrist. It is made of a flexible

and durable elastomer material and looks like a sport watch. It has a touch screen where users can instantly check their physical data. The Fitbit Surge has an automatic and wireless syncing feature, which can connect to tablets, computers and 200+ leading iOS, Android and Windows smartphones using Bluetooth 4.0 wireless technology. Syncing to computers requires an Internet connection and a USB port, whereas syncing to mobile devices requires Bluetooth and an Internet connection [49].

The Jawbone UP3 wristband is a thin and light wearable tracker. It has a strap made of medical-grade hypoallergenic TPU rubber. The Jawbone UP3 is built on an advanced multi-sensor platform that contains a newly designed tri-axis accelerometer, bio-impedance sensors, as well as skin and ambient temperature sensors [50] [51]. Unlike Fitbit Surge, there is no screen to display users' physical data. Instead, it has three single color LEDs that show the mode of the band: an orange light for sleep mode, a blue light to indicate activity mode, and a white light for notifications from the UP application [50] [51].

A. Method

This stage took place over 17 days and consisted of two sub-phases. With the need to check the accuracy and reliability of the devices in recording distance walked and steps taken, specific physical activities was performed throughout the days of the experiment. In Sub-phase 1 of the experiment, a treadmill walk activity was selected, along with a standard distance value, to be compared with the output of the trackers. The trackers were worn at the same time while walking on a treadmill for a specific distance at a constant speed. This method follows the previous technique used for validating the three types of physical activity self-monitoring technologies in Stage 2 [45], which followed the methods reported in other literature [15] [30]. For seven days, the experiment focused on the metric distance recorded by the two fitness bands. On each day, ten trials were performed; therefore, a total of 70 observations were collected. Each trial was a 500m walk on a treadmill at a speed of 4.5 km/h with the two tracking wristbands worn simultaneously. In each round, the author put on the two bands, started on the treadmill, walked for 500m, stopped the treadmill, and recorded the output of each tracker before resetting the distance and starting over for the next trial. By the end of the test period, the distance recorded by each tracker was compared with the treadmill output.

In Sub-phase 2 of the experiment, a specific value of steps was set and taken while wearing both trackers, in order to compare the trackers' outputs with the actual number of steps. This phase of the experiment took place over ten days. On each day, ten trials were performed; so generating data collection of a total of 100 observations for each device. Each trial comprised of 51 steps taken through climbing 3 sets of 17 stairs. In each round, the bands were worn simultaneously while climbing a set of the stairs up, down and finally up, ending with 51 stairs having been climbed in total. The next round reversed the method, starting with walking down the stairs, then up, and finally down again. After each trial, the researcher stopped and recorded the output of each tracking device before moving onto the next round. This method of stair

climbing was selected in order to avoid any errors associated with manual step counting. Therefore, each step recorded while climbing the stairs, was equal to one exact step recording. The method of stair climbing in general has already been used in previous research [31], however the particular stair climbing procedure employed in this research is distinctive from such.

B. Data and Analysis

The data were analyzed using the JMP and SPSS data analysis software. The significance level is set at $p < 0.05$.

In Sub-phase 1 (Distance Validation), the first analysis test was a Shapiro-Wilk W. Based on this test's results, the outcome variable "distance walked" for both the Fitbit Surge (FS) and the Jawbone UP3 (JU) devices were negatively skewed (FS: $W=0.893$, $P<0.001$; JU: $W=0.648$, $P<0.001$). However, the distribution is moderately skewed (skewness of FS=-0.532; JU=-0.696). Furthermore, the combined sample size is over 100. Therefore, the Independent Sample T test was conducted to compare the difference in the distance walked measurement between the two devices. Fig. 1 shows the boxplots of the distance walked, recorded by each tracker.

In Sub-phase 2 (Steps Validation), the same procedure of analysis as in the previous phase, was followed. This involved firstly the application of a Shapiro-Wilk W analysis test. The Shapiro-Wilks W test showed that the JU steps data were skewed while the FS steps data were normally distributed (FS: $W=0.983$, $P=0.208$; JU: $W=0.910$, $P=0.000$). However, the distribution of the Jawbone UP3 steps data were only moderately skewed (skewness=-0.590). In addition, the combined sample size was 200. Therefore, the Independent Sample T test was conducted to see whether the recordings of the steps taken by the two trackers were different from each other. Fig. 2 shows the boxplots of the number of steps recorded by each tracker. This figure demonstrates the differences between the trackers in recording the steps taken, and shows a variation in the number of steps recorded in each of the tracker's output over all of the days of the experiment.

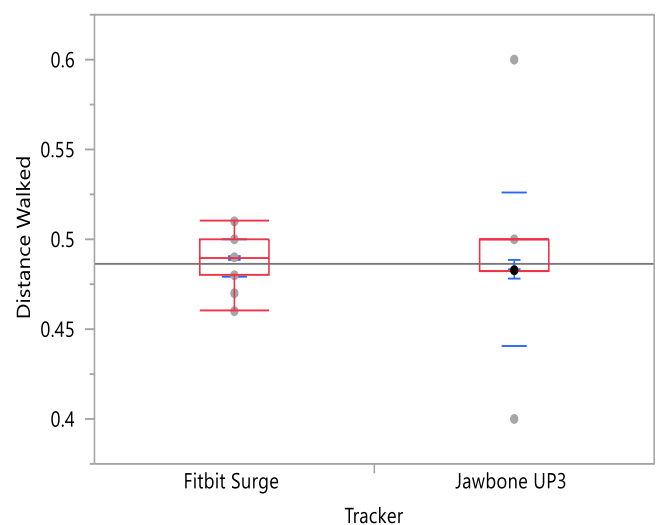


Fig. 1: Analysis of distance walked by each tracker

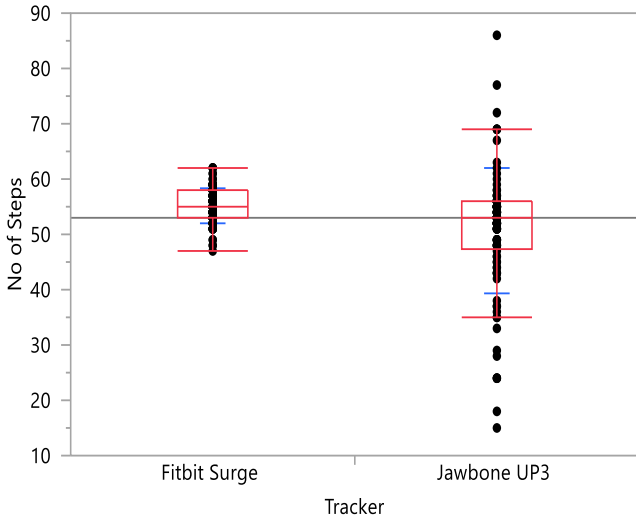


Fig. 2: Analysis of the no of steps recorded by each tracker

The accuracy refers to the agreement between the measurement and the true or actual value. As the actual value is known, the Mean Absolute Error (MAE) and the Mean Absolute Percentage Error (MAPE) of each device have been calculated, based on the following equations:

$$MAE = \frac{1}{n} \sum_{i=1}^n |Estimated - Actual| \quad (1)$$

$$MAPE = \frac{1}{n} \sum_{i=1}^n \frac{|Estimated - Actual|}{Actual} \times 100 \quad (2)$$

Actual value, in (1) and (2), refers to the value of 0.5 km for distance validation and to the value of 51 steps for the steps validation. The Estimated value refers to the device's recordings. The value n refers to the number of errors. Positive values of errors mean that the tracker had overestimated the measurements, while negative errors mean that the tracker had underestimated the measurements. The absolute error shows the difference between the estimated value and the true or actual value, whereas the MAE refers to the average of all absolute errors. The MAPE measures the size of the devices' errors in percentage terms. The MAE as well as the MAPE are presented in Table 1. In addition, Table 1 offers the descriptive statistics generated for each tracking device, including the mean, median, standard deviation, and the interquartile range.

C. Results

From the data collected under the condition of Sub-phase 1 as well as the statistical analysis provided above, a number of results can be drawn, as follows:

TABLE I: DESCRIPTIVE STATISTICS OF DISTANCE WALKED AND STEPS TAKEN METRICS

Sub-phase	Sub-phase 1 Distance Validation (0.5 Km)		Sub-phase 2 Steps Validation (51 Steps)	
	FS	JU	FS	JU
Tracker				
No. of Observations	70	70	100	100
Mean	0.49	0.48	55.31	50.68
Median	0.49	0.5	55	53
Std. Dev	0.01	0.04	3.177	11.249
IQR	0.02	0.02	5	9
MAE	0.015	0.065	4.88	8.09
MAPE	3.08%	13.10%	9.57%	15.85%

- The results of the Independent-Samples T Test show that there is no statistically significant difference between the distance measurement of the Fitbit Surge (Mean=0.49, SD=0.01, Median=0.49) and the Jawbone UP3 (Mean=0.48, SD=0.04, Median=0.5), $t(77.888) = 1.184$, $p=0.240$.
- The One-Sample T Test shows that each tracker differs with regard to treadmill output, in recording the measurement of the distance walked (FS: $t(69) = -8.226$, $p=0.000$; JU: $t(69) = -3.313$, $p=0.001$).
- It appears that the Fitbit Surge had a mean closest to the treadmill ($M = 0.49$) and the smallest standard deviation ($SD=0.01$).
- Both the Fitbit Surge and the Jawbone UP3 had underestimated the distance walked. The MAPE in the Fitbit Surge (3.08%) was smaller than the MAPE in the Jawbone UP3 (13.10%).

The results of Sub-phase 2 of the experiment, include the following findings:

- Based on the p value of the Independent-Samples T Test, the tracking devices were different in their recordings of the steps counted, $t(114.695) = 3.961$, $p = 0.000$.
- The One-Sample T Test shows that the step count recorded by Fitbit Surge was different from the real count of steps (the number of stairs climbed), $t(99) = 13.565$, $p=0.000$. On the other hand, the step count recorded by the Jawbone UP3 was not statistically different from the real count of steps, $t(99) = -0.284$, $p=0.777$.
- While the Jawbone UP3 tracker was more accurate than the Fitbit Surge (mean of 50.68 compared to 55.31), the Jawbone UP3 was much less precise (SD of 11.249 compared to 3.177).
- The Fitbit Surge had overestimated the steps count with a MAPE equal to 9.57%, while the Jawbone UP3 underestimated the steps count with a MAPE equal to 15.85%.

D. Findings and Discussion

Based on the conditions and the results of the two sub-phases of this experiment, both the Fitbit Surge and the Jawbone UP3 are considered as valid PAMTs for recording distance walked and number of steps taken. They both measured what they were supposed to measure as they had recorded valid metrics of distance walked and steps taken. These recordings helped in the assessment of the devices' accuracy and reliability.

Accuracy. In terms of the metric "distance walked", results show that there is no significant difference between the Fitbit Surge and the Jawbone UP3 in their recordings of distance walked. However, these recordings were different from the treadmill measurement. The Fitbit Surge band was more accurate, as the mean was the closest to the distance value of the treadmill (Mean=0.49, SD=0.01). However, both the Fitbit Surge and the Jawbone UP3 had underestimated the distance walked measurement with a mean absolute percentage error, 3.08% and 13.10% respectively. The mean of the Fitbit Surge, and the Jawbone UP3 recordings of distance walked, were slightly different, leading to the finding that both devices are accurate and therefore valid in their recordings of distance walked while walking on a treadmill at a constant speed.

With regard to the steps taken recordings, we found that there is a statistically significant difference between the Fitbit Surge and the Jawbone UP3 in their recordings of steps taken. The Jawbone UP3 recorded the most accurate number of steps (Median=53, Mean=50.68), compared to the true number of steps, which was 51 steps. However, the Jawbone UP3 underestimated the steps count, with a higher MAPE equal to 15.85% compared to the Fitbit Surge, which overestimated the steps count, with a MAPE equal to 9.57%. Again, the difference between both trackers in terms of accuracy, was minor (a mean of 50.68 in the Jawbone UP3 compared to 55.31 in the Fitbit Surge), which means that both trackers are considered valid in their recordings of steps taken. The Jawbone UP3 and the Fitbit Surge wristband devices, are therefore both considered as valid tools for tracking steps taken while climbing a set number of stairs.

Reliability. In terms of the distance walked measurement, the Fitbit Surge was more reliable, as it provided the most consistent recordings of distance each time the activity was repeated, SD=0.01. However, the Jawbone UP3 also had a high consistency with a small SD value equal to 0.04. Therefore, both the Fitbit Surge and the Jawbone UP3 can be considered as reliable tools for recording the distance walked data, as they both consistently and accurately recorded the distance walked data (Fitbit Surge SD=0.01, Jawbone UP3 SD=0.04). While there is a significant difference between the two trackers and the treadmill in their measurement of distance walked, it is of no practical difference for this study. The Jawbone UP3 and the Fitbit Surge wristband devices are both valid and reliable tools in tracking the distance walked while walking on a treadmill at a constant speed. Therefore, either of the two trackers are suitable for use in recording the distance metric.

In terms of the precision and consistency of the recording of the 'steps taken' measurement, the Fitbit Surge was more precise (SD 3.177 compared to 11.249), and therefore more

reliable. The Jawbone UP3 was more accurate in recording step count, but it was less precise and therefore less reliable in recording the steps taken (SD=11.249). Nevertheless, the Jawbone UP3 and the Fitbit Surge devices are both valid tools in tracking steps taken while climbing a set of stairs. Therefore, either of the two trackers are suitable for use in recording metric steps.

It has been reported that some models of Fitbit trackers overestimated the number of steps taken in free-living settings [52] [19]. The results of this study also confirm that the Fitbit Surge overestimated step count in a stair climbing setting. Furthermore, it has been reported that activity monitors underestimated step count while walking upstairs and downstairs [31]. However, the present study found that the Fitbit Surge overestimated step count while the Jawbone UP3 underestimated step count during stair climbing activities. A previous research reported that the Fitbit Surge consistently and significantly undercounted steps [40], whereas the results of this experiment agree that the steps recorded by the Fitbit Surge significantly differed from the true value, by over-counting the step measurement (M=55.31). While it has been reported that the Fitbit monitor was inaccurate in calculating the distance travelled [15], this study found that the Fitbit Surge recorded the closest mean and smallest variation of distance walked, compared to the Jawbone UP3. The present study demonstrates the reliability, as well as the less variability of the Fitbit Surge tracker in recording both the steps taken and the distance walked. A recent work demonstrated the reliability of the Fitbit Surge and the Jawbone UP3 in measuring the number of steps and distance [44]. This is consistent with the present study in terms of distance measurements. However, in terms of the recording of the steps, the Fitbit Surge was less accurate and more reliable, while the Jawbone UP3 was more accurate and less reliable. The results of this study support other findings about the accuracy, validity and reliability of Fitbit trackers for measuring step count [12] [18] [15] [20] [27] [29] [30] [33] [53] and distance walked [36].

As Fitbit trackers have an altimeter sensor that can discover when users are going up or down in elevation, these PAMTs permit the counting of floors climbed. The Fitbit tracker records one floor when a user climbs about ten feet at one time, but it does not record floors when users go down [54]. Investigating this feature throughout the second phase of this experiment proves the accuracy and reliability of this tracking technique. Each round of this phase consisted of climbing three sets of 17 stairs, and composing two types of rounds: twice-up and twice-down. In the twice-up round, the researcher climbed up twice and down once by following an up-down-up climb pattern. In the next round – twice-down – the researcher proceeded in reverse, climbing down twice and up once by following a down-up-down climb pattern. Each time of undertaking the twice-up round, the researcher observed that the Fitbit Surge band recorded "floors climbed" data as 2 floors. On the other hand, in each attempt of the twice-down round, the researcher observed that it recorded "floors climbed" data as 1 floor. This confirms the Fitbit Surge data monitor's accuracy in detecting and tracking user movements while walking up stairs.

E. Limitation

The pilot study presented in this paper has a number of limitations. Firstly, the tests were undertaken by only one person: the first author of this paper. The reason behind this limitation was the time constraint, as these preliminary experiments were a fundamental and preliminary part of an overarching research project. However, testing a number of trackers using a single person has been previously employed in literature [27]. Secondly, using two specific types of physical activity – walking on a treadmill in distance validation and manually counting the steps in step validation – limited the demonstrated validity of the trackers used in this research. A reliable tracker for distance and step recordings for the provided type of physical activity may not be valid for other types of physical activities, such as running. Thirdly, the focus of this study was on the distance walked and steps taken measurements. Therefore, all other physical data recorded by a tracker, such as active minutes and calories burned, were excluded. However, the step count validation was the most important measurement within the context of this research, as it will be implemented and utilized in the active living technology application. Nevertheless, this study makes a valuable contribution within the area of valid trackers in the treadmill walking activity and manual counting of steps taken in a stair climbing activity. The validity of the distance walked as shown by trackers, was assessed, during a session of treadmill walking using methods similar to previous research on activity monitoring validation. The distance of 0.5 km was determined as a standard distance value in all trials, which would so offer more validation for the results generated from the 70 observations collected for each tracker.

V. CONCLUSION

The pilot study presented in this paper advances knowledge about physical activity self-monitoring technologies used for the objective assessment of physical activity in terms of steps taken and distance walked. Based on the data collected over many observations and the statistical analysis presented in this paper, both the Fitbit Surge and the Jawbone UP3 can be considered as valid and reliable devices in measuring the distance walked metric. The Fitbit Surge is a useful, valid and reliable PAMT, which had the smallest variation in terms of steps taken. On the other hand, the Jawbone UP3 is more accurate with a higher percentage of error in detecting the steps taken. While it is not the intention of this research to promote any individual physical activity monitoring technology, it is hoped that this part of the research will assist other researchers in their choice of reliable equipment to use in research that involves reliable and accurate distance and steps calculation. Finally as technology evolves so quickly, there should be a standard qualification of factors developed in the framework to assess the validation of every new type of technology that comes onto the field of physical activity tracking technologies.

REFERENCES

- [1] U.S. Department Of Health And Human Services (HHS), Centers for Disease Control and Prevention (CDC), National Center for Chronic Disease Prevention and Health Promotion (NCCDPHP), and The President's Council on Physical Fitness and Sports (PCFSN), "Physical Activity and Health - A Report of the Surgeon General—Executive Summary," 1996.
- [2] M. Hoos, H. Kuipers, W.-J. Gerver, and K. Westerterp, "Physical activity pattern of children assessed by triaxial accelerometry," *European journal of clinical nutrition*, vol. 58, no. 10, pp. 1425-1428, 2004.
- [3] W. B. Strong et al., "Evidence based physical activity for school-age youth," *The Journal of pediatrics*, vol. 146, no. 6, pp. 732-737, 2005.
- [4] G. J. Norman, M. F. Zabinski, M. A. Adams, D. E. Rosenberg, A. L. Yaroch, and A. A. Atienza, "A review of eHealth interventions for physical activity and dietary behavior change," *American journal of preventive medicine*, vol. 33, no. 4, pp. 336-345. e16, 2007.
- [5] H. Oh, C. Rizo, M. Enkin, and A. Jadad, "What is eHealth (3): a systematic review of published definitions," *J Med Internet Res*, vol. 7, no. 1, p. e1, 2005.
- [6] P. W. Lau, E. Y. Lau, D. P. Wong, and L. Ransdell, "A systematic review of information and communication technology-based interventions for promoting physical activity behavior change in children and adolescents," *Journal of medical Internet research*, vol. 13, no. 3, p. e48, 2011.
- [7] C. R. Nigg, "Technology's influence on physical activity and exercise science: the present and the future," *Psychology of Sport and Exercise*, vol. 4, no. 1, pp. 57-65, 2003.
- [8] S. Consolvo, K. Everitt, I. Smith, and J. A. Landay, "Design requirements for technologies that encourage physical activity," in *Proceedings of the SIGCHI conference on Human Factors in computing systems*, 2006, pp. 457-466: ACM.
- [9] J. J. Lin, L. Mamykina, S. Lindtner, G. Delajoux, and H. B. Strub, "Fish'n'Steps: Encouraging physical activity with an interactive computer game," in *International Conference on Ubiquitous Computing*, 2006, pp. 261-278: Springer.
- [10] I. Anderson et al., "Shakra: tracking and sharing daily activity levels with unaugmented mobile phones," *Mobile networks and applications*, vol. 12, no. 2-3, pp. 185-199, 2007.
- [11] V. H. Heyward and A. L. Gibson, "Technology can boost physical activity promotion " in *Advanced Fitness Assessment and Exercise Prescription*, Seventh Edition With Online Video, 2014.
- [12] F. Guo, Y. Li, M. S. Kankanalli, and M. S. Brown, "An evaluation of wearable activity monitoring devices," in *Proceedings of the 1st ACM international workshop on Personal data meets distributed multimedia*, 2013, pp. 31-34: ACM.
- [13] P. J. Mancuso, M. Thompson, M. Tietze, S. Kelk, and G. Roux, "Can patient use of daily activity monitors change nurse practitioner practice?," *The Journal for Nurse Practitioners*, vol. 10, no. 10, pp. 787-793. e4, 2014.
- [14] B. C. Choi, A. W. Pak, and J. C. Choi, "Daily step goal of 10,000 steps: a literature review," *Clinical & Investigative Medicine*, vol. 30, no. 3, pp. 146-151, 2007.
- [15] J. Takacs, C. L. Pollock, J. R. Guenther, M. Bahar, C. Napier, and M. A. Hunt, "Validation of the Fitbit One activity monitor device during treadmill walking," *Journal of Science and Medicine in Sport*, vol. 17, no. 5, pp. 496-500, 2014.
- [16] D. R. Bassett Jr et al., "Accuracy of five electronic pedometers for measuring distance walked," *Medicine and science in sports and exercise*, vol. 28, no. 8, pp. 1071-1077, 1996.
- [17] S. E. Crouter, P. L. Schneider, M. Karabulut, and D. R. Bassett, Jr., "Validity of 10 electronic pedometers for measuring steps, distance, and energy cost," (in eng), *Med Sci Sports Exerc*, vol. 35, no. 8, pp. 1455-60, Aug 2003.
- [18] J. Adam Noah, D. K. Spierer, J. Gu, and S. Bronner, "Comparison of steps and energy expenditure assessment in adults of Fitbit tracker and Ultra to the Actical and indirect calorimetry," *Journal of medical engineering & technology*, vol. 37, no. 7, pp. 456-462, 2013.
- [19] M. A. Tully, C. McBride, L. Heron, and R. F. Hunter, "The validation of Fitbit Zip™ physical activity monitor as a measure of free-living physical activity," *BMC research notes*, vol. 7, no. 1, p. 952, 2014.

- [20] K. M. Diaz et al., "Fitbit®: An accurate and reliable device for wireless physical activity tracking," *International journal of cardiology*, vol. 185, pp. 138-140, 2015.
- [21] H. Issa, A. Shafae, S. Agne, S. Baumann, and A. Dengel, "User-sentiment based evaluation for market fitness trackers-evaluation of Fitbit One, Jawbone Up and Nike+ Fuelband based on Amazon. com customer reviews," in *ICT4AgeingWell*, 2015, pp. 171-179.
- [22] Fitabase. (2015). Fitbit Research Library. Available: <https://www.fitabase.com/research-library/>
- [23] R. Gusmer, T. Bosch, A. Watkins, J. Ostrem, and D. Dengel, "Comparison of FitBit® Ultra to ActiGraph™ GT1M for assessment of physical activity in young adults during treadmill walking," *The Open Sports Medicine Journal*, vol. 8, no. 1, 2014.
- [24] G. C. Le Masurier and C. Tudor-Locke, "Comparison of pedometer and accelerometer accuracy under controlled conditions," *Medicine and Science in Sports and Exercise*, vol. 35, no. 5, pp. 867-871, 2003.
- [25] C. G. Ryan, P. M. Grant, W. W. Tigbe, and M. H. Granat, "The validity and reliability of a novel activity monitor as a measure of walking," *British journal of sports medicine*, vol. 40, no. 9, pp. 779-784, 2006.
- [26] B. Dijkstra, W. Zijlstra, E. Scherder, and Y. Kamsma, "Detection of walking periods and number of steps in older adults and patients with Parkinson's disease: accuracy of a pedometer and an accelerometry-based method," *Age and ageing*, vol. 37, no. 4, pp. 436-441, 2008.
- [27] M. L. Dontje, M. de Groot, R. R. Lengton, C. P. van der Schans, and W. P. Krijnen, "Measuring steps with the Fitbit activity tracker: an inter-device reliability study," *Journal of medical engineering & technology*, vol. 39, no. 5, pp. 286-290, 2015.
- [28] F. El-Amrawy and M. I. Nounou, "Are currently available wearable devices for activity tracking and heart rate monitoring accurate, precise, and medically beneficial?," *Healthcare informatics research*, vol. 21, no. 4, pp. 315-320, 2015.
- [29] T. Ferguson, A. V. Rowlands, T. Olds, and C. Maher, "The validity of consumer-level, activity monitors in healthy adults worn in free-living conditions: a cross-sectional study," *International Journal of Behavioral Nutrition and Physical Activity*, vol. 12, no. 1, p. 42, 2015.
- [30] T. J. Kooiman, M. L. Dontje, S. R. Sprenger, W. P. Krijnen, C. P. van der Schans, and M. de Groot, "Reliability and validity of ten consumer activity trackers," *BMC sports science, medicine and rehabilitation*, vol. 7, no. 1, p. 24, 2015.
- [31] Y. Huang, J. Xu, B. Yu, and P. B. Shull, "Validity of FitBit, Jawbone UP, Nike+ and other wearable devices for level and stair walking," *Gait & posture*, vol. 48, pp. 36-41, 2016.
- [32] K. N. Deyarmin, K. M. Snyder, A. G. Mihalik, and T. A. Hargens, "Accuracy of wrist and hip-worn commercial physical activity monitors in free living conditions: 2775 Board #298 June 3, 9: 30 AM - 11: 00 AM," *Medicine & Science in Sports & Exercise*, vol. 48, no. 5S, p. 781, 2016.
- [33] H.-S. An, G. C. Jones, S.-K. Kang, G. J. Welk, and J.-M. Lee, "How valid are wearable physical activity trackers for measuring steps?," *European journal of sport science*, vol. 17, no. 3, pp. 360-368, 2017.
- [34] R. E. Reid et al., "Validity and reliability of Fitbit activity monitors compared to ActiGraph GT3X+ with female adults in a free-living environment," *Journal of science and medicine in sport*, vol. 20, no. 6, pp. 578-582, 2017.
- [35] J. M. Bock, L. A. Kaminsky, M. P. Harber, and A. H. Montoye, "Determining the reliability of several consumer-based physical activity monitors," *Technologies*, vol. 5, no. 3, p. 47, 2017.
- [36] C. J. Marton, "Validity of the Fitbit® distance traveled feature among multiple speed trials: 2672 Board# 192 June 2 9," *Medicine & Science in Sports & Exercise*, vol. 49, no. 5S, p. 762, 2017.
- [37] K. R. Evenson, M. M. Goto, and R. D. Furberg, "Systematic review of the validity and reliability of consumer-wearable activity trackers," *International Journal of Behavioral Nutrition and Physical Activity*, vol. 12, no. 1, p. 159, 2015.
- [38] Z. Beattie et al., "Estimation of sleep stages in a healthy adult population from optical plethysmography and accelerometer signals," *Physiological Measurement*, vol. 38, no. 11, p. 1968, 2017.
- [39] Z. Gao et al., "Accuracy of smartwatches in assessing college students' energy expenditure in exercise with different intensities: 1660 Board #335 June 1 8: 00 AM - 9: 30 AM," *Medicine & Science in Sports & Exercise*, vol. 49, no. 5S, p. 474, 2017.
- [40] F. Modave et al., "Mobile device accuracy for step counting across age groups," *JMIR mHealth and uHealth*, vol. 5, no. 6, 2017.
- [41] A. Shcherbina et al., "Accuracy in wrist-worn, sensor-based measurements of heart rate and energy expenditure in a diverse cohort," *Journal of personalized medicine*, vol. 7, no. 2, p. 3, 2017.
- [42] O. Binsch, T. Wabeke, and P. Valk, "Comparison of three different physiological wristband sensor systems and their applicability for resilience-and work load monitoring," in *Wearable and Implantable Body Sensor Networks (BSN)*, 2016 IEEE 13th International Conference on, 2016, pp. 272-276: IEEE.
- [43] M. A. Smith, "Accuracy of steps, energy expenditure, and distance in nine activity trackers: 1341 Board #16 June 1 9: 00 AM - 10: 30 AM," *Medicine & Science in Sports & Exercise*, vol. 49, no. 5S, p. 362, 2017.
- [44] D. Wen, X. Zhang, X. Liu, and J. Lei, "Evaluating the consistency of current mainstream wearable devices in health monitoring: a comparison under free-living conditions," *Journal of medical Internet research*, vol. 19, no. 3, 2017.
- [45] R. I. Altamimi and G. D. Skinner, "Validation of contemporary physical activity tracking technologies through exercise in a controlled environment," *World Academy of Science, Engineering and Technology, International Journal of Medical, Health, Biomedical, Bioengineering and Pharmaceutical Engineering*, vol. 10, no. 1, pp. 31-42, 2016.
- [46] R. Altamimi and G. Skinner, "An experimental analysis of active living technologies to review device accuracy," in *Region 10 Conference (TENCON)*, 2016 IEEE, 2016, pp. 337-343: IEEE.
- [47] J. P. Biddix, "Research rundowns_instrument, validity, reliability," ed, 2009.
- [48] D. L. Streiner and G. R. Norman, "'Precision' and 'Accuracy': two terms that are neither," *Journal of Clinical Epidemiology*, vol. 59, no. 4, pp. 327-330, 2006/04/01/ 2006.
- [49] Fitbit. (2017). Surge_specifications. Available: <https://www.fitbit.com/surge#specs>
- [50] Jawbone. (2017). UP3. Available: <https://jawbone.com/fitness-tracker/up3>
- [51] P. Lamkin. (2015). Jawbone UP3 review. Available: <https://www.wearable.com/jawbone/jawbone-up3-review>
- [52] L. J. Leininger, B. J. Cook, and K. J. Adams, "Validation and accuracy of FITBIT Charge: a pilot study in a university worksite walking program," *Journal of Fitness Research*, vol. 5, 2016.
- [53] G. Mammen, S. Gardiner, A. Senthinathan, L. McClemon, M. Stone, and G. Faulkner, "Is this bit fit? Measuring the quality of the FitBit step-counter," *Health Fit J Can*, vol. 5, no. 4, pp. 30-9, 2012.
- [54] Fitbit. (2017, August 2017). How does my tracker count floors? Available: https://help.fitbit.com/articles/en_US/Help_article/1141

Modernising Asthma Management: Personalised Asthma Action Plans Using a Smartphone Application

Nikita Isaac, Naveenaa Sampath and Valerie Gay

*Faculty of Engineering and IT
University of Technology Sydney
Broadway NSW 2007, Australia
Email: Valerie.Gay@uts.edu.au*

Asthma is a chronic disease affecting one in nine Australians. With symptoms such as coughing, wheezing and shortness of breath, asthma can significantly impact a patient's quality of life. Asthma action plans are said to be one of the most effective asthma interventions available. However, in Australia only one in five people aged 15 and over, with asthma, have a written asthma action plan. Even less of which, refer to their plan. A review of related literature and work showed a gap regarding accessibility of information on asthma action plans in a written form. In an attempt to mitigate this problem, this paper focuses on the design and development of a smartphone application. The application is currently a high-fidelity prototype designed and built using proto.io software. In addition to this conversion, the application incorporates aspects of the Internet of Things (IoT) whereby real-time data regarding environmental triggers such as temperature, humidity and pollen in surroundings, can be accessed from the application. The application ultimately aims to help asthmatics improve their health and quality of life by providing them, or their carer with the knowledge needed to better understand and manage their asthma, when and where they need it.

Keywords—Asthma management; mobile technology; smartphone application; asthma action plans; internet of things

I. INTRODUCTION

Asthma is a chronic disease affecting one in nine Australians [1]. As of 2014, 1.5 out of every 100, 000 deaths in Australia were due to asthma [2]. People with asthma have sensitive airways which react to environmental triggers, causing 'flare ups'. This is when muscles in the wall of airways tighten and swell, narrowing the airway itself. This, in combination with the production of mucus can block the airway to varying degrees. Resulting in symptoms such as coughing, wheezing, tightness in the chest and shortness of breath, making it extremely difficult to breathe [3].

There is no cure for asthma, even when patients feel fine, they still have asthma and flare ups can occur at any time [4]. Asthma varies in severity from mild to severe. In severe asthma, breathing difficulties can be life threatening [5].

Asthma Australia's 2015-16 annual report, stated the individual cost of having asthma as \$11 741 per asthmatic, and the direct and indirect costs of asthma to the Australian economy was an estimated \$28 billion per annum. With \$1.2 billion being costs to the health system by means of prescriptions and hospitalisations. In the Australian Institute of

Health and Welfares 2014-15 report, there were 39 500 hospitalisations and a totalled 419 deaths from due to asthma.

Asthma can be managed by taking an active role in its management via ongoing treatment and building a strong partnership with doctors and other health care providers [1]. Asthma action plans are said to be one of the most effective asthma interventions available. A Written asthma action plan is key to effective asthma management, because it is written by the patient, in conjunction with their doctor. Such that they can both easily recognize changes in the patient's asthma severity and provide clear instructions on how to respond. It is important to note that as a patient's asthma severity changes so should the advice on their asthma action plan. Hence regular updates are essential [3]. However, despite the recommendation that all asthmatics in Australia be given a personalised asthma action plan (PAAP), only one in five people aged 15 and over with asthma, have a written asthma action plan in Australia [2], even less of whom refer to it.

The biggest challenge with asthma control is daily adherence. Consequently, this projects goal is to increase the awareness and use of Asthma action plans as a key asthma intervention for regular control over symptoms.

In this paper section II consists of an evaluation of related work regarding the benefits and current limitations of PAAPs, the current use of smartphone applications and the Internet of Things (IoT) in health care. The overlap of these three themes leads to the design and development of a high-fidelity prototype in sections III and IV. This is followed by a discussion in section V and conclusion in section VI which evaluates the application for future improvements and general biases.

II. RELATED WORK

A. Asthma Action Plan

In the UK asthmatics without a PAAP are said to be four times more likely to be hospitalised for asthma related purposes [5]. PAAPs are noted by Gatheral et al (2017) to be fundamental in the achievement of asthma control. Asthmatics are frequently sent to the ED for reasons that could be easily handled with proper understanding of their asthma and how to treat it at home [6]. Steady increases in ED admissions for asthma causes in patients aged 14-19 years old in the UK, indicated a need for a

clinically appropriate program to encourage effective asthma management [5]. This need can be further supported as Asthma flare-ups were the top cause for ED visits for children in the US over 2011 [7]. Consequently, Lynch et al (2016) conducted an asthma review where participants were to use a peak flow meter and an Asthma Action Plan (AAP) for two months with weekly telephone check-ups on their condition. The results showed improved consistency of exacerbations, self-reported wellbeing and reduced hospitalisations, with 75% of participants having a better understanding of their own asthma and as a result of this, with 83% of patients feeling more in control of their asthma. Overall half of the participants experienced improved asthma symptoms as a result of their reliance on their AAP.

While all these studies demonstrate how beneficial PAAPs can be to an asthmatic, PAAPs are not without current limitations. The National Health Service in Lanarkshire, Scotland and the National Service for Health Improvement in the UK, developed an adult version of the PAAP and assessed its usefulness within the local population. Smith et al (2016) conducted the study to understand the impact of a structured consultation delivered by a respiratory nurse or specialist on a patient use of a PAAP and consequently their asthma. As part of a structured annual review and educational program, 136 patients were provided with a PAAP in consultation with a respiratory nurse specialist team. Over the next 6 months, 27.2% of participants experienced asthma exacerbations. At the 6-month follow up point, 82.2% remembered getting their PAAP but only 64.9% of participants still had theirs and only 20.7% of participants had properly used their PAAP. Additionally, 43.4% of patients were not able to name even one item or task on their PAAP. These results indicate that within a short 6-month time period, one third of patients had not stuck to their PAAP and this was largely due to their reported difficulties in recalling and accessing its content. This highlights the need for constant access to the information on a PAAP in order for its continuous and effective use.

B. Smartphone Application

In the face of inconsistent and ignored face-to-face and paper-based tools evidenced by the 1 in 5 usage rate of written asthma action plans in Australia [1], apps are increasingly recognized by policy makers as a potential avenue of supporting self-management in long term conditions, such as asthma [8]. Huckvale, Car, Morrison & Car (2012) conducted a review on the extent to which current smartphone apps suitably support people with asthma, by way of comprehensive information, evidence-based advice and compliance with best practice health principles. After performing a search in Android and iOS app stores against an inclusion and exclusion criteria, 94 English apps were found. Of which, 43 apps were sources of written information about asthma, 13 were multimedia apps and the outstanding 47 were tools supporting aspects of asthma self-management. Despite this, they found no English language app that combined information and management tools, identifying that the potential complexity of these tasks highlights an opportunity to combine information and management tools. In 2015, they conducted a review of the 2012 data, to highlight the evolution of smartphone apps for asthma, and noted that with

the rapid evolution of mobile technologies, opportunities for health capabilities by means of wearable devices are emerging. Between 2011 – 2013, the number of apps for asthma doubled. Based on the previously mentioned inclusion and exclusion criteria apps from both studies were screen again and an updated analysis was performed on 147 unique asthma apps. 83% of asthma apps available in 2013 gave details of asthma pathophysiology. But only half provided information on basic asthma management. Even less addressed self-management skills inclusive of allergen and trigger avoidance, self-monitoring skills or how to appropriately use treatment. Furthermore, less than a third of apps addressed how to recognize signs of deterioration or failed to identify the importance of personalized treatments and goal setting.

At the same time, there is no current smartphone health or fitness app that meets the need of every patient [8]. Huckvale, Car, Morrison & Car (2012) found 103 English apps, but none of them combined comprehensive, evidence based information with supportive tools. The review showed that paper based asthma action plans lack the interactive treatment recommendations offered by most app based plans in the review. However, asthma apps enabling the development and updating of asthma action plans or data into diaries, were noted as being in need of a new way to populate records in a timely fashion. As a result, the quality of an app may be judged differently by different patient users of the app specific to their own goals such that it stimulates sustained use. The range of app functions for asthma demonstrated in this literature review highlights the potential value of patient and professional input into health app designs.

C. Internet of Things

Although recent years have seen a vast improvement in medications to control asthma symptoms, asthma management still proves a challenging task as it requires an understanding of asthma causes and the consequent triggers to avoid. Both of which are multi-factorial and individualistic in nature [9]. Additionally, it is not possible for doctors to constantly monitor each patient's health with respect to their environmental triggers.

Several prototype devices and systems incorporating IoT and asthma are currently being developed. Sheth et al (2017) published a research paper outlining their work on putting together 'kHealth' which is a model for the ongoing monitoring of a patients personal, public and population-based health signals. Using this information, it can send alerts regarding the severity of a patient's asthma condition to both the patient and their clinician. In a similar, yet alternative way, Bozkart (2015) and his team at The National Science Foundation (NSF) Nanosystems Engineering Research Centre for Advanced Self-Powered Systems of Integrated Sensors and Technologies (ASSIST) research centre developed a wearable sensor system composed of a wristband and chest patch which together, pull correlating information about an individual's environmental exposure and its impact on their asthma conditions.

kHealth enables the clinician to gather information regarding their patients triggers and put together a prevention plan for the future. Furthermore, it gives patients the chance to take control of their asthma management [10]. kHealth attempts to personalise and contextualise the information it gathers using multi-modal data, to help better understand asthma control. This program is currently undergoing trials at the Dayton Children's hospital in Ohio, with 200 patients. Part of the study used the Foobot sensor to measure indoor air quality. Indoor environments vary significantly depending on how they are being used. Indoor air conditions change while performing certain tasks or activities such as cooking, vacuuming or smoking. The study showed that combinations of these activities had a great effect on asthma in children. Consequently, a continuous monitoring system was set up to observe and understand the indoor air quality of asthma patients. Data was collected from 7 environments over 15 days and was examined to successfully determine that high concentrations of particulate matter, carbon dioxide and volatile organic compounds during cooking and smoking events, do have an impact on children with asthma. Using a control of when no event was taking place, they detected cooking with an error rate of 11%, smoking with an error rate of 1%, obtaining an overall 95.7% percent classification accuracy across all three events.

III. DESIGN OF APPLICATION

Using the prototype software and design tools of Proto.io, a high-fidelity prototype of the proposed asthma action plan app was designed. In order to ensure further consistency, the graphics and terminology used in the National Asthma Council Australia's written asthma action plan were kept and adapted to the smartphone applications digital environment and needs. **Figure 3.1.** is a flowchart outlining the high-level storyboard of events within the app. At the end of each page there is an option to return to the homepage. **Figure 3.2** is a detailed flowchart outlining the steps taken for initial set-up of the application. Once the user reaches the IoT tab, depending on what information they desire, they will be directed to either *AccuWeather* for temperature and humidity or *WeatherZone* for pollen.

A baseline survey of 32 patients was conducted regarding the future use of a PAAP smartphone application. The establishment of patients need and desire for the PAAP smartphone application lead to the end-user ranking of app features, cross-referenced with clinical design requirements already in place by the National Asthma Council Australia, plus the addition of an IoT feature.

This feedback revealed that features such as knowing when to seek urgent medical help, and information regarding call-to-action responses and management of increased severity were of the most importance to users. However, all features were found to be at least somewhat important, with majority of participants indicting that all features were 'important' or 'very important'.

Consequently, all features were incorporated into the PAAP smartphone application, with emphasised important put on the top three features as chosen by participants.

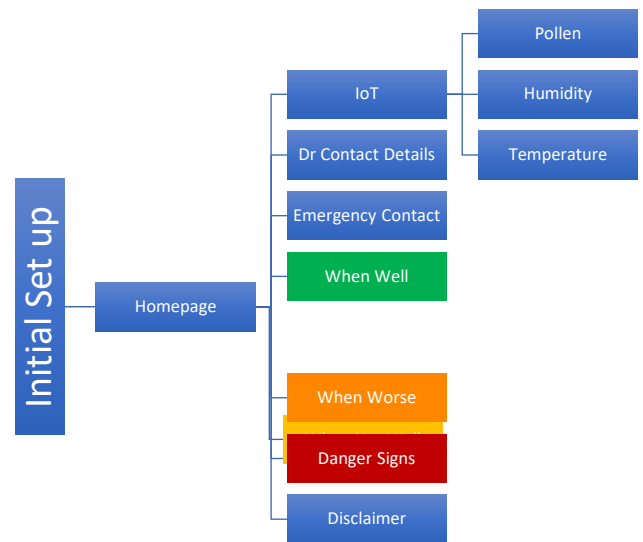


Figure 3.1 High level flowchart of PAAP app

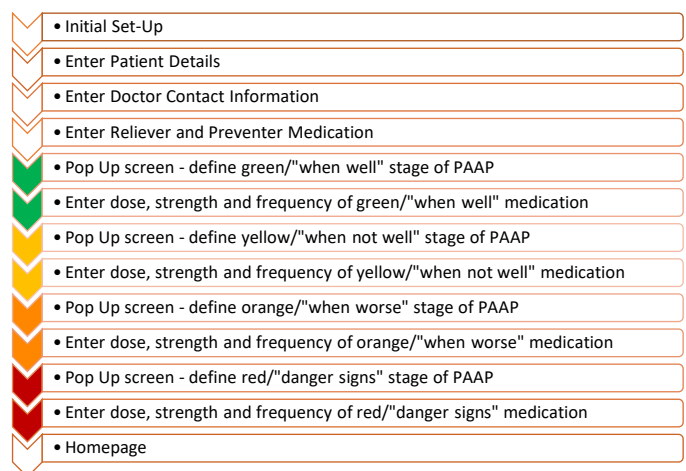


Figure 3.2 Detailed flowchart of initial set up

IV. RESULTS

In addition to assessing the current contextual use of PAAPs, the Asthma Action Plan Survey also addressed the feasibility of an asthma action plan smartphone application in terms of user perspective, requirements and desire for such a platform.

When asked about whether or not participants think an app version of hand-written AAPs would increase their use 87.5% said yes. Additionally, when asked if they would be interested in using said app, 93.8% said yes. Of the 32 responses to the survey, 68.8% do not currently use any type of health or fitness tracking application. The remaining 31.1% that do, list their

ease of use, convenience and monitoring capabilities as the three most common reasons for using these health applications. Top- 5 valued features as ranked my participants were:

- Danger signs - when and how to seek urgent medical help
- Contain information on what action to take in response to exacerbations
- Managing increased severity
- Treating exacerbations
- Contain information for users to recognise exacerbations

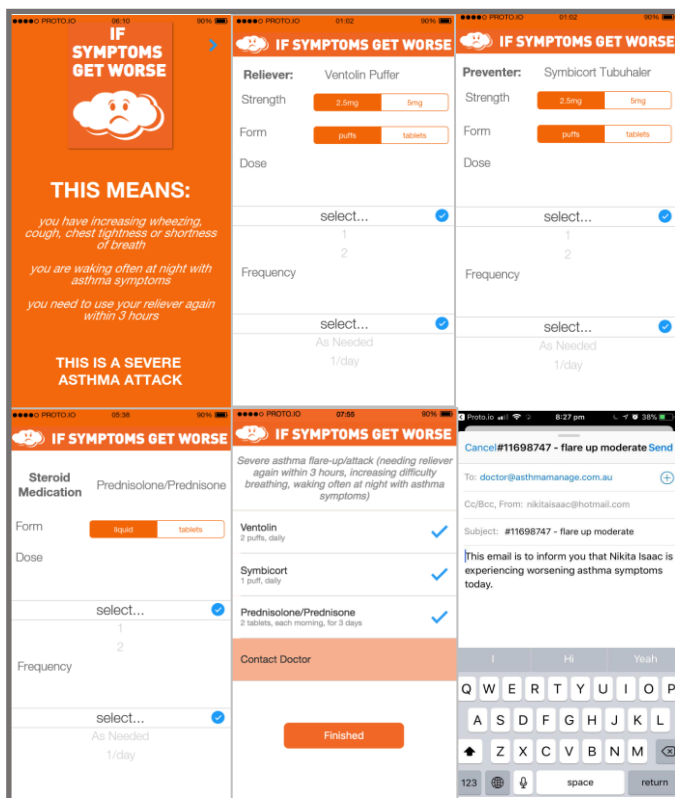


Figure 4.1 Six stages of 'Orange – if symptoms get worse' within application

With all these factors in mind, a high-fidelity prototype was made. The app functions fully as a prototype allowing the user to enter the details of themselves and their doctor, followed by their doctors recommended treatments for each stage of exacerbations. The application explicitly outlines how to identify the severity of a flare up. It has an integrated checklist system making it easy to use and track progress of treatment at the time. Here the 'Orange – If symptoms get worse' level is used to demonstrate how the application will work and how key features from the survey were integrated into the app.

Taking into consideration feedback from the forms and the requirements on the existing written PAAP forms, when a patient is experiencing worsening symptoms it is advised that

they contact their physician to let them know. Accordingly, as shown in **Figure 4.1**, when in the 'Orange – If symptoms get worse' section of this application, rotating the device automatically sends your entered physician an email notification to let them know.

V. DISCUSSION

It is important to note that survey data was collected from online asthma help-groups. Patients therefore, are likely to have a preference for technology as a solution for their asthma. Consequently, a key improvement to be made is to increase the number of patients that complete the forms. The responses of 32 patients alone are not sufficient to make definitive conclusions. This would also even out the potential technology bias. This design of the smartphone application is largely focused on patient's requirements and incorporates some aspects of the carers perspective. However, in order to gain a complete and holistic application, significantly more input from carers and more importantly, doctors will be required.

Another aspect to be considered in further detail for the future is the security of personal health data. Especially with the use of IoT there will be need to ensure the security of this information. One way might be through the use on encryptions that only patient, carer and doctor are aware of.

As previously mentioned, the current PAAP smartphone application is a high-fidelity prototype. As a result, it has present limitations and requires improvements by means of continued development of the application, so it is fully functional. More specifically, this includes improvements regarding user interface, to be more attuned with natural hand movements and gestures made when using smartphone applications. As well as having more embedded IoT connections within the app. Rather than selecting the IoT tab and having it leave the application to a website that displays temperature, pollen or humidity levels.

The application would also benefit from more tracking and time sensitive capabilities, making it particularly beneficial in cases where patients are required to wait a certain period of time before taking next-steps. As they move down their PAAP checklist the timer could automatically start and keep track of this progression. Moreover, the addition of personalised notifications as an appropriate way to remind users of daily preventative medications. is a Finally, with significant development the PAAP smartphone application has the potential to be compatible with existing wearable devices which would allow for a greater accumulation of personal data in order to specifically assist the user in controlling their asthma

In the big picture, PAAPs as a smartphone application offers asthmatics an alternative way to control their asthma by giving them the knowledge, means and opportunity to do so in a technologically appropriate and convenient way.

VI. CONCLUSION

This paper looked into asthma management and ways to increase the use of Personalised Asthma Action Plans as an asthma intervention. The main aim of this research was to determine if the conversion from hand-written asthma action plans to a smartphone application, would improve their potential utilisation by asthmatics. It was hence hypothesised that Asthma action plans are more likely to be used when accessible via a smartphone application due to societies increased convenience and reliance on mobile devices. Based on primary research and an extensive review of related work the crossover point of the IoT, PAAPs and smartphone applications was deemed an appropriate solution to address the underutilisation of PAAPs.

The resulting creation of a high-fidelity prototype where features of importance as determined by patients were incorporated into the application, in order to further enhance user experience and encourage increased use of PAAP smartphone application. In particular, the apps ability to access information regarding temperature, humidity and pollen levels within the environment gives asthmatics more personalised control over their asthma.

Consequently, results from primary research showing that over 80% of patients would use the PAAP smartphone application and believe that the change from a written to digital platform would increase their use of PAAPs as it is more convenient. This shows the original hypothesis to be true, making the PAAP smartphone application a step in the right direction for the future of asthma management and control.

With the technology of today, this integration and digital upgrade is a feasible and appropriate way to improve individual knowledge about asthma management and hence improve the utilisation of asthma action plans, as an asthma intervention.

REFERENCES

- [1] Asthma Australia, 2017
- [2] Australian Institute of Health, 2016
- [3] National Asthma Council Australia, 2016
US Department of Health & Human Services – National heart, lung and blood institute, 2014
- [4] Woolcock Institute of Medical Research, 2017
- [5] Lynch, S., Kearney, S., Hueppe, M., Day, T., Dominey, R. & Dewey, A. 2016, 'Owning my asthma: an enhanced self-management initiative for 14-19 year olds', *npj Primary Care Respiratory Medicine*, vol. 26, no. 16077.
- [6] Engel, T., Rizvanolli, L., Pidgeon, H. & Palter, J. 2017, '413 Incorporation of a Novel Asthma Action Plan to Improve Knowledge and Symptom Management in the Low Acuity Asthmatics Presenting to the Emergency Department', *Annals of Emergency Medicine*, vol. 70, no. 4, pp. S162.
- [7] Joshua S Davis, Maoyun Sun, Alvin T Kho, Kip G Moore, Jody M Sylvia, Scott T Weiss, Quan Lu & Kelan G Tantisira 2017, 'Circulating microRNAs and association with methacholine PC20 in the Childhood Asthma Management Program (CAMP) cohort', *PLoS One*, vol. 12, no. 7, pp. e0180329.
- [8] Huckvale, K., Morrison, C., Ouyang, J., Ghaghda, A. & Car, J. 2015, 'The evolution of mobile apps for asthma: an updated systematic assessment of content and tools', *BMC medicine*, vol. 13, no. 1, pp. 58.
- [9] Jaimini, U. 2017, 'PhD Forum: Multimodal IoT and EMR Based Smart Health Application for Asthma Management in Children', IEEE, pp. 1-2.
- [10] Sheth, A., Jaimini, U., Thirunarayan, K. & Banerjee, T. 2017, 'Augmented personalized health: How smart data with IoTs and AI is about to change healthcare', IEEE, pp. 1-6.

Performance Study for Multimodal Client Identification System using Cardiac and Speech Signals

Hadri Hussain, Sh-Hussain Salleh*, Chee-Ming Ting, Fuad Noman, MM Mohammad
Universiti Teknologi Malaysia,
81310, Skudai, Johor Baharu, Malaysia.
e-mail: hadri_hussain@yahoo.com

Ahmad Zubaidi Abdul Latif
Universiti Sultan Zainal Abidin,
21300, Gong Badak,
Kuala Terengganu,
Malaysia.

Osamah Al-Hamdani
Cisco System,
R&D Wireless Department,
4125, Highlander Pkwy, Richfield, Ohio,
USA.

Abstract— A person's physiological or behavioral characteristic can be used as a biometric and provides automatic identification. There are several advantages of this identification method over the traditional approaches. Overall, biometric techniques can potentially prevent unauthorized access. Unlike the traditional approaches which uses keys, ID, and password, these approaches can be lost, stolen, forged and even forgotten. Biometric systems or pattern recognitions system have been acknowledged by many as a solution to overcome the security problems in this current times. This work looks into the performance of these signals at a frequency samples of 16 kHz. The work was conducted for Client Identification (CID) for 20 clients. The building block for these biometric system is based on MFCC-HMM. The purpose is to evaluate the system based on the performance of training data sets of 30%, 50% and 70%. This work is evaluated using biometric signals of Electrocardiogram (ECG), heart sound (HS) and speech (SP) in order to find the best performance based on the complexity of states and Gaussian. The best CID performance was obtained by SP at 95% for 50% training data at 16 kHz. The worst CID performance was obtained by ECG achieving only 53.21% for 30% data training.

Keywords— *Electrocardiogram, Hidden Markov Model, Mel-Frequency Cepstral Coefficients, Client Identification.*

I. INTRODUCTION

Signals of any source can be analyzed and classified for any application. The process involves the following important steps: recording or capturing the data, pre-processing, classification, decision score, and performance evaluations. The method and techniques used in capturing the signals may vary from signal to signal. This may be due to the interface of the sensor with the desired subject being analyzed. Capturing accurate signals also depends on the quality of the sensor sensitivities. Pre-processing is the initial stage of processing the raw signal. It is used to prepare the signal for another procedure of pre-processing. Generally, it is described as any type of process performed on raw data. A classifier adds specific information to the predicate meaning of the data. There are various types of classifiers. The

classifier has to be trained with the input data, and the purpose of the classifier is to test the classifier using an unknown data set. The complexity of the classifier algorithm plays a role in the performance. The ideal case for a classifier would be to train it using a minimal data set, and it performs at a high accuracy decision score. Decision scoring and performance evaluation is the final phase, in which the data is plotted to make sense of the data classification results. Filtering of the data can be implemented in different phases or stages. Some filtering methods may enhance the resulting performance, whereas, some do the complete opposite. Knowledge of the types and purpose of the filtering methods used can help filter out unwanted desired noise.

In order to use brain print, for brain identification, new approach such as Markov Switching is needed to segment the heart sound. Segmentation involve segmenting the heart signals into four different regions such as the first heart sound, systolic, second heart sound and diastolic. Currently, work is carried out towards understanding the correlations of these four specific areas with the brain activities. Selecting the Region of interest (ROI) of the brain requires huge data processing which deters the possibility of applying brain biometrics. Factor model can be used [1] and [2] to compress the data to the right amount to provide sufficient data features which can lead to the possibility of using these techniques to be applied for brain identification biometric.

Traditional identification methods that utilize password such as iris, fingerprint, speech or face scans [3], [4], [5] are vulnerable to forge input. Moreover, most provide neither reliable nor efficient identification performance. Liveliness checks, is one form of technological computers measures to spoofing artefacts. Traditional biometrics in this core would include finger, face, hand, and iris. The method, however need a high-resolution computer system. Special devices are required when using such methods. As for the palm or finger print recognition the client is required to place his hand or finger on

* Research supported by Project No (RUG Q.J130000.2507.13H47) and (TRGS R.J130000.7809.4L840).

the scanner, his/her eye near a vision system and speak into a microphone for speech recognition. It is rather difficult and complex when applying such technologies to human beings.

This work focuses on the development of a feature extraction and classification for biometric performance [6], [7], [8], [9], [10], [11], [12], [13], and [14]. A biometric evaluation platform is composed of a start/end point, feature extraction, and classification. In this study, a Markov model approach was proposed in order to enhance the performance of the biometric system.

II. METHODOLOGY

Fig. 1 shows the biometric evaluation platform. The experimental results are evaluated based on each of the biometric signals (ECG, HS and SP), percentage split of training data (30%, 50% and 70%), the increments of the client, and complexity of the states and Gaussian classifications. The database consists of 3 biosignals, and the first evaluation of the biometric system is the CID experiments. The performance of HMM varies strongly along with the amount of data being trained.

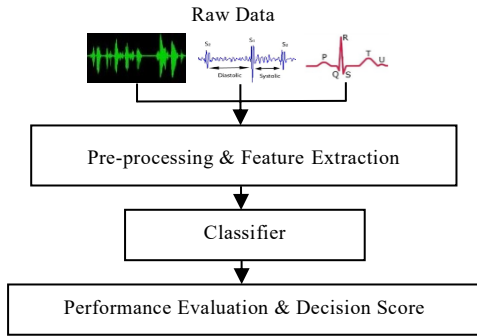


Figure 1: Block diagram of the biometric system.

A. Database

The database used for the purpose of evaluating the proposed multimodal biometric system is collected from 20 clients for ECG and HS signals and digit-speech signals. The database is split into train and test datasets in three different percentage folds, such that the training dataset varies and takes percentages of 30%, 50%, and 70% of the total data, the rest assigned to testing dataset.

The HMM is trained using the training dataset to construct the client's individual models. The utilized continuous distribution HMM (CDHMM) further evaluated on different experiment setups, where different number of Markov states and Gaussian mixtures are used to construct the models with different complexities.

The frame sizes are 20ms with 15ms overlap. Using standard MFCC analysis [15], [16], the feature vector consists of 12 MFCC coefficients which were extracted every 20msec from the

speech. The same feature extraction technique was carried out for the other two biosignals.

B. Feature Extraction

The MFCC coefficient have been calculated by using the Discrete Cosine Transform (DCT) of the logarithmic spectrum scale subsequent to its warping to Mel scale, in a similar manner as the perceptual linear predictive analysis in the case of the sound signals [17] and [18].

In sound processing, the MFCC is a representation of the short-term power spectrum of a sound based on a linear cosine transform of a log power spectrum on a nonlinear Mel scale of frequency. Mel-frequency cepstral coefficients (MFCCs) are coefficients that collectively make up an MFCC [19].

$$\text{Mel}(f) = 2595 \log(1 + f/700) \quad (1)$$

The biometric system is based on MFCC. The MFCC features are robust (especially speech and heart sound) [20]. The signals undergo several steps, which are pre-emphasis, Hamming windowing, Fast Fourier Transform (FFT), triangular band pass filter, and Discrete cosine transform (DCT). 12 MFCC is used to run all the experiments.

C. Classification

The HMM model is an extended version of the Markov chains, wherein each state does not correspond to any of the observable events but is able to connect to a set of probability distributions of a state. The HMM model is identified as a very effective model that is popular in the speech processing domains [21], [22], [23], [24].

The HMM model used in this study is a 5-state left-to-right HMM model which is shown in Fig. 2. Fig. 3 show the flow of the block diagram of training the HMM model.

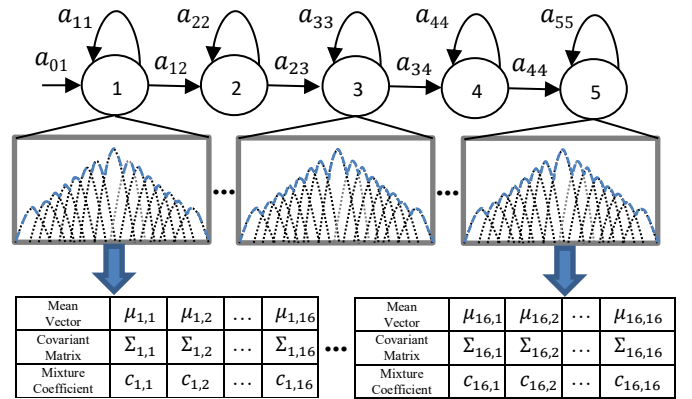


Figure 2: Representation of the left-to-right HMM.

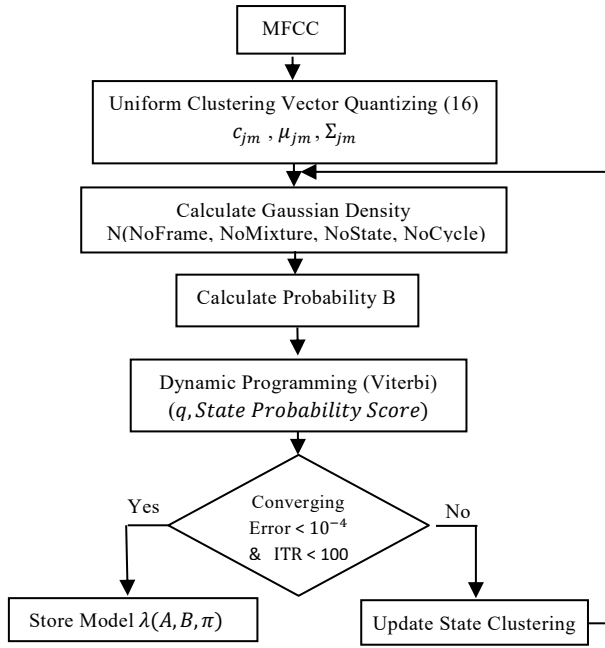


Figure 3: Flow diagram of training the HMM model.

The following parameters characterize the HMM model $\lambda = (A, B, \pi)$:

- π represent the initial state probability vector.
- $A = [a_{ij}]$, $1 \leq i, j \leq N$ is the state transition matrix probability transition.
- $B = [b_j(X)]$, in the case of $1 \leq j \leq N$, where B represents the observation probability functions, which is related to every state j . The HMM observation probability distribution can be modelled by the continuous probability density function (PDF) of predefine Gaussians mixtures, such that,

$$b_j(X) = \sum_{m=1}^M c_{jm} N(x, \mu_{jm}, \Sigma_{jm}) \quad 1 \leq j \leq N \quad (2)$$

where x represents the vector that is modelled, c_{jm} refers to the mixture coefficient of m^{th} mixture component present in the state j , $N(x, \mu_{jm}, \Sigma_{jm})$ is a multivariate Gaussian probability distribution function with mean vector $\mu_{jm} = [\mu_{jmd}]$ and the covariance matrix of $\Sigma_{jm} = [\Sigma_{jmd}]$ in the case of the m^{th} mixture component present in the state j , for $1 \leq d \leq D$, where D is the dimensions of the feature vectors.

III. RESULTS AND DISCUSSION

Table I shows the CID at 16 kHz for 20 clients. The three biometric signals are conducted for 30%, 50%, and 70% training data. Fig. 4 shows a bar diagram illustrating the comparison between the various percentage splits of training data. Based on the bar plot itself, it is observed that an increase in the training data, results in a slight improvement in performance.

TABLE I BEST CID FOR 16 KHZ

Best Client Identification for 16 kHz for 20 clients			
	30 %	50 %	70 %
ECG	53.21	59.41	57.50
HS	87.13	90.04	91.29
SP	93.93	95	92.67

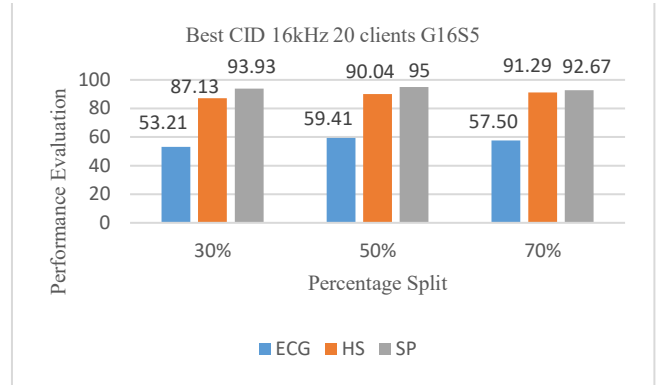


Figure 4: Best CID for 16 kHz for 20 clients.

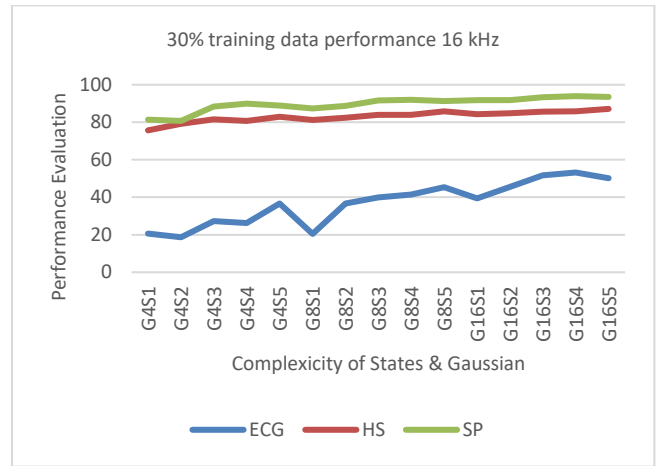


Figure 5: Performance based on 30% training data.

Based on the trends in the bar plots observed in Fig 4, all three percentages split of training data have a similar pattern. All three percentage splits show gradual increments in performance as the training data increased. The best result is obtained from 50% training data which gives an accuracy of 95% for SP.

Fig. 5, Fig. 6, and Fig. 7, the graphs show that for each 30%, 50%, and 70% percentage split of training data, the performance of HS and SP are very close to one another. The performance of both signals increases slowly and seems to be more stable. However, this is not the case with the ECG signal performance, which starts off at a low point for all 3 percentage splits of training data and then drastically increases towards the end. These gradual increments can be seen in Fig. 5, Fig. 6, and Fig. 7.

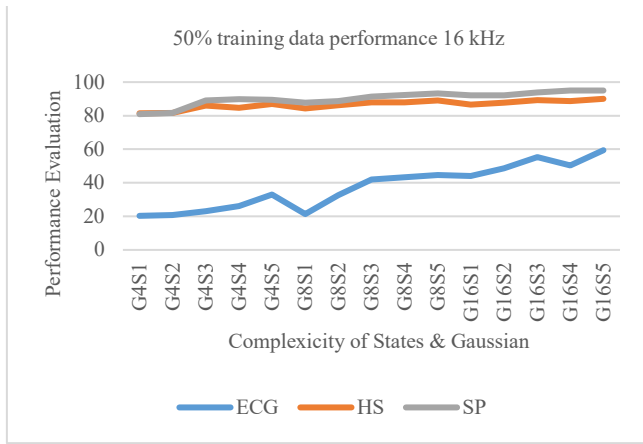


Figure 6: Performance based on 50% data training.

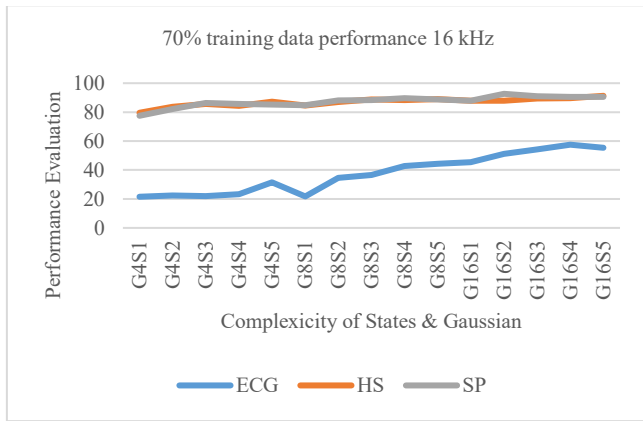


Figure 7: Performance based on 70% data training.

In terms of performance based on the biometric signals, Fig. 8 shows that SP gives the best performance for all percentage splits of training data (30%, 50% and 70%). For all cases of training data, ECG has the lowest performance, followed by HS, and finally, SP with the best performance.

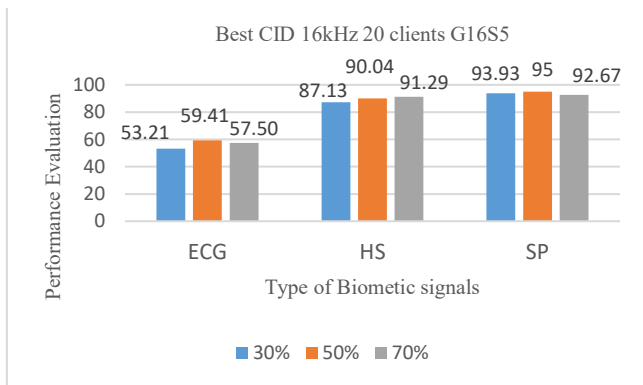


Figure 8: Best CID for 16 kHz for 20 clients.

Fig. 9, Fig. 10, and Fig. 11 shows the performance categorized in terms of ECG, HS, and SP signals. The performance is also evaluated in terms of the complexity of states and Gaussian using 30%, 50% and 70% of training data. Based on the graph,

all three percentage splits of training data show a gradual increase in performance as the complexity of states and Gaussian increase.

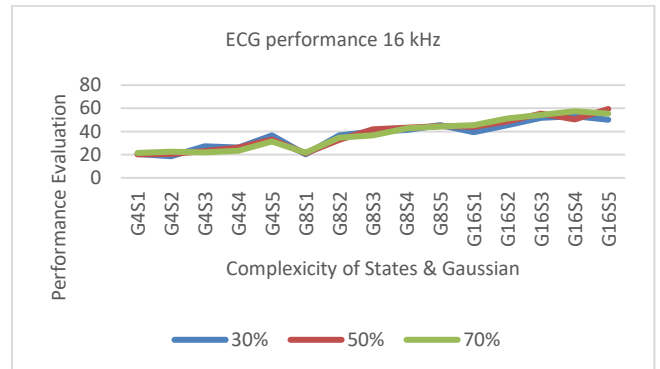


Figure 9: Performance based on ECG biometric signal.

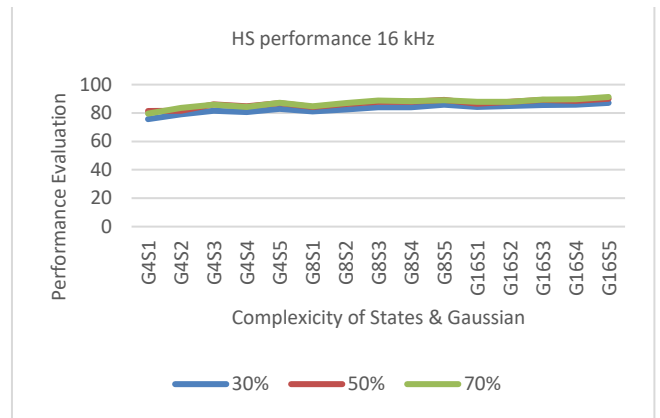


Figure 10: Performance based on HS biometric signal.

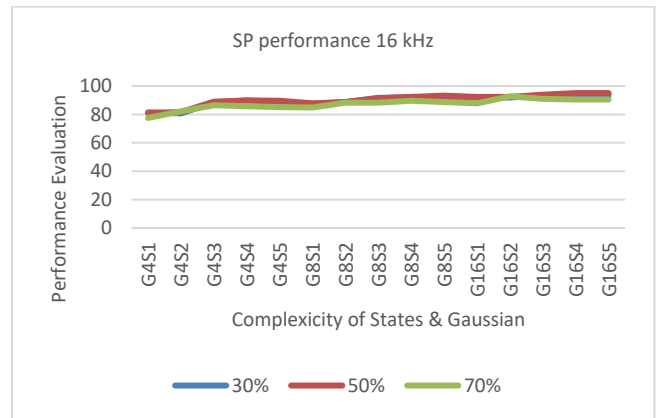


Figure 11: Performance based on SP biometric signal.

The performance of ECG increases gradually as the states and Gaussian reach the maximum complexity of State 5 and Gaussian 16 respectively. ECG shows the most drastic increments for 30%, 50% and 70% of training data in comparison to HS and SP.

IV. CONCLUSION

The best overall performance at 16 kHz for 20 clients obtained an accuracy of 95% for SP using 50% of training data. The worst overall performance was obtained for ECG using 30% training data which had an accuracy of 53.21%. Overall performance shows that there is a significant improvement in performance as the training data increases from 30% to 50% and to 70% at the maximum complexity of states and Gaussian of State 5 and Gaussian 16. In this work, ECG and HS are currently a new topic that has managed to capture the attention of researchers around the world.

There is a need to find a more efficient way for a system to be sure that the live biometric of a user is presented at all times when needed. Biosignals of the ECG and HS can be defined as signals that can be continuously measured and maintained from biological beings. The terms of biosignal can mean bio-electrical signal which refer to both electrical and nonelectrical signal such as HS [25], [26], and [27]. Since this work emphasize on the use of biosignals for authentication, this study shows that the biosignal is unique from one person to another. The study also shows the use of these two suggested biosignal is practical for this application.

V. FUTURE WORK

Currently, more experiments are carried out in order to determine whether the higher states and Gaussian with sampling data of 44 kHz increased the performance. Fusion of this three biosignals will be one of solutions to improve the authentication performance of biometric systems.

The focus of this paper was based on the three biometric characteristics of SP, HS and ECG, where SP is considered as traditional approached because of its commonly used in a biometric system, while the other approaches like HS and ECG are gradually gaining popularity. It was noted previously that the performance varied significantly from client to client with different biometric traits. The future work will discuss the performance of the three-biometric system with more than one source of information combined to form a fusion system that can overcome the limitation of a single biometric system.

In addition, we are also studying the effects of heart activity on brain function. Although, there is much to understand, it appears that the current proposed solutions could show the Region of Interest (ROI) are inter-connected within common function and anatomical domains, revealing distinct pattern that can be used in applications such as brain diagnosis for epilepsy, stroke, and even brain signals biometrics.

ACKNOWLEDGMENT

The authors would like to express their appreciation to the Universiti Teknologi Malaysia, the Ministry of Higher Education of Malaysia (MOHE), Project No (Q.J130000.2507.13H47) and (TRGS R.J130000.7809.4L840) for their support and UTM Zamalah Scholarship.

REFERENCES

- [1] Lam, C., & Yao, Q. (2012). Factor modeling for high-dimensional time series: inference for the number of factors. *The Annals of Statistics*, 40(2), 694-726.
- [2] Ting, C. M., Seghouane, A. K., Salleh, S. H., & Noor, A. M. (2014, June). Estimation of high-dimensional brain connectivity from fMRI data using factor modeling. In *Statistical Signal Processing (SSP), 2014 IEEE Workshop on* (pp. 73-76). IEEE
- [3] Cao, K., Yang, X., Chen, X., Zang, Y., Liang, J., & Tian, J. (2012). A novel ant colony optimization algorithm for large-distorted fingerprint matching. *Pattern Recognition*, 45(1), 151-161.
- [4] Zhang, H., Nasrabadi, N. M., Zhang, Y., & Huang, T. S. (2012). Joint dynamic sparse representation for multi-view face recognition. *Pattern Recognition*, 45(4), 1290-1298.
- [5] Jain, A. K., Ross, A., & Pankanti, S. (2006). Biometrics: a tool for information security. *IEEE transactions on information forensics and security*, 1(2), 125-143.
- [6] Rowe, R. K., Nixon, K., and Corcoran, S. (2005). *Multispectral fingerprint biometrics*. Paper presented at the Proceedings of the Sixth Annual IEEE SMC Information Assurance Workshop, 14-20
- [7] Ross, A., and Jain, A. K. (2004). *Multimodal biometrics: An overview*. Paper presented at the Signal Processing Conference, 2004 12th European, 1221-1224
- [8] Ribaric, S., and Fratric, I. (2006). *Experimental evaluation of matching score normalization techniques on different multimodal biometric systems*. Paper presented at the MELECON 2006-2006 IEEE Mediterranean Electrotechnical Conference, 498-501.
- [9] M. U., Tariq, A., and Khan, S. A. (2011). *Retinal recognition: Personal identification using blood vessels*. Paper presented at the Internet Technology and Secured Transactions (ICITST), 2011 International Conference for, 180-184.
- [10] Phua, K., Chen, J., Dat, T. H., and Shue, L. (2008). Heart sound as a biometric. *Pattern Recognition*, 41(3), 906-919
- [11] Ting, C.-M., and Salleh, S.-H. (2010). *ECG-based personal identification using extended Kalman filter*. Paper presented at the Information Sciences Signal Processing and their Applications (ISSPA), 2010 10th International Conference on, 774-777.
- [12] Zhao, Z., and Wang, J. (2011, 9-11 Sept. 2011). *Heart sound identification system*. Paper presented at the Electronics, Communications and Control (ICECC), 2011 International Conference on, 2079-2082.
- [13] Tanprasert, C., Wutiwivatchai, C., and Sae-Tang, S. (1999). *Text-dependent speaker identification using the neural network on distinctive Thai tone marks*. Paper presented at the Neural Networks, 1999. IJCNN'99. International Joint Conference on, 2950-2953.
- [14] Al-Hamdani, O., Chekima, A., Dargham, J., Salleh, S.-H., Noman, F., Hussain, H., et al. (2013). Multimodal biometrics based on identification and verification system. *Journal of Biometrics & Biostatistics*, 2013.
- [15] Chee-Ming, T. and S.H.Salleh, 2007. Text-independent Speaker Identification using Gaussian mixture model, on. In international Conference on Intelligent and Advanced Systems, ICIAS 2007. Kula Lumpur, 2007. IEEE.
- [16] Chee-Ming, T., Salleh, S.-H. and Ariff, A.K., 2009. Malay continuous speech recognition using fast HMM match algorithm. In 4th IEEE Conference on Industrial Electronics and Applications, ICIEA., 2009.
- [17] Hang Wu, Chong Kim, and Keunsung Bae, 2010, Hidden Markov Model with Heart Sound Signals for Identification of Heart Diseases, Proceeding of 20th International Congress on Acoustics, ICA 2010.
- [18] Muda, L., Begam, M., & Elamvazuthi, I. (2010). Voice Recognition Algorithms using Mel Frequency Cepstral Coefficient (MFCC) and Dynamic Time Warping (DTW) Techniques, 2(3), 138-143
- [19] Pramanik, A., & Raha, R. (2013). Speaker Independent Word Recognition Using Cepstral Distance Measurement. In A. Abraham & M. S. Thampi (Eds.), *Intelligent Informatics: Proceedings of the International Symposium on Intelligent Informatics ISI'12 Held at August 4-5 2012, Chennai, India* (pp. 225-235)
- [20] Hang Wu, Chong Kim, and Keunsung Bae, 2010, Hidden Markov Model with Heart Sound Signals for Identification of Heart Diseases, Proceeding of 20th International Congress on Acoustics, ICA 2010.

- [21] Rahman, M. M. B. I. I. (2010). *Performance evaluation of MLPC and MFCC for HMM-based noisy speech recognition*. Paper presented at the 13th International Conference Proceedings on Computer and Information Technology (ICCIT 2010), Dhaka, Bangladesh, 273--276.
- [22] Dey, N. S., Mohanty, R., and Chugh, K. (2012). *Speech and Speaker Recognition System Using Artificial Neural Networks and Hidden Markov Model*. Paper presented at the Communication Systems and Network Technologies (CSNT), 2012 International Conference on, 311-315.
- [23] Biswas, S., Ahmad, S., and Mollad, M. K. I. (2007). *Speaker identification using Cepstral based features and discrete Hidden Markov Model*. Paper presented at the 2007 International Conference on Information and Communication Technology, 303-306.
- [24] Nakagawa, S., and Markov, K. P. (1997). *Speaker verification using frame and utterance level likelihood normalization*. Paper presented at the Acoustics, Speech, and Signal Processing, 1997. ICASSP-97., 1997 IEEE International Conference on, 1087-10
- [25] Revett, K., Deravi, F., and Sirlantzis, K. (2010). Biosignals for user authentication towards cognitive biometrics? Paper presented at the Emerging Security Technologies (EST), 2010 International Conference on, 71-76
- [26] Brooks, D. J., Hunter, P. J., Smaill, B. H., and Titchener, M. R. (2010). BioSignalML-a meta-model for biosignals. Paper presented at the Conference proceedings: Annual International Conference of the IEEE Engineering in Medicine and Biology Society. IEEE Engineering in Medicine and Biology Society. Annual Conference, 5670-5673
- [27] Spasic, S. (2007). Spectral and fractal analysis of biosignals and coloured noise. Paper presented at the 2007 5th International Symposium on Intelligent Systems and Informatics.

Monitoring and controlling two applications of a magnetic screw in the gastrointestinal tract

Hidetoshi Ohta

Department of Gastroenterology
Sapporo Orthopaedics and Cardiovascular Hospital
Sapporo, Japan

Abstract— Several magnetic devices have been introduced into the gastroenterology. We have developed a magnetic navigation system for controlling a capsule endoscopy in the gastrointestinal tract. We have applied this system to intragastric balloon therapy and the preparation of capsule colonoscopy. Though both procedures are well-known as non-invasive modalities, there are some drawbacks such as an unstable efficacy of the body weight loss for long term or the poor acceptability due to onerous amount of preparation.

In this study, we clarified that the volume of the intragastric balloon could be changed by using a handheld magnet to operate the magnetic screw. Also, the magnetic cleansing device could reduce the amount of preparation to an acceptable dose. To date, there are no real-time monitoring systems for frequently checking the balloon volume or cleansing effects during preparation. We have also developed a simple method for estimating the volume of the balloon and flow from the cleansing device in real time. It measured shifts in the resonant frequencies of the coils on the devices and the accuracy of this method was within 20%. The monitoring data provided useful feedback for controlling the two devices.

Keywords—*Extracorporeal control, Real-time monitoring, Estimation of volume and flow, Severe acidic condition*

I. INTRODUCTION

Obesity is worldwide epidemic disease. These days, bariatric surgery is recommended to patients who cannot reduce or control their weight through lifestyle changes such as healthy eating habits and/or physical exercise [1]. Endoscopic bariatric treatment (EBT) is believed to be a less invasive modality than bariatric surgery, though the long term effectiveness of EBT seems to be inferior to that of bariatric surgery [2].

The intragastric balloon (IGB) is improving rapidly in terms of safety, the rate of adverse events and the method of placement [3-5]. To be able to continually reduce weight over several years, we need to develop a simple balloon structure which is not corroded by the severe acidic conditions in the stomach and add a volume control function so that the volume can be changed to suit the patient's obesity level and also to control the amount of the food intake. Currently there are no IGBs which can be controlled under real time monitoring. As the severe acidic conditions in the stomach are capable of degrading most materials, a thick protective coating is inevitable to prevent the circuits from corroding. Only several

materials such as gold, platinum, glass and some chemical compounds (polyethylene, polyvinylidene chloride, though hydrogen chloride gas can pass through them easily.) can withstand the harsh gastric conditions for long time. For implants and other devices to be able to keep working in stomach for a long time, they need to be made from materials that are unreactive and safe for human use so that they do not generate any toxic products. From the point of chemical stability, gold and platinum are suitable materials for using in the GI tract. Circuits made from them or used as a coating may make them a good option for long-term use in such a challenging environment.

On the other hand, to avoid missing colorectal cancers or polyps which are known to be precursors of cancer, there is a high demand for good preparation before colonoscopies. The easiest way to guarantee that the colon is cleanse properly is to increase the volume of preparation liquid, however the volume is already over the acceptable range for older subjects especially the volume for a colon capsule endoscopy. To date, various kinds of preparation solution have been developed but there have been no proposals about mechanical cleansing devices for cleansing the colon. Such a device in the digestive tract has similar issues to those mentioned earlier. Not only in stomach but also in other digestive organs, severe chemical and mechanical conditions such as the detergent and alkaline conditions which are generated by bile acid. The polycarbonate outer sheath of a capsule endoscope is able to protect the electronic circuits against the severe chemical and mechanical conditions for the short-term duration of the screening. Every implant or device in the digestive tract has to be protected in a similar way to a capsule endoscope so that they continue working and do not cause any problems whilst they are there.

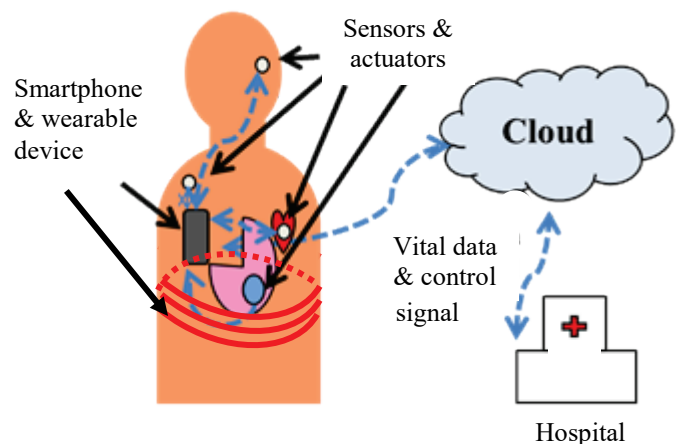


Fig.1 System architecture for sensing and interventions

We are developing a volume controllable intragastric balloon for bariatric therapy and a cleansing device for improving colonic preparation. They are both fitted with a magnetic screw which is controlled extracorporeally with a magnetic paddle. During the designing phase we took into consideration the necessary mechanical and chemical protection they would need in the GI tract.

When we design sensors for monitoring the conditions in the stomach we are faced with the same problems, in particular, it is not possible to stop them coming into contact with gastric juice. Sensors exposed to gastric juice have to keep their characteristics for the duration of time they are in the stomach. In the case of an IGB, the sensors would be expected to monitor the balloon volume, food intake and the emptying speed (peristaltic activity) in stomach in real-time for six months or more. In the stomach, moreover, the sensors for monitoring should keep their structural and electrical characteristics against mechanical (due to peristalsis), thermal and chemical attacks which are generated by various ingredients, secreted acid and enzymes. We have developed an IGB prototype with these inevitable monitoring functions. It is equipped with simple volumetric sensors that are capable of working safely for over 6 months and a cleansing device with a simple pump. The monitoring data from these sensors is available not only for controlling the magnetic screw in both devices. Also it could be sent to extracorporeal wearable devices and be uploaded to the medical cloud with the technology that is already available today [6], including IoT (Fig.1). In this paper we present two ingestible devices for the GI tract which can be monitored and controlled remotely.

II. MAGNETIC POWER TRANSFER TO THE SCREW IN THE GI TRACT

The two applications of the magnetic screw are shown in Fig.2 (IGB) and Fig.3 (colonic cleansing device) respectively. Both of these intra body devices were placed inside a gelatin capsule before the test and they were transformed to working structures at their destination (stomach or cecum). The IGB was composed of a gelatin capsule, a waterproof poly-ethylene bag, a magnetic screw pump and stop valves to prevent water from entering or leaving the balloon (Fig.2). The balloon capsule was placed in a phantom and hot water was then

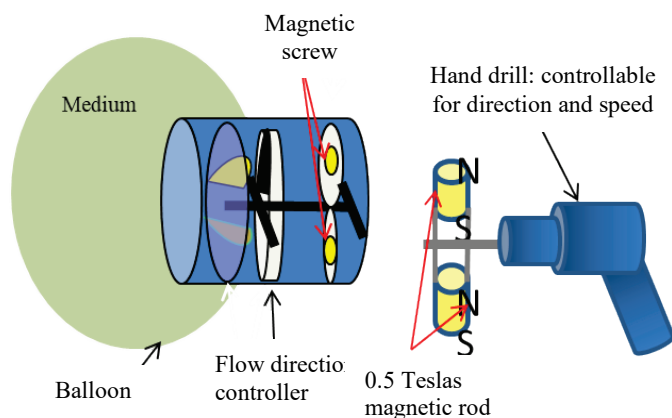


Fig.2 Volume controllable intragastric bariatric balloon

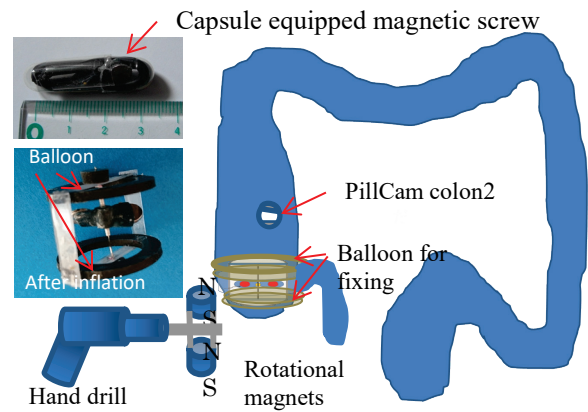


Fig. 3 Equipment for colonic cleansing

poured into it. An extracorporeal smart magnetic paddle [7] (Fig.4) was used to navigate and confirm the position of the balloon. Two magnetic sensors in the magnetic smart paddle detected the minute magnetic field generated by the magnetic screw in the stomach of the phantom. The rotator was then used to fill the balloon with water by operating the screw pump. After that it was used to change the volume of the balloon a number of times. At the end of the simulation in the phantom, the balloon was emptied to confirm that it could be excreted easily.

A capsule containing the colonic cleansing device (balloon + coil+ cylinder) was placed in the phantom and navigated to the cecum. When the smart magnetic paddle detected the colonic cleansing capsule in the cecum, the smart paddle switched on the carbon dioxide gas generation which was produced from a chemical reaction between sodium hydrogen carbonate and citrate. Carbon dioxide inflated the balloon for fixing the cleansing unit to the cecal wall. The rotating screw generated an alternating current in the coil wound over the cylinder. This current was proportional to the flow speed.

A. How to measure the volume of the IGB or flow speed from colon cleansing machine

The coils over the balloon were used as volume sensors in our system. The inductance is dependent on the length, cross section, arrangement of the coils and the magnetic permeability of the medium in the coil. Compression of the balloon changed the cross section of the coils and led to shifts in their resonant

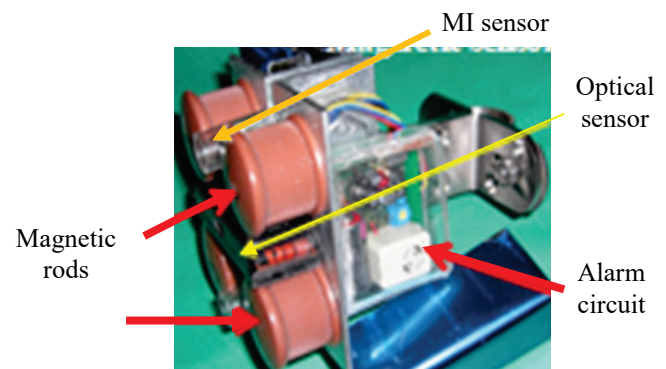


Fig.4 Smart magnetic paddle

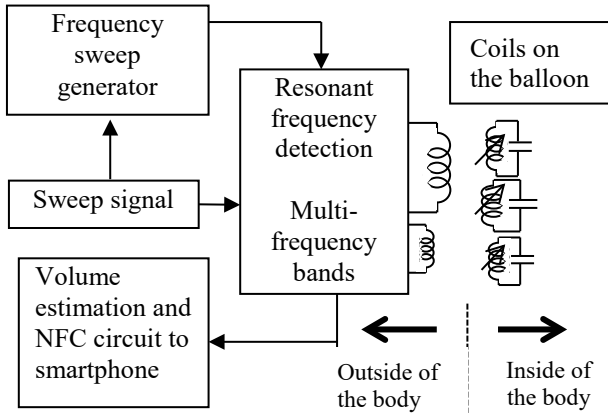


Fig. 5 Block diagram for volume estimation

frequencies. To improve the precision of the volume estimation, we arranged three different length coils over the balloon in the IGB. Also, these coils served us to monitor the simulation of peristalsis and food intake. In exactly the same way as the IGB, the coils over the balloons for fixing the cleansing unit at the cecum worked for measuring the flow speed of the liquid from it. The fundamental structure is shown in Fig.5 as a block diagram.

Generally speaking, the interaction between the two coils can be described using the simplified circuit structure in Fig.6 [8]. Tx coil with a radius of r_x generates the magnetic field H_{xy} along the central axis at a distance of d_{xy} . (according to the Biot-Savart law)

$$H_{xy} = r_x^2 I_x / 2(r_x^2 + d_{xy}^2)^{3/2} \quad (1)$$

The coupling coefficient k_{xy} has a value between 0 and 1, which can be expressed as follows:

$$k_{xy} = M_{xy} / (L_x L_y)^{1/2} \quad (2)$$

Mutual inductance is derived from the flux in the Rx coil as follows:

$$M_{xy} = \mu_0 H_{xy} \pi r_y^2 \cos \theta / I_x \quad (3)$$

Combining (1),(2), and (3) creates a well-known expression in geometric terms (coil radii r_x and r_y , horizontal displacement factor d_{xy} and angle θ) for the coupling coefficient:

$$k_{xy} = \mu_0 \pi r_x^2 r_y^2 \cos \theta / 2(L_x L_y)^{1/2} (r_x^2 + d_{xy}^2)^{3/2} \quad (4)$$

where μ_0 is the permeability of the medium, and r_x and r_y are

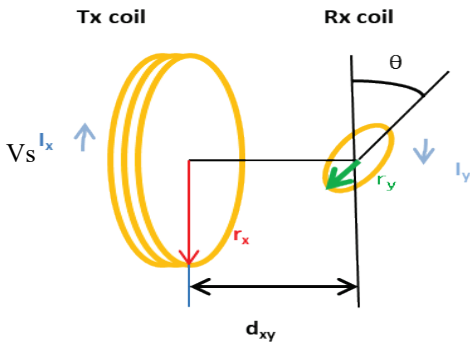


Fig.6 Monitoring the volume by measuring shifts in the resonant frequencies of the coils

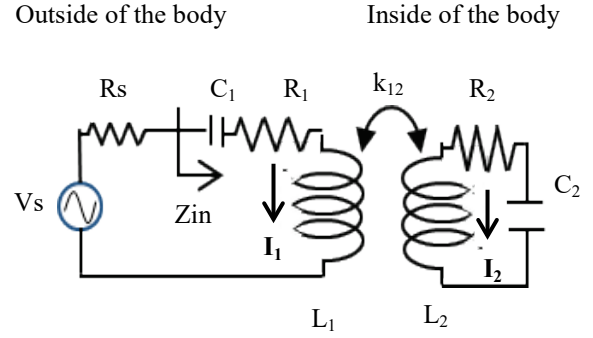


Fig.7 Simplified equivalent circuits

the coil radii. L_1 and L_2 are the inductance values of the coils. d_{xy} is the distance between the coils.

This equation indicates that the coupling coefficient could be controlled using the vertical displacement factor d_{xy} and the angle θ . If the radius of the T_x coil satisfies $r_x \gg d_{xy}$, k_{xy} is dependent on the radius of the R_x coil and misalignment of θ .

III. IMPEDANCE AND RESONANT FREQUENCY

Fig.7 shows the equivalent circuit of the four-coil MR-WPT system. At the resonance condition $j(\omega L_x - 1/\omega C_x)$ is zero, and I assume that $R_s + R_1 = R_s$, and R_2 is small. The currents in the power and load coil are indicated by (5).

$$I_2 = \frac{J \omega^3 k_{12} L_2 (L_1)^{1/2} V_s}{(R_s R_2 + \omega^2 k_{12}^2 L_1 L_2) (R_1 R_3)} \quad (5)$$

This formula can also be expressed alternatively with Q factors,

$$Q_1 = \omega L_1 / R_1, \quad Q_2 = \omega L_2 / R_2, \quad (6)$$

where Q_1 and Q_2 are the Q-factors of the resonators.

$$I_2 = \frac{k_{12} Q_2 (Q_1)^{1/2} V_s}{(1 + k_{12}^2 Q_1 Q_2) / ((R_s + R_1) (R_2))^{1/2}} \quad (7)$$

If the impedance matching condition $k_{12}^2 Q_1 = Q_2$ is satisfied and if the following variables are replaced with X to simplify the formula, (6) has its optimal value expressed as

$$I_{Lopt} = X / (1 + 2X) V_s / ((R_s + R_1) (R_2))^{1/2} \quad (7)^*$$

$$X = k_{12} \cdot Q_2 (Q_1)^{1/2} \quad (8)$$

The input impedance can be expressed by the following equation:

$$Z_{in} = V_1 / I_1 = k_{12} (L_1 L_2)^{1/2} / (Q_2 (1 - 1/\gamma^2)) \quad (9)$$

$$\gamma = \omega / \omega_0 \quad (9)^*$$

We can know that the input impedance changes around the resonant frequency but the resonant frequency is dependent on the coil inductance. As the inductance L_2 changed easily and intensively due to compression of the IGB, the resonant frequency and input impedance could be good markers for monitoring the information of food intake.

III EXPERIMENTAL RESULTS

A. Mechanical characteristics of the magnetic screw in the phantom

The controllability and mechanical ability of the IGB in the phantom are shown in Fig.8.

- 1) The magnetic paddle was used to identify the position of the screw pump (Fig.4). Two magnetic sensors (MI sensor: Aichi Engineering Nagoya, Japan) were equipped at the magnetic field free position on the smart magnetic paddle to cancel the strong magnetic field generated by the four magnetic rods and it could provide the precise 2-dimensional localization of the magnetic screw. The precision of the screw localization was within 1cm. This paddle could also navigate the IGB in a more optimal direction and position in the stomach of the phantom.
- 2) The leakage of water from the balloon made from polyethylene (thickness 0.08mm) was less than 1% over a period of 6 months. The balloon was ruptured only by pressure over 5 atm.
- 3) The prototype IGB was small when deflated, so it should not have any problems being excreted from the gut. (Fig.8)
- 4) The magnetic screw could be driven up to 15cm from the surface of the phantom effectively. Over 20cm the screw rotation was rotated slower than extracorporeal magnetic rotator because of asynchronous rotation due to slipping (Fig.8).
- 5) The average speed of inflation was 3ml/sec and deflation was 2ml/sec. (Fig.8)

B. Evaluation of the precision of volume estimation

The accuracy of the volume estimation of the IGB was examined in three volunteers by two non-invasive modalities; the newly developed resonant frequency method and ultrasonography. The results are shown in Fig.9. The margins of error for estimating the volume of the balloon by resonant frequency and ultrasonography were within 5% and 17% respectively between 300ml and 500ml (Fig.9).

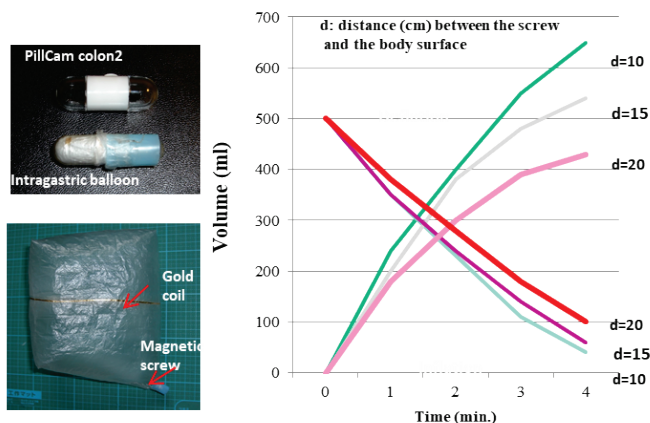


Fig.8 Inflation speed and distance

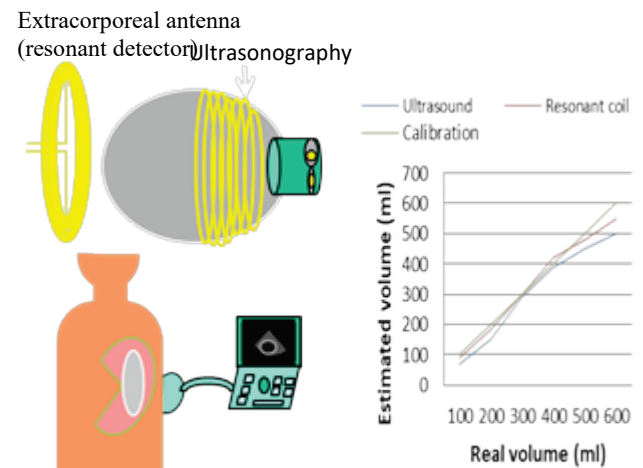


Fig. 9 Accuracy of volume estimation

IV. DISCUSSION

The various robots are being developed for working inside the body [9-12]. The motor driven robot (so called radio-control robot) is a popular approach to realize such a machine in the body. Though it is easier to realize outside of the body, it is much harder inside the body because there are some high barriers to overcome, such as long battery life, safety of the materials and mechanical stability. On the other hand, there are some simple alternative methods which do not include risky materials or energy sources, though they are not so efficient or sophisticated. One of the alternatives is the magnetic approach. Several researchers [13] have proposed equipping a capsule endoscope with a magnetic fin or disc driven by the rotational magnetic field generated by giant electric coil similar to a MRI. Keller [14] proposed a capsule endoscope that included magnetic discs and Otsuka [15] developed the Mermaid a capsule endoscope with a magnetic fin. Though their systems did not include risky materials for human such as lithium batteries, they are neither portable nor cheap. We also equipped a capsule endoscope with magnetic discs but it was navigated by solid magnetic rods. In this study, we used a hand drill and two magnetic rods for generating the rotational magnetic field and a pair of magnetic discs for the screw. This method is more portable, cheaper and simpler than reported magnetic devices. We chose a hand drill (Ryobi BD122, Tokyo Japan) which allowed us to change the rotational speed and direction easily.

Unlike the working time for a capsule endoscope (8-10 hours), an IGB has to remain in the stomach for half of a year or more. This can cause parts of the device to corrode and become unsafe. Most metals including neodymium dissolve in a strong acid such as gastric juice. There have been cases of an infant ingesting a button battery or a magnet so it is well-known that they can cause perforations of the GI tract. Therefore if we want to use such materials in the digestive tract, they need to be coated with a tough protective material similar to the polycarbonate outer sheath of a capsule endoscope, but much tougher because the polycarbonate

sheath can only protect the electronic circuits for several days. Otherwise, we have to choose materials that are not affected by strong acids.

Even though gold is expensive, it is stable and unaffected by strong acids and it has good electric conductivity. That is why gold is used in electronic circuits. Many medical implants such as pacemakers use platinum or gold because they are stable and have low resistance.

IGBs are very useful devices for treating obese people. However a drawback is that they lack a monitoring system. We hit on the idea of building a sensor composed of gold. Our aim is to increase weight loss and over a longer period of time by introducing a monitoring system into our IGB therapy, so that it can match the weight loss achieved by bariatric surgery.

Also, we want to reduce the onerous amount of preparation that patients have to drink for capsule colonoscopy. Clinical trials [16], [17] have indicated that cleanliness is dependent upon the amount of the preparation is important for reducing the missing rate. The results for my cleansing device in the phantom indicated that it could be used to significantly reduce the amount of preparation and keep visibility (no data shown). The cleansing device works like a washing machine. This device could be improved by equipping it with sensors for evaluating the cleanliness of the colon and the flow speed of the preparation liquid which is related to the transition time for the capsule endoscope in the colon. The flow speed of a colon capsule endoscope is crucial for improving the detection rate for lesions. As this cleansing system only needs to work for 2 to 3 hours in the colon and would be excreted from the anus after examination, the requirements for the materials are quite different from those for the IGB. Therefore, it might be possible to power the device using button batteries such as those used in current capsule endoscopes. They could also be used to power tiny body sensors. However, there would be complicating if batteries are retained in the GI tract, so I am thinking of using simple sensors composed of only passive elements.

The prototypes are still in the laboratory stage. The interface between the wearable device and the cloud is still under investigation. There are also several technical problems to overcome such as intragastric infections, perforations caused by over-inflation and reduction in the screw's power due to a weakening of the magnetic force in large patients with thicker layers of adipose tissue over 20cm.

Limiting the amount of exposure to magnetic fields is an important issue. ICNIRP guidelines [18] recommend a limit of 2W/Kg for the trunk of the human body in the frequency range of 100 kHz to 300 GHz. Our experiments were within these criteria.

CONCLUSION

Non-invasive modalities for diagnosing and treating epidemic diseases such as obesity and colon cancer are rapidly developing, due to the availability of various minute sensors and networking for medical information. An advantage of our intra body magnetic screw devices is that they do not require

any complicated materials, only simple materials such as gold, polyethylene, a neodymium magnet and a silicon rubber balloon. The tests in the phantom went very well and indicated that the two magnetic screw devices could work for a long time in the GI tract. We are planning to refine these devices before carrying out clinical trials.

REFERENCES

- [1] A. Skinner, JA Skelton "prevalence and trends in obesity and severe obesity among children in the United States 1999-2012" JAMA Pediatr 2014; pp.561-566
- [2] J. Vidal, R. Corcelles, A. Jimenez, L. Flores, AM. Lacy "Metabolic and Bariatric Surgery for Obesity" Gastroenterology vol.152(7), pp.1780-90, 2017
- [3] BK. Abu. Dayyer, SA. Edmundowicz, CC. Thompson et al. ASGE BARIATRIC TASK FORCE "Endoscopic bariatric therapies" Gastrointest Endosc. Vol 81, No5, pp.1073-86, 2015
- [4] S. Sullivan, SA. Edmundowicz, CC. Thompson, "Endoscopic Bariatric and Metabolic Therapies: New and Emerging Technology" Gastroenterology vol.152(7), pp.1791-9801, 2017
- [5] H. Ohta, S. Katsuki, "A New Bariatric Balloon Capsule Therapy without a Filling Tube Indicates a Reduction in Visceral Fat and Insulin Resistance", Gastroenterology, Supplement vol1, pp. 241, 2017
- [6] K. Tweed "Working on Smart contact Lens to Monitor Diabetes" IEEE Spectrum : Working-on-smart-contact-lens-to-monitor-diabetes Jan.17, 2014
- [7] H. Ohta, "Innovations leading capsule endoscopy into the new frontier: screening and therapy at home" IEICE Trans. COMMUN vol.E98-B NO.4, pp.526-534, 2015
- [8] H. Ohta, "Using Magnetic Resonance Wireless Power Transfer to Operate a Scalpel on a Prototype of a Robotic Therapeutic Endoscope," IEEE ISMICT, Proceeding Tec. Session 5, Worcester, 2016
- [9] S. Yim, and M. Sitti, "Design and rolling locomotion of a magnetically actuated and compliant capsule endoscopy robot," In Proc. IEEE Int. Conf. Robot. Autom, pp. 4810-4815, May 2011.
- [10] G. Ciuti, P. Valdastrì, A. Menciasì, P. Dario, "Robotic magnetic steering and locomotion of capsule endoscope for diagnostic and surgical endoluminal procedures," *Robotica*, vol. 28, no. 2, pp. 199-207, Oct. 2009.
- [11] I. Iris De Falco I, G. Tortora, P. Dario, et al., "A integrated system for wireless capsule endoscopy in a liquid-distended stomach," IEEE Trans. Biomed. Eng., vol.61, pp.794-804, March 2014
- [12] P. Valdastrì, C. Quaglia, E. Susilo, et al., "Wireless therapeutic endoscopic capsule: in vivo experiment," *Endoscopy*, vol.40, pp.979-82, 2008
- [13] Jo.F. Rey, H. Ogata, N. Hosoe, et al., "Feasibility of stomach exploration with a guided capsule endoscope," *Endoscopy*, vol.42, pp.541-5, 2010
- [14] J. Keller, C. Fibble, F. Volke, et al., "Remote magnetic control of a wireless capsule endoscope in the esophagus is safe and feasible: results of a randomized, clinical trial in healthy volunteers," *Gastrointest Endosc*, vol.72, pp.941-6, 2010
- [15] E. Morita, N. Ohtsuka, Y. Shindo, et al., "In vivo trial a driving system for a self-propelling capsule endoscope using a magnetic field," *Gastrointest Endosc*, vol.72, no.4, pp.836-40, 2010
- [16] C. Spada, SF. Pasha, SA. Gross et al. "Accuracy of First and Second-Generation Colon Capsules in Endoscopic Detection of Colorectal Polyps," *Clin Gastroenterol Hepatol*, pp.1533-1543, Nov, 2016
- [17] DK. Rex, SN Adler, J. Aisenberg et al. "Accuracy of capsule colonoscopy in detecting colorectal polyps in a screening population," *Gastroenterology*, pp.948-957 May 2015
- [18] ICNIRP GUIDELINES Health PHYSICS 99(6):818-836; 2010

Applying Multi-channel Flooding to Vital Data Monitoring of a Large Number of Exercisers: Mobility and Link Modeling and Performance Evaluation

Shintaro Yamaguchi[†], Atushi Niino[†], Hirofumi Ogura^{††}, Hiroyuki Yomo[†],
 Ryusuke Miyamoto^{†††}, Shinsuke Hara^{††}, and Takashi Kawabata^{††††}
[†]Graduate School of Science and Engineering, Kansai University
^{††}Graduate School of Engineering, Osaka City University
^{†††}School of Science and Technology, Meiji University
^{††††}Graduate School of Health and Well-being, Kansai University

Abstract—In recent years, there have been significant research effort on vital data monitoring of people playing sports, which provides us with the information on their physical conditions and training effect. In this paper, we assume a system configuration in which sensor nodes attached to exercisers with their back-waist positions sense vital data and send them to a sink node. In order to evaluate data collection performance by computer simulations, we first conduct experiments to collect position data of people playing football and footrace. Furthermore, we measure communication performance of sensor nodes with IEEE802.15.4g with experiments. Based on these experimental data, we construct mobility model and radio link model, which are applied to computer simulations investigating the performance of data collection employing a location-based flooding with multi-channel setting. Based on the obtained simulation results, we analyze the trade-off between the alleviation of congestion level and reduction of connectivity, which are observed when varying the number of allocated channels in the location-based flooding.

I. INTRODUCTION

In recent years, there have been significant research effort on vital data monitoring of people playing sports, which provides us with the information on their physical conditions and training effect [1]. The information can be used not only for giving advices on training menu, but also for checking the risk of injuries and diseases during exercises.

In order to realize such vital data monitoring, it is essential to collect vital data in real-time, simultaneously, periodically, and reliably. To this end, WSN (Wireless Sensor Network) can be employed, which is composed of sensor nodes that sense the vital data of exercisers and a data collection node (sink) that aggregates the sensed data. In this work, we focus on WSN following the communication standard of IEEE802.15.4g operating with 920MHz band. We assume that sensor nodes are attached to exercisers with their back-waist positions. In this case, it is expected that the communication range of each sensor node has directivity because of

shadowing of human body. Furthermore, we assume a highly mobile environment where exercisers' positions and orientations change frequently. These directivity and mobility can greatly influence data transmission characteristics, therefore, it is necessary to model the mobility of exercisers as well as the directivity of communication range.

In this work, we first construct a node mobility model under exercises of football game and footrace at a sports-day event of school, and a radio link model of IEEE802.15.4g with nodes attached to exercisers' back-waist positions based on our experimental results. For constructing mobility model, we employ an object-tracking technique that is applied to video data of actual football game and footrace. The link model is created based on experimental data of received power measured for different distance and directivity between IEEE 802.15.4g nodes. Then, we evaluate the vital data collection characteristics by computer simulations by using those models. We focus on a location-based flooding [2] as a data transmission method, where appropriate relay nodes are selected according to their locations in order to suppress redundant relay packets. With flooding, each node has multiple routes to deliver its data to a sink node, therefore, it is expected that the influence of link fluctuation caused by mobility and directivity of communication range can be small. However, since our work aims to collect vital data from a large number of nodes, the disadvantage of flooding, namely, the congestion due to redundant packets, can be dominant. Therefore, we try to suppress redundant packets by applying multi-channel transmissions to the location-based flooding. While the usage of multiple channels can reduce the congestion level by distributing the traffic, if the number of channels is excessively increased, the connectivity among nodes deteriorates due to the decrease of the number of relay nodes. For this reason, it is necessary to select an appropriate number of channels in the location-

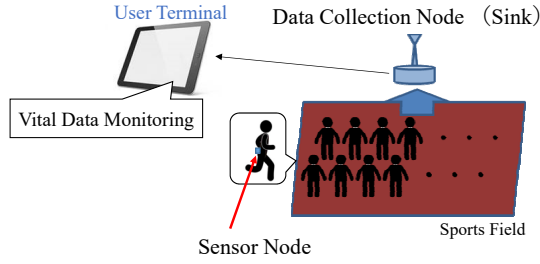


Fig. 1. System model of vital data monitoring.

based flooding using multi-channel transmissions. Therefore, in this work, we evaluate the performance of the location-based flooding in a multi-channel environment by using the mobility model and radio link model constructed based on the results obtained by our experiments.

II. SYSTEM MODEL AND PROBLEM DEFINITION

A. System Model

In this work, as shown in Fig. 1, we assume a system configuration in which sensor nodes attached to exercisers with their back-waist positions sense vital data and send them to a sink node. Vital data monitoring becomes possible by transmitting the collected vital data from the sink node to a user terminal. Each sensor node generates six types of data: heart-rate, energy expenditure, body temperature, humidity, GPS position and sequence number. It is assumed that these vital data are collected every 10 seconds. This data collection cycle is known to be sufficiently short from the viewpoint of sports physiology and medical health care [1]. Heart-rate data is the output of PPG (photoplethysmography) sensor [1], and its data size is assumed to be 200 bytes. The data sizes of energy expenditure, body temperature, humidity, GPS position, and sequence number are respectively assumed to be 2bytes, 2bytes, 2bytes, 4bytes, and 1byte. As a communication module, we adopt ARIB STD-T108 [3] which is based on IEEE802.15.4g standard as physical layer (PHY) operating over 920MHz band and IEEE802.15.4 as MAC layer. Furthermore, we assume that the transmission rate per channel is 100 kbps. In this paper, we focus on two models with different types of exercises, which are football and footrace. Football is a group game suitable for evaluating wireless communication because it includes various movements such as jumping and sliding [4]. On the other hand, footrace, which is a typical exercise played during a sports-day event at schools in Japan, is a game which includes rapid changes of positions of nodes over time due to the dash action of each player. In this paper, we call these vital data collection models as football model and footrace model.

B. Data Collection Method

In this work, it is assumed that sensor nodes are attached to exercisers with their back-waist positions. In this case, the communication range is expected to be smaller than that of

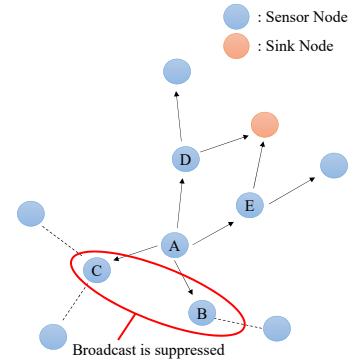


Fig. 2. An example of operation of location-based flooding.

the line-of-sight environment due to the influence of shadowing of human body. Therefore, in this work, multi-hop data transmission is adopted. Here, we focus on a flooding-based data transmission method. With the flooding, multi-hop data transmissions are realized by repeating broadcast of relay nodes. Since multiple neighboring nodes receive the data broadcasted by a sensor node, the influence of link directivity and mobility, which are the main sources of packet losses in our scenario, is expected to be smaller than that of a routing-based data transmission method. In this work, a location-based flooding is applied in order to alleviate the congestion caused by the flooding-based data transmission method. With this method, only relay nodes that are located closer to the sink node than the sender of the received packet repeat the broadcast. An example of packet transmissions in the location-based flooding is shown in Fig. 2. In this example, the sensor node A performs a flooding-based data transmission to the sink node. We assume that each sensor node has the location information of itself and the sink node. The node A first transmits a packet including its own location information by broadcast transmission. The transmitted packets are received by the sensor nodes B, C, D, and E existing within the communicable range of the node A. Each receiving node uses the location information of itself and that included in the received packet to compare the distance from itself to the sink node and distance from the node A to the sink node. Then, sensor nodes D and E find that the distance from themselves to the sink node is closer than that from node A, and rebroadcast the packet. On the other hand, sensor nodes B and C find that they are located farther than sensor node A toward the sink node, and suppress the broadcast. With these operations, it is possible to reduce redundant broadcast and reduce the congestion level of the communication band.

C. Problem Definition

In this work, we aim to collect vital data from a large number of nodes, therefore, it is expected that the problem of packet congestions caused by the flooding becomes severe. Therefore, the data collection rate can deteriorate even when the location-based flooding is applied. In order to further

alleviate the congestion problem, we consider applying multi-channel communication to the location-based flooding. Through multi-channel communication, the number of communication nodes per channel is reduced, which can reduce traffic load over each channel. However, as the number of channels increases, the number of relay candidates that use the same channel decreases. This degrades the connectivity among nodes and the data collection rate is expected to deteriorate. Thus, the reductions of congestion level and connectivity are in a relationship of trade-off though the number of applied channels. For this reason, we need to select the appropriate number of channels, and verify the effectiveness of the location-based flooding when using multi-channel communication in an environment where the position and direction of a large number of sensor nodes with link directivity change frequently with mobility. In order to investigate these issues with computer simulations, it is necessary to construct a radio link model of the sensor nodes attached to the back-waist positions of exercisers and the mobility model of exercisers when they perform football and footrace. In this work, we obtain these models through experiments in a real environment.

III. MODEL CONSTRUCTION FOR SIMULATION EVALUATION

A. Node Mobility Model

In order to construct a node mobility model, we conducted an experiment at a gymnasium. The subjects in this experiment are 30 males whose ages range from 21 to 24. The size of experimental area is $57\text{m} \times 36\text{m}$. Within this area, the subjects are instructed to make exercises simulating football and footrace, which are recorded with video cameras. Then, by applying an object tracking technique to the recorded video data, the position data of all subjects are created.

Fig. 3 shows an overview of the experiment for constructing the mobility data in the football model. In the football model, 22 subjects are supposed to play a football game for 30 minutes in the field with its size of $57\text{m} \times 36\text{m}$. In the experiment, 22 players played 3 sets of football games for 10 minutes each.

Next, the movement pattern of exercisers in the footrace model is shown in Fig. 4, where the number of exercisers is 100. First, 100 exercisers start in a state where 20 people are lined up in 5 rows in the entrance position. Subsequently, the exercisers are supposed to perform the following three operations:

- (1) Exercisers move from an entrance position to the standby position A.
- (2) Exercisers are divided into 20 groups, with a group consisting of 5 people. Each group makes 50-meters dash in turn. After the race, they move to the standby position B.
- (3) Exercisers move to an exit position after all races are completed.

Here, there are only 30 subjects for the experiment, which does not reach the number of exercisers assumed in the

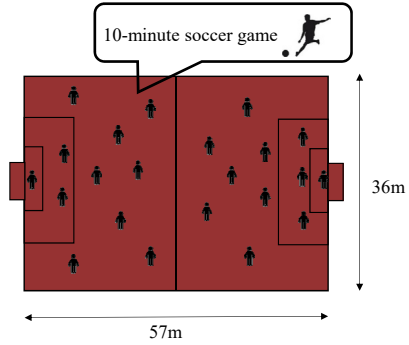


Fig. 3. An overview of experiments to construct a mobility model in the football model.

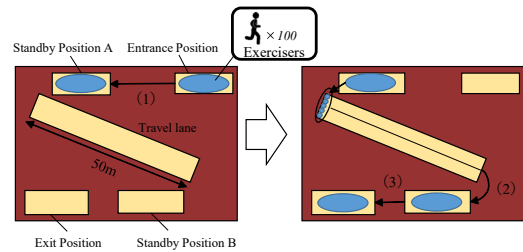


Fig. 4. An overview of experiments to construct a mobility model in the footrace model.

footrace model. Therefore, in the experiment, we separately recorded movements of 25 people in 5 rows four times with shifted locations, and combined them to create a model with 100 exercisers shown in Fig. 4.

B. Radio Link Model

The radio link model was constructed based on the experimental results using sensor nodes conforming to ARIB STD-T108 standard. In particular, we conducted experiments to obtain results on distance attenuation and directivity between sensor nodes attached to the back-waist positions of human phantoms [5].

Fig. 5 shows an overview of experiments for evaluating the distance attenuation between sensor nodes attached to the back-waist position of each exerciser. In this experiment, transmitter and receiver are attached to a position with its height of 60cm of a container. The size of container with a height of 120cm and a circumference of 63cm assumes the body of an elementary school child, and the height of the node position assumes its back-waist position. Then, the distance between transmitter and receiver is varied with equal intervals on a log scale from 0.1m to 30m, and the RSSI (Received Signal Strength Indicator) is measured. The experimental results of the distance attenuation obtained from this experiment are shown in Fig. 6. From Fig. 6, it can be seen that the attenuation increases as the distance between the transmitter and receiver increases and the amount of change also increases over the range of long distance.

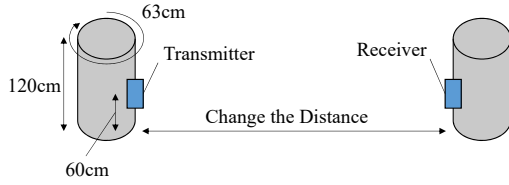


Fig. 5. An overview of experiment to evaluate distance attenuation.

Next, an overview of experiments for evaluating the communication directivity between sensor nodes attached to the back-waist position of each exerciser is shown in Fig. 7. Here, the same container and node position as those used in the experiment for evaluating the distance attenuation is employed. This container is filled with a 0.18 mass % saline to imitate a human body. Then, the RSSI value received by the receiver located 1m apart from the transmitter is measured while rotating the container with the step of 10 degrees. The results on the directivity obtained from this experiment are shown in Fig. 8. Here, the direction of 0 degree corresponds to the back-side of the exerciser. From Fig. 8, it can be seen that the attenuation is hardly observed in the backward direction of the exerciser, however, the RSSI value largely decreases in the horizontal direction and the forward direction due to the shadowing of human phantom.

IV. SIMULATION EVALUATION

We constructed a node mobility model and a radio link model by using the position variation data and RSSI data obtained by the experiments described in Section III. With these models, we conducted simulations to evaluate the data collection rate of the location-based flooding in the multi-channel setting. In simulations, the received RSSI value at each node is calculated based on the position and orientation data of each exerciser taken from the node mobility model and radio link model shown in Fig. 6 and Fig. 8. In this

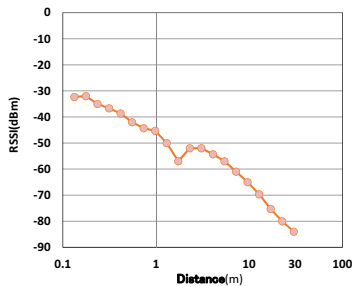


Fig. 6. The experimental results on distance attenuation.

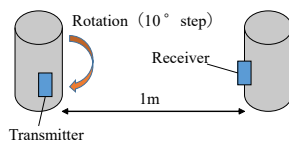


Fig. 7. An overview of experiment to evaluate directivity.

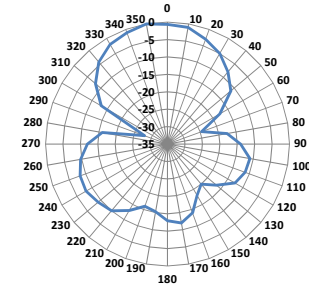


Fig. 8. The experimental results on communication directivity.

evaluation, we used a network simulator Scenargie [6]. The position of the sink node is at the midpoint of the upper long side of the sports field shown in Fig. 1, and the operating channel is randomly assigned to each sensor node so that the number of sensor nodes using each channel becomes almost equal. The sink node is assumed to be equipped with multiple interfaces operating with different channels selected by sensor nodes. The maximum waiting time before each rebroadcast in the location-based flooding is set to be 1 second. The other simulation parameters are shown in Table I. Here, the field size and mobility data of the football model is scaled up in order to set it to an official size of FIFA (International Federation of Association Football) .

Fig. 9 shows the data collection rate against the number of allocated channels for the football model. The data collection rate is defined as the ratio of the number of successfully collected packets at sink node to that of generated packets at all sensor nodes. As can be seen from this figure, in the football model, the data collection rate has the maximum value when 2 channels are randomly allocated to sensor nodes. However, comparing the result when the multi-channel communication is not applied (i.e., the case with 1 channel) and that with 2 channels, there is no significant difference in the data collection rate. Thus, in the football model, there is no improvement in the data collection rate by applying multi-channel communication. In the football model, the number of sensor nodes is 22, which is relatively a small number. For this reason, it is considered that the traffic congestion due to flooding in the football model is not so severe. On the other hand, the number of isolated nodes is increased by allocating more channels since the

TABLE I
SIMULATION PARAMETERS

	Football Model	Footrace Model
Field Size	101.58m × 81.18m	57m × 46m
Number of Nodes	22	100
Transmission Power	20 mW	
Receiver Sensitivity	-95 dBm	
Simulation Duration	10 minutes	
Data Size	211 Bytes	
Transmission Rate	100 kbps	
macMinBE	3	
macMaxBE	5	
macMAXCSMABackoffs	4	
Max. Hop Count	10	
Number of Simulation Trials	10	

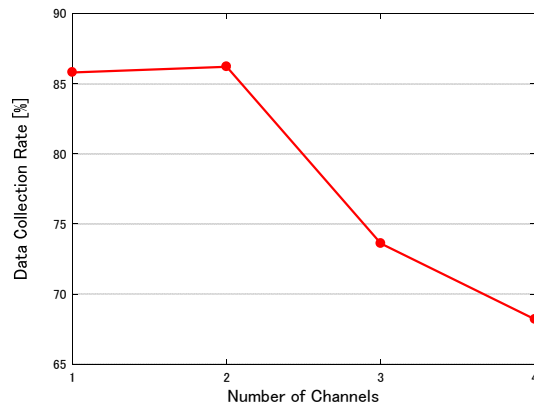


Fig. 9. The simulation results for the football model.

number of nodes operating over each channel is decreased which reduces the connectivity among nodes. This is the reason why we have worse performance with larger number of channels for the football model.

Fig. 10 shows the data collection rate against the number of allocated channels for the footrace model. From the result, we can see that the data collection rate is improved with the increase of the number of allocated channels until it reaches 16 channels, and no further deterioration is observed. In the footrace model, the operation where a large number of sensor nodes move with high density is included, in which many sensor nodes rebroadcast data packets. Therefore, by applying multi-channel communication, the data collection rate is improved by distributing the traffic into different channels. In addition, the data collection rate is not degraded with the increase of the number of channels. This is probably because, in the considered field size, many nodes can transmit sensing data toward the sink node with a single hop, and the number of isolated nodes is not increased so much with the increase of the number of channels.

V. CONCLUSIONS

In this work, we focused on vital data monitoring of exercisers who perform exercises such as football and footrace. We adopted a location-based flooding with multi-channel setting as a data collection method and conducted simulations using the mobility model and radio link model constructed based on our experimental results. As a result, in the football model, we found that the number of isolated nodes is increased by allocating more channels since the number of nodes operating over each channel is decreased, which reduces the connectivity among nodes. The increase of the isolated node is dominant over the reduction of traffic congestion when applying multi-channel communication to the football model, and its performance is degraded as the number of allocated channels is increased. On the other hand, in the footrace model, we observed that the data collection rate is improved by distributing the traffic into different channels. From this result, it was confirmed that the reduction of traffic congestion is dominant over the increase

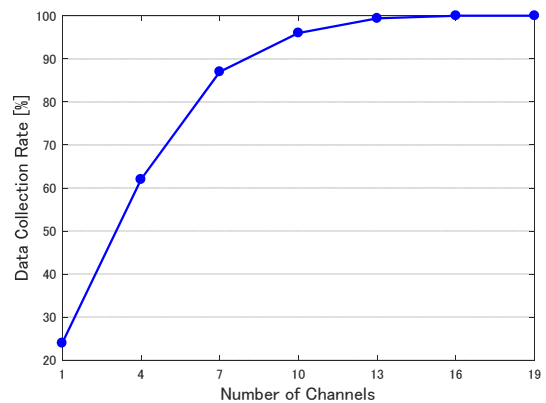


Fig. 10. The simulation results for the footrace model.

of the isolated node in the footrace model, which contributes to the improvement of the data collection rate.

In our future work, in order to examine the influence of mobility characteristics on the data collection rate, simulation evaluation is planned with various exercise models. In addition, we will investigate the effectiveness of the location-based flooding by comparing its performance with the routing-based data transmission methods.

VI. ACKNOWLEDGEMENT

This work was supported by the Research and Development of Innovative Network Technologies to Create the Future of National Institute of Information and Communications Technology (NICT) of Japan.

REFERENCES

- [1] S. Hara, H. Okuhata, T. Kawabata, H. Nakamura, and H. Yomo, "Real-Time Vital Monitoring for Persons during Exercises-Solutions and Challenges," *IEICE Trans. Commun.*, vol. E99-B, no. 3, pp. 556-564, March 2016.
- [2] Y.-B. Ko and N.H. Vaidya, "gLocation-aided Routing (LAR) in Mobile Ad Hoc Networks," *Proc. of Mobicom 98*, pp. 66-75, 1998.
- [3] Association of Radio Industries and Businesses, ARIB STD-T108, version 1.0, 2011.
- [4] S. Hara, H. Yomo, T. Kawabata, and H. Nakamura, "Challenges in Wireless Networking for Real-Time Vital Sensing from Persons in Exercises," *Proc. of ISMICT 2016*, March 2016.
- [5] H. Ogura, T. Hamagami, R. Miyamoto, H. Yomo, and S. Hara, "A Network Simulator to Develop Wireless Networking Protocols Suited for Vital Information Collection from a Group of Exercisers," *Proc. of ISMICT 2018*, Sydney, Australia, March 2018.
- [6] Space Time Engineering, <https://www.spacetime-eng.com/jp>

Resource-Constrained Device for Unobtrusive Estimation of Sleep Stages using R-R Interval Data

Jaspal Singh

Electronics & Embedded Computing,
Center for Development of Advanced Computing,
Mohali, India
Jaspal_sng@yahoo.com

Rajender Sharma

Prof., Electronics & Communications Engg Dept,
National Institute of Technology,
Kruksheeta, India
Mail2drrks@gmail.com

Abstract— Identifying the Sleep stages is an essential component of sleep studies. It is normally done by observing collective behavior of various physiological signals, including EEG, EMG, EOG, etc. Recently it has been demonstrated that respiration and ECG can be computationally augmented to reasonably estimate the sleep stages. This paper describes a dedicated wireless device developed to acquire the cardio-respiratory data to distinguish the sleep stages. The device extracts R-R intervals and respiration data from the ECG and transmits it over the Bluetooth. The miniature hardware device and its energy efficient firmware design, presented in this work, are tested against the standard ECG machine for accuracy of R-R interval periods and ECG derived respiration (EDR). The experimental results show very good agreement of observed data with that obtained using commercial wired machine. The device can be very useful in unobtrusively screening the patients suffering with sleep related problems, especially in an out of center setting.

Keywords— *R-R intervals, Sleep Staging, Polysomnography, wireless, energy efficiency*

I. INTRODUCTION

Sleep is an essential part of our life. It is a non-homogenous process consisting of alternating cycles of rapid-eye-movement (REM) stage and three types of NREM stages. With changing lifestyles, sleep related problems are increasingly becoming common. These problems are diagnosed after elaborate sleep studies that often involve assessing changes in pattern/ duration of these stages. Sleep studies involve full-night recording of over eight different physiological parameters and then annotating the sleep stage for every 30-sec epoch of the entire sleep record [1]. The different stages are identified by collective behavior of the physiological parameters. The standard instrumentation for sleep studies is Polysomnography (PSG). It requires the patient to sleep in a specially equipped facility (sleep-lab) with an array of sensors attached to different parts of his body [1]. This is highly inconvenient, and may even affect the sleep that is being observed. The limited availability of specially designed sleep-labs and trained technicians is a big bottleneck. In view of all this, for greater patient convenience and shorter waiting times, it is highly desirable to be able to undertake in-home / out-of-center (OOC) sleep studies.

To address the issue, researchers have explored signals and methods that enable studies with either lesser number of

electrodes/ parameters or with various unobtrusively monitored parameters. One set of methods that increase the patient-friendliness, leverage computational processing of a smaller number of signals to distinguish the sleep stages. EEG, is a suitable candidate and it yields good results [2]. However, it is a comparatively sensitive and difficult to acquire signal. So, researchers have increasingly started focusing on more robust ECG and other signals [3]. Second set of methods promising greater patient friendliness are based on using instrumented beds (or bed sheets) [4], video monitoring [5] etc. Another approach to increase unobtrusiveness is to use wireless data acquisition, as in [6] using multiple wireless modules. Based on our study of respiration and variations of ECG's R-R intervals with REM sleep stages in Montreal Archive of Sleep studies (MASS) sleep database [7], it is planned to combine the idea of using a wireless device along with using computational augmentation of cardio-respiratory signals. While there can be several well proven methods of getting cardiorespiratory data for the entire night (including standard multi-parameter patient monitors, etc.), but they are either not so unobtrusive or are more of an overkill for the purpose. On the other hand, the consumer heart-rate devices, although very friendly, are mostly wrist based. They, primarily, rely on averaging over multiple cycles, and are thus, not suitable for our purpose. For our specific purpose, we developed a wearable wireless module that extracts the R-R Intervals and EDR data from the ECG and transmits it wirelessly. The cardiorespiratory data is processed to indicate the sleep stage. The overview of the arrangement is shown in Fig1. The present paper describes the design of hardware and the resource optimizing firmware for it. This wearable can be particularly useful in several healthcare scenarios including unobtrusive sleep monitoring in an out-of-center setting.

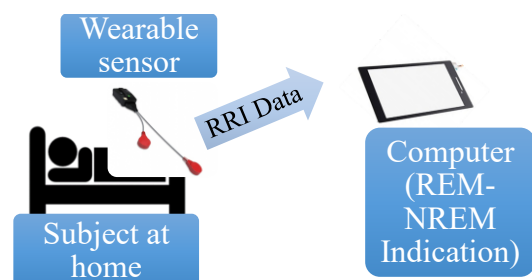


Fig. 1. Overview of the system

II. THE WIRELESS DEVICE

A. The Hardware Design

The proposed device consists of electronics for ECG acquisition, R-wave detection, deriving the respiration data, forming the data packets and their wireless transmission. A block diagram of the device is shown in Fig 2.

The Analog Front end (AFE) of the device is based on application-specific integrated circuit (IC) from 'Analog Devices Inc.', AD3282. The left-arm (LA) and right-arm (RA) signal is fed to the instrumentation amplifier with gain of 100. Their common mode signal is fed to the right leg drive; enabling CMRR of more than 80dB. Two pole filtering, implemented with an OP-AMP and passive components, is designed for bandwidth of 0.4 to 40 Hz. A second stage amplifier is used to raise total gain to 1000.

The signal is also fed to comparators for sensing the leads-off condition that drives the signal path to saturation in either direction in this single supply rail to rail system. Additionally, mid-supply reference is also generated. The amplified and filtered signal is fed to the differential mode ADC of the Silicon Labs micro-controller, C8051F300-GM. The controller is specifically selected for its energy efficient operation with low supply voltage (3V), calibrated internal oscillator (24.5MHz) and it's small (11-pin QFN) footprint. The ADC is configured for 8-bit sampling at 300 Hz.

R-wave detection, R-R interval extraction, buffering, encoding and packetisation are implemented in the microcontroller. The occurrence of artefacts (like leads-off) which drive the signal to saturation are detected with range comparator in the AFE. Such conditions are used to trigger a subroutine in microcontroller which outputs a code for every one second of the occurrence of condition. This is detected and considered accordingly at the receiver end. The complete sensor circuit is implemented on a circular double sided printed circuit board (PCB) with $\phi = 30\text{mm}$. The PCB is assembled with carefully selected components and 1206 SMT passives. Electrode wires and battery were soldered to it. To keep the cost low and for our testing purposes we used off-the shelf Bluetooth module (BlueSMiRF Silver from www.sparkfun.com). Fig 3. shows the assembled PCB and

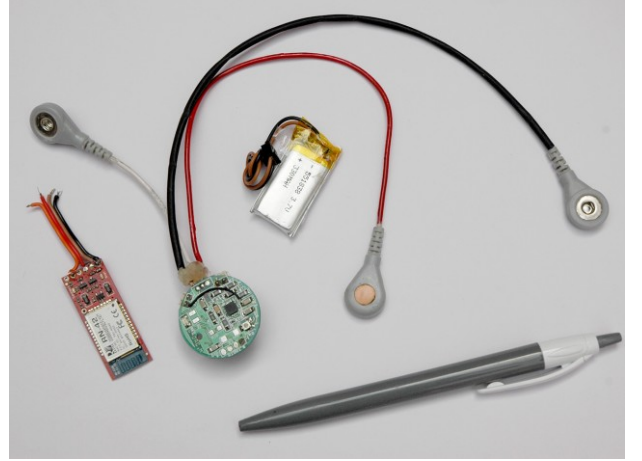


Fig. 3. Assembled PCB and other components shown alongside a pen

other components alongside a pen to show the miniature size.

Considerations for unobtrusiveness required us to assemble the hardware on a small board. Its optimal performance demanded resource constrained R-wave detection and energy optimized transmission. The major effort, thus, lies in resource constrained firmware design. It is described below.

B. R-Wave Detection

A simplified algorithm based on [8] was implemented for detection of R-wave in ECG. We know, the QRS complex has a specific shape and lasts about 0.06 to 0.1 sec. So, we calculate the slope in a moving window of 0.03 sec on the left and right of every sample, as given below.

$$\Delta_l = \frac{1}{i} (ECG_n - ECG_{n-i}) \quad (1)$$

$$\Delta_r = \frac{1}{i} (ECG_n - ECG_{n+i}) \quad (2)$$

Here, ECG_n represents the n th sample of ECG signal; and as sampling frequency, $f_s = 300 \text{ Hz}$, and, $i = 0.03f_s$. So, i , corresponding to 0.03s is taken as 9 here.

We know, QRS complex has a sharp slope up followed by slope down, so, we check $\text{sign}(\Delta_l) = -\text{sign}(\Delta_r)$. If the given n th sample passes this test we calculate, a parameter, ' t ' given

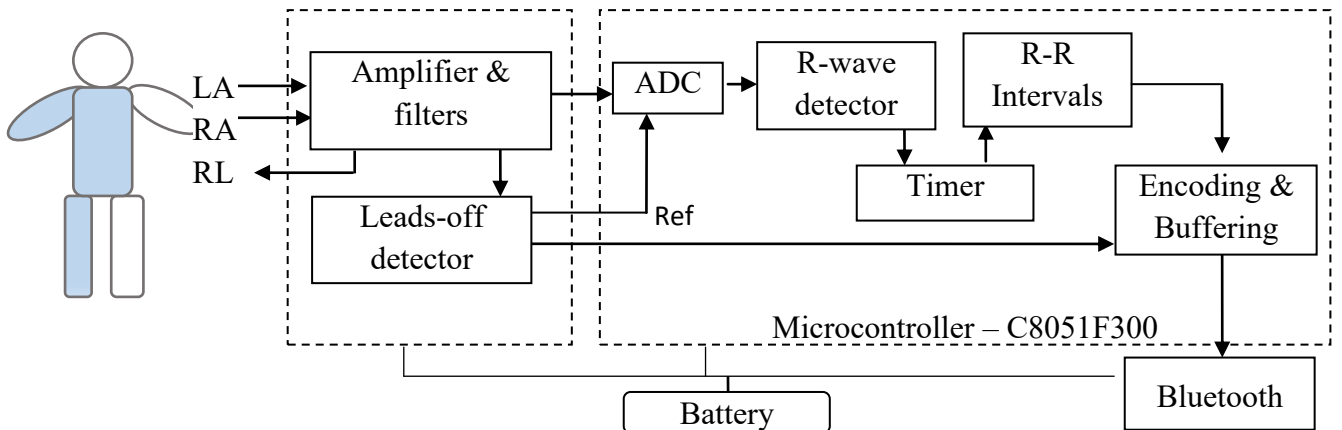


Fig. 2. Block Diagram of the Device

as,

$$t_n = \text{abs}(\Delta_l)_n * \text{abs}(\Delta_r)_n. \quad (3)$$

This t_n is then compared with an adaptive threshold, T_a , initialized as one half of the maxima in first ten seconds of the ECG record. Thereafter, T_a was updated as one third of the previous maxima of t_n . Thus, R-wave was considered located at local maxima of,

$$t_n > T_a \quad (4)$$

The method uses less than 25% of the hardware resources required for implementing popular Pan-Tompkins method [9] and is rated numerically efficient. Once the R-wave instant was located (Fig 4. shows the use of ' t_n '), corresponding ECG signal was noted as R-peak for EDR signal and calculation of slope was suspended for next 109 samples as next R wave is not expected in less than 0.3 seconds (i.e. heart rate is not expected to be normally more than 200bpm). Each R-wave event was used to reset and trigger a counter working on the internal oscillator calibrated at 24.5MHz. The time (count) from one R-wave to next R-wave is extracted as R-R interval (RRI).

C. Considerations for efficient wireless transmission

For wireless connection, standard Bluetooth was preferred due to its popularity in commercial computing devices and convenience in personal usage. Bluetooth protocol in a master-slave configuration undergoes a series of steps like device discovery, pairing, authentication and bonding before data transfer happens in 'send slots'. Data transfer includes sending access code, header and payload in every 'send slot' of 625 micro-second. To improve the energy efficiency, energy hungry stage of Bluetooth should be minimized. The Bluetooth specifications reveal that Sniff mode current is about 10mA, whereas transmission (Tx) mode current is about 50-80mA. The Tx mode actually accounts for up to 80% of the Bluetooth energy consumption [10].

So, the key is to use minimal transmission slots for given data or equivalently, maximize payload per transmitted packet to achieve higher efficiency. To achieve this, we buffered the RRI interval and EDR data, before transmitting them in bursts.

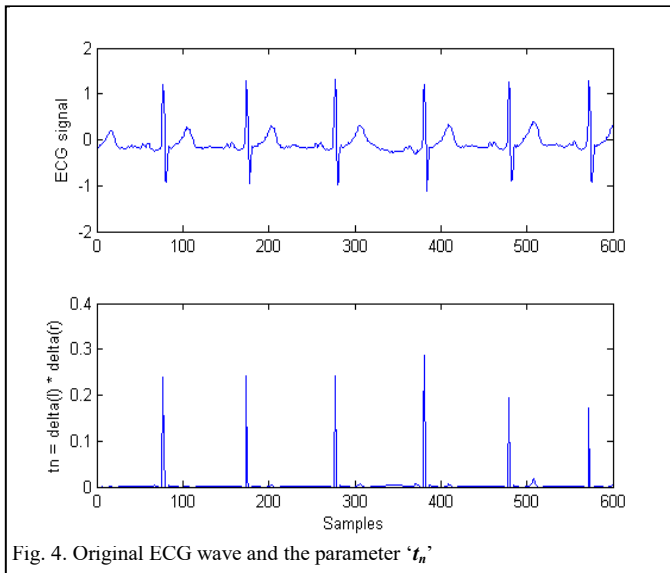


Fig. 4. Original ECG wave and the parameter ' t_n '

As our algorithm of sleep staging is based on 60 second epochs of sleep [7], we preferred buffering data for 60 seconds. The Bluetooth was configured to spend maximal time in sniff mode and send the entire buffered data in allocated transmit slots in one go. This minimizes the number of transmission slots used per transmitted byte and reduces repeated transmissions of access code and headers in send slots. Thus, we could achieve better performance as compared to unbuffered method of sending data as soon as it is made available. Also, this enables keeping the radio more in sniff mode for longer durations. In this device we employed buffering of one-minute data and dedicated bonding for fast reconnection. This enabled improvement in average operable time of a charged battery from about 8 hours to over 20 hours.

III. TESTING THE SYSTEM

To test the system performance, the hardware device was assembled as explained above. A battery (3.7V, 450mA rechargeable Li-ion battery, Jackli, Mohali, India), selected to last 10 hours of continuous operation, and Bluetooth module (BlueSMiRF silver) were connected to the circuit. The microcontroller was configured as described above. For receiving the data, we used a Bluetooth enabled computer so as to easily analyze and process the data. The data can be received on a mobile phone also, which can then be used to send the packets over to internet. At the computer end, the data packets were received and concatenated. A dot-net software was designed to capture the streaming input data from the Bluetooth module. Raw RRI data stream is recovered by truncating the signaling bytes and decoding. The packets are stored as separate time stamped files or as single file made by concatenation of the input data in the computer.

In order to test the device, it was attached to the patient using three pre-gelled electrodes as shown in the Fig 5. For comparison, commercially available PC based ECG machine CardioAssist (Maestros Mediline, Mumbai) in long term monitoring mode was also attached to the subject simultaneously. The recordings were done for 1 hour on each of the 10 healthy young volunteers (six males aged 21 – 29 years, 4 females aged 20 and 25 years) while sitting comfortably on a chair. The two data sets of R-R Intervals were tabulated and evaluated for using NCSS statistical software.

IV. RESULTS

One hour of RRI data and EDR from our wireless device and that from the commercial wired device was obtained for each case. The combined overall RRI data with the two methods showed a very good correlation with the series obtained from CardioAssist (correlation coefficient, $r = 0.996$).

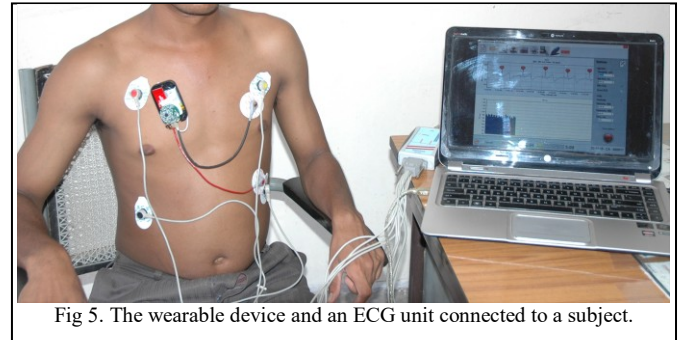


Fig 5. The wearable device and an ECG unit connected to a subject.

Considering the R wave detections by the commercial device as reference, we compared them with our detections and are reported in Table I. For EDR, the common method of comparing breaths per minute (bpm) was used. The cumulative average error in observed breaths as reported by our device and that obtained by using the ECG wave recorded with wired device was found to be 4.2 %.

To compare the agreement between two methods of obtaining a quantitative variable, Bland-Altman plot (BA plot aka difference plot) is a suitable statistic [11]. It is a scatter plot of difference in observations versus the average of two observations. BA plot was made in each of the 10 cases for RRI, and it was observed that 99% of the difference values fall within the ± 1.96 SD of the respective standard value data set. This showed a very good agreement between RRI obtained by two methods. One such BA plot for recordings of subject 1 is shown in Fig.6. It shows observations to be within 6ms (± 1.96 SD) of the standard values.

TABLE I. COMPARISON OF RR INTERVALS

Sub ject	Reference RRI (ms)		RRI by our device (ms)	
	Mean	SD	Mean	SD
1	864.2	38.0	859.3	38.4
2	797.7	47.5	787.7	46.6
3	849.6	28.3	854.5	28.3
4	728.1	42.4	737.2	42.6
5	956.2	84.8	933.4	69.6
6	774.2	42.1	758.9	44.2
7	803.6	37.6	812.3	38.3
8	792.4	68.3	787.2	64.2
9	829.6	74.9	823.3	72.9
10	853.3	53.2	861.2	52.6

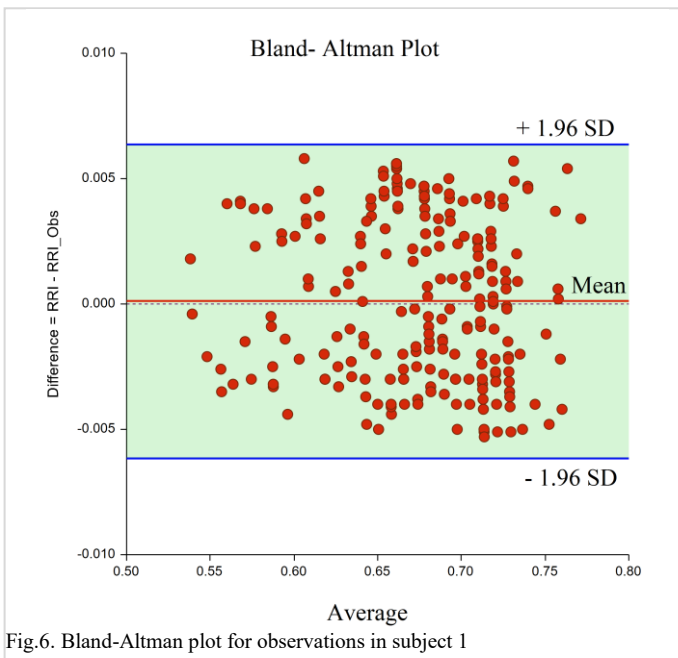


Fig.6. Bland-Altman plot for observations in subject 1

V. CONCLUSION

The BA plot and results show a very good agreement between RRI obtained from our device and that from a normal wired system. The device is a good implementation for obtaining cardiorespiratory data in a resource constrained setting. With further improvements it should be useful, not only for online sleep staging but also for several other remote monitoring applications.

ACKNOWLEDGMENT

The authors acknowledge the technical support and lab resources provided by VLSI Design Lab at NIT Kurukshetra under MeitY's SMDP-C2SD project.

REFERENCES

- [1] R. B. Berry, R. Brooks, and B. Vaughn, "The AASM manual for the scoring of sleep and associated events: rules, terminology, and technical specifications, version 2.2," Darien, IL, 2015.
- [2] S. F. Liang, C. E. Kuo, Y. H. Hu, Y. H. Pan, and Y. H. Wang, "Automatic stage scoring of single-channel sleep EEG by using multiscale entropy and autoregressive models," *IEEE Trans. Instrum. Meas.*, vol. 61, no. 6, pp. 1649–1657, 2012.
- [3] Ying Chen, Xin Zhu, and Wenxi Chen, "Automatic sleep staging based on ECG signals using hidden Markov models," 37th Annu. Int. Conf. IEEE Eng. Med. Biol. Soc., pp. 530–533, 2015.
- [4] L. Samy, M. C. Huang, J. J. Liu, W. Xu, and M. Sarrafzadeh, "Unobtrusive sleep stage identification using a pressure-sensitive bed sheet," *IEEE Sens. J.*, vol. 14, no. 7, pp. 2092–2101, 2014.
- [5] C. W. Wang, A. Hunter, N. Gravill, and S. Matusiewicz, "Unconstrained video monitoring of breathing behavior and application to diagnosis of sleep apnea," *IEEE Trans. Biomed. Eng.*, vol. 61, no. 2, pp. 396–404, 2014.
- [6] D. Chang, Y. Liu, C. Young, J. Chen, Y. Chen, C. Chen, Y. Hsu, F. Shaw, and S. Liang, "Design and Implementation of a Modularized Polysomnography System," *IEEE Trans. Instrum. Meas.*, vol. 61, no. 7, pp. 1933–1944, 2012.
- [7] J. Singh, R. K. Sharma, and A. K. Gupta, "A method of REM-NREM sleep distinction using ECG signal for unobtrusive personal monitoring," *Comput. Biol. Med.*, vol. 78, no. September, pp. 138–143, Nov. 2016.
- [8] H. Khamis, R. Weiss, Y. Xie, C. W. Chang, N. H. Lovell, and S. J. Redmond, "QRS Detection Algorithm for Telehealth Electrocardiogram Recordings," *IEEE Trans. Biomed. Eng.*, vol. 63, no. 7, pp. 1377–1388, 2016.
- [9] J. Pan and W. J. Tompkins, "A real-time QRS detection algorithm," *Biomed. Eng. IEEE Trans.*, vol. 1, no. 3, pp. 230–236, 1985.
- [10] A. Dementyev, S. Hodges, S. Taylor, and J. Smith, "Power consumption analysis of Bluetooth Low Energy, ZigBee and ANT sensor nodes in a cyclic sleep scenario," in *IEEE International Wireless Symposium (IWS)*, 2013, pp. 1–4.
- [11] R. Zaki, A. Bulgiba, N. Nordin, and N. A. Ismail, "A systematic review of statistical methods used to test for reliability of medical instruments measuring continuous variables," *Iranian Journal of Basic Medical Sciences*, vol. 16, no. 6, pp. 803–807, 2013.

Modeling of a Cardiovascular System to Investigate Factors Affecting Hypertension

Kento KADOYA

Department of Mechanical Engineering
The University of Tokyo
Tokyo, Japan
kkadoya@fiv.t.u-tokyo.ac.jp

Shigehiko KANEKO

Department of Mechanical Engineering
The University of Tokyo
Tokyo, Japan
kaneko@mech.t.u-tokyo.ac.jp

Abstract—In this study, we construct a cardiovascular model considering the interaction of cardiac and vascular systems, and investigate factors affecting hypertension. In the cardiovascular model, stroke volume, the blood volume pumped by a heart per beat, is determined based on the operating conditions of the system. In addition, positions of baroreceptors, pressure sensors of cardiac system, in blood vessels are also considered. Consequently, the functions proportionally controlling the baroreceptor activities and determining the activities of autonomic nerves have significant effects on hypertension, which are comparable to those of aortic stiffness.

Keywords—cardiovascular system; hypertension; baroreceptor; stroke volume.

I. INTRODUCTION

In recent years, cardiovascular diseases have been major causes of death and have become significant social problems, in particular, in developed countries, which are facing a growth in aging population. Therefore, it is necessary to prevent the diseases.

An important factor for monitoring the onset risk of cardiovascular diseases is blood pressure, which displays a correlation with the risk [1]. Hence, it is important to prevent the diseases by identifying factors that highly affect hypertension and by conducting appropriate treatment.

Although the factors are usually attributed to aortic insufficiency and arteriosclerosis, many kinds of the factors have not been clinically identified [2]. Therefore, it is necessary to examine the effects of cardiovascular characteristics on blood pressure and investigate the causes of hypertension in another way.

In this study, we aim to achieve the aforementioned objective by modeling a cardiovascular system, which consists of cardiac and vascular systems. The cardiac system controls heartbeat generation based on the conditions of autonomic nerves and the vascular system carries blood all over the body through a vascular network; both systems interact with each other in a body. However, in research fields, these two systems are dealt with independently [3], [4], and as of today, there is no model which considers the interaction of both the systems.

This study aims to construct a cardiovascular model where we consider the interactions between cardiac and vascular systems, and identify the effects of cardiovascular characteristics on hypertension.

II. NOMENCLATURE

Cardiac model

c_{cNe}	: concentration of cardiac norepinephrine [-]
c_{vNe}	: concentration of vascular norepinephrine [-]
p	: blood pressure [g/(s ² cm)]
R	: respiratory activity [-]
RR	: heartbeat interval [s]
t	: time [s]
v_b	: baroreceptor activity [-]
ϕ	: sinus node phase [-]

Vascular model

A	: cross sectional area [cm ²]
f	: arterial stiffness [g/(s ² cm)]
P	: blood pressure [g/(s ² cm)]
R_{min}	: truncation radius [cm]
r_0	: initial radius [cm]
t	: time [s]
x	: axial coordinate [cm]
μ	: viscosity [g/ (cm s)]
ρ	: density [g/cm ³]

Cardiovascular model

DBP	: diastolic blood pressure [g/(s ² cm)]
MBP	: mean blood pressure [g/(s ² cm)]
RR	: heartbeat interval [s]
SBP	: systolic blood pressure [g/(s ² cm)]
SV	: stroke volume [cm ³]

III. CONSTRUCTION OF A CARDIOVASCULAR MODEL

In this section, we first describe a cardiac and vascular model. Then, we explain the construction of a cardiovascular model. Finally, we validate the calculations of the cardiovascular model.

A. Cardiac Model

Kotani et al. [3] constructed models which could reproduce effects of autonomic nerves on a cardiac system. We describe a schematic of the cardiac model below.

Fig. 1 shows the schematic of the cardiac model, which mainly consists of three elements: baroreceptor, central nervous system, and sinus node. The model performs calculations by transmitting each state quantity through these elements.

1) *Baroreceptor*: Firstly, baroreceptor activity v_b is determined by the blood pressure p [mmHg] and its first derivative, as described in (1).

$$v_b = k_1(p - p_0) + k_2 \frac{dp}{dt} + \xi \quad (1)$$

(default parameters: $k_1 = 0.02 \text{ mmHg}^{-1}$, $k_2 = 1.25 \times 10^{-3} \text{ s mmHg}^{-1}$, $p_0 = 50 \text{ mmHg}$, and $\xi = 0.16$)

2) *Central nervous system*: The v_b subsequently determines sympathetic and parasympathetic nerve activities (v_s and v_p) as in (2), after being modulated by respiratory activity R as calculated in (3).

$$\begin{aligned} v_s' &= v_{s0} - k_s^b v_b + k_s^r (1 - R) \\ v_s &= v_s' \left[\tanh(v_s' \times 100) + 1.0 \right] / 2.0 \\ v_p' &= k_p \left[v_{p0} + k_p^b v_b + k_p^r (1 - R) \right] \\ v_p &= v_p' \left[\tanh(v_p' \times 100) + 1.0 \right] / 2.0 \end{aligned} \quad (2)$$

($v_{s0} = 0.95$, $k_s^b = 0.8$, $k_s^r = 3.0 \times 10^{-4}$, $k_p = 1.1$, $v_{p0} = 0.01$, $k_p^b = 0.036$, and $k_p^r = 4.5 \times 10^{-3}$)

$$\begin{aligned} \frac{dr'}{dt} &= \frac{1}{T_{resp}} - G \times (v_{trig} - v_b) \\ \frac{dr}{dt} &= \frac{dr'}{dt} \left[\tanh \left(\frac{dr'}{dt} \times 100 \right) + 1.0 \right] / 2.0 \\ R &= \cos(2\pi r) \\ (T_{resp} &= 3.5 \text{ s}, G = 0.2, \text{ and } v_{trig} = 1.3) \end{aligned} \quad (3)$$

In addition, at the central nervous system, the concentration of the sympathetic neurotransmitter,

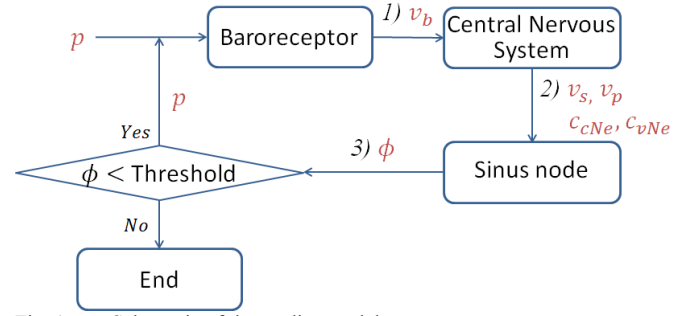


Fig. 1. Schematic of the cardiac model

“norepinephrine (Ne)” is also calculated by (4); c_{cNe} and c_{vNe} represent the cardiac and vascular concentrations respectively.

$$\begin{aligned} \frac{dc_{cNe}}{dt} &= -\frac{c_{cNe}}{\tau_{cNe}} + k_{cNe}^s \times v_s (t - \theta_{cNe}) \\ \frac{dc_{vNe}}{dt} &= -\frac{c_{vNe}}{\tau_{vNe}} + k_{cNe}^s \times [v_s (t - \theta_{vNe}) + k_v] \end{aligned} \quad (4)$$

($\tau_{cNe} = 2.0 \text{ s}$, $k_{cNe}^s = 0.7$, $\theta_{cNe} = 1.65 \text{ s}$, $\tau_{vNe} = 2.0 \text{ s}$, $k_{cNe}^s = 0.5$, $\theta_{vNe} = 2.0 \text{ s}$, and $k_v = 0.2$)

3) *Sinus node*: The sinus node plays the role of a cardiac pacemaker based on its pacemaker phase ϕ , whose velocity is a function of both sympathetic (f_s) and parasympathetic (f_p) influences on the sinus node, as described in (5).

$$\begin{aligned} f_s &= 1 + k_\phi^{cNe} \left[c_{cNe} + (\hat{c}_{cNe} - c_{cNe}) \times \frac{(c_{cNe})^{n_{cNe}}}{(\hat{c}_{cNe})^{n_{cNe}} + (c_{cNe})^{n_{cNe}}} \right] \\ f_p &= 1 - k_\phi^p [v_p (t - \theta_p) + (\hat{v}_p - v_p (t - \theta_p)) \\ &\quad \times \frac{v_p (t - \theta_p)^{n_p}}{(\hat{v}_p)^{n_p} + v_p (t - \theta_p)^{n_{cNe}}}] \end{aligned} \quad (5)$$

$$\frac{d\phi}{dt} = \frac{1}{T_0} f_s f_p$$

($k_\phi^{cNe} = 1.6$, $\hat{c}_{cNe} = 2.0$, $n_{cNe} = 2.0$, $k_\phi^p = 9.5$, $\theta_p = 0.5$, and $n_p = 2.0$)

When ϕ is smaller than its threshold of 1.0, systolic blood pressure, SBP, is determined using the diastolic pressure (d_{i-1}) and the heartbeat interval (RR_{i-1}) of the previous beat, as in (6), where t_i is the time of last contraction onset and cardiac contraction period (τ_{sys}) is 0.125 s, and diastolic blood pressure, DBP, is described by the relaxation of Windkessel arteries, as in (7). Then, when, ϕ reaches the threshold, ϕ is reset to zero and the calculation of the beat ends.

As a result, by using the cardiac model, the cardiac blood pressure and heartbeat interval can be obtained.

$$\begin{aligned}
S_i' &= S_0 + k_s^c \cdot c_{cNe} + k_s^t \cdot RR_{i-1} + k_s^v c_{vNe} \\
S_i &= S_i' + (\hat{S} - S_i') \frac{(S_i')^{n_s}}{(S_i')^{n_s} + (\hat{S})^{n_s}} \\
p_{SBP} &= d_{i-1} + S_i \frac{t - t_i}{\tau_{sys}} \exp\left(1 - \frac{t - t_i}{\tau_{sys}}\right)
\end{aligned} \quad (6)$$

$$\begin{aligned}
\tau_v(t) &= \tau_{v0} - \bar{\tau}_v \left[c_{vNe} + (\hat{c}_{vNe} - c_{vNe}) \times \frac{(c_{vNe})^{n_{vNe}}}{(\hat{c}_{vNe})^{n_{vNe}} + (c_{vNe})^{n_{vNe}}} \right] \\
\frac{dp_{DBP}}{dt} &= -\frac{p_{DBP}}{\tau_v(t)}
\end{aligned} \quad (7)$$

$$\begin{aligned}
(S_0 = -13.8 \text{ mmHg}, k_s^c = 10.0 \text{ mmHg}, k_s^t = 45 \text{ mmHg s}^{-1}, k_s^v = \\
20 \text{ mmHg}, \hat{S} = 70 \text{ mmHg}, n_s = 2.5, \tau_{v0} = 2.8 \text{ s}, \bar{\tau}_v = 1.2 \text{ s}, \\
\hat{c}_{vNe} = 1.0, \text{ and } n_{vNe} = 1.5)
\end{aligned}$$

B. Vascular Model

In this study, we used a proposed numerical simulation for pulse wave propagation in arterial network [4] as the vascular model, which focuses on the 55 arteries shown in Fig. 2.

1) *Governing equations*: The vascular model consists of three governing equations. The two equations that ensure conservation of mass and momentum are given in (8). Here, density, $\rho = 1.055 \text{ g/cm}^3$ and viscosity, $\mu = 0.049 \text{ g/(cm s)}$ are kept constant.



Fig. 2. Arterial network model

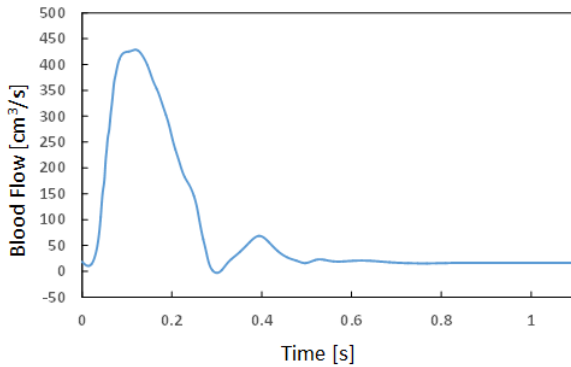


Fig. 3. Pumped blood flow in ascending aorta

$$\begin{aligned}
\frac{\partial A}{\partial t} + \frac{\partial UA}{\partial x} &= 0 \\
\frac{\partial U}{\partial t} + U \frac{\partial U}{\partial x} &= -\frac{1}{\rho} \frac{\partial P}{\partial x} - \frac{22\mu\pi U}{\rho A}
\end{aligned} \quad (8)$$

In addition to (8), the equation on tube law, which relates local cross-sectional area to the local radial pressure, should be added, as shown in (9), where f represents the stiffness of each artery determined as the function of its initial radius, r_0 , as in (10).

$$P = P_e + \frac{4}{3} f \left(1 - \sqrt{\frac{A_0}{A}}\right) \quad (9)$$

$$f = a_1 \exp(a_2 r_0) + a_3 \quad (10)$$

$$\begin{aligned}
(P_e = 25 \text{ mmHg}, a_1 = 2.00 \times 10^7 \text{ g/(s}^2\text{cm)}, a_2 = -22.53 \text{ cm}^{-1}, \\
\text{and } a_3 = 8.65 \times 10^5 \text{ g/(s}^2\text{cm)})
\end{aligned}$$

Then, P, U , and A of each artery can be obtained from the input cardiac blood pressure at the contraction onset in the vascular model.

2) *Boundary conditions*: Equations (8), (9), and (10) focus on single vessel. In order to extend the vascular model to the arterial network, it is necessary to establish three boundary conditions: (a) at the inlet of the arterial network, (b) at each bifurcation where the three vessels, i.e., one parent and two daughter vessels, meet at each junction, and (c) at the outlet of each terminal vessel of the arterial network.

a) *Inlet boundary condition*: At the inlet of the arterial network, the flow is given based on magnetic resonance measurement of the pumped blood flow in the ascending aorta, as shown in Fig. 3 [4].

b) *Bifurcation boundary condition*: Considering the loss of energy at each bifurcation, we derived a mass-conservation equation and the Bernoulli equation.

c) *Outlet boundary condition*: In this study, we considered symmetrical trees in peripheral vessels [5]. Each such tree has several generations, before the radius of the vessel reaches a truncation radius, R_{\min} , giving resistance and compliance to each terminal vessel of the arterial network. Here, we set the value of R_{\min} to 0.02 cm.

3) *Numerical method*: Now that we have the governing equations and the boundary conditions of the arterial network, the simulation can be performed numerically by Richtmeyer's two-step version of the Lax-Wendroff method. The calculations were done by the time-discretization $\Delta t = 3.125 \times 10^{-5} \text{ s}$ and the spatial-discretization $\Delta x = 0.2 \text{ cm}$.

C. Cardiovascular Model

In this section, we construct the cardiovascular model considering the interaction of the cardiac and vascular systems. In order to combine the cardiac and vascular models, we describe the state quantities which are transferred 1) from the

cardiac model to the vascular model and 2) from the vascular model to the cardiac model.

1) *Cardiac model* \rightarrow *Vascular model*: As described above, from the cardiac model, cardiac blood pressure and heartbeat interval of a beat can be obtained. Inserting these two state quantities into the vascular model, simulation of pulse wave propagation works with the cardiac blood pressure at the onset of contraction until t reaches the heartbeat interval.

Here, considering that one stroke volume (SV), i.e., the blood volume pumped from a heart per beat, fluctuates at each beat, it is necessary to change the pumped blood flow in response to the condition of the cardiovascular system (Fig. 3). Hence, we should determine the SV based on the cardiovascular condition, and change the vertical scale of the pumped blood flow such that SV equals an integrated value of the pumped blood flow per heartbeat interval.

Then, we decided to estimate SV of a beat based on the condition at the beat and the previous beat. Fig. 4 shows the determination process of SV at a beat of number “N”, which focuses on the state quantities at beats of number “N” and “N-1”. Generally, the SV is mainly dependent on three factors: pre-load, contraction, and after-load; pre-load is the force that pushes blood out and increases with the pressure of venous return; contraction is the force of cardiac contraction and autonomic nerves have a significant impact on the force; after-load is the force of arterial blood that resists pumped blood [6]. As shown in Fig. 4, these three factors at the beat “N” are considered to be mainly determined by the arterial blood pressure and SV at the beat “N-1”, and heartbeat interval at the beat “N”. Therefore, we determined SV at the beat “N” by using an estimating formula which consists of three state quantities: systolic blood pressure (SBP) and SV at the beat “N-1”, and heartbeat interval (RR) at the beat “N”. Then, we conducted experiments to form an estimating formula and to evaluate its estimation accuracy.

a) *Experiment*: We conducted experiments by using a bloodless and continuous hemomanometer (FINOMETER MIDI) on three subjects in their twenties (subject A, B, and C). Here, the hemomanometer can measure all the three factors. Then, we divided the experimental data into those for forming an estimating formula and for evaluating its estimation

accuracy for each subject. It should be noted that these experiments were approved by the research ethics committee of the University of Tokyo and the consent of each subject was obtained.

b) *Forming an estimating formula*: In order to estimate the SV, we formed a formula that consists of the above three factors, as defined in (11), and determined coefficients $A_1 \sim A_6$ by applying the least squares method to the data for forming an estimating formula. Here, $[]$ in the equation means that original data for each factor are divided by its corresponding mean value and made dimensionless.

$$[SV_{(N)}] = A_1 \times [SBP_{(N-1)}]^{A_2} \times [SV_{(N-1)}]^{A_3} \times [RR_{(N)}]^{A_4} \quad (11)$$

c) *Evaluating estimation accuracy*: Fig. 5 shows the estimation result where the estimating formula is applied to the data for evaluating the estimation accuracy for subject A. As shown in this graph, the estimation accuracy is good and determination coefficient (R^2) displays a high value (0.62). In addition, approximately 98% of the data are in the region where prediction errors are within $\pm 10 \text{ cm}^3$. Moreover, for subject B and C, the same kind of results was obtained. Hence, the estimation accuracy of the estimating formula (11) was guaranteed, and we decided to use this formula to calculate the SV and determine the inlet condition in the vascular model.

2) *Vascular model* \rightarrow *Cardiac model*: In the vascular model, based on cardiac blood pressure, heartbeat interval, and SV, pulse wave propagation in the arterial network is simulated. Here, in order to consider the effect of vascular system on cardiac system, we focused on the positions of the baroreceptors, which are pressure sensors of the cardiac system, in the arterial network.

Generally, baroreceptors which react to fluctuation of blood pressure are located at the aortic arch and carotid [6]. In Fig. 2, the aortic aorta corresponds to an artery “2” and the

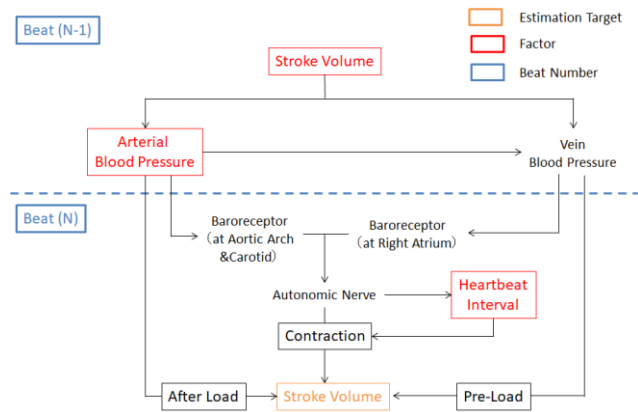


Fig. 4. Process for the determination of SV at a beat of number “N”

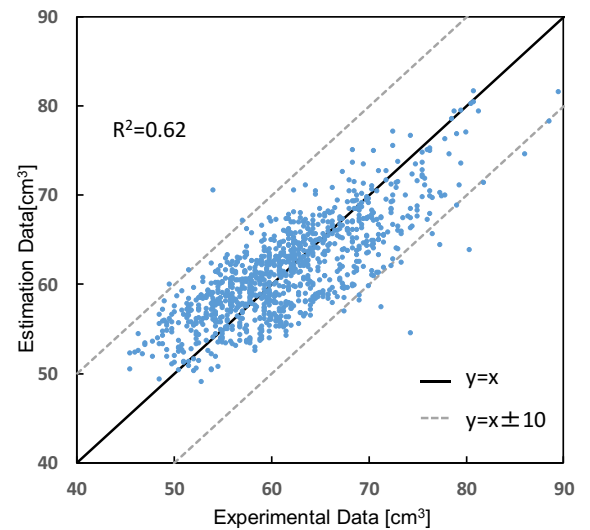


Fig. 5. Comparison of SV measured by experiment and obtained by estimation

carotid corresponds to arteries “5” and “15”. Therefore, we used the mean value of diastolic pressure of these three arteries as an input value to the cardiac model. Calculations for the next beat start based on this value.

D. Validation of the cardiovascular model

In this section, we examine if the cardiovascular model can reproduce blood pressure waveform in a real body.

Firstly, comparison of the calculated blood pressure waveforms at the ascending aorta and radial is shown in Fig. 6 (1), where the reflected wave (the 2nd peak) becomes more prominent and the rising phase is delayed further at the radial than at ascending aorta. This is due to peripheral resistance and these results comply with physiological knowledges.

Further, comparison of the calculated and measured blood pressure waveforms at the radial is shown in Fig. 6 (2), where the biological data, such as the systolic and diastolic blood pressures, peak phase, and heartbeat interval, are accurately calculated using the model.

Finally, the effect of autonomic nerves on the calculated blood pressure at the ascending aorta is calculated as shown in Fig. 6 (3), where blood pressure rises and heart beat interval decreases at the state of sympathetic nerves predominance. This result also corresponds with physiological knowledges.

Based on the above, we can say that the cardiovascular model can reproduce the real blood pressure waveform.

IV. EFFECT OF CARDIOVASCULAR CHARACTERISTICS ON HYPERTENSION

In this section, we examine the effects of cardiovascular characteristics on hypertension by using the cardiovascular model constructed in the preceding section. We focus on baroreceptor reflex, regulation of norepinephrine (Ne) concentration, and aortic stiffness. Here, the effect of aortic stiffness is examined to compare it with that of the other two characteristics (baroreceptor reflex and regulation of Ne concentration). First, we describe the role of each characteristic and then, we perform parameter study to examine the effects.

A. Cardiovascular characteristics

1) *Baroreceptor reflex*: As mentioned above, baroreceptors are blood pressure sensors and control the activities of the autonomic nerves (inhibit sympathetic nerves and promote parasympathetic nerves) in response to an increase in blood pressure. Therefore, failure in their functioning is considered one of the major causes of hypertension; however, there is no research which quantitatively evaluates this effect.

Baroreceptor reflex has two functions: (a) controlling the baroreceptor activity based on the detected blood pressure, and (b) controlling the activities of the autonomic nerves, both of which weaken by aging.

The function (a) is expressed in (1) as the two parameters, k_1 and k_2 , which are the proportional and derivative gains, respectively. If these parameters decrease, blood pressure

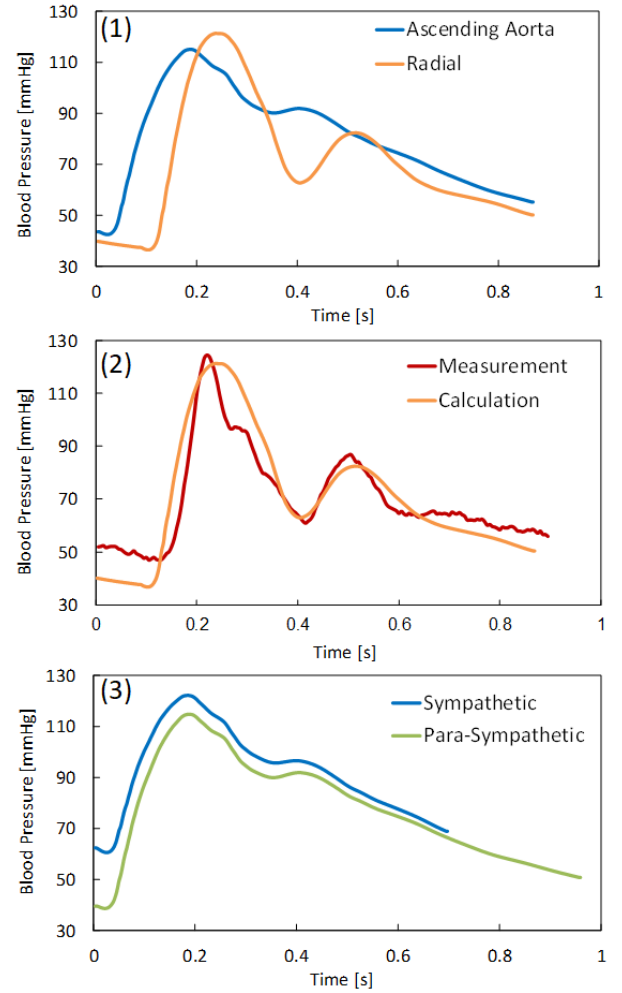


Fig. 6. Comparisons of blood pressure waveforms
 (1): Calculated waveforms at ascending aorta and radial
 (2): Calculated and measured waveforms at radial
 (3): Calculated waveforms at ascending aorta at the state of sympathetic and parasympathetic nerves predominance

cannot be controlled normally, which would lead to hypertension.

The function (b) is expressed in (2) as the parameters, k_s^b and k_p^b , which represent the effects of the baroreceptor activity on the autonomic nerves. If these parameters decrease, it becomes impossible to control the activity of the autonomic nerves, which would also lead to hypertension.

2) *Regulation of Ne concentration*: Norepinephrine (Ne) is a neurotransmitter of sympathetic nerves and its concentration increases with increase in sympathetic nerve activities. In addition, Ne stimulates sympathetic nerves, which constrict blood vessels [6].

In this study, to represent the condition where the Ne concentration is chronically high, we changed the time constants τ_{cNe} and τ_{vNe} in (4). If these two constants increase, the concentration decreases slowly, which would be a cause of hypertension.

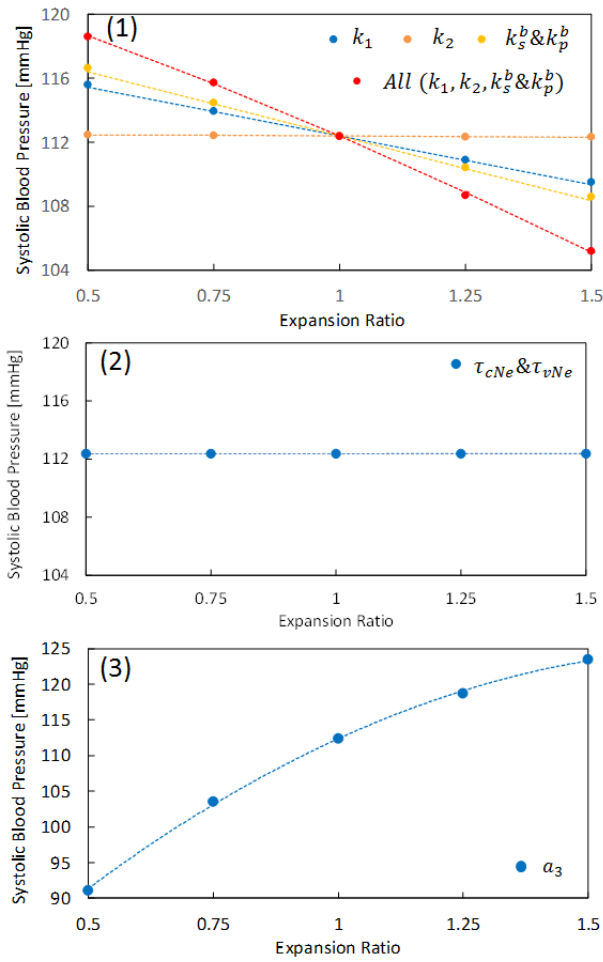


Fig. 7. Systolic blood pressure (SBP) in response to a change in the cardiovascular characteristics: (1) Baroreceptor reflex, (2) Regulation of Ne concentration, and (3) Aortic stiffness

TABLE I. Variation value of SBP for each characteristic

		Systolic Blood Pressure [mmHg]	
		Min	Max
Baroreceptor reflex	k_1	-2.87	3.22
	k_2	-0.05	0.11
	k_s^b and k_p^b	-3.75	4.28
	All	-7.18	6.23
Norepinephrine	τ_{cNe} and τ_{vNe}	-0.00	0.00
Aortic stiffness	a_3	-21.22	11.13

3) *Aortic stiffness*: As mentioned above, aortic stiffness is considered a major cause of hypertension. In the cardiovascular model, aortic stiffness is expressed in (10) as a parameter of f . In this study, to examine the effect of aortic stiffness on hypertension, we changed constant term a_3 of

ascending aorta, aortic arch, thoracic aorta and abdominal aorta.

B. Parameter study

In this section, we examine the effect of each cardiovascular characteristic on hypertension by changing the corresponding parameter. Here, each parameter is changed from 50 % to 150 % at an interval of 25 %.

Fig. 7 shows the SBP at the ascending aorta for the changing corresponding parameter, and Tab.1 summarizes the variation value of SBP for each characteristic. As shown in this, it was found that the functions which proportionally control the baroreceptor activity (expressed as k_i) and determine the activities of autonomic nerves (k_s^b and k_p^b) significantly affect the hypertension, the combination of which has pressure-rise effects equal to approximately 60% of those of aortic stiffness. On the other hand, it was also revealed that the functions which derivatively control the baroreceptor activity (expressed as k_2) and regulate Ne concentration have little influence.

V. CONCLUSIONS

In this study, we constructed a cardiovascular model where the interaction of the cardiac and vascular system was considered for the first time and examined the effects of cardiovascular characteristics on hypertension by using the model. The results obtained in this study are as follows:

- The functions which proportionally control baroreceptor activities and determine the conditions of the autonomic nerves have significant effects on hypertension. Such effects are comparable to the effect of aortic stiffness.
- Each of the functions which derivatively control the baroreceptor activities and determine concentration of norepinephrine has little contribution to a rise in blood pressure.

REFERENCES

- [1] Prospective Studies Collaboration, "Age-specific relevance of usual blood pressure to vascular mortality: a meta-analysis of individual data for one million adults in 61 prospective studies," *Lancet* 2002, vol. 360, pp. 1903-1913, December 2002.
- [2] M. Sakamoto et al., "Evaluation of the autonomic nervous activity based on transfer entropy of biological signals," *SICE*, 2012.
- [3] K. Kotani, Zbigniew R. Struzik, K. Takamasu, H. Eugene Stanley, and Y. Yamamoto, "Model for complex heart rate dynamics in health and disease," *Physical review E*, no. 72, vol. 4; pp. 1-8, 2005.
- [4] Olufsen, M.S, Peskin, C.S, Kim, W.Y, Pedersen, E.M, Nadim, A, and Larsen, J, "Numerical simulation and experimental validation of blood flow in arteries with structured-tree outflow conditions," *Annals of Biomedical Engineering*, vol. 28, pp.1281-1299, 2000.
- [5] K. Yasuda, S. Kaneko, "Numerical simulation of pulse wave propagation arteries with structured-tree outflow conditions," *ASME*, 2012.
- [6] T. Okada et al., "An introduction to cardiovascular physiology (5th edition)," *MEDSI*, 2013.

Impact of Enhancement Features on Image Registration for Liver Cancer Interventions using CT Images

Luu Manh Ha^{1,2}, Hoang Hong Son^{1,2}, Nguyen Hong Thinh^{1,2}, Adriaan Moelker³, Tran Duc Tan², Theo van Walsum³

¹ AVITECH Institute, University of Engineering and Technology, VNU, Hanoi, Vietnam

² Faculty of Electronics and Telecommunications, University of Engineering and Technology, VNU, Hanoi, Vietnam

³ Department of Medical Informatics and Radiology, Erasmus MC, Rotterdam, Netherlands

halm@vnu.edu.vn

list of abbreviations: CT, dCECT, iCECT, iDECT, CE_N, DE_N, DE_R

Abstract—In minimally invasive interventions for liver cancer treatment, image registration is a powerful technique to align diagnostic information, such as tumors and vessels, to the interventional images. In this paper, we investigate how the contrast-enhanced features in computed tomography (CT) images i.e. the tumors and the vessels, help the registration. For this, we de-enhance the contrast-enhanced CT image (iDECT) of the liver acquired during the intervention; and then we compare the accuracy of the registration between the diagnostic contrast-enhance CT image (dCECT) and the original interventional contrast-enhanced image (iCECT) versus the dCECT image and the de-enhanced image (iDECT). In addition, we use a rigidity term to improve the registration using the de-enhanced image. The method is evaluated on 11 clinical datasets.

Keywords—liver cancer; imageregistration; CT image; de-enhanced; Enhancement features; rigidity;

I. INTRODUCTION

Primary liver cancer is a severe disease and has become more common in developing countries in Southeast Asia [1]. Minimal invasive interventions under image guidance such as Radiofrequency ablation (RFA) and Cryoablation are typical for liver cancer treatments [1,2]. In an RFA procedure, an applicator (needle) is inserted into the tumor and destroys it by locally heating the tissues around the tip of the applicator, while in a Cryoablation procedure, the destruction of the tissues is performed in a locally freezing process using a cryoprobe. During these procedures using a CT imaging modality, both pre-operative images (diagnostic) and intra-operative images (interventional) are used to aid radiologists to localize the tumors, to guide them in placing the applicator [1,4]. Contrast agent use in CT is preferably limited because its use may cause harm to the kidneys. Also, contrast agent can be used only once during a CT acquisition but is readily excreted by the kidneys. Absence of contrast agent on the other hand results in poor visualization of the liver tumors and the liver vessels in the intra-operative CT images. Therefore interventional radiologist mentally maps the position of the tumors and the vessels from the pre-operative image to the

intra-operative images, which is inconvenient. Mental mapping may not be sufficiently accurate, because the liver changes its size and shape between the pre-operative section and the intra-operative section due to differences in patient pose and respiration.

Image registration is a powerful technique which may improve image guidance in the interventions, and could be a potential assistance or substitution for the mental mapping method [4,9]. In image registration, the pre-operative image non-rigidly deforms to match the intra-operative image. Subsequently, information of the liver tumors and the vessels in the pre-operative image can be transferred to the intra-operative image; hence, this helps the radiologist to obtain a better localization of the tumors and the vessels during the interventions.

There have been several image registration methods published in literature designed specifically for liver interventions. Elhawary et al. [1] proposed a non-rigid registration method using a B-spline based non-rigid transformation model to align diagnostic MRI image to intra-operative CT image. Archip et al. [2] introduced a finite element based method (FEM) to align diagnostic MRI images to intra-operative CT images of the liver for RFA. Wang et al. [9] described a registration method based on a biomechanical model for liver CT image. Our previous studies [4,5] used B-spline modelling to register liver CT images for liver RFA interventions.

Registration between contrast-enhanced CT images and non-contrast enhanced CT images may result in poor performance because a lack of corresponding information between the two images [6]. To the best of our knowledge, there has been no study investigating the impact of contrast enhancement features on registration of the liver CT images. As an extension of our previous study, this paper focuses on the evaluation of the impact of liver features, i.e. liver tumors and liver vessels, on image registration of the CT images acquired during minimally invasive liver interventions. In addition, we propose a registration approach to deal with the

problem caused by the lacking of the visibility of corresponding liver tumor and vessel features in the de-enhanced CT image (dCECT).

II. METHOD

In this section, we describe the methods to investigate the impact of the anatomic features on image registration. We first virtually remove the effect of contrast agent, which enhance the liver vessels and the liver tumors, from the intra-operative CT image (iCECT) using contrast de-enhancement method introduced in [6]. Secondly, we quantitatively evaluate two registration approaches: (1) registration CE_N between dCECT image and iCECT image; and (2) registration DE_N between the dCECT image and the iDECT image. The main difference in the two registrations is that both the dCECT image and the iCECT image are contrast-enhanced images in the portal-venous phase, while the iDECT image in the registration DE_N is the virtually de-enhanced CECT image. To this end, we describe a registration approach, called DE_R, for the dCECT- iDECT image registration using an additional rigidity term.

A. Image registration and impact of the contrast enhanced features

Image registration is a method which transforms a moving image $I_M(\mathbf{x})$ to match a target image $I_F(\mathbf{x})$ [4,7-9]. Mathematically, it is an optimization process which finds the best transformation $\mathbf{T}(\mathbf{x}) = \mathbf{x} + \mathbf{u}(\mathbf{x})$ that relates the two images such that the transformed moving image $I_M(\mathbf{T}(\mathbf{x}))$ spatially matches the target image $I_F(\mathbf{x})$ at every position of \mathbf{x} , where a similarity metric $M(I_F(\mathbf{x}), I_M(\mathbf{T}(\mathbf{x})))$ is used to quantify the quality of the match. In our study, we use the pre-operative image (dCECT) as the moving image and iCECT/iDECT image as the target image, and mutual information (MI) as the similarity metric for the registration.

The registration accuracy can be quantitatively evaluated using target registration error measurement (TRE) [4,7]. We use 8-15 pairs of landmark, manually annotated by a radiologist, at bifurcations of the liver vessels for the evaluation stage. Subsequently, TRE of the registration characterized by transformation \mathbf{T} is computed by the following equation:

$$TRE = \frac{1}{n} (\sum_{i=1}^n |a_i - \mathbf{T}(b_i)|) \quad (1)$$

where n is the number of pair of landmarks, and a_i, b_i denote landmark location in the dCECT and iCECT images correspondingly; and \mathbf{T} is the transformation of the registrations.

By comparing TRE of the registration of the dCECT images to the iCECT images versus that of the registration of the dCECT images to the iDECT images, we can verify the impact of the contrast-enhancement on the registration method.

B. Image registration with rigidity

Our hypothesis is that the registration of the dCECT images to the iDECT images has worse performance than the registration of the dCECT images to the iDECT images due to the absence of the corresponding features in the iDECT image.

As a result, the deformation inside the liver, e.g. at tumor regions and vessel regions may not reliable. Therefore, we use rigidity term [5,8]. This additional term restricts the deformation inside these regions; meanwhile it does not affect global non-rigid deformation of the moving image [8], thereby potentially improving the registration accuracy.

First, we segment the liver tumors and the liver vessels using the method proposed by Luu [10]. The liver tumor and liver vessel segmentations are used as a mask in dCECT image where deformation is locally restricted. Mathematically, the cost function of the registration can be written as:

$$C(\mathbf{T}; I_F, I_M) = -MI(\mathbf{T}; I_F, I_M) + \alpha R(\mathbf{T}; I_M) + \beta B(\mathbf{T}) \quad (2)$$

where $MI(\mathbf{T}; I_F, I_M)$ is mutual information between the moving image and the target image; $R(\mathbf{T}; I_M)$ is the rigidity term; $B(\mathbf{T})$ is the bending energy term; α and β are weights to balance both terms.

We also evaluate the accuracy of the registration using the rigidity term by using mean of squared difference measurement (MSD). The registration result of dCECT and iCECT images, i.e. the transformed dCECT image, is used as a reference ($I_R(\mathbf{x})$). The liver vessel segmentation and/or the tumor segmentation in the dCECT images are utilized as the region of interest to compute MSD of the output image of the registration with the reference image. The MSD measurements can be formulated as:

$$MSD = \frac{1}{m} \{ \sum_{i=1}^m (I_R(\mathbf{x}_i) - I_M(\mathbf{T}(\mathbf{x}_i)))^2 \} \quad (3)$$

where m is the total number of voxels inside the liver tumor and liver vessel segmentations of iCECT image; $I_R(\mathbf{x}_i)$ denotes intensity value of the voxel \mathbf{x}_i in the reference image (inside the segmentations); and $I_M(\mathbf{T}(\mathbf{x}_i))$ denotes intensity value of the voxel \mathbf{x}_i in the transformed moving image with transformation $\mathbf{T}(\mathbf{x})$ characterizing for either the DE_N or the DE_R registration.

III. EXPERIMENTS AND RESULTS

A. Data

We randomly selected 11 anonymized, portal-venous CT liver datasets of patients that underwent ablation therapy for liver tumors. The datasets were acquired on a Siemens CT Scanner in the Erasmus MC, University Medical Center Rotterdam.

The CT image resolution is 0.56 - 0.89 mm with slice spacing is 2.5-3 mm. The images were converted to mhd format with voxel intensity of the dataset ranging from 0 to 4096.

B. Registration framework

We used *Elastix*, an image registration framework, to perform the registration algorithms [7]. The parameter settings were chosen as in [5]. In this study, a manual annotated liver mask was used as region of interest for the liver registration [4,5]. All of the annotations and evaluations and visualization were performed by using Mevislab. The registrations and segmentations were performed using a 64 bit Window 7 PC

equipped with Intel Xeon quad-core 2.66 GHz and 16GB RAM.

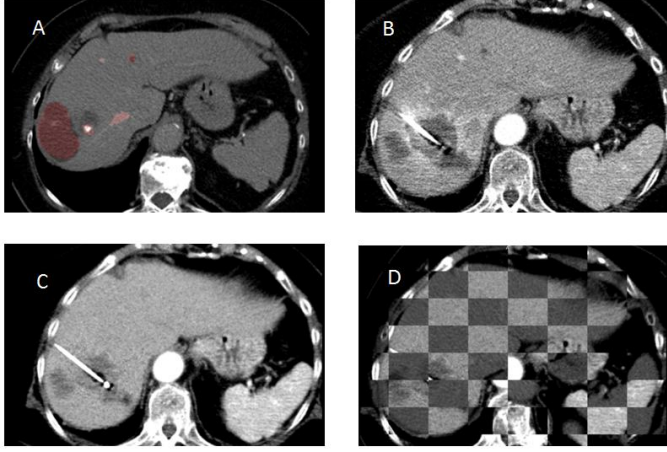


Fig. 1. Example of a registration result between adCECT image and aniDECT image. (A) is the dCECT image with the liver tumor and liver vessel segmentation. (B) the iCECT image. (C) the iDECT image. (D) checkerboard view of the transformed dCECT image and the iDECT image.

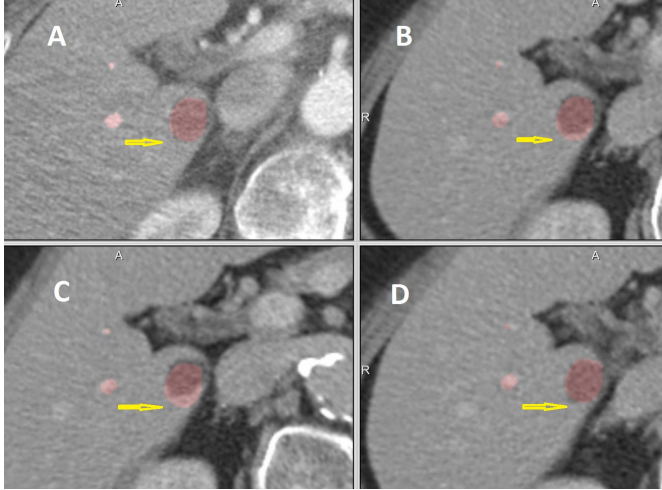


Fig. 2. Illustration of the difference at the tumors and the vessel regions by different registration methods: (A) aniCECT image overlaid with the tumor segmentation and the vessel segmentation; (B) the DE_R registration with the rigidity term; (C) is the DE_N registration; (D) is the CE_N registration. The arrows point out the tumor regions where the overlaps of the same tumor are different.

Figure 1 is an example of the registration using the rigidity term and Figure 2 is an illustration of the differences in performance at the tumor and vessel regions of the registration results.

C. Evaluation of registration result

1) Evaluation using TRE

The evaluation results for the registration methods mentioned in section II using TRE are illustrated in figure 3. The median values of TRE of the registrations using the iCECT image (CE_N), the iDECT image (DE_N) and the iDECT with rigidity term (DE_R) are 4.3 ± 2.5 mm, 5.7 ± 3.7 mm and $5.1 \pm$

3.07 mm respectively. Moreover, we performed paired T-test of the TRE results of the registrations using the iCECT image, the iDECT image and the iDECT with the rigidity term. The results are 0.0027, 0.178, and 0.001 suggesting that the TRE results of the registration using iCECT images is statistically significantly better than the registration using the iDECT images, and iDECT images with rigidity term, while the TRE results of the registrations using the iDECT images and using the dCECT images are not statistically significantly different.

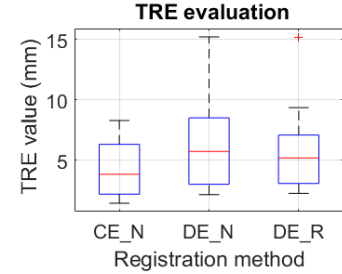


Fig. 3. Evaluation of the registration approaches using TRE.

2) Evaluation using MSD

Figure 4 illustrates evaluation result of the registration methods mentioned in section II using the MSD metric. The DE_N and DE_R registration methods have a mean of MSD of 23.75 ± 7.1 and 21.95 ± 7.2 respectively. A paired T-test comparing the two MSD results in $p=0.012$, implying that the difference inside the vessels and/or tumor regions is statistically significant.

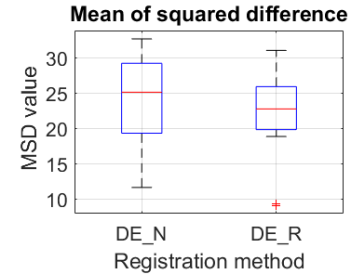


Fig. 4. Boxplot of MSD evaluation of the DE_N registration approach and the DE_R registration approach.

Table I contains the computational time for each registration strategy and the liver vessel segmentation processing time. The DE_R registration method requires additional liver vessel segmentation; its total computational time is approximately 20 minutes on average while the computational times of the CE_N and DE_N methods are approximately 2 minutes.

TABLE I. COMPUTATIONAL TIME

Method	Mean (sec)	Std (sec)
CE_N registration	126	29
DE_N registration	132	31
DE_R registration	925	112

<i>Method</i>	<i>Mean (sec)</i>	<i>Std (sec)</i>
Liver vessel segmentation	142	63

IV. DISCUSSION AND CONCLUSION

In this study, we evaluated the impact of the contrast-enhancement in liver CT imaging, used for image guidance in liver cancer interventions. We compared results of the registration between pre-operative image and intra-operative images, and its de-enhanced version where the effect of the contrast agent was removed. Subsequently, a registration approach with rigidity inside liver vessels and liver tumors was evaluated.

In section III.C.1, we found the median TRE values of the registrations CE_N, DE_N, DE_R are 4.3 ± 2.5 mm, 5.7 ± 2.9 mm and 5.1 ± 3.1 mm, respectively. Those are similar to the previous studies using a different dataset, i.e. a mean corresponding distance of 5.3 mm. Note that the slice spacing of the CT images is 2.5-3 mm. In addition, a result from our previous study showed that the intra-observer test for in-plane annotation error is around 1 mm [5]. Those errors account to some extent for the registration error in the evaluation stage. Using the T-test, the TRE value of the CE_N registration is statistically significantly different from the TRE values of the DE_N, DE_R registrations suggesting that contrast enhancement features, i.e. the liver vessels and liver tumors, are important factors to the registration. Thus, registration using unenhanced CT image may perform differently and this should be taken into account in future research.

The TRE values of the registration DE_N and DE_R are not statistically significantly different. We may conclude that the registration using rigidity term does not improve the accuracy at liver vessel bifurcations. We note that the rigidity term mainly affects the registration inside the liver tumors and liver vessels, thus it may not improve the registration in other regions.

From the MSD T-test in section III.C.2, we draw a conclusion that, in the region of interest, the output of the registration using the rigidity term has better similarity to the reference image inside the liver tumor and the liver vessels. Moreover, this conclusion also can be appreciated from Figure 2. Obviously, the liver tumor in the transformed pre-operative image by using transformation from the DE_R registration has better matching to those in the transformed pre-operative image using them from the DE_N registration. The reference image, i.e. the transformed pre-operative image using transformation from the CE_N registration, has the best visual matching with iCECT images. We note that the tumor in the pre-operative images and intra-operative images may be different in size because the intra-operative images are acquired 3 – 10 weeks after the diagnostic pre-operative images. As a result, the liver tumor may have grown and changed in appearance.

A limitation of the registration method using a rigidity term is its time consumption (approximately 20 minutes). However, in the near future, computation enhancing hardware (graphical

processing units) could be a potential solution which enables the use of the registration method in the interventions.

There are some limitations in our study. First, the number of data involved in this study is small. A limited number may cause bias in evaluation. However, based on the similarity to the registration results of other previous studies, we suppose that the data are representative for the evaluations. Second, the experiment was carried out on a single registration framework. Nevertheless, other intensity-based registration frameworks using mutual information may perform similarly to what experimented in our study.

In conclusion, we presented a study on the impact of contrast enhancement on image registration using CT images of the liver. The liver tumor and liver vessel regions have essential roles in the registration. Additionally, the registration between the contrast enhanced CT image and the de-enhanced CT image of the liver acquired during minimally invasive interventions can be improved by using the registration with a rigidity term. This registration method has the potential to improve tumor targeting and treatment outcome.

ACKNOWLEDGMENT

Theo van Walsum was supported by ITEA project 13031: Benefit.

REFERENCES

- [1] A. Mahnen, P. Pereira, T. Baere. "Interventional oncologic approaches to liver metastases". *Radiology*, 2013, 266(2): pp 407-30.
- [2] H. Elhawary, S. Oguro, K. Tuncali, P. Morrison, S. Tatli, P. Shyn, et al. "Multimodality non-rigid image registration for planning, targeting and monitoring during CT-guided percutaneous liver tumor cryoablation." *Academic radiology*, 2010, vol 17, no. 11, pp 34-44.
- [3] N. Archip, S. Tatli, P. Morrison, F. Jolesz, S. K. War eld, and S. Silverman, "Non-rigid registration of pre-procedural MR images with intra-procedural unenhanced CT images for improved targeting of tumors during liver radiofrequency ablations," *International Conference on Medical Image Computing and Computer-Assisted Intervention*, 2007, vol. 10, no. 2, pp. 969-977.
- [4] H. Luu, C. Klink, W. Niessen, A. Moelker, T. Walsum. "Non-Rigid Registration of Liver CT Images for CT-Guided Ablation of Liver Tumors." *PloS one*, 2016, vol 11, no. 9: e0161600.
- [5] H. Luu, C. Klink, W. Niessen, A. Moelker, T. Walsum. "An automatic registration method for pre- and post-interventional CT images for assessing treatment success in liver RFA treatment." *Medical physics*. 2015, vol. 42, no. 9, pp. 59-67.
- [6] H. Luu, H. Boulkhrif, A. Moelker, T. Walsum, "Registration evaluation by virtual unenhancing CT images," *submitted*.
- [7] S. Klein, M. Staring, K. Murphy, M. Viergever, J. Pluim. "elastix: a toolbox for intensity-based medical image registration." *IEEE transactions on medical imaging*, 2010, vol. 29, no. 1, pp. 196-205.
- [8] M. Staring, S. Klein and J. Pluim, "A Rigidity Penalty Term for Nonrigid Registration," *Medical Physics*, 2007, vol. 34, no. 11, pp. 4098-4108.
- [9] B. Wang, C. Ying, "Liver medical image registration based on biomechanical model." *Multimed Tools Appl*, 2017, vol. 76, no. 19 pp 19927-19944.
- [10] H. Luu, C. Klink, A. Moelker, W. Niessen, T. Walsum, "Quantitative evaluation of noise reduction and vesselness filters for liver vessel segmentation on abdominal CTA images." *Phys. Med. Biol*, 2015, vol 60, pp. 3905-3926.

Electronic Design of a Semi-Automated Micromanipulator Cell Injection System

Asad Hameed, Nabeel Kamal, Saad Bin Qaiser and
Osman Hasan
School of Electrical Engineering and Computer Science
National University of Sciences and Technology (NUST)
Islamabad, Pakistan
{asad.hameed, nabeel.kamal, saad.qaiser,
osman.hasan}@seecs.nust.edu.pk

Nasir Jalal
School of Pharmaceutical Science and Technology
Tianjin University
Nankai district, Tianjin, China
twaindoc@yahoo.com

Abstract— A cell microinjection system is a widely used tool in the domain of cell biology and it allows us to deliver a specific amount of substance into a cell using a fine tipped needle (or a microinjection pipette) under the observation of a microscope. Cell microinjection systems are widely used for delivering drugs to a single cell for the treatment of diseases, like Cancer, Alzheimer's, Sickle cell anemia and Cystic fibrosis etc., developing organs, like heart, lungs and kidney, and in-vitro fertilization. This paper surveys the state-of-the-art microinjection techniques and cell microinjections systems and proposes an electronic design for the semi-automated micro cell injection system, which works on the principle of capillary pressure microinjection (CPM). The distinguishing feature of the proposed system is its low cost without compromising on the accuracy or movement precision.

Keywords— *Micro Cell Injection; Capillary Pressure Microinjection; Micro Manipulation; Robotic Micromanipulation.*

I. INTRODUCTION

Cell Microinjection is a process in which a fine tipped needle (microinjection pipette) is inserted inside a cell to deliver a clearly predefined amount of substance. The substance is injected into the desired cell by holding it with the help of holding pipettes. Once the substance is injected, the injection pipette is removed from the cell. During the entire process the movements of holding the cell and microinjection pipettes are controlled by a micromanipulator, which is visually observed under a specialized microscope. The entire procedure is carried out with the help of a cell microinjection system.

A cell microinjection system is a widely used tool in the domain of cell biology and it allows us to deliver a specific amount of substance into a cell using a fine tipped needle (or a microinjection pipette) under the observation of a microscope. Cell microinjection systems are widely used for delivering drugs to a single cell for the treatment of diseases, like Cancer, Alzheimer's, Sickle cell anemia and Cystic fibrosis etc., developing organs, like heart, lungs and kidney, and in-vitro fertilization (commonly known as test tube babies).

Cell microinjection systems can be broadly classified in three categories: manual, semi-automated and full automated. Manual Microinjection systems, depicted in Figure 1, are the ones in which the operator performs cell microinjection manually with the assistance of several mechanical knobs. The position of the cell holding and injection / suction pipettes can be adjusted by rotating the mechanical knobs. Cell microinjection is a very delicate process and operators need several years of training to become proficient in performing microinjection. Despite such rigorous training, the success rate of manual microinjection is very low [2]. Operators need to spend hours in front of microscopes in uncomfortable positions to perform microinjection procedures manually. The main limitations of manual microinjection systems include low efficiency and poor reproducibility, which is a result of

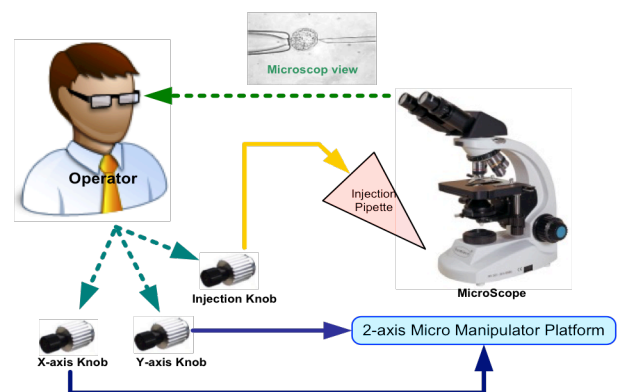


Fig. 1. Manually operated cell microinjection system

the fact that a slight vibration in human hands may cause undesired movements and wobbly effect during the procedure.

Semi-Automated Micromanipulator cell injection procedure is carried out using a micromanipulator controller a kind of joystick and an interactive graphical user interface (GUI) where the operator can see the real-time video on a computer screen as shown in Figure 2. Semi-automation is achieved through treating cell microinjection process as a computer game. The operator interacts with the system through a visual feedback device, such as monitor, and a

micromanipulator controller as a controlling device. Customized micromanipulator controller is designed as an input device for all motion commands that allows the operator to control the fine movements of the injection pipette through precise motorized control system. The wobbly effect in human hands can be overcome by deploying dedicated filters. The GUI allows the user to perform the microinjection with ease by just watching the monitor screen. It converts a tedious and exhausting manual microinjection task into a computer game. The interactive GUI for microinjection puts the operator in front of a computer screen instead of microscope and this new

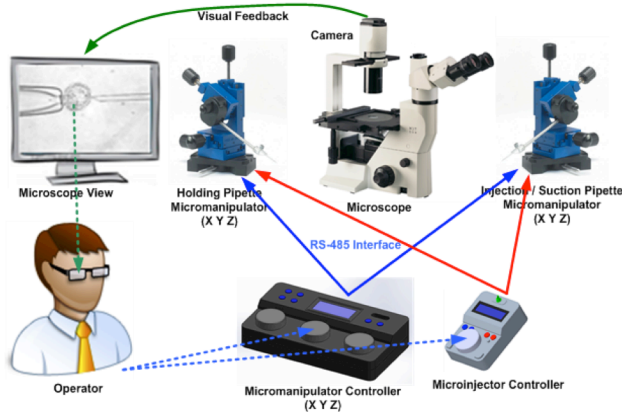


Fig. 2. Semi-Automated Micromanipulator Cell Injection System Block Diagram

position and operating environment is much more comfortable and user friendly. Semi-Automated system provides higher accuracy, which enables the operator to work in delicate narrow spaces with high precision.

In order to eliminate the errors made by humans and to perform cell microinjections more quickly and reliably, fully autonomous microinjection systems have also been recently proposed [3]. It starts with the acquisition of a real-time video from a Charge Couple Device (CCD) camera, which is then ripped off into multiple frames. The colored image is transformed to gray for enhanced image identification process. The Digital Image Processing (DIP) algorithms automatically identify the location and keep the track of cell nucleolus, injection and holding pipette from the grabbed frame. This DIP algorithm uses a state-of-the-art method for tracking pipette and cells in real time. Cells are then segmented using well-known image processing techniques. These accurate position coordinates are fed to a motion control algorithm, which decides the most optimum path to perform cell microinjection procedure without the direct involvement of human. However, most of these systems are still in the development stage and the ones that are developed do need some sort of human intervention.

In this paper, we provide a comprehensive tutorial and survey about the existing technologies used in the development of cell microinjection systems. The intent is to provide a comprehensive overview of the domain to facilitate further research and development in this multidisciplinary area

of research, involving mechanical, electrical and software engineering and biological sciences. To the best of our knowledge, there is no review of microinjection systems available in the literature.

The rest of the paper is organized as follows: We present various microinjection techniques in Section II. This is followed by a comprehensive literature survey of existing cell microinjection systems in Section III. Based on our literature survey, we propose an electronic design for a cost-effective and accurate semi-automatic cell injection system in Section IV. Finally, we conclude the paper in Section V.

II. MICROINJECTOR CONTROLLER

There are different types of microinjection techniques that are currently in use in various microinjection systems. The methods of delivery are based on different properties, such as chemical, optical, electrical and mechanical etc.

A. Chemical Based Systems

Chemically automated micro injector is an autonomous a micro fluidic device that does not need external electrical signals. It usually consists of chemically actuated micro injectors and micro fluidic networks. In some cases, the operation of the micro injectors depends on the change of volume of the oxygen bubbles produced by the hydrogen peroxide decomposition.

B. Optical Based Systems

Optical micro-injector is an ultrasonic actuator of silicon-nitride micro injectors. The injectors are longitudinally vibrated with tip velocities controllable by actuation frequency and voltage using piezoelectric actuators. Electro mechanical system (MEMS) based force sensors are used to measure the forces.

C. Electrical Based Systems

Electrical micro injectors, also called piezoelectric micro injectors, are controlled by electric current. So the voltage given will determine the force with which the injector is able to inject into a cell or pull out of a cell, without damaging the cell or causing cell death. Another type of electrically controlled method for injection is the cytoplasmic delivery method, which is unique as it manipulates transgenes using electrical forces. MEMS based devices use electrostatic charge to physically pick up transgenes and place them in the cytoplasm. From there, they are propelled and electroporated into the pronuclei by electrical pulses [13].

D. Mechanical Based Systems

Capillary pressure microinjection (CPM) allows penetrating a thin micro capillary on a cell membrane and thus delivering the filing liquid from the capillary to the cell. It is the most suitable technique that allows the injection of a large number of molecules [7]. Manually operated CPM is error prone and thus have a poor efficiency, and is susceptible to contamination [10]. It also comes with a risk of contamination

due to the involvement of human operators during the microinjection process [15].

III. STATE-OF-THE-ART

Microinjections have been used since early 1900s to facilitate micro manipulation of single cells [16] and suspended cells [4]. This mechanical technique has enabled massive advancements in the field of genetic engineering and transgenic. By far this technology has made possible the delivery of proteins, cDNA constructs, peptides, drugs and particles into transfection-challenged cells. Direct-pressure microinjection is an important tool for introducing a range of substances into the cytoplasm or nucleus of a cell. This procedure remains the most direct method to gain insights into the dynamics and functions of intracellular components, to produce transgenic organisms, or to overcome infertility and other such problems. Microinjection technique has been used for transgenic animal production, in vitro fertilization and RNA interference [16]. In 2007, this technique was used to inject a batch culture of embryo of zebra fish [10]. Blastocysts stem cell therapy was also enabled by designing a semi-automated microinjection system [11]. Manipulation of blastocyst had been used to create knocked-out or gene targeted-mice, which had genetically altered embryonic stem (ES) cells microinjected during the blastocyst stage into early embryo [12] introduced xanthine dehydrogenase gene of *Drosophila* into parental element along with an intact helper P-element which was microinjected into embryo deficient for this gene. Such embryos were used to develop flies with rosy colored eyes than mosaic eyes as in the first parental generation. Microinjection of *Xenopus* oocytes had also been made possible and rendered easier because of the large size of oocytes [14].

Recently a fully automated cell injection has been developed [1]. This system provides an automated methodology for in vitro cell injection using robotic systems and image processing by assembling commercially available micromanipulation systems and a GUI build in Open CV and C++. In this system, cells have been identified with the help of bright-field microscopy without using chemical markers. Use of Eppendorf FemtoJet micro injector and actuators make this system highly non-customizable and expensive. Similarly, an in-house microinjection system has been reported in [17] just to rotate a batch of oocyte to desired orientation. Using this system, the mechanical trajectory (MT) has been used for Injection Micropipette (IM) to calculate minimum exerted force for cell manipulation. This system helps scientists to orient batch of oocytes without any mechanical deformation and accuracy. But this system cannot perform injection or extraction from a single cell. Another microinjection system has been reported in [9] for studying the mechanical behavior of cells. This system has been assembled using commercial actuators and injectors that make it a bit unattractive based on the “ease of manufacturing” and cost point of view.

There are various other components of a microinjection system including an inverted light microscope, micromanipulator, micropipette holder, gas pressure regulator, micropipette puller, glass capillary tubing, micrometer syringe and vibration isolation table [5]. More elaborate systems can be assembled according to the experimental needs of the investigator, e.g., specimen incubator, CCD (charge-coupled device) camera, digital image processing software and computer.

IV. PROPOSED MICRO INJECTION SYSTEM

The biggest limitation of existing microinjection systems, in terms of using them in a developing nation like Pakistan, is their huge costs. The purchase of these systems not only requires a significant amount of foreign exchange upfront but also a hefty after sales support cost. Just a disposable needle can cost as much as \$1000, while the whole system could cost somewhere close to \$100,000. This constraint disallows the scientists of developing nations to compete with the rest of the world and to test their locally manufactured synthesized drugs on cellular cultures. The system, proposed in this paper, is expected to cost around \$5000 and due to the local design and manufacturing the aftersales support would cost a fraction of the cost in the case of imported solutions.

A semi-automated micro-injection has two main components; a cell holding pipette, and a cell injection/suction micropipette. The cell injection/suction micropipette is used to deliver contents into the cell or sub-cellular compartment and the needle is removed. The whole procedure is performed under a micromanipulator setup. The semi-automated system requires high efficiency and experience to obtain desirable results [8]. However, even all the training and experience did not produce desired results and the survival rates of microinjected cells were often found to be ranging from 40% and 70% [6]. Therefore, while minimizing the cost, another major objective of the system is to improve on the accuracy and precision of the system.

A mechanical setup has been designed, as shown in Figure 3, for the Semi-Automated micro cell injection. Two sets of micromanipulators have been placed on both sides of the OPTIKA IM-2 microscope for the injection and holding purposes.

The position coordinates of a cell holding and a cell injection/suction pipette micromanipulators are governed by the Micromanipulator Controller whereas the pressure of the

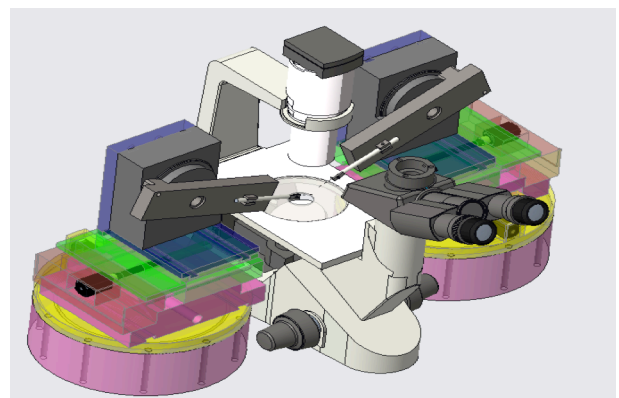


Fig. 3. Semi Automated Micro Cell Injection System

cell holding and cell injection/suction pipettes are managed by the Microinjector Controller. The operator controls the controllers by observing the microscope view on the monitor.

The primary task of the Mechanical Interface is to track the movements made by an operator's hand and to transfer this data to the Micromanipulator and Microinjector with high precision. The purpose of developing customized Micromanipulator Controller and Microinjector Controller is to facilitate the operator in performing the entire procedure. The two input mechanical interface devices "Micromanipulator Controller" and "Microinjector Controller" are depicted in Figures 4a and 4b, respectively.



Fig. 4. Overview of Controlling Devices of Micromanipulation and Microinjection. (a) Micromanipulator Controller (b) Microinjector Controller

The electrical design related aspects of the proposed system are discussed in following sections. The system primarily comprises of Micromanipulator Controller Interface, Micromanipulator Controller Interface Unit, Communication Link, Micromanipulator Drive Unit and Micromanipulator as shown in Figure 5.

A. Micromanipulator Controller Interface

The Micromanipulator Controller Interface consist of three rotary knobs, one LCD and seven buttons. The rotary knobs

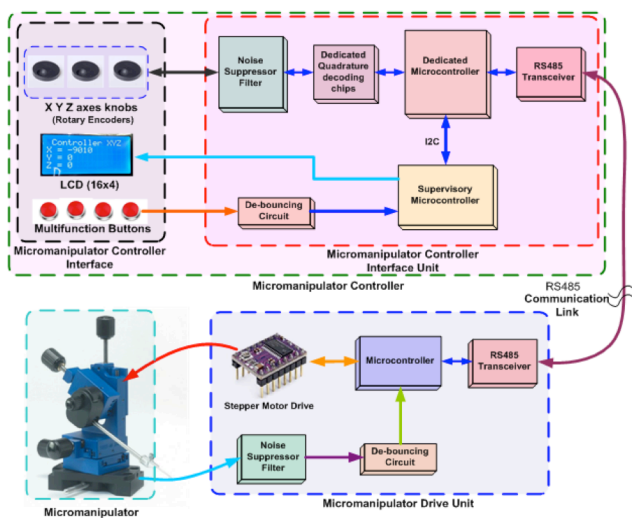


Fig. 5. Micromanipulator System Block Diagram

are directly coupled to position sensing sensors. The optical encoders precisely track the hand movement. The buttons and

LCD allows the operator to adjust the operating parameters according to the operating conditions.

B. Micromanipulator Controller Interface Unit

The micromanipulator controller interface unit mainly comprises of five key components. The noise suppressor filter is fundamentally a passive low pass filter that eliminates any high frequency noise contents caused by the switching of inductive electrical loads. The dedicated quadrature decoding chip decodes the optical encoders position signals and feeds it to the microcontroller for further computation. The microcontrollers are configured in master-slave topology and are responsible for performing all the key tasks, i.e., reading the knobs position, performing all the computations, displaying the position coordinates on LCD, converting the data according to the customized protocol and transmitting it to the Micromanipulator Drive Unit. The RS-485 transceiver converts the TTL signal into a differential signal. The de-bouncing circuit discards any false signals generated due to the mechanical contacts of the switch. The input devices fabricated circuit boards are depicted in Figure 6.

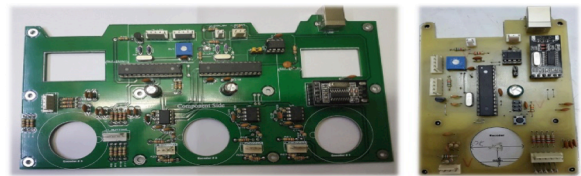


Fig. 6. Micromanipulator and Microinjector Controllers Circuit Boards

C. Communication Link and Customized Protocol

The RS-485 bus standard communication is selected for our system because of its wide acceptance in industrial and instrumentation applications. The differential transmission ability of RS-485 makes it noise immune, compatible for long distance communication and ensures a reliable link. The half-duplex communication mode is pertained because most of the data flows from the controllers to the manipulators. The data transmission baud rate of 230.4kb/s is selected and to transmit one character serially 10 bits (start 1 bit + data 8 bit + stop 1 bit) are required. The maximum character transmission frequency can be calculated as 23040 characters per second with the baud rate of 230.4kb/s.

D. Micromanipulator Drive Unit:

The main task of the Micromanipulator Drive Unit (MDU) is to drive the micromanipulator actuators in a controlled manner. It gets the position coordinate commands from the micromanipulator controller then translates the RS-485 bus communication standard to TTL UART and feeds it to the microcontroller. The microcontroller extracts the position information and computes the stepper motor drive signals by applying the position control algorithm. The proximity sensors mounted on each axis of micromanipulator sends the data to microcontroller through the noise filter and de-bouncing circuit. Finally, the stepper motor driver drives the stepper motor. The stepper motor drive is configured in 1/16 micro stepping modes. The motor can complete one revolution in 16

$\times 200 = 3200$ steps with a resolution of $360^\circ / 3200 = 0.1125$ degrees / step. The MDU PCB artwork and fabricated circuit board is depicted in Figure 7.

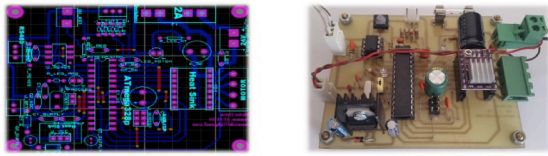


Fig. 7. Micromanipulator Drive Unit PCB Artwork and Fabricated PCB

MCI system comprises of 8 independent Micromanipulator Drive Units, out of which 3 MDUs are dedicated for cell holding pipette micromanipulator, 3 MDUs are devoted for cell injection/suction pipette micromanipulator and remaining 2 MDUs are committed for holding pipette and injection/suction pipette pressure generation. Each MDU represents a degree of freedom (DoF) of the micromanipulator. All Micromanipulator Drive Units are replica copy of each other. They are tuned independently as all of them performs different task.

E. Micromanipulator:

The micromanipulators are the mechanical components with the help of which cell injection procedures are performed. In each micromanipulator there are three motors and six limit switches, i.e. one motor and two limit switches for each axis. The motors play a significant role in accurately maneuvering the micromanipulator platform and the microinjection pipette with high accuracy. For precise movements, we have selected fine motion stepper motors to drive the actuation mechanism. The limit switches inform the MDU when certain axis reaches its maximum limit. The motors are directly coupled to the lead screw based mechanical mechanism. The pitch of the lead screw is chosen as 1mm, i.e., it can travel a distance of 1mm in one complete revolution. The resolution of the micromanipulator platform is $1\text{mm} / 3200 = 0.3125\mu\text{m} \approx 0.5\mu\text{m}$ per step. The maximum speed of the motor can be calculated as 23040 steps per second with the transmission baud rate of 230.4 kb/s, i.e., $23040 / 3200 = 7.2$ revolutions / second = 432 RPM or 2592 degree per second. The maximum speed of the linear stage is $7.2 \times 1\text{mm} = 7.2\text{mm}$ per second = $7200\mu\text{m}$ per second.

V. CONCLUSIONS

Cell microinjection systems are widely used to conduct cell biology experiments. In this paper, we present a comprehensive overview of a cell microinjection system and its underlying technologies and kinds. This information can play a vital role in the design of next generation cell microinjection systems as, to the best of our knowledge, no system level design specifications for a cell microinjection system exists in the literature. Moreover, we have proposed an electronic design of a semi-automatic cell microinjection system in this paper. The simple and robust mechanisms, the usage of locally available hardware components and in-house

fabrication of customized micromanipulators has contributed towards the reduction of the overall cost of the proposed system and without compromising on the accuracy and precision. We are currently manufacturing the mechanical components of a semi-automated system to be able to test the proposed electronic design in the real-world setting.

REFERENCES

- [1] G. Becattini, L.S. Mattos, and D.G. Caldwell. 2014. A Fully Automated System for Adherent Cells Microinjection. *IEEE J. Biomed. Heal. Informatics* 18, 1 (January 2014), 83–93.
- [2] D.H. Kim, S. Yun, and B. Kim. 2004. Mechanical force response of single living cells using a microrobotic system. In *IEEE International Conference on Robotics and Automation, 2004. Proceedings. ICRA '04. 2004*, 5013–5018 Vol.5.
- [3] E. Hodneland, N.V. Bukoreshtliev, T.W. Eichler, Xue-Cheng Tai, S. Gurke, A. Lundervold, and H.-H. Gerdes. 2009. A Unified Framework for Automated 3-D Segmentation of Surface-Stained Living Cells and a Comprehensive Segmentation Evaluation. *IEEE Trans. Med. Imaging* 28, 5 (May 2009), 720–738.
- [4] H.B. Huang, Dong Sun, J.K. Mills, and Shuk Han Cheng. 2009. Robotic Cell Injection System With Position and Force Control: Toward Automatic Batch Biomanipulation. *IEEE Trans. Robot.* 25, 3 (June 2009), 727–737.
- [5] Y. Komarova, J. Pelloquin, and G. Borisy. 2011. Components of a microinjection system. *Cold Spring Harb. Protoc.* 6, 8 (2011), 935–939.
- [6] R. Kumar, A. Kapoor, and R.H. Taylor. 2003. Preliminary experiments in robot/human cooperative microinjection. In *Proceedings 2003 IEEE/RSJ International Conference on Intelligent Robots and Systems (IROS 2003)* (Cat. No.03CH37453), 3186–3191.
- [7] J. Kuncova and P. Kallio. 2004. Challenges in capillary pressure microinjection. In *The 26th Annual International Conference of the IEEE Engineering in Medicine and Biology Society*, 4998–5001.
- [8] J.H. Lee, S.M. Jeong, B. H. Lee, H.S. Noh, B.K. Kim, J. Kim, H. Rhim, H.C. Kim, K.M. Kim, and S.Y. Nah. 2004. Prevention of ginsenoside-induced desensitization of Ca^{2+} -activated Cl^- current by microinjection of inositol hexakisphosphate in *Xenopus laevis* oocytes: Involvement of GRK2 and arrestin I. *J. Biol. Chem.* 279, 11 (March 2004), 9912–9921.
- [9] F. Liu, D. Wu, and K. Chen. 2013. Mechanical behavior of cells in microinjection: A minimum potential energy study. *J. Mech. Behav. Biomed. Mater.* 24, (August 2013), 1–8.
- [10] Z. Lu, P.C.Y. Chen, J. Nam, R. Ge, and W. Lin. 2007. A micromanipulation system with dynamic force-feedback for automatic batch microinjection. *J. Micromechanics Microengineering* 17, 2 (February 2007), 314–321.
- [11] L. Mattos, E. Grant, and R. Thresher. 2006. Semi-automated blastocyst microinjection. In *Proceedings 2006 IEEE International Conference on Robotics and Automation, 2006. ICRA 2006.*, 1780–1785.
- [12] G. Rubin and A. Spradling. 1982. Genetic transformation of *Drosophila* with transposable element vectors. *Science* (80-.). 218, 4570 (October 1982), 348–353.
- [13] A. Tsoukalas and A. Tzes. 2011. Modelling and Adaptive Control of Nanowire-Driven Micromanipulators. *J. Intell. Robot. Syst.* 62, 3–4 (June 2011), 419–450.
- [14] M. P. Wickens and R. A. Laskey. 1981. Expression of cloned genes in cell-free systems and in microinjected *Xenopus* oocytes. (1981).
- [15] Z.X. Xi, X. Li, J. Li, X.Q. Peng, R. Song, J. Gaal, and E.L. Gardner. 2013. Blockade of dopamine D_3 receptors in the nucleus accumbens and central amygdala inhibits incubation of cocaine craving in rats. *Addict. Biol.* 18, 4 (July 2013), 665–677.
- [16] Y. Zhang and L.C. Yu. 2008. Microinjection as a tool of mechanical delivery. *Curr. Opin. Biotechnol.* 19, 5 (2008), 506–510.
- [17] Q. Zhao, M. Sun, M. Cui, J. Yu, Y. Qin, and X. Zhao. 2015. Robotic Cell Rotation Based on the Minimum Rotation Force. *IEEE Trans. Autom. Sci. Eng.* 12, 4 (October 2015), 1504–1515.

Resource Allocation in PDMA with Wireless Information and Power Transmission

Chang Wang², Jie Zeng¹, Bei Liu¹, Mingyao Peng³, Xin Su¹, Shihai Shao² and Qi Liu⁴

¹ Tsinghua National Laboratory for Information Science and Technology
Research Institute of Information Technology, Tsinghua University, Beijing, China

² National Key Laboratory of Science and Technology on Communications
University of Electronic Science and Technology of China, Chengdu, China

³ Broadband wireless access laboratory of Communication and Information Engineering
Chongqing University Of Posts And Telecommunications, Chongqing, China

⁴ China Unicom, Beijing, China
Email: suxin@tsinghua.edu.cn

Abstract—With the development of the fifth generation (5G) wireless systems, the mobile medical will face a profound change. Pattern division multiple access (PDMA) is a novel non-orthogonal multiple access scheme proposed to increase throughput and the number of connections by combining the design of transmitters and receivers. In this paper, we propose a resource allocation scheme to achieve the trade-off between rate and energy. In our system model, we also exploited energy harvesting to optimize the efficiency of the entire system, although this make it harder to solve the problem. To figure out the problem, an iterative algorithm based on optimized power allocation and the pattern matrix is proposed to improve the performance of downlink PDMA networks. Simulation results show that the proposed algorithm needs less total transmitting power when reaching the same rate and energy value.

Index Terms—pattern division multiple access (PDMA), medical communication, energy harvesting, pattern matrix.

I. INTRODUCTION

The fifth generation (5G) wireless systems is the next step in the development of mobile communications and is expected to be implemented by 2020. The goal of 5G is to provide connectivity for any type of device and any type of application that may benefit from the connection, including mobile connections for various objects in both humans and user environments[1]. In order to improve spectral efficiency and peak data rate, four generations of mobile communication systems have been designed. It is foreseeable that other standards such as energy efficiency or radiation exposure will also play an very important role in the design of such communication systems. Computer technology, modern devices and ICTs bring e-health to healthcare solutions, and the integration of portable devices, medical sensors and mobile computing in a healthy environment makes mobile healthcare a mobile health space. Mobile healthcare (M-health) is a model of combined healthcare and the latest in wireless communication technology, a constantly evolving paradigm.[2]. Since the introduction of mobile broadband networks, many mobile health scenarios

have been successfully deployed around the world to meet the vision of popularizing connected healthcare anytime, anywhere[3]. It is well known that the development of fourth generation (4G) wireless systems will have a significant impact on future m-health applications that require medical diagnostic quality with high transmission rates and high reliability[4]. It is foreseeable that in the realization of 5G, electronic health will face greater changes. By 2020, when the 5G is implemented, the number of devices can reach tens or even hundreds of billions. In order to be able to achieve this connectivity, high data rates, low latency, and very high device densities must be met. The 5G should include an innovative set of technologies that are directed through the introduction of the telemedicine IoT and the latest developments or improvements in the biomedical arena Fifth Generation Health Care Applications and Services Paradigm. In order to give full play to the advantages of Content-Centric Networking (CCN),[5] proposed a WBG 5GCCN architecture based on the Internet of Things. This 5G-CCN framework provides the right conditions for e-Health communications, with regard to how low-cost, low-power devices can improve the quality of life of people with chronic or emergency problems. Increased security with the concept of digital signatures that protect the privacy of patient medical data. The Internet of Things using various sensors and smart medical devices can be used, for example, for tele-auscultation, remote health monitoring, remote diagnostics and possible treatments, and geriatric care. Medical Internet of Things (IMedT) refers to the Internet of Things (IoT) specifically used in health field[6]. IMedT is expected to reduce consulting and transportation costs and narrow the gap among those living in isolated areas where physicians are not working. 5G Healthnet is a cloud framework for storing medical records that is encrypted with a two-key algorithm and wirelessly authorized for access. If the patient has been monitoring and diagnosis, you can save a lot of life in time. Therefore, the integration of 5G with WBSNs may be the best solution for

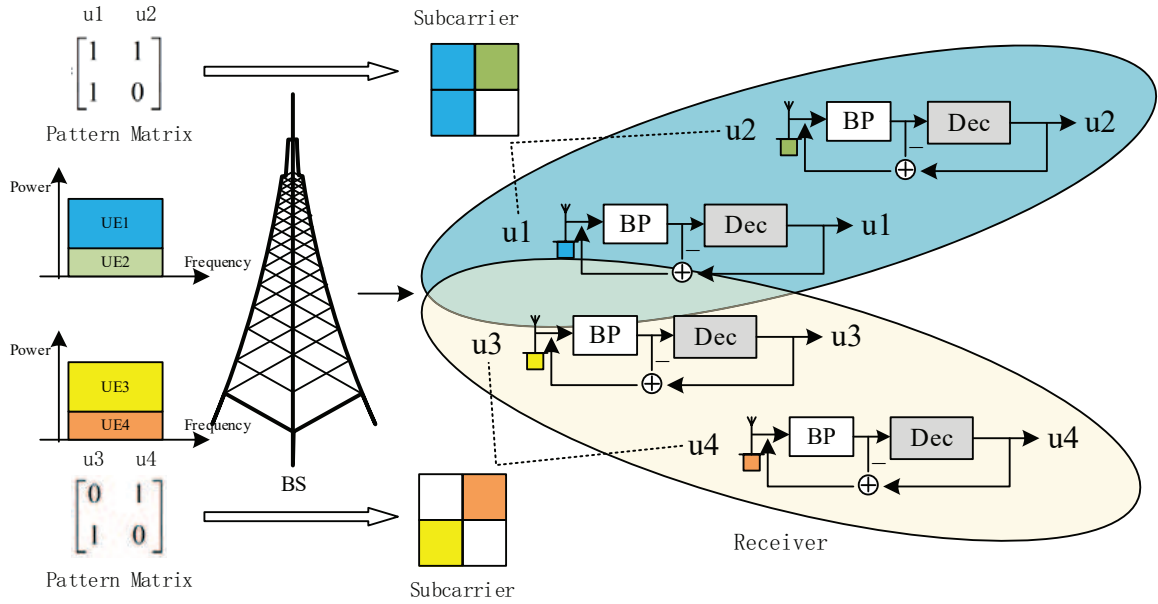


Fig. 1. the system model of downlink PDMA.

telemedicine applications[7]. The evolution of 5G networks is a key part of the rapid spread of M2M communications and the Internet of Things (IoT). The future of 5G can play an important role in improving the medical experience, including remote monitoring of health data, robotic-assisted remote surgery and the management of hospital assets.

As a key technology of 5G, pattern division multiple access (PDMA) technology can greatly improve the performance of wireless system, but also can communicate with multiple users in the same frequency band[8]. 5G technology has the following key features, including very low latency, long battery life, security, bandwidth scalability, network capacity and a large number of devices. All of these capabilities make 5G technology a more useful method of real-time health monitoring. This paper presents a scheme to achieve the rate and energy balance in a PDMA system. Compared with other schemes, the same transmission information can be used to lower the power and reduce the radiation. The rest of this article is organized as follows. In section II, we introduce the proposed system model of tradeoff between rate and energy. In section III, we propose an iterative search algorithm to solve this model. In section IV, we made a comparative analysis of the proposed algorithm. Finally, the conclusion illustrates the superiority of our proposed algorithm in section V.

II. SYSTEM MODEL AND PROBLEM FORMULATION

A. System Model

We assume a downlink PDMA system with one base station (BS), K users, N subcarriers. Each subcarrier transports L ($L < N$) non-zero entries at most. The mapping relationship is determined by the pattern matrix G , where

$g_{k,n} = 1$ if user k uses the n th subcarrier, otherwise $g_{k,n} = 0$. In PDMA, due to the sparseness of the PDMA pattern matrix, multi-user data can be transmitted on the same subcarrier at the same time. To quantify this process in detail, we let $P = (P_{k,n})$ denote the power allocation, which the $P_{k,n}$ represents the transmit power of user k using the n th subcarrier. Thus, the total transmit power of the BS is $P^{tot} = \sum_{k=1}^K \sum_{n=1}^N g_{k,n} P_{k,n}$.

In order to more clearly explain the PDMA system operation process, we draw a simple model in Figure 1. In this short paragraph, we will highlight the distinctiveness of the pattern matrix, which is significantly different from other multiple-access techniques. Data streams of multiple users can be multiplexed onto a same subcarrier for non-orthogonal transmission by different PDMA patterns, and the PDMA system uses patterns matrix to define a sparse mapping from data streams to a subcarrier[9]. This pattern matrix is usually expressed by a binary vector. "1" in the vector indicates that the data is mapped to the subcarrier corresponding to the resource group, $G_{PDMA}^{[N,K]}$ commonly used, for convenience, usually abbreviated as G . In order to understand, we give the process of four user receive data from base station in the figure. Each user is marked with a different color. First, the PDMA system gives the resource allocation strategy according to the preset algorithm, that is, the power allocation scheme and the pattern matrix. Then, the user's data is mapped to the corresponding subcarriers according to the pattern matrix, and then the corresponding power is matched according to the power allocation parameter of each user. At the receiver, each user receives all the data, and then destroys the signal they need based on successive interference cancellation. Other interfering signals can be used for energy harvesting.

Without loss of generality, we assume that both the base station and the user equipment have only one antenna, the PDMA pattern corresponding vectors of each user are $g_1 = [1, 1, 1, 1]^T$, $g_2 = [1, 1, 1, 0]^T$, $g_3 = [1, 0, 1, 0]^T$ etc. Then the data received by user k in the downlink of PDMA system can be written as follows.

$$\mathbf{y}_k = \text{diag}(\mathbf{h}_k) \sum_{k=1}^K \mathbf{g}_k x_k + \mathbf{n}_k = \text{diag}(\mathbf{h}_k) \mathbf{G} \mathbf{x} + \mathbf{n}_k \quad (1)$$

where $\mathbf{h}_k = [h_{1,k}, h_{2,k}, \dots, h_{N,k}]^T$ represents the channel response for user k , $h_{n,k}$ represents the channel gain of user k on the n th resource. $n_{k,n}$ represents the noise power received by each user. Set $H_k = \text{diag}(h_k) G_{PDMA}^{[N,K]}$, $x = [x_1, x_2, \dots, x_K]^T$, (1) can be written as

$$\mathbf{y}_k = \mathbf{H}_k \mathbf{x} + \mathbf{n}_k, k = 1, 2, \dots, K \quad (2)$$

For power allocation to a designated user, the transmitting power P^{tot} is finally allocated to the corresponding subcarrier. However, unlike the OFDMA network, the size of the transmitting power $p_{k,n}$ is determined according to a given pattern matrix G and power allocation factor $\alpha_{k,n}$ ($0 < \alpha_{k,n} < 1$ when $g_{k,n} = 1$ and $\alpha_{k,n} = 0$ when $g_{k,n} = 0$). Without loss of generality, we suppose that the receiver decodes from user 1 to user K in order. According to the PDMA downlink system model introduced earlier, the signal-to-noise ratio (SNR)[10] of user k when using the n th subcarrier can be expressed as

$$\Gamma_{k,n} = \frac{\alpha_{k,n} p_{k,n} h_{k,n}}{\sigma_k^2 + \sum_{k'=k+1}^K \alpha_{k',n} p_{k',n} h_{k',n}} \quad (3)$$

where σ_k^2 is the noise power and $h_{k,n}$ is the channel gain from the BS to user k on subcarrier n .

According to the power allocation method in [11], each user k can decode his own information from its own signal, and harvest energy from all the signals it receives. Therefore, the data rate of user k is

$$R_k = \sum_{n=1}^N \frac{g_{k,n}}{2} \log_2(1 + \rho_k \Gamma_{k,n}) \quad (4)$$

where ρ_k is the power allocation ratio for information decoding. Accordingly, the harvested energy of user k is given by

$$E_k = \zeta_k (1 - \rho_k) \sum_{k'=1}^K \sum_{n=1}^N \alpha_{k',n} g_{k',n} p_{k',n} h_{k',n} \quad (5)$$

where $0 < \zeta_k < 1$ represents the energy conversion efficiency.

B. Problem Formulation

The weighted rate and energy maximization problem by considering power allocation P , pattern matrix G , and power coefficient ρ_k is formulated as

$$\begin{aligned} \max_{P, G} \quad & \sum_{k=1}^K w_k^r R_k + \sum_{k=1}^K w_k^e E_k \\ \text{s.t.} \quad & C1: R_k \geq R_k^{req}, \forall k \\ & C2: P^{tot} \leq P^{\max} \\ & C3: \sum_{k=1}^K g_{k,n} \leq D, \forall n \\ & C4: \sum_{k=1}^K \alpha_{k,n} \leq 1, \forall n \\ & C5: \alpha_{k,n} \in [0, 1] \\ & C6: p_n \geq 0, \forall n \\ & C7: 0 \leq \rho_k \leq 1, \forall k \end{aligned} \quad (6)$$

Where w_k^r and w_k^e are weighted coefficients.

In (6), C1 specifies the rate requirement for each user, C2 limits the maximum power transmitted by the BS, C3 guarantees that each subcarrier can not be multiplexed beyond a certain value D , and C4 and C5 together represent the power allocation among multiple users.

III. DESCRIPTION OF PROPOSED ALGORITHM

In this section, an iterative search algorithm based on Karush-Kuhn-Tucker (KKT) conditions and Lagrange multiplier is proposed to solve 6. The algorithm optimizes the power allocation ratio and resource allocation through iteration, so that the target value increases continuously until convergence.

A. Optimization for the Power Allocation Ratio

Give the resource allocation strategy $\{P, G\}$, the original problem (6) can be decomposed into K independent sub-problems, each of which can be expressed as

$$\begin{aligned} \max \quad & w_k^r R_k + w_k^e E_k \\ \text{s.t.} \quad & C1: R_k \geq R_k^{req}, \forall k \\ & C7: 0 \leq \rho_k \leq 1, \forall k \end{aligned} \quad (7)$$

To learn more about how ρ_k affects system work, we analyze the closed expression of each ρ_k and describe it in detail later. The optimal power splitting ratio ρ_k for (7) is given by

$$\rho_k^* = \begin{cases} \bar{\rho}_k, & \text{if } \hat{\rho}_k < \bar{\rho}_k \\ \hat{\rho}_k, & \text{if } \bar{\rho}_k \leq \hat{\rho}_k \leq 1 \\ 1, & \text{if } \hat{\rho}_k > 1 \end{cases} \quad (8)$$

where $\bar{\rho}_k$ and $\hat{\rho}_k$ are solutions of the following two equations (which can be tackled by dichotomy).

$$\sum_{n=1}^N g_{k,n} \log_2(1 + \bar{\rho}_k \Gamma_{k,n}) = R_k^{req} \quad (9)$$

$$\sum_{n=1}^N \frac{w_k^r g_{k,n} \Gamma_{k,n}}{\ln(4)(1 + \hat{\rho}_k \Gamma_{k,n})} = Q_k \sum_{k'=1}^K \sum_{n=1}^N \alpha_{k',n} g_{k',n} p_{k',n} h_{k',n} \quad (10)$$

where $Q_k = w_k^e \zeta_k$

Lemma 1 illustrates the user's state at different values of ρ_k . Detailedly, when $\hat{\rho}_k < \bar{\rho}_k$, User k requires energy,

so most of the power is used for energy harvesting, except for the energy used to meet the minimum requirements. Nevertheless, in the case of $\hat{\rho}_k > 1$, User k prefers to obtain a higher data rate, so all the received energy is used for information decoding. In other cases, the power partition coefficient should be optimized in order to achieve a balance between data rate and energy harvest.

B. Optimization for the Resource Allocation

When ρ is confirmed, the model is still a mixed integer non-convex programming, it is difficult to solve. We define a new variable $C(C = (c_{k,n}) = (g_{k,n}p_{k,n}))$, so the model can be transformed into a convex optimization problem.

$$\begin{aligned} \max_{C, G} \quad & \sum_{k=1}^K \sum_{n=1}^N w_k^r \frac{g_{k,n}}{2} \log_2 \left(1 + \frac{\rho_k \sum_{n=1}^N \alpha_{k,n} c_{k,n} h_{k,n}}{\sigma_k^2 g_{k,n} + \sum_{k'=1}^K \alpha_{k',n} c_{k',n} h_{k,n}} \right) \\ & + \sum_{k=1}^K Q_k (1 - \rho_k) \sum_{k'=1}^K \sum_{n=1}^N \alpha_{k',n} c_{k',n} h_{k,n} \\ \text{s.t.} \quad & C1: \sum_{n=1}^N \frac{g_{k,n}}{2} \log_2 \left(1 + \frac{\rho_k \sum_{n=1}^N \alpha_{k,n} c_{k,n} h_{k,n}}{\sigma_k^2 g_{k,n}} \right) \geq R_k^{req}, \forall k \\ & C2: \sum_{k=1}^K \sum_{n=1}^N g_{k,n} p_{k,n} \leq P^{\max} \\ & C3: \sum_{k=1}^K g_{k,n} \leq D, \forall n \\ & C4: c_{k,n} \geq 0, \forall k, n \\ & C5: \sum_{k=1}^K \alpha_{k,n} \leq 1, \forall n \\ & C6: \alpha_{k,n} \in [0, 1] \end{aligned} \quad (11)$$

Although the relaxation-rounding approach usually leads to sub-optimal solutions, we will show that the optimal (6) solution to the relaxation constraint can still be obtained with a given ρ . For (9), we use the dual decomposition technique to find the optimal resource allocation strategy $\{C, G\}$, and then get $\{P, G\}$ for (6). In order to reduce the binary variable and improve the convergence rate, we construct the partial Lagrangian of (11) given by (12), where $\lambda = (\lambda_1, \dots, \lambda_k)$ and μ correspond to the Lagrange multipliers of C1 and C2 in (11).

$$L(C, G, \lambda, \mu) = \sum_{k=1}^K [w_k^r R_k + w_k^e E_k + \lambda_k (R_k - R_k^{req})] + \mu (P^{\max} - P^{tot}) \quad (12)$$

Since (11) is convex and meet Slater's condition, The dual problem of (11) exists the optimal solution when the dual gap is zero[12]. Thus, we can get the best control strategy by solving the following dual problems.

$$\min_{\lambda, \mu} \max_{C, G} L(C, G, \lambda, \mu) = \min_{\lambda, \mu} \max_C \max_G L(C, G, \lambda, \mu) \quad (13)$$

With IWF algorithm and KTT conditions, we can obtain the optimal transmitting power by several iterations with given $\{P, G\}$. The result is given below.

$$p_{k,n}^* = \frac{(w_k^r + \lambda_k) / \ln(4)}{\mu - \sum_{k'=1}^K \sum_{n=1}^N Q_{k'} (1 - \rho_{k'}) \alpha_{k,n} h_{k',n}} - \frac{\sigma_k^2}{\rho_k \sum_{n=1}^N \alpha_{k,n} h_{k,n}} \quad (14)$$

Substitution the calculated p_n^* into (11) and reorganize it, then we can get a linear programming (LP) for G .

$$\begin{aligned} \max_G \quad & \sum_{k=1}^K \sum_{n=1}^N v_{k,n} g_{k,n} \\ \text{s.t.} \quad & C3, C4, C5 \end{aligned} \quad (15)$$

where $v_{k,n} = p_{k,n}^* \sum_{k'=1}^K \sum_{n=1}^N \alpha_{k',n} h_{k',n} Q_{k'} (1 - \rho_{k'}) - \mu p_{k,n}^* + \frac{w_k^r + \lambda_k}{2} \log 2(1 + \rho_k \Gamma_{k,n})$, $\forall k, n$ is a constant.

In order to solve the external minimization problem of (13) (also called master dual problem), a sub-gradient method can be used to update the bivariate and assign it as

$$\lambda_k(t+1) = [\lambda_k(t) - \theta_k(t)(R_k(t) - R_k^{req})]^+ \quad (16)$$

$$\mu(t+1) = [\mu(t) - \theta_0(t)(P^{\max} - R^{tot}(t))]^+ \quad (17)$$

where $\theta_k(t)$ is adequately small positive step size.

Here, all the variables that need to be solved have been given. The following briefly describes the solution process. If the allocated power of user k on the n th subcarrier $P_{k,n} = 0$, then set $g_{k,n} = 0$. Then calculate the maximum number of users mapped to the subcarriers, that is, the maximum rank of the pattern matrix. If the condition C3 is not satisfied, take out the corresponding k and n from the minimum sum of weighted rate and energy, and cancel the correspondence between the user k and the subcarrier n , that is, set $g_{k,n} = 0$. Repeat these processes until the condition C3 is satisfied. The specific algorithm process as shown in Algorithm 1.

Algorithm 1 Iterative resource allocation algorithm (IRAA).

Initialization:

- Set $G_{PDMA}^{[N,K]} = 1$
- Set $L, L_{\max} = \|G_{PDMA}^{[N,K]}\|_{\infty}$
- 1: **while** $L_{\max} > D$ **do**
- 2: The optimized power allocation $p_{k,m}^*$ is obtained by (14)
- 3: **if** $P_{k,n} = 0$ **then**
- 4: $\alpha_{k,n} = 0$
- 5: **end if**
- 6: Update $L_{\max} = \|G_{PDMA}^{[N,K]}\|_{\infty}$
- 7: **if** $L_{\max} > D$ **then**
- 8: $(k, n) = \arg \min (w_k^r R_k + w_k^e E_k)$
- 9: Set $\alpha_{k,n} = 0$
- 10: **end if**
- 11: According to $\alpha_{k,n}$ update the pattern matrix $G_{PDMA}^{[N,K]}$
- 12: Uniformization power allocation factor $\alpha_{k,n}$
- 13: **end while**

IV. SIMULATION RESULTS

In this section, we compare the proposed IRRA scheme and FTPA with optimized pattern matrix, and FTPA with random pattern assignment through simulation. Suppose

users are randomly distributed in a base station area, the channel fading factor $\alpha_c = 3.5$. In the simulations, wireless channels are randomly generated and obey Rayleigh fading.

We assume that there are 4 to 10 users mapped to 4 subcarriers, so that the overload factor is between 1 and 2.5, and each subcarrier is allocated to 3 users at most, that is, $D = 3$. The total transmitting power P^{tot} range is from 0 to 100, and the initial power allocation factor $\alpha_{k,n} = 0.5, \forall k, n$, and set energy conversion efficiency $\zeta = 0.5$. For the pattern matrix, we set $L = 3$. Due to the user experience rate is more important, we set the weight of the data rate slightly greater than the weight of energy, that is $W_k^r = 0.6, W_k^e = 0.4$. In order to ensure the validity of the results, we conducted a simulation 5000 times to give the average simulation graphics.

With IRRA we can get the following optimization pattern matrix, interestingly, the optimal pattern matrix is the same no matter how many times the simulation is done. We can see from the following matrix that the PDMA pattern matrix is sparse and there are no more than three user data transmitted on each subcarrier. It meets the model requirements.

$$G_{PDMA}^{4,6} = \begin{bmatrix} 1 & 0 & 1 & 1 & 1 & 0 \\ 1 & 1 & 0 & 1 & 0 & 1 \\ 1 & 1 & 1 & 0 & 1 & 0 \\ 0 & 1 & 1 & 0 & 0 & 1 \end{bmatrix}$$

with the optimal pattern matrix, we compare the IRRA scheme with the FTPA scheme, and also show the performance of the IRRA using a random pattern matrix. Specific simulation results shown in Figure 1.

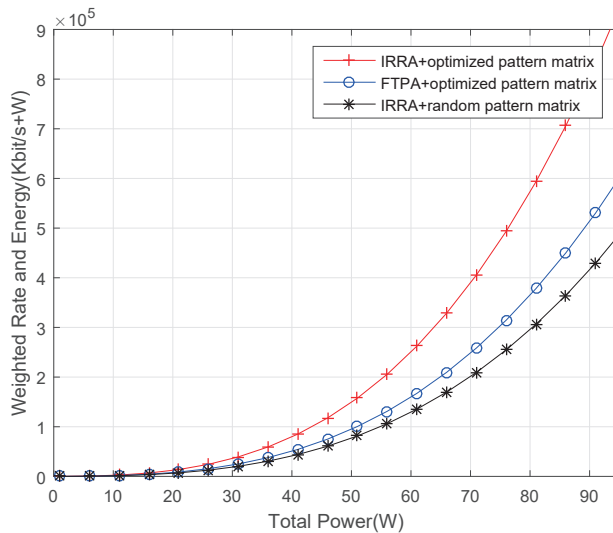


Fig. 2. Weighted rate and energy of three different power allocation scheme and pattern matrix scheme, when $N=4, K=6, L=3$.

From Fig.1. Compared to the FTPA scheme, we can see that the proposed IRRA scheme can signally improve the sum of weighted rate and energy. On the other hand, com-

pared with random pattern matrix, the optimized pattern matrix provides significant rate and energy gain.

V. CONCLUSION

In this paper, we propose an efficient iterative algorithm to achieve the trade-off between rate and energy in a PDMA network enhanced by SWIPT. The proposed IRRA scheme can not only get each user suboptimal power partition coefficient, but also get the optimal pattern matrix, and the pattern matrix maintains a certain sparseness, so that the decoding of the receiver is not overly complicated. The simulation results show that, compared with FTPA and random pattern, the IRRA scheme can significantly improve the sum of weighted rate and energy.

REFERENCES

- [1] J. Zeng, B. Li, X. Su, L. Rong, and R. Xing, Pattern division multiple access (PDMA) for cellular future radio access, in *2015 International Conference on Wireless Communications and Signal Processing, WCSP 2015*, 2015, pp1-5.
- [2] R. S. H. Istepanian, E. Jovanov and Y. T. Zhang, "Guest Editorial Introduction to the Special Section on M-Health: Beyond Seamless Mobility and Global Wireless Health-Care Connectivity," in *IEEE Transactions on Information Technology in Biomedicine*, vol. 8, no. 4, pp. 405-414, Dec. 2004.
- [3] M. G. Martini, "Wireless broadband multimedia health services: Current status and emerging concepts," *2008 IEEE 19th International Symposium on Personal, Indoor and Mobile Radio Communications, Cannes*, pp. 1-6, 2008.
- [4] R. S. H. Istepanian and Y. T. Zhang, "Guest Editorial Introduction to the Special Section: 4G HealthThe Long-Term Evolution of m-Health," in *IEEE Transactions on Information Technology in Biomedicine*, vol. 16, no. 1, pp. 1-5, Jan. 2012.
- [5] K. N. Lal and A. Kumar, "E-health application over 5G using Content-Centric networking (CCN)," *2017 International Conference on IoT and Application (ICIOT)*, Nagapattinam, 2017, pp. 1-5.
- [6] W. D. de Mattos and P. R. L. Gondim, "M-Health Solutions Using 5G Networks and M2M Communications," in *IT Professional*, vol. 18, no. 3, pp. 24-29, May-June 2016.
- [7] N. K. Ardi and N. Joshi, "Poster Abstract: 5GHealthNet : A Cloud Based Framework for Faster and Authorized Access to Private Medical Records through 5G Wireless Network," *2016 IEEE/ACM Symposium on Edge Computing (SEC)*, Washington, DC, 2016, pp. 89-90.
- [8] J. Zeng, D. Kong, B. Liu, X. Su, and T. Lv, RlePDMA and BP-IDD-IC detection, *EURASIP J. Wirel. Commun. Netw.*, vol. 2017, no. 1, p. 12, 2017.
- [9] S. Chen, B. Ren, Q. Gao, S. Kang, S. Sun and K. Niu, "Pattern Division Multiple AccessA Novel Nonorthogonal Multiple Access for Fifth-Generation Radio Networks," in *IEEE Transactions on Vehicular Technology*, vol. 66, no. 4, pp. 3185-3196, April 2017.
- [10] D. Zhai, M. Sheng, X. Wang, Y. Li, J. Song and J. Li, "Rate and Energy Maximization in SCMA Networks With Wireless Information and Power Transfer," in *IEEE Communications Letters*, vol. 20, no. 2, pp. 360-363, Feb. 2016.
- [11] R. Zhang and C. K. Ho, "MIMO broadcasting for simultaneous wire-less information and power transfer," *IEEE Trans. Wireless Commun.*, vol. 12, no. 5, pp. 1989C2001, May 2013.
- [12] S. Boyd and L. Vandenberghe, *Convex Optimization*. Cambridge University Press, 2004.

Beacon-based Localization Middleware for Tracking in Medical and Healthcare Environments

Kevin Casareo and Zenon Chaczko
Faculty of Engineering and Information Technology
University of Technology, Sydney, Australia
kevin.casareo, zenon.chaczko@uts.edu.au

Abstract—This research paper proposes a Middleware model for a Localization System that may be applied in Healthcare environments such as Hospitals or Nursing Homes to track staff, patients, visitors and equipment. It investigates literature regarding indoor localization methods and limitations to determine a suitable algorithm that may be implemented in an infrastructure oriented software. The methodology used to build and test the software is explained. It then illustrates the concept of the Localization Middleware and how it might be used when deployed indoor premises, inside such rooms as a hospital wards. In terms of the functional responsibilities, it is expected to offer an effective implementation of the distance measurement algorithm for Received Signal Strength and the Linear Least-Squares localization algorithm. The simulations of the localization algorithm with the given simulation results are looking promising. However, the real-time tests demonstrated that the range measurement was insufficiently precise to be reliable. Given a more accurate and reliable distance measurement, a more precise localization result could be attained.

Keywords— *localization; linear least-squares; received signal strength; trilateration*

I. BACKGROUND

Localization is the means of determining the location of an object or person in an environment. This helps ensure that what is localized cannot be lost, and can be navigated or navigated to, which could be valuable in a busy medical facility such as a Hospital or a Clinic. A commonly used example of this is the use of the Global Positioning System to track the location of a vehicle or person in the world. GPS, however, has the limitation of being unreliable and insufficiently precise when used in an indoor environment.

Hospitals would benefit from a localization system to track the positions of equipment, patients and personnel within their premises. Allow a means for a patient to be recovered if they wander from their room, or guiding critical personnel such as doctors and nurses to places where they are needed could be valuable in ensuring that the operations of the facility can be run more efficiently. They may also open up avenues to developing automated systems such as automated stretchers or hospital beds to navigate through these facilities.

This paper proposes a middleware solution for an Android mobile device that may be integrated into a tracking system as described above. The scope of the proposed solution is limited to providing the location of a tracked Android phone relative to the position of trusted broadcasting beacons (anchors).

II. LITERATURE OVERVIEW

A. Localization

Localization is the main service to be provided by the middleware solution. One means of attempting position estimation is to use trilateration. The distance r from an anchor node may be represented with a circle around the coordinate position $[x_n, y_n]$ is given by the expression below [1]:

$$(x_n - x_0)^2 + (y_n - y_0)^2 - r_n^2 = 0 \quad (1)$$

Where n is corresponds to an anchor node. For two-dimensional localization, three anchor nodes are required. In ideal circumstances, the object being localized (the mobile node) will lie in the intersection of all three points, resulting in the following set of equations [2]:

$$r_1^2 = r_2^2 = r_3^2 \quad (2)$$

$$r_1^2 - r_3^2 = r_2^2 - r_3^2 \quad (3)$$

Due to the imprecise nature of measuring distance in reality, it is assumed that there will be error that needs to be accounted by the localization algorithm. One method of doing so will be to utilise trigonometry to determine the positions where two of the three circumferences intersect [3]. The coordinates given by these intersections are averaged to estimate the location of the mobile node.

Another option is to use a least-squares algorithm to estimate the position of the node. Although a non-linear method would have less computational complexity [4], it was determined that a working linear least-squares approximation would be far easier to implement whilst still being sufficiently reliable.

Expanding out the left side expression in (3) will result in the following:

$$r_1^2 - r_3^2 = (x_1 - x_0)^2 + (y_1 - y_0)^2 - (x_3 - x_0)^2 + (y_3 - y_0)^2 \quad (4)$$

After further expanding and rearranging this equation will result in the following:

$$2x_0(x_1 - x_3) + 2y_0(y_1 - y_3) = r_1^2 - r_3^2 - x_1^2 + x_3^2 - y_1^2 + y_3^2 \quad (5)$$

Since all terms on the right hand side and the coefficients of x_0 and y_0 are known, the result is in the form of a linear equation $Ax + By + C$. By applying the same steps to the right

hand side of equation (3), we get two linear equations that can be written in the following system:

$$\begin{bmatrix} 2x_1 - 2x_3 & 2y_1 - 2y_3 \\ 2x_2 - 2x_3 & 2y_2 - 2y_3 \end{bmatrix} \begin{bmatrix} x_0 \\ y_0 \end{bmatrix} = \begin{bmatrix} r_1^2 - r_3^2 - x_1^2 + x_3^2 - y_1^2 + y_3^2 \\ r_2^2 - r_3^2 - x_2^2 + x_3^2 - y_2^2 + y_3^2 \end{bmatrix} \quad (6)$$

Letting A equal the coefficient matrix and B equivalent to the right-hand side, $\begin{bmatrix} x_0 \\ y_0 \end{bmatrix}$ can be solved with linear least squares:

$$A^{-1} \cdot A \cdot \begin{bmatrix} x_0 \\ y_0 \end{bmatrix} = A^{-1} \cdot B \quad (7)$$

B. Distance Ranging

Ranging refers to the measurement of the distance between the mobile node and the anchor nodes. With bluetooth signals this may be achieved by deriving the distance by the signal's Time of Arrival, the Angle of Arrival of the wireless signal, or by using the Received Signal Strength Indicator measurement. Due to time constraints, it was determined that measuring RSSI would be the simplest to implement. The relationship between distance and signal strength is expressed by the equation below [5]:

$$d = 10^{\frac{A - RSSI}{10n}} \quad (8)$$

The values of the constant A (the signal strength when $d = 1$), and n (the pathloss exponent) must be determined after calibration. The latter of which is dependant upon the qualities indoor environment. This presents a weakness in using RSSI, as the sensitivity of the signal when it bounces off or attenuates through surfaces will result in a much weaker recieved signal. A variation on (8) also applies a penalty based on the number of walls that the signal may pass through [6], however this may not be simple for the software to account for during runtime.

III. METHODOLOGY

A. Tools

This middleware solution was written using Java and the Android Software Development Kit. It utilises the Android SDK's capability for handling Bluetooth Low-Energy connections and the services that may be provided by BLE beacons. This middleware utilised by a consumer application with an Android mobile device (mobile node) as a deploy target. The mobile node will measure its distance from each anchor node with a known position and use this to estimate its own position. Should the method of localization provided by the middleware be insufficiently accurate, it may be replaced by a more suitable method.

The BLE beacons used for testing are Texas Instruments CC2650 Sensortags. These are consumer embedded devices that can expose a variety of onboard sensors with BLE Services, including a temperature sensor and accelerometer. Software that handles these services are not demonstrated within the middleware solution, which emphasises the use of the beacons for localization.

B. Testing

In order to demonstrate the functions of the middleware, a test application was written using the Android SDK. This test application demonstrates the localization service provided by the solution and is used to qualify the reliability of the localization.

The first test is used to calibrate the constants used in the distance estimation calculation outlined in section II.B of this paper. This is performed by first finding the signal strength measured at 1 metre, then using this measurement in the distance estimation to determine what path loss factor is suitable. Once these constants are determined, they are utilised in the middleware application to determine distance based on the RSSI.

The second test for assessing localization is to simulate the localization algorithm in Scilab to assess its quality with ideal conditions. This means that the coordinate positions of each anchor node and the distances are assumed to be correct. The localization algorithm is then adapted for use in middleware solution in Java Code. The localization algorithm used for the middleware is a trilateration algorithm outlined in section II.A of this paper.

The final test is to evaluate the quality of the localization using the distance estimation constants derived in the second test. The quality of the localization algorithm given actual circumstances is to be assessed.

IV. ARCHITECTURE

A. Conceptual

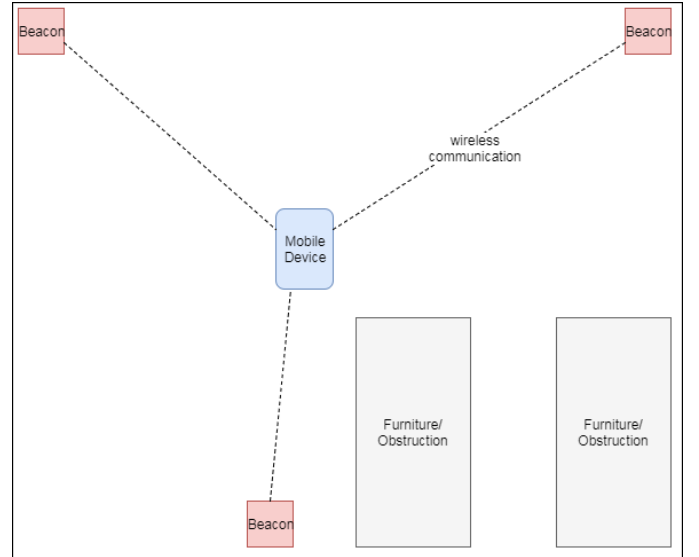


Fig. 1. Indoor Wireless Beacon Localization Concept

The Hospital environment is populated with a wireless beacon sensor net, which act as the anchor nodes for the purposes of localization. The mobile node communicates with beacons in the sensor net, identifies them and measures the distance from each one. This may then be used to track the position of the person within the premises of the the Hospital, or used to aid in navigating automated beds or other

equipment. Fig. 1 above illustrates the system used to track an object or person (in this case, a phone) within a hospital ward.

Each wireless beacon is an anchor node within the room. The mobile device would be able to infer the position of each node based on an identifier such as UUID or address. The position estimation would then be presented to the user of the device, or exported to a system external to the mobile device. This external system could, for instance, be a navigation system for autonomous beds, with the mobile node broadcasting its position in the Hospital.

B. Execution

1) *Application Stack*: The software is built on the Android SDK as a Service to be consumed by the user application or other services. The user application could be presenting the localization information to the user as a map, or exporting the data to another operations system. Fig. 2 below illustrates the application stack of the system, with the middleware solution highlighted blue, labelled *Localization Software*.

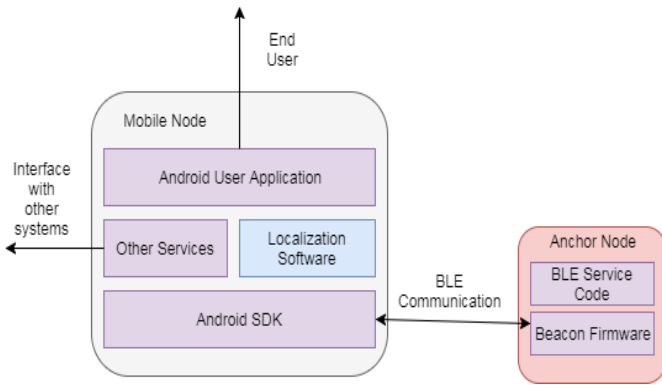


Fig. 2. Application Stack

The separation of Localization Software into its own service was to ensure that it could be reused by another user application or other service running on the Android mobile device.

Other Services consist of other services managed or created by the Application that it consumes. Other than communicating with the front end application, they may also consume the services offered by the Localization Software.

2) *Services and Components*: The main services to be consumed are illustrated in Fig. 3 with the components. These include identifying the beacons to be used for measurement; updating the position for an identified beacon; and localizing the position of the mobile node. These are provided by the *Localization Service* component, which communicates with a number of anchor nodes that may offer BLE services.

The *User Software* component is what tells the localization service what beacon should be included in the localization algorithm and where each of them are. This component represents any user interface or broker that presents or exports the localization information.

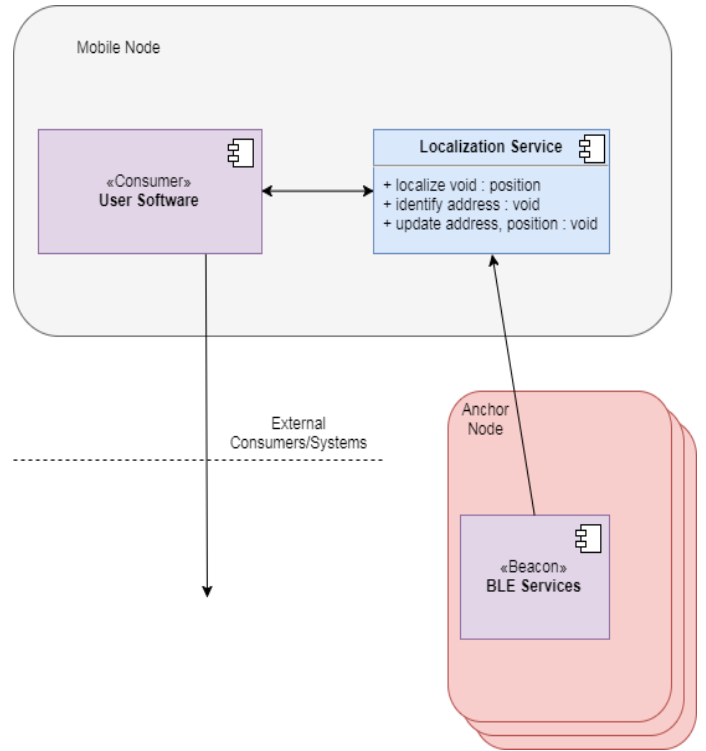


Fig. 3. Services and Components

C. Implementation

1) *Localization Algorithm*: The localization algorithm used

was first written in SciLab for verification. The simulation code in Fig. 4 utilises Equations (1) through to (7), before it is adapted into Java Code. The code was then adapted into Java and uses the Apache Commons library for matrix math capabilities.

```

1 function [x, y]=localise(node1, node2, node3)
2   an = 2*node2(1) - 2*node1(1);
3   bn = 2*node2(2) - 2*node1(2);
4   cn = node1(3) ** 2 - node2(3) ** 2 - node1(1) ** 2 + node2(1)
      ↳ ** 2 - node1(2) ** 2 + node2(2) ** 2;
5   dn = 2*node3(1) - 2*node1(1);
6   en = 2*node3(2) - 2*node1(2);
7   fn = node1(3) ** 2 - node3(3) ** 2 - node1(1) ** 2 + node3(1)
      ↳ ** 2 - node1(2) ** 2 + node3(2) ** 2;
8   A = [ an bn ; dn en];
9   B = [ cn; fn ];
10  val = (inv(A)*B)';
11  plot(val(1), val(2), '*')
12  x = val(1)
13  y = val(2)
14  endfunction

```

Fig. 4. Scilab Localize Algorithm

2) *Class Diagram*: The class diagram shown in Fig. 5 shows the class structure of the Localization Service. Service functionality is exposed with the *IBeaconService* interface, which is outlined in an *Android Interface Definition Language* file. The implementation of *IBeaconService* is contained within the *BeaconService* class, and creates and accesses an instance of the *Beacons* class to handle the creation and management of Bluetooth connections to the beacons; and the method of Localization.

Other vital classes include the *SignalDatum* class, which represents the state of an anchor node at a single point in time, and the *SignalData* class, which stores all states of connected anchor nodes at the same point in time, which is to be exposed to client applications.

The Localization implementation is written in the classes *DimensionTwo* and *DimensionThree*, both of which implement a virtual method *Localize* from abstract class *Localiser*. The input is a collection of beacons with known positions and distance measurements.

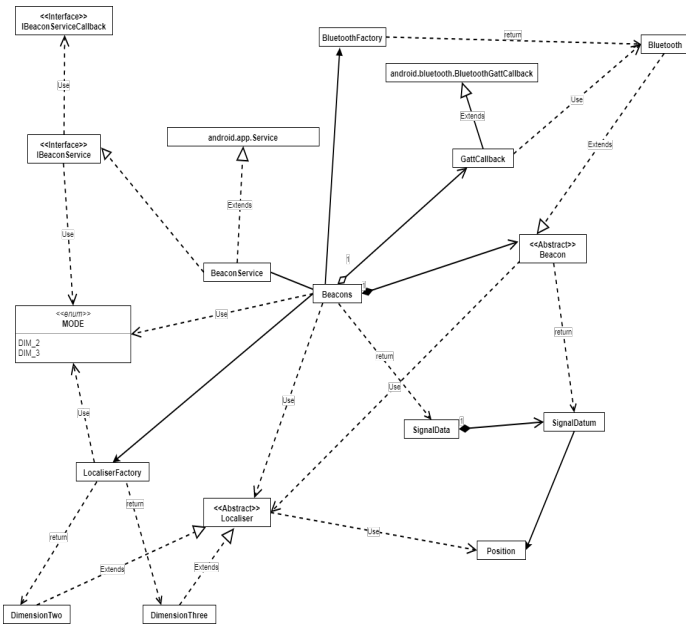


Fig. 5. Class Diagram

3) *Packaging*: The root folder of the package is split into two branches for Android Interface Definition Language interfaces and Java source code. The AIDL package tree is used to define objects and service functionality that is to be passed interprocess.

The implementation code is saved under the Java source path. In order to utilise the Localization Service offered by the middleware solution, the consuming Android Activity or Service has to start the *BeaconService* and implement a callback handler *IBeaconServiceCallback*. This callback will handle the responses to calls to the *localize* method, which can be presented in a suitable User Interface.

Fig. 6 shows the package structure for the Localization service source code.

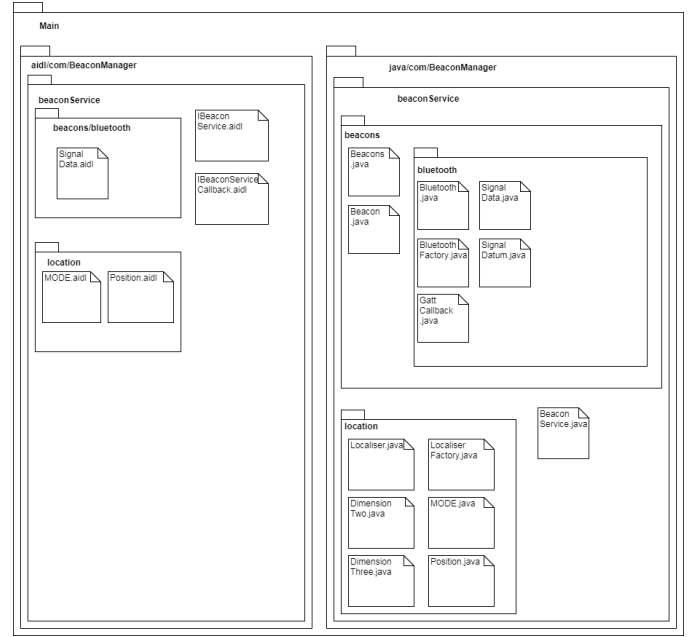


Fig. 6. Package Structure

V. RESULTS

A. Calibration Tests

These tests use Equation 8 for Free Space Path Loss [5]. After determining the signal strength when the distance between mobile and anchor node is one meter, the path loss factor in this case is determined by measuring the signal strength when the distance is increased to two. A spreadsheet with Equation 8 is used to find the path loss factor given the measurements at one metre and two metres.

1) *Line of Sight*: Line of Sight refers to a clear path between the mobile node and the anchor node. The beacon and the mobile device were suspended from separate racks at a one metre and two metre distance. The average result of 20 samples for each measurement is shown in the first row of Table I below.

2) *Room Deployment*: In this test, the test beacon is placed within an indoor office to resemble a deployed sensor net. The beacon was taped to a wall and the signal strength readings at one metre and two metres was recorded

B. Localization Algorithm Verification

The tests for algorithm verification were written in Scilab using the Localization Algorithm from Fig 4 and listed in Table II below.

Fig 7. on the next page shows the result for an *ideal measurement*, where all 3 circumferences representing the

TABLE I. CALIBRATION TESTS

Calibration Test	Average Signal Strength at Distance		Path Loss Factor
	1 metre (m)	2 metre (m)	
Free Space	-47.45	-56.15	2.84
Room Deployment	-61.4	-68.05	2.2

Results of Calibration Tests with Beacon

TABLE II. LOCALIZATION VERIFICATION

Test Type	Distance in metres (m)			Result [x, y]
	A[4.0, 0.0]	B[0.0, -4.0]	C[0.0, 4.0]	
Ideal Circumstances	4.0	4.0	4.0	0.0, 0.0
One Under-measured	2.0	3.0	4.0	1.5,0.0
Two Under-measured	2.0	3.0	4.0	1.06, -0.438
All Under-measured	2.0	3.0	1.0	0.125,0.5
All Over-measured	8.0	8.0	8.0	0.0, 0.0
Two Over-measured	1.0	8.0	8.0	7.88, 0.0
One Over-measured	1.0	2.0	16.0	16.1,-15.8

Results for Scilab Localization Simulation

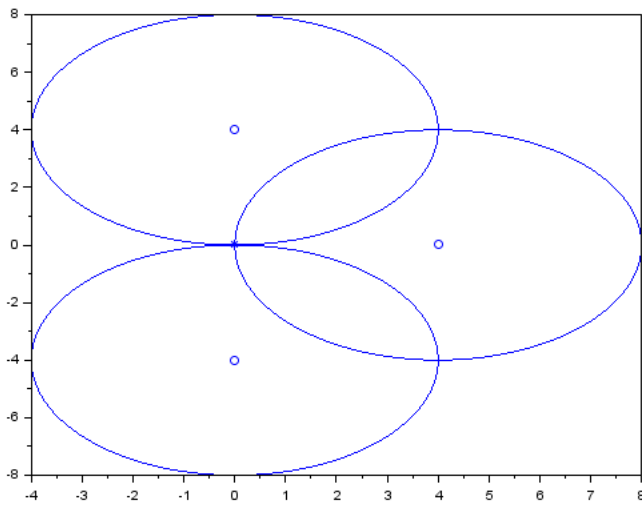


Fig. 7. Ideal Circumstance Simulation

range measurement intersect at the exact same point. Most of the proceeding results demonstrate a result that has minimal reliability, apart from the sixth result, which has one measurement significantly more weighted than the last. This result is shown in Fig. 8 on the next page.

Due to the simulated distance measured for one of the anchor nodes being far greater than the other two, it weighted far more and produced an unreliable result. However, in reality, there would be more than three beacons placed indoors. Ignoring severe outliers such as those shown in Fig. 8 would be the best course of action.

C. Integrated Testing

This test was conducted in an office indoors. The localization is test for the mobile node residing at [0.0,0.0] and [0.0, 1.5]. Table III displays the results for these tests.

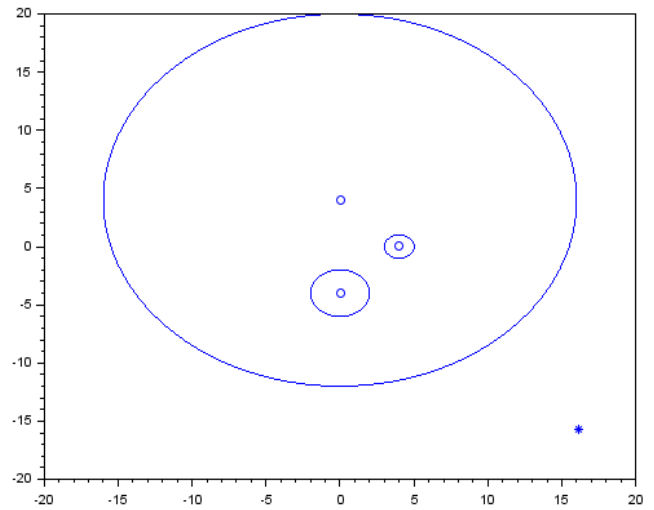


Fig. 8. One Over-measured Simulation

What is immediately noticeable in Table III is the unreliability of the localization result. The distance measurements appear to fluctuate significantly, resulting in an imprecise and inaccurate reading. One solution would be to change the method of distance measurement used by the localization algorithm. One of the goals of the middleware solution is to provide an avenue for software developers to replace components of the solution with more suitable ones, including the distance measurement method.

TABLE III. INTEGRATION TEST OF LOCALIZATION SOFTWARE

Test Coordinates	Distance in metres (m)			Result [x, y]	Error
	A[3.2, -1.5]	B[-1.0, 1.0]	C[0.0, -3.5]		
[0.0, 0.0]					
1	1.87	1.37	3.16	1.06,0.00	+1.06,+0.00
2	1.23	1.00	3.16	1.08,-0.18	+1.08,-0.18
3	1.11	1.00	3.16	1.11,-0.19	+1.11,-0.19
4	1.87	1.23	2.57	1.31,0.51	+1.31,-0.51
5	1.37	1.11	2.08	1.63,0.78	+1.63,-0.78
6	1.87	1.37	2.57	1.38,0.55	+1.38,-0.55
[0.0, -1.5]					
1	0.81	1.67	2.57	1.25,-0.45	+1.25,+1.05
2	1.69	1.69	3.51	1.38,0.22	+1.38,+1.72
3	3.51	1.23	3.16	-0.18,-0.24	-0.18,+1.26
4	2.57	1.11	3.51	0.77,0.26	+0.77,+1.74
5	2.08	1.11	4.33	1.57,1.16	+1.57,+2.66
6	1.69	1.23	3.90	1.52,0.72	+1.52,+2.22

Results of Localization Integration Test

VI. CONCLUSION

This paper demonstrates a solution for a localization system that could be used in a Hospital environment. The middleware solution developed has shown a potential means to track persons and objects within an indoor environment, and can therefore be modified to be used to track patients, staff and equipment. Future work for this middleware include adapting it to aid in navigation of robotics, such as autonomous beds and trolleys and finding a more suitable method of distance estimation with wireless communications. For indoor scenarios, the channel model applied in the prediction is rather simplistic and may not always be able to yield accurate results. In future work we would like to consider the time of flight, similar to Radar applications taking advantages of OFDM based systems and for channel estimation purposes using the channel impulse response approach.

REFERENCES

- [1] F. Ileri and M. Akar, "Rssi based position estimation in zigbee sensor networks," in *8th WSEAS Conference on Circuits, Systems, Signal and Communications (CSST 2014)*, January 2014, pp. 62–73.
- [2] S. Kahnemouyi and A. Poushafiee, "Localization of rf nodes using trilateration in a network," UC Santa Cruz, Tech. Rep., December 2014.
- [3] Z. Chaczko, R. Klempous, J. Nikodem, and M. Nikodem, "Methods of sensors localization in wireless sensor networks," in *14th Annual IEEE International Conference and Workshops on the Engineering of Computer-Based Systems (ECBS'07)*, March 2007.
- [4] Y. Zhou, "An efficient least-squares trilateration algorithm for mobile robot localization," in *IEEE/RSJ International Conference on Intelligent Robots and Systems*, St. Louis, USA, March 2009, pp. 3474–3479.
- [5] A. Jayakody, S. Lokuliyana, D. Chathurangi, and D. Vithana, "Indoor positioning: Novel approach for bluetooth networks using rssi smoothing," *International Journal of Computer Applications*, vol. 137, no. 13, pp. 26–32, 2016.
- [6] R. Faragher and R. Harle, "An analysis of the accuracy of bluetooth low energy for indoor positioning applications," in *27th International Technical Meeting of The Satellite Division of the Institute of Navigation (ION GNSS+ 2014)*, Tampa, FL, USA, September 2014, pp. 201–210.

Resource Allocation in Multi-user NOMA Wireless Systems

Mingyao Peng¹, Jie Zeng², Bei Liu², Jiajia Mei³, Xin Su², Xibin Xu² and Limin Xiao²

¹ Broadband Wireless Access Laboratory

Chongqing University of Posts and Telecommunications, Chongqing, China

² Tsinghua National Laboratory for Information Science and Technology

Research Institute of Information Technology, Tsinghua University, Beijing, China

³ National Key Laboratory of Science and Technology on Communications

University of Electronic Science and Technology of China, Chengdu, China

Email: suxin@mail.tsinghua.edu.cn

Abstract—Non-orthogonal multiple access (NOMA) has been considered as a key candidate technology for 5G wireless systems due to its superior spectral efficiency and system capacity. With the ever-development of wireless body sensor networks (WBSNs) and wireless communications, supporting real-time communications in the telemedicine communication becomes a very important challenge. In this article, our goal is to maximize the overall system throughput by optimizing sub-band allocation and power allocation, thereby improving real-time performance in telemedicine communications. Assuming that the base station could obtain perfect channel state information (CSI), we propose a suboptimal sub-band allocation algorithm with low complexity. In the power allocation scheme, the closed-form expressions of power allocation factors for multiplexed users on each sub-band are obtained based on the Karush-Kuhn-Tucker (KKT) optimality conditions. Simulation results demonstrate that the proposed resource allocation scheme is closest to the ideal sub-band allocation based on exhaustive search and is superior to other schemes.

Index Terms—Non-orthogonal multiple access (NOMA), telemedicine communication, maximum sum rate, sub-band allocation, power allocation

I. INTRODUCTION

With the ever-development of wireless body sensor networks (WBSNs) and wireless communications, telemedicine is becoming more and more important [1]. The widespread use of telemedicine to monitor and diagnose patients may be the savior of many precious lives. Therefore, supporting real-time communications between a patient's WBSN and a remote server becomes a very important challenge [2]. Future 5G wireless systems will make significant headway on many human health issues, such as real-time sharing of patients' personal medical records, robotic-assisted teletherapy, remote monitoring of human indicators, and remote drug use [3]. As a promising candidate key technology for 5G, non-orthogonal multiple access (NOMA) can achieve higher spectral efficiency

and system capacity of wireless systems. Therefore, the use of NOMA technology in 5G wireless networks for telemedicine communications may be a promising trend.

To date, NOMA has been widely studied in academia. For example, [4] mainly focus on improving the design of spectrum efficiency (SE). In [5], the authors studied the energy efficiency (EE) optimization of downlink NOMA systems and proposed a low-complexity sub-optimal user scheduling algorithm. Reference [6] propose several power allocation schemes, in which exhaustive search for power allocation (ESPA) can achieve the best performance in these schemes, but the computational complexity is very high. Compared with ESPA, fractional transmit power allocation (FTPA) get worse performance, but the computational complexity is expressively lower. In addition, in [7] and [8], the authors obtained a closed-loop expression of power allocation among users according to Karush-Kuhn-Tucker (KKT) optimization conditions and proved that this power allocation scheme can get better system performance than other schemes.

In this paper, we are dedicated to addressing the issue of maximizing the sum rate on the downlink NOMA wireless systems to support real-time communication between patients' WBSN and remote servers in future telemedicine communications. Since the issue of maximizing the system sum rate is a non-convex problem, it is too difficult to get the global optimal solution. Therefore, with the total system transmits power constraint and the minimum rate of each user constraint, we use sub-band allocation and power allocation as sum rate optimized solutions. Firstly, we propose a sub-optimal and low-complexity sub-band allocation algorithm. Then allocation the transmit power between each sub-band by using FTPA. Finally, the closed-form expressions of power allocation proportional factors among users in each sub-band are obtained according to KKT optimization conditions. The simulation results illustration that the proposed resource allocation scheme is helpful in improving NOMA performance. The results also verify that compared with the sub-optimal matching

This work was supported by the China's 863 Project (No.2015AA01A706), the National S&T Major Project (No.2016ZX03001017), Science and Technology Program of Beijing (No.D171100006317002), and Ministry of Education-China Mobile Research Fund(No.MCM20160105).

for sub-band allocation (SOMSA) proposed in [5], our proposed sub-band allocation algorithm shows comparable performance and lower complexity.

The rest of this article is arranged as follows. We introduce the system model of downlink multi-user NOMA in Section II, and the problem formulation is also presented in this Section. In Section III, we propose a suboptimal sub-band allocation algorithm and analyze its computational complexity. The scheme of power allocation between sub-bands and the scheme of power allocation among users on sub-bands are respectively proposed in Section IV, whereas Section V shows the simulation results. In the final section, we conclude this paper.

II. SYSTEM MODEL AND PROBLEM FORMULATION

A. Network Model

A downlink NOMA wireless system is considered with SIC applied at the receiver. As shown in Fig. 1, the system total bandwidth is B , which is divided into N sub-bands on average, and the bandwidth of each sub-band is $B_n = B/N$, where $n \in \{1, 2, \dots, N\}$ and n th sub-band (SB_n) is allocated with index n . Providing the radius of this cell is R and BS has perfect channel state information (CSI). As can be observed in [9], one sub-band can serve multiple different users simultaneously. Assuming M users are accidentally distributed in this cell and M_n users are allocated on each sub-band, where $M_n \in \{M_1, M_2, \dots, M_N\}$. In addition, if the total system transmit power is P_{tot} and the transmit power on SB_n is P_n , where $\sum_{m=1}^{M_n} P_{m,n} = P_n$, $\sum_{n=1}^N P_n = P_{tot}$, where $m \in \{1, 2, \dots, M\}$ and user m is allocated with index m .

Without loss of generality, we assume that the equivalent channel gain order in the cell is sorted as $|H_{1,n}| \geq |H_{2,n}| \geq \dots \geq |H_{M_n,n}|$, the transmitted signal on SB_n can be written as

$$s_n = \sqrt{P_{1,n}}s_{1,n} + \sqrt{P_{2,n}}s_{2,n} + \dots + \sqrt{P_{M_n,n}}s_{M_n,n} \quad (1)$$

where s_n denote the transmitted signal of SB_n at the BS, $s_{m,n}$ denote the BS transmit symbol of user m (U_m) at SB_n , and $E[|s_{m,n}|^2] = 1$. Therefore, the received signal of U_m at SB_n is

$$y_{m,n} = h_{m,n}s_n + \omega_{m,n} \quad (2)$$

where $h_{m,n}$ denotes the coefficient between $s_{m,n}$ and U_m , $h_{m,n} = g_{m,n} \cdot PL^{(-1)}(d)$, and where $g_{m,n}$ denotes the Rayleigh fading channel gain, $PL^{(-1)}(d)$ denotes the path loss function, d denotes the distance between the SB_n from BS to U_m . Let $\omega_{m,n}$ be the additive white Gaussian noise (AWGN). We define the equivalent channel gain $H_{m,n} = |h_{m,n}|^2/N_0B_n$, where N_0 is the noise power spectral density.

With the SIC decoding order, if $h_{i,n} > h_{j,n}$ and $j > i$, user i will execute SIC to cancel the interference of user j . Else user i will not execute SIC and the user j

will as interference signal for user i . Thus, the achievable throughput of U_m on SB_n can be expressed as

$$R_{m,n} = B_n \log_2 \left(1 + \frac{P_{m,n} H_{m,n}}{1 + \sum_{i=1}^{m-1} P_{i,n} H_{m,n}} \right) \quad (3)$$

The throughput of SB_n can be expressed as (4) and the overall system throughput can be written as (5).

$$R_n = \sum_{m=1}^{M_n} R_{m,n} \quad (4)$$

$$R = \sum_{n=1}^N \sum_{m=1}^{M_n} R_{m,n} \quad (5)$$

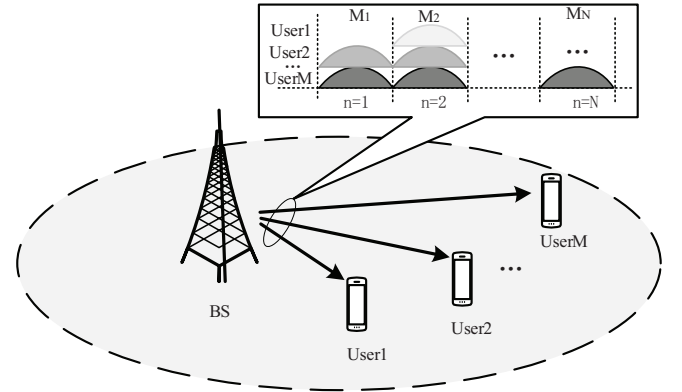


Fig. 1. Downlink multi-user NOMA wireless system with N sub-bands.

B. Problem formulation

With the total system transmits power constraint and the minimum rate of each user constraint, our purpose is to maximize the throughput in NOMA wireless systems. This optimization problem can be formulated as follows

$$\max_{P_{m,n}} \sum_{n=1}^N R_n \quad (6)$$

$$s.t. C1 : \sum_{n=1}^N \sum_{m=1}^{M_n} P_{m,n} \leq P_{tot} \quad (6.1)$$

$$C2 : R_{m,n} \geq R_{m,n}^{\min} \quad (6.2)$$

where $R_{m,n}^{\min}$ denotes the minimum data rate requirement for U_m on SB_n . Constraint C1 is the total system transmit power constraint of the BS and constraint C2 is the minimum data rate requirements of each user. From equation (6) we can see, sub-band allocation and power allocation are affect each other. Thus, the optimization problem of (6) is non-convex optimization problem, and it is very hard to obtain the global optimal solution. To get a better solution, we decompose the optimization problem into two sub-problems: the sub-band allocation sub-problem and the power allocation sub-problem. Firstly,

we propose a suboptimal sub-band allocation algorithm with a low-complexity. Then allocation the transmit power between each sub-band allocation by using FTPA. Finally, the closed-form expressions of power allocation proportional factors among users in each sub-band are obtained according to KKT optimization conditions.

III. PROPOSED SUB-BAND ALLOCATION ALGORITHM

In this section, the sub-optimal sub-band allocation algorithm (SOSA) with low-complexity is proposed and the computational complexity of the algorithm is also analyzed.

A. Sub-band Allocation Algorithm

With existing SIC technology of downlink NOMA system, we can observe that the more users that are allocated on the same sub-band, the greater complexity of implementing the SIC on the receiver side. If so, the downlink signaling overhead and false propagation due to incorrect SIC decoding will be increased. Therefore, to make the receiver have a lower complexity, we consider a simple case that one sub-band is allocated only two users and each user can only be assigned to one sub-band. This assumption can effectively limit the error propagation and reduce the downlink signaling overhead.

Considering two users are multiplexed on the same sub-band, we assume $M = 2N$ due to the complexity of the decoding [10]. In practice, the optimal solution to sub-band allocation is very difficult to obtain since it requires searching all possible combinations of every two users in the system. Therefore, we propose a sub-optimal sub-band allocation algorithm (SOSA) with low-complexity.

Algorithm 1 describes the proposed suboptimal sub-band allocation process. We represent S_{UnAll} as a group of users that have not been assigned to any sub-bands. In the matching process, we first identify the users with the largest channel gain and the second largest users in each sub-band, and then sum the channel gains corresponding to the two users. If the sum gain of sub-band n is the largest among N sub-bands, the corresponding two users are preferentially allocated for SB_n . Until all users are assigned, the assignment process terminates.

B. Complexity Analysis

The exhaustive search is the optimal sub-band allocation scheme by searching for all possible pairs and selecting one of the pairs which can obtain the maximizes the overall system throughput, with a computational complexity of $O(\frac{(2N)!}{2^N})$. The complexity of SOMSA which is proposed in [5] is $O(2N^2)$. Compared with SOMSA, the proposed sub-band allocation algorithm has a lower complexity. By taking the natural logarithm method to compare the complexity of SOSMA and exhaustive search, $O(\ln N) < O(N \ln N)$. Therefore, the complexity of the proposed sub-band allocation algorithm is significantly less than the optimal sub-band allocation scheme and less than SOMSA.

Algorithm 1 Suboptimal Sub-band Allocation Algorithm.

- 1: Initialize the pairing list $S_{Match}(n)$ to record the paired sub-bands and users.
- 2: Initialize the collection S_{UnAll} to record users that have not been assigned to any sub-bands.
- 3: **while** $\{S_{UnAll}\} \neq \emptyset$ **do**
- 4: **for** $n = 1$ to N **do**
- 5: $\{S_{UnMatch}'\} = \{S_{UnMatch}\}$
- 6: Each user sends a signal requesting pairing to SB_n
- 7: $H_{m_1,n} = \arg \max_{m \in \{S_{UnMatch}'\}} H_{m,n}$
- 8: Remove user m_1 from $S_{UnMatch}'$
- 9: $H_{m_2,n} = \arg \max_{m \in \{S_{UnMatch}'\}} H_{m,n}$
- 10: $H_n = H_{m_1,n} + H_{m_2,n}$
- 11: **end for**
- 12: $H_{n^*} = \arg \max_{n \in \{1,2,\dots,N\}} H_n$
- 13: SB_{n^*} adds user m_1 and m_2 to $S_{Match}(n)$, and removes user m_1 and m_2 from $\{S_{UnMatch}\}$
- 14: **end while**

IV. PROPOSED POWER ALLOCATION SCHEME

After the sub-band allocation is obtained from Section III, in this section, we are committed to solving the power allocation. Closed-form expressions of power allocation proportional factors among users in each sub-band are obtained according to KKT optimization conditions.

A. Sub-band power allocation scheme

Consider that two users are multiplexing on SB_n , the sum of the two user channel gains is H_n . In previous studies, it was generally considered to divide the total system transmits power to sub-bands with equal power allocation (EPA) scheme [5]. According to the expression in (3), the power allocated to SB_n will affect the achievable throughput on each sub-band. Thus, the sub-band power allocation scheme should be optimized. To date, the power allocation scheme of FTPA with a low computational complexity is very mature. Therefore, we present to assign different transmit powers to sub-bands based on FTPA, which can be expressed as follows

$$P_n = P_{tol} \frac{H_n}{\sum_{i=1}^N H_i} \quad (7)$$

B. Sub-band users power allocation scheme

According to the abovementioned power allocation scheme between sub-bands, the transmit power of each sub-band is obtained. Considering two users are multiplex in the same sub-band, the concept of NOMA with SIC of sub-band n as shown in Fig. 2. On SB_n , the center-cell channel gain is represented by H_n^l and the edge-cell user channel gain is represented by H_n^s , where $H_n^l > H_n^s$. If the center-cell user transmit power on SB_n is $\beta_n P_n$, thus

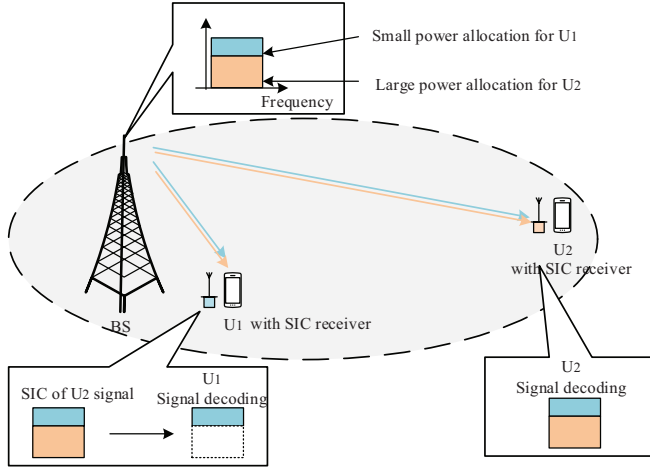


Fig. 2. Downlink NOMA system with two users on each sub-band.

the edge-cell user transmit power is $(1 - \beta_n)P_n$, where $0 < \beta_n \leq 0.5$. Therefore, the throughput of the SB_n can be expressed as

$$R_n^l = B_n \log(1 + \beta_n P_n H_n^l) \quad (8)$$

$$R_n^s = B_n \log\left(1 + \frac{(1 - \beta_n)P_n H_n^s}{1 + \beta_n P_n H_n^s}\right) \quad (9)$$

$$R_n = B_n \log_2\left(1 + \beta_n P_n H_n^l\right) + B_n \log_2\left(1 + \frac{(1 - \beta_n)P_n H_n^s}{1 + \beta_n P_n H_n^s}\right) \quad (10)$$

According to the optimization problem (6), the overall system throughput is the sum of the N sub-bands throughput. Therefore, to achieve the overall system throughput maximizes, the throughput of each sub-band must be maximized, so the optimization problem (6) can be updated as follows

$$\max_{P_{m,n}} R_n \quad (11)$$

$$s.t. C1 : 0 < \beta_n \leq 0.5 \quad (11.1)$$

$$C2 : R_{i,n} \geq R_{i,n}^{\min}, i = 1, 2 \quad (11.2)$$

The optimization problem (11) is still a non-convex problem, and the global optimal solution is difficult to determine. Therefore, in our work, we find the optimal solution that satisfies the KKT [11] optimization conditions, and then the Lagrange optimization problem can be formulated as

$$\begin{aligned} \mathcal{L}(\beta_n, \lambda, \mu) = & B_n \log_2\left(1 + \beta_n P_n H_n^l\right) \\ & + B_n \log_2\left(1 + \frac{(1 - \beta_n)P_n H_n^s}{1 + \beta_n P_n H_n^s}\right) \\ & + \lambda(0.5 - \beta_n) + \mu_1\left(\beta_n P_n H_n^l - (\varphi_1 - 1)\right) \\ & + \mu_2\left((1 - \beta_n)H_n^s - \beta_n P_n H_n^s \times (\varphi_2 - 1)\right) \end{aligned} \quad (12)$$

where λ , μ_1 and μ_2 are the Lagrange multipliers. Also, $\varphi_i = 2^{\frac{R_{i,n}^{\min}}{B_n}}$. Taking derivatives of (11) w.r.t. β_n , λ , μ_i , we can write KKT optimization conditions as follows

$$\begin{aligned} \frac{\partial \mathcal{L}}{\partial \beta_n^*} = & \frac{B_n P_n H_n^l}{1 + \beta_n P_n H_n^l} - \frac{B_n P_n H_n^s}{1 + \beta_n P_n H_n^s} - \lambda + \mu_1 P_n H_n^l \\ & - \mu_2 P_n H_n^s - \mu_2 P_n H_n^s \times (\varphi_2 - 1), \\ & \forall n = 1, 2, \dots, N, \end{aligned} \quad (13)$$

$$\frac{\partial \mathcal{L}}{\partial \lambda^*} = 0.5 - \beta_n \geq 0, \text{ if } \lambda^* \geq 0, \quad (14)$$

$$\frac{\partial \mathcal{L}}{\partial \mu_1^*} = \beta_n P_n H_n^l - (\varphi_1 - 1) \geq 0, \text{ if } \mu_1^* \geq 0, \quad (15)$$

$$\begin{aligned} \frac{\partial \mathcal{L}}{\partial \mu_2^*} = & ((1 - \beta_n)P_n H_n^s - \beta_n P_n H_n^s \times (\varphi_2 - 1)) \geq 0, \\ & \text{if } \mu_2^* \geq 0, \end{aligned} \quad (16)$$

From the KKT optimization conditions, the closed-form solution of users power allocation coefficients in SB_n can be given as follows:

- If $\lambda > 0$, $\beta_n^* = 0.5$.
- If $\lambda = 0$, $\mu_1 > 0$, $\mu_2 = 0$, $\beta_n^* = \frac{\varphi_1 - 1}{P_n H_n^l}$.
- If $\lambda = 0$, $\mu_1 = 0$, $\mu_2 > 0$, $\beta_n^* = \frac{1}{\varphi_2}$.
- If $\lambda = 0$, $\mu_1 > 0$, $\mu_2 > 0$, $\beta_n^* = \frac{\varphi_1 - 1}{P_n H_n^l} = \frac{1}{\varphi_2}$.

V. SIMULATION RESULTS

In this section, we evaluated the performance of the multi-user NOMA wireless system with the proposed sub-band allocation and power allocation schemes. We assume that one BS placed in the cell center with the perfect CSI. To keep the demodulation complexity of the SIC receiver is lower, we assume that each user can only be assigned to one sub-band and only two users are allocated per sub-band. For the simulation, we let the minimum data rates for each user requirement to be equal. Table 1 shows the detailed simulation parameters.

TABLE I
SIMULATION PARAMETERS

Parameter Name	Value
No. of Subcarriers (SB)	3
No. of Users (U)	6
Noise Power Density (N_0)	-174dBm/Hz
Total Bandwidth (B)	5MHz
Range of system transmit power (P_{tot})	20dBm~40dBm
Minimum rate requirement ($R_{m,n}^{\min}$)	0.5Mbps
Cell Diameter (d)	500m

To compare with other schemes, we simulated the proposed resource allocation scheme SOSA + FTPA + KKT, SOSA + EPA + KKT, SOMSA + EPA + KKT and the optimal NOMA.

Figure 3 below shows the throughput of all the comparison schemes. In general, as the total system transmits

power increases, the trend of simulation curves is also increasing. As can be observed in this figure, our proposed scheme displays better performance than other schemes. It is also the closest one to the optimal. In our proposed scheme, the use of EPA for power allocation between sub-bands shows a lower performance than using FTPA, but the power allocation mechanism is simpler. In addition, we also compared with the sub-band allocation algorithm SOMSA proposed by [5] and find that the SOSA proposed in this paper can achieve almost the same performance and a lower complexity.

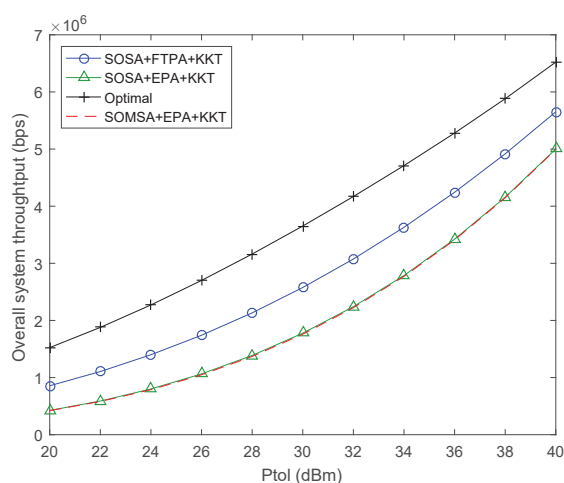


Fig. 3. Overall sum rate evaluates against increasing system transmit power.

VI. CONCLUSIONS

In this paper, we investigated the throughput optimization problem of the downlink NOMA system, and propose a low complexity sub-optimal resource allocation scheme. Simulations demonstrate that the proposed scheme has the closest performance to the optimal scheme and is superior to other schemes. The results also show that

the proposed sub-band allocation algorithm can get the comparable performance as the SOMSA proposed in [5], and the complexity is low. In addition, system performance obtained with EPA during sub-channel power allocation is significantly lower than that of FTPA. In a word, the proposed optimized scheme can get better system performance with lower complexity and improve real-time performance of telemedicine communication.

REFERENCES

- [1] X. Lin, R. Lu, X. Shen, Y. Nemoto, and N. Kato, "SAGE: A strong privacy-preserving scheme against global eavesdropping for ehealth systems," *IEEE J. Sel. Areas Commun.*, vol. 27, no. 4, pp. 365- 378, May 2009.
- [2] G. Samadi, Mohammad, and A. Mehrangiz. "OPCA: Optimized Prioritized Congestion Avoidance and Control for Wireless Body Sensor Networks," *International Journal of Sensors Wireless Commun. and Control*, vol. 6, no. 2, pp. 118-128, 2016.
- [3] M. De, D. Willian, and G. Paulo. "M-Health Solutions Using 5G Networks and M2M Communications," *IT Professional*, vol. 18, no. 3, pp. 24-29, 2016.
- [4] Y. Saito, Y. Kishiyama, A. Benjebbour, T. Nakamura, A. Li and K. Higuchi, "Non-Orthogonal Multiple Access (NOMA) for Cellular Future Radio Access," in *Pro. IEEE VTC Spring*, Jun. 2013, pp. 1-5.
- [5] F. Fang, H. Zhang, J. Cheng and V. C. M. Leung, "Energy efficiency of resource scheduling for non-orthogonal multiple access (NOMA) wireless network," in *Pro. IEEE Int. Conf. on Commun. (ICC)*, May. 2016, pp. 1-5.
- [6] A. Benjebbour, A. Li, Y. Saito, Y. Kishiyama, A. Harada, and T. Nakamura, "System-level performance of downlink nomu for future lte enhancements," in *Pro. IEEE Globecom Workshops (GC Wkshps)*, Atlanta, GA, 2013, pp. 66-70.
- [7] S. N. Datta and S. Kalyanasundaram, "Optimal power allocation and user selection in non-orthogonal multiple access systems," in *Pro. IEEE Wireless Commun. and Networking Conf.*, Apr. 2016, pp. 1-6.
- [8] M. S. Ali, H. Tabassum and E. Hossain, "Dynamic User Clustering and Power Allocation for Uplink and Downlink Non-Orthogonal Multiple Access (NOMA) Systems," *IEEE Access*, vol. 4, no., pp. 6325-6343, Oct. 2016.
- [9] Y. Saito, A. Benjebbour, Y. Kishiyama, and T. Nakamura, "System-level performance evaluation of downlink non-orthogonal multiple access (NOMA)," *IEEE PIMRC*, pp. 611-615, Sep. 2013.
- [10] S. Park, D. Cho, "Random Linear Network Coding based on Non-Orthogonal Multiple Access in Wireless Networks," *IEEE Commun. Lett.*, vol. 19, no. 7, pp.1273-1276, 2015.
- [11] S. Boyd and L. Vandenberghe, *Convex Optimization*, U.K.: Cambridge Univ. Press, 2004.

A Low Complexity SCMA Detector Based on Avoiding Redundant Iterations

Shuliang Hao¹, Xin Su², Jie Zeng², Xin Ma³, Tiejun Lv⁴

¹Chongqing University of Posts and Telecommunications, Chongqing, China

²Tsinghua University, Beijing, China

³Beijing Gongjin Electronics Co., Ltd, Beijing, China

⁴Beijing University of Posts and Telecommunications, Beijing, China

Email: suxin@tsinghua.edu.cn

Abstract—Sparse code multiple access (SCMA), a competitive air-interface technology with the message passing algorithm (MPA) employed at the receiver, has a broad application prospect. However, the computational complexity of MPA is still an extreme challenge for SCMA decoding. In this paper, a low complexity multiuser detection algorithm based on avoiding redundant iterations, namely Avoiding Redundant Iterations-MPA (ARI-MPA), is proposed for the uplink SCMA system. ARI-MPA can achieve low complexity by avoiding redundant iterations, in which the number of iterations required is determined by the convergence rate of codeword probability. Numerical results demonstrate that the proposed scheme can achieve an affordable trade-off between bit error ratio (BER) performance and decoding complexity for the SCMA system.

Keywords—Sparse code multiple access, message passing algorithm, avoiding redundant iterations, multiuser detection

I. INTRODUCTION

Medical monitoring systems employing implant vital sensors or wearable and wireless communication systems will receive more attention in the future [1]-[3]. However, various types of sensors in a wearable vital sensor node have varying data rates, and that the allowable communication error ratio and the delay have higher accuracy requirements. As a result, the fifth generation (5G) mobile communication systems should support many different types of medical services with tighter requirements: lower latency, higher level of quality of service and more massive connectivity. To satisfy these demands, some potential candidates have been proposed to address challenges of 5G, such as ultra dense network (UDN) [4], large-scale MIMO (multiple-input multiple-output) [5], device to device (D2D) [6], non-orthogonal multiple access (NOMA) [7], and so on. NOMA can be a feasible solution to meet these requirements.

Sparse code multiple access (SCMA) [8]-[10] is one of NOMA technologies, which is commonly considered as one promising candidate to tackle these challenges in 5G. The major challenges of SCMA are its codebook design at the transmitter side and decoding complexity at the receiver side. This paper mainly focuses on the low complexity decoding algorithm at the receiver side. Message passing algorithm (MPA) [11] can achieve low decoding complexity, due to exploiting the sparsity of the SCMA structure. Its decoding

complexity can be lower than maximum-likelihood (ML) based on exhaustive method. Furthermore, MPA can achieve the shaping gain of the multi-dimensional codebooks efficiently, by combination quadrature amplitude modulation (QAM) and sparse spreading. However, as the number of iterations or connected users increases, the decoding complexity of the MPA increases dramatically. To reduce the decoding complexity, [12] proposed a log-domain based MPA, in which messages are computed in log domain. The complexity is further reduced by max-log-MPA proposed in [13]. Max-log-MPA uses maximization operation max instead of Jacobian logarithm max*. But it can result in some performance loss. In [14], a low complexity MPA detection algorithm based on edge selection was proposed, where unselected edges apply Gaussian approximation. The authors in [15] investigated a list sphere decoding based multiuser detection algorithm. However, most of these works mentioned above are mainly focused on algorithm optimization in each iteration. In this paper, we attempt to design a low complexity detector from the perspective of the number of iterations.

Since the convergence of codeword probability at different time slots is different, the number of iterations required should be different. MPA with a uniform fixed number of iterations may have some redundant iterations. Motivated by this, an avoiding-redundant-iterations based low complexity SCMA multiuser detection algorithm is proposed in this paper, Avoiding Redundant Iterations-MPA (ARI-MPA), which can avoid redundant iterations by determining the optimal number of iterations to reduce the decoding complexity. The convergence rate of probability is defined as the codeword probability difference of both the current iteration and the previous iteration. ARI-MPA calculates the convergence rate of all the codewords before the end of each iteration. If the convergence rates of all codewords are less than the preset threshold, it can be considered that an acceptable convergence is achieved. These remaining redundant iterations are unnecessary to be involved in the rest of the decoding process. Simulation results demonstrate that the ARI-MPA can achieve a reasonable trade-off between bit error ratio (BER) performance and complexity for the system.

The paper has the following structure. The system model is described in Section II. Original MPA and ARI-MPA

algorithms are described in Section III. Simulation results are shown in Section IV. Section V draws the conclusions.

II. SYSTEM MODEL

A SCMA encoding procedure is regarded as a mapper from $\log_2(M)$ incoming bits to complex domain codebooks, which is the combination of modulation and sparse code spreading. Each codebook consists of M codewords, every one of which contains N non-zero elements and $(K - N)$ zeros. Each user has a unique codebook, which is selected from the set of J codebooks. The overloading is defined as $\lambda = J/K$.

A SCMA uplink system with $J = 6$ users and $K = 4$ resource elements (REs) is depicted in Fig.1. $M = 4$ dimensional codebook is applied in this system. The overloading of this system is 150%. Each $\log_2(M) = 2$ incoming binary bits of user j are first mapped to a $K = 4$ dimensional codeword \mathbf{x}_j . Then, 6 codewords are superimposed over 4 resource elements.

$$\mathbf{y} = \sum_{j=1}^J \text{diag}(\mathbf{h}_j) \mathbf{x}_j + \mathbf{n} \quad (1)$$

$$y_k = \sum_{j=1}^J h_{k,j} x_{k,j} + n_k \quad (2)$$

The received signal at the base station side is indicated by Equation (1). Where $\mathbf{x}_j = (x_{1,j}, \dots, x_{K,j})^T$ is the codeword, which is mapped from $\log_2(M)$ bits. $\mathbf{h}_j = (h_{1,j}, \dots, h_{K,j})^T$ is the channel vector. Vector \mathbf{n} denotes the Gaussian noise, of which the mean is zero and the variance is σ^2 . For the k -th resource element, the received signal can be written as Equation (2). The subscript j is the index of user, k is the index of a RE.

III. DETECTION SCHEMES

Perfect channel state information at the receiver is assumed. ML algorithm can be used to detect the received signal. The most likely transmitted signal $\hat{\mathbf{x}}$ minimizes the squared Euclidean distance:

$$\hat{\mathbf{x}} = \arg \min \left\| \mathbf{y} - \sum_{j=1}^J \text{diag}(\mathbf{h}_j) \mathbf{x}_j \right\|^2 \quad (3)$$

Although the ML algorithm can achieve optimal system performance, it has very large complexity, $O(M^J)$, that can increase polynomially with the codebook size M and exponentially with the number of user J .

A. Original MPA Detection Review

SCMA codewords can be decoded by MPA. MPA is an iterative suboptimal algorithm with lower complexity than ML. The complexity is $O(M^{d_f})$, where the d_f represents the number of users occupying every RE. During the decoding, soft information of codewords are exchanging between function nodes (FN) and variable nodes (VN) in an iterative way until the preset number of iteration is reached. During each iteration,

two main steps are involved: FN update and VN update. For FN update, messages from VNs are first sent to FNs. And then, each FN calculates extrinsic information for each codeword, and the previously received information is to be sent back to the VNs. For VN update, the extrinsic information from VN to FN will be updated. The two steps are defined as Equation (4) and (5). $I_{f_k \rightarrow v_j}^t$ and $I_{v_j \rightarrow f_k}^t$ represent FN update and VN update in the t -th message passing iteration, respectively.

$$I_{f_k \rightarrow v_j}^t(\mathbf{x}_j) = \sum_{\mathbf{x}_j} \left\{ \frac{1}{\sqrt{2\pi}\sigma} \exp \left(-\frac{1}{2\sigma^2} \left\| \mathbf{y}_k - \sum_{m \in \xi_k} h_{k,m} x_{k,m} \right\|^2 \right) \times \prod_{l \in \xi_k / \{j\}} I_{v_l \rightarrow f_k}^{t-1}(\mathbf{x}_l) \right\} \quad (4)$$

$$I_{v_j \rightarrow f_k}^t(\mathbf{x}_j) = \prod_{m \in \zeta_j / \{k\}} I_{f_m \rightarrow v_j}^t(\mathbf{x}_j) \quad (5)$$

Where ξ_k and ζ_j donate the set of non-zeros index in the k -th row and j -th column respectively.

When the maximum iteration T_{max} is reached, the soft output for each codeword can be expressed as Equation (6).

$$Q(\mathbf{x}_j) = \prod_{k \in \zeta_j} I_{f_k \rightarrow v_j}^{T_{max}}(\mathbf{x}_j) \quad (6)$$

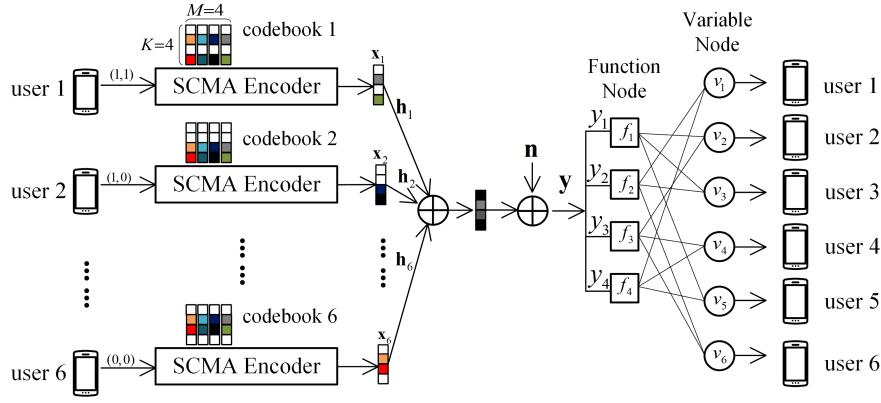
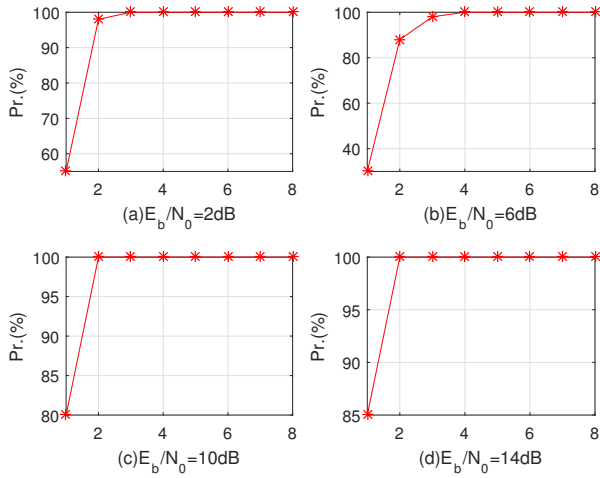
Last, bitwise soft output can be computed by the bit-to-codeword mapping.

B. Proposed ARI-MPA

In the original MPA algorithm, although the maximum number of message passing iterations has been set, the decoding process does not require so many iterations at different time slots. Fig.2 shows the convergence of a codeword probability in different E_b/N_0 under the original MPA algorithm, where the number of iterations T_{max} is 8. When $E_b/N_0 = 2\text{dB}$, this codeword only needs $t = 3$ iterations. However, when $E_b/N_0 = 6\text{dB}$, the codeword need $t = 4$ iterations. Thus, these remaining $(T_{max} - t)$ iterations, regarded as redundant iterations, should be deleted to reduce the complexity.

Based on the above existing problems, the ARI-MPA algorithm can be used to reduce the complexity by avoiding redundant iterations that may exist in each time slot. This algorithm first obtains the convergence rate of all codewords $w^t(\mathbf{x}_j)$. And if the $w^t(\mathbf{x}_j)$ is less than the preset threshold h_A ($0 \leq h_A \leq 1$), it means that the best convergence has been achieved. ARI-MPA with a lower threshold have a better convergence, and can achieve a higher BER performance gain. The definition of convergence rate can be expressed as Equation (7), where $Q^t(\mathbf{x}_j)$ is the codeword probability of user j .

$$w^t(\mathbf{x}_j) = |Q^t(\mathbf{x}_j) - Q^{t-1}(\mathbf{x}_j)| \quad (7)$$

Fig. 1. SCMA uplink system ($J = 6, K = 4, M = 4$)Fig. 2. Convergence of codeword probability under different E_b/N_0 for MPA

Based on the above analysis, the ARI-MPA algorithm can determine the optimal number of iterations, eliminate the redundant iterations effectively. The detailed algorithm is shown in Algorithm 1. Where $LLR_{j,i}$ denotes soft output of the i -th bit for user j , $1 \leq i \leq \log_2(M)$.

Different from the original MPA algorithm, ARI-MPA needs to calculate the convergence rate of each possible codeword before the end of each iteration and compare it with a preset threshold. These operations make that ARI-MPA are more complex at each iteration than the original MPA. However, ARI-MPA without redundant iterations can reduce the complexity in the whole decoding process. ARI-MPA algorithm can effectively determine the optimal number of iterations and avoid redundant iterations.

C. Complexity Analysis

The complexity of the SCMA multi-user detection algorithm is mainly reflected in the exponentiation and the number of iterations.

Algorithm 1 The ARI-MPA algorithm

Input: $\mathbf{y}, \mathbf{H}, \sigma^2, T_{max}$
Output: $LLR_{j,i}$
Initialization: $Q^0(\mathbf{x}_j) = 1/M$, $I_{v_j \rightarrow f_k}^0(\mathbf{x}_j) = 1/M$
 $\max(w^0(\mathbf{x}_j)) = 1$, $t = 1$

- 1: **while** $((t \leq T_{max}) \&\& (\max(w^{t-1}(\mathbf{x}_j)) \geq h_A))$ **do**
- 2: **for** $k = 1, 2, \dots, K$ **do**
- 3: Equation (4) // FN update
- 4: **end for**
- 5: **for** $j = 1, \dots, J$ **do**
- 6: Equation (5) // VN update
- 7: $Q^t(\mathbf{x}_j) = \text{normalize}(\prod_{k \in \zeta_j} I_{f_k \rightarrow v_j}^t(\mathbf{x}_j))$
- 8: Equation (7) // Calculation of convergence rate
- 9: **end for**
- 10: $t = t + 1$
- 11: **end while**
- 12: **for** $j = 1, \dots, J$ **do**
- 13: $LLR_{j,i} = \log \left(\frac{\sum_{b_{\mathbf{x}_j,i}=0} Q^{t-1}(\mathbf{x}_j)}{\sum_{b_{\mathbf{x}_j,i}=1} Q^{t-1}(\mathbf{x}_j)} \right)$
- 14: **end for**
- 15: **return** $LLR_{j,i}$

The decoding complexity of original MPA and ARI-MPA is analyzed here. To obtain $h_{k,m}x_{k,m}$ ($k = 1, \dots, K, m = 1, \dots, M$), $2MKd_f$ additions and $4MKd_f$ multiplications must be involved. During the process of FN update, for one variable node, MPA need $(2d_f + 1)M^{d_f-1}$ additions, $(d_f + 2)M^{d_f-1}$ multiplication, and M^{d_f-1} exponentials. During the process of VN update, for one variable node, $d_v - 1$ additions are involved. The main difference between ARI-MPA and MPA is the process of VN update. Since this process needs to calculate the convergence rate of the codeword probability for each iteration, extra $2MJ$ multiplications and MJ comparisons are required for each iteration. The complexity of MPA and ARI-MPA is shown in Table I, where ADD, MUL, EXP and CMP respectively represent addition, multiplication, exponential and comparison operations, T_{max} is the maximum number of iterations, t_{slot}^A is the number of iterations for

ARI-MPA at different time slots, d_v represents the number of resources that occupied by every user.

TABLE I
COMPLEXITY COMPARISON

Algorithms	MPA	ARI-MPA
ADD	$(2d_f + 1)M^{d_f}Kd_fT_{max}$ $+(d_v - 2)MKd_fT_{max}$ $+2MKd_f$	$(2d_f + 1)M^{d_f}Kd_ft_{slot}^A$ $+(d_v - 2)MKd_ft_{slot}^A$ $+2MKd_f$
MUL	$(d_f + 2)M^{d_f}Kd_fT_{max}$ $+4MKd_f$	$(d_f + 2)M^{d_f}Kd_ft_{slot}^A$ $+4MKd_f + 2MJt_{slot}^A$
EXP	$M^{d_f}Kd_fT_{max}$	$M^{d_f}Kd_ft_{slot}^A$
CMP	0	JMt_{slot}^A

The reduced complexity of ARI-MPA is mainly achieved by the reduction of the number of message passing iterations. Due to the different time slots, it is difficult to see the advantages of complexity for ARI-MPA. To compare the complexity of MPA and ARI-MPA precisely, the exact number of passing message iterations for ARI-MPA must be known first. The complexity of ARI-MPA algorithm will be further discussed next part.

IV. SIMULATION RESULTS

In this part, the BER performance and complexity of SCMA with MPA and ARI-MPA are evaluated. In this simulation, $J = 6$ users are multiplexed over $K = 4$ REs, and the dimension of codebook $M = 4$. The maximum number of iterations $T_{max} = 5$. The codebook used in this simulation is 4-dimensional codebooks in [16].

A. The BER Performance

BER performance of SCMA systems with original MPA and ARI-MPA in an additional white gaussian noise channel is evaluated in Fig.3. When E_b/N_0 is 10 dB, the original MPA and ARI-MPA with $h_A = 0.001$ have the same BER value. It can also be seen from Fig.3 that the original MPA and ARI-MPA with $h_A = 0.001$ have exactly the same BER performance curves. At this time, the ARI-MPA with $h_A = 0.010$ has poorer BER performance than the two mentioned above, but it is still within tolerance. However, the BER performance of the ARI-MPA with $h_A \geq 0.050$ has much performance loss. From the simulations below, the average number of message passing iterations for ARI-MPA with $h_A = 0.100$ is about two. However, it has a better BER performance than the original MPA with $T_{max} = 2$.

B. Complexity

The advantage of ARI-MPA is the elimination of redundant iterations at each time slot. As can be seen from Table I, the difference between MPA and ARI-MPA algorithm is mainly reflected in the number of iterations. Therefore, we first simulate the number of iterations under the ARI-MPA algorithm.

The average number of message passing iterations for ARI-MPA at different E_b/N_0 is shown in Fig.4. It can be observed from the Fig.4, that the average number of message passing

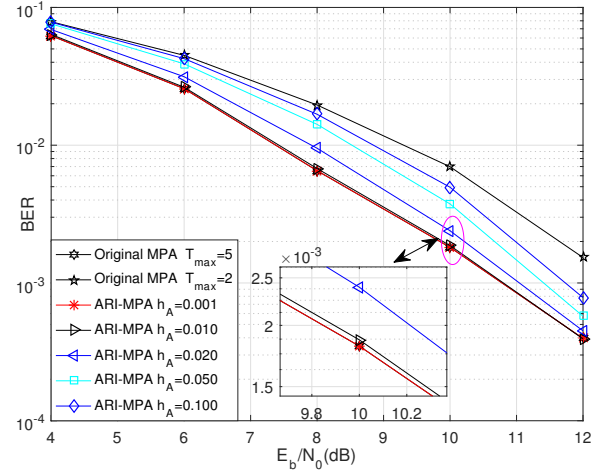


Fig. 3. The BER performance comparison between MPA and ARI-MPA

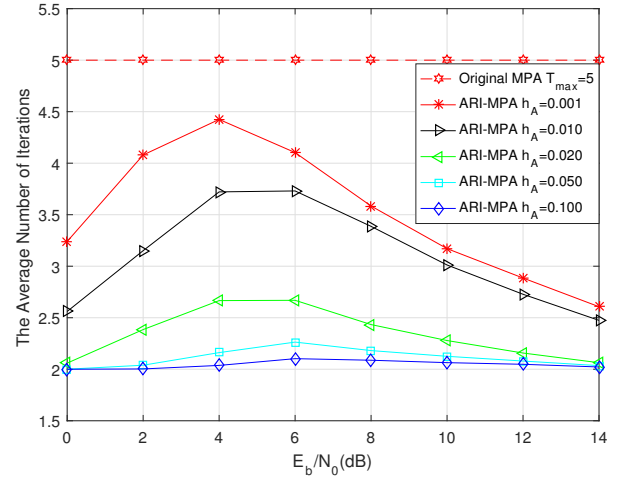


Fig. 4. The average number of iterations of ARI-MPA under different E_b/N_0

iterations of the ARI-MPA is less than the maximum number of iterations T_{max} . As can also be seen from the figure, the average number of iterations does not have a linear correlation with E_b/N_0 . The relationship between them should be further studied.

After obtaining the average number of iterations of the ARI-MPA under different E_b/N_0 , the complexity comparison between ARI-MPA and MPA can be easily derived from Table I. The computational complexity reduction ratio (CCRR) is used to compare the complexity of these two algorithms. The CCRR is defined as the ratio of the complexity difference, of both original MPA and ARI-MPA, and the complexity of original MPA. The ARI-MPA algorithm needs a certain comparison operation, which has been neglected in this paper due to its low complexity. Fig.5 shows the CCRR cures of ARI-MPA over the original MPA with $T_{max} = 5$. It can be seen from the figure that when the is 0.001, the maximum

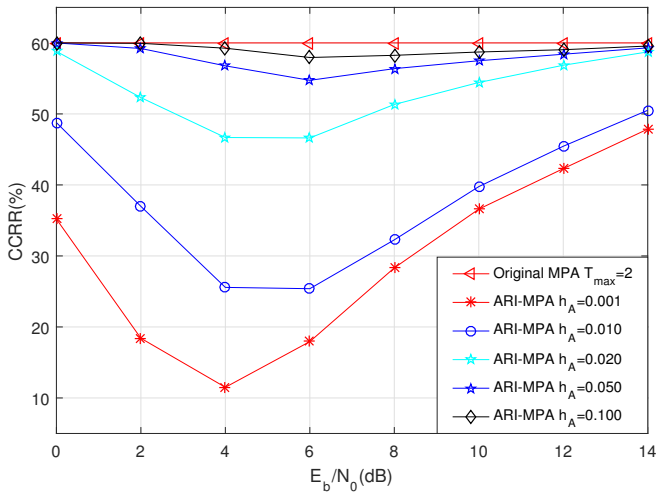


Fig. 5. The CCRR of ARI-MPA over original MPA with $T_{max} = 5$

CCRR value of ARI-MPA with the best BER performance is 47.86% and the minimum is 11.50%. And the CCRR becomes larger as the value of h_A becomes larger. Which all shows the effectiveness of reducing complexity by the method of avoiding redundant iteration.

V. CONCLUSION

In this paper, we have proposed a low complexity multiuser detection algorithm based on avoiding redundant iterations that can reduce the decoding complexity by removing redundant iterations in the SCMA uplink system. Compared with the original MPA, ARI-MPA can achieve a low decoding complexity with a better BER performance. The idea based on avoiding redundant iterations can be also applied in the log-domain MPA, which may have a lower complexity than ARI-MPA.

REFERENCES

- [1] Min Chen, Sergio Gonzalez, Athanasios Vasilakos, et al. Body Area Networks: A Survey[J]. Mobile Networks and Applications, 2011, 16(2):171-193.
- [2] Viswanathan H, Chen B, Pompili D. Research challenges in computation, communication, and context awareness for ubiquitous healthcare[J]. Communications Magazine IEEE, 2012, 50(5):92-99.
- [3] Bachmann C, Ashouei M, Pop V, et al. Low-power wireless sensor nodes for ubiquitous long-term biomedical signal monitoring[J]. IEEE Communications Magazine, 2012, 50(1):20-27.
- [4] Jie Zeng, Qi Zhang, Xin Su, et al. An Improved Dynamic Clustering Algorithm Based on Uplink Capacity Analysis in Ultra-Dense Network System[C]// International Wireless Internet Conference. Springer, Cham, 2016:218-227.
- [5] Su X, Zeng J, Rong L P, et al. Investigation on Key Technologies in Large-Scale MIMO[J]. Journal of Computer Science & Technology, 2013, 28(3):412-419.
- [6] Khandaker M R A, Masouros C, Wong K K. Secure Full-Duplex Device-to-Device Communication[J]. 2017.
- [7] Zeng J, Kong D, Liu B, et al. RIePDMA and BP-IDD-IC detection[J]. Eurasip Journal on Wireless Communications & Networking, 2017, 2017(1):12.
- [8] Wang P, Xiao J, Ping L. Comparison of orthogonal and non-orthogonal approaches to future wireless cellular systems[J]. Vehicular Technology Magazine IEEE, 2006, 1(3):4-11.

- [9] Dai L, Wang B, Yuan Y, et al. Non-orthogonal multiple access for 5G: solutions, challenges, opportunities, and future research trends[J]. IEEE Communications Magazine, 2015, 53(9):74-81.
- [10] Nikopour H, Baligh H. Sparse code multiple access[C]// IEEE, International Symposium on Personal Indoor and Mobile Radio Communications. IEEE, 2013:332-336.
- [11] Kschischang F R, Frey B J, Loeliger H A. Factor graphs and the sum-product algorithm[C]// IEEE Transactions on Information Theory. 1998:498-519.
- [12] Xiao K, Xiao B, Zhang S, et al. Simplified multiuser detection for SCMA with sum-product algorithm[C]// International Conference on Wireless Communications & Signal Processing. IEEE, 2015:1-5.
- [13] Zhang S, Xu X, Lu L, et al. Sparse code multiple access: An energy efficient uplink approach for 5G wireless systems[C]// Global Communications Conference. IEEE, 2014:4782-4787.
- [14] Du Y, Dong B, Chen Z, et al. Low-Complexity Detector in Sparse Code Multiple Access Systems[J]. IEEE Communications Letters, 2016, 20(9):1812-1815.
- [15] Wei F, Chen W. Low Complexity Iterative Receiver Design for Sparse Code Multiple Access[J]. IEEE Transactions on Communications, 2017, 65(2):621-634.
- [16] Altera Innovate Asia website, Presentation 1st 5G Algorithm Innovate Competition-ENV1.0-SCMA, Web: <http://www.innovateasia.com/5g/en/gp2.html>.

A Channel Estimation Method Based on the Improved LMS Algorithm for MIMO-OFDM Systems

Zhenfeng Zhang
Broadband Wireless Access Laboratory
Chongqing University of Posts
and Telecommunications
Chongqing, China
Email: 981831456@qq.com

Limin Xiao, Xin Su, Jie Zeng, Xibin Xu
Tsinghua National Laboratory for Information Science
and Technology Research Institute of Information Technology
Tsinghua University
Beijing, China
Email: xiaolm@tsinghua.edu.cn,
suxin@tsinghua.edu.cn,
zengjie@mail.tsinghua.edu.cn

Abstract—The least mean square (LMS) algorithm is a kind of typical adaptive filter algorithms. The algorithm of channel estimation algorithm based on LMS is no need to know the characteristics of channel and noise statistics, which make full use of channel correlation between front and back to reduce the influence of noise on channel estimation performance. In this paper, the LMS algorithm has been improved under the MIMO-OFDM systems. Then, a revised method for variable step size has been put forward, which accelerates the rate of convergence to improve channel estimation performance preferably. The simulation results show that the algorithm proposed in this paper not only has the fastest convergence compared with LMS and NLMS algorithm, but also has a better channel estimation(CE) performance than other estimation algorithms.

Keywords—MIMO-OFDM; channel estimation; the least mean square algorithm; variable step size; NLMS

I. INTRODUCTION

MIMO-OFDM technology is the core of the forth generation of wireless communication(4G) technology [1], which can support high speed data transmission and has a series of advantages, such as decreasing frequency selective fading and higher spectrum efficiency. High speed data transmission has promoted the development of digital medical treatment and smart medical treatment. Technologies such as big data, cloud computing, virtualized radio access Network [2][3] and Internet of things have been applied to the medical field. Through digital mode, medical resources can be shared by many people and the occurrence of diseases can be effectively reduced and controlled. The development of modern technology lays the foundation for people to provide a better life, This new form of smart medical technology is formally conducive to solving one of the most difficult problems in China, such as the difficulty of seeing a doctor, the inefficiency of a hospital, and the imbalance of medical resources. In MIMO-OFDM system, accurate channel state information(CSI) is needed for space-time coding and so on. Achieving frequent and accurate CE

is key to guaranteeing the stability and reliability of system transmission.

Usually the CE algorithm is divided into based on the pilot-CE and the blind-CE algorithm. The blind-CE algorithm [4] needn't sending pilot sequences, but using the received information sequence to make channel estimation. The Pilot-based channel estimation algorithm generally includes the Least squares (LS) algorithm, Minimum Mean Square Error (MMSE) algorithm [5], and the Linear Minimum Mean Square Error (LMMSE) algorithm [6]. The MMSE algorithm is difficult to apply to the actual system due to the large calculation of matrix inversion and the channel information that have to be known (such as self-related functions). Therefore, literatures [7][8] have studied the singular value decomposition and discrete fourier transform(DFT) and other improved methods respectively in order to make a compromise between calculation complexity and estimation performance.

The LMS algorithm is proposed in Widrow and Hoff research pattern recognition. In order to solve shortcomings of the traditional fixed-step LMS algorithm, Many domestic and foreign scholars have made some improvements about the algorithm. The step size factor not only controls the convergence speed of the algorithm, but also determines the steady-state error of the algorithm. Therefore, the step size factor is an inconsistent amount during the iteration of the algorithm[9][10]. In order to overcome this shortcoming, many variable-length LMS algorithms have been proposed. Literature [11] proposed an adaptive channel tracking and estimation method, which is a kind of channel tracking and estimation method that doesn't need channel statistics and based on the LMS algorithm.

With the convergence problem in LMS algorithm, this paper improves the step size of LMS algorithm, and puts forward a MIMO-OFDM channel estimation method on the improved LMS algorithm. This method does not require the channel statistics and the transcendental channel information, moreover, there is faster convergence and higher accuracy to

reach target of tracking effectively. At the same time, it reduces the complexity of the implementation by avoiding the inverse matrix of the matrix. If put the method into to intelligent medical treatment and digital medical treatment will benefit the modernization of medical service where be improve in our country.

II. THE IMPROVED VARIABLE STEP SIZE LMS ALGORITHM

A. System model

MIMO-OFDM system model based on the STBC description of typical is shown in Fig.1.

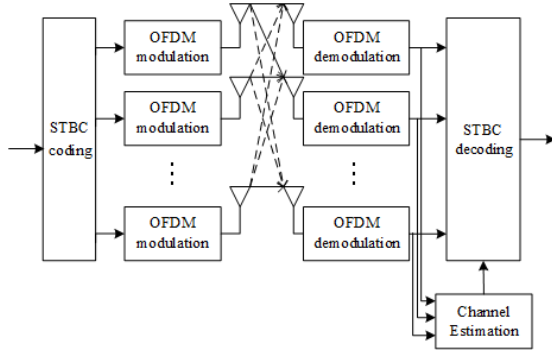


Fig. 1. MIMO-OFDM system model

In MIMO-OFDM system, there are N_t transmitting antennas and N_r receiving antennas. firstly, transmitting antennas modulates a binary data bit stream $\{b[n, k] : k = 0, 1, \dots\}$, then N_t parallel data streams are generated through the MIMO encoder and modulated into a signal of OFDM $\{x_i[n, k] : i = 0, 1, \dots, N_t; k = 0, 1, \dots\}$ which is sent out by different antennas. At the receiver, the signal of each receiving antenna is the sum of multipath signals and noise, which is denoted as $\{y_j[n, k] : i = 0, 1, \dots, N_r; k = 0, 1, \dots\}$.

So, system model can be written as

$$\mathbf{Y} = \mathbf{H}\mathbf{X} + \mathbf{Z} \quad (1)$$

where \mathbf{X} is a matrix with value of pilot signal on its diagonal, \mathbf{H} is channel transfer function, \mathbf{Z} is Gaussian noise vector, \mathbf{Y} is received signal vector.

B. The LMS algorithm

Adaptive system can rely on a certain pre-determined criteria, without knowing the priori knowledge of the statistical properties of the input signal. It adjusts the parameters of the filtering system automatically to achieve the optimal filtering under this criterion.

The LMS algorithm is developed on the basis of Wiener filtering, according to the idea of the steepest descent method. The method is simple which neither need calculating the correlation function nor need inverse matrix. The rule of LMS algorithm is to minimize the mean square error between actual output from filter and desired output. The block diagram is shown in Fig.2.

The LMS algorithm is summarized as follows[12]

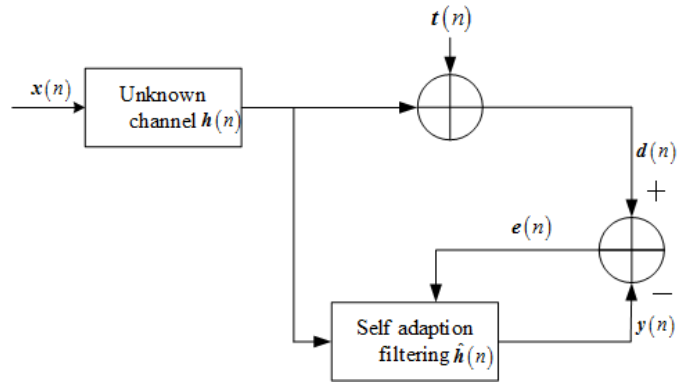


Fig. 2. Self-adaption algorithm schematic diagram

Step 1: Initialization $\mathbf{w}(0) = 0$;

Step 2: Renew: $n = 1, 2, \dots$

$$e(n) = d(n) - \mathbf{w}^H \mathbf{x}(n) \quad (2)$$

$$\mathbf{w}(n) = \mathbf{w}(n-1) + \mu e^*(n) \mathbf{x}(n) \quad (3)$$

(1) if $\mu = C$, C expression constant, is called the basic LMS algorithm.

(2) if $\mu = \frac{\alpha}{\beta + \mathbf{x}^H(n) \mathbf{x}(n)}$, $\alpha \in (0, 2)$, $\beta \geq 0$, is called NLMS.

In the formula above, $\mathbf{x}(n)$ is the input vector; $\mathbf{w}(n)$ is the tap weight vector; $e(n)$ is the estimation error at n time of filter; $d(n)$ represents the desired signal; μ stands for the step-size.

The step size parameter μ in LMS algorithm determines the renewal amounts of the tap weight vector at each iteration. It is also the key parameter which can effect the convergence rate.

C. The improved variable step size LMS algorithm

The classical LMS algorithm is easy to implement due to the simplicity and low complexity. However, there is a conflict between the steady state error and the convergence rate. In order to obtain a faster convergence rate under the premise of convergence, the step size factor μ should set larger. The large step size factor is, the large steady state error is. Thus, this results a decrease in accuracy. On the contrary, the smaller the steady state error is, the slower the convergence rate is. In order to solve the contradiction, the convergence factor with variable step size is adopted. The algorithm replaces the fixed length μ with the variable $\mu(k)$. We adopt a larger step size in order to obtain faster convergence speed and tracking speed at the beginning of the algorithm. Then, the step size is decreased gradually for a smaller steady state error.

$\mathbf{h}(k) = [\mathbf{h}_0(k), \mathbf{h}_1(k), \dots, \mathbf{h}_{M-1}(k)]$ is the channel impact response of the unknown system, and M represents for the number of taps in the filter, $\hat{\mathbf{h}}(k) = [\hat{\mathbf{h}}_0(k), \hat{\mathbf{h}}_1(k), \dots, \hat{\mathbf{h}}_{M-1}(k)]$ represents the channel impulse response estimation at the time of k . Then the LMS is updated to

$$\hat{\mathbf{h}}(k+1) = \hat{\mathbf{h}}(k) + \mu(k) e(k) \mathbf{x}(k) \quad (4)$$

In the formula above, $d(k)$ represents the desired signal, (\bullet) represents the inversion of vector, $\mu(k)$ is variable step size, $e(k)$ is the error between the desired signal and the output signal, $z(k)$ is noise signal, which is

$$d(k) = e(k) + s(k) \quad (5)$$

$$s(k) = \mathbf{x}^T(k) \hat{\mathbf{h}}(k) \quad (6)$$

$$d(k) = \mathbf{x}^T(k) \mathbf{h}(k) + z(k) \quad (7)$$

The excess error is defined as

$$\eta(k) = e(k) - z(k) \quad (8)$$

and the deviation is defined as

$$\gamma(k) = \mathbf{h}(k) - \hat{\mathbf{h}}(k) \quad (9)$$

Substituting equation (5), equation (7) and equation (9) into equation (8), the relationship between the excess error and the deviation vector can be formulated as

$$\eta(k) = \gamma(k)^T \mathbf{x}(k) \quad (10)$$

To derive the optimal step size, we make those assumptions as follows:

A.1. Step size $\mu(k)$ and $e(k)$, $\mathbf{x}(k)$ and $\eta(k)$, are independent of each other.

A.2. The noise $z(k)$ and the excess error signal $\eta(k)$ are independent.

A.3. The input signals are statistically fixed and $\|\mathbf{v}\|^2$ can be approximated as a constant $M\sigma^2$, $\|\bullet\|^2$ is the square Euclidean mode operation.

The optimal step size of the LMS algorithm formulated in [13] is defined as the value which can obtain the largest decrease of the MSD $E\{\|\gamma(k)\|^2\}$ at each iteration. The largest decrease of the MSD is obtained by maximizing $f(k) = E\{\|\gamma(k)\|^2\} - E\{\|\gamma(k+1)\|^2\}$.

$$f(k) = -\mu^2(k)E\{e^2(k)\|\mathbf{x}(k)\|^2\} + 2\mu(k)E\{e(k)\gamma^T(k)\mathbf{x}(k)\} \quad (11)$$

substituting equation (10) into equation(11), we obtain equation (12) as follows.

$$f(k) = -\mu^2(k)E\{e^2(k)\|\mathbf{x}(k)\|^2\} + 2\mu(k)E\{e(k)\eta(n)\} \quad (12)$$

By setting $\partial E\{\|\gamma(k)\|^2\} - E\{\|\gamma(k+1)\|^2\}/\partial\mu(k) = 0$ The best step size is expressed as

$$\mu_{opt}(k) = \frac{E\{e(k)\eta(n)\}}{E\{e^2(k)\|\mathbf{x}(k)\|^2\}} \quad (13)$$

Utilizing A.2 and A.3, Substituting the equation (8) into the equation (13) obtained the optimal step size

$$\mu_{opt}(k) \approx \frac{E\{\eta^2(k)\}}{\|\mathbf{x}(k)\|^2 E\{e^2(k)\}} \quad (14)$$

Theoretically, optimal step size come up by equation (14) gives the general guidance for the design of the variable step

size LMS algorithm, but the algorithm is impractical because the noise and its power are difficult to be obtained.

To deal with this problem, use A.2 to substitute equation (8) into equation (15), Then, equation (14) can be rewritten as:

$$\mu_{opt}(k) \approx \frac{E\{\eta^2(k)\}}{\|\mathbf{x}(k)\|^2 (E\{z^2(k)\} + E\{\eta^2(k)\})} \quad (15)$$

Taking advantage of A.3, equation (15) is rewritten as

$$\mu_{opt}(k) \approx \frac{E\{\frac{\eta(k)\mathbf{x}^T(k)}{\|\mathbf{x}(k)\|^2} \frac{\eta(k)\mathbf{x}(k)}{\|\mathbf{x}(k)\|^2}\}}{\|\mathbf{x}(k)\|^2 [\frac{E\{z^2(k)\}}{\|\mathbf{x}(k)\|^2} + E\{\frac{\eta(k)\mathbf{x}^T(k)}{\|\mathbf{x}(k)\|^2} \frac{\eta(k)\mathbf{x}(k)}{\|\mathbf{x}(k)\|^2}\}]} \quad (16)$$

Then, variable step size could be calculated by approximating the term $\frac{E\{z^2(k)\}}{\|\mathbf{x}(k)\|^2}$ as C, and the term $E\{\frac{\eta(k)\mathbf{x}^T(k)}{\|\mathbf{x}(k)\|^2} \frac{\eta(k)\mathbf{x}(k)}{\|\mathbf{x}(k)\|^2}\}$ as $\|\mathbf{g}(k)\|^2$

$$\mu_{opt}(k) \approx \frac{\mu_{max}\|\mathbf{g}(k)\|^2}{\|\mathbf{x}(k)\|^2 (C + \|\mathbf{g}(k)\|^2)} \quad (17)$$

where

$$\mathbf{g}(k) = \lambda \mathbf{g}(k-1) + (1-\lambda) \frac{\mathbf{x}(k)}{\|\mathbf{x}(k)\|^2} e(k) \quad (18)$$

In the formula above, $\mathbf{g}(0) = 0$ and λ is smoothing parameter that close to 1. μ_{max} is fixed step size which is set as 1.

III. THE MIMO-OFDM CHANNEL ESTIMATION METHOD BASED ON IMPROVED LMS ALGORITHM

A. The LS algorithm

The LS algorithm whose estimator is unbiased. The algorithm only needs one multiplication when it estimate the fading coefficient of each channel. The disadvantage is that affected by the noise greatly. It is one of several basic estimation algorithms with low computational complexity. At the same time, its channel estimation accuracy is not too low, and it can meet the requirements of the actual communication system. Therefore, it has become one of the most commonly channel estimation algorithms.

Define the cost function as shown in the formula (19)

$$\mathbf{J}(\mathbf{H}) = \min(\mathbf{Y} - \mathbf{H}\mathbf{X})^H (\mathbf{Y} - \mathbf{H}\mathbf{X}) \quad (19)$$

$$\frac{\partial \mathbf{J}(\mathbf{H})}{\partial \mathbf{H}} = 2\mathbf{X}^H (\mathbf{Y} - \mathbf{H}\mathbf{X}) \quad (20)$$

By setting $\partial \mathbf{J}(\mathbf{H})/\partial \mathbf{H} = 0$, the channel estimation formula can be express

$$\mathbf{H}_{LS} = \mathbf{X}^{-1}\mathbf{Y} \quad (21)$$

B. MIMO-OFDM channel estimation method based on improved LMS algorithm

In this paper, the adaptive channel estimation algorithm is derived from the LMS adaptive estimation algorithm. It makes the most of step size as the key to convergence rate and the characteristic of low computational complexity on the LMS adaptive algorithm. This method major includes the following steps.

Step.1: Using the LS to estimate the frequency domain, the estimated results can be expressed as

$$\mathbf{H}_{LS}(k) = \frac{\mathbf{Y}(k)}{\mathbf{X}(k)} \quad (22)$$

where $\mathbf{Y}(k)$ represents the receiving pilot signal, and $\mathbf{X}(k)$ represents the pilot sequence signal.

Step.2: Transform the gained channel frequency response to the time domain:

$$\mathbf{h}(k) = IDFT[\mathbf{H}_{LS}(k)] \quad (23)$$

Step.3: Obtain the initial channel estimation to carry out adaptive filtering and calculate the estimated error $e(k)$.

Step.4: Adjust the adaptive weights according to the improved variable step size.

$$\hat{\mathbf{h}}(k+1) = \hat{\mathbf{h}}(k) + \frac{\mu_{max} \|\mathbf{g}(k)\|^2}{\|\mathbf{x}(k)\|^2 (C + \|\mathbf{g}(k)\|^2)} \mathbf{e}(k) \mathbf{x}(k) \quad (24)$$

Step 5: Repeat Steps.3 and Steps.4 until the algorithm converges.

Step 6: Then the interpolation process, to obtain the entire data channel estimation results.

IV. SIMULATION RESULTS AND ANALYSIS

The simulation parameters are set as follows: the MIMO-OFDM system used in this simulation is configured as 2*2; the loop prefix is 16; the total sub-carrier number is 64; the number of pilot frequencies is 16, and is modulated by QPSK. The bandwidth is 20MHz and the carrier spacing is 312.5 kHz; the simulation channel is the Rayleigh fading channel of Jakes model; the number of channel taps is 6; FFT/IFFT sampling point is 512; Multi-antenna empty time code samples STBC encoding. The noise is named Gaussian, whose mean value is 0 and the variance is 0.01. The tap length is set to $M = 8$; μ_{max} is set to 1; λ is set to 0.999 and C is set to $2 * 10^{-4}$.

The algorithm comparison Fig.3 shows that the proposed algorithm in this paper needs fewer iterations to achieve the optimal solution compared with LMS and NLMS algorithm.

As can be seen from the Fig.4, with the SNR increasing gradually, the estimation performance of the adaptive algorithm based on variable step size proposed on this article is superior to the traditional LS algorithm and the LMS adaptive algorithm, and approximates the optimal MMSE algorithm. But because the proposed algorithm neednt channel statistics and transcendental state information, the algorithm has better

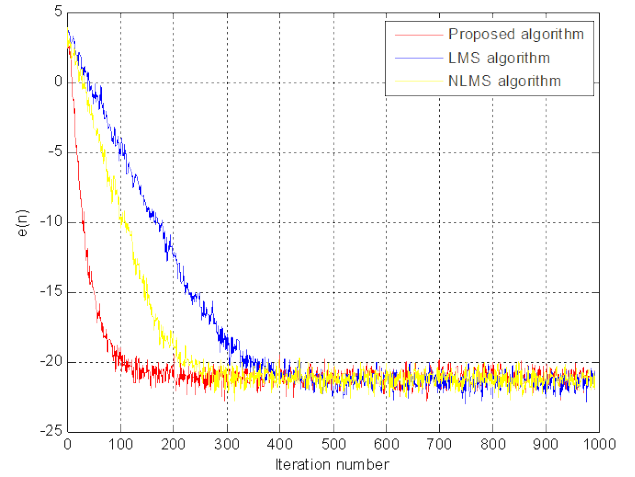


Fig. 3. Algorithm convergence comparison diagram

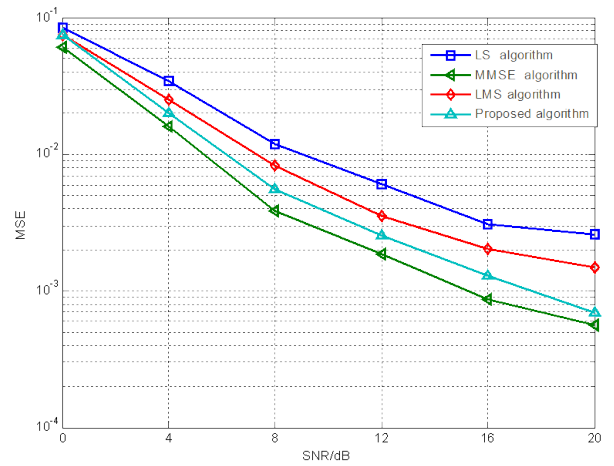


Fig. 4. Comparison of channel estimation MSE performance

applicability than MMSE algorithm which has higher complexity. so it is more suitable for time-varying fading channel on the harsh environment.

V. CONCLUSIONS

A novel estimation algorithm of variable step size adaptive channel has been put forward in this paper. Through the mathematical derivation and simulation, this algorithm can significantly reduce the MSE of the channel estimation and computational complexity under the premise that does not require any channel statistical information and priori information. In addition, the multi-antenna space-time coding technique is also combined, which has great significance to MIMO-OFDM system channel estimation.

REFERENCES

- [1] J. Li, J. Zeng, X. Su, W. Luo, and J. Wang, Self-optimization of coverage and capacity in LTE networks based on central control and decentralized fuzzy Q-Learning, *Int. J. Distrib. Sens. Networks*, vol. 2012, 2012.

- [2] J. Zeng, X. Su, J. Gong, L. Rong, and J. Wang, "5G Virtualized Radio Access Network Approach Based on NO Stack Framework", in *IEEE International Conference on Communications*, 2017, pp. 1C5.
- [3] J. Zeng, X. Su, J. Gong, L. Rong, and J. Wang, "A 5G Virtualized RAN Based on NO Stack", *China Commun.*, vol. 14, no. 6, pp. 199C208, 2017.
- [4] Morelli M, Mengali U, "A comparison of pilot-aided channel estimation methods for OFDM systems", *IEEE Transactions on Signal Processing*, 2002, 49(12):3065-3073.
- [5] Shin C, Heath R.W, Powers E, "Blind Channel Estimation for MIMO-OFDM systems Vehicular Technology", *IEEE Trans.*[2]2007, 3(56):670-685.
- [6] Wang S, Hu C, Peng T, et al, "A low complexity channel estimation approach of LTE downlink system", *IEEE, International Conference on Communication Technology. IEEE*, 2012:143-147.
- [7] Edeskar, T. "OFDM channel estimation by singular value decomposition", 2015.
- [8] Zhu H, Ge Y, Chen X. "DFT-based adaptive channel estimation for OFDM systems", *Communication Technology (ICCT), 2015 IEEE 16th International Conference on. IEEE* , 2015: 515-517.
- [9] W. Ang and B. Farhang-Boroujeny. "A new class of gradient adaptive step size LMS algorithms", *IEEE Trans. Signal Processing* , 2001,49(4):805-801P
- [10] E. Eweda. "Convergence analysis and design of an filter with finite-bitpower-of-two quantizer error", *IEEE Trans.on Circuits and System II:Analog and Digital Signal Processing* , vol.39, pp.113-115, Feb.1992.
- [11] Schafhuber D, Rupp M, Matz G, et al. "Adaptive identification and tracking of doubly selective fading channels for wireless MIMO-OFDM systems", *Signal Processing Advances in Wireless Communications, 2003. Spawc 2003. IEEE Workshop on. IEEE* ,2003:417-421.
- [12] Vetterli M C. "Modern signal-processing", 2001.
- [13] Mathews V J, Xie Z. "A low complexity channel estimation approach of LTE downlink system", *IEEE, International Conference on Communication Technology. IEEE* , 2012:143-147.

Method of CS-IC Detection in the Grant-Free NOMA System

Bin Fan¹, Xin Su², Jie Zeng², Xin Ma³, Tiejun Lv⁴

¹Chongqing University of Posts and Telecommunications, Chongqing, China

²Tsinghua University, Beijing, China

³Beijing Gongjin Electronics Co., Ltd, Beijing, China

⁴Beijing University of Posts and Telecommunications, Beijing, China

Email: suxin@tsinghua.edu.cn

Abstract—With the development of mobile communications and the Internet of Things, non-orthogonal multiple access (NOMA) may be one of the candidates for 5G. In the uplink NOMA system, there are a large number of connected users with multi-user detection, fewer active users and sparse signals in a certain time duration. In this paper, we propose a compressive sensing based multi-user interference cancellation (CS-IC) method to detect the active users and data of the grant-free non-orthogonal multiple access (GF-NOMA) system. It greatly reduces the signaling overhead and control transmission delay, because the active users do not send the active status information to the base station and do not need to interact with the base station in advance. Simulation results show that the proposed CS-IC multi-user detection can obtain much better BLER performance than the IC and MMSE-IC multi-user detection, greatly improving the spectrum efficiency.

Keywords—5G; Non-orthogonal Multiple Access; Grant-free; Compressive Sensing; Interference Cancellation; Multi-user Detection

I. INTRODUCTION

In order to support the development of the mobile Internet and the Internet of Things, the fifth generation mobile communication system(5G) will gradually become the primary scheme for the wireless network access of human to human, machine to human and machine to machine communications in the future [1].The 5G will support three typical scenarios, including enhanced Mobile Broadband (eMBB), mass Machine Type Communication (mMTC) and Ultra-Reliable and Low Latency Communications (URLLC) [2]. Wise Information Technology of 120(WIT120)is a typical application of 5G low latency communications. WIT120 utilizes new sensors, Internet of Things, cognitive radio [3][4]and other technologies combined with modern medical concepts. Through the 5G network, doctors use handheld Personal Digital Assistant (PDA) to connect various medical instruments conveniently.

Multiple access is a way to achieve multi-user communications using common channels. Multiple access is one of the core technologies of the wireless physical layer. Frequency Division Multiple Access (FDMA) in the first generation of mobile communication system (1G), Time Division Multiple Access (TDMA) in the second generation mobile communication system (2G), Code Division Multiple Access (CDMA)

in the third generation mobile communication system (3G), and Orthogonal Frequency Division Multiple Access (OFDMA) in the fourth generation mobile communication system (4G) adopts orthogonal resource allocation. For 2020 and the future, 5G not only needs to improve system spectrum efficiency, but also needs to have the ability to support massive equipment connection. Resource utilization of 5G multiple access technology must be more flexible and efficient. Non-orthogonal multiple access (NOMA) technology is proposed in this context.

In Orthogonal Multiple Access, the number of users is limited by the amount of available orthogonal resources and it is difficult to meet the requirements of large-scale connection in the 5G system. However, Non-orthogonal multiple access breaks shackles of the orthogonality of resource allocation [5]. Digital imaging equipment, such as CT, MRI, CR, DR and ECT, are the main parts of the digitization of medical equipment that forms a 5G non-orthogonal network. Medical institutions provide real-time access to disease data through 5G non-orthogonal information exchange platforms. By introducing non-orthogonal resource allocation and controllable interference, NOMA achieves the efficient use of limited resources at the expense of appropriately increasing the complexity to meet the high spectral efficiency and mass connection need in 5G networks.

In 5G, the target of uplink and downlink user delay should be 0.5ms, and the reliability requirement of a 32-byte transmit data packet is that the user waiting time is 1ms [6]. In [7][8], NO Stack framework could reduce the signaling and delaying. In the uplink grant-free Non-orthogonal Multiple Access (GF-NOMA) system, users could transmit data randomly. With proper resource pre-configuration and the corresponding multi-user detection algorithm, extra signaling overhead and transmission delay introduced by uplink requests and downlink resource scheduling be reduced. WIT120 introduced GF-NOMA system, effectively reduced the transmission delay of the system and implemented preventive verification and monitored sensitive data. In [9], a Partial Marginalization (PM) detection is proposed, which can achieve the BLER performance of Message Passing Algorithm (MPA) with low complexity. In [10], a priori judgment of the high confidence

user is proposed, which simplifies the receiver detection algorithm. In [11], an iterative algorithm is proposed to reduce the complexity. In [12][13], MMSE-IC detection algorithm was proposed, which can reduce the receiver complexity by abolishing the search process and finding the minimum value estimated in Soft Bit Information (SBI). In this letter, we put forward a compressive sensing-based multi-user interference cancellation (CS-IC) method to detect the active users and information of the GF-NOMA system.

The rest of the paper is organized as follows. In Section II, we introduce the uplink NOMA system model and analysis the grant-free design scheme. The signal reconstruction algorithm and the proposed CS-IC detection method are illustrated in Section III. The algorithm BLER performance, delay characteristics, and simulation results are analyzed in Section IV. In Section V, we discuss the possible future research directions in grant-free NOMA briefly. Finally, Section VI concludes this paper.

II. SYSTEM MODEL

A. Uplink NOMA System Model

We consider the ideal symbol synchronization without channel coding in the uplink of a single-cell GF-NOMA system. There are totally K users and one base station (BS), and the activity of the user is η , the number of active users at the same time is ηK . As shown in Fig.1, active users are sparse. The active users communicate with the base station through a wireless multipath channel, and the noise is Gaussian white noise.

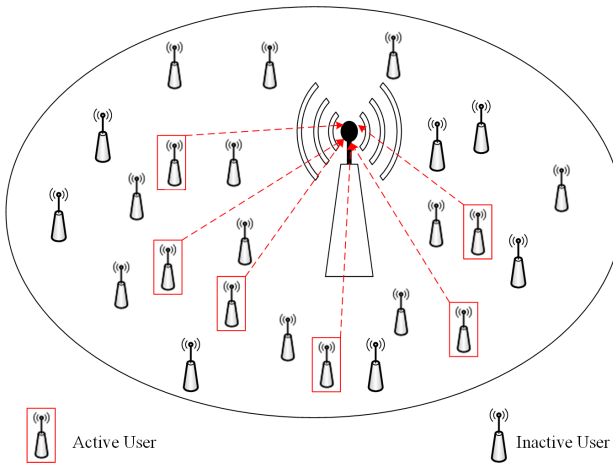


Fig. 1. Sparse user scenes

In this system, the transmission symbol of the active user is non-zero, and the transmission symbol of the inactive user is zero. Then the transmission symbol vector $\mathbf{X} = [x_1, x_2, \dots, x_K]$ of the entire system is sparse. All active users are transmitted on N orthogonal OFDM subcarriers. System model shown in Fig.2. The reception signal is $\mathbf{y} = [y_0, y_1, \dots, y_{N-1}]$. $\mathbf{a}_k = [a_{0,k}, \dots, a_{N-1,k}]$ and $\mathbf{v} = [v_0, v_1, \dots, v_{N-1}]$ represent the k th user's influence signal and noise vector respectively. Assuming that all users are precisely

aligned in time. The discrete form of the received signal for all user signals is

$$\begin{aligned} \mathbf{y} &= \sum_{k=1}^K \mathbf{a}_k \mathbf{x}_k + \mathbf{v} \\ &= \mathbf{A} \mathbf{x} + \mathbf{v} \end{aligned} \quad (1)$$

Where $\mathbf{A} = [a_1, a_2, \dots, a_K]^T$ is vector that affects the received signal, $\mathbf{x} = [x_1, x_2, \dots, x_K]^T$ is transmission symbol, and $\mathbf{v} \sim \mathcal{CN}(0, \sigma^2 \mathbf{I}_N)$.

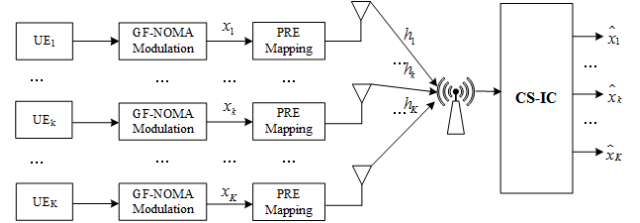


Fig. 2. Uplink GF-NOMA system model

The influence signal vector \mathbf{a}_k of the user k is a convolution of the new spreading sequence \mathbf{s}'_k and the instantaneous channel response \mathbf{h}_k formed by the user k after being mapped. The channel response length is L , denoted as $\mathbf{h}_k = [h_{1,k}, h_{2,k}, \dots, h_{L,k}] \in \mathbb{C}^{L \times 1}$. The influence signal vector \mathbf{a}_k of user k can be expressed as

$$\begin{aligned} \mathbf{a}_k &= \mathbf{h}_k * \mathbf{s}'_k \\ &= \begin{bmatrix} h_{1,k} & \dots & 0 & \dots & 0 \\ h_{2,k} & \dots & 0 & \dots & 0 \\ \vdots & \dots & \vdots & \dots & \vdots \\ h_{L,k} & \dots & \vdots & \dots & \vdots \\ 0 & \dots & h_{1,k} & \dots & 0 \\ 0 & \dots & h_{2,k} & \dots & 0 \\ \vdots & \dots & \vdots & \dots & \vdots \\ 0 & \dots & h_{L,k} & \dots & h_{1,k} \end{bmatrix} \begin{bmatrix} s'_{1,k} \\ s'_{2,k} \\ \vdots \\ \vdots \\ s'_{N-L,k} \\ s'_{N-L+1,k} \\ \vdots \\ s'_{N,k} \end{bmatrix} \end{aligned} \quad (2)$$

The new spreading sequence \mathbf{s}'_k of user k is formed by the unique mapping of shared initial spreading sequence \mathbf{s}_k by user k .

B. Grant-Free Design

For the grant-free transmission in NOMA, the user does not need to send a Scheduling Request (SR) / Buffer Status Report (BSR), and the base station does not need to feedback the uplink scheduling. Therefore, the non-scheduling can eliminate the SR / BSR and uplink scheduling related delay, and only keep sending and receiving delay.

On grant-free based transmission for NOMA, the resource utilization can be separated from grant-based transmission. For grant-free UE, because of non-centralized scheduling, the access resource is uncertain. Therefore, if more than one UE

randomly select the same access resource for the uplink transmission and use the same signature, such as code, sequence, or demodulation reference signal, collision will occur, as illustrated in Fig.3. As a result, the data of multiple users will be overlap together and the receiver would have difficulty to recognize the transmission data and then retransmission would be introduced.

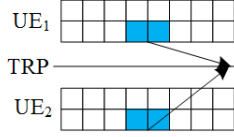


Fig. 3. Grant-Free transmission for two users

In the premise of effective control of user conflicts, uplink grant-free transmission can achieve lower signaling overhead and latency. Therefore, grant-free is used in NOMA systems to achieve stringent latency requirements and reduce overhead in the case of sparse packet transmission. The key to achieve uplink grant-free transmission is the corresponding transmission format and flow. Fig.4 is a set of preamble, uplink control channel and data transmission format design.

- Preamble: used for BS to detect UL signal transmission. Preamble sequence may be different depending on whether Random Access Channel (RACH) procedure is completed or omitted.
- UL control channel: used to carry ID to identify UE, buffer status report, UL control information, etc. A robust channel design against a collision may be necessary.
- Data transmission: to carry URLLC data and small packet. Collision handling for data channel may be needed. For example, code division multiplexing (CDM) and non-orthogonal multiplexing can be considered.



Fig. 4. Example of transmission format for RACH-less and UL grant-free transmission

III. MULTIUSER DETECTION BASED ON CS-IC

A. Signal Reconstruction

In 5G, some users typically transmit their data with high probability in neighboring time slots, and resulting in a temporal correlation of active user sets in multiple sequential time slots [14]. Further, the received signals of reconstruction signals $\mathbf{x} = [x^{[1]}, x^{[2]}, \dots, x^{[M]}]$ is $\mathbf{y} = [y^{[1]}, y^{[2]}, \dots, y^{[M]}]$ in M continuous time slots. According to formula (1) get

$$\mathbf{y}^{[m]} = \mathbf{H}^{[m]} \mathbf{x}^{[m]} + \mathbf{v}^{[m]}, m = 1, 2, \dots, M \quad (3)$$

where $\mathbf{H}^{[m]}$ is the channel response matrix in the m th time slot, which can be changed in different time slots. The CS detection problems can be written as formula (2). And the sparsity of \mathbf{X} is measured by the number of non-zero elements, and the support of $\mathbf{x}^{[m]}$ is express as

$$\begin{aligned} \mathbf{J}^{[m]} &= \|\mathbf{X}\|_0 \\ &= \{k : x_k^{[m]} \neq 0\} \end{aligned} \quad (4)$$

which denotes the index set of nonzero elements in $\mathbf{x}^{[m]}$. CS detection methods are mainly divided into three categories: convex optimization, greedy tracking and combination algorithm.

Compressive Sampling Matching Pursuits (CoSaMP) Algorithm flow is as follows, where \mathbf{r}_i is the residual signal, i is the quantity of iterations, \emptyset represents the empty set, Λ_i represents the set of indices for the i th iteration, α_j represents the j th column of the matrix \mathbf{A} , θ represents the sparse signal, Φ is the observation matrix, Ψ is the transformation matrix, and \mathbf{A} is the sensing matrix.

Algorithm 1 CoSaMP Algorithm

Input: (1) $M \times N$ sensor matrix is $\mathbf{A} = \Phi\Psi$;

(2) The observation vector of the $N \times 1$ dimension is \mathbf{y}

Output: (1) The coefficient estimates $\hat{\theta}$;

(2) The residuals $N \times 1$ dimensional is $\mathbf{r}_k = \mathbf{y} - \mathbf{A}_k \hat{\theta}_k$

1: Initialization: $\mathbf{r}_0 = \mathbf{y}$, $\Lambda_0 = \emptyset$, $\mathbf{A}_0 = \emptyset$, $i = 0$.

2: Calculate $\mathbf{u} = \text{abs}[\mathbf{A}^T \mathbf{r}_{i-1}]$

3: Assume $\Lambda_i = \Lambda_{i-1} \cup \mathbf{J}_0$

4: $\mathbf{A}_i = \mathbf{A}_{i-1} \cup \alpha_j$ (for all $j \in \mathbf{J}_0$).

5: Find the least squares solution of $\mathbf{y} = \mathbf{A}_i \theta_i : \hat{\theta} = \argmin \|\mathbf{y} - \mathbf{A}_i \theta_i\| = (\mathbf{A}_i^T \mathbf{A}_i)^{-1} \mathbf{A}_i^T \mathbf{y}$.

6: $\hat{\theta}_{iS} = \max\{\hat{\theta}_i, 0 < i < N\}$

7: $\hat{A}_{iS} = \max\{\hat{A}_i, 0 < i < N\}$

8: update $\Lambda_i = \Lambda_{iS}$.

9: $\mathbf{r}_i = \mathbf{y} - \mathbf{A}_{iS} \hat{\theta}_{iS} = \mathbf{y} - \mathbf{A}_{iS} (\mathbf{A}_{iS}^T \mathbf{A}_{iS})^{-1} \mathbf{A}_{iS}^T \mathbf{y}$
 $i = i + 1$.

10: if $i < K$

return (2)

11: else if $i > K$ or $\mathbf{r}_i = 0$

return (7)

12: end if

13: end if

14: The reconstruction $\hat{\theta}$ has a non-zero item at Λ_{iS} .

In [15], the statistics of mobile traffic during busy hours show that the actual number of active users is relatively small. In addition, some users typically transmit their information in neighboring time slots with a high probability, which results in a time-dependent group of active user groups in multiple sequential time slots.

B. CS-IC Detection

In order to achieve signal recovery by exploiting the temporal correlation of active user sets, the support set of the $(m+1)$ th slot can be obtained according to the active user support set of the m th slot ($m = 1, 2, \dots, M-1$). Accordingly, we propose the CS-IC multi-user detection to detect active users and data with compression sensing technology.

At the receiver using multi-user IC detection technology, can effectively reduce the system complexity and transmission

delay. According to the Algorithm 1, the iteration signal is updated, and the support set of the i th iteration of the active user on the m th time slot is

$$\hat{\Gamma}^{[m][i]} = \hat{\Gamma}^{[m][i-1]} \cup \arg\max |(\mathbf{h}_k^{[m]})^H \mathbf{r}^{[m][i-1]}|^2 \quad (5)$$

$$\mathbf{r}^{[m][i]} = \mathbf{y}^{[m]} - \mathbf{H}_{\hat{\Gamma}^{[m][i]}}^{[m]} \hat{\mathbf{x}}^{[m][i]} \quad (6)$$

Where $\mathbf{h}_k^{[m]}$ is the k th column of $\mathbf{H}_{\hat{\Gamma}^{[m][i]}}^{[m]}$. Taking the joint sparse of data as the standard, we could select the subspace that can accurately reconstruct the original station data. The Restricted Isometry Property (RIP) was introduced to assess the reliability of sparse signal reconstruction and compression. By CS quantization, the j th constraint equidistance constant of the observation matrix is set to ξ_j ($0 \leq \xi_j \leq 11$) then

$$(1 - \xi_j) \|\mathbf{x}\|_2^2 \leq \|\mathbf{H}_x\|_2^2 \leq (1 + \xi_j) \|\mathbf{x}\|_2^2 \quad (7)$$

$$\hat{\mathbf{x}}^{[m][i]} = (\mathbf{H}_{\hat{\Gamma}^{[m][i]}}^{[m]})^\dagger \mathbf{y}^{[m]} \quad (8)$$

After obtaining the updated active user set, the sparse transmitted signal vector in the m th slot is recovered by the Least Squares (LS). The CS-IC takes into account the user's sparsity, making the detected data and the original data minimum error. According to CS-IC detection method combined with the formula (7)(8) can be error signal

$$\begin{aligned} \|\hat{\mathbf{x}} - \mathbf{x}\|_2 &\leq \|\mathbf{x}_{\hat{\Gamma}} - \mathbf{H}_{\hat{\Gamma}}^\dagger\|_2 + \|\mathbf{x}_{\Gamma \setminus \hat{\Gamma}}\|_2 \\ &= \lambda \|\mathbf{v}\|_2 \end{aligned} \quad (9)$$

Where $\|\mathbf{v}\|_2$ is noise power,
 $\lambda = \frac{2 + \sqrt{S} + \xi_2 S + 1 + \xi_2^2 S + 1}{\xi_2 S + 1(1 - \xi_2 S + 1)}$ is a constraint.

IV. PERFORMANCE ANALYSIS

In this section, the proposed algorithm is compared with the traditional IC algorithm and the classic MMSE-IC algorithm. Parameter settings in TABLE 1. According to the standard of LTE-Advanced, the number of consecutive slots is set to $M = 7$ [16].

As can be seen from Fig.5, the BLER performance of MMSE-IC and CS-IC are obviously better than that of IC when $0\text{dB} < \text{SNR} < 16\text{dB}$. With SNR increases, CS-IC gets better and better BLER performance gain than MMSE-IC algorithm.

For the application scenarios with high reliability and low latency in the future 5G, this paper performs further delay detection for the CS-IC and MMSE-IC algorithms, mainly in the running time of the algorithm, and the result is shown in Fig.6. In the case of a certain length of the spreading code, the running time of the CS-IC detection is much lower than that of the MMSE-IC algorithm. When the number of users covered by single BS is $K = 160$, the CS-IC detection method is operated at a speed of 54%. Analysis shows that this method effectively improves the performance of the grant-free system.

TABLE I
SIMULATION PARAMETERS

Parameter	Value
Carrier frequency	2GHz
System bandwidth	10MHz
Scheduling	Grant free
Spreading matrix	Toeplitz matrix
Channel coding	LTE Turbo 1/2
Modulation	QPSK
Max HARQ	1
Channel model	Uma
Channel estimation	Ideal
Overload factor	200%

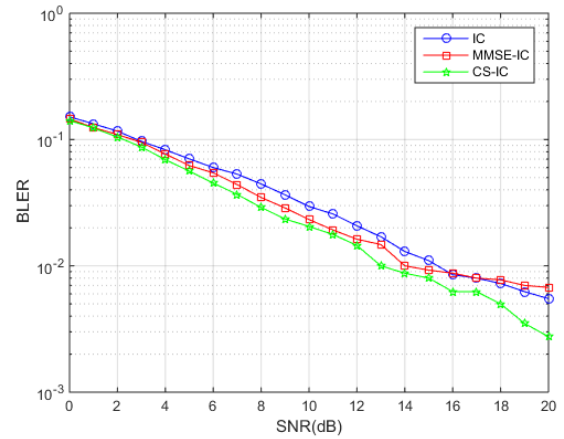


Fig. 5. Three kinds of interference cancellation algorithm

V. FUTURE RESEARCH

Based on our current probe and ponder, the further research can be executed from the following possible directions.

A. Grant-Free for URLLC

- 1) Study how to meet wireless access network requirements on latency and reliability using at least one HARQ retransmission for DL data and UL data.
 - Further study TTI duration and achievable latency based on at least one retransmission.
 - Further study details of HARQ operation in DL and UL taking into account reliability of overall HARQ signaling procedure (control, data and feedback channels).

- 2) This does not preclude studying single transmission to meet the wireless access network requirements on latency and reliability.

B. Further Performance Evaluation of UL Grant-Free NOMA

- 1) Collision of time/frequency resources from different UEs, solutions potentially including code, sequence, interleaver pattern.

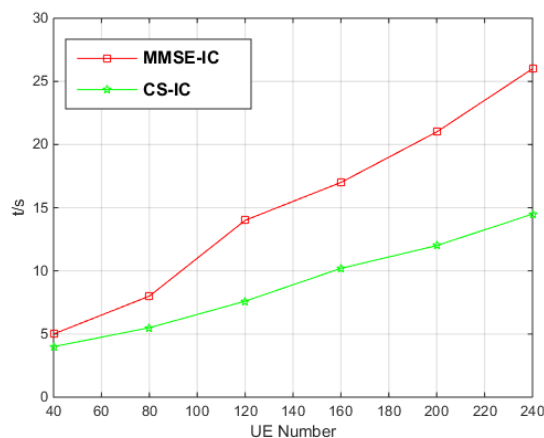


Fig. 6. Algorithm run time comparison

- 2) Multiuser detection based on dynamic CS receiver. By designing the measurement matrix reasonably, the perceptual matrix is directional, which can effectively restrain the noise interference and improve the reconstruction performance of sparse signals under low SNR. And developing own CS reconstruction algorithm based on CoSaMP.

VI. CONCLUSIONS

This paper has mainly studied the IC based CS multi-user detection method for uplink GF-NOMA system. The method utilizes the temporal correlation of active subscriber sets to enable active users and data detection in the uplink GF-NOMA system within multiple contiguous time slots. Furthermore, the simulation results have shown that the CS-IC detection method can get better BLER performance than the MMSE-IC detection algorithm when the active users are sparse in the uplink GF-NOMA system. Simultaneously, the simulation results have revealed that the algorithm also achieves a great advantage in operation efficiency. Overall, the CS-IC is an efficient method of multi-user detection.

REFERENCES

- [1] J. G. Andrews et al., "What Will 5G Be?," in *IEEE Journal on Selected Areas in Communications*, vol. 32, no. 6, pp. 1065-1082, June 2014.
- [2] H. Tullberg, P. Popovski, Z. X. Li, M. A. Uusitalo, A. Høglund, et al. "The METIS 5G system concept: meeting the 5G requirements," *IEEE Commun. Mag.*, vol. 54, no. 12, pp. 132-139, December 2016.
- [3] X. Lu, X. Su, J. Zeng, and H. J. Wang, "A single FPGA embedded framework for secondary user in cognitive network," in *International Conference on Communication Technology Proceedings, ICCT*, no. 2009, pp. 881C884, 2010.
- [4] H. Liu, X. Su, Y. You, and J. Zeng, "A reconfigurable software radio framework for accessing diverse resources in distributed nodes," in *Ultra Modern Telecommunications and Control Systems and Workshops (ICUMT)*, 2011 3rd International Congress on, pp. 1C5, 2011.
- [5] Z. Ding, L. Dai and H. V. Poor, "MIMO-NOMA Design for Small Packet Transmission in the Internet of Things," in *IEEE Access*, vol. 4, pp. 1393-1405, 2016.
- [6] 3GPP TR 38.913 V14.0.0, "Study on Scenarios and Requirements for Next Generation Access Technologies."

- [7] J. Zeng, X. Su, J. Gong, L. Rong, and J. Wang, "5G Virtualized Radio Access Network Approach Based on NO Stack Framework," in *IEEE International Conference on Communications*, pp. 1C5, 2017.
- [8] J. Zeng, X. Su, J. Gong, L. Rong, and J. Wang, "A 5G Virtualized RAN Based on NO Stack," *China Commun.*, vol. 14, no. 6, pp. 199C208, 2017.
- [9] H. Mu, Z. Ma, M. Alhaji, P. Fan and D. Chen, "A Fixed Low Complexity Message Pass Algorithm Detector for Up-Link SCMA System," in *IEEE Wireless Communications Letters*, vol. 4, no. 6, pp. 585-588, Dec. 2015.
- [10] K. Xiao, B. Xiao, S. Zhang, Z. Chen and B. Xia, "Simplified multiuser detection for SCMA with sum-product algorithm," 2015 International Conference on Wireless Communications & Signal Processing (WCSP), Nanjing, 2015, pp. 1-5.
- [11] J. Zeng, D. Kong, B. Liu, X. Su, and T. Lv, "RlePDMA and BP-IDD-IC detection," *EURASIP J. Wirel. Commun. Netw.*, vol. 2017, no. 1, p. 12, 2017.
- [12] L. Fang, L. Xu, Q. Guo, D. Huang and S. Nordholm, "A low complexity iterative soft-decision feedback MMSE-PIC detection algorithm for massive MIMO," 2015 IEEE International Conference on Acoustics, Speech and Signal Processing (ICASSP), South Brisbane, QLD, 2015, pp. 2939-2943.
- [13] M. Zhang, C. Li, S. Kim and S. Ahmed, "Low-complexity iterative PIC-MMSE based detection with symbol mapping," 2016 IEEE/CIC International Conference on Communications in China (ICCC), Chengdu, 2016, pp. 1-5.
- [14] B. Wang, L. Dai, T. Mir and Z. Wang, "Joint User Activity and Data Detection Based on Structured Compressive Sensing for NOMA," in *IEEE Communications Letters*, vol. 20, no. 7, pp. 1473-1476, July 2016.
- [15] J. P. Hong, W. Choi and B. D. Rao, "Sparsity Controlled Random Multiple Access With Compressed Sensing," in *IEEE Transactions on Wireless Communications*, vol. 14, no. 2, pp. 998-1010, Feb. 2015.
- [16] Evolved Universal Terrestrial Radio Access (E-UTRA), "Physical Channels and Modulation (Release 12)", document 3GPP TS-36.211, Jan. 2016.

Author index

Author by Session

Author	Session	Start page	Title
A			
Abdul Rahman, Abdul Wahab	S1.6	34	
Abed-Meraim, Karim	S3.4	114	
Al-Hamdani, Osamah	S4.8	175	
Alam, Muhammad	S4.1	137	
	O1.1		
Altamimi, Reem	S4.6	162	
B			
Balasingham, Ilanko	S2.1	40	
Bjørnevik, Anders	S2.1	40	
C			
Cai, Yixin	Special 1.4	83	
Casareo, Kevin	S6.2	215	
Chaczko, Zenon	S2.4	60	
	S6.2	215	
Chaudhry, Junaid	S2.3	50	
Cheng, Yongqiang	S3.5	120	
Crowley, Michael	S2.3	50	
D			
D'Souza, Andrea	S4.2	143	
Diao, Yinliang	Special 1.4	83	
Do Duc, Dong	S1.5	28	
Douseki, Takakuni	Special 1.1	70	
Dutkiewicz, Eryk	Special 1.2	74	
	S1.3	16	
E			
Elshakankiri, Maher	S3.7	131	
Esselle, Karu	Special 1.3	80	
F			
Fan, Bin	S6.6	236	
Feng, Jiewei	Special 1.5	86	
Feng, Shilun	Special 1.3	80	
Floor, Pål Anders	S2.1	40	
Fuglevand, Andrew	S1.3	16	
G			
Gay, Valérie	S4.7	170	
	S3.6	125	
Gupta, Samir	Special 1.5	86	
H			
Ha, Luu	S5.5	201	
Haddad, Assal	S3.1	97	
Hamagami, Takuma	S3.3	109	
Hämäläinen, Matti	S4.4	153	
	S4.2	143	
Hameed, Asad	S5.6	205	
Hao, Shuliang	S6.4	226	
Hara, Shinsuke	S5.2	186	

	S3.3	109
Hasan, Osman	S5.6	205
Hoang, Son	S5.5	201
Hussain, Hadri	S4.8	175
I		
Ichikawa, Yuki	S4.5	158
Iinatti, Jari	S4.4	153
Isaac, Nikita	S4.7	170
	S3.6	125
J		
Jalal, Nasir	S5.6	205
Jon Haass, Jon	S2.3	50
K		
Kadoya, Kento	S5.4	195
Kamal, Nabeel	S5.6	205
Kamaruddin, Norhaslinda	S1.6	34
Kaneko, Shigehiko	S5.4	195
Karmakar, Nemai	Special 1.5	86
Kawabata, Takashi	S5.2	186
Khadirnaikar, Seema	S3.8	
Khan, Rida	S4.1	137
	O1.1	
Kikuchi, Makoto	S1.2	10
Kim, Minseok	S4.5	158
Kohno, Ryuji	S1.1	5
Kumar, Vimal	S2.2	45
Kumpuniemi, Timo	S4.4	153
L		
Latif, Zubaidi Abdul	S4.8	175
Leong, Philip	S1.3	16
Leung, Sai Wing	Special 1.4	83
Li, Mengze	Special 1.4	83
Linh-Trung, Nguyen	S3.4	114
	S1.5	28
Liu, Bei	S6.3	221
	S6.1	210
	S4.3	148
Liu, Qi	S6.1	210
	S4.3	148
Lv, Tiejun	S6.6	236
	S6.4	226
M		
Ma, Xin	S6.4	226
	S6.6	236
Mai, Ha	Special 1.2	74
McEwan, Alistair	S1.3	16
Mei, Jiajia	S6.3	221
	S4.3	148
Minh-Chinh, Truong	S3.4	114
Miyamoto, Ryusuke	S5.2	186
	S3.3	109
Moelker, Adriaan	S5.5	201
Mohamad, Mohd Murtadha	S4.8	175
Mohd Nasir, Mohd Hafiz	S1.6	34
Mrema, Edward	S2.2	45
Mucchi, Lorenzo	S4.2	143

N		
Nag, Anindya	S3.2	103
	Special 1.6	92
Nakajima, Yo	Special 1.1	70
Nguyen, Diep	Special 1.2	74
	S1.3	16
Nguyen, Hong Thinh	S5.5	201
Nguyen, Viet-Dung	S3.4	114
Niino, Atsushi	S5.2	186
	O1.2	1
Noman, Fuad	S4.8	175
O		
Ogura, Hirofumi	S5.2	186
	S3.3	109
Ohta, Hidetoshi	S5.1	181
Okita, Kazuki	O1.2	1
Omuro, Yuto	S2.5	66
Onasanya, Adeniyi	S3.7	131
Oweis, Khalid	S3.1	97
P		
P, Aparna	S3.8	
Peng, Mingyao	S6.3	221
	S6.1	210
Pfahringner, Bernhard	S1.4	22
Pham, Thuy	Special 1.2	74
	S1.3	16
Pomalaza Raez, Carlos	S4.4	153
Q		
Qaiser, Saad	S5.6	205
Quteishat, Hussam	S3.1	97
R		
Roberts, Peter	S2.3	50
Robinson, Reece	S1.4	22
S		
Safaei, Farzad	O1.3	3
Sakakibara, Katsumi	S2.5	66
Sakamoto, Hiroya	Special 1.1	70
Sakuma, Yoshitomo	S1.1	5
Salleh, Sh-Hussain	S4.8	175
Sampath, Naveenaa	S4.7	170
	S3.6	125
Särestöniemi, Mariella	S4.4	153
Sayem, Abu Sadat Md.	Special 1.3	80
Shao, Shihai	S4.3	148
	S6.1	210
Sharma, Rajender	S5.3	191
Shehab, Shahriar	Special 1.5	86
Shnoudi, Tamer	S2.4	60
Simorangkir, Roy B. V. B.	Special 1.3	80
Singh, Jaspal	S5.3	191
Skinner, Geoff	S4.6	162
Slehat, Shaher	S2.4	60
Su, Xin	S4.3	148
	S6.6	236
	S6.3	221
	S6.4	226

	S6.1	210
	S6.5	231
Suematsu, Ryota	Special 1.1	70
Sun, Weinong	Special 1.4	83
T		
Takabayashi, Kento	S2.5	66
Tanaka, Ami	Special 1.1	70
Thai Dinh, Phuc	S1.5	28
Ting, Chee-Ming	S4.8	175
Tran, Le Chung	O1.3	3
Tran, Tan	S5.5	201
V		
Valli, Craig	S2.3	50
van Walsum, Theo	S5.5	201
Viittala, Harri	S4.2	143
Vũ, Ngọc Anh	S1.5	28
W		
Wang, Chang	S6.1	210
	S4.3	148
X		
Xiao, Limin	S6.3	221
	S6.5	231
Xu, Xibin	S6.3	221
	S6.5	231
Y		
Yamaguchi, Shintaro	S5.2	186
	O1.2	1
Yang, Yang	Special 1.4	83
	Special 1.3	80
	Special 1.5	86
Ye, Hangyang	S3.5	120
Yomo, Hiroyuki	S5.2	186
	O1.2	1
	S3.3	109
Z		
Zeng, Jie	S4.3	148
	S6.6	236
	S6.3	221
	S6.4	226
	S6.1	210
	S6.5	231
Zgoul, Moudar	S3.1	97
Zhang, Edmond	S1.4	22
Zhang, Hongyun	O1.3	3
Zhang, ZhenFeng	S6.5	231
Zhu, Jin	S3.5	120
Zhu, Xi	Special 1.4	83

Author by Title

A B C D E F G H I J K L M N O P Q R S T V W X Y Z

Abdul Rahman, Abdul Wahab

EEG Affective Modelling for Dysphoria Understanding

Abed-Meraim, Karim

A Non-Linear Tensor Tracking Algorithm for Analysis of Incomplete Multi-Channel EEG Data

Ahmed, Nadeem

Assistive Tool for Speech Disorder Diagnosis and Remote Therapy Progress Monitoring

Ahmedy, Ismail

Assessing the Impact of Multipath Fading on Spectrum Sensing for Mobile Rescue Operation

Al-Hamdani, Osamah

Performance Study for Multimodal Client Identification System Using Cardiac and Speech Signals

Alam, Muhammad

Body-to-Body Communication: Applications, System Design Aspects and Performance Evaluation

Joint PHY-MAC Realistic Performance Evaluation of Body-to-Body Communication in IEEE 802.15.6 and SmartBAN

Ali, Jawad

Application of Machine Learning Techniques in Categorizing Breast Cancer Severity

Altamimi, Reem

Evaluating Contemporary Physical Activity Self-Monitoring Technology Performance

Balasingham, Ilanko

On Path Length Estimation for Wireless Capsule Endoscopy

Bjørnevik, Anders

On Path Length Estimation for Wireless Capsule Endoscopy

Cai, Yixin

Safety Consideration for Emerging Wireless Technologies - Evaluations of Temperature Rise in Eyes for RF Radiations Up to 10GHz

Casareo, Kevin

Beacon-based Localization Middleware for Tracking in Medical and Healthcare Environments

Chaczko, Zenon

Beacon-based Localization Middleware for Tracking in Medical and Healthcare Environments

Game-Theory Based Cognitive Radio Policies for Jamming and Anti-Jamming in the IoT

Chaudhry, Junaid

POSTCODE Middleware for Post-market Surveillance of Medical Devices for Cyber Security in Medical and Healthcare Sector in Australia

Chembe, Christopher

Assessing the Impact of Multipath Fading on Spectrum Sensing for Mobile Rescue Operation

Cheng, Yongqiang

PPG Based Respiration Signal Estimation Using VMD-PCA

Crowley, Michael

POSTCODE Middleware for Post-market Surveillance of Medical Devices for Cyber Security in Medical and Healthcare Sector in Australia

D'Souza, Andrea

Performance Comparison Between ETSI SmartBAN and Bluetooth

Diao, Yinliang

Safety Consideration for Emerging Wireless Technologies - Evaluations of Temperature Rise in Eyes for RF Radiations Up to 10GHz

Do Duc, Dong

An Efficient Ant Colony Optimization Algorithm for Protein Structure Prediction

Douseki, Takakuni

Self-powered Wireless Urinary-incontinence Sensor System Detecting Urine Amount and Diaper Change Timing in Under 10 Minutes

Dutkiewicz, Eryk

Feature Analysis for Discrimination of Motor Unit Action Potentials

Non-Laboratory-Based Risk Factors for Automated Heart Disease Detection

Elshakankiri, Maher

Secured Cancer Care and Cloud Services in IoT/WSN Based Medical Systems

Esselle, Karu

PDMS-Embedded Conductive Fabric: A Simple Solution for Fabricating PDMS-Based Wearable Antennas with Robust Performance

Fan, Bin

Method of CS-IC Detection in Grant-Free NOMA System

Feng, Jiewei

A Design and Implementation of an Ambulatory Electrocardiogram (ECG) Acquisition Circuit for Emergency Application

Feng, Shilun

Design and Microfabrication of Microfluidics Needle for Delivery/ Sampling Chemicals with Resolution

PDMS-Embedded Conductive Fabric: A Simple Solution for Fabricating PDMS-Based Wearable Antennas with Robust Performance

Simulation Modeling of Microfluidics Deterministic Lateral Displacement Array for Cell Enrichment

Floor, Pål Anders

On Path Length Estimation for Wireless Capsule Endoscopy

Fraz, Muhammad

Assistive Tool for Speech Disorder Diagnosis and Remote Therapy Progress Monitoring

Fuglevand, Andrew

Feature Analysis for Discrimination of Motor Unit Action Potentials

Gay, Valérie

Modernising Asthma Management; Personalised Asthma Action Plans Using a Smartphone Application

SAM: Smart Asthma Monitoring: Focus on Air Quality Data and Internet of Things (IoT)

Goldys, Ewa

Design and Microfabrication of Microfluidics Needle for Delivery/ Sampling Chemicals with Resolution

Gupta, Samir

A Design and Implementation of an Ambulatory Electrocardiogram (ECG) Acquisition Circuit for Emergency Application

Ha, Luu

Impact of Enhancement Features on Image Registration for Liver Cancer Interventions Using CT Images

Haddad, Assal

A Study on the Effect of Sports on Academic Stress Using Wearable Galvanic Skin Response

Hamagami, Takuma

A Network Simulator to Develop Wireless Networking Protocols Suited for Vital Information Collection from a Group of Exercisers

Hämäläinen, Matti

Impact of the Sternotomy Wires and Aortic Valve Implant on the On-Body UWB Radio Channels

Performance Comparison Between ETSI SmartBAN and Bluetooth

Hameed, Asad

Electronic Design of a Semi-Automated Micromanipulator Cell Injection System

Hao, Shuliang

A Low Complexity SCMA Detector Based on Avoiding Redundant Iterations

Hara, Shinsuke

A Network Simulator to Develop Wireless Networking Protocols Suited for Vital Information Collection from a Group of Exercisers

Applying Multi-channel Flooding to Vital Data Monitoring of a Large Number of Exercisers: Mobility and Link Modeling and Performance Evaluation

Hasan, Osman

Electronic Design of a Semi-Automated Micromanipulator Cell Injection System

Hoang, Son

Impact of Enhancement Features on Image Registration for Liver Cancer Interventions Using CT Images

Hussain, Hadri

Performance Study for Multimodel Client Identification System Using Cardiac and Speech Signals

Ichikawa, Yuki

Simulation-based Body Motion Classifier Using Radio Channel Characteristics

Iinatti, Jari

Impact of the Sternotomy Wires and Aortic Valve Implant on the On-Body UWB Radio Channels

Inglis, David

Design and Microfabrication of Microfluidics Needle for Delivery/ Sampling Chemicals with Resolution

Simulation Modeling of Microfluidics Deterministic Lateral Displacement Array for Cell Enrichment

Isaac, Nikita

Modernising Asthma Management; Personalised Asthma Action Plans Using a Smartphone Application

SAM: Smart Asthma Monitoring: Focus on Air Quality Data and Internet of Things (IoT)

Jalal, Nasir

Electronic Design of a Semi-Automated Micromanipulator Cell Injection System

Jiang, Lianmei

Design and Microfabrication of Microfluidics Needle for Delivery/ Sampling Chemicals with Resolution

Jon Haass, Jon

POSTCODE Middleware for Post-market Surveillance of Medical Devices for Cyber Security in Medical and Healthcare Sector in Australia

Kadoya, Kento

Modeling of a Cardiovascular System to Investigate Factors Affecting Hypertension

Kamal, Nabeel

Electronic Design of a Semi-Automated Micromanipulator Cell Injection System

Kamaruddin, Norhaslinda

EEG Affective Modelling for Dysphoria Understanding

Kaneko, Shigehiko

Modeling of a Cardiovascular System to Investigate Factors Affecting Hypertension

Karmakar, Nemaï

A Design and Implementation of an Ambulatory Electrocardiogram (ECG) Acquisition Circuit for Emergency Application

Kawabata, Takashi

Applying Multi-channel Flooding to Vital Data Monitoring of a Large Number of Exercisers: Mobility and Link Modeling and Performance Evaluation

Khadirnaïkar, Seema

Design and Implementation of Portable Health Monitoring System

Khan, Rida

Body-to-Body Communication: Applications, System Design Aspects and Performance Evaluation

Joint PHY-MAC Realistic Performance Evaluation of Body-to-Body Communication in IEEE 802.15.6 and SmartBAN

Kikuchi, Makoto

Proposal for Feature Enhancement of Bioinformation Using Attractor Pattern and Frequency Analysis

Kim, Minseok

Simulation-based Body Motion Classifier Using Radio Channel Characteristics

Kohno, Ryuji

A Dynamic Model Estimation Scheme for Model Predictive Control of Anesthesia Using Recurrent Neural Network

Kumar, Vimal

Fine Grained Attribute Based Access Control of Healthcare Data

Kumpuniemi, Timo

Impact of the Sternotomy Wires and Aortic Valve Implant on the On-Body UWB Radio Channels

Kunda, Douglas

Assessing the Impact of Multipath Fading on Spectrum Sensing for Mobile Rescue Operation

Latif, Zubaidi Abdul

Performance Study for Multimodel Client Identification System Using Cardiac and Speech Signals

Leong, Philip

Feature Analysis for Discrimination of Motor Unit Action Potentials

Leung, Sai Wing

Safety Consideration for Emerging Wireless Technologies - Evaluations of Temperature Rise in Eyes for RF Radiations Up to 10GHz

Li, Mengze

Safety Consideration for Emerging Wireless Technologies - Evaluations of Temperature Rise in Eyes for RF Radiations Up to 10GHz

Linh-Trung, Nguyen

A Non-Linear Tensor Tracking Algorithm for Analysis of Incomplete Multi-Channel EEG Data

An Efficient Ant Colony Optimization Algorithm for Protein Structure Prediction

Liu, Bei

A New Optimal Relay Selection Strategy for the Coincident Multi-user Access

Resource Allocation in Multi-user NOMA Wireless Systems

Resource Allocation in PDMA with Wireless Information and Power Transmission

Liu, Guozhen

Design and Microfabrication of Microfluidics Needle for Delivery/ Sampling Chemicals with Resolution

Liu, Qi

A New Optimal Relay Selection Strategy for the Coincident Multi-user Access

Resource Allocation in PDMA with Wireless Information and Power Transmission

Lv, Tiejun

A Low Complexity SCMA Detector Based on Avoiding Redundant Iterations

Method of CS-IC Detection in Grant-Free NOMA System

Ma, Xin

A Low Complexity SCMA Detector Based on Avoiding Redundant Iterations

Method of CS-IC Detection in Grant-Free NOMA System

Mahmood, Imran

Assistive Tool for Speech Disorder Diagnosis and Remote Therapy Progress Monitoring

Mai, Ha

Non-Laboratory-Based Risk Factors for Automated Heart Disease Detection

McEwan, Alistair

Feature Analysis for Discrimination of Motor Unit Action Potentials

Md Noor, Rafidah

Assessing the Impact of Multipath Fading on Spectrum Sensing for Mobile Rescue Operation

Mei, Jiajia

A New Optimal Relay Selection Strategy for the Coincident Multi-user Access

Resource Allocation in Multi-user NOMA Wireless Systems

Minh-Chinh, Truong

A Non-Linear Tensor Tracking Algorithm for Analysis of Incomplete Multi-Channel EEG Data

Miyamoto, Ryusuke

A Network Simulator to Develop Wireless Networking Protocols Suited for Vital Information Collection from a Group of Exercisers

Applying Multi-channel Flooding to Vital Data Monitoring of a Large Number of Exercisers: Mobility and Link Modeling and Performance Evaluation

Moelker, Adriaan

Impact of Enhancement Features on Image Registration for Liver Cancer Interventions Using CT Images

Mohamad, Mohd Murtadha

Performance Study for Multimodel Client Identification System Using Cardiac and Speech Signals

Mohd Nasir, Mohd Hafiz

EEG Affective Modelling for Dysphoria Understanding

Mrema, Edward

Fine Grained Attribute Based Access Control of Healthcare Data

Mucchi, Lorenzo

Performance Comparison Between ETSI SmartBAN and Bluetooth

Nag, Anindya

Development of Novel Gold/PDMS Sensors for Medical Applications

Development of Printed Sensors for Shoe Sensing Applications

Nakajima, Yo

Self-powered Wireless Urinary-incontinence Sensor System Detecting Urine Amount and Diaper Change Timing in Under 10 Minutes

Nayab, Durr

Application of Machine Learning Techniques in Categorizing Breast Cancer Severity

Nguyen, Diep

Feature Analysis for Discrimination of Motor Unit Action Potentials

Non-Laboratory-Based Risk Factors for Automated Heart Disease Detection

Nguyen, Hong Thinh

Impact of Enhancement Features on Image Registration for Liver Cancer Interventions Using CT Images

Nguyen, Viet-Dung

A Non-Linear Tensor Tracking Algorithm for Analysis of Incomplete Multi-Channel EEG Data

Niino, Atsushi

Applying Multi-channel Flooding to Vital Data Monitoring of a Large Number of Exercisers: Mobility and Link Modeling and Performance Evaluation

Performance Comparison of Routing Protocols for Vital Data Monitoring from a Large Number of Exercisers

Noman, Fuad

Performance Study for Multimodel Client Identification System Using Cardiac and Speech Signals

Ogura, Hirofumi

A Network Simulator to Develop Wireless Networking Protocols Suited for Vital Information Collection from a Group of Exercisers

Applying Multi-channel Flooding to Vital Data Monitoring of a Large Number of Exercisers: Mobility and Link

Ohta, Hidetoshi

Monitoring and Controlling Two Applications of a Magnetic Screw in the Gastrointestinal Tract

Okita, Kazuki

Performance Comparison of Routing Protocols for Vital Data Monitoring from a Large Number of Exercisers

Omuro, Yuto

Detection Scheme of Selfish Node in WBAN Utilizing CSMA/CA Based on IEEE 802.15.6

Onasanya, Adeniyi

Secured Cancer Care and Cloud Services in IoT/WSN Based Medical Systems

Oweis, Khalid

A Study on the Effect of Sports on Academic Stress Using Wearable Galvanic Skin Response

P, Aparna

Design and Implementation of Portable Health Monitoring System

Peng, Mingyao

Resource Allocation in Multi-user NOMA Wireless Systems

Resource Allocation in PDMA with Wireless Information and Power Transmission

Pfahringner, Bernhard

Deep Holistic Representation Learning from EHR

Pham, Thuy

Feature Analysis for Discrimination of Motor Unit Action Potentials

Non-Laboratory-Based Risk Factors for Automated Heart Disease Detection

Pomalaza Raez, Carlos

Impact of the Sternotomy Wires and Aortic Valve Implant on the On-Body UWB Radio Channels

Qaiser, Saad

Electronic Design of a Semi-Automated Micromanipulator Cell Injection System

Quteishat, Hussam

A Study on the Effect of Sports on Academic Stress Using Wearable Galvanic Skin Response

Roberts, Peter

POSTCODE Middleware for Post-market Surveillance of Medical Devices for Cyber Security in Medical and Healthcare Sector in Australia

Robinson, Reece

Deep Holistic Representation Learning from EHR

Safaei, Farzad

Autocorrelation Based Transmission Power Control in WBANs

Sakakibara, Katsumi

Detection Scheme of Selfish Node in WBAN Utilizing CSMA/CA Based on IEEE 802.15.6

Sakamoto, Hiroya

Self-powered Wireless Urinary-incontinence Sensor System Detecting Urine Amount and Diaper Change Timing in Under 10 Minutes

Sakuma, Yoshitomo

A Dynamic Model Estimation Scheme for Model Predictive Control of Anesthesia Using Recurrent Neural Network

Salleh, Sh-Hussain

Performance Study for Multimodel Client Identification System Using Cardiac and Speech Signals

Sampath, Naveenaa

Modernising Asthma Management; Personalised Asthma Action Plans Using a Smartphone Application

SAM:Smart Asthma Monitoring: Focus on Air Quality Data and Internet of Things (IoT)

Särestöniemi, Mariella

Impact of the Sternotomy Wires and Aortic Valve Implant on the On-Body UWB Radio Channels

Sayem, Abu Sadat Md.

PDMS-Embedded Conductive Fabric: A Simple Solution for Fabricating PDMS-Based Wearable Antennas with Robust Performance

Shao, Shihai

A New Optimal Relay Selection Strategy for the Coincident Multi-user Access

Resource Allocation in PDMA with Wireless Information and Power Transmission

Sharma, Rajender

Resource-Constrained Device for Unobtrusive Estimation of Sleep Stages Using R-R Interval Data

Shehab, Shahriar

A Design and Implementation of an Ambulatory Electrocardiogram (ECG) Acquisition Circuit for Emergency Application

Shnoudi, Tamer

Game-Theory Based Cognitive Radio Policies for Jamming and Anti-Jamming in the IoT

Simorangkir, Roy B. V. B.

PDMS-Embedded Conductive Fabric: A Simple Solution for Fabricating PDMS-Based Wearable Antennas with Robust Performance

Singh, Jaspal

Resource-Constrained Device for Unobtrusive Estimation of Sleep Stages Using R-R Interval Data

Skelly, Alison

Simulation Modeling of Microfluidics Deterministic Lateral Displacement Array for Cell Enrichment

Skinner, Geoff

Evaluating Contemporary Physical Activity Self-Monitoring Technology Performance

Slehat, Shaher

Game-Theory Based Cognitive Radio Policies for Jamming and Anti-Jamming in the IoT

Su, Xin

A Channel Estimation Method Based on the Improved LMS Algorithm for MIMO-OFDM Systems

A Low Complexity SCMA Detector Based on Avoiding Redundant Iterations

A New Optimal Relay Selection Strategy for the Coincident Multi-user Access

Method of CS-IC Detection in Grant-Free NOMA System

Resource Allocation in Multi-user NOMA Wireless Systems

Resource Allocation in PDMA with Wireless Information and Power Transmission

Suematsu, Ryota

Self-powered Wireless Urinary-incontinence Sensor System Detecting Urine Amount and Diaper Change Timing in Under 10 Minutes

Sun, Weinong

Safety Consideration for Emerging Wireless Technologies - Evaluations of Temperature Rise in Eyes for RF Radiations Up to 10GHz

Takabayashi, Kento

Detection Scheme of Selfish Node in WBAN Utilizing CSMA/CA Based on IEEE 802.15.6

Tanaka, Ami

Self-powered Wireless Urinary-incontinence Sensor System Detecting Urine Amount and Diaper Change Timing in Under 10 Minutes

Thai Dinh, Phuc

An Efficient Ant Colony Optimization Algorithm for Protein Structure Prediction

Ting, Chee-Ming

Performance Study for Multimodel Client Identification System Using Cardiac and Speech Signals

Tran, Le Chung

Autocorrelation Based Transmission Power Control in WBANs

Tran, Tan

Impact of Enhancement Features on Image Registration for Liver Cancer Interventions Using CT Images

Valli, Craig

POSTCODE Middleware for Post-market Surveillance of Medical Devices for Cyber Security in Medical and Healthcare Sector in Australia

van Walsum, Theo

Impact of Enhancement Features on Image Registration for Liver Cancer Interventions Using CT Images

Viittala, Harri

Performance Comparison Between ETSI SmartBAN and Bluetooth

Vũ, Ngọc Anh

An Efficient Ant Colony Optimization Algorithm for Protein Structure Prediction

Wang, Chang

A New Optimal Relay Selection Strategy for the Coincident Multi-user Access

Resource Allocation in PDMA with Wireless Information and Power Transmission

Xiao, Limin

A Channel Estimation Method Based on the Improved LMS Algorithm for MIMO-OFDM Systems

Resource Allocation in Multi-user NOMA Wireless Systems

Xu, Xibin

A Channel Estimation Method Based on the Improved LMS Algorithm for MIMO-OFDM Systems

Resource Allocation in Multi-user NOMA Wireless Systems

Yamaguchi, Shintaro

Applying Multi-channel Flooding to Vital Data Monitoring of a Large Number of Exercisers: Mobility and Link Modeling and Performance Evaluation

Performance Comparison of Routing Protocols for Vital Data Monitoring from a Large Number of Exercisers

Yang, Yang

A Design and Implementation of an Ambulatory Electrocardiogram (ECG) Acquisition Circuit for Emergency Application

PDMS-Embedded Conductive Fabric: A Simple Solution for Fabricating PDMS-Based Wearable Antennas with Robust Performance

Safety Consideration for Emerging Wireless Technologies - Evaluations of Temperature Rise in Eyes for RF Radiations Up to 10GHz

Ye, Hangyang

PPG Based Respiration Signal Estimation Using VMD-PCA

Yomo, Hiroyuki

A Network Simulator to Develop Wireless Networking Protocols Suited for Vital Information Collection from a Group of Exercisers

Applying Multi-channel Flooding to Vital Data Monitoring of a Large Number of Exercisers: Mobility and Link Modeling and Performance Evaluation

Performance Comparison of Routing Protocols for Vital Data Monitoring from a Large Number of Exercisers

Zeng, Jie

A Channel Estimation Method Based on the Improved LMS Algorithm for MIMO-OFDM Systems

A Low Complexity SCMA Detector Based on Avoiding Redundant Iterations

A New Optimal Relay Selection Strategy for the Coincident Multi-user Access

Method of CS-IC Detection in Grant-Free NOMA System

Resource Allocation in Multi-user NOMA Wireless Systems

Resource Allocation in PDMA with Wireless Information and Power Transmission

Zgoul, Moudar

A Study on the Effect of Sports on Academic Stress Using Wearable Galvanic Skin Response

Zhang, Edmond

Deep Holistic Representation Learning from EHR

Zhang, Hongyun

Autocorrelation Based Transmission Power Control in WBANs

Zhang, ZhenFeng

A Channel Estimation Method Based on the Improved LMS Algorithm for MIMO-OFDM Systems

Zhu, Jin

PPG Based Respiration Signal Estimation Using VMD-PCA

Zhu, Xi

Safety Consideration for Emerging Wireless Technologies - Evaluations of Temperature Rise in Eyes for RF Radiations Up to 10GHz

Sponsors

Sponsors



Technically Sponsors

